Final Task Report

Determining Bearing Resistance of Cantilever Sheet Piles

FDOT Contract No: BDV31 977-90
UF Project No: AWD03567

Submitted to:
Juan Castellanos
Project Manager
Florida Department of Transportation

Principal Investigator:
Xiaoyu Song, Ph.D.

Research Assistant:
Amirata Taghavi, Ph.D.
Shashank Menon, Ph.D.
Kaiqi Wang, Ph.D.
Zhe Zhang

04/19/2022

University of Florida
Department of Civil and Coastal Engineering

Technical Report Documentation Page

1. Report No.	2. Government Accession No.	3. Recipient's Catalog No.
4. Title and Subtitle Determining Bearing Resistance of Cantilever Sheet Piles		5. Report Date April 19, 2022
		6. Performing Organization Code
7. Author(s) Xiaoyu Song, Amirata Taghavi, Shashank Menon, Kaiqi Wang, Zhe Zhang		8. Performing Organization Report No. AWD03567
9. Performing Organization Name and Address Department of Civil and Coastal Engineering, University of Florida, Gainesville FL- 32611		10. Work Unit No. (TRAIS)
		11. Contract or Grant No. BDV31 977-90
12. Sponsoring Agency Name and Address FDOT Research Center Phone: (850) 414-5260 605 Suwannee Street Tallahassee, Florida 32399-0450 Email: research.center@dot.state.fl.us		13. Type of Report and Period Covered Final Report: Apr 2018 – Apr 2022
		14. Sponsoring Agency Code
15. Supplementary Notes		

16. Abstract

Sheet pile walls are structures that FDOT has only used for permanent and temporary lateral support. The Department has not allowed these elements to be used as vertical load bearing elements because of the inability to confirm bearing resistance during construction. Current FDOT practice requires discrete deep foundation (piles or drilled shafts) for bearing purposes, which may or may not be combined with permanent sheet piles for lateral retaining purposes. Some designers have previously considered using sheet piles to support both vertical bridge loads and lateral earth loads; however, the concept has not survived final design due to the inability to confirm the capacity of these elements in the field and accept them as bearing piles. For end bents of small bridges, there is a potential for realizing savings if we can verify the axial resistance of the sheet piling and eliminate the need for separate deep foundations. This would relieve the complications that arise in construction when driving piles and sheet piles in close proximity.

17. Key Word	18. Distribution Statement
Sheet pile wall, centrifuge, bearing capacity, finite elements, design equations	No Restriction

19. Security Classif. (of this report)	20. Security Classif. (of this page)	21. No. of Pages	22. Price
Unclassified	Unclassified	300	

Form DOT F 1700.7 (8-72) Reproduction of completed page authorized

Disclaimer

This research is funded by Florida Department of Transportation. The opinions, findings, and conclusions expressed in this publication are those of the authors and not necessarily those of the Florida Department of Transportation.

Acknowledgements

The authors would like to thank the Florida Department of Transportation (FDOT) for providing the funding that made this project possible.

Executive Summary

Sheet pile walls are structures that FDOT has only used for permanent and temporary lateral support. The Department has not allowed these elements to be used as vertical load bearing elements because of the inability to confirm bearing resistance during construction. Current FDOT practice requires discrete deep foundation (piles or drilled shafts) for bearing purposes, which may or may not be combined with permanent sheet piles for lateral retaining purposes. Some designers have previously considered using sheet piles to support both vertical bridge loads and lateral earth loads; however, the concept has not survived final design due to the inability to confirm the capacity of these elements in the field and accept them as bearing piles. For end bents of small bridges, there is a potential for realizing savings if we can verify the axial resistance of the sheet piling and eliminate the need for separate deep foundations. This would relieve the complications that arise in construction when driving piles and sheet piles in close proximity (RFRP-17/18-002).

The objectives of this project are to (1) quantify the bearing capacity of permanent steel sheet pile walls and evaluate both the skin friction and end bearing components; (2) develop practical recommendations for designers to estimate the bearing capacity of steel sheet pile walls; and (3) develop practical methods to determine and verify the bearing capacity in the field. These objectives will be achieved through collecting and reviewing existing literature and documents dealing with steel sheet piles used as axial load bearing elements (Chapter 1), developing a numerical model to simulate the bearing capacity mechanism of steel sheet piles (Chapter 2), designing and developing centrifuge tests to represent the problem at hand, to help calibrate and validate the numerical model, and to compare with the theoretical models (Chapter 3), and develop and propose field load test procedures (Chapter 4). Chapter 5 will summarize the findings and close out the project.

In summary, upon the completion of the project, we aim to recommend detailed methods for determining axial load capacity of sheet piles considering both the side friction and end bearing resistance under a variety of site conditions, structural properties, and loading regimes. A detailed practical design method with several examples for axially loaded sheet pile foundations will be established. Moreover, a practical protocol will be developed to conduct static and quasi-static axial load tests on cantilever sheet piles and determine the bearing capacity in the field.

TABLE OF CONTENTS

LIST OF FIGURES:

LIST OF TABLES

CHAPTER 1: LITERATURE REVIEW AND INFORMATION COLLECTION

1.1 Background

Sheet pile walls are structures that FDOT has only used for permanent and temporary lateral support. The Department has not allowed these elements to be used as vertical load bearing elements because of the inability to confirm bearing resistance during construction. Current FDOT practice requires discrete deep foundation (piles or drilled shafts) for bearing purposes, which may or may not be combined with permanent sheet piles for lateral retaining purposes. Some designers have previously considered using sheet piles to support both vertical bridge loads and lateral earth loads; however, the concept has not survived final design due to the inability to confirm the capacity of these elements in the field and accept them as bearing piles. For end bents of small bridges, there is a potential for realizing savings if we can verify the axial resistance of the sheet piling and eliminate the need for separate deep foundations. This would relieve the complications that arise in construction when driving piles and sheet piles in close proximity (RFRP-17/18-002).

The objectives of this project are to (1) quantify the bearing capacity of permanent steel sheet pile walls and evaluate both the skin friction and end bearing components; (2) develop practical recommendations for designers to estimate the bearing capacity of steel sheet pile walls; and (3) develop practical methods to determine and verify the bearing capacity in the field. These objectives will be achieved through collecting and reviewing existing literature and documents dealing with steel sheet piles used as axial load bearing elements (task 1), developing a numerical model to simulate the bearing capacity mechanism of steel sheet piles (task 2), designing and developing centrifuge tests to represent the problem at hand, to help calibrate and validate the numerical model, and to compare with the theoretical models (task 3), and develop and propose field load test procedures (task 4). Task 5 will include drafting the final report and setting up the closeout teleconference. The final report will be prepared through task 6. The following section describes task 1.

In this task, we have collected and reviewed existing literature and documents dealing with steel sheet piles used as axial load bearing elements. This includes reviewing design methods, numerical methods, small-scale lab models, and field load testing procedures that have been attempted or performed by others to study the axial load behavior of sheet piles and evaluate their bearing resistance. The review identifies what current theoretical methods will be used to compare with the results of the small-scale lab testing and numerical modeling (tasks 2 and 3).

1.2 Review of design methods

After obtaining information about geotechnical site conditions through subsurface investigations and laboratory tests, the type of sheet pile section for a cantilever sheet pile foundation should be determined. For the cases where bending could control the design, Z-shaped profiles are usually used. After finalizing the type of cross section, the design of all elements of the bridge structure shall be performed according to AASHTO (2014) LRFD bridge design specification. Although analyses and design methods are developed for pile foundations, there are not such well-defined methods to analyze sheet piles under combined axial and lateral loads. Different research, therefore, has used AASHTO (2014) to design axially loaded sheet piles (ASTM D1143/D1143M, 2013; Evans, White, & Klaiber, 2012; Underwood & Greenlee, 2010). A review of the current practice reveals that the sheet pile walls are designed separately for axial and lateral loading (Chung, Yoo, Oh, & Kim, 2004; Evans et al., 2012; Yandzio, 1998). According to AASHTO (2014), nominal pile bearing resistance can be verified in the field during pile installation using a variety of methods including static load tests.

1.2.1 Static load test

The load test needs to follow the procedures specified in ASTM D1143/D1143M (2013). Unless specified otherwise by the engineer, according to AASHTO (2014), the nominal bearing resistance will be determined from the test data utilizing the Davisson Method (Davisson, 1972) for piles with a diameter of 24 in or less. For piles greater than 36 in, the following equation should be used as the Davisson method usually under-predicts the bearing resistance for these cases:

$$s_f = \frac{QL}{12AE} + \frac{B}{2.5}$$

where Q = test load; L = pile length; A = pile cross-sectional area; E = pile modulus; and B = pile diameter (length of side for square piles). A linear interpolation between the results obtained by the aforementioned two methods should be performed to obtain the bearing resistance for piles having a diameter less than 36 in but greater than 24 in. The presented procedure(s) to determine the nominal bearing resistance of piles shall be modified to account for sheet pile-specific and site-specific conditions when dealing with sheet piles.

1.2.2 Analyses and design for axial loading

In order to obtain the ultimate bearing capacity of sheet piles under axial loading, they can be considered as driven piles (Chung et al., 2004; Evans et al., 2012; Yandzio, 1998). According to AASHTO (2014) the following equation defines the bearing capacity of driven piles:

$$R_R = \emptyset R_n = \emptyset_{stat} R_p + \emptyset_{stat} R_s$$

in which:

$$R_p = q_p A_p$$

$$R_s = q_s A_s$$

where $\emptyset_{stat}$ = resistance factor for the bearing resistance of a single pile (obtained from FDOT SDG Table 3.1 for driven piles or AASHTO (2014) Article 10.5.5.2.3); R_p= pile tip resistance; R_s = pile side resistance; q_p = unit tip resistance of pile; q_s = unit side resistance of pile; A_s = surface area of pile side; and A_p = area of pile tip.

1.2.2.1 Nominal bearing capacity according to FDOT guidelines

In order to estimate the nominal static axial capacity of driven piles, two types of analyses based on SPT and CPT shall be used. SPT methodology is based on empirical correlations between cone penetrometer tests and standard penetration tests for typical Florida soils. Unit end bearing resistance and unit skin friction resistance versus SPT-N values are given in the FDOT research bulletin No. 121-A (Schmertmann, 1967) and 121-B (Nottingham & Renfro, 1972), for the different soil types. To safeguard against punching failure in obtaining the end bearing capacity, the methods shall account for soils 3.5B (B is pile width) below and 8.0B above the pile tip. In obtaining the ultimate side friction, a weighted average technique to establish the ultimate unit skin friction in each layer shall be used accounting for soil layers above the bearing layer and in the bearing layer. Corrections for critical depth/pile width ratio shall be applied for both end bearing and skin friction.

Driven pile capacity calculated using CPT data can be determined by three separate methods. The first method is the Schmertmann method proposed by Schmertmann (1978). The second method is the University of Florida method proposed by Bloomquist, McVay, and Hu for FDOT in 2007 (Bloomquist, McVay, & Hu, 2007).The third method is the LCPC method proposed by Bustamante and Gianeselli for the French Highway Department in 1982 (M.G. Bustamante & Gianeselli, 1982).

1.2.3 Analyses and design for lateral earth pressure

Walls capable of moving away from the soil mass behind them, should be designed for the earth pressures between the rest and active conditions. The amount of this movement to mobilize active or passive lateral earth pressures on the wall depends on the soil type and wall height and is provided in AASHTO (2014), Table C3.11.1-1. There are several theoretical methods to predict the lateral earth loads on the walls such as Rankin, Coulomb, and Log-Spiral (Bowles, 1996). Predictions of Coulomb and log-spiral methods have been proven more accurate as they consider the wall-soil friction. ASCE (1996) suggests using Coulomb's theory to design sheet pile walls. However, as suggested by United States Steel (1984), in case Coulomb's theory is used, an appropriate safety factor should be applied as this theory overestimates passive loads. Another option would be using the logarithmic spiral method. Lateral effective earth pressure is proportional to vertical effective pressure (due to soil weight, pore water pressure, and surcharge loading) by an earth pressure coefficient, K:

$$K = \frac{\sigma'_h}{\sigma'_v}$$

For the active (minimum) limit-state, the pressure is given by:

$$P_a = \gamma z K_a - 2c\sqrt{K_a}$$

and the passive (maximum) limit-state is given by:

$$P_p = \gamma z K_p + 2c\sqrt{K_p}$$

Coulomb theory determines K_a and K_p (active and passive pressure coefficients) as:

$$K_a = \frac{cos^2(\phi-\theta)}{cos^2\,\theta\cos(\theta+\delta)\left[1+\sqrt{\frac{\sin(\theta+\delta)\sin(\phi-\beta)}{\cos(\delta+\phi)\cos(\beta-\phi)}}\right]^2}$$

$$K_p = \frac{cos^2(\phi-\theta)}{cos^2\,\theta\cos(\theta+\delta)\left[1-\sqrt{\frac{\sin(\phi+\delta)\sin(\phi-\beta)}{\cos(\delta+\phi)\cos(\beta-\phi)}}\right]^2}$$

where:

σ'_h = lateral effective earth pressure

σ'_v = vertical effective earth pressure

γ = unit weight of homogeneous soil

ϕ = angle of internal soil friction

c = cohesive strength of the soil

δ = angle of wall friction

θ = angle between the wall and the failure plane

z = depth below the ground surface

β = slope of the soil surface

A review of failure mechanism of laterally loaded sheet piles is provided in the following section.

1.2.3.1 Failure mechanism of sheet pile walls under lateral earth pressure

For analyzing sheet piles as retaining structures, U.S. Army Corps of Engineers (1994) presented different failure modes for steel sheet pile systems: deep-seated failure, rotational failure due to inadequate sheet pile penetration, overstressing of the sheet pile, and anchorage failure (Figure 1). Deep-seated failure occurs when the entire soil mass containing the retaining wall system rotates along a single failure surface. In this failure type, soil failure is independent of the structural capacity of the wall and the anchorage system. The second failure type occurs when the retaining wall rotates due to the excessive lateral earth pressure. This type of failure can be prevented by either increasing the wall penetration into the soil, or by implementing an anchorage system. Overstressing of the sheet pile due to both lateral and axial loads will result in the development of

plastic hinge(s) leading to a structural failure. A passive anchorage failure occurs when the anchor moves laterally within the soil due to the force exerted on it. The tie rod may fail if it does not have the required tensile capacity.

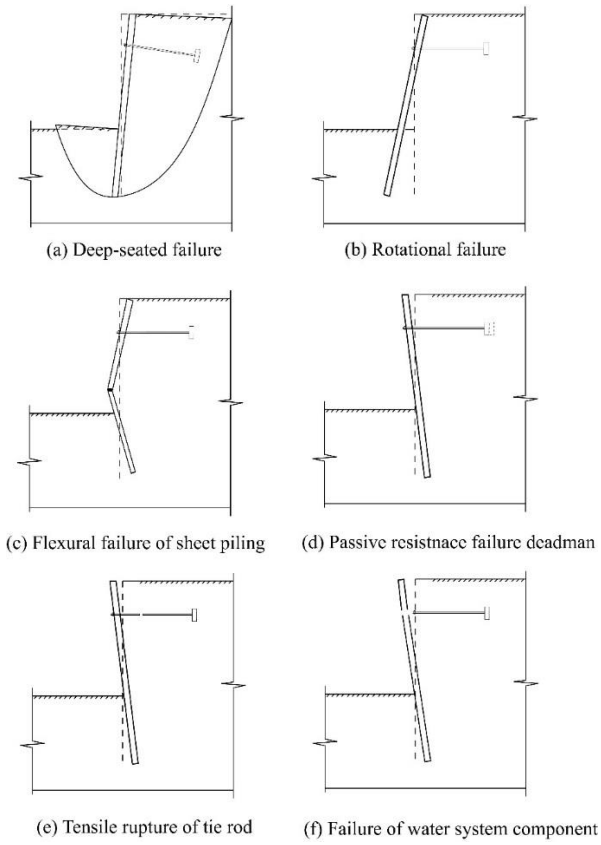

Figure 0-1. Failure types of laterally loaded sheet pile retaining walls (U.S. Army Corps of Engineers, 1994)

1.2.4 Surcharge loads

Surcharge loads can affect the amount and distribution of the lateral earth pressure on the wall. Different types of surcharge loads including uniform, strip, line, ramp, triangular, area, and point loads can be considered. The contribution of the different types of nonuniform surcharge loads on the lateral earth pressure are calculated mostly based on the theory of elasticity and are provided in AASHTO (2014) Section 3.11.6 and other references (Bowles, 1996; Peck, Hanson, & Thornburn, 1974).

For a uniformly loaded strip (parallel to the wall) applying pressure, p (psf), the lateral pressure, ΔP_H (ksf), is given by Equation:

$$\Delta P_H = \frac{2p}{\pi}[\alpha - sin\alpha cos(\alpha + 2\delta)]$$

For a point load, P (kip), the lateral pressure is given by Equation:

$$\Delta P_H = \frac{p}{\pi R^2}\left[\frac{3ZX^2}{R^3} - \frac{R(1-2v)}{R+Z}\right]$$

For an infinitely long line load, Q (k/ft), parallel to the wall, the lateral pressure is given by Equation:

$$\Delta P_H = \frac{4Q}{\pi}\frac{X^2 Z}{R^4}$$

For a finite line load, Q (k/ft), perpendicular to the wall, the lateral pressure is given by Equation:

$$\Delta P_H = \frac{Q}{\pi Z}\left(\frac{1}{A^3} - \frac{1-2v}{A+\frac{Z}{x_2}} - \frac{1}{B^3} + \frac{1-2v}{A+\frac{Z}{x_1}}\right)$$

in which:

$A = \sqrt{1+\left(\frac{z}{x_2}\right)^2}$ and $B = \sqrt{1+\left(\frac{z}{x_1}\right)^2}$.

1.2.5 Structural design using LRFD methods

For structural design of steel sheet piles under *combined* axial and lateral loading, based on AASHTO (2014), the axial compressive load, P_u, and concurrent moments, M_{ux} and M_{uy}, calculated for the factored loadings by elastic analytical procedures shall satisfy the following relationship:

$$If\ \frac{P_u}{P_r} < 0.2, \qquad then \quad \frac{P_u}{2.0\ P_r} + \left(\frac{M_{ux}+M_{uy}}{M_{rx}+M_{ry}}\right) \le 1.0$$

$$If\ \frac{P_u}{P_r} \ge 0.2, \qquad then \quad \frac{P_u}{P_r} + \frac{8.0}{9.0}\left(\frac{M_{ux}+M_{uy}}{M_{rx}+M_{ry}}\right) \le 1.0$$

where P_r = factored compressive resistance (specified in Article 6.9.2.1 (AASHTO, 2014)); M_{rx} = factored flexural resistance about the *x*-axis (specified in Article 6.10, 6.11 or 6.12 (AASHTO, 2014)); M_{ry} = factored flexural resistance about the *y*-axis (specified in Article 6.12 (AASHTO, 2014)); M_{ux} = factored flexural moment about the *x*-axis; M_{uy} = factored flexural moment about the *y*-axis; and φ_f = resistance factor for flexure (specified in Article 6.5.4.2 (AASHTO, 2014)).

AASHTO (2014) Section 3.4 should be used in calculating appropriate load factors and combinations so that all loads used in the above equations are the maximum loads, including second order effects.

1.2.5.1 Limiting slenderness ratio

There are analytical solutions available in the literature to determine the buckling behavior of embedded deep foundations, but the methods are quite complex. A method is provided by Bowles (1996) which is easier to use and implement. Assuming that the pile is not supported laterally by the soil, a simplistic calculation can be also performed. AASHTO (2014) Section 3.4 requires that all primary compression members satisfy the slenderness requirements given below:

$$\frac{K\ell}{r} \leq 120$$

where K = effective length factor (specified in Article 4.6.2.5 (AASHTO, 2014)); ℓ = unbraced length ; r = radius of gyration.

1.2.6 Remarks on design methods

After performing site investigations and analyzing geotechnical site conditions, the limit equilibrium methods can be used to investigate the overall stability of the sheet piles under different failure mechanisms. Once performed, the section type and size of sheet pile would be selected. Three criteria should be satisfied when choosing the section size for sheet piles: First, the minimum size for successful pile driving (drivability criteria) and maximum driving length should be considered. Second, the full structural capacity of the sheet pile wall should be taken into account. Finally, both corroded and non-corroded part properties should be determined.

Next, superstructure imposed vertical loads should be determined and stability and capacity requirements should be satisfied. As such, an easiest solution to increase the capacity and satisfy the stability might be increasing the penetration depth. Sheet pile internal forces can be determined using two methods: First, the limit equilibrium method can be used to determine bending moments and forces induced by lateral loading. Second, soil-structure interaction-based analysis and methods can be used to calculate the forces acting on the pile due to lateral loading. The last step is determining whether the section size is adequate. The design work is completed if the sheet pile section size is adequate. Otherwise, the loop should be repeated from checking the stability and vertical load capacity requirement after modifying section size.

1.3 Review of numerical methods

1.3.1 Purpose of numerical modeling

In geotechnical engineering applications, many retaining structures are particularly used for protecting excavations and structures near underground water area. These retaining structures include sheet walls used as temporary retaining structures, and pile walls used as permanent retaining structures. Many studies have also investigated how piles behave to support offshore structures under pure lateral loads and inclined loads. However, the investigation of the behavior of such side supporting systems under axial load cannot be thoroughly investigated.

It is extremely difficult to determine the behavior of a large-scale problem in the laboratory (i.e., the vertical settlement or subsidence of the soil behind the steel sheet piled wall at different

distances from the piled wall edge). However, finite element method is one of the most powerful approximate solution methods that can be applied to solve the soil vertical deformation for the model test at different distances from the piled wall edge.

Thus, this review focus on reviewing the papers which are using numerical modeling to determine bearing capability of steel sheet piles under different conditions (i.e., soil type, steel pile type, and combined loading).

1.3.2 Different numerical modeling

The common types of side-supporting systems include gravity, cantilever, or embedded walls; sheet pile walls and diaphragm walls. Previous studies on the behavior of such schemes provided useful information for the numerical modeling. An investigation about cantilever sheet pile wall penetrating sand in the absence of a water table using the finite difference method software, FLAC was sated by Smith (2006) and Shiau and Smith (2013). The results obtained from the numerical model (Figure 2) developed in FLAC were compared to the analytical solutions to discuss the advantages and disadvantages. The depth of embedment was varied to identify the effect exerted on the sheet pile wall by analyzing the bending moment, wall deflection, and ground settlement. This investigation demonstrated that FLAC produced similar results to the limit equilibrium methods. The outputs obtained were also found to be more accurate when compared to the limit equilibrium method solutions. However, according to Amer (2013), important serviceability considerations are not considered when using the limit equilibrium methods. This is because information about the wall deformation could not be obtained by this analytical method. Amer (2013) investigated sheet pile walls behavior by varying the soil conditions for both the cantilever and anchored sheet pile walls. Finite element analysis was then used to perform numerical modeling to analyze the behavior of the walls and the structural response. It was found that wall deformations reduced with increasing wall penetration depth for both wall types and the bending moments significantly reduced with increasing wall penetration depth.

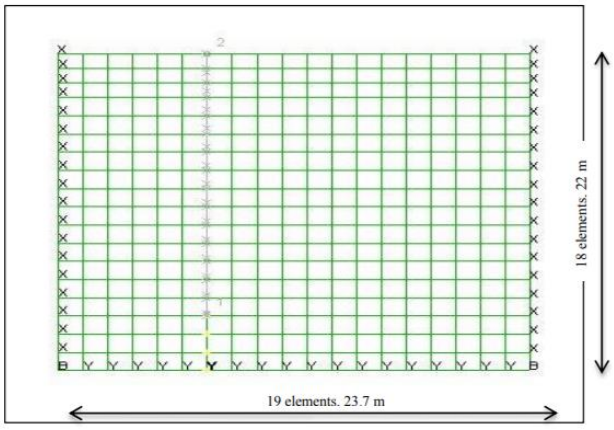

Figure 0-2. Sheet Pile Wall Model (Shiau & Smith, 2013)

For seismic stability, the side supporting system was found to be stable when using the SSI method after analyzing the results of sheet pile wall subjected to earthquake load. The results were obtained from three different engineering approaches: the limit equilibrium methods, the p-y method and the time history soil structure (SSI) analysis method (Zhai, 2009).

However, above publications present an analytical study of cantilever sheet pile walls under lateral loading by using the finite-element approach. FDOT Project considers the problem of using the piled retaining wall as a permanent part of the foundation and studied how to transfer its load safely to the foundation without changing its location. The following part focus on studying the bearing capacity of steel sheet pile since the above structure load.

Several different numerical modeling methods for analysis and design of steel piles near foundations have also been described. The study about the screw piles in sand were modeled using three-dimensional finite element analysis based on the assumption of symmetry about the vertical plane under combined lateral and vertical load by (Al-Baghdadi, Brown, Knappett, & Al-Defae, 2017). The useful information about the numerical modeling as below. The top boundary was free to move in all directions whereas the bottom boundary was fully fixed and the vertical side boundaries were allowed only vertical deformation. The pile-soil interfaces were modeled using twelve nodes interface elements with a Mohr–Coulomb model compatible with the six nodes triangular sides of both the plate and soil elements. The interface elements had zero thickness as each node pair was identical and had the same coordinates. In order to obtain accurate results, the mesh was divided into different zones to allow localized mesh refinement close to the pile and reduce the element size gradually near the screw pile geometry. After that, two types of pile loading regime were applied. One is simulations were undertaken under purely axial and lateral loading to study the influence of combined loading on ultimate vertical pile capacity, another is piles subjected to pure lateral loading to determine the ultimate lateral pile capacity. For both pile types the lateral performance degraded under short-pile or long-pile modes. However, the influence of the vertical tension load on the lateral capacity was more significant in short piles than in long piles.

Another three-dimensional finite element analysis (Figure 0-3) presented by Karthigeyan, Ramakrishna, and Rajagopal (2006) showed that the significant influence of vertical loads on a pile's lateral response which was performed in sandy soils. The information about this article is given below: The pile was treated as a linear elastic material. The Von Mises constitutive model with associated flow rule for clayey soils and the Drucker-Prager constitutive model with non-associated flow rule for sandy soils were used to predict the stress-strain behavior. Based on the symmetry, only half the pile section in the direction of lateral load is analyzed. The 20-node brick elements are used to mesh the pile and the soil continuum. The interface between the pile and the soil has been modeled using 16-node joint elements of zero thickness. The same finite element analysis conducted by Karthigeyan, Ramakrishna, and Rajagopal (2007) presented that the influence of interaction between the vertical and lateral loads on steel pile in both homogeneous clayey soils and homogeneous sandy soils. Both articles show through a series of 3D FE analysis of piles that the presence of vertical loads increases the lateral load capacity of piles in sandy soil and decreases it in clayey soil. Hussien, Tobita, Iai, and Rollins (2012), using simplified soil-pile interaction FE models (Figure 0-4), reported slight increase in the lateral capacity of free-head

piles installed in sandy soil due to the presence of vertical loads and attributed this increase to the increase in the confining pressures in the sand deposit surrounding the upper part of the pile.

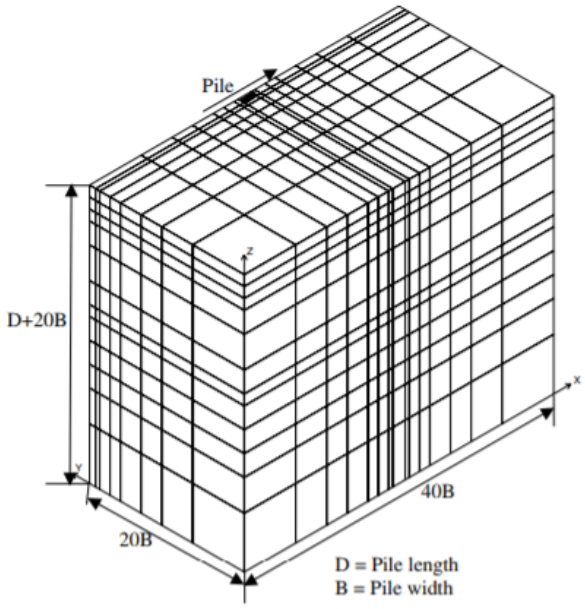

Figure 0-3. Typical mesh for three-dimensional finite element analyses (Karthigeyan et al., 2006)

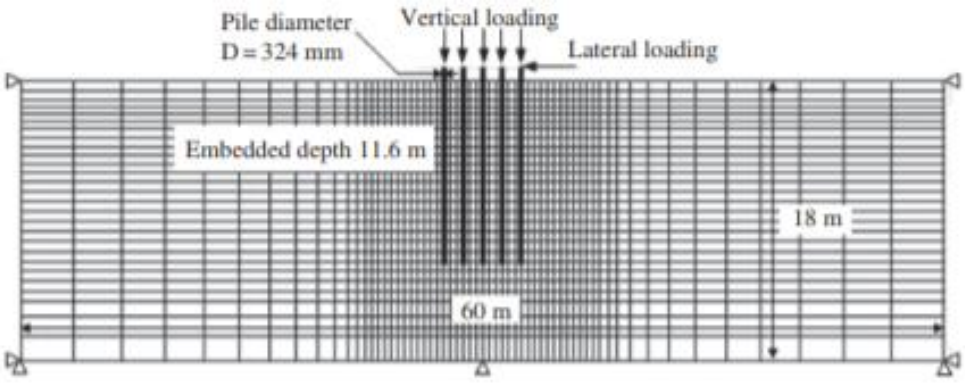

Figure 0-4. General layout and meshing of the finite element model (Hussien et al., 2012)

However, the scopes of the previous attempts examining problems using three-dimensional finite element models have been limited to the behavior of piles installed in homogeneous sandy or clayey soils. The mechanisms regarding the influence of vertical loads on the lateral response of pile foundations in inhomogeneous soils may be quite different from those of piles in ideal homogeneous situations. Hazzar, Hussien, and Karray (2017) presented and discussed the results of a series of three-dimensional finite difference analysis (Figure 0-5) carried out using FLAC 3D in order to evaluate the influences of vertical loads on the lateral response as well as internal forces of piles installed in four idealized sandy and clayey soil profiles, i.e. a homogeneous sandy layer,

a clayey layer with constant undrained shear strength, a clayey layer with undrained shear strength proportional to depth, and two-layered strata. The results of the lateral capacities and the bending moments of piles were determined and compared for piles subjected to pure lateral loads and to combined vertical and lateral loads for several values of vertical loads corresponding to 25%, 50%, 75% and 100% of the pile ultimate vertical capacity. It can be concluded that the lateral load capacity of piles under lateral load is not influenced by the presence of vertical load in loose, dense or very dense sandy soil. However, the presence of vertical loads decreases the lateral load capacity by as much as 20% and the maximum bending moment by as much as 30% of piles in clayey soil depending on the level of vertical load and the value of the lateral deflection. Considering the multi-layers, the effect of vertical loads on the lateral capacity of a pile embedded in two-layered strata with a clay layer thickness (H) ranging from 2B to 10B is not significant and almost similar to that observed in the sandy soil. When the clay thickness increases, the effect of vertical loads becomes pronounced and leads to a significant reduction in the lateral capacity of the pile. The dependence of vertical load effect on the characteristics of the soil layer under the pile tip may be attributed to the difference in pile function in terms of load transfer.

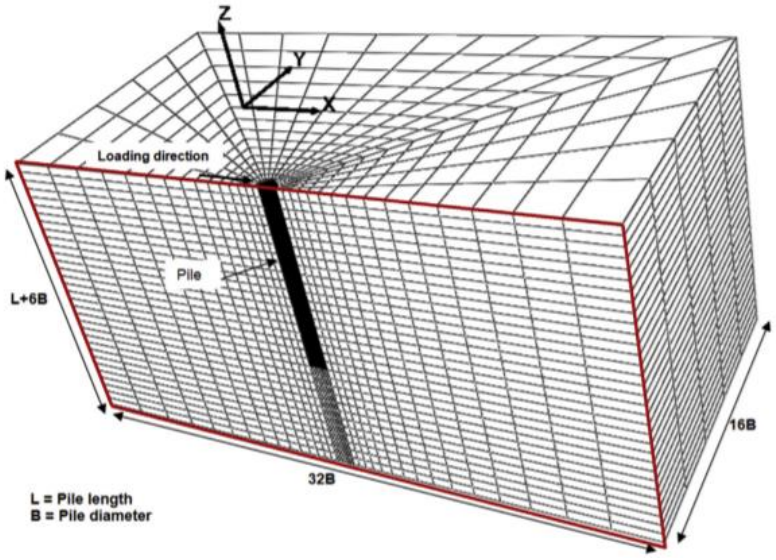

Figure 0-5. The general layout and meshing of the FD half model used for the analysis of the soil-pile system (Hazzar et al., 2017).

The study provided by Azzam and Elwakil (2017), the numerical simulations about the piled retaining wall under axial load were carried out using a plane strain, two-dimensional finite element program (Figure 0-6). The shear stress parameters were used to define the failure behavior of sand. The sand was modeled using the elastoplastic Mohr-Coulomb model. The five essential parameters of the Mohr-Coulomb model can be determined from basic tests on soil samples. The interface element for the interaction between the soil and piled wall element was used for all embedment piled wall depth. An elastoplastic model was used to describe the behavior of interfaces for modeling the soil structure interaction. The influence of different penetration depth of piles and different surcharge loading for different densities sand were studied. The simulation results indicate that increasing the normalized penetration depth increased the maximum bending

moment along the axially loaded-piled wall under the value of penetration depth ratio below the 1.67. At the same time, the relative density of the sand had a major influence on the maximum bending moment along the piled wall. Increasing the shear angle increased the maximum bending moment along the piled wall as a result of the significant increase in the ultimate capacity of the piled system. It also can be concluded that the lower sand relative density, the lower increasing in the maximum bending moment under different surcharge intensities. A summary of the results for the piled wall prototype at different sand densities and penetration depths is shown in Table 2. As a result of the remarkable increase in the lateral top deformation of the piled system, a progressive failure rapidly occurred when the piled wall was vertically loaded; as a result, the ultimate axial capacity of the piled wall steadily decreased (Figure 0-7).

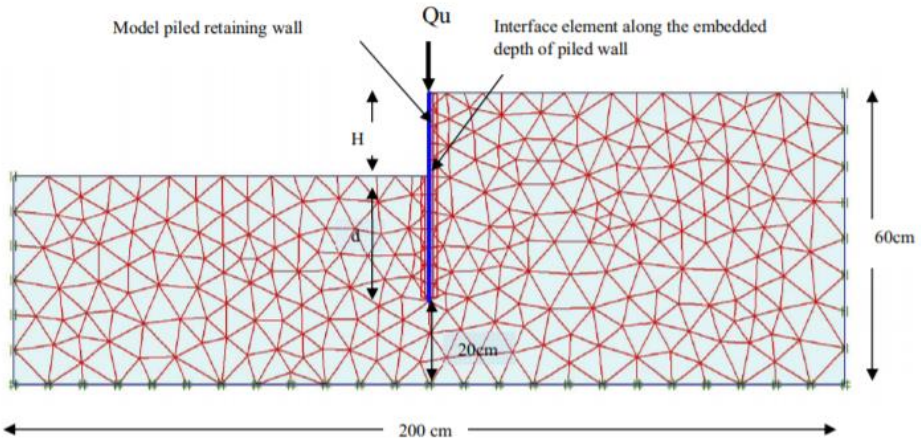

Figure 0-6. Geometry, generated mesh, and boundary conditions of sheet pile model (Azzam & Elwakil, 2017)

Table 0-1. Summary of the FE Results of Large-Scale Piled Wall in Test Series (Azzam & Elwakil, 2017)

	$\phi = 41$			$\phi = 35$			$\phi = 24$		
Observed parameter for series of $L/Dp = 21$	$d/h = 3$	$d/h = 1.67$	$d/h = 1$	$d/h = 3$	$d/h = 1.67$	$d/h = 1$	$d/h = 3$	$d/h = 1.67$	$d/h = 1$
Qu (kN·m)	225	190	154	124	93	56	84	45	32
δ_{Hmax} (mm)	0.74	0.87	0.99	1.06	1.45	1.29	1.12	1.67	1.87
S_{vmax} (mm)	1.3	1.39	1.48	1.39	1.47	1.67	1.5	1.83	2.21
Maximum bending moment (kN·m/m)	11.3	10.5	9.98	9	8.2	7.87	8.4	6.7	5.35

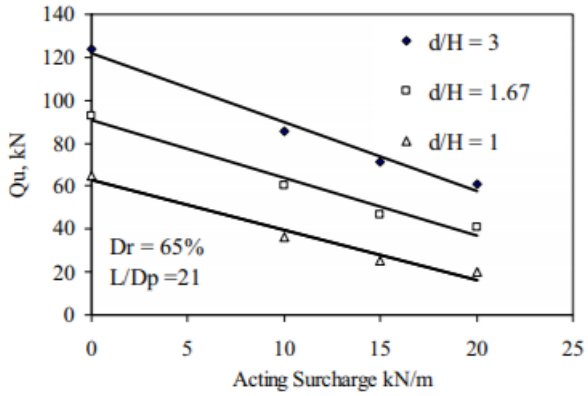

Figure 0-7. Variation of the surcharge intensity of piled wall prototype with ultimate axial capacity (Azzam & Elwakil, 2017)

1.3.3 Remarks on numerical modeling

After reviewing the numerical modeling about bearing capacity of pile under vertical and lateral load, we can recapitulate the conclusion and consider the several aspects of numerical modeling in the next step study as follows. Above numerical simulations indicate that increasing the penetration depth increase the maximum bending moment along the axially loaded-piled wall in sandy soil under single pile and sheet pile conditions. Second, the relative density of the sand has a major influence on the maximum bending moment along the piled wall but has no influence on the lateral load capacity of piles. It also can be concluded that the lower sand relative density, the lower increasing in the maximum bending moment under different surcharge intensities. Though the numerical simulations about the steel sheet pile wall under axial load were carried out using a plane strain, two-dimensional finite element program, there are still many factors should be considered. Since the results of piles in clayey soil from Hazzar et al. (2017), the bearing capacity of steel sheet pile under axial load should be simulated under the different type soil and multi-layer conditions. In addition, the three-dimensional simulation should be conducted for sheet pile wall to study the real engineering problems.

1.4 Physical modeling of sheet pile bridge abutment systems: literature review

Experimental study of the axially loaded sheet piles can be done by conducting full-scale field tests and model-scale lab tests. Field tests have the advantage of closely modeling the in-situ conditions. The main drawback of these tests is that they are expensive and might be time consuming.

1.4.1 Full-scale field testing

A few full-scale top-down axial load tests have been performed on sheet pile foundations. M.G. Bustamante and Gianeselli (1991) conducted a series of static full-scale static load tests on sheet pile walls in dense sand and in plastic clay. To do the load tests, successive loads maintained for 15 to 60 minutes, with no unloading between load levels. They illustrated that sheet piles could carry large axial loads and suggested that they can be used as foundations. At the same embedment

length, the ultimate load reached by the wall element (Figure 0-8a) made of four sheet piles was about 210% of that of the open box-pile (Figure 0-8b) and 120% of that of the closed-end box-pile in sand. In stiff clay, depending on the clay stiffness, the ultimate load carried by the sheet pile wall was about 280 to 230% of that of the closed box pile. It should be noted that, the enclosed cross-sectional area of the wall element (consisted of two sheet piles) were almost the same as that for the box-pile. Therefore, for a two-sheet pile wall element only, these figures should be divided by two.

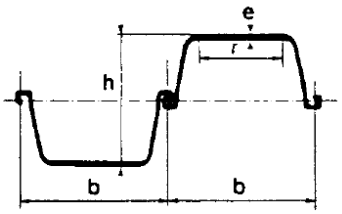

Sheet pile type	B	H	E	R	Perimeter	Weight	Sa
		(mm)			(cm/ml)	(kg/m)	(cm^2/m)
IIs	500	340	12.3	280	282	139	177
IIn	400	270	9.5	250	293	122	156

a. Sheet pile wall element

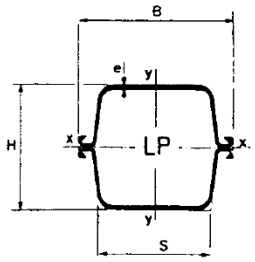

Sheet type	B	H	E	S	Perimeter	Weight	Sa
		(mm)			(cm)	(kg/m)	(cm^2)
Box pile LPIIs	533	385	12.3	342	164	139	177

b. Box-pile

Figure 0-8. Section and characteristics of the sheet pile element and the box-pile (M.G. Bustamante & Gianeselli, 1991)

Width of each pile	600.0 mm
Embedment	GL-11.2 m
Sectional area	207.8 cm^2/Double
Perimeter	3790 mm/Double
Plug area	unknown

a. Sheet pile wall element

Width of each pile	600.0 mm
Embedment	GL-11.2 m
Sectional area	207.8 cm^2/Box
Perimeter	1895 mm/Box
Plug area	1798.0 cm^2/Box

b. Box-pile

Figure 0-9. Section and characteristics of the sheet pile wall element and the box-pile (J. Taenaka et al., 2006)

J. Taenaka, Otani, Tatsuta, and Nishiumi (2006) performed static full-scale axial load tests on sheet piles in sand by increasing the load in stages, which was maintained for 30 minutes, and then unloading and leaving off until the load was zero. The sheet pile was then reloaded to the working load and to the next higher stages, and the test continued to the planned maximum load. The main objective of these tests was to obtain the ultimate load capacity, which was determined from a settlement equal to 10% of a pile diameter. Considering that the tests were performed on sheet piles, pile diameter was substituted with the effective width of each sheet pile (600 mm for their tests). For comparison purposes, a box-pile was also load tested (Figure 0-9).

According to their test results, the ultimate load of the sheet pile was about 167% of that of the box-pile (Figure 0-10). Although the tip resistance of sheet piles are usually ignored in Japan and the U.S., their test results revealed that the end resistance could be high. Plugging contributed to the high tip resistance which was confirmed through X-ray tomography in small-scale tests performed in 1-g. Their load tests revealed that the sheet pile can have much higher capacity than the comparable box pile.

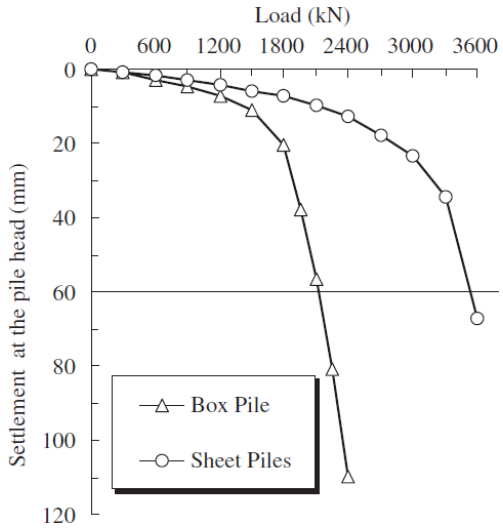

Figure 0-10. Comparison of load-settlement curves of the box-pile and the sheet piles (J. Taenaka et al., 2006)

S. Taenaka et al. (2016a) performed full-scale static axial load tests on sheet piles with closed section (Figure 0-11) at the bottom in a soil profile consisted of altering layers of sand and silt. The closed cross section was used to increase the bearing capacity through plugging. The load tests revealed that increasing the cross-sectional area and length of the closed section at the bottom of sheet pile can increase the bearing resistance and decrease the settlement.

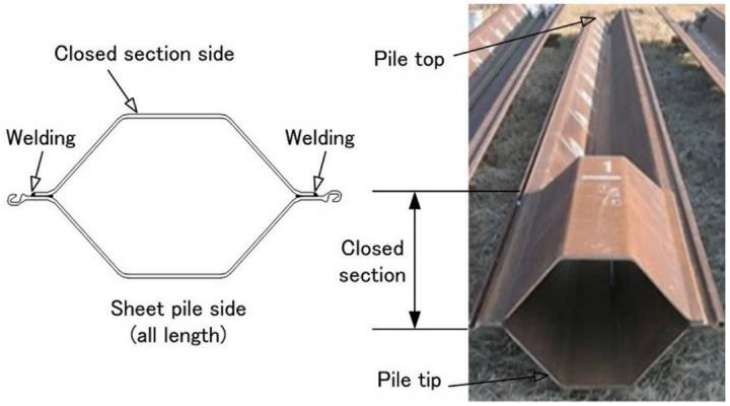

Figure 0-11. Sheet pile with closed section at bottom (S. Taenaka et al., 2016b)

Sylvain et al. (2017) considered using sheet piles for the double function of scour protection and axial load bearing. They conducted axial load tests on a pair of PZ 27 sheet piles as well as a HP 12×53 H-pile (for comparison purposes) in a site located in Matthews, North Carolina. Both the sheet pile and the pile had a total length of 6.1 m. SPT and CPTu soundings revealed that the soil profile consists of generally cohesionless soils including dense gravel with sand fill, medium dense clayey sand, soft to medium stiff silt, loose clayey sand, and medium dense to dense silty sand extending to the final depth investigated of 10.15 m and 14.48 m for two SPT borings. The test sheet pile and pile were first installed to an initial embedment depth of 2.4 m using a vibratory hammer (ICE Model 28C hammer) and then driven to the final embedment depth of 5.2 m using an impact hammer (ICE Model I-12 hammer).

Pile driving analysis (PDA) measurements were obtained on both piles during restrike performed 11 days after driving with the same impact hammer. Static load testing was performed on both the sheet pile and H-pile (see Figure 12) in general accordance with ASTM D1143/D1143M (2013). Testing was performed using the constant rate of penetration (about 0.13 mm/min) as well as the quick load test procedures. Prior to axial load testing, the axial load capacities of both sheet pile and pile were estimated using CPT-based LCPC method (M.G. Bustamante & Gianeselli, 1982) and SPT-based Meyerhof method (Meyerhof, 1976) assuming no plugging will happen at the tip. The axial load capacity estimates and measurements are presented in Table 2. The test results revealed that the axial stiffness and load capacity of the sheet pile was comparable to the response recorded in the comparison H-pile when normalized for differences in the tip and surface areas. However, as the load at the toe was not measured, the skin friction and end bearing contributions remained unknown.

Table 0-2. Predicted and measured capacity (Sylvain et al., 2017)

Test Pile Type	Measured (Axial load test and PDA dynamic measurements)			Predicted (Static methods)	
	Load at 7 mm Displacement (kN)	Failure Load[1] (kN)	Restrike PDA Capacity[2] (kN)	LCPC[3] (kN)	Meyerhof[4] (kN)
Sheet pile	165	158	196	285	157
H-pile	100	101	40	189	76

Notes: ([1]): Reported failure load is based on the Chin-Kondner failure criterion (Chin 1970).
([2]): Axial load capacity estimate based on PDA dynamic measurements during restrike (11 days after installation) and the CASE damping model (damping CRX 7).
([3]): LCPC based on Bustamante and Gianeselli (1982).
([4]): Based on Meyerhof (1976).

a. Photo of the test pile and the reaction frame

b. Photo of the test H-pile prior to static load test

Figure 0-12. Photos of the test setup for the axial load test (Sylvain et al., 2017)

Doubrovsky and Meshcheryakov (2015) conducted press-in full-scale tests (Figure 13a) as well as large-scale laboratory tests (Figure 0-13b) on sheet piles with U profile in different soil conditions. The aim of this research was to study the dependencies between the applied forces and the developed friction in the interlocks by physical modeling and using it to calibrate and verify interlock forces in numerical modeling. The experimental program made it possible to determine the main components of soil resistance in sheet pile driving, and to consider the influence of soil types and soil densities.

a. Press-in piling machine SO-450

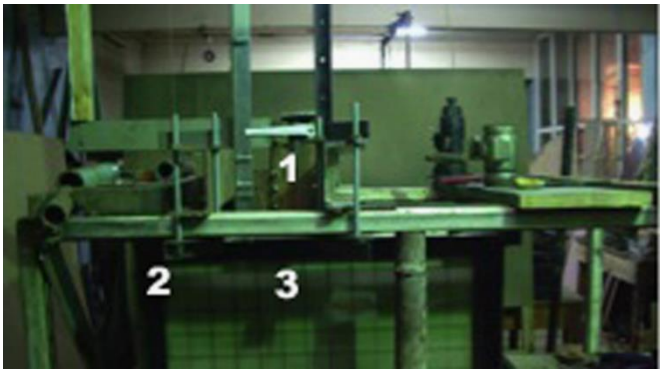

b. Laboratory test set-up showing sheet pile elements (1), soil container (2), and glass walls (3)

Figure 0-13. Set-ups for investigating interlock friction of sheet piles (Doubrovsky & Meshcheryakov, 2015)

Evans et al. (2012) utilized different alternative anchored sheet pile abutments for short-span bridges on low-volume roads with mainly cohesive materials in Iowa. They constructed three new bridges where (1) the sheet pile wall driven into shallow bedrock was directly bearing the superstructure load; or the sheet pile wall combined with a Geosynthetically Reinforced Soil (GRS) system was used as the primary abutment foundation element and backfill retaining system for (2) single-span, or (3) multi-span bridges. A hybrid design approach was utilized to design axially loaded sheet pile walls. That is, for determining the lateral loads experienced by the abutment, the sheet pile wall was analyzed as a retaining wall and for determining the bearing capacity of the sheet pile elements, they were analyzed as driven piles. The tests revealed that generally the measured stresses and deflections were different from the design values, where the differences reflected conservatisms and the complex field conditions. According to the authors, additional research is needed to optimize the design procedures for axially loaded sheet piles. Given below is the brief description of each project including the details of the foundation systems and outcomes of each project:

(1) Black Hawk County Bridge

Site characterization was performed by conducting SPT and CPT sounding, where it was revealed that the majority of material was clay with sandy seams occurring near stream level. Weathered limestone was encountered at depths of $16ft$ - $17ft$. Groundwater table was encountered at about $10ft$ - $12ft$ depth. Custom precast beam-in-slab units ($40.75ft$ long) were used in the bridge superstructure. Each abutment consisted of a precast abutment cap directly bearing on “PZ 22” sheet pile sections driven into shallow bedrock. The main wall of the abutment required 20 sheet pile elements with each of the wing walls consisting of 6 elements. Both vibratory and impact hammers were used to drive sheet pile elements. To increase the lateral resistance of the system, an anchoring system (i.e. tie rod attached to deadman) was used with the wall (Figure 0-14). Because the sheet piles were driven into the bedrock and also restrained by wing walls, it was

assumed the wall was restrained against translation at the base. The bridge superstructure was assumed to provide restraint against translation at the top of the wall; thus, the designed element was assumed to be simply-supported at both ends of the section. Based on these reasons, at-rest (K_0) conditions were assumed to design the wall against lateral earth pressure. Figure 0-15 depicts pictures of the abutment caps and the completed bridge. Analysis of the live load test results showed that maximum axial stresses occurring in the piles were comparable to the predicted analyzed values. Flexural stresses, however, were significantly less than those estimated by analysis. Earth pressures recorded during live load testing were also significantly lower than earth pressures estimated by analysis.

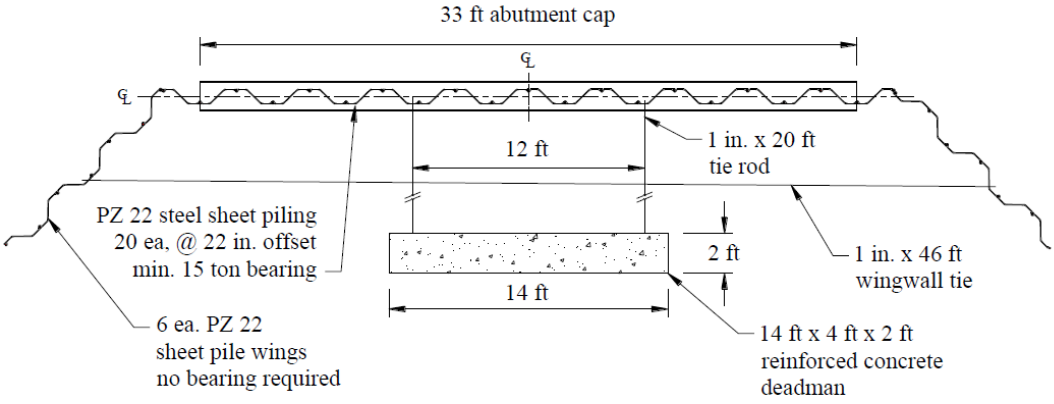

Figure 0-14. Plan view of the sheet pile abutment and backfill retaining system (Evans et al., 2012)

a. Placement of abutment caps on sheet pile walls

b. Side view of the completed bridge

Figure 0-15. Black Hawk County bridge resting on sheet pile walls (Evans et al., 2012)

(2) Boone County Bridge

The second demonstration project was aimed to investigate the feasibility of sheet piling combined with a Geosynthetically Reinforced Soil (GRS) system for use as the primary abutment foundation element and backfill retaining system (Figure 0-16). The site was consisted of cohesive soils underlain by a granular base, where dense granular materials and overconsolidated fine grained soil deposits were found below depths of 34 ft. Groundwater was encountered at about 16 ft depth. The bridge (a 30 ft wide, 100 ft long three-span continuous concrete slab with a 30 degree skew) was a replacement for an existing old bridge. The bridge deck was a 33.17 ft wide continuous concrete slab structure with a depth of 1.48 ft along the spans and 2.46 ft over the piers. Each pier consisted of eight, 80 ft long piles made monolithic with the bridge deck. The bridge deck-abutment cap system was designed to bear on a reinforced concrete spread footing (6 ft wide and 1 ft thick) on a GRS system retained by an anchored sheet pile wall (i.e. tie rod attached to deadman). Accounting for a 6 ft depth of scour, the required depth of the sheet pile wall for stability was approximately $25ft$. However, as an additional factor of safety, 30 ft long PZ 22 sheet pile sections were driven with a vibratory pile driver. The GRS system was created using 6 layers of biaxial geogrid with a granular backfill. In this foundation system, the reinforced concrete spread footing provided a larger bearing surface area for the abutment caps. The sheet pile wall and reinforced concrete deadman anchor system were designed to resist all loads (Figure 0-16 and Figure 0-17). According to the authors, the contribution of the GRS system was, however, neglected in this project due to the limited existing research on long-term performance of GRS systems. Analyses of the live load test results revealed that the maximum flexural stress experienced in the sheet pile elements were 3% of the expected value by analysis. Vertical and horizontal earth pressures in the backfill and the maximum lateral earth pressure experienced at the face of the sheet pile wall were lower than the estimated values concluding that the design methods, in general, were significantly conservative. Due to the inherent potential for settlement of spread footings, use of this type of sheet pile bridge abutment system for relatively long bridges with multiple spans must include strict requirements for compaction and reduction of voids in the backfill material.

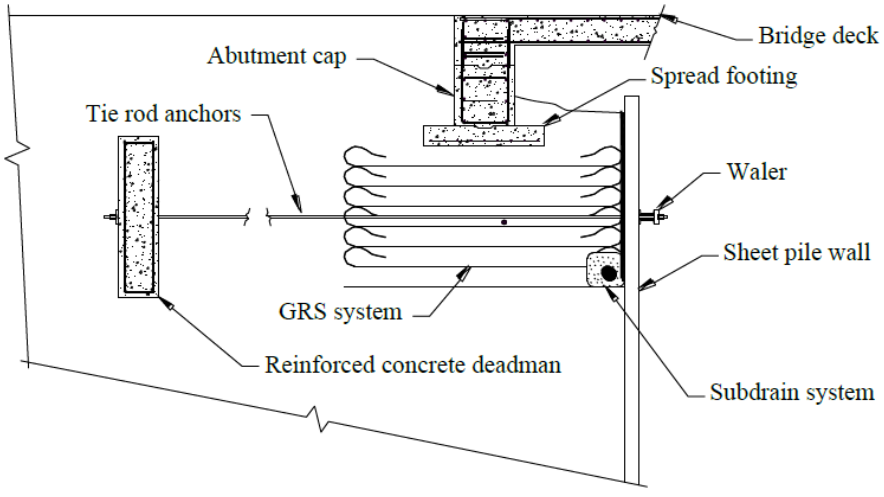

Figure 0-16. Cross-section of sheet pile abutment foundation system (Evans et al., 2012)

a. Deadman and tie rods anchoring the west abutment sheet pile wall

b. side view of the finished bridge

Figure 0-17. Boone County bridge resting on sheet pile walls (Evans et al., 2012)

(3) Tama County Bridge

Based on CPT sounding results, the site was consisted of cohesive soils underlain by a granular base with very soft material in the upper 6 ft to 20 ft, granular deposits that extend to approximately 37 ft and fine-grained Pre-Illinoian glacial in the remaining lower portion of each sounding. Groundwater was encountered at 20 ft depth. Similar to the project in Boone County, this project was aimed to investigate the feasibility of using anchored sheet piling combined with a GRS system for the primary abutment foundation element and backfill retaining system (Figure 17). However, the bridge was single span (Figure 18) utilizing two 89 ft long railroad flatcars (RRFC's) for the superstructure in which significant differential abutment settlements might not be detrimental to the superstructure (Figure 19). A 10 ft × 10 ft timber-made footing was bolted to both ends of each RRFC. The substructure for the bridge utilized a GRS system with an anchored steel sheet pile retaining wall consisted of PZC 13 sections. To avoid the need for significant earthwork required to construct a deadman, tie rods were directly attached to the RRFC superstructure. With this system, the sheet pile wall was anchored by developing axial compressive forces in the RRFC superstructure. The anchored sheet pile wall system was designed to resist all loads from the bridge and backfill surcharge. Unlike the bridge in Boone County, the design of this sheet pile abutment retaining system considered the contribution of the GRS system in redefining the applied lateral pressure to the wall causing significantly smaller sheet pile sections and anchorages to be required. As at the time of their report, construction of the bridge was not completed, the results of live load tests were not reported.

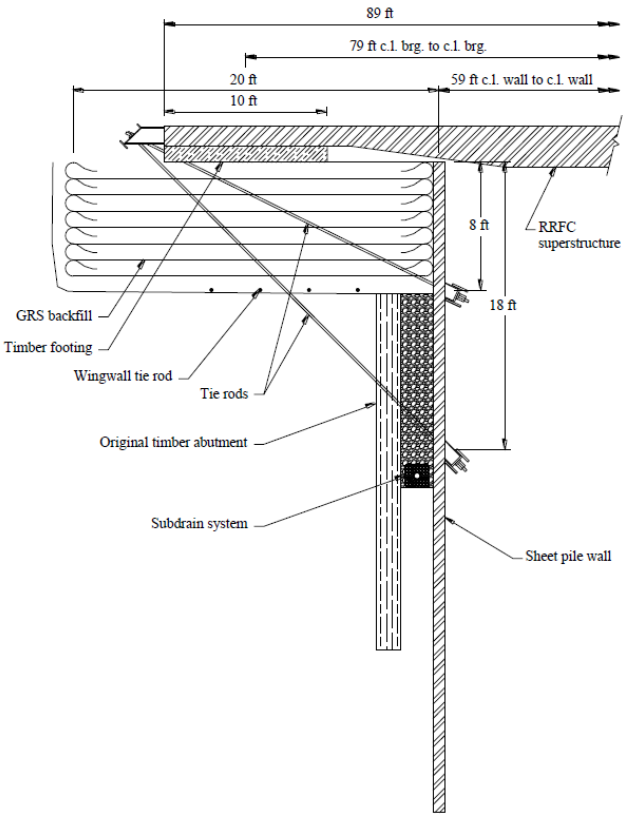

Figure 0-18. Design details of the sheet pile bridge abutment and backfill retaining system (Evans et al., 2012)

a. Completed abutment looking south

b. Side view of the completed bridge

Figure 0-19. Tama County bridge resting on sheet pile walls (Evans et al., 2012)

Underwood and Greenlee (2010) reported conducting high strain dynamic testing with a Pile Driving Analyzer (PDA) to verify the bearing capacity of sheet piles in Minnesota. The sheet piles were designed to carry uniform wall loads in the range of 5 to 12 kips per linear foot and concentrated loads of up to 251 kips. As construction stage loading typically controls the sheet pile section and the required embedment, they followed conventional design methodology considering each stage of construction. Their results revealed that permanent cantilever sheet pile foundations can be cost effective where it is necessary to construct one or more below grade levels with building foundation walls close to the property lines. Figure 20a shows the use of sheet pile walls for below grade building levels where the floor provides a lateral constraint. Figure 20b depicts finished sheet pile foundation walls in below grade parking garages where a precast beam bears on a bracket, welded to the flanges of the sheet pile.

(a) Sheet pile wall under the construction stage

(b) Finished sheet pile foundation walls in below grade parking garages

Figure 0-20. Steel sheet piles used as permanent foundation and retention systems (Underwood & Greenlee, 2010)

1.4.2 Small-scale testing

1.4.2.1 Tests in 1-g

Small-scale model tests conducted in a 1g gravitational field have been used to study the behavior of sheet piles under axial loading. Small-scale tests conducted in a 1g field in large containers might have the advantage of modeling Soil-Sheet-Pile-Interaction (SSPI) with dimensions comparable to the prototype scale. However, it is difficult to account for high gravitational stresses associated with deep soil profiles and constructing large models can be time consuming. Authors are also not aware such tests in large containers studying SSPI. Given below is a review of this type of tests to study the behavior of axially loaded sheet piles:

Punrattanasin, Gasaluck, Muktabhant, Angsuwotai, and Patjanasuntorn (2009) investigated the capacity changes of shallow foundations enclosed with sheet pile walls along their length. They used sheet piles with lengths of 25 *mm*, 50 *mm*, 75 *mm*, and 100 *mm* resulting in sheet pile length to shallow foundation width ratios (L/B) ratios of 0.5, 1.0, 1.5, and 2.0 (Figure 21a). Dense sand

profiles with relative density of 70% were constructed by pluviating sand into a rigid rectangular container with dimensions of 800 *mm* × 400 *mm* × 800 *mm* (L×W×H). The static load tests results illustrated the effectiveness of sheet piles in increasing the capacity of shallow foundation. Although the higher the sheet pile length, the greater the increase in capacity (Figure 21b), the authors recommended using L/B = 1, considering both construction cost and the foundation capacity.

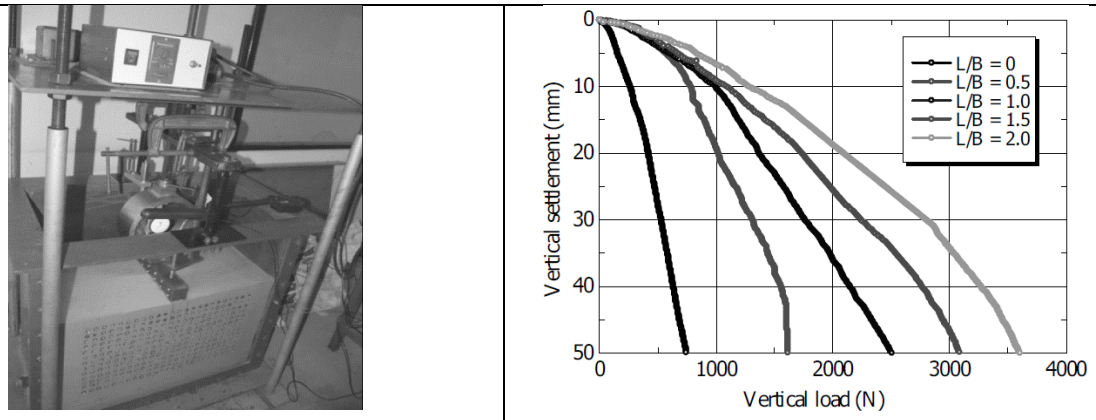

a. Load testing set up

b. Load-settlement curves for the foundation systems

Figure 0-21. Load testing of shallow foundations enclosed by sheet piles (Punrattanasin et al., 2009)

Nishioka, Koda, Hirao, and Higuchi (2010) conducted a series of static load tests to investigate the behavior of a shallow foundation enclosed by sheet piles (Figure 22). They showed an enhancement in the performance of these foundation systems in terms of both bearing capacity and lateral resistance.

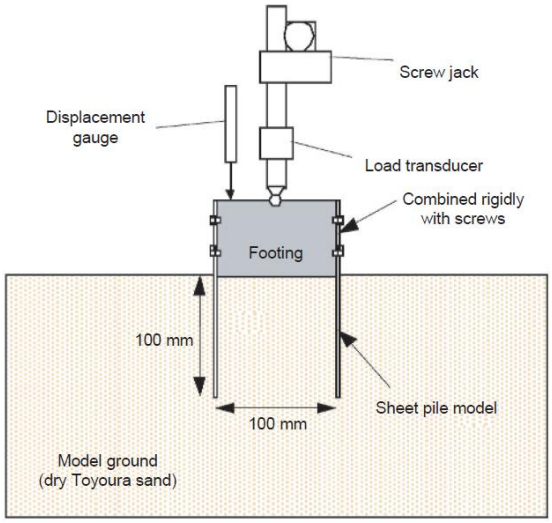

Figure 0-22. Axial loading test of the shallow foundation enclosed by sheet piles (Nishioka et al., 2010)

Azzam and Elwakil (2017) conducted small-scale tests in 1-g gravitational field and investigated the effects of penetration depth, pile stiffness, and sand relative density on the behavior of piled retaining walls under axial loads. Figure 23 depicts schematic diagram of the test setup. Pictures of the sheet pile under axial loading are shown in Figure 24. Their results reveled that increasing the soil relative density from 50 to 88% can increase the ultimate axial capacity of the sheet piles by 72%. Increasing the sheet pile penetration depth and the sheet pile stiffness also increased the capacity.

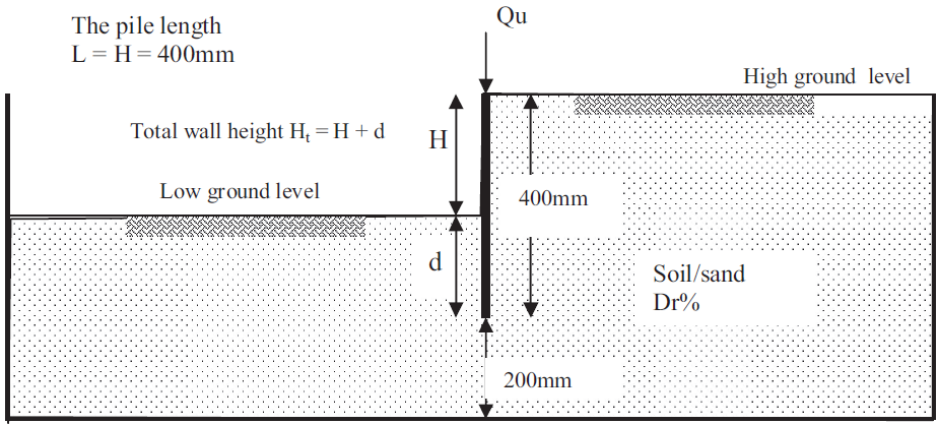

Figure 0-23. Schematic diagram of the test setup (Azzam & Elwakil, 2017)

Figure 0-24. Pictures of the sheet pile under axial loading (Azzam & Elwakil, 2017)

It is worth mentioning that there are other small-scale laboratory tests performed in 1-g gravitational field; however, the behavior of sheet piles are studied only under lateral loading. Among others, Bica and Clayton (1998) investigated the effects of wall embedment depth and effective angle of wall friction on the earth pressure distribution on two sides of the wall. They showed that relatively large earth pressures, associated with high effective angles of wall friction,

were mobilized just below the soil surface in front of the wall. On the retained side of the wall and below the center of rotation, earth pressures were smaller than those estimated by Rankin's passive values as the wall friction acted downwards below the pivot point. At a given effective angle of friction, bending moments increased with wall embedment depth. Pula and Rybak (1984) investigated the behavior of a foundation system consisted of a strip footing enclosed by sheet piles using 2D numerical analysis and small-scale model tests in 1g field. Their analyses and model tests showed the effects of using sheet pile walls in increasing the bearing capacity of the strip footing.

1.4.2.2 Centrifuge Testing

Craig (1985) showed that driving piles at 1g instead of prototype-scale g-levels in small-scale models would significantly alter the bearing capacity and the behavior of axially loaded pile foundations in sands. This is due to the loss of similarity associated with failure in modeling the volume change in sands during driving deep foundations. To overcome these problems, centrifuge tests can be used to investigate the behavior of such foundation systems. Compared to field experiments, soil profiles can be well defined in centrifuge tests. Moreover, in centrifuge tests, the stress condition at any point of the model and, therefore, the overall model behavior (e.g. displacement and failure mechanisms) is similar to that in the full-scale prototype. However, to the best knowledge of the authors, there are no centrifuge tests studying the behavior of axially loaded sheet piles especially in sand. The previous centrifuge tests have been only done on sheet piles in cohesive soils to study their behavior under lateral earth pressure without subjecting them to axial loading. This is mainly because equipped centrifuge modelling facilities capable of driving sheet piles into sand in-flight and conduct load tests are rare. Given below is the review of these tests:

Bolton and Powrie (1987) and Bolton and Powrie (1988) conducted centrifuge model tests to form the basis of research into the soil-structure interaction behavior following the excavation of soil in front of a pre-constructed wall. Their centrifuge tests were designed to illustrate aspects of the collapse of stiff cantilever retaining walls embedded in overconsolidated clay. To simulate the effects of staged excavation, a heavy fluid stored in front of the wall was drained in flight. A typical centrifuge model used in their tests is shown in Figure 25 and represents a section of a long wall. The length of the model wall section was 150 mm, corresponding to 18.75 m in the prototype scale. Two modes of collapse were observed with unpropped walls. The walls with small penetration were failed by the hydraulic action of a water-filled crack opening on the retained side of the wall (Figure 26a). The walls with deeper penetration showed accumulation of distributed strains in 'active' and 'passive' zones which could lead ultimately to sliding on shear rupture surfaces (Figure 26b). Centrifuge tests made possible to validate simplified "geostructural mechanisms" which were based on lower bound stress fields, but which incorporate consistent strain fields. The strain fields indicated that wall rotation, $\delta\theta$, could mobilize a shear strain increment $\delta\gamma = 2\delta\theta$ within the neighboring zones of deformation, whether the wall rotated about the top or the base of the adjacent soil layer.

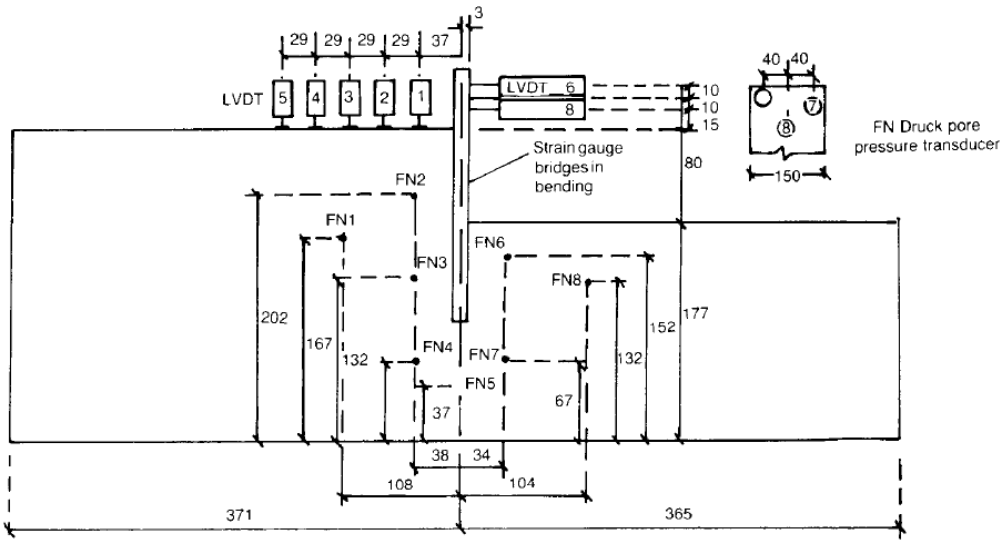

Figure 0-25. Instrumentation of a typical model; dimensions in millimeters (Bolton & Powrie, 1987)

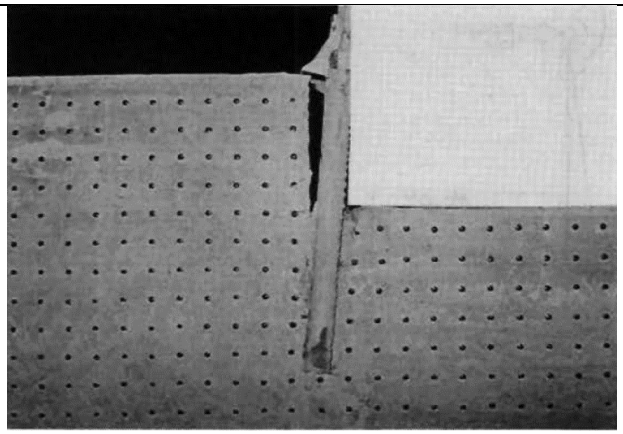

(a) Flooded tension crack failure in the wall with shallow penetration

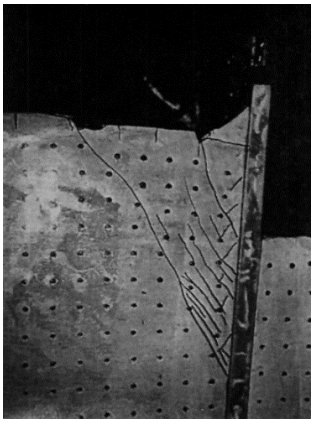

(b) Post-flight view of the wall with deeper penetration

Figure 0-26. Observed modes of collapse (Bolton & Powrie, 1987)

Madabhushi and Chandrasekaran (2005) proposed a minimization of moment ratio technique to determine the point of rotation (pivot point) for sheet pile walls with cohesive or cohesionless backfills. The location of the pivot point obtained by the minimization of the moment ratio approach was validated against their centrifuge data. One of their typical centrifuge models with a rigid sheet pile wall penetrated in cohesive backfill is shown in Figure 27. The soil model was created by compacting six layers of Bombay marine clay mixed at 54% moisture content, resulting in the undrained shear strength of 32.5 kPa. Centrifuge tests were conducted for the D/H ratio of the sheet pile wall equal to 0.76 and 0.44. In all tests, it was observed that the minimization of the

moment ratio approach gave satisfactory results that compared well with the experimentally determined location of the pivot point.

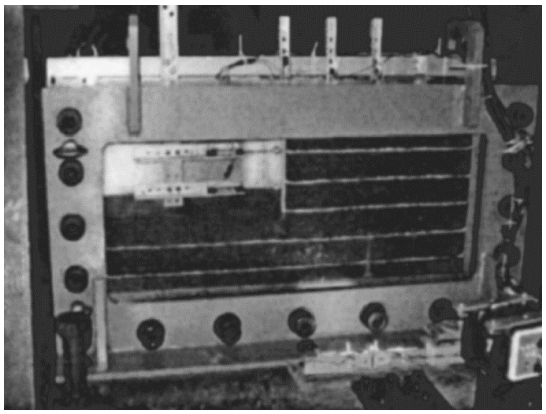

Figure 0-27. View of the sheet pile model in the centrifuge container (Madabhushi & Chandrasekaran, 2005)

Madabhushi and Chandrasekaran (2008) conducted centrifuge tests to establish the failure mechanisms suffered by the sheet pile walls. Sheet pile walls with two varying depths of penetration were used (namely, D/H=0.76 and 0.44). Schematic diagram of the centrifuge model with D/H=0.76 is shown in Figure 28. In both centrifuge tests the observed failure mechanism was similar and confirmed the failure mechanism employed in practice. The sheet pile walls suffered severe rotation about a point just above the base subjecting the backfill soil to active earth pressures and the soil in front of the toe to passive earth pressures. As the sheet pile wall rotated outwards, excessive tension cracking was observed in the backfill (Figure 29). Passive wedges developed in the toe region of the wall. Also horizontal tension crack was observed on the passive side.

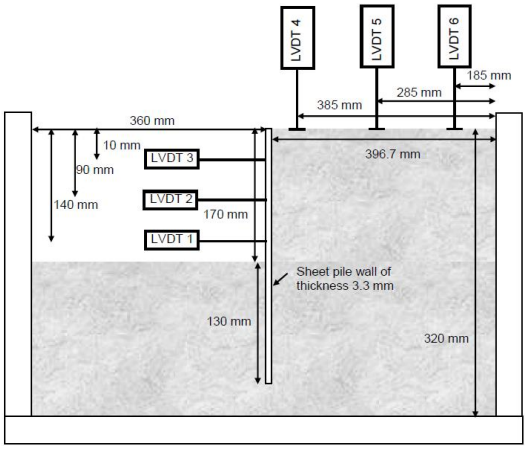

Figure 0-28. Schematic diagram of the cross-section of the centrifuge model (Madabhushi & Chandrasekaran, 2008)

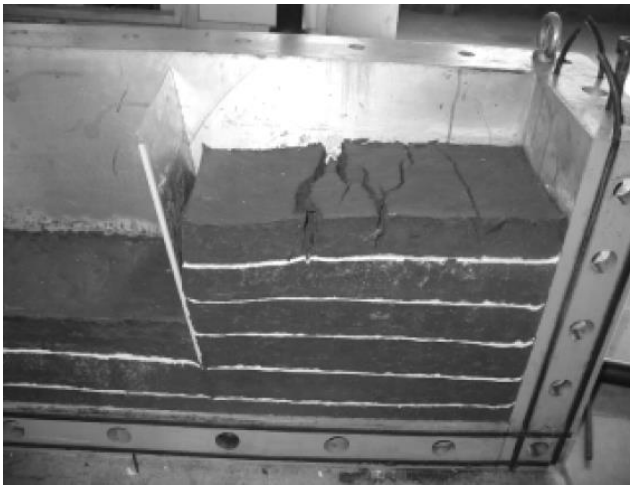

Figure 0-29. View of the model after the test showing the rotation of the sheet pile wall and the tension cracks in the backfill (Madabhushi & Chandrasekaran, 2008)

Viswanadham, Madabhushi, Babu, and Chandrasekaran (2009) conducted centrifuge tests to investigate the structural failure of the sheet pile elements because of high stresses or loss of serviceability due to large deformation. To conduct the tests, a rigid container having internal dimensions of 760 *mm* length, 410 *mm* depth and 200 *mm* width was used (Figure 30). The cantilever sheet pile wall was modelled by a 3.3 *mm* thick plate made of aluminum alloy. Centrifuge tests were carried out by subjecting the model to varied g-levels (in steps of 5 g from 10 g onwards) up to a maximum set target g-level of 75 g or to excessive deformation of wall, whichever occurred first. The relative density of the sand in the container was 55%. Direct shear tests were conducted to determine the soil–wall interface friction angle δ, which was found to be 16°. Centrifuge tests results were used to validate and verify the predictions of the finite element method and closed form solutions implementing Coulombs earth pressure theory. Location of the maximum bending moment predicted by the finite element method and closed form solution agreed well with that observed by the centrifuge tests. The finite element analysis was able to capture the formation of the plastic hinge observed in the sheet pile walls during the centrifuge model tests.

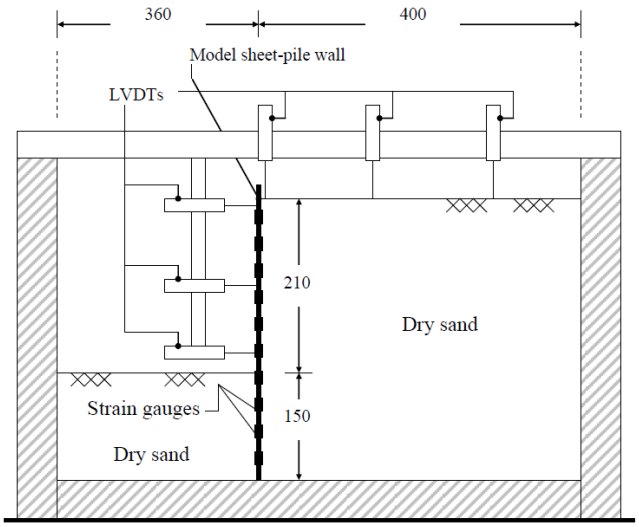

Figure 0-30. Cross-section view of experimental set-up; all dimensions are in mm (Viswanadham et al., 2009)

1.4.3 Sheet pile bridge abutment systems in practice: case studies

There have been a variety of highway structures built using steel sheet piling as the permanent structural elements of bridge piers, abutments, and wingwalls. Carle and Whitaker (1989) presented design concepts for highway structures utilizing steel sheet piles as a part of their permanent foundation system. They reviewed cases in Europe where (1) bulkhead sheet pile walls were used as an abutment for a highway bridge to resist both horizontal soil pressure and vertical loads from the bridge (Figure 31); (2) the top of the sheet pile was fixed into the concrete bridge structure and vertical loads from the bridge were transferred to the firm soil below through the box piles extending below the bottom of the sheet pile; (3) the toe of the sheet pile wall was placed in a steel channel to distribute the loads to the underneath bearing rock layer; (4) sheet pile wall abutment was tied back with a driven and grouted steel batter pile; and (5) heavy vertical loads from a 233 ft long truss bridge were carried by a sheet pile wall and by the second row of intermittent double piles. In the United States, they reviewed cases where (1) a single span integral abutment bridge is supported on HP8x36 H-piles with steel sheet piling driven immediately behind the H-piles and braced by steel channels spanning between the H-piles (Figure 32); (2) a bridge with a span of 37 ft 6 in and a useable width of 34 ft is borne on concrete footings immediately behind and structurally attached to the sheet piling abutment walls; (3) a 79 ft 4 in. span bridge supported directly on a sheet pile wall is driven to rock where fitted cast steel tips are used to help seat the wall in the rock. Sheet pile wingwalls were tied back to concrete deadmen using steel tie rods (Figure 33); (4) a 42 ft single span highway bridge is borne directly on a sheet pile wall with the top of the sheet pile abutment capped with reinforced concrete bearing on a steel plate; and (5) a 3-span ACROW panel bridge with a total length of 415 ft 9 in and a curb to curb width of 11 ft 3 in is supported at the abutments and the piers by circular sheet piling cells with 21.5 ft diameter. The bridge loads were transferred to the compacted granular cell fill by reinforced concrete footings (Figure 34). Carle and Whitaker (1989) illustrated the need for a comprehensive

research project in order to take advantage of the potential savings and other benefits associated with the use of steel sheet piling for bridge abutments and wingwalls.

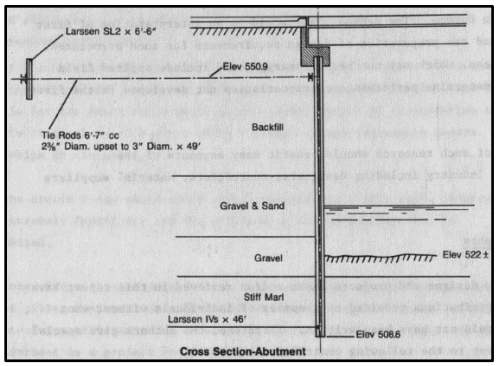

Figure 0-31. Highway bridge over a branch of the Moselle river in Europe (Carle & Whitaker, 1989)

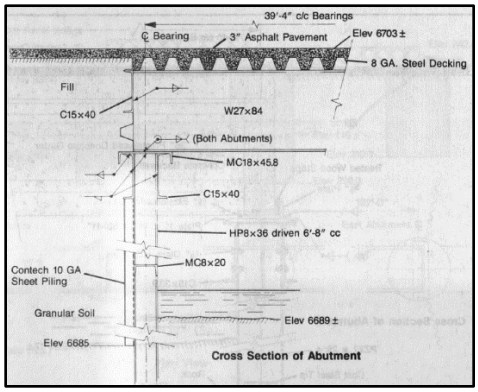

Figure 0-32. Peyton Highway Bridge, El Paso County, Colorado (Carle & Whitaker, 1989)

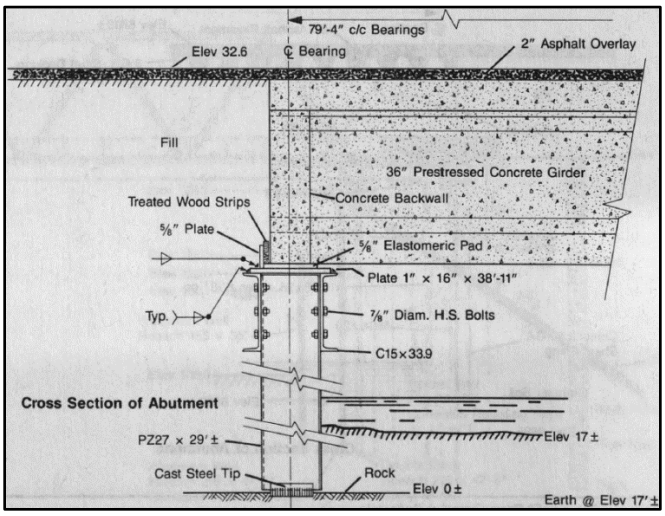

Figure 0-33. Small Creek Bridge, Seward, Alaska (Carle & Whitaker, 1989)

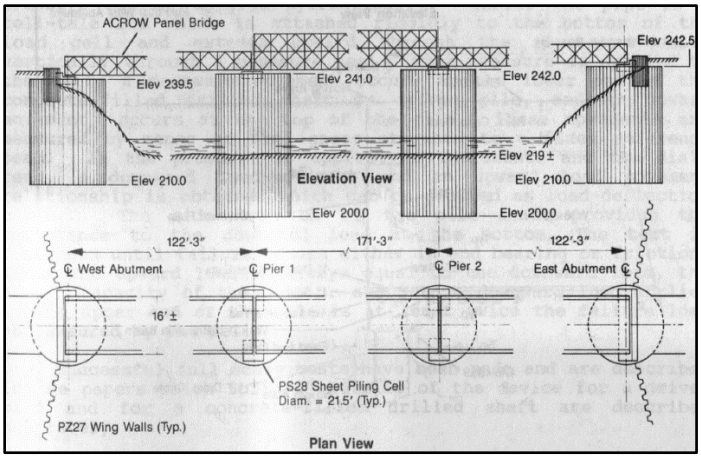

Figure 0-34. Highway Bridge, Russell, Massachusetts (Carle & Whitaker, 1989)

Recently, use of steel sheet piling bridge abutment systems have been received further attention in the U.S. In Iowa, as mentioned earlier, several bridges with sheet pile abutments have been constructed mostly as parts of research projects where the performance of sheet piles under axial loading was studied. An example in Iowa is shown in Figure 35a. The bridge has three spans with the two piers consisted of steel capped H-piles and the bridge structure supported by the sheet pile abutments using stiffened angles bolted to the wall. Figure 35b illustrates a view of the pier and abutment.

a. View of abutment and pier

b. Stiffened angles bolted to piling supporting superstructure

Figure 0-35. Overview of sheet pile bridge abutment in Winnebago County, Iowa (Evans et al., 2012)

1.4.4 Remarks on experimental modeling

The review of literature pertaining experimental modeling provided useful information and details on different research addressing the problem of axially loaded sheet pile walls. Insights on the load testing procedures, instrumentation, sheet pile behavior, failure types, and analyses methods are obtained and will be considered in designing and conducting our small-scale laboratory tests and full-scale tests. Relevant results from literature will be quantitatively or qualitatively compared with the physical modeling results obtained from this current study to validate or verify our tests results and seek the reasons for the observed likely differences.

1.5 References

AASHTO. (2014). *AASHTO LRFD bridge design specifications* (7 ed.). Washington, D.C.: American Association of State Highway and Transportation Officials (AASHTO).

Al-Baghdadi, T. A., Brown, M. J., Knappett, J. A., & Al-Defae, A. H. (2017). Effects of vertical loading on lateral screw pile performance. *Proceedings of the Institution of Civil Engineers-Geotechnical Engineering, 170*(3), 259-272.

Amer, H. A. R. (2013). *Effect of wall penetration depth on the behavior of sheet pile walls.* University of Dayton.

ASCE. (1996). Design of Sheet Pile Walls - Technical Engineering and Design Guides as Adapted from the US Army Corps of Engineers, (Vol. No. 15).

ASTM D1143/D1143M. (2013). Standard Test Methods for Deep Foundations Under Static Axial Compressive Load. West Conshohocken, PA: ASTM International.

Azzam, W. R., & Elwakil, A. Z. (2017). Performance of Axially Loaded-Piled Retaining Wall: Experimental and Numerical Analysis. *International Journal of Geomechanics, 17*(2), 04016049. doi: doi:10.1061/(ASCE)GM.1943-5622.0000710

Bica, A. V. D., & Clayton, C. R. I. (1998). An experimental study of the behaviour of embedded lengths of cantilever walls. *Géotechnique, 48*(6), 731-745. doi: 10.1680/geot.1998.48.6.731

Bloomquist, D., McVay, M. C., & Hu, Z. (2007). Updating Florida Department of Transportation's (FDOT) Pile/Shaft Design Procedures Based on CPT and DTP Data (Vol. BD-545, RPWO #43). Florida Department of Transportation: University of Florida.

Bolton, M. D., & Powrie, W. (1987). The collapse of diaphragm walls retaining clay. *Géotechnique, 37*(3), 335-353. doi: 10.1680/geot.1987.37.3.335

Bolton, M. D., & Powrie, W. (1988). Behaviour of diaphragm walls in clay prior to collapse. *Géotechnique, 38*(2), 167-189. doi: 10.1680/geot.1988.38.2.167

Bowles, J. E. (1996). *Foundation analysis and design* (5 ed.). New York: McGraw-Hill.

Bustamante, M. G., & Gianeselli, L. (1982). *Pile Bearing Capacity Predictions by Means of Static Penetrometer CPT*. Paper presented at the 2nd European Symposium on Penetration Testing (ESOPT-II), Amsterdam, Netherlands.

Bustamante, M. G., & Gianeselli, L. (1991). *Predicting the bearing capacity of sheet piles under vertical load*. Paper presented at the Proceedings of the 4th International Conference on Piling And Deep Foundations,, Stresa, Italy.

Carle, R. J., & Whitaker, S. S. (1989). *Sheet Piling Bridge Abutments*. Paper presented at the 4th Annual Members' Conference, "Realizing DFI's Potential, A Parallel to Baltimore's Renaissance", Baltimore, Maryland.

Chung, H. I., Yoo, J., Oh, I. K., & Kim, B. (2004). Application of Steel Sheet Pile Embedded Retaining Wall as a Bridge Abutment *Geotechnical Engineering for Transportation Projects*.

Craig, W. H. (1985). Modeling pile installation in centrifuge experiments *11th International Conference on Soil Mechanics and Foundation Engineering* (Vol. 2, pp. 1101-1104). San Francisco, California.

Davisson, M. T. (1972). *High capacity piles*. Paper presented at the Innovations in foundation construction : proceedings of lecture series, January to May 1972, sponsored by Soil Mechanics and Foundation Division, Illinois Section., Illinois Section, Chicago.

Doubrovsky, M., & Meshcheryakov, G. (2015). Physical modeling of sheet piles behavior to improve their numerical modeling and design. *Soils and Foundations, 55*(4), 691-702.

Evans, R., White, D., & Klaiber, W. (2012). Modified Sheet Pile Abutments for Low-Volume Road Bridges (Vol. IHRB Project TR-568): Iowa Department of Transportation and Iowa Highway Research Board.

Hazzar, L., Hussien, M. N., & Karray, M. (2017). Influence of vertical loads on lateral response of pile foundations in sands and clays. *Journal of Rock Mechanics and Geotechnical Engineering, 9*(2), 291-304.

Hussien, M. N., Tobita, T., Iai, S., & Rollins, K. M. (2012). Vertical loads effect on the lateral pile group resistance in sand. *Geomechanics and Geoengineering, 7*(4), 263-282.

Karthigeyan, S., Ramakrishna, V., & Rajagopal, K. (2006). Influence of vertical load on the lateral response of piles in sand. *Computers and Geotechnics, 33*(2), 121-131.

Karthigeyan, S., Ramakrishna, V., & Rajagopal, K. (2007). Numerical investigation of the effect of vertical load on the lateral response of piles. *Journal of geotechnical and geoenvironmental engineering, 133*(5), 512-521.

Madabhushi, S. P. G., & Chandrasekaran, V. S. (2005). Rotation of Cantilever Sheet Pile Walls. *Journal of Geotechnical and Geoenvironmental Engineering, 131*(2), 202-212. doi: doi:10.1061/(ASCE)1090-0241(2005)131:2(202)

Madabhushi, S. P. G., & Chandrasekaran, V. S. (2008). Centrifuge Testing of a Sheet Pile Wall with Clay Backfill. *Indian Geotechnical Journal, 38*(1), 1-20.

Meyerhof, G. G. (1976). Bearing Capacity and Settlement of Pile Foundations. *Journal of the Geotechnical Engineering Division, 102*(3), 195-228.

Nishioka, H., Koda, M., Hirao, J., & Higuchi, S. (2010). Vertical and combined loading tests for sheet pile foundation. *International Journal of Physical Modelling in Geotechnics, 10*(2), 25-34. doi: 10.1680/ijpmg.2010.10.2.25

Nottingham, L. C., & Renfro, R. H. (1972). A Computer Program to Estimate Pile Load Capacity from Standard Penetration Test Results (Vol. FDOT Research Bulletin No. 121-B): Florida Department of Transportation.

Peck, R. B., Hanson, W. E., & Thornburn, T. H. (1974). *Foundation engineering* (2 ed.). New York: John Wiley & Sons, Inc.

Pula, O., & Rybak, C. (1984). *The Improvement of Strip Footings Through the Use of Sheet Pile Walls*. Paper presented at the Proceedings of the Sixth Budapest Conference on Soil Mechanics and Foundation Engineering, Budapest, Hungary.

Punrattanasin, P., Gasaluck, W., Muktabhant, C., Angsuwotai, P., & Patjanasuntorn, A. (2009). *The effect of sheet pile length on the capacity of sheet pile foundation*. Paper presented at the The 17th International Conference on Soil Mechanics and Geotechnical Engineering, Alexandria, Egypt.

Schmertmann, J. H. (1967). Guidelines For Use In The Soils Investigation and Design of Foundations For Bridge Structures In The State Of Florida (Vol. Research Report 121-A): Florida Department of Transportation.

Schmertmann, J. H. (1978). Guidelines for Cone Penetration Test - Performance and Design (Vol. TS-78-209): FHWA.

Shiau, J., & Smith, C. (2013). Developing numerical models for the design of cantilever sheet pile wall. *Research, development, and practice in structural engineering and construction*, 533-538.

Smith, C. (2006). Development of numerical models for geotechnical design: USQ.

Sylvain, M. B., Pando, M. A., Whelan, M. J., Rice, C. D., Ogunro, V. O., Park, Y., & Koch, T. (2017). Case History of a Full Scale Axial Load Test of Sheet Piles *Geotechnical Frontiers* (pp. 355-365).

Taenaka, J., Otani, S., Tatsuta, M., & Nishiumi, K. (2006). Vertical bearing capacity of steel sheet piles *Physical Modelling in Geotechnics*: Taylor & Francis.

Taenaka, S., Kato, A., Toda, K., Harata, N., Otsushi, K., Nakayama, H., & Tanaka, R. (2016a). Development of New Steel Sheet Pile Foundation Method: Nippon Steel and Sumitomo Metal.

Taenaka, S., Kato, A., Toda, K., Harata, N., Otsushi, K., Nakayama, H., & Tanaka, R. (2016b). Development of New Steel Sheet Pile Foundation Method (Vol. Technical Report No. 113): Nippon Steel and Sumitomo Metal

U.S. Army Corps of Engineers. (1994). Design of Sheet Pile Walls. Washington, DC.

Underwood, C. A., & Greenlee, R. M. (2010). Steel Sheet Pile Used as Permanent Foundation and Retention Systems-Design and Construction *Earth Retention Conference 3*.

United States Steel. (1984). Steel Sheet Piling Design Manual. U.S.A.

Viswanadham, B., Madabhushi, S. P. G., Babu, K., & Chandrasekaran, V. (2009). Modelling the failure of a cantilever sheet pile wall. *International Journal of Geotechnical Engineering, 3*(2), 215-231. doi: 10.3328/IJGE.2009.03.02.215-231

Yandzio, B. (1998). Design Guide for Steel Sheet Pile Bridge Abutments *SCI Publication 187*.

Zhai, E. (2009). A Comparison Study of Engineering Approaches for Seismic Evaluation of Anchored Sheet Pile Walls *TCLEE 2009: Lifeline Earthquake Engineering in a Multihazard Environment* (pp. 1-11).

2 CHAPTER 2: NUMERICAL MODELING OF CANTILEVER SHEET PILES

2.1 Task 2a: Details of proposed numerical modeling

Piled retaining walls are used in a wide range of applications to solve the geotechnical problem of excavation near foundations. In-situ pile retaining walls are rows of concrete or steel piles installed directly tangent to existing structures to safeguard the foundations from deformation and collapse. The benefits of such piled walls are less soil disturbance and low noise, or vibration compared with that produced by the installation of solid piles or sheet piles. The stability of the excavation is the major design criterion avoid excavation deformation and collapse. Investigations of the behavior of piled retaining walls in supporting the excavation and adjacent foundations have also been undertaken. In this research, the behavior of the steel sheet wall system will be investigated using a physical model. In addition, a comparison was made between the two modes of free end piles and fixed end piles. Most of the literature has investigated, either experimentally or numerically, the different methods used to retain the excavation and adjacent structures. However, the investigation of the behavior of such side-supporting systems under combined load (lateral and axial load) cannot be thoroughly investigated. This project considered the problem of using the piled retaining wall as a permanent part of the foundation and studied how to transfer its load safely to the foundation without changing its location.

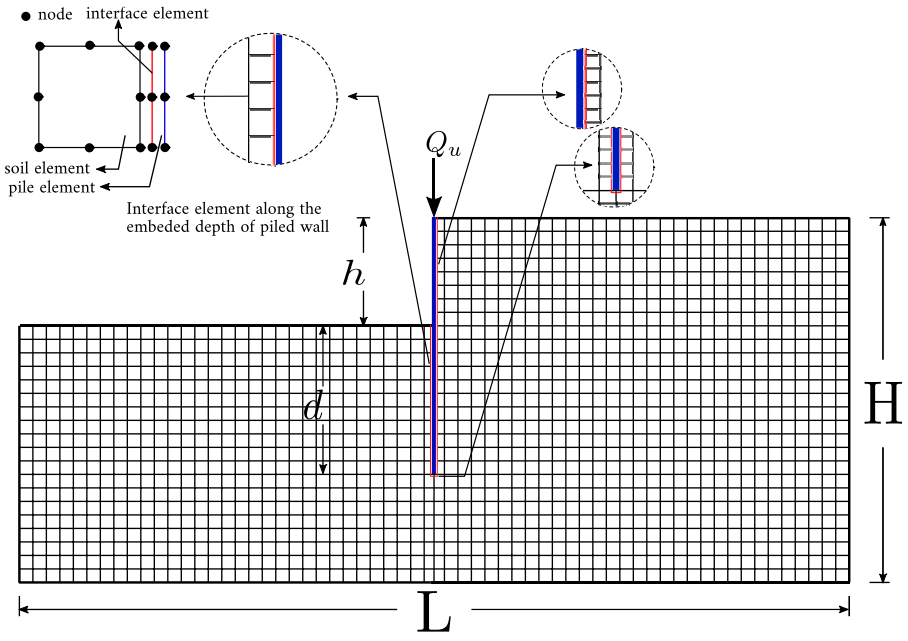

Figure 2-1. Geometry, generated mesh, soil-pile interaction elements, and the finite element model under the plane strain condition.

For this project, a commercial finite element analysis tool (PLAXIS 3D) for geotechnical engineering will be adopted. PLAXIS 3D is a powerful and user-friendly finite element package intended for three-dimensional analysis of deformation and stability in geotechnical engineering and rock mechanics. PLAXIS 3D is used worldwide by top engineering companies and institutions in the civil and geotechnical engineering industry. Applications range from

excavations, foundations, to tunneling, mining, and dynamic analyses and modeling. Therefore, we will use PLAXIS 3D to conduct the major numerical analysis detailed in the following sections. At the end of the project, a step-by-step guideline for modeling and analyzing the behavior of axially loaded sheet piles using PLAXIS 3D will be presented.

2.1.1 Nonlinear finite element program

In this project, numerical simulations were carried out using a three-dimensional (3D) finite element (FE) program. The elastoplastic FE analysis was carried out using PLAXIS 3D. All FE calculations were based on ten-node tetrahedral elements using a four-point Gaussian integration rule to calculate the element stiffness matrix. The shear stress parameters were used to define the failure behavior of sand. The sand was modeled using the elastoplastic Mohr-Coulomb model. The five essential parameters of the Mohr-Coulomb model are well known to most geotechnical engineers and can be determined from basic tests on soil samples. These parameters are Young's modulus, Poisson's ratio (or bulk and shear moduli), cohesion, friction angle, and dilation angle. These parameters can be readily determined from the proposed basic laboratory tests on soil samples such as direct shear tests and triaxial compression tests. These parameters can be used as the starting estimates for the preliminary study. However, for the numerical analysis conducted in this task, soil parameters for sands will be calibrated and obtained from the results of laboratory and centrifuge tests (Task 3).

In this project, modeling of the steel sheet pile wall as a 3D model was carried out in PLAXIS 3D. The pilled wall was analyzed with the linear elastic and nonlinear FE models, which involved the analysis of a 3D strip piled wall with equivalent depth. A ten-node element was used to model the piled wall as a sheet pile wall. The mathematical model for the problems under investigation is shown in Figure 2-1, which presents the different elements used to simulate the practical problems. The displacements were prescribed to zero in both the x-, y- and z-directions at the bottom and in the horizontal direction at the sides. The cluster embracing the piled wall was introduced to prepare for a simple mesh optimization with the use of the refine cluster option during mesh generation. The interface element for the interaction between the soil and piled wall element was used for all embedment piled wall depth. An elastoplastic model was used to describe the behavior of interfaces for modeling the soil-structure interaction. The interface strength was taken as a rigid type between sand and steel piles. The interface elements were connected to soil elements by three pairs of nodes. The stiffness matrix for interface elements was obtained with the use of Newton–Cotes integration points. The interface friction angle and adhesion between the contact surfaces were modeled by assigning a suitable value for the strength-reduction factor at the interface compared with the corresponding soil strength. The Coulomb criterion was used to distinguish between elastic behavior, where small displacements can occur with the interface, and plastic interface behavior (slip). The material properties used in the FE analysis are listed in Table 1. A series of FE analyses was carried out by applying vertical incremental loads to the nodes at the piled wall with different studied parameters to reach the failure point. The staged constriction feature in PLAXIS 3D makes it possible to simulate real-time construction, excavation, and backfilling processes by activating and deactivating the soil cluster, application of loads, and installation of the piled wall. The excavation on one side of the wall was carried out using this

staged construction option in the calculation phase by deactivation at a given depth of soil cluster in each stage, one after the other, until the system reached failure under the applied axial load.

2.1.2 Calibration and validation of the numerical model

Numerical models including the three-dimensional model of PLAXIS 3D need to be calibrated and validated before they can be used to investigate the bearing capacity of axially loaded sheet pile walls. Closed-form solutions for walls under lateral earth pressure and also the results from laboratory element-scale tests and centrifuge tests described in Task 3 will be used for calibration and validation of both numerical models.

2.1.2.1 Validation against closed-form solutions

In order to validate our FE simulation tools, we did the following boundary value problem by the PLAXIS 3D. The bending moment in the sheet pile wall obtained and derived from Coulomb's theory would be compared with the results achieved from numerical analysis under the same boundary conditions. The meshed 3D sheet pile wall model was shown in Figure 8. The bottom surface was fixed in three directions and the lateral surfaces were added the roller in horizontal direction. The soil of whole domain was Soil 1. The property of the Soil 1 was shown in Table1. The depth (d) of sheet pile wall equals 4m and the ratio of d/h =1. In order to compare the bending moment of the sheet pile wall between the analytical solution and numerical modeling. We need to calculate the active pressure (P_a) and passive pressure (P_p) by Coulomb's theory (Figure 2-2).

$$P_a = \frac{1}{2} K_a \gamma (h + d)^2$$
$$P_p = \frac{1}{2} K_p \gamma d^2,$$

where the K_a and K_p is the active pressure coefficient and passive pressure coefficient, respectively.

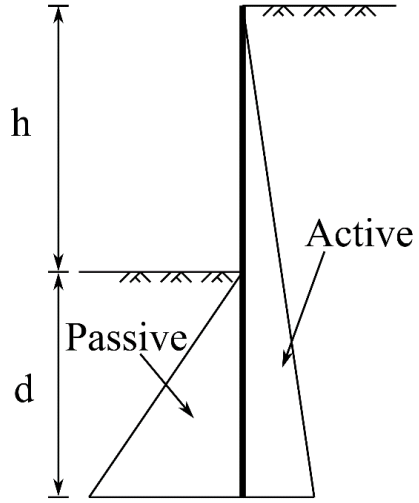

Figure 2-2. Coulomb's theory concept to calculate the pressure.

Figure 2-3 showed the bending moment contour of the sheet pile wall. Figure 2-4 showed the bending moment comparison for sheet pile wall between the closed form solution and simulation result.

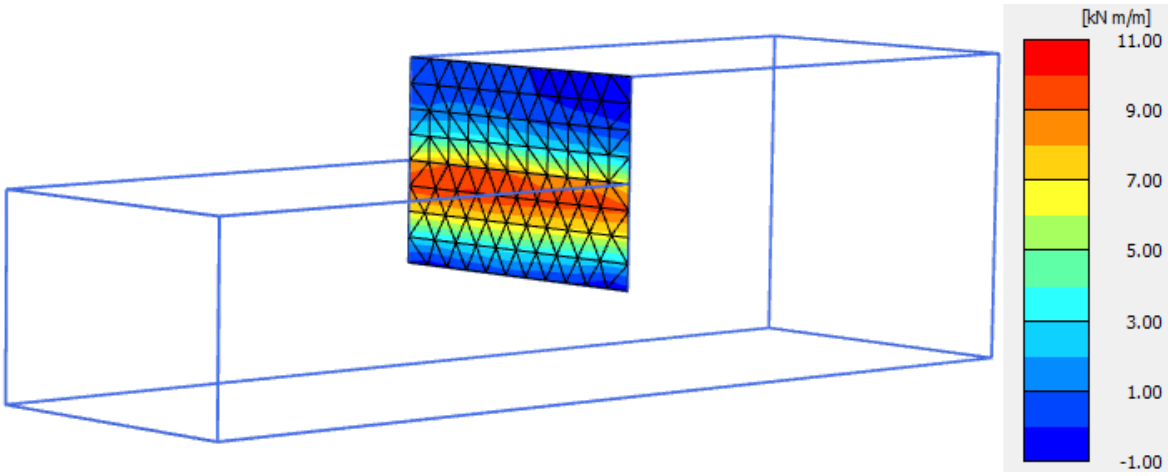

Figure 2-3. Bending moment of the sheet pile wall.

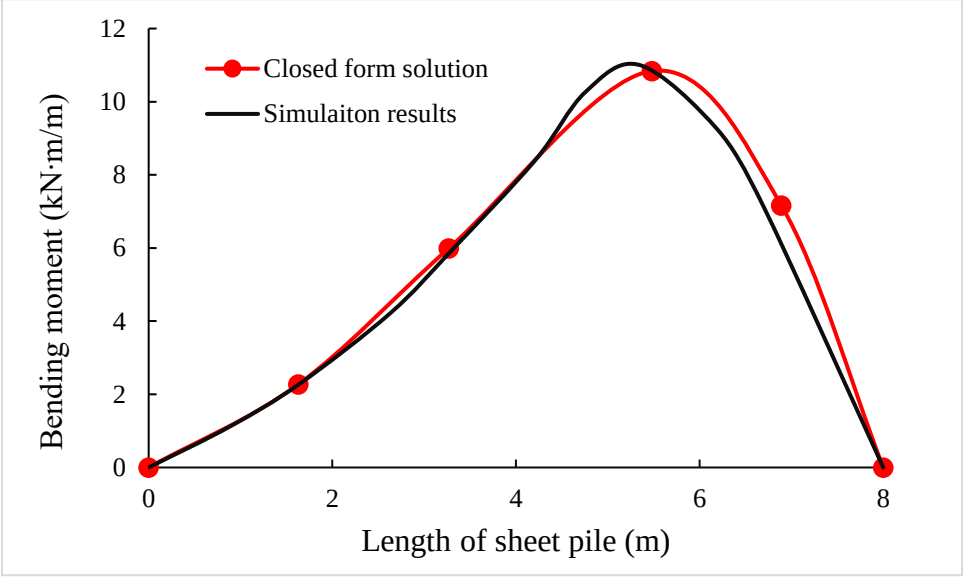

Figure 2-4. Bending moment comparison between the closed form solution and simulation result.

2.1.2.2 Validation against the results in the literature

The results from available research on the axially loaded sheet piles such as that conducted by Azzam and Elwakil (2017) was compared with the results of similar problems obtained by the numerical model. The comparisons and validation was performed in different forms including the earth pressure distribution (e.g., passive earth pressure in front of the sheet pile) in the adjacent soil mass and settlement and deflection of sheet piles.

Numerical analysis was used to validate the laboratory model test results and to give insight into the deformation behavior of both the piled wall and the adjacent soil mass. It also helped in measuring the variety of parameters that cannot be investigated in the laboratory. The lab-scale model (i.e., the soil domain was 60 cm in width, 60 cm in depth in the active zone, and 200cm in length) was used. The pile length was constant and equal to 40 cm. The 3D model (Figure 2-5) was created to run the simulation and compare the results with experimental test and 2D simulation (Figure 2-1) results. After ensuring the program's capability through the validation process, the analysis further investigated the behavior of a large-scale problem model under new parameters.

Initially, the numerical model was verified via the results obtained from the experimental test program of this investigation. The boundary condition of the model was assumed that the bottom surface was fixed in z-direction, the lateral surface was fixed in the normal direction of each surface. The constant load was added on the top of the sheet pile wall. The interface element was added on both sides of the steel sheet pile wall. The material properties were shown in table 1.

Figure 2-6 and Figure 2-7 showed the similarity between the load-displacement curves for the experimental and theoretical analyses of the axially loaded-piled wall. Good conformity was achieved between the experimental and the current FE modeling for the case of d/h = 3, L/D =21 (L is length of sheet pile, D is diameter of pile). The values of ultimate load capacity of the piled wall in the FE results were the same, but the displacement (vertical and horizontal) values were slightly lower (approximately 5%) than the experimentally predicted values. The numerical results follow the trend of the model test results, and acceptable agreement is achieved with a minimum difference around 10%. Thus, the adopted PLAXIS 3D model was shown to be proficient in predicting the behavior of prototype in the field in comparison with the small model test.

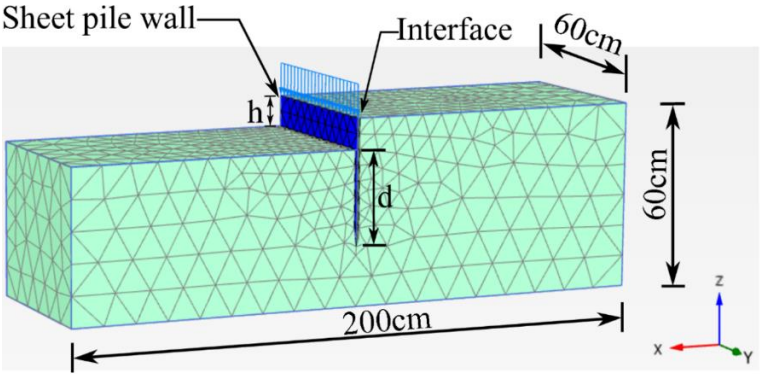

Figure 2-5. Meshed 3D sheet pile wall model under the vertical load.

Table 2-1. Material properties used in the finite element simulations

Parameter	Sheet pile wall	Very dense sand
Material model	Elastic	Mohr-Coulomb

Young's modulus	$2.1*10^7$	113000
Cohesion	-	0
Poisson ratio	0.25	0.3
Friction angle	-	41

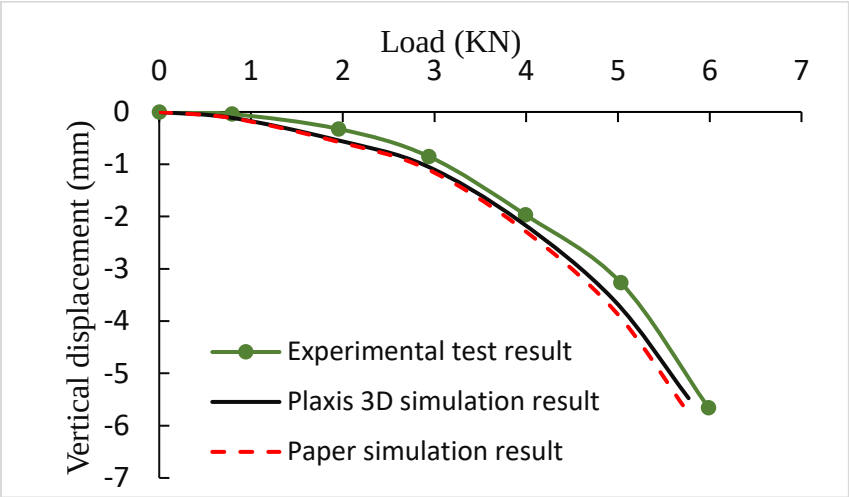

Figure 2-6. Comparison of experimental versus 2D and 3D numerical results for the model test (load-vertical displacement curve).

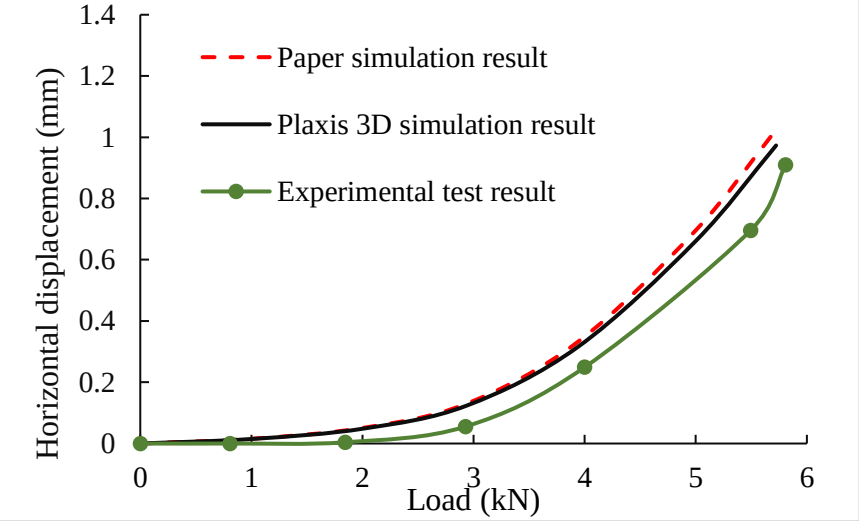

Figure 2-7. Comparison of experimental versus 2D and 3D numerical results for the model test (load-horizontal displacement curve).

2.1.2.3 Validation against the centrifuge test results

Results from the numerical models will be compared with the results from centrifuge tests in Task 3 to mimic the centrifuge test results and validate the numerical model. Bending moment and axial force distribution along sheet piles and axial load-settlement behavior obtained from system-scale axial static and quasi-static load tests performed in the centrifuge tests will be used for validation of numerical models.

2.1.3 Influence factors

Parametric studies were conducted under different scenarios simulating the variety of conditions that may frequently encounter in the field. This section explains the scenarios to be investigated by numerical modeling. For all simulations, the displacements were prescribed to zero in both the x-, y- and z-directions at the bottom and in the horizontal direction at the sides. The axial load and surcharge loading were different in each simulation sets. The material general material properties were same as the validation part.

2.1.3.1 Studied scenarios in numerical analysis

Once the numerical model is validated, extensive parametric studies will be conducted investigating the behavior of prototype-scale sheet pile walls under static and quasi-static axial loading through different scenarios. Key parameters and factors at the design stage capable of affecting the capacity of steel sheet pile foundations under axial loading will be studied. These include wall free length and wall embedment depth (the ratio of d/h), wall stiffness, soil properties (e.g. relative density) and layering, boundary conditions of the pile head (i.e. free or fixed), and general stability and buckling instability. The following sections provide justifications for studying the specified scenarios through numerical modeling. The studied scenarios model was shown in Figure 2-8.

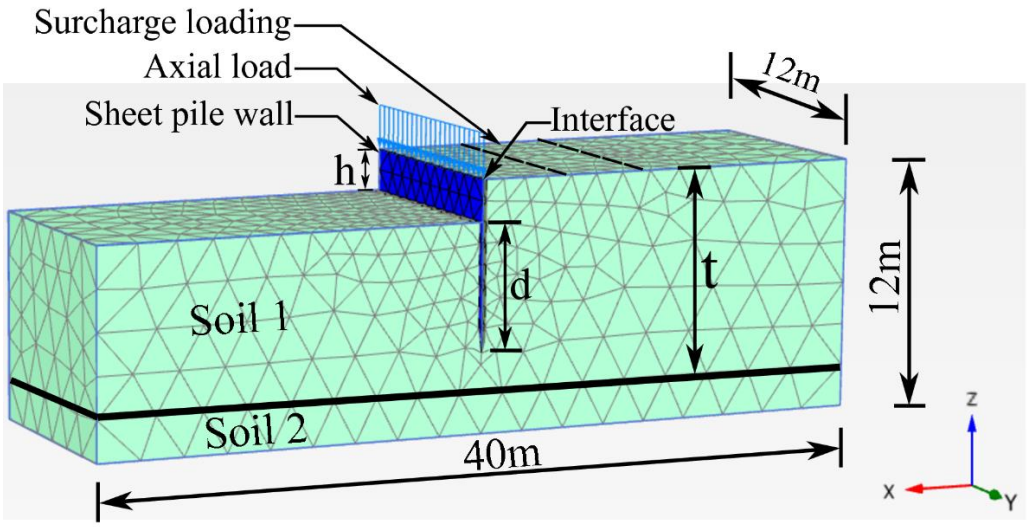

Figure 2-8. Meshed 3D sheet pile wall model under the vertical load.

2.1.3.2 Effect of penetration depth and unsupported length

The passive resistance of the soil in front of the wall provides stability for the cantilever sheet pile walls against lateral earth pressure. For a sheet pile wall under lateral earth pressure, assuming that a structural failure does not occur, a cantilever sheet pile wall of penetration (d) will fail as a rigid body by rotation about an axis lying in the plane of the wall at an unknown distance below the level of the excavation. It is possible that if the sheet pile wall is driven to insufficient depth, the passive resistance in the embedded portion of the wall may be overcome in which the toe of the wall moves laterally with substantial soil heave at the toe (Figure 2-9 (a)). Moreover, the penetration depth will affect the amount of mobilized and ultimate skin friction for the axially loaded sheet piles. An increase in the penetration depth can result in a fixed earth support and might lead to a decrease in the horizontal displacement of the sheet pile wall. An increase in unsupported length can make the wall susceptible for buckling causing a structural failure (Figure 2-10 (b)). Through performing numerical modeling, the effects of unsupported length and penetration depth on the axial behavior of sheet piles will be studied. The effects of these parameters on the failure mechanism and also buckling of the wall will be investigated. The potential failure mode of sheet piles under the axial loading will be studied via numerical modeling.

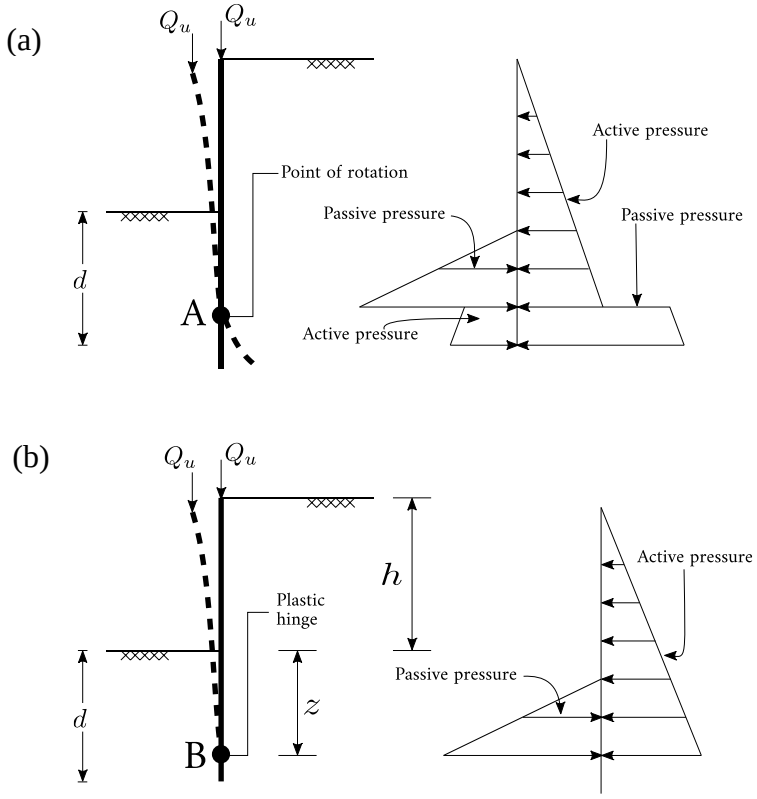

Figure 2-9. Failure modes of cantilever sheet pile walls: (a) Failure due to rotation about point A and (b) Failures due to the form of a plastic hinge at point B.

We simulated the different ratio of d/h to consider the effect of the penetration depth of the piled wall on the ultimate axial capacity of the system for one layer soil. We used the d/h which equals 3, 1.67, and 1. The material properties were shown in Table 1. Figure 2-10 showed the vertical

displacement and Figure 2-11 showed the horizontal displacement contour. Figure 2-12 showed the load versus vertical displacement curve and Figure 2-13 showed the load versus vertical displacement curve. Figure 2-14 showed the plastic shear strain contour.

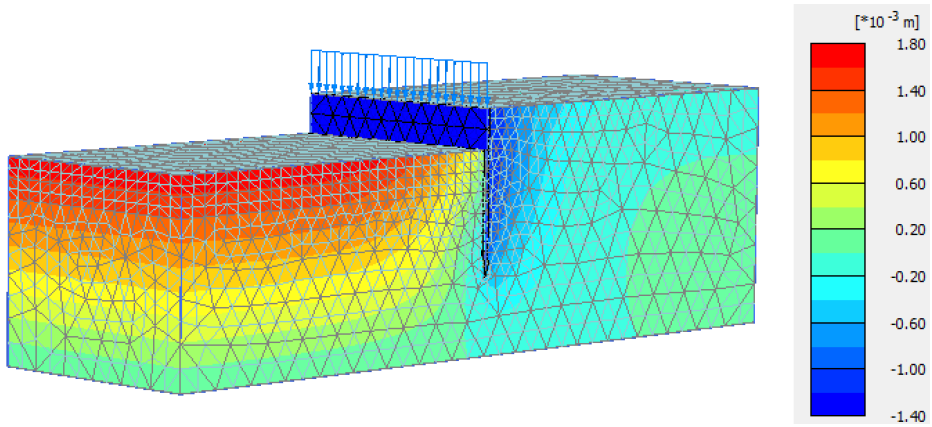

(a)

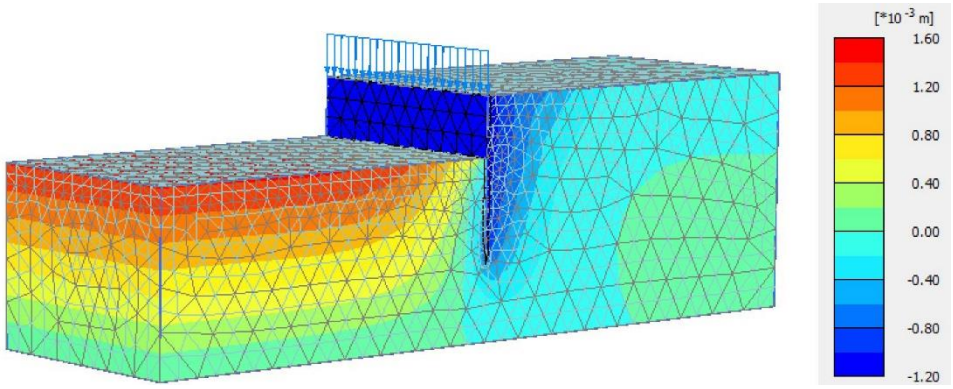

(b)

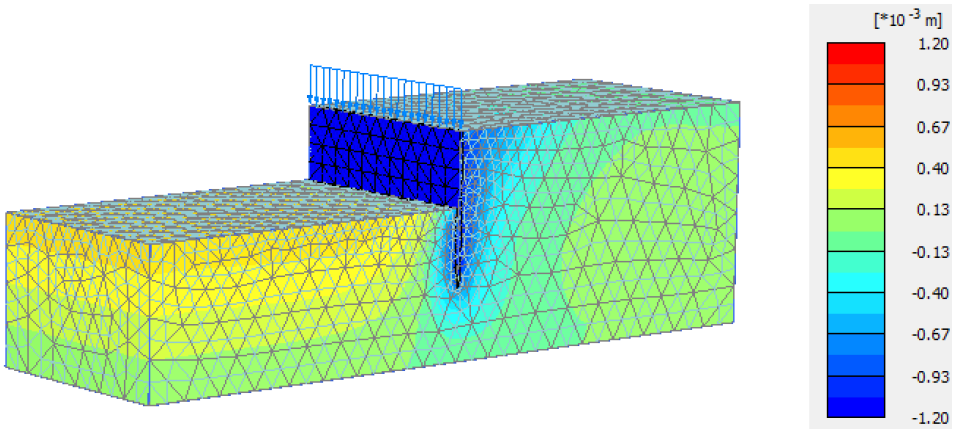

(c)

Figure 2-10. Vertical displacement contour at last time step; (a) d/h = 3; (b) d/h =1.67; (c) d/h =1.

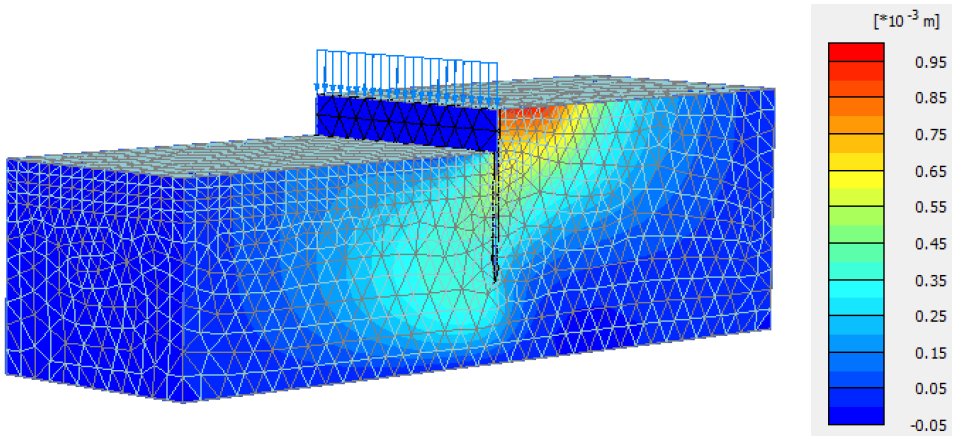

(a)

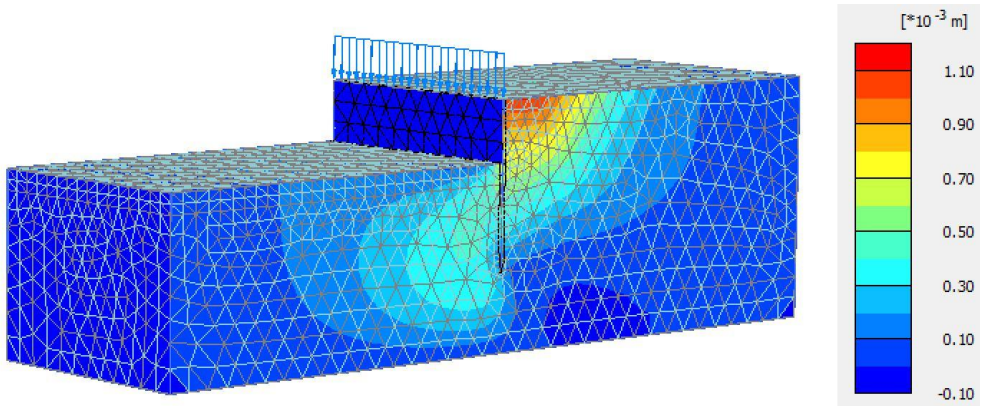

(b)

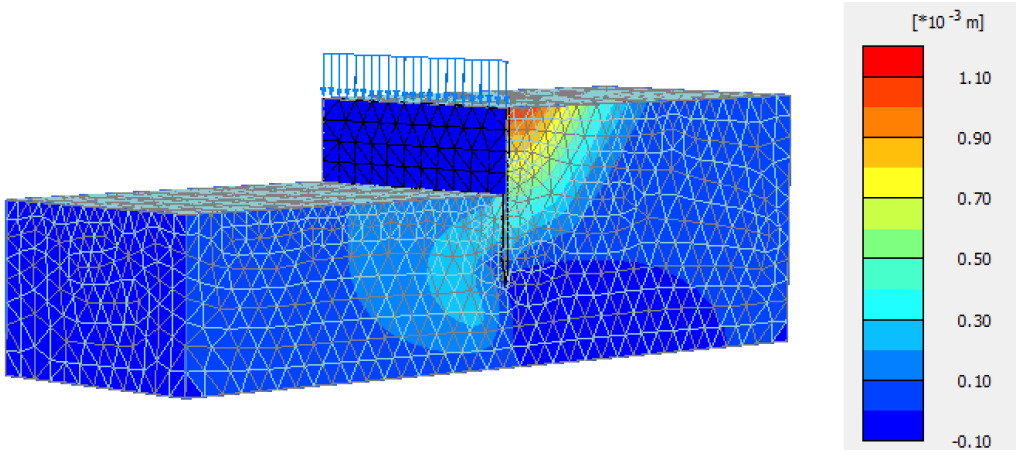

(c)

Figure 2-11. Horizontal displacement contour at last time step; (a) d/h = 3; (b) d/h =1.67; (c) d/h =1.

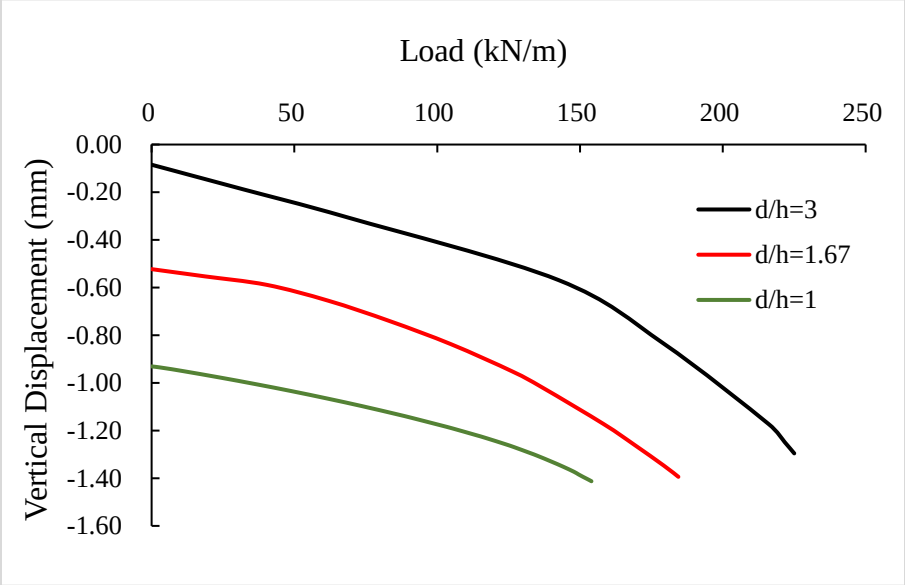

Figure 2-12. Load versus vertical displacement curve for different ratio of d/h.

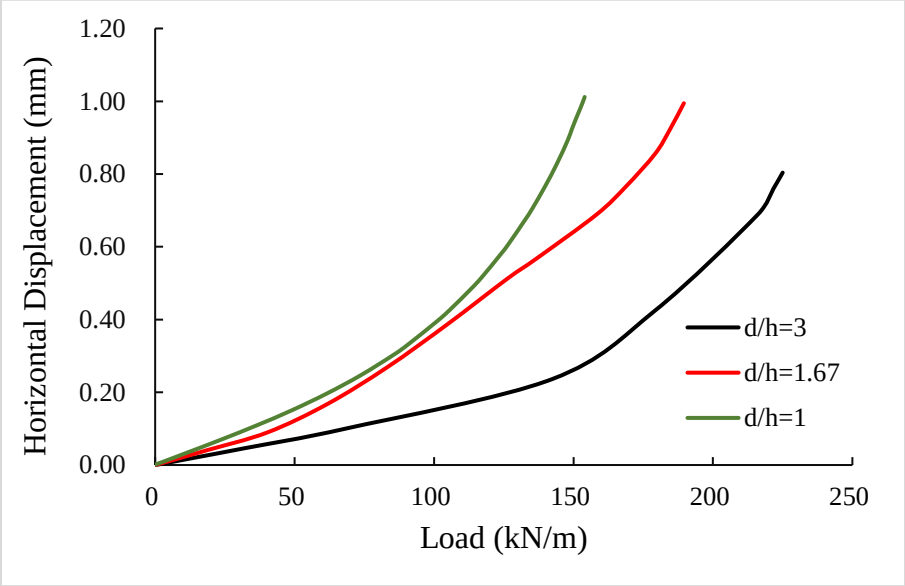

Figure 2-13. Load versus horizontal displacement curve for different ratio of d/h.

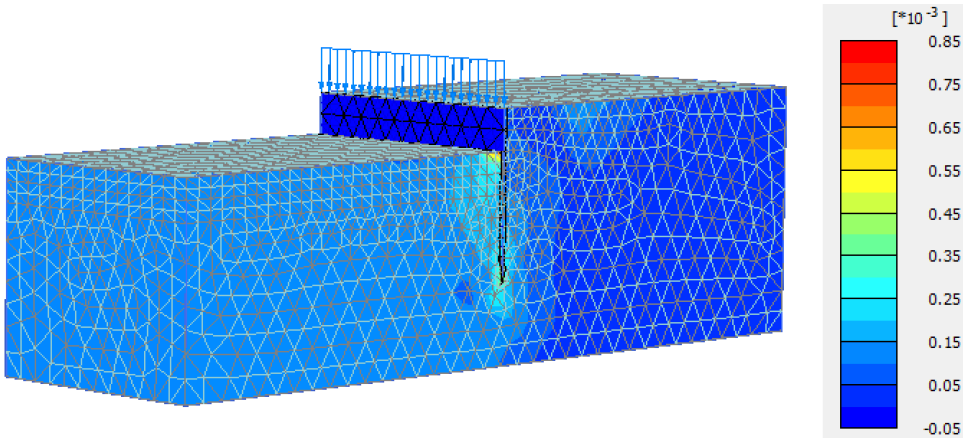

(a)

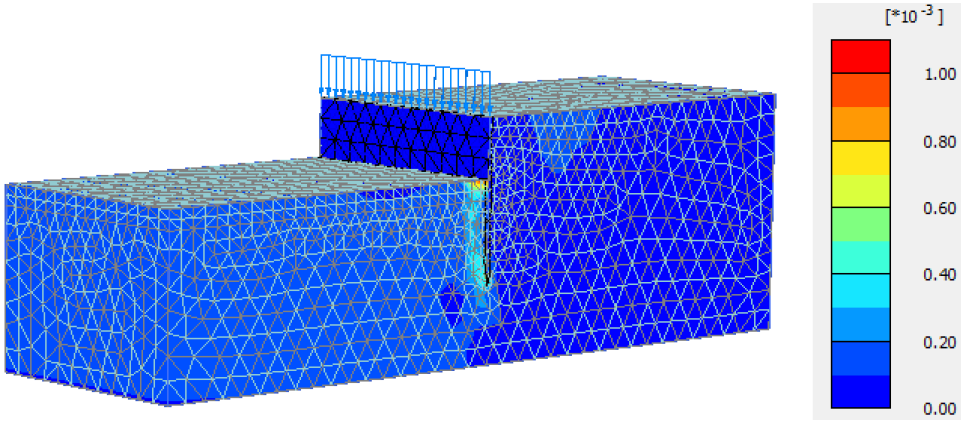

(b)

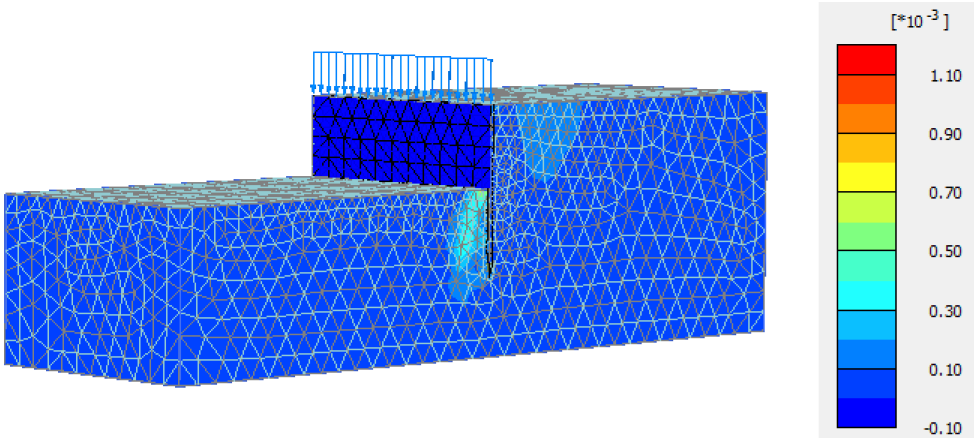

(c)

Figure 2-14. Plastic shear strain; (a) d/h = 3; (b) d/h =1.67; (c) d/h =1.

2.1.3.3 Effect of sheet pile wall stiffness

Z-shaped sheet pile profiles are commonly used in the U.S. Four commonly rolled Z-shaped sheet pile sections in the U.S. are the PZ 22, PZ 27, PZ 35, and PZ 40. Larssen type profiles are also popular U-shaped sheet piles mostly used in Europe. Both these profiles follow the concept for a "wave-shaped" profile but the Z-type shapes have the added advantage that the interlocks are formed on the outer elements of the section. Sheet pile stiffness can affect its buckling behavior under axial loading. Flexural stiffness also plays and important role in the bending moment distribution and wall deflections. Structural failure of the sheet pile elements because of the developed high stresses and formation of plastic hinges, as suggested by Eurocode 3, should be considered in design of sheet pile wall foundation systems. Through numerical modeling, the effects of flexural and axial stiffness of the sheet pile elements on their bearing capacity and deformation characteristics will be studied. In the numerical simulation, we will change the Young's modulus to study the influence of the wall stiffness on the bearing capacity. Two cases were conducted for different Young's modulus. The Young's modulus is $21 \times 10^7\ kN/m^2$ in the first case. The Young's modulus is $10 \times 10^7\ kN/m^2$ in the second case. Figure 2-15 showed the deformed vertical displacement and Figure 2-16 showed the deformed horizontal displacement contour.

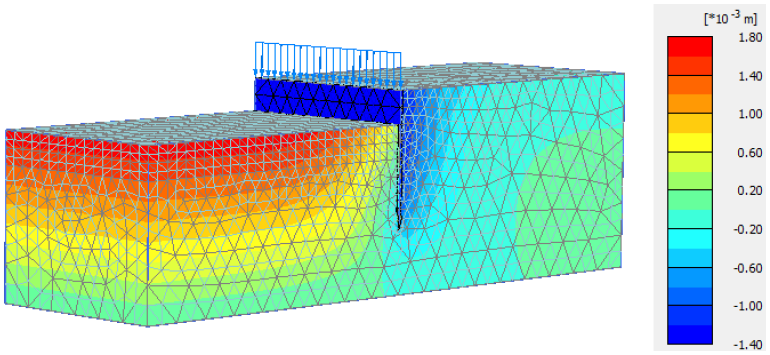

(a)

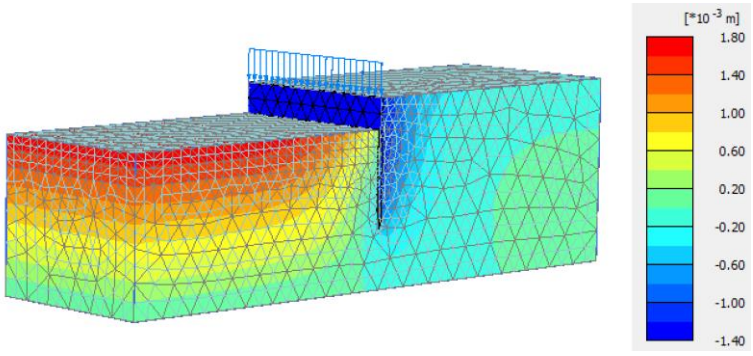

(b)

Figure 2-15. Vertical displacement contour at last time step; (a) E=21×10^7kN/m^2; (b) E=10×10^7kN/m^2.

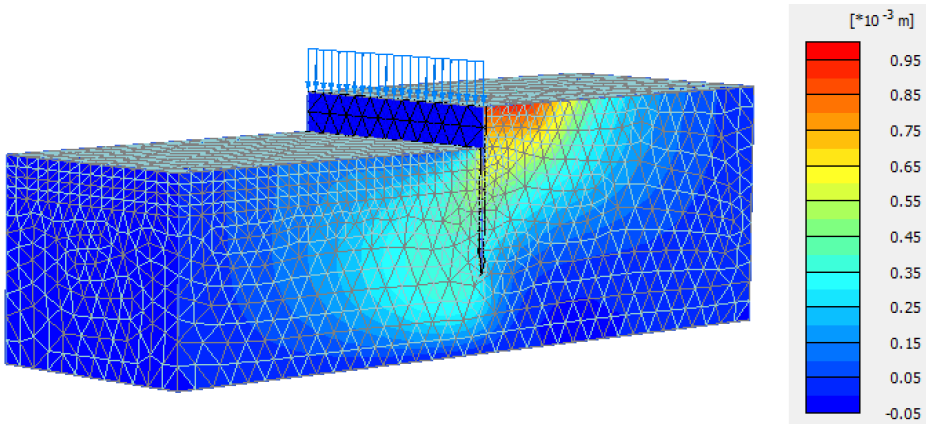

(a)

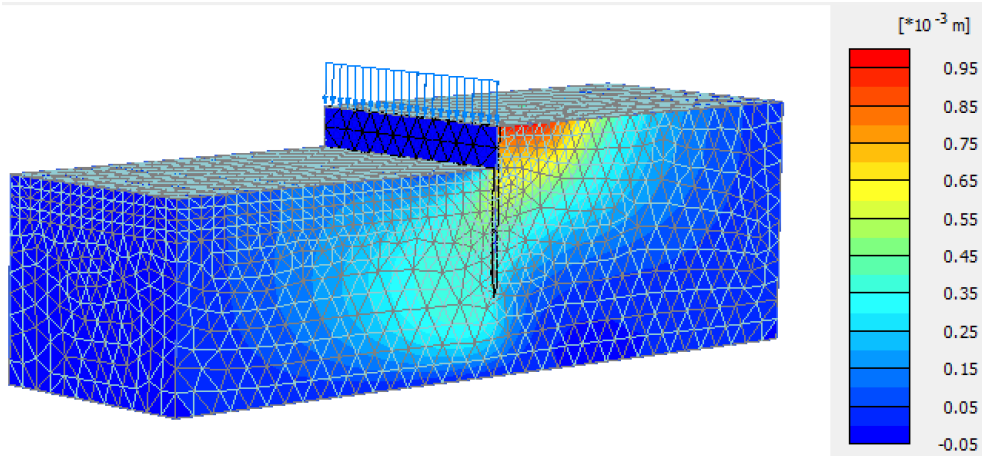

(b)

Figure 2-16. Horizontal displacement contour at last time step; (a) $E=21 \times 10^7 kN/m^2$; (b) $E=10 \times 10^7 kN/m^2$.

Figure 2-17 (a) showed the load versus vertical displacement curve and Figure 2-17 (b) showed the load versus vertical displacement curve. Figure 2-19 showed the plastic shear strain contour.

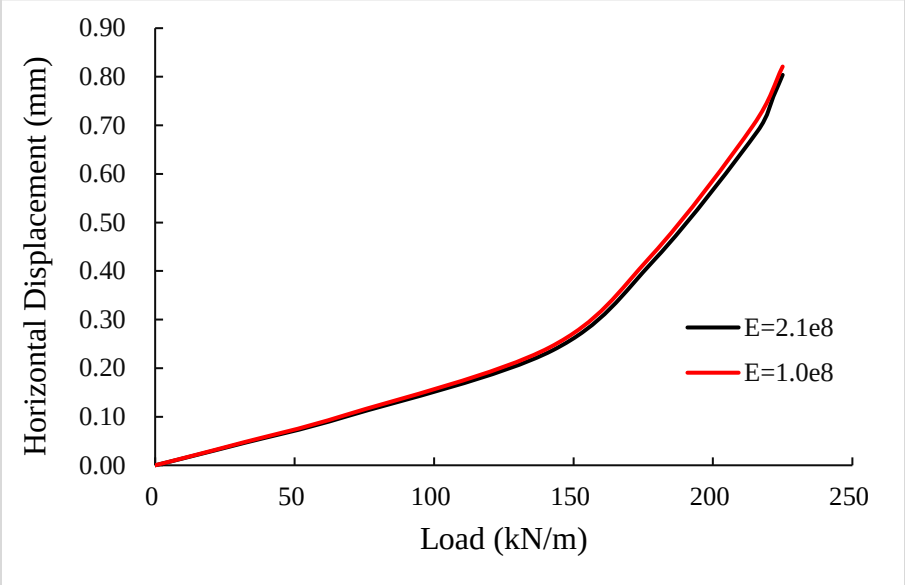

(a)

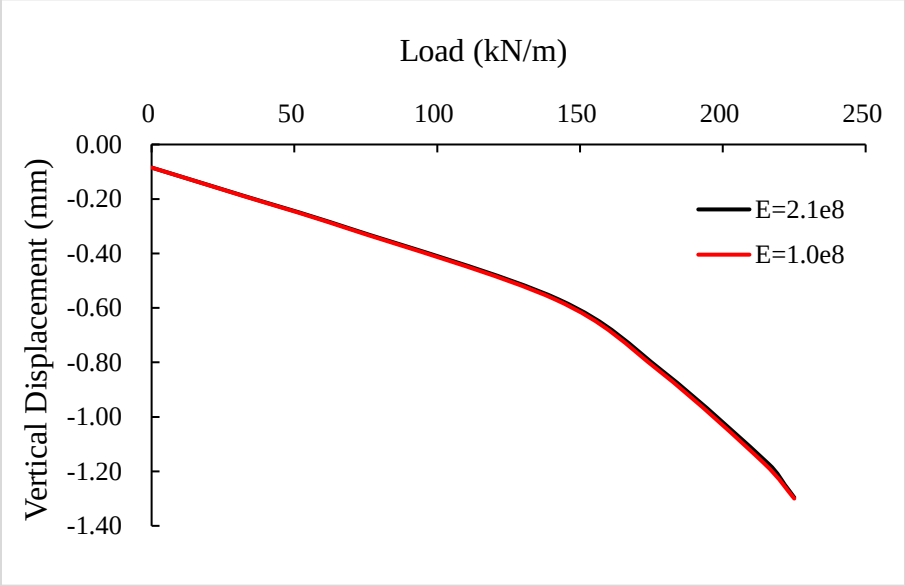

(b)

Figure 2-17. Load versus horizontal displacement curve for different Young's modulus of sheet piles.

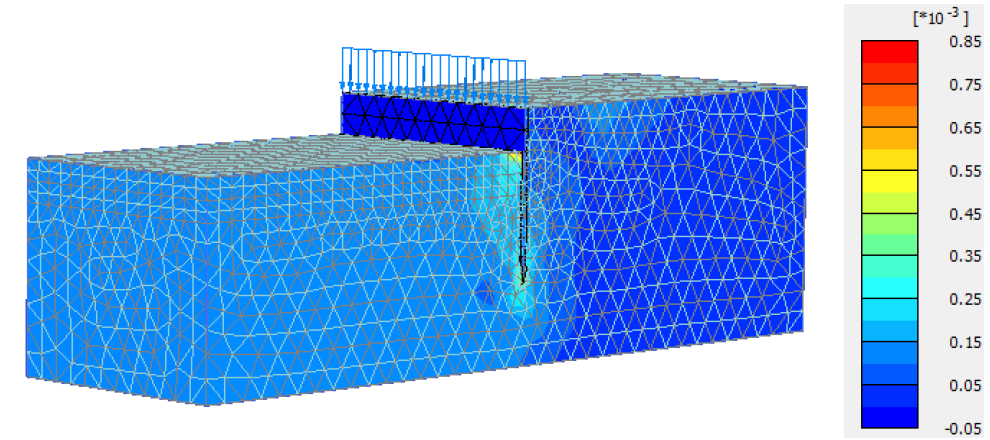

(a)

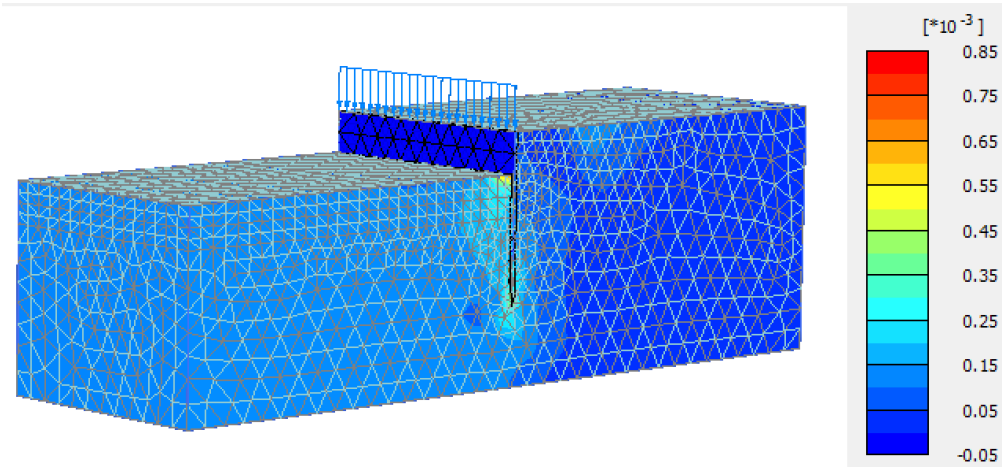

Figure 2-18
(b)

Figure 2-19. Plastic shear strain; (a) E=21 × 10^7kN/m^2; (b) E=10 × 10^7kN/m^2.

2.1.3.4 Effect of sand relative density and layering

An axially loaded sheet pile will support that load partly by shear generated over its length, due to the soil-sheet pile skin friction or adhesion, and partly by normal stresses generated at the base or tip of the sheet pile, due to end bearing resistance of the soil. The relative magnitudes of the mobilized wall friction and end bearing resistances and their ultimate values depend on the geometry of the sheet pile and the soil relative density and layering. A so-called “end bearing sheet pile” is embedded in a relatively soft layer of soil but bears on a firmer stratum. On the other hand, if no firmer layer is available on which to found the sheet pile, the sheet pile will be so called “friction sheet pile.” The effects of sand relative density and layering (e.g. dense sand layer at the sheet pile tip) on the mobilized and ultimate skin friction and end bearing of the sheet pile will be

investigated through numerical modeling. The effects of hard stratum at the tip of the sheet pile on buckling behavior, bending moment and axial force distribution of the wall will be investigated in detail through finite element analyses. Relative density of sand is defined as the ratio of the difference between the void ratio of a cohesion- less soil in the loosest state and in-situ void ratio to the difference between its void ratios in the loosest and the densest states. For the different relative density (50%, 65%, and 88%) of sand, we were changing relative density of sand from dense sand to loose sand while keeping the ratio of d/h= 3. Figure 2-20 showed the deformed vertical displacement and Figure 2-21 showed the deformed horizontal displacement contour.

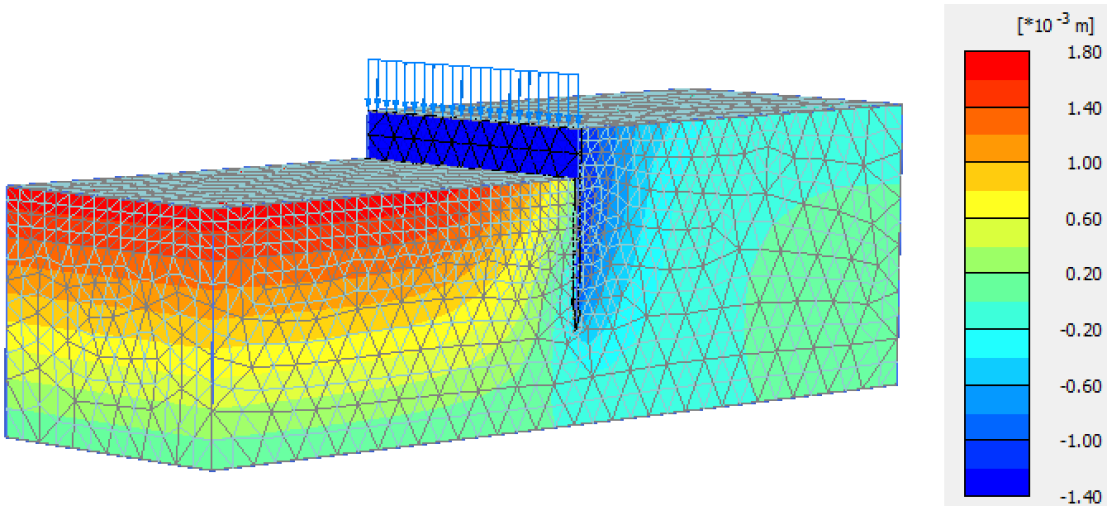

(a)

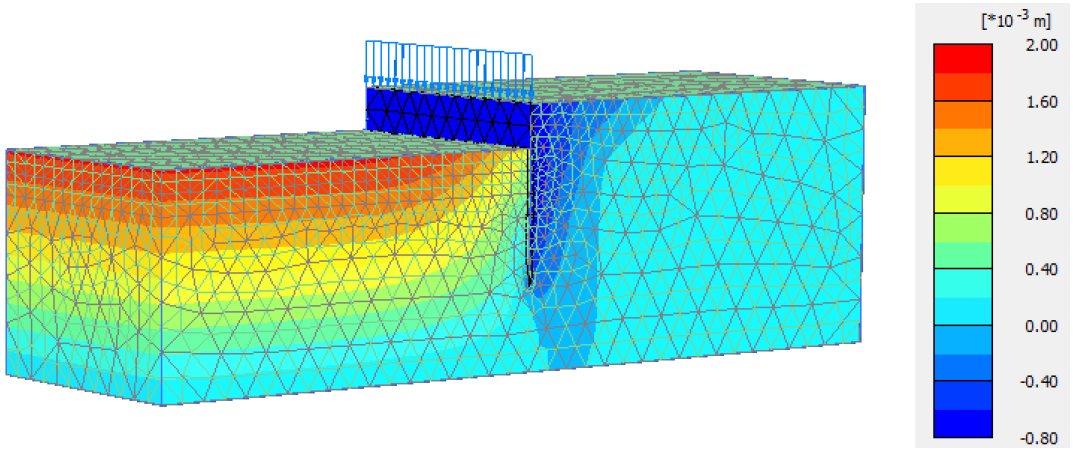

(b)

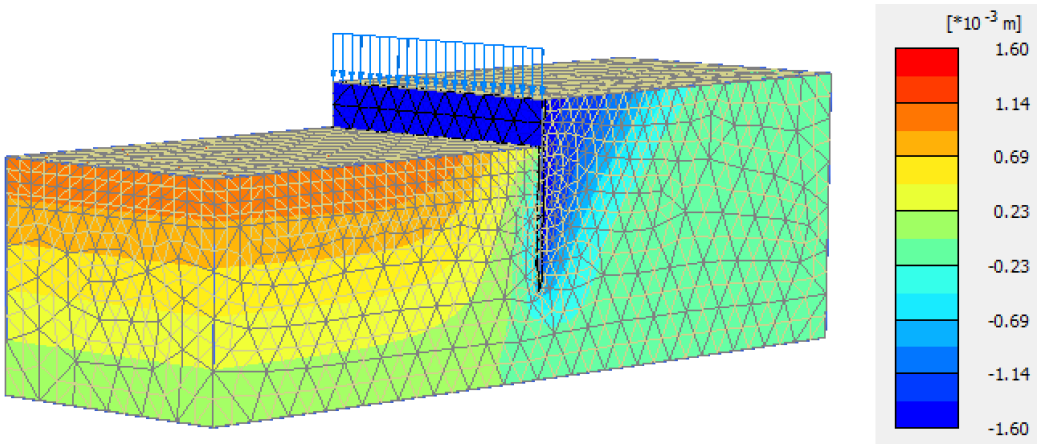

(c)

Figure 2-20. Vertical displacement contour at last time step; (a) Very dense sand; (b) Dense sand; (c) Loose sand.

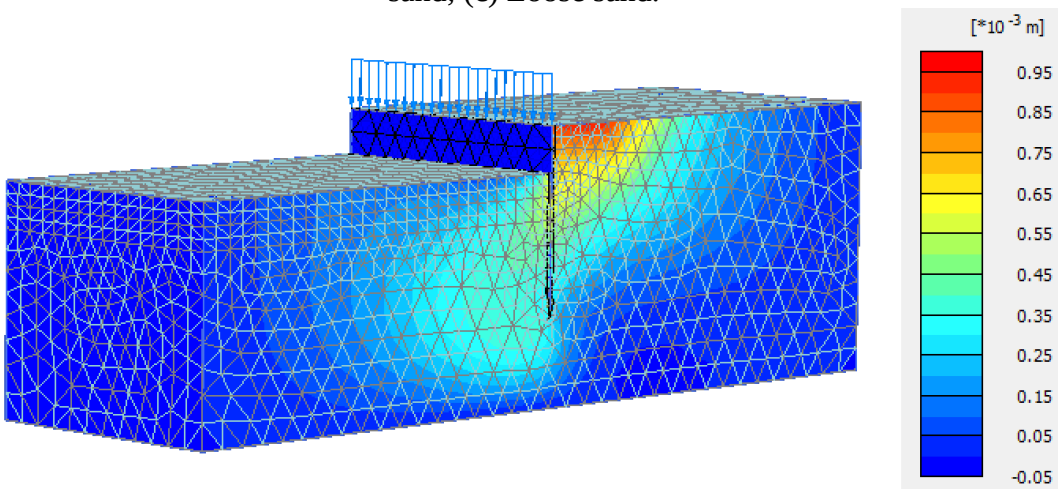

(a)

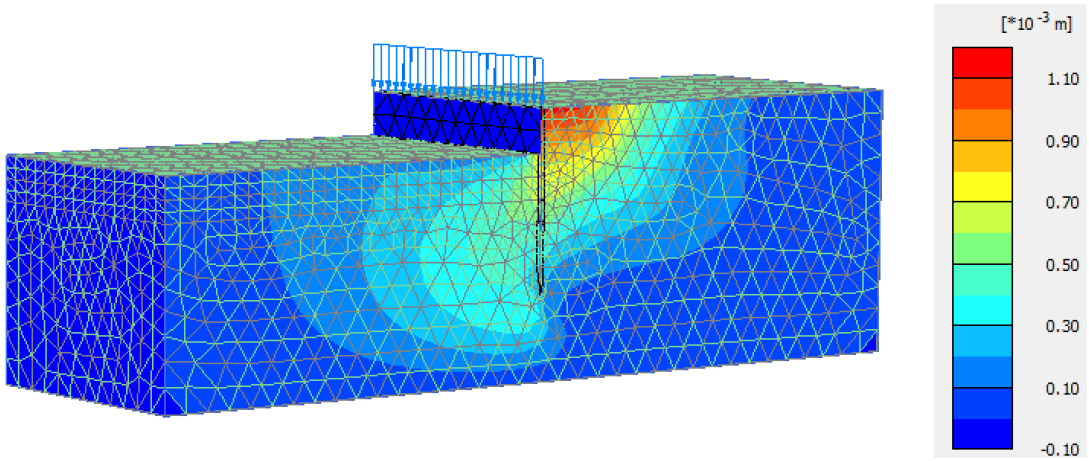

(b)

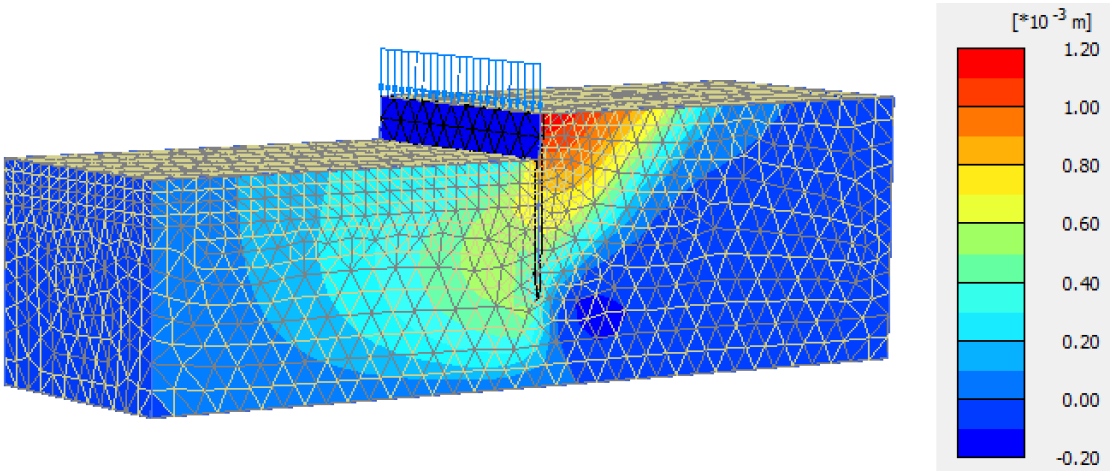

(c)

Figure 2-21. Horizontal displacement contour at last time step; (a) Very dense sand; (b) Dense sand; (c) Loose sand.

Figure 2-22 showed the load versus vertical displacement curve and Figure 2-23 showed the load versus vertical displacement curve. Figure 2-24 showed the plastic shear strain contour.

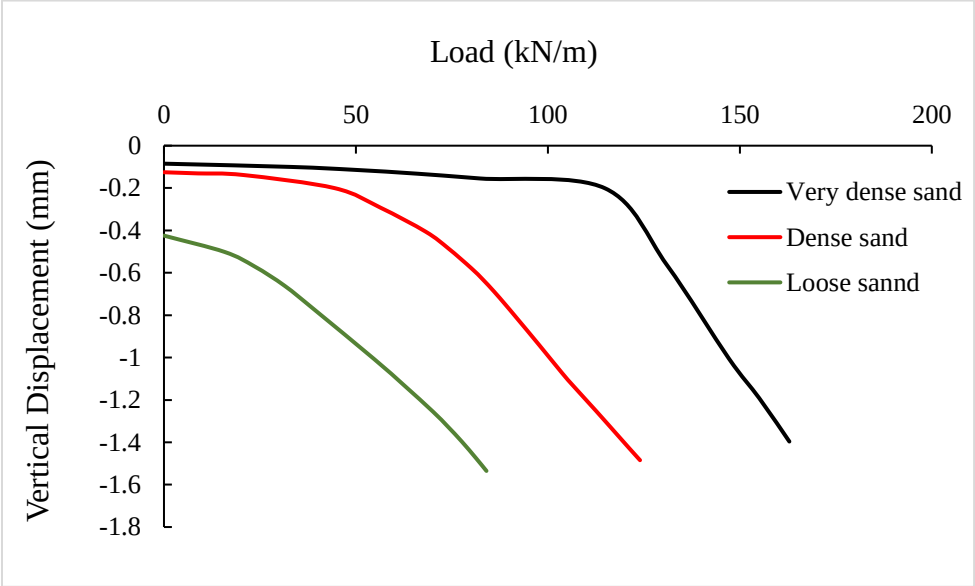

Figure 2-22. Load versus vertical displacement curve for different sands.

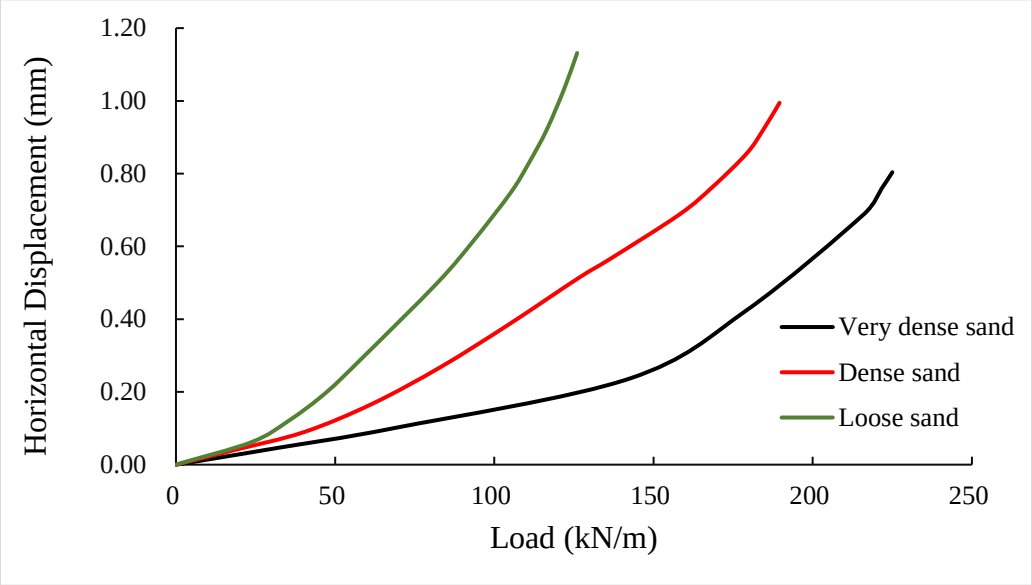

Figure 2-23. Load versus horizontal displacement curve for different sands.

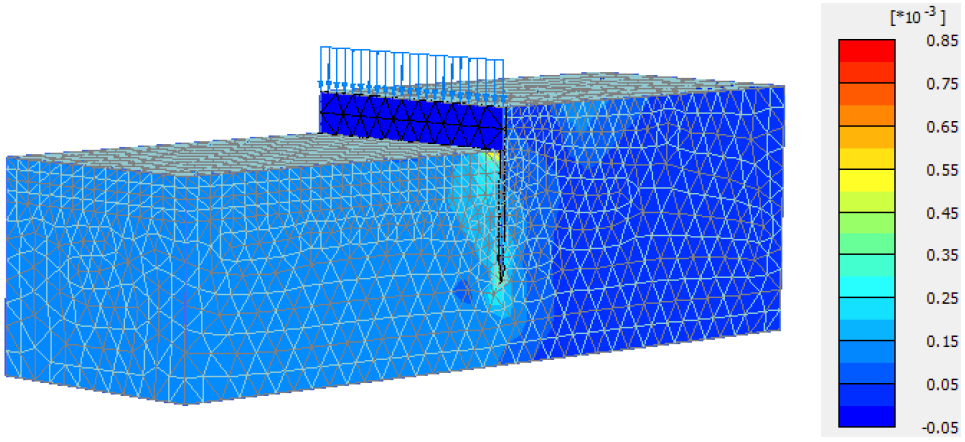

(a)

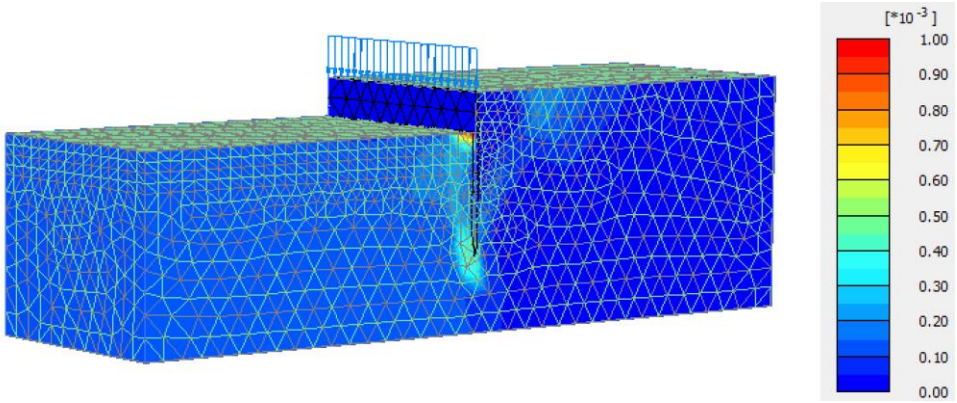

(b)

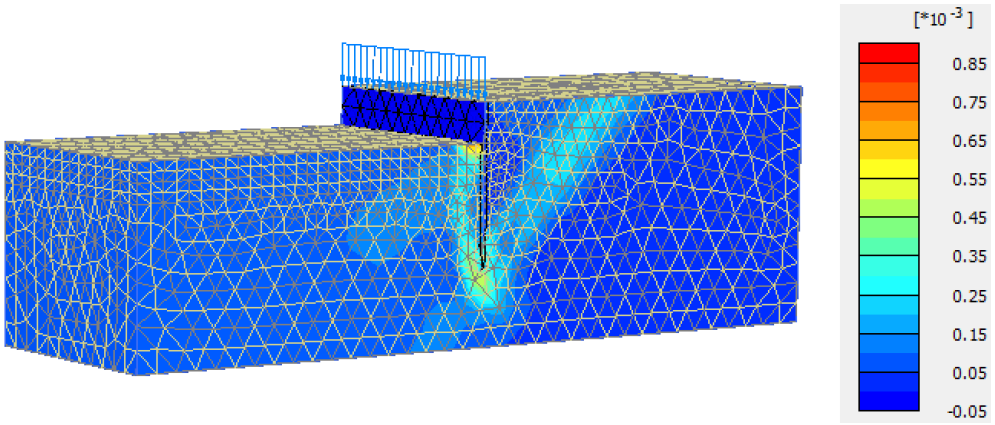

(c)

Figure 2-24. Plastic shear strain; (a) Very dense sand; (b) Dense sand; (c) Loose sand.

For the two-layer model, we were using the soil 1 (see Figure 2-8) as loose sand (relative density 50%) and soil 2 as very dense sand (relative density 88%). Figure 2-25 showed the vertical displacement and Figure 2-26 showed the deformed horizontal displacement contour. Figure 2-27 showed the bending moment of sheet pile wall and Figure 2-28 showed the axial force distribution of sheet pile wall. Figure 2-29 showed the plastic shear strain contour.

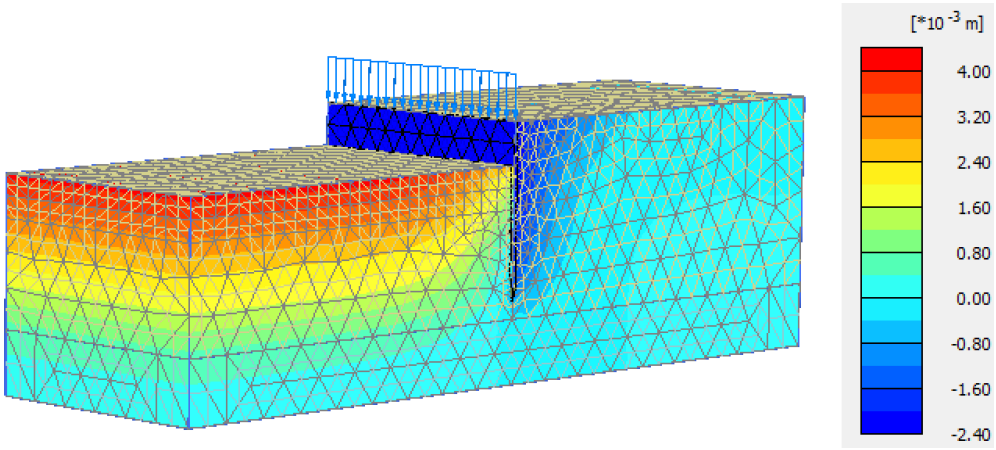

Figure 2-25. Vertical displacement contour at last time step.

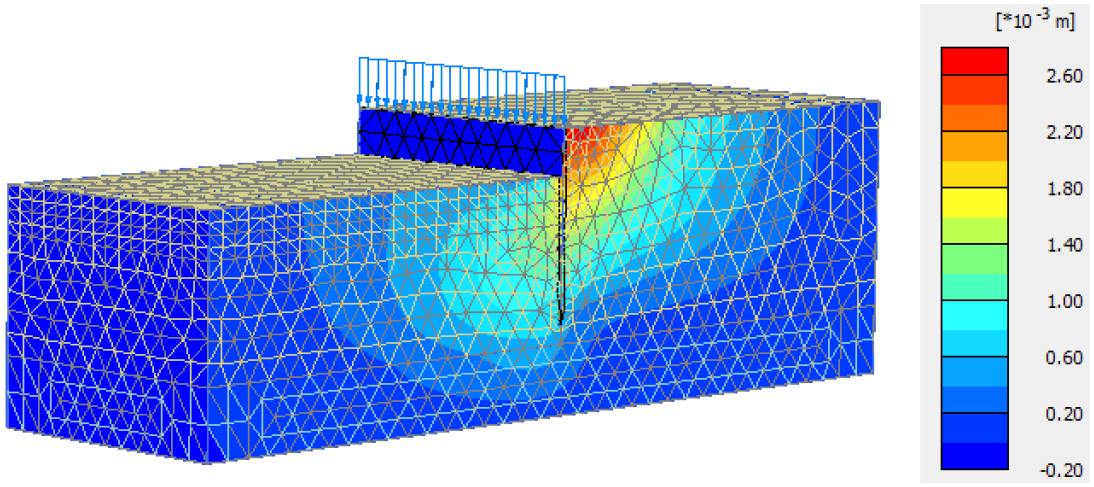

Figure 2-26. Horizontal displacement contour at last time step.

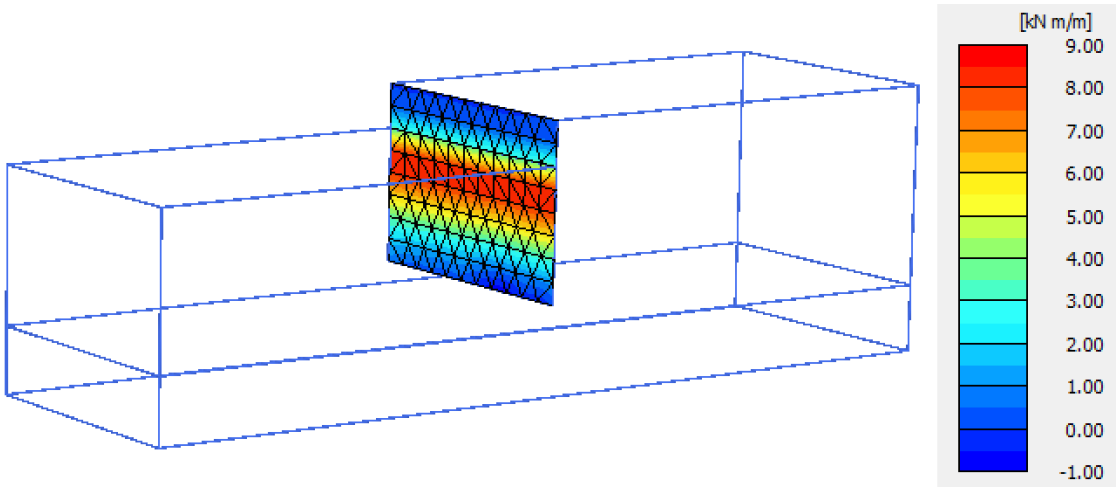

Figure 2-27. Bending moment of sheet pile wall.

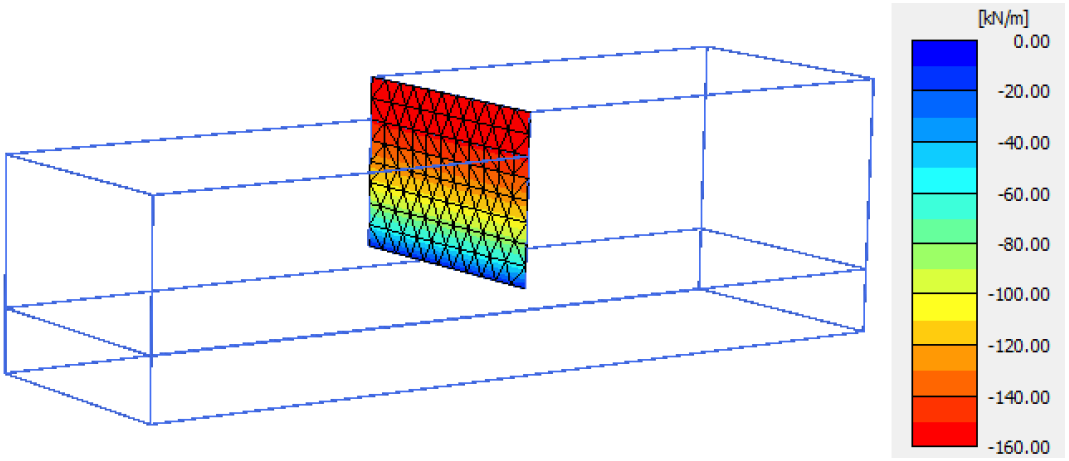

Figure 2-28. Axial force distribution of the sheet pile wall.

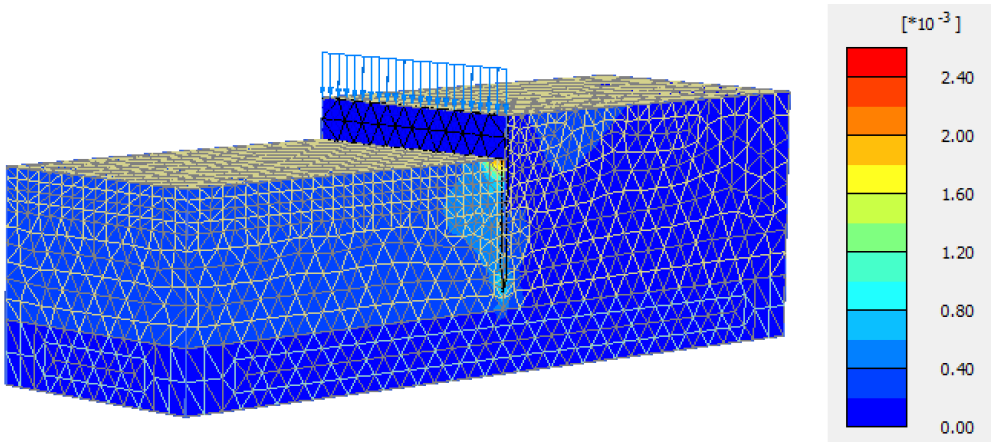

Figure 2-29. Plastic shear strain.

2.1.3.5 Effect of the sheet pile head fixity

Although in practice, the design of the sheet pile abutment to resist axial load is undertaken independently of the lateral loading case, the behavior of the soil adjacent to the wall needs to be considered as the wall displaces laterally. In a sheet pile wall with a free head condition, provided that wall tilts sufficiently, the soil on the retained side of the wall has an active earth pressure and moves down relative to the wall in order to mobilize friction in the beneficial direction (Figure 29a). On the passive side, the displaced soil has to move upward. If the axially loaded sheet pile abutment moves downward, the shaft friction on the active side will diminish. On the other hand, if the top of the sheet pile wall is restrained (e.g. by the bridge superstructure), the skin friction on both sides of the sheet pile might be considered (Figure 29b).

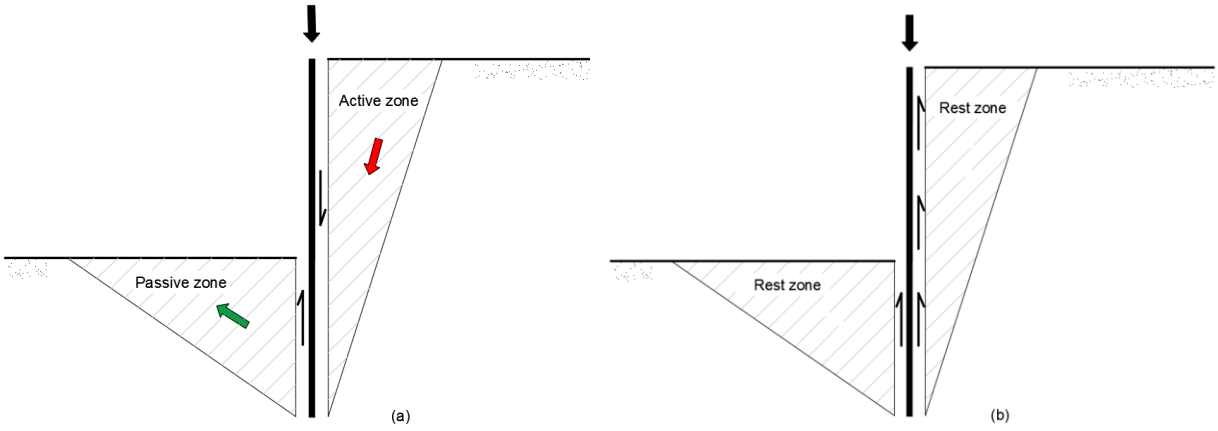

Figure 2-30. Skin friction developed in the axially loaded sheet pile: (a) free head conditions; and (b) fixed head conditions.

To study the influence of the sheet pile head conditions, we did the simulation which the pile head (Figure 8) was fixed in three directions. The soil was very dense sand (relative density is 88%). We used the same boundary conditions which were used in the previous simulations. The

following figures showed the horizontal displacement, vertical displacement and plastic shear strain. We will compare the results for the free and fixed pile head in the parametric studies of the task 2b.

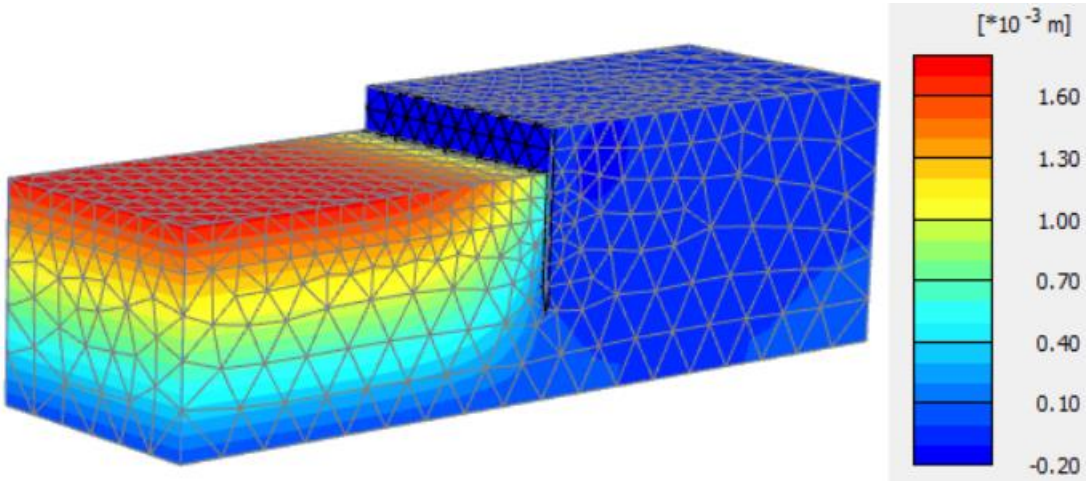

Figure 2-31. Vertical displacement contour at last time step.

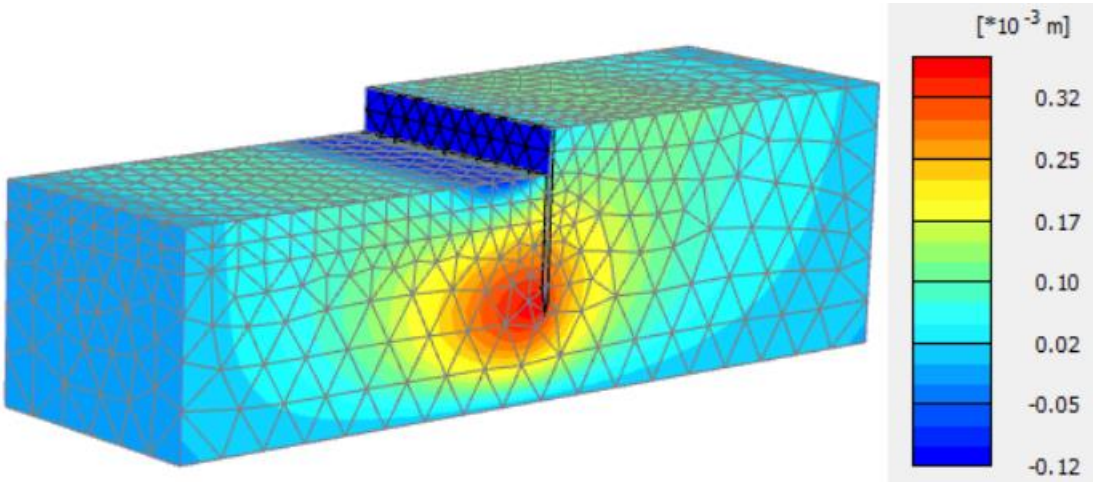

Figure 2-32. Horizontal displacement contour at last time step.

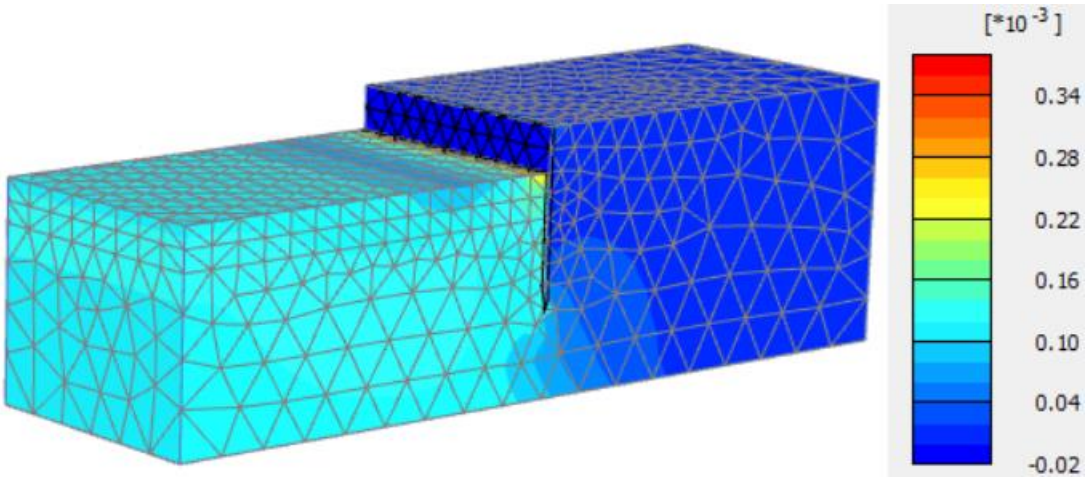

Figure 2-33. Plastic shear strain.

2.1.3.6 Effect of surcharge loading

Surcharge loads exert additional lateral pressures on the sheet pile wall system. Surcharge loads may result from traffic loads, equipment, construction materials, and other factors. Therefore, numerical modeling of axially loaded sheet pile walls at different surcharge intensities will be conducted to investigate the effect of surcharge loads on the general behavior (e.g., axial bearing capacity, lateral movement and induced bending moment) of sheet pile walls. The following two simulations showed sheet pile wall under the two different surcharge loading. The surcharge loading area (blue arrow in Figure 2-34) was 36 m^2. The soil was very dense sand (relative density is 88%) in both simulations. We used the same boundary conditions which were used in the previous simulations. The following figures showed the horizontal displacement, vertical displacement and plastic shear strain and bending moment contour of sheet pile walls.

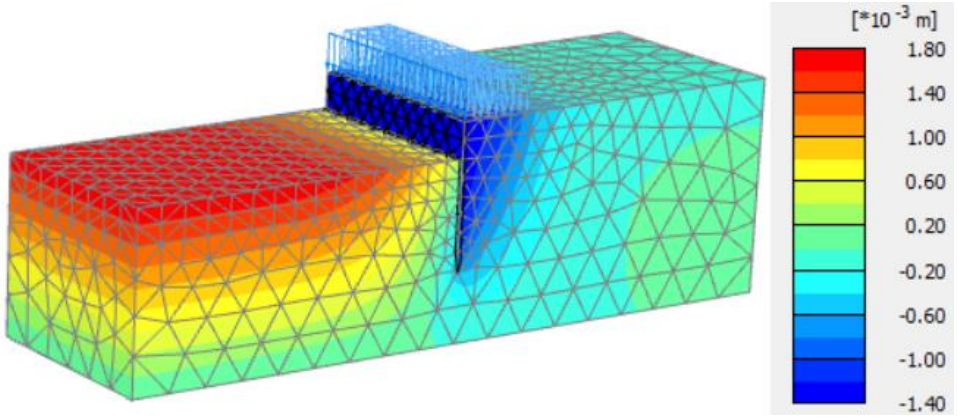

(a)

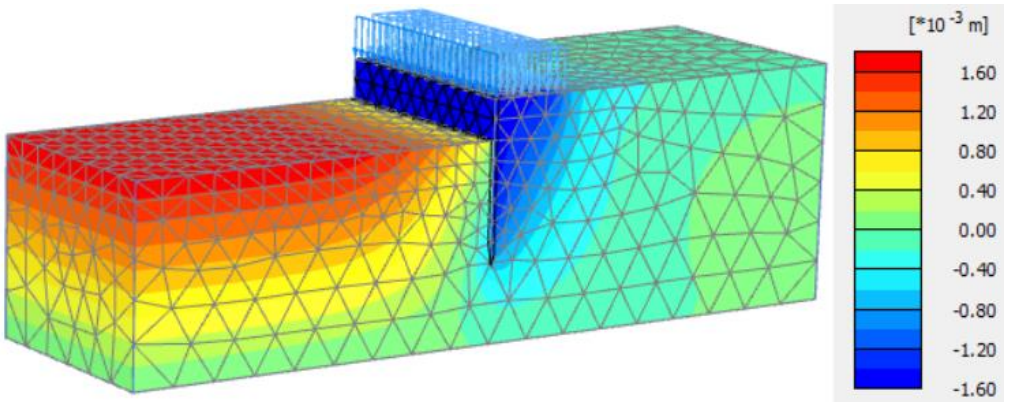

(b)

Figure 2-34. Vertical displacement contour at last time step; (a) Surcharge loading 10 kN/m^2; (b) Surcharge loading 20 kN/m^2.

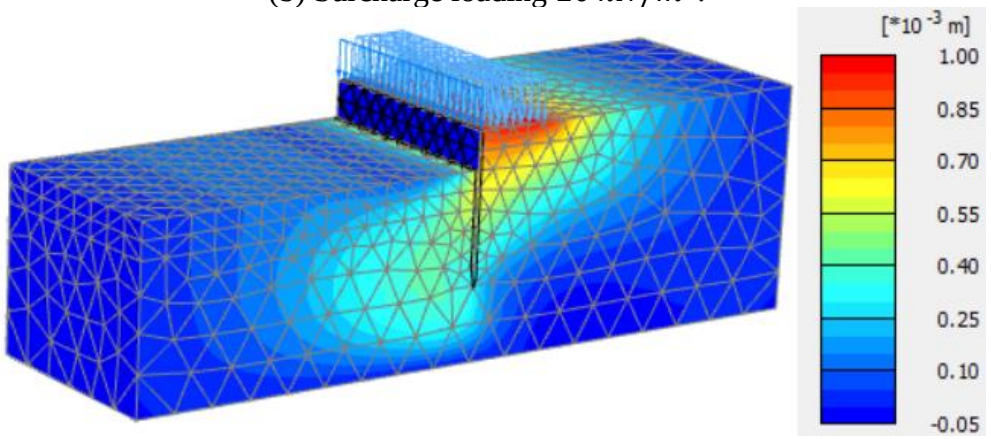

(a)

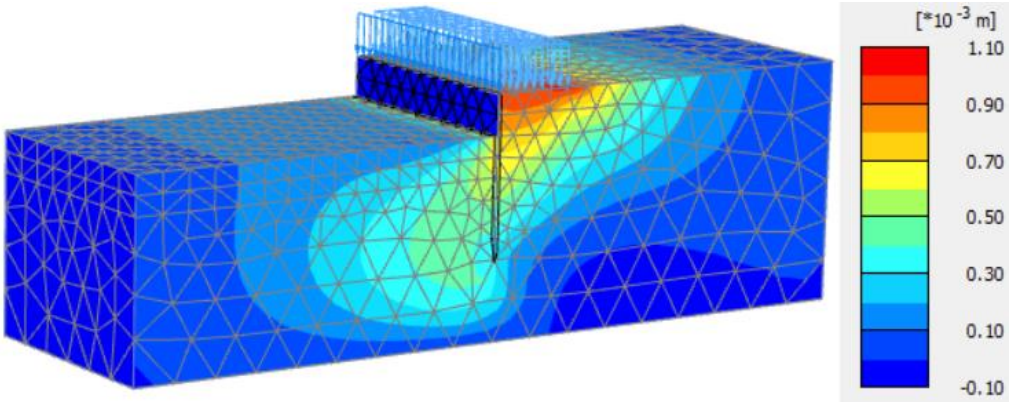

(b)

Figure 2-35. Horizontal displacement contour at last time step; (a) Surcharge loading 10 kN/m^2; (b) Surcharge loading 20 kN/m^2.

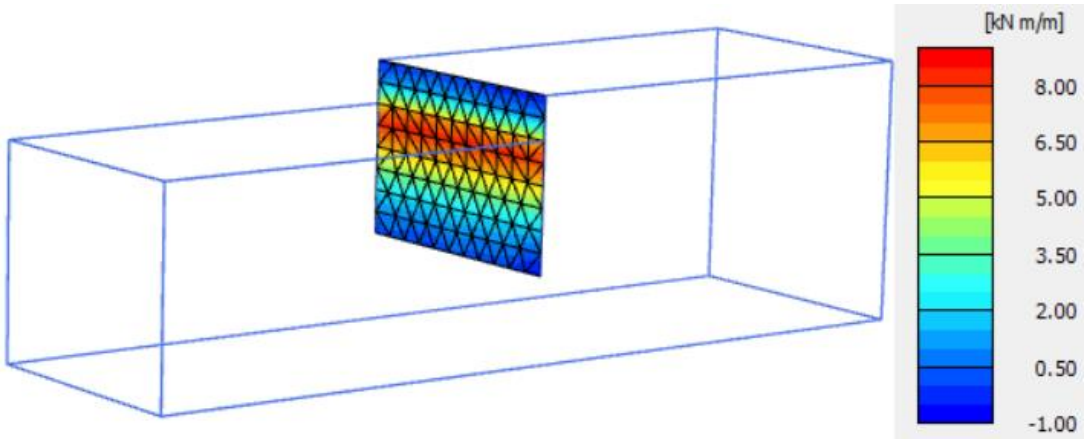

(a)

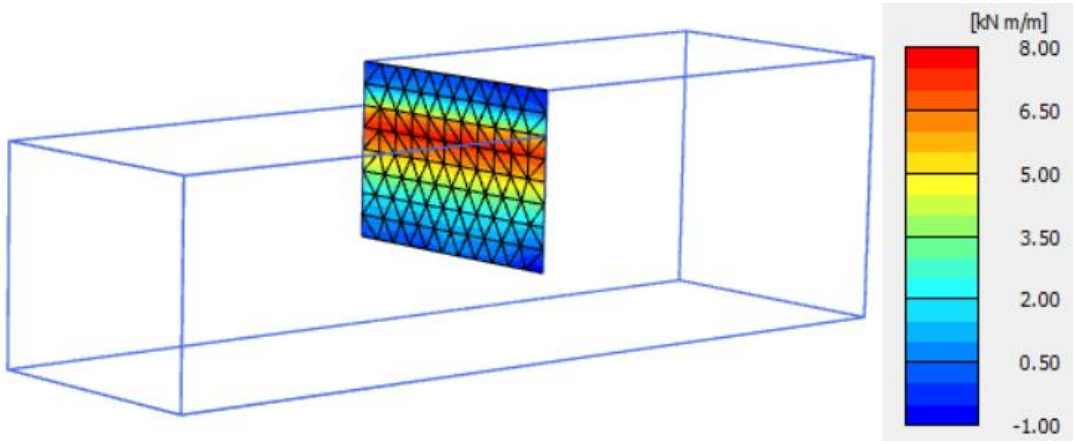

(b)

Figure 2-36. Bending moment of sheet pile wall at last time step; (a) Surcharge loading 10 kN/m^2; (b) Surcharge loading 20 kN/m^2.

2.1.3.7 Summary of the proposed scenarios for numerical analysis

Table 2 summarizes the scenarios for numerical analysis. These simulations include the validation and parametric studies. Different soil layers are considered in the simulations.

Table 2-2. Summary of scenarios for numerical analysis

		Pile Embedment	**Pile stiffness**	**Pile head constraints**	**Surcharge**	**Total cases**
One layer	**Loose**	3	3	2	2	36
	Dense	3	3	2	2	36
	Very Dense	3	3	2	2	36
Two layer	**Loose**	3	3	2	2	36
	Dense	3	3	2	2	36
	Very Dense	3	3	2	2	36
					Sum	216

2.1.3.8 Products of numerical analysis

Numerical analyses are expected to provide the relationships between the axially loaded sheet pile wall response and variable parameters including sheet pile free length, sheet pile embedment depth, sheet pile stiffness, and the surcharge. A rational relation for determining the ultimate axially loaded sheet pile walls at different parameters and factors identified above, for instance, the axial load - vertical displacement relationship for sheet pile walls.

2.2 Task 2b: Parametric studies of bearing capacity of cantilever steel sheet piles

For this project, a commercial nonlinear finite element analysis tool (PLAXIS 3D) for geotechnical engineering is adopted to conduct the major numerical analysis detailed in the following sections. Figure 2-37 shows the finite element model for the soil-pile interaction problem under 3D condition. Upon completion of the project, a step-by-step guideline for modeling and analyzing the behavior of axially loaded sheet piles using PLAXIS 3D is presented.

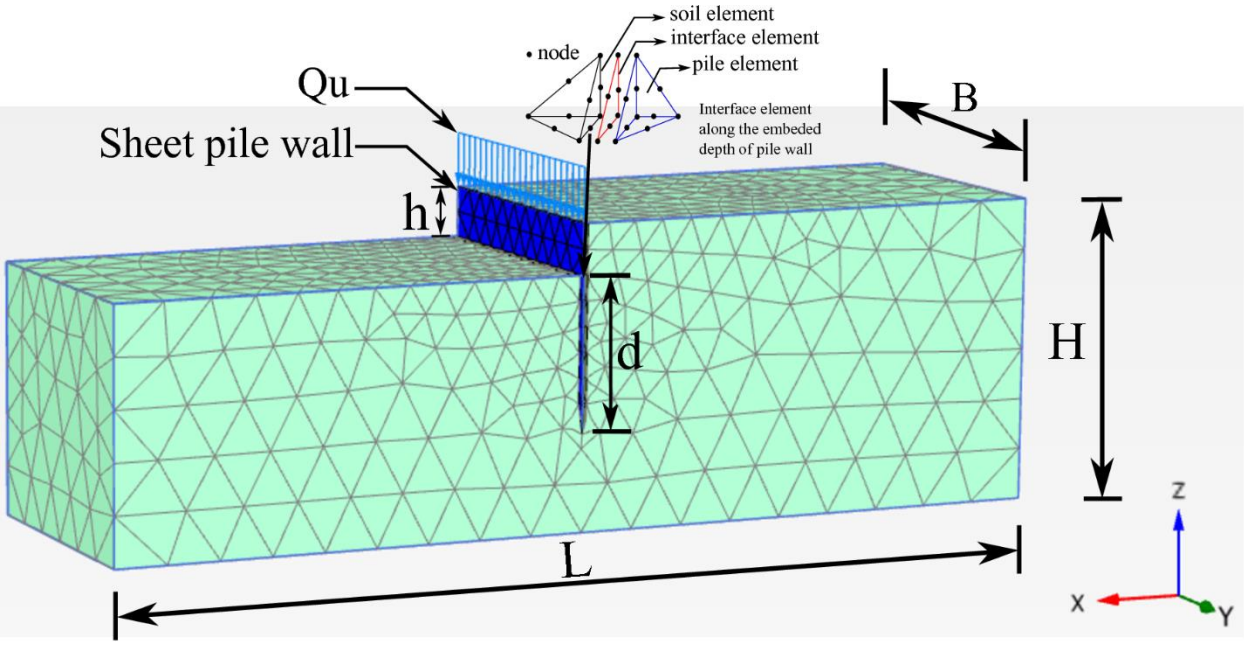

Figure 2-37. Mesh, soil-pile interaction elements, and the finite element model under 3D condition.

2.2.1 Nonlinear finite element program

2.2.1.1 Models for soil, sheet pile, and soil-sheet pile interface

In the numerical model, sands are represented by ten-node tetrahedral elements and a four-point Gaussian integration rule is utilized to calculate the element stiffness matrix. The mechanical behavior is modeled by the elastoplastic Mohr-Coulomb model. The five essential parameters of the Mohr-Coulomb model are Young's modulus, Poisson's ratio, cohesion, friction angle, and dilation angle. These parameters are determined from the basic laboratory tests on soil samples such as direct shear tests and triaxial compression tests. These parameters are compared to typical values for loose, dense sands and very dense sand for the parametric studies reported here.

In the numerical model, the steel sheet pile wall is characterized as a strip pile wall available in PLAXIS3D. A ten-node tetrahedral plate element (Figure 2-37) is used to model the pile wall as a sheet pile wall. The finite element model for the problems under investigation is shown in Figure 2-41. We define the same boundary conditions in all simulations. The bottom surface is fixed in the x-, y- and z- directions. The front and back surfaces are fixed in the y-direction and the left and

right surfaces are fixed in the x-direction. Note that the cluster embracing the pile wall is introduced to prepare for a simple mesh optimization with the use of the refined cluster option for the mesh generation. Interface elements (Figure 2-37) based on the Coulomb's friction law are used to simulate soil-pile wall interaction in terms of slippage at interface surface. An elastic model is used to describe the mechanical behavior of the interface element for modeling the soil-structure interaction. The interface strength is taken as a rigid type between sands and steel piles. The interface elements are connected soil elements and plate elements by six nodes. The stiffness matrix for interface elements is obtained by using Newton–Cotes integration points. The interface friction angle and adhesion are modeled by assigning a suitable value for the strength-reduction factor at the interface compared with the corresponding soil strength. The Coulomb criterion is used to distinguish between elastic behavior, where small displacements can occur with the interface, and plastic interface behavior (slip). The material properties used in the FE analysis are listed in Table 2-3. FE analyses are carried out by applying vertical incremental loads on the top of the pile wall. The staged construction feature in PLAXIS 3D is used to simulate real-time construction and excavation processes by activating and deactivating the soil cluster, application of loads, and installation of the pile wall. For instance, the excavation on one side of the wall is carried out using this staged construction option in the calculation phase by deactivation at a given depth of soil cluster in each stage, one after the other, until the pile wall system reaches failure under the applied axial load.

Table 2-3. Material properties used in the finite element simulations

Parameter	Sheet pile	Very dense sand	Dense sand	Loose sand	Interface elements
Material model	Elastic	Mohr-Coulomb	Mohr-Coulomb	Mohr-Coulomb	Mohr-Coulomb
Young's modulus	438594.12 ksf	2360.1 ksf	2360.1 ksf	2360.1 ksf	2360.1 ksf
Cohesion	-	0	0	0	0
Poisson ratio	0.25	0.3	0.3	0.3	0.3
Friction angle	-	35	32	27	25

2.2.1.2 Sheet pile wall settings

The sheet pile wall is modeled as linear-elastic and can therefore never go to failure. To simulate retaining structures, PLAXIS 3D uses the construction element "Plate". To get a satisfying behavior of the sheet pile wall in three dimensions, the behavior in different directions must be realistic. Since a pile wall element for practical reasons must be drawn as a straight line, its "Z type" shape must be simulated using anisotropic material properties. This will give the sheet pile wall different flexural rigidity in different directions. In PLAXIS 3D, the element "Plate" could

have anisotropic properties. So the challenge is to find the properties that would simulate a realistic behavior of the sheet pile wall to be used in the soil/structure model in the parametric studies. This means that the properties of the "Z type" sheet pile wall with its anisotropic geometry must be transformed to a wall with isotropic geometries and anisotropic properties. The procedure for doing this is discussed in the following section. The local system of axis and properties in all directions are shown in Figure 2-38. The sheet pile wall (Plate element) parameters in PLAXIS 3D is presented in Table 2-4.

Table 2-4. Material properties for the sheet pile wall with linear elastic behavior.

Parameters	Unit	Definition
d, thickness	ft	The cross-section area of the wall across its major axial direction per 1 ft width
E_1, Young's modulus	lb/ft^2	Modulus of elasticity in first axial direction
E_2, Young's modulus	lb/ft^2	Modulus of elasticity in second axial direction
G_{12}, Shear modulus	lb/ft^2	In plane shear modulus
G_{13}, Shear modulus	lb/ft^2	Out-of-plane shear modulus related to shear deformation over first direction
G_{23}, Shear modulus	lb/ft^2	Out-of-plane shear modulus related to shear deformation over second direction

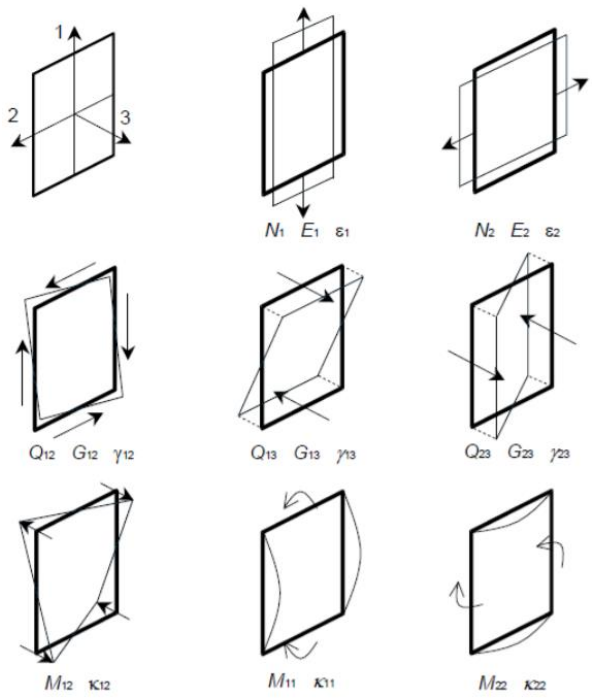

Figure 2-38. The local system of axes in the plate (sheet pile wall) element and various quantities.

The flexural rigidities must be found in each direction. For a sheet pile wall, bending around the first and the second axis is of most importance, together with the resistance against torsion. To describe this, each column of Figure 2-38 shows parameters that affects the flexural rigidity in each direction. The procedure for determine these is described under the following sections.

The flexural rigidity around the first axis

The flexural rigidity around the first axis is usually important in a 3D analysis. The parameters are described in Figure 2-39.

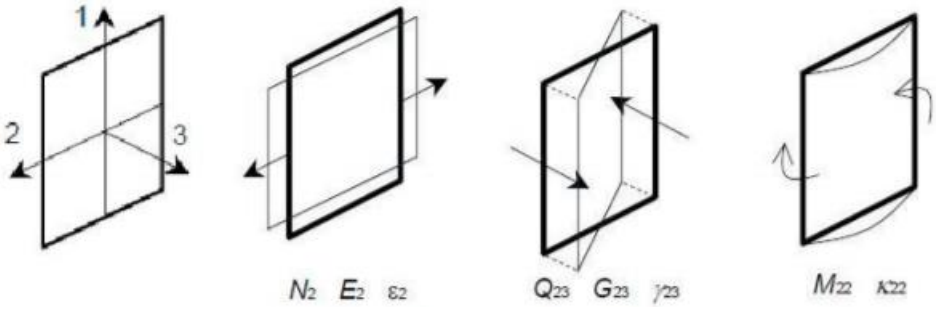

Figure 2-39. Definition of the parameters describing flexural rigidity around the first axis.

The flexural rigidity in this direction is determined by E_2 and G_{23} and is defined in Equation (1.1) and (1.2). These equations are according to PLAXIS 3D user manual.

$$E_2 = \frac{12E_{steel} \cdot I_2}{d^3} \tag{1.1}$$

$$G_{23} = \frac{E_{steel} \cdot A_{23}}{2(1+\nu)d} \tag{1.2}$$

where A_{23} is effective against shear deformation over the horizontal direction and is 1/10 of the value of A, (Brinkgreve, 2012). According to PLAXIS user manual, I_2 can be defined as $I_1/20$. This recommendation can be questioned since the flexural rigidity in this direction is much weaker. The flexural rigidity is also influenced by the interaction between the single sheet piles. Slip in the interlocks makes the wall much weaker compared to a solid wall and this effect is hard to estimate. Also assumptions regarding angle displacement in the interlocks will affect the behavior. If not weld, which usually is the case, sliding is only prevented by friction in the interlocks, and the friction coefficient is unknown. Even if the interlocks are welded the stiffness is hard to estimate.

The flexural rigidity around the second axis

The flexural rigidity around the second axis is also important in a 3D analysis. The parameters are described in Figure 2-40.

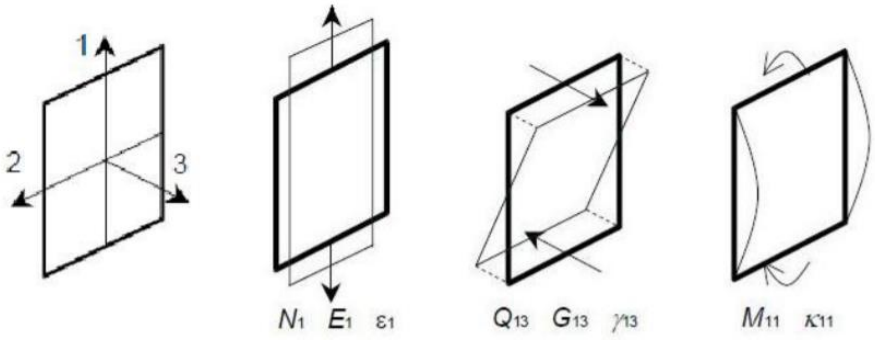

Figure 2-40. Definition of the parameters describing flexural rigidity around the second axis.

When subjected to a moment force, M_{11}, the resistance is determined by Young´s modulus E_1 and the shear modulus G_{13}.

$$E_1 = \frac{12E_{steel} \cdot I_1}{d^3} \tag{1.3}$$

$$G_{13} = \frac{E_{steel} \cdot A_{13}}{2(1+\nu)d} \tag{1.4}$$

where I_1 is the moment of inertia around the second axis. A is the cross-section area per 1 foot wall that is effective against shear forces. These two properties can be found in specifications from manufactures. For A_{13}, which is working over the vertical direction, the value is approximated to 1/3 of A. In three dimensions the behavior of the wall is much more complex, and more material parameters are needed to describe the behavior.

2.2.2 Parametric studies in uniform soil

Key parameters and factors at the design stage that can affect the axial loading capacity of steel sheet pile foundations include wall free length and wall embedment depth (the ratio of d/h), wall stiffness, soil properties (e.g., relative density) and layering, boundary conditions of the pile head (i.e. free or fixed), and general stability and buckling instability.

This section states the scenarios to be investigated by numerical modeling. The material properties are same as the ones used for the validation simulations (Table 1). The section modulus of sheet pile wall is 30.2 in^3/ft. Figure 8 shows a generic numerical model for the simulations. For all simulations, the displacements are prescribed zero in all x-, y- and z-directions at the bottom surface. The side surfaces are fixed in the lateral directions and are free to move in the vertical direction. The total simulation time (or load steps) of each case is 1000 s.

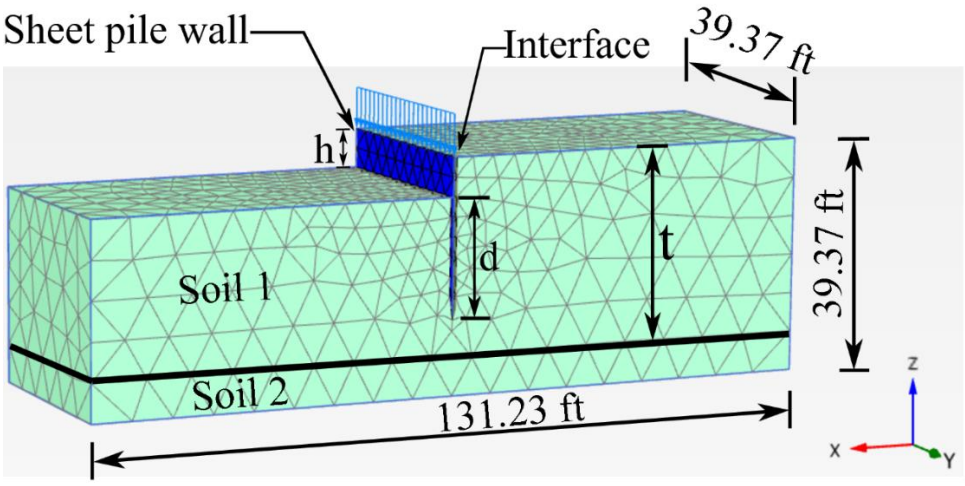

Figure 2-41. 3D sheet pile wall-soil interaction finite element model.

2.2.2.1 Effect of penetration depth and unsupported length

The passive resistance of the soil in front of the wall provides stability for the cantilever sheet pile walls against lateral earth pressure. For a sheet pile wall under lateral earth pressure, if a structural failure does not occur, a cantilever sheet pile wall of penetration (d) will fail as a rigid body by rotation about an axis lying in the plane of the wall at an unknown distance below the level of the excavation. Through performing numerical modeling, the effects of unsupported length and penetration depth on the axial behavior of sheet piles is studied. We have simulated three different ratios of d/h to study the effect of the penetration depth of the pile wall on the ultimate axial capacity of the system for one-layer soils. Three different (friction angle) soils are simulated in the following three cases. The retained height of soil (h), is varied from 6.56ft to 13.12 ft. Thus, the range of d/h from 3 to 1 are adopted. The material properties are shown in Table 2-3.

In the first case, we conduct the simulation for the very dense sand. Figure 2-42 shows the load versus vertical displacement curve. Figure 2-43 plots the load versus horizontal displacement curve for the pile wall at three different ratios of d/h. Figures 6 and 7 show that the ultimate axial sheet

pile wall capacity increases with an increase of the pile penetration depth. Finally, the contours of the computed plastic shear strains for a loading state are shown in Figure 2-44. The rupture surface (shear failure) is developing front interface between the pile wall and soil and to the bottom of the pile wall.

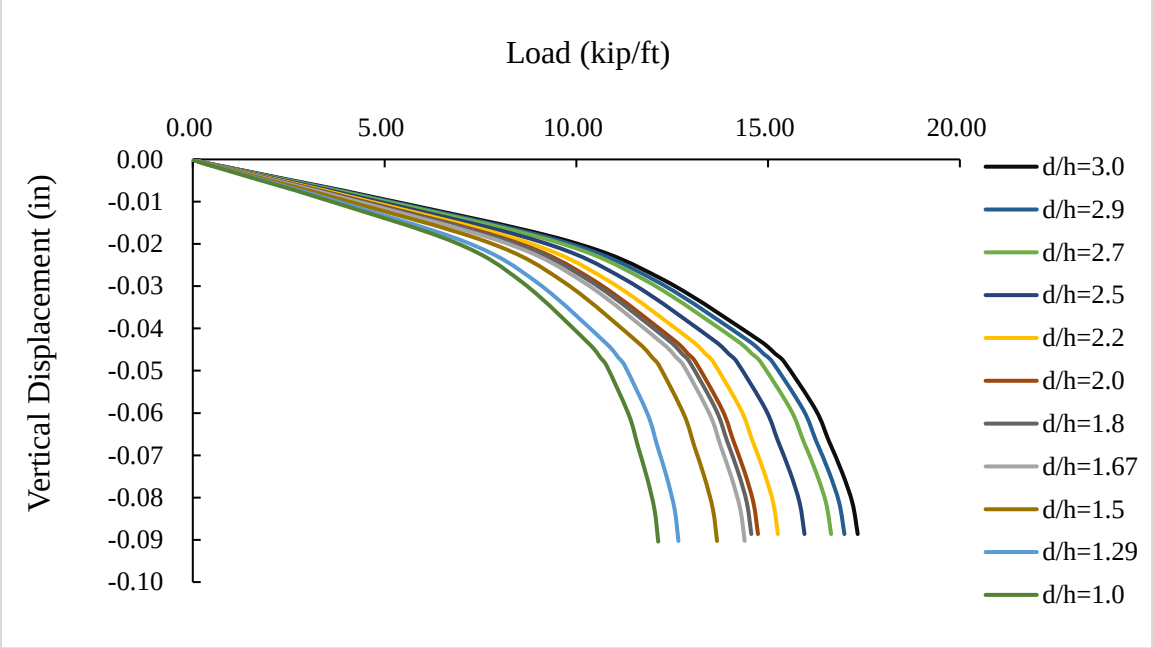

Figure 2-42. Load versus vertical displacement curve of very dense sand for different ratio of d/h.

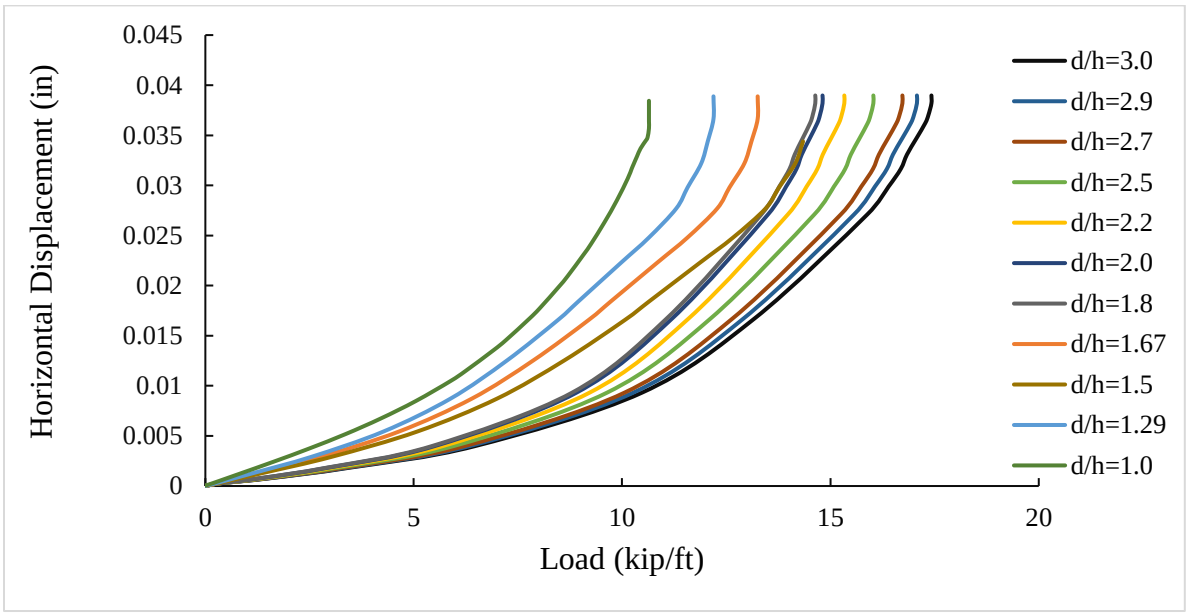

Figure 2-43. Load versus horizontal displacement curve of very dense sand for different ratio of d/h.

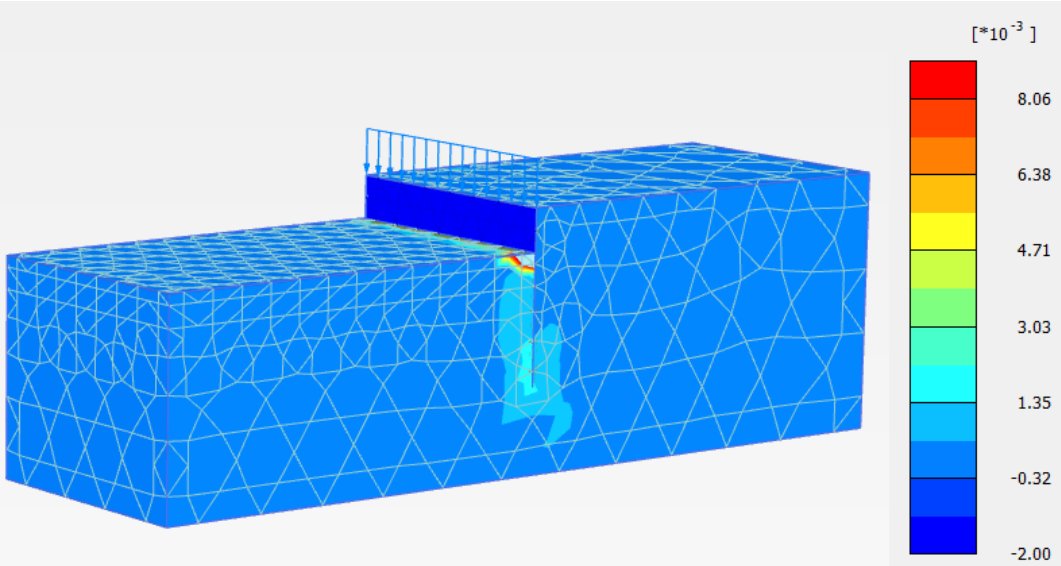

Figure 2-44. Contour of plastic shear strain of very dense sand d/h = 3 at vertical displacement 0.09in.

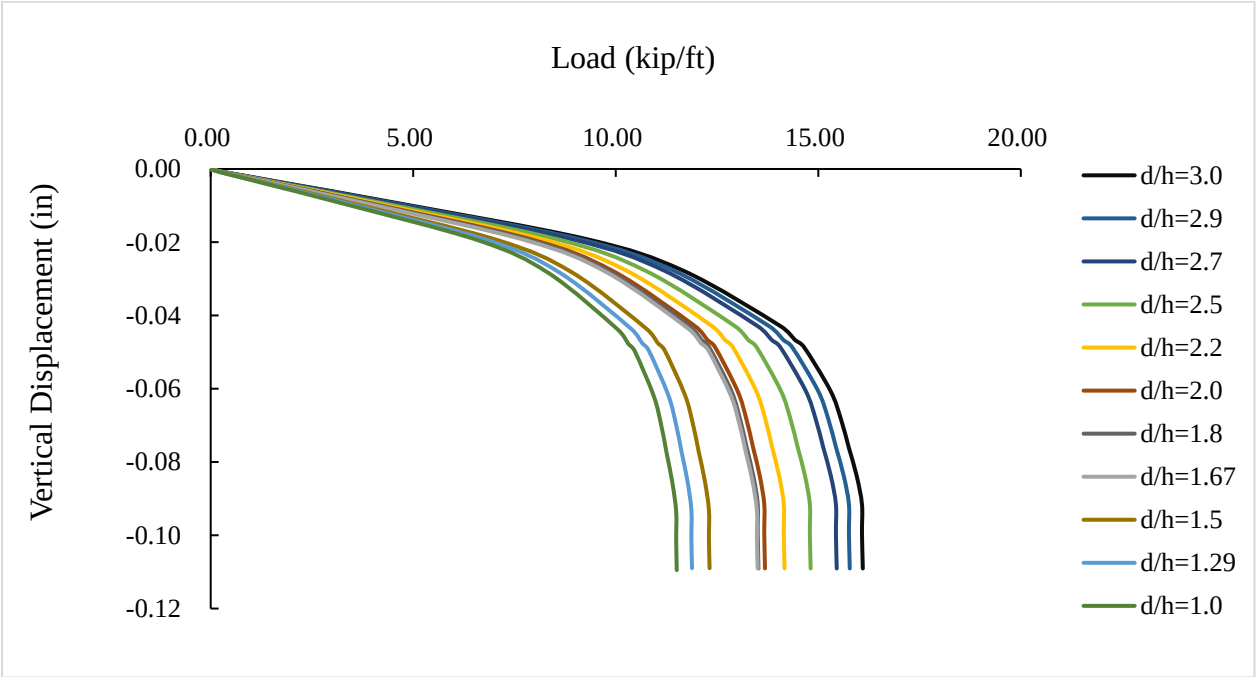

Figure 2-45. Load versus vertical displacement curve of dense sand for different ratio of d/h.

In the second case, we conduct the simulation for the dense sand. Figure 2-45 shows the load versus vertical displacement curve. Figure 2-46 plots the load versus horizontal displacement curve for the pile wall at three different ratios of d/h. Figure 2-45 and Figure 2-46 show that the ultimate axial sheet pile wall capacity increases with an increase of the pile penetration depth. Finally, the contours of the computed plastic shear strains for a loading state are shown in Figure 2-47. The

rupture surface (shear failure) is developing front interface between the pile wall and soil and to the bottom of the pile wall.

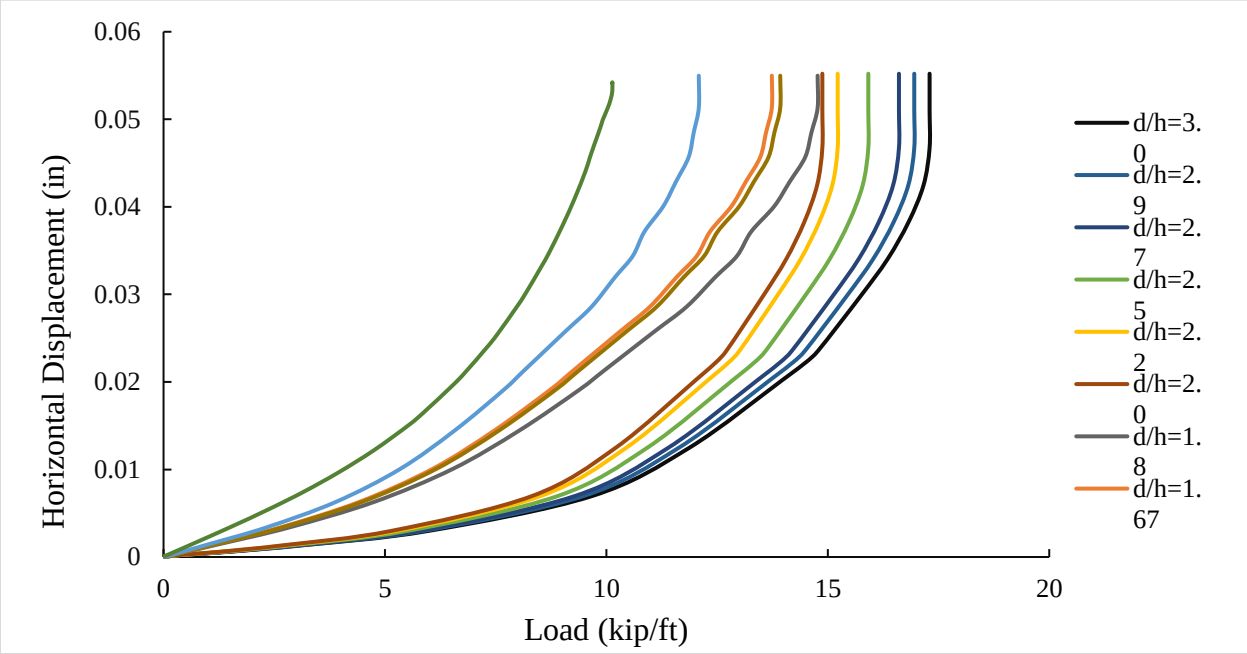

Figure 2-46. Load versus horizontal displacement curve of dense sand for different ratio of d/h.

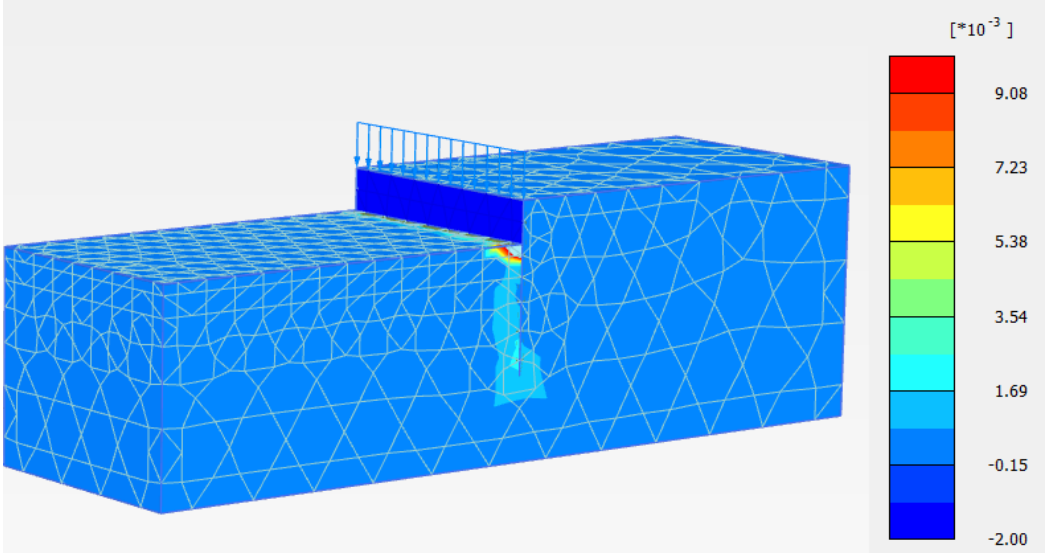

Figure 2-47. Contour of plastic shear strain of dense sand d/h = 3 at vertical displacement 0.104in.

In the third case, we conduct the simulation for the loose sand. Figure 2-48 shows the load versus vertical displacement curve. Figure 2-49 plots the load versus horizontal displacement curve for the pile wall at three different ratios of d/h. Figure 2-48 and Figure 2-49 show that the ultimate axial sheet pile wall capacity increases with an increase of the pile penetration depth. Finally, the contours of the computed plastic shear strains for a loading state are shown in Figure 2-50. The rupture surface (shear failure) is developing front interface between the pile wall and soil and to the bottom of the pile wall.

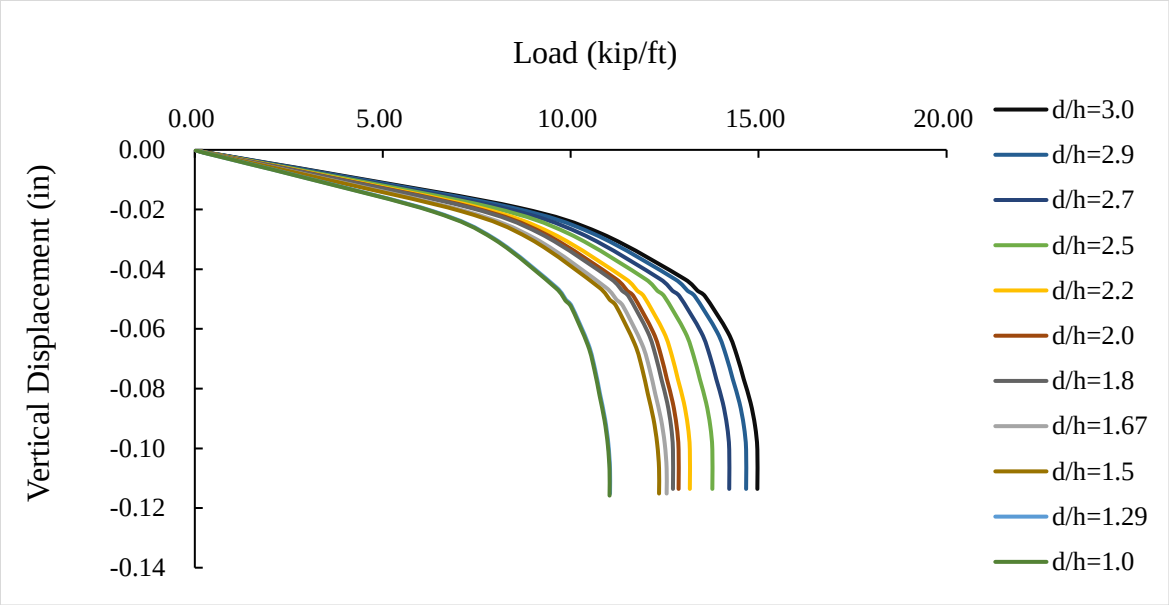

Figure 2-48. Load versus vertical displacement curve of loose sand for different ratio of d/h.

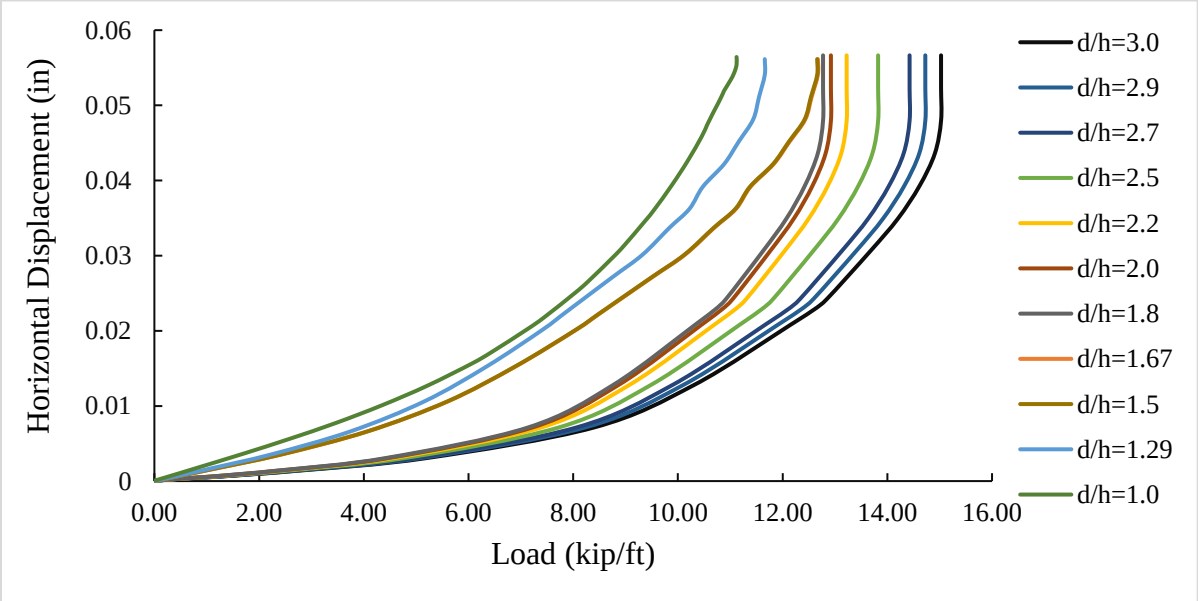

Figure 2-49. Load versus horizontal displacement curve of loose sand for different ratio of d/h.

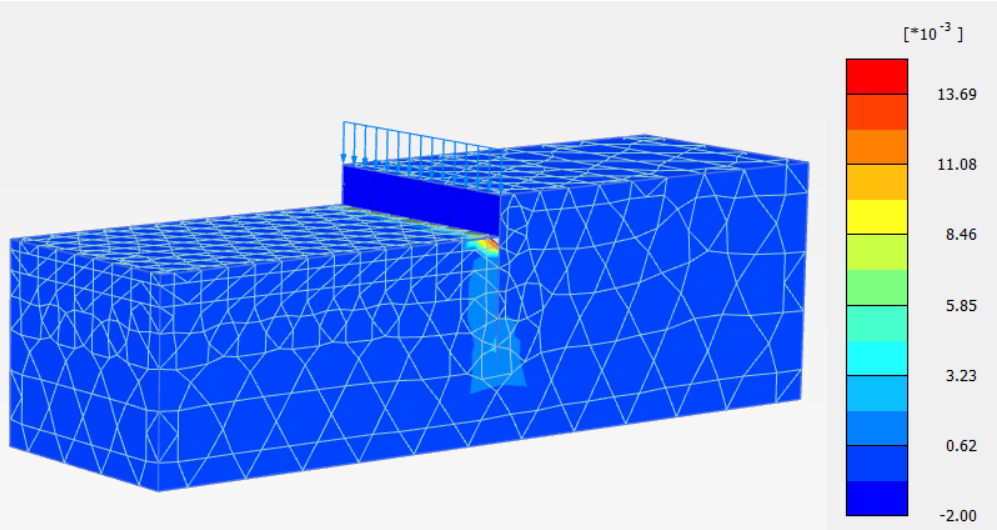

Figure 2-50. Contour of plastic shear strain of loose sand d/h = 3 at vertical displacement 0.118in.

Discussion:

In this section, the investigation mainly focused on determining the effect of the penetration depth and relative density of sand under the effect of axial loading conditions. The main conclusions that can be deduced from the numerical modeling results comparison. The numerical results obtained in the above simulations are outlined as follows:

1. The ultimate axial piled wall capacity increased with an increase in penetration depth under three different soils condition (Figure 2-42 - Figure 2-49).
2. The ultimate axial piled wall capacity increased with an increasing in relative density (Figure 2-51 - Figure 2-52).
3. Figure 2-44, Figure 2-47 and Figure 2-50 show the induced plastic shear strain in the soil at different sand densities for the case of d/h=3. In the three different soil conditions, the plastic shear strain is reduced to the lowest value as a result of soil resistance in the passive zone, as shown in Figure 2-44 (a), Figure 2-47 (a) and Figure 2-50 (a). The gradual increase in the plastic shear strains is observed with a decrease in sand density. (Figure 2-44, Figure 2-47 and Figure 2-50 (b and c)). The failure occurs mainly at the left top edge of interface between the soil and the pile wall, which transferred the axial stresses to the deep soil at the toe of the wall. These strains were easily observed at the bottom of the piled wall in the case of the dense condition, which produced a higher axial capacity. It can be concluded that because the penetration depth exceeded the free height (d > H), there is less slip failure. The axial load effect resulted in the sheet pile wall transferring its major load to the deeper soil below the toe and around the pile surface area.

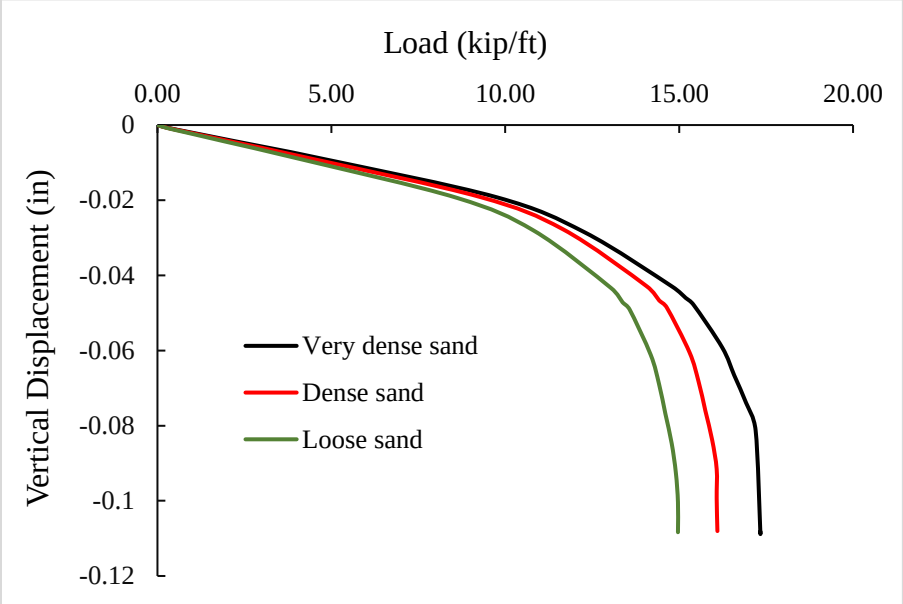

Figure 2-51. Load versus vertical displacement curve of different density sand at ratio of d/h=3.

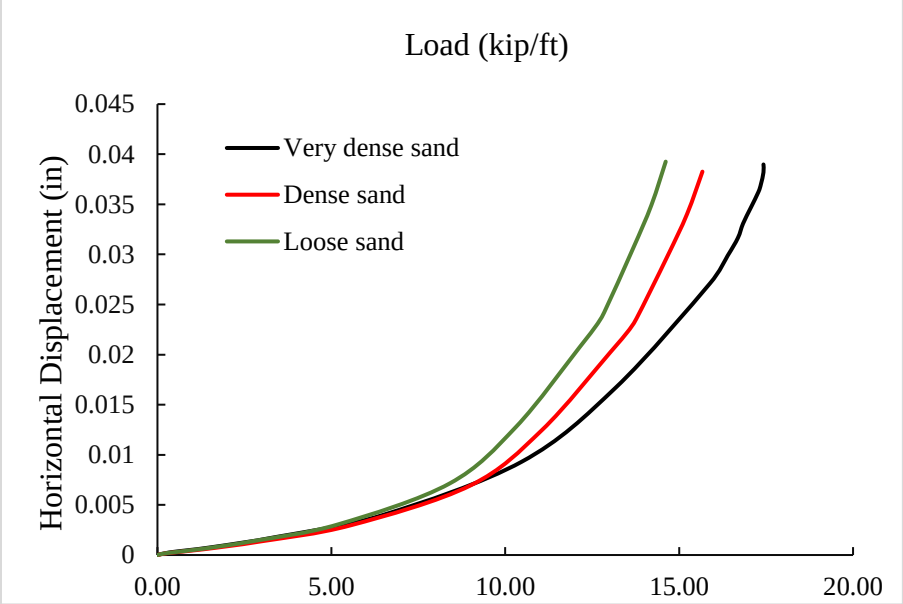

Figure 2-52. Load versus horizontal displacement curve of different density sand at ratio of d/h=3.

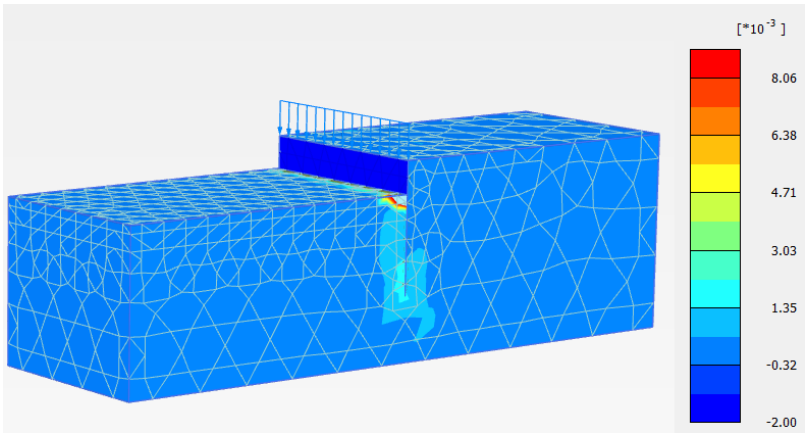

(a)

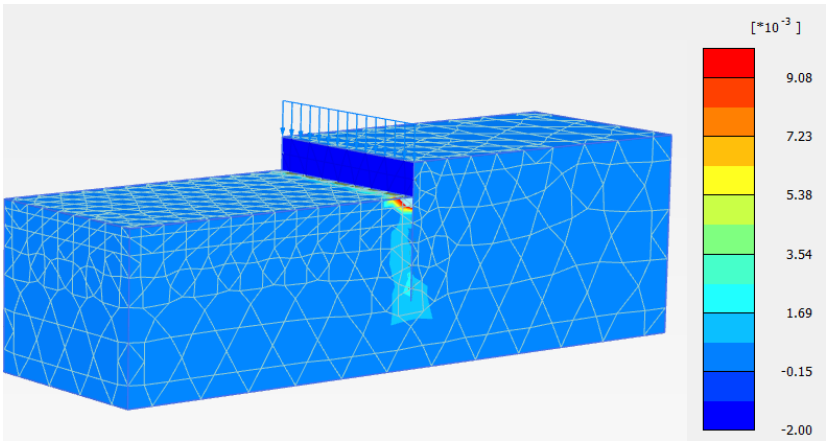

(b)

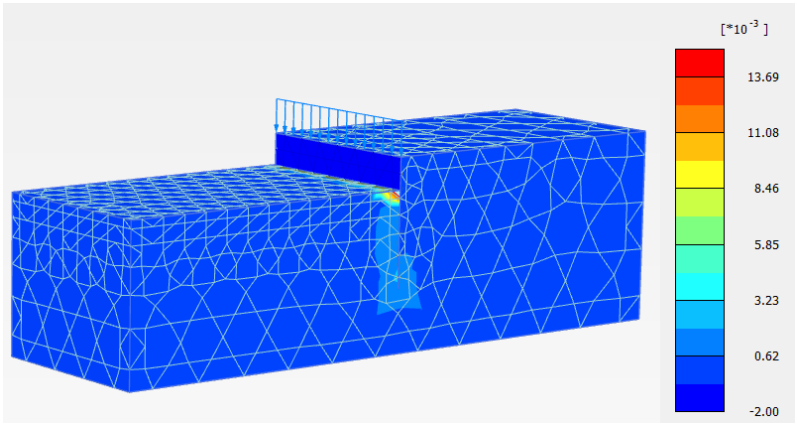

(c)

Figure 2-53. Contour of plastic shear strain for d/h = 3; (a) Very dense sand; (b) Dense sand; (c) Loose sand.

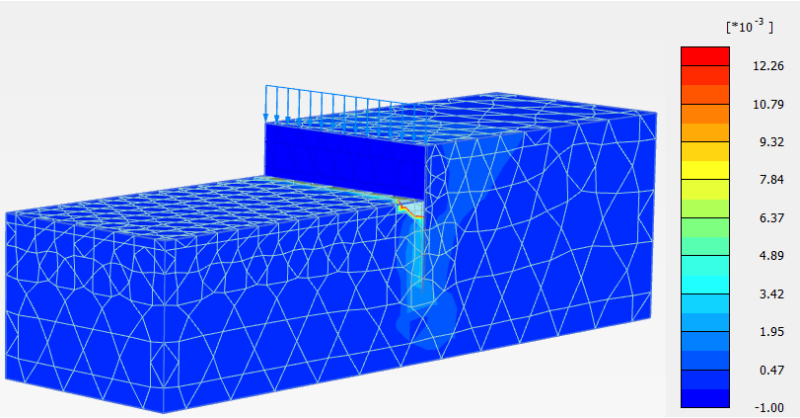

(a)

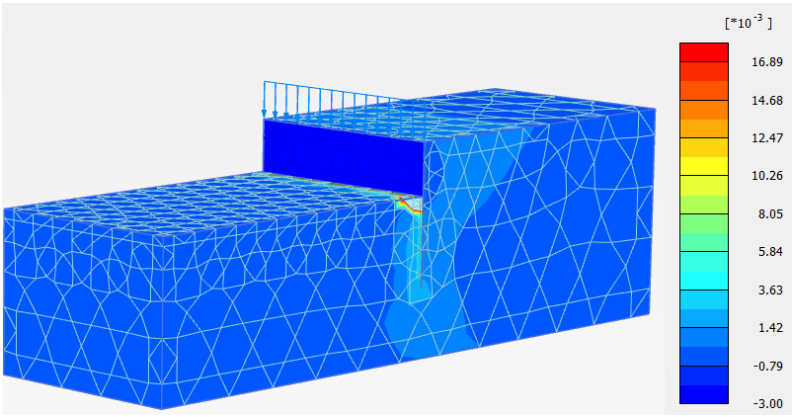

(b)

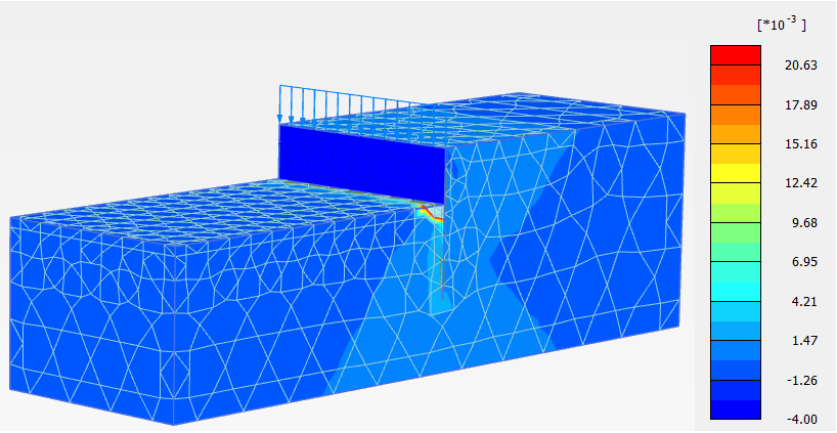

(c)

Figure 2-54. Contour of plastic shear strain for d/h = 1.67; (a) Very dense sand; (b) Dense sand; (c) Loose sand.

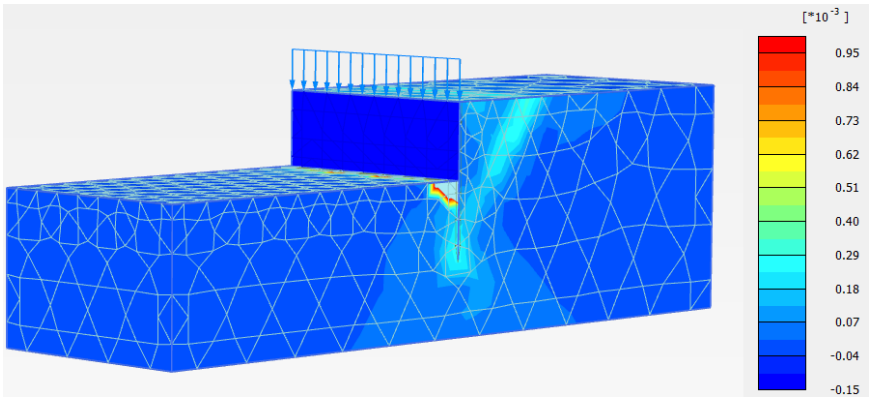

(a)

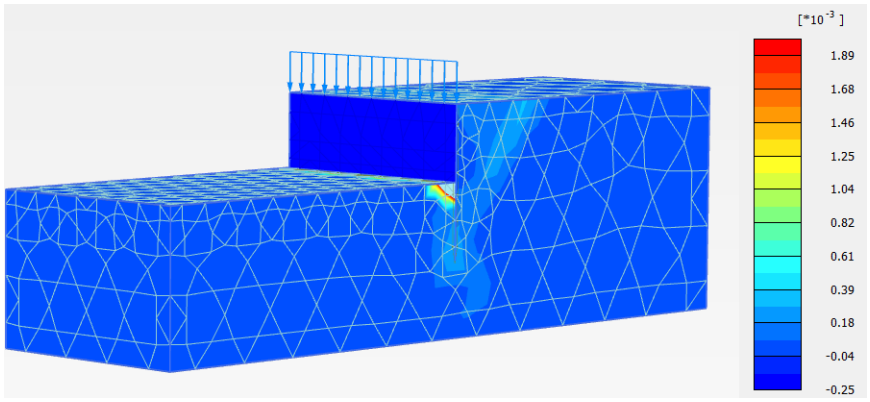

(b)

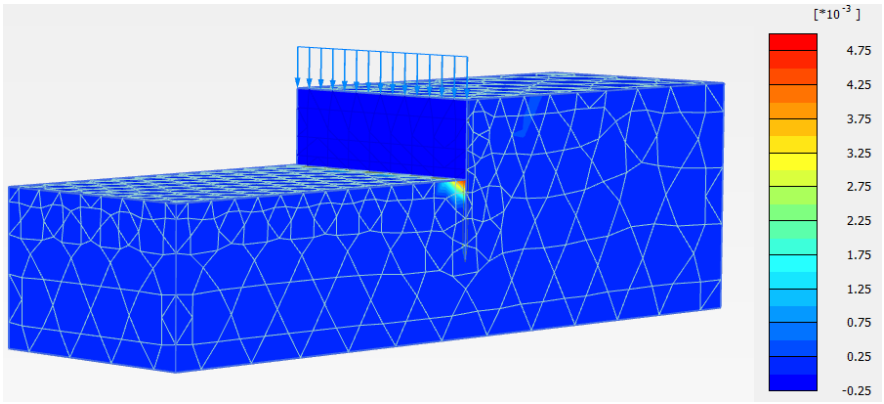

(c)

Figure 2-55. Contour of plastic shear strain for d/h = 1; (a) Very dense sand; (b) Dense sand; (c) Loose sand.

2.2.2.2 Effect of sheet pile wall stiffness

Z-shaped sheet pile profiles are commonly used in the U.S. Four commonly rolled Z-shaped sheet pile sections in the U.S. are the PZ 22, PZ 27, PZ 35, and PZ 40. Larssen type profiles are also popular U-shaped sheet piles mostly used in Europe. Both these profiles follow the concept for a "wave-shaped" profile but the Z-type shapes have the added advantage that the interlocks are formed on the outer elements of the section. Sheet pile stiffness can affect its buckling behavior under axial loading. Flexural stiffness also plays an important role in the bending moment distribution and wall deflections. Through numerical modeling, we have studied the effects of flexural and axial stiffness of the sheet pile elements on their bearing capacity and deformation characteristics. In the preliminary numerical simulation, we have studied the influence of the wall stiffness on the bearing capacity by using the two different Young's moduli for sheet piles, $2.10 \times 10^6\ tsf$ (case 1) and $1.05 \times 10^5\ tsf$ (case 2). The three different soils are shown in Table 2-3. The ratio of d/h equals 3 in both cases.

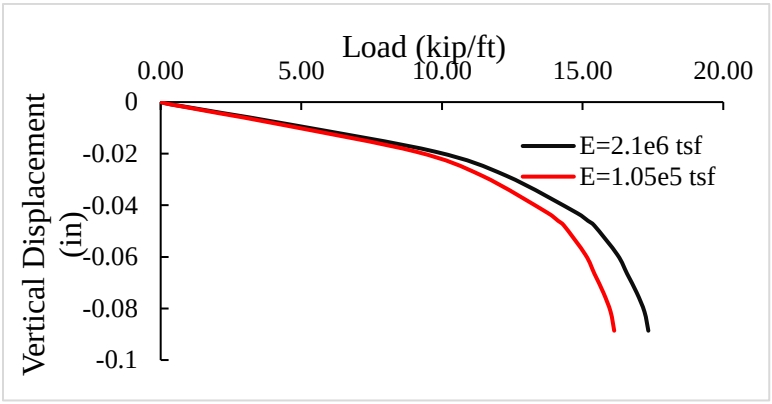

(a)

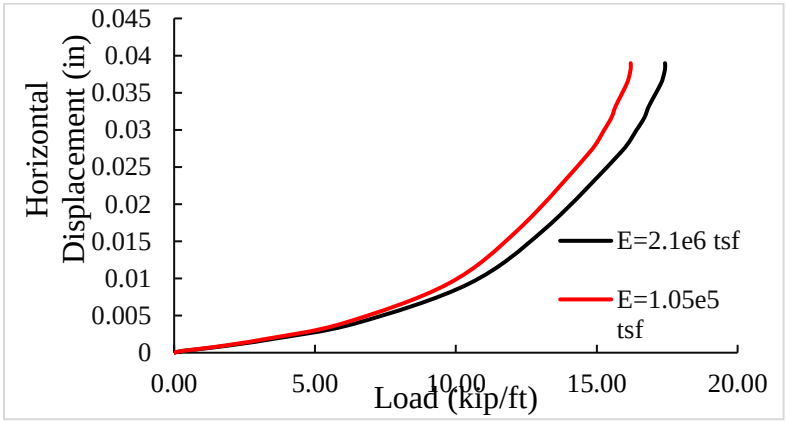

(b)

Figure 2-56. Load versus displacement curve for different Young's modulus of sheet piles for very dense sand.

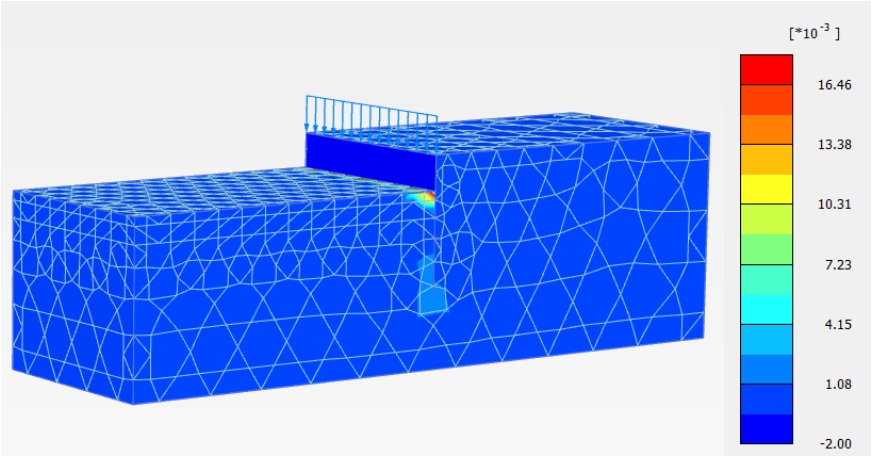

(a)

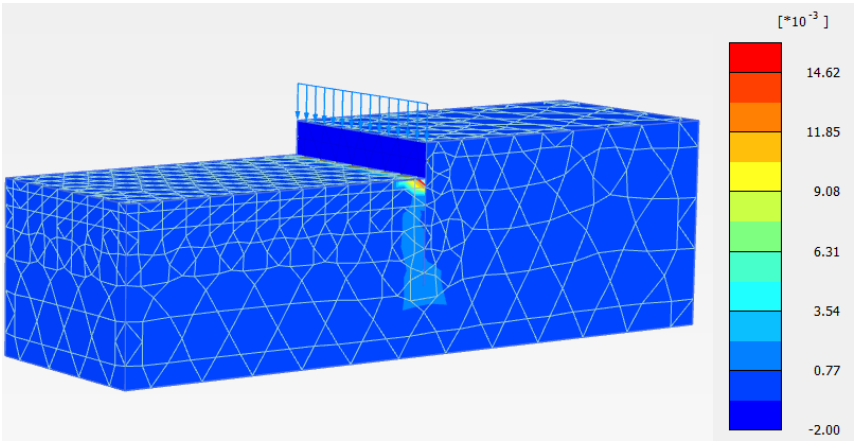

(b)

Figure 2-57. Contour of plastic shear strains for very dense sand: (a) E= $2.10 \times 10^6\ tsf$; (b) E=$1.05 \times 10^5\ tsf$.

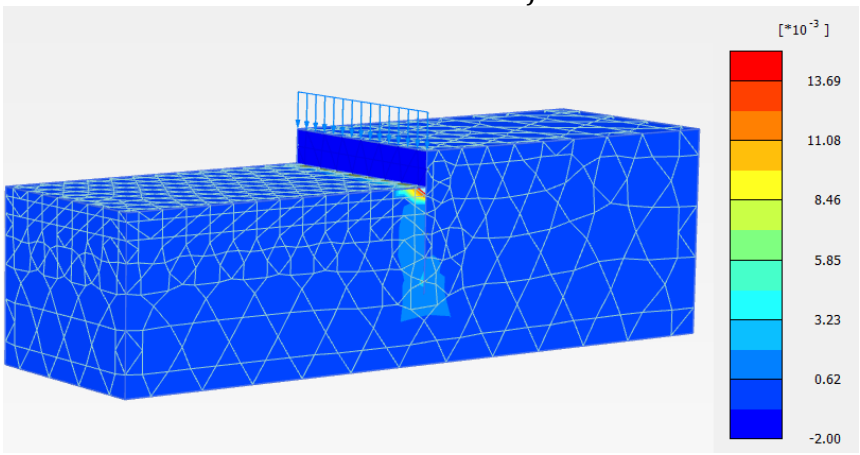

(a)

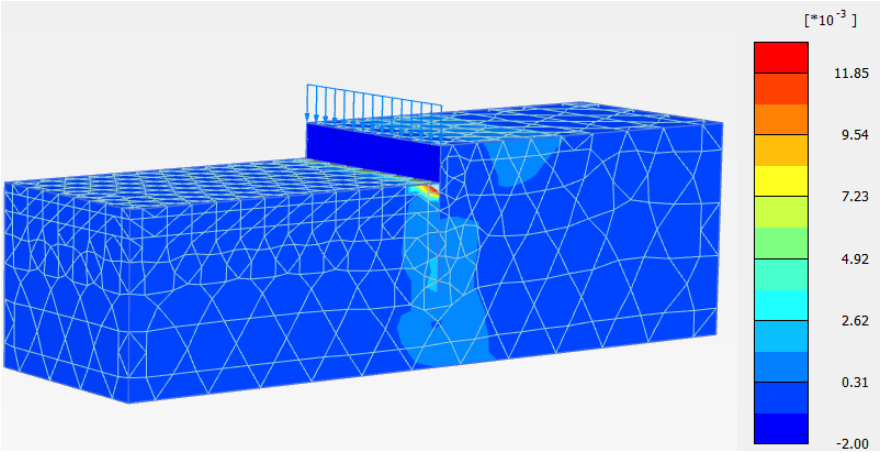

(b)

Figure 2-58. Contour of plastic shear strains for dense sand: (a) E= $2.10 \times 10^6\ tsf$; (b) E=$1.05 \times 10^5\ tsf$.

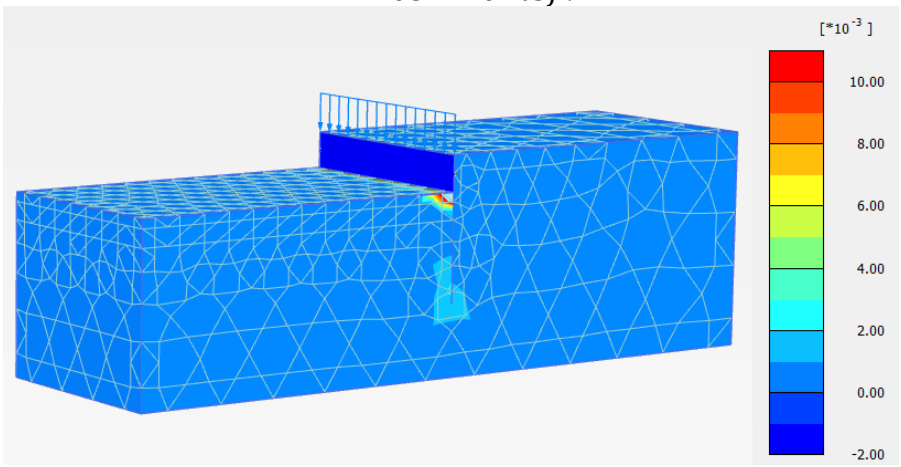

(a)

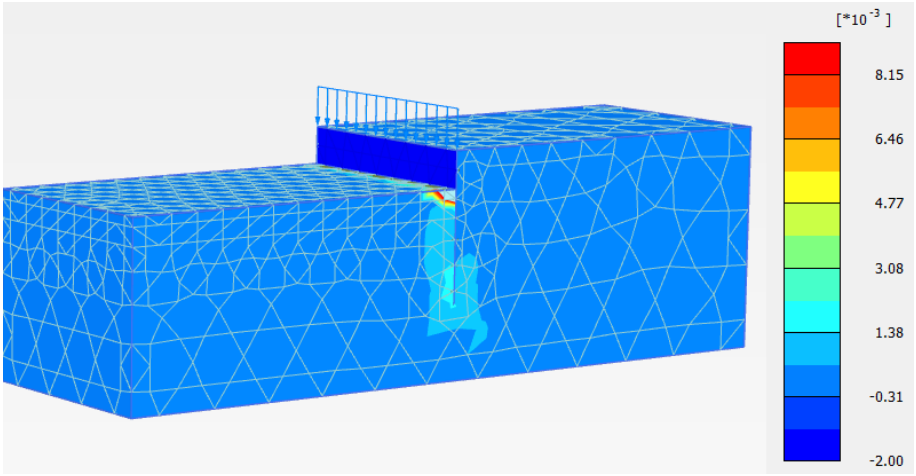

(b)

Figure 2-59. Contour of plastic shear strains for loose sand: (a) E= $2.10 \times 10^6\ tsf$; (b) E=$1.05 \times 10^5\ tsf$.

Discussion:

Figure 2-56 (a) shows the load versus vertical displacement curve and Figure 2-56 (b) shows the load versus horizontal displacement curve for the different stiffness piles. Figure 2-57-Figure 2-59 show the contours of plastic shear strains for different sand. These numerical results show that the pile wall stiffness affects the axial loading capacity and plastic shear zone around the sheet pile. The ultimate axial piled wall capacity increased with an increase in sheet pile wall stiffness. The failure of the pile retaining wall occurred at interface position between the excavation soil and sheet pile.

2.2.2.3 Effect of surcharge loading

Surcharge loads exert additional lateral pressures on the sheet pile wall system. Surcharge loads may result from traffic loads, equipment, construction materials, and other factors. Therefore, numerical modeling of axially loaded sheet pile walls at different surcharge intensities will be conducted to investigate the effect of surcharge loads on the general behavior (e.g., axial bearing capacity, lateral movement and induced bending moment) of sheet pile wall. The following simulations show sheet pile wall under the two different surcharge loading for three different soil conditions. The surcharge loading area is 393.7 ft^2. The soil properties are shown in Table 2-3. The ratio of d/h is 3 in each simulation.

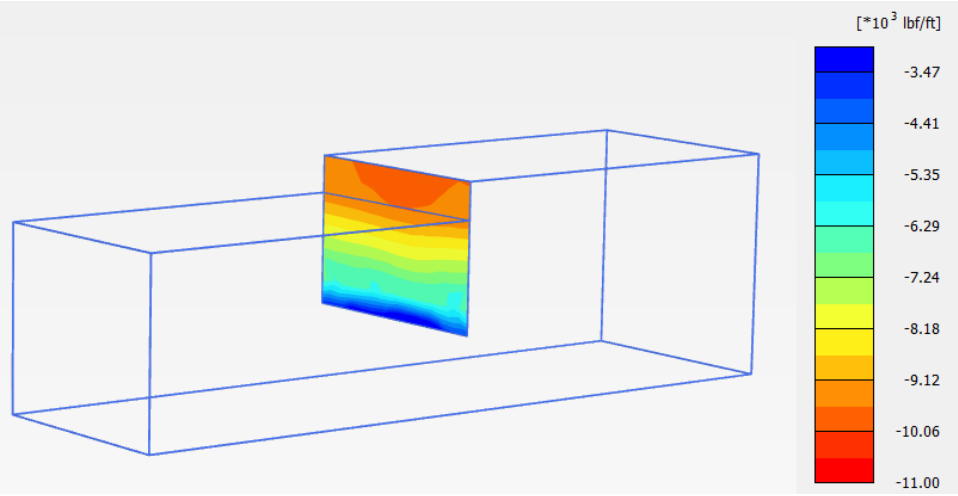

(a)

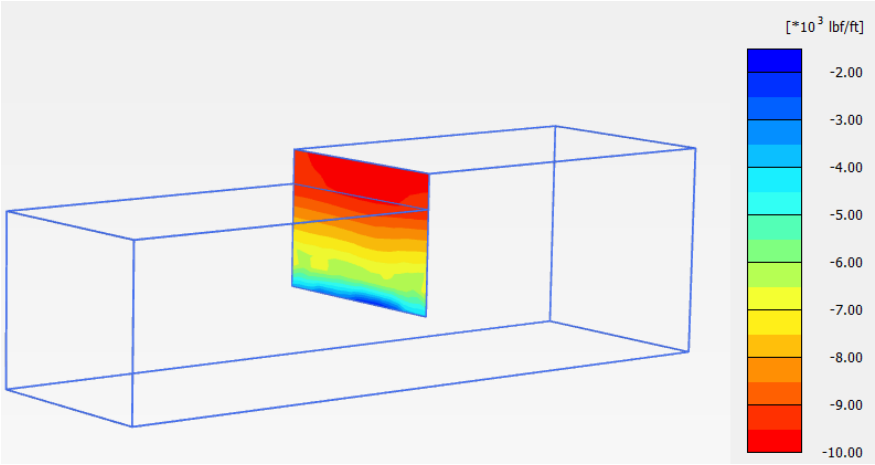

(b)

Figure 2-60. Contours of axial capacity of sheet pile wall in very dense sand; (a) Surcharge loading 208.85 psf; (b) Surcharge loading 417.71 psf.

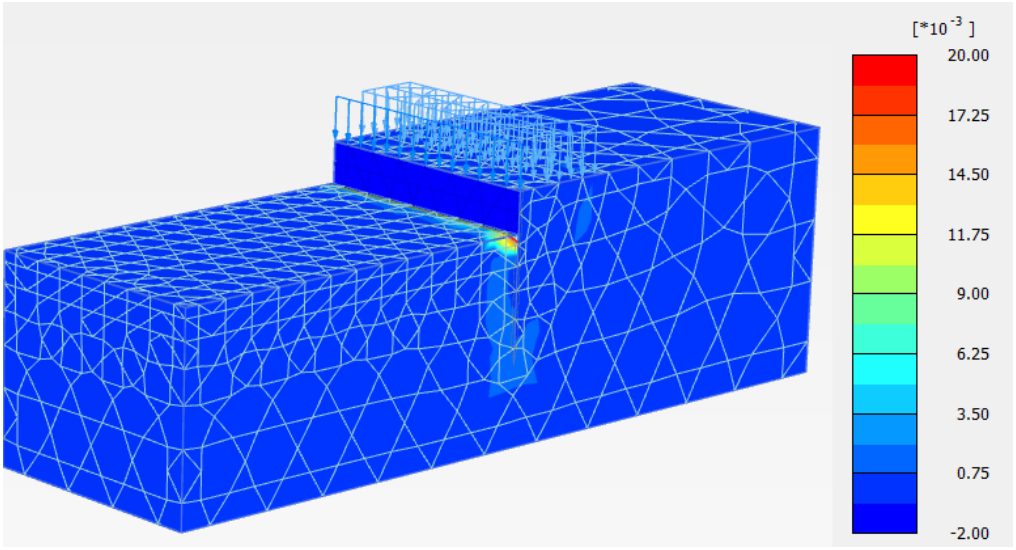

(a)

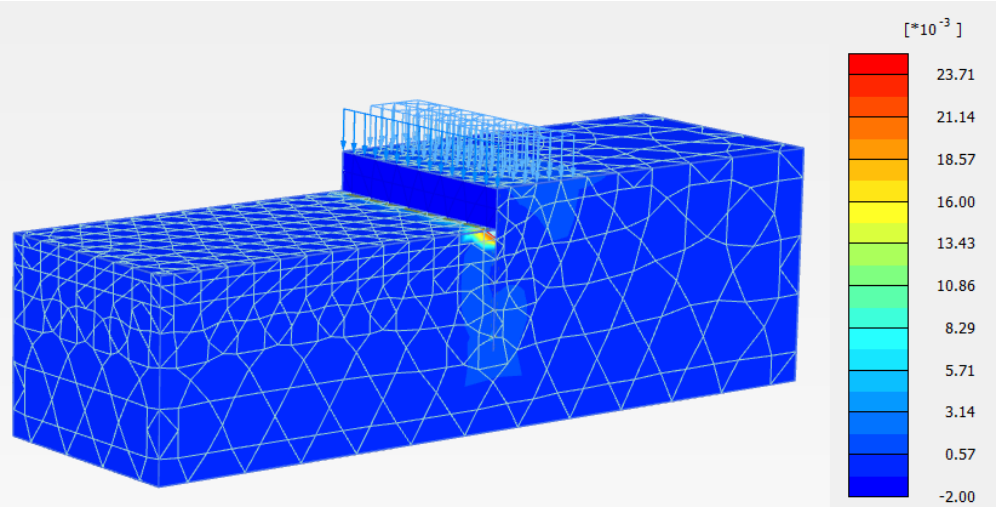

(b)

Figure 2-61. Contours of plastic shear strain in very dense sand; (a) Surcharge loading 208.85 psf; (b) Surcharge loading 417.71 psf.

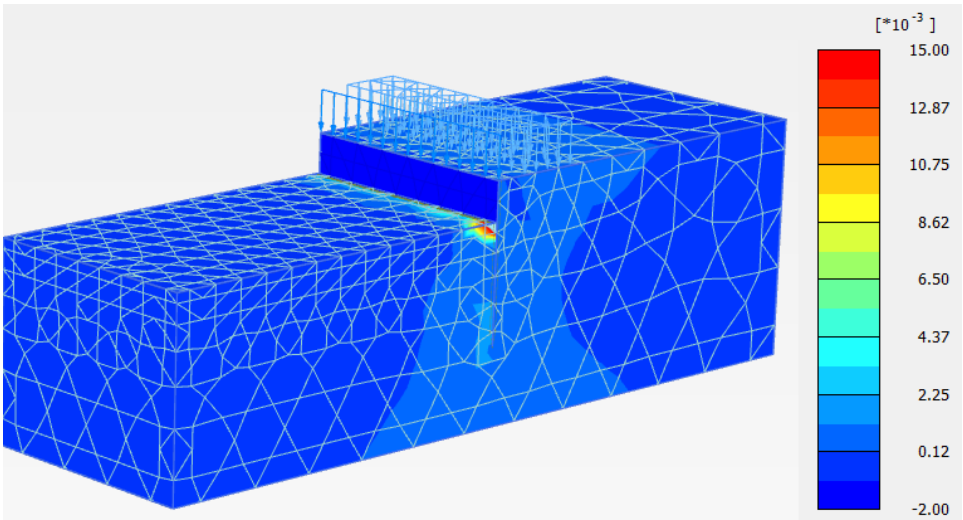

(a)

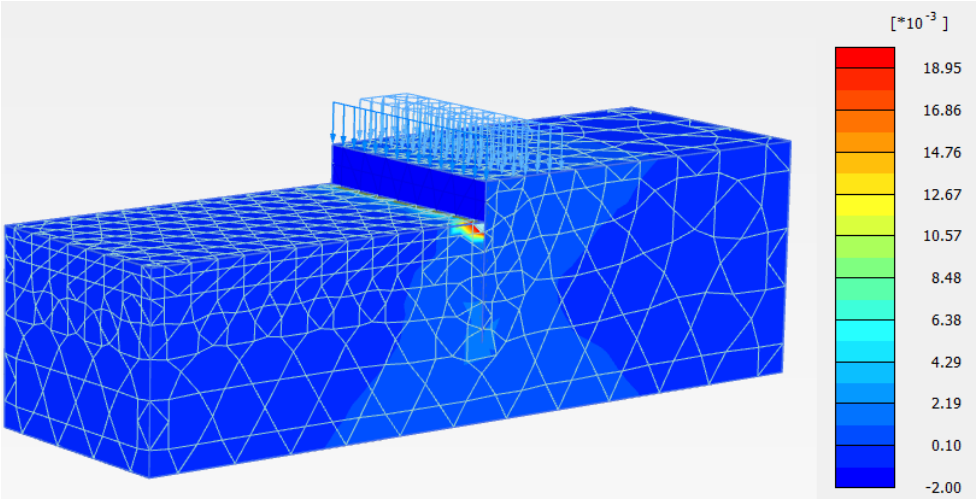

(b)

Figure 2-62. Contours of plastic shear strain in dense sand; (a) Surcharge loading 208.85 psf; (b) Surcharge loading 417.71 psf.

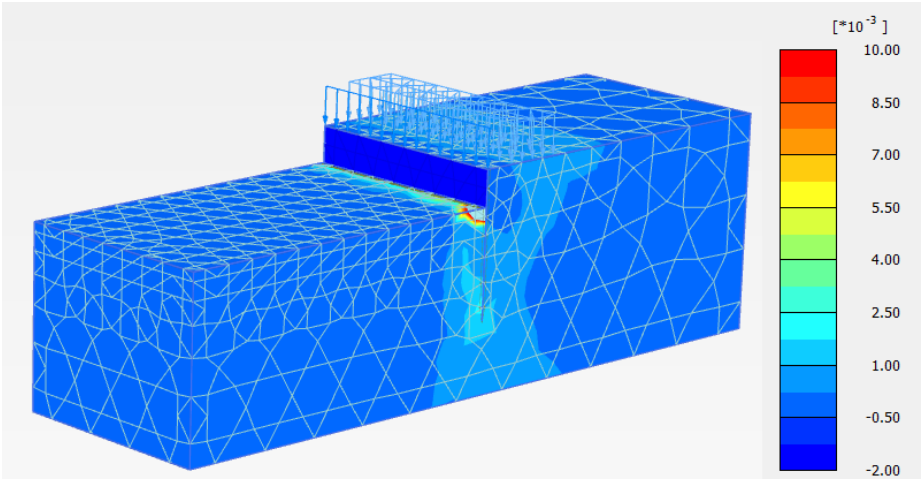

(a)

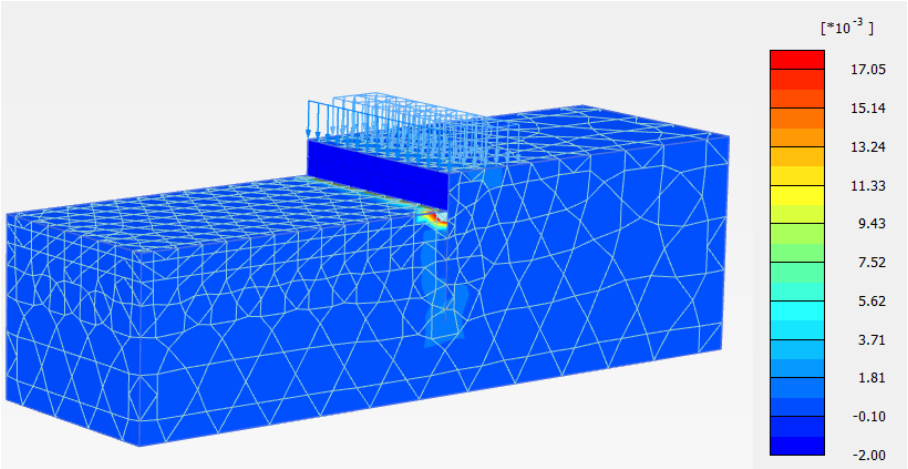

(b)

Figure 2-63. Contours of plastic shear strain in loose sand; (a) Surcharge loading 208.85 psf; (b) Surcharge loading 417.71 psf.

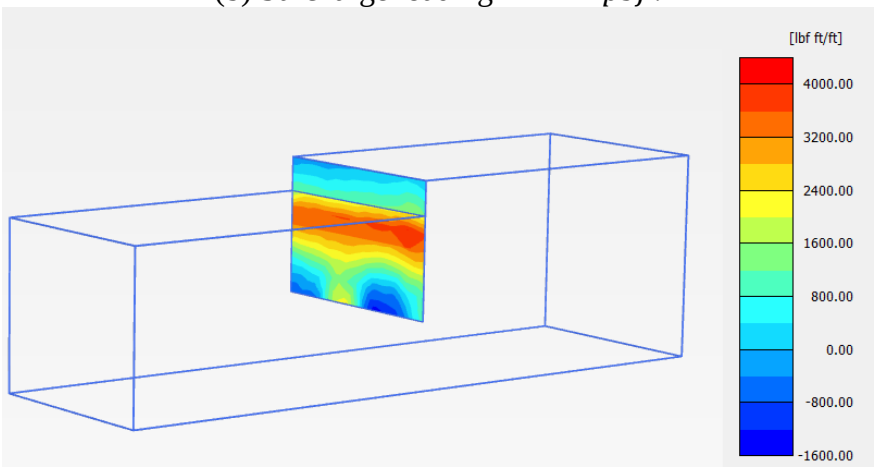

(a)

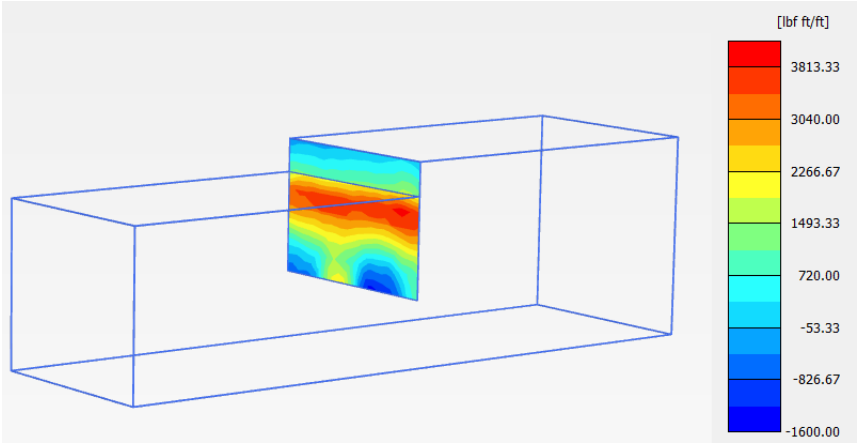

(b)

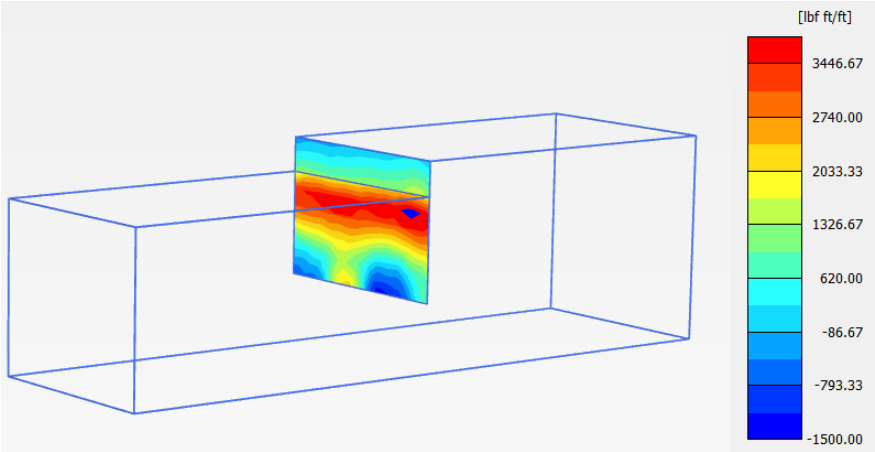

(c)

Figure 2-64. Contours of bending moment (M_{11}) for sheet pile wall under surcharge loading 417.71 psf ; (a) Very dense sand; (b) Dense sand; (c) Loose sand.

Discussion:

Figure 2-60 - Figure 2-64 show the contours of axial capacity of sheet pile wall, plastic shear strain, and bending moment contour of sheet pile wall, respectively. With an increase in the surcharge load, the lateral wall deformation increases. The FE analysis showed that the existence of surcharge in the active zone can substantially reduce the ultimate axial capacity of the piled wall, with a remarkable increase in lateral wall deformation. The bending moment of sheet pile was increasing with increase the relative density of sand. At a surcharge intensity of 417.71 psf and d/h = 3 the percentage increases in the maximum bending moments were 61, 47, and 35% for friction angles of 35, 32, and 27°, respectively.

2.2.2.4 Effect of the sheet pile head fixity

In a sheet pile wall with a free head condition, if wall tilts sufficiently, the soil on the retained side of the wall has an active earth pressure and moves down relative to the wall to mobilize friction in the beneficial direction (Figure 2-65 a). On the passive side, the displaced soil will move upward. If the axially loaded sheet pile abutment moves downward, the shaft friction on the active side will diminish. On the other hand, if the top of the sheet pile wall is restrained (e.g. by the bridge superstructure), the skin friction on both sides of the sheet pile might be considered (Figure 2-66 b).

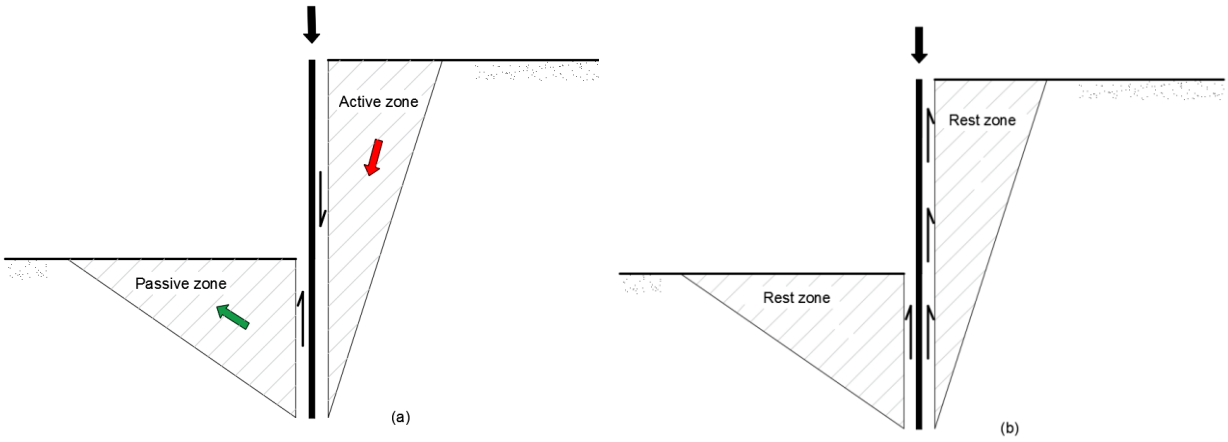

Figure 2-67. Skin friction developed in the axially loaded sheet pile: (a) free head conditions; and (b) fixed head conditions.

To study the influence of the sheet pile head conditions, we performed simulations with the pile head (Figure 2-37) fixed in all directions. The soil is assumed very dense sand, dense sand, and loose sand. We use the ratio of d/h equals 3. Figure 2-68 shows the contours of plastic shear strain for the very dense sand.

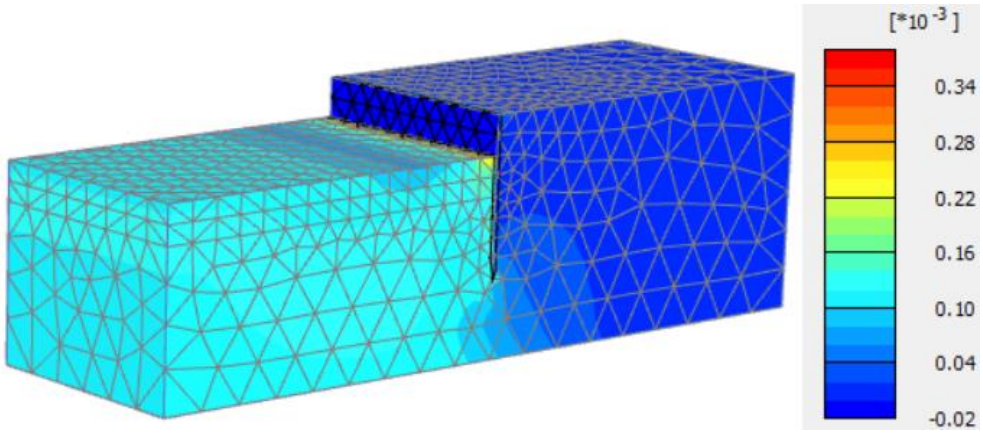

Figure 2-68. Contour of plastic shear strains.

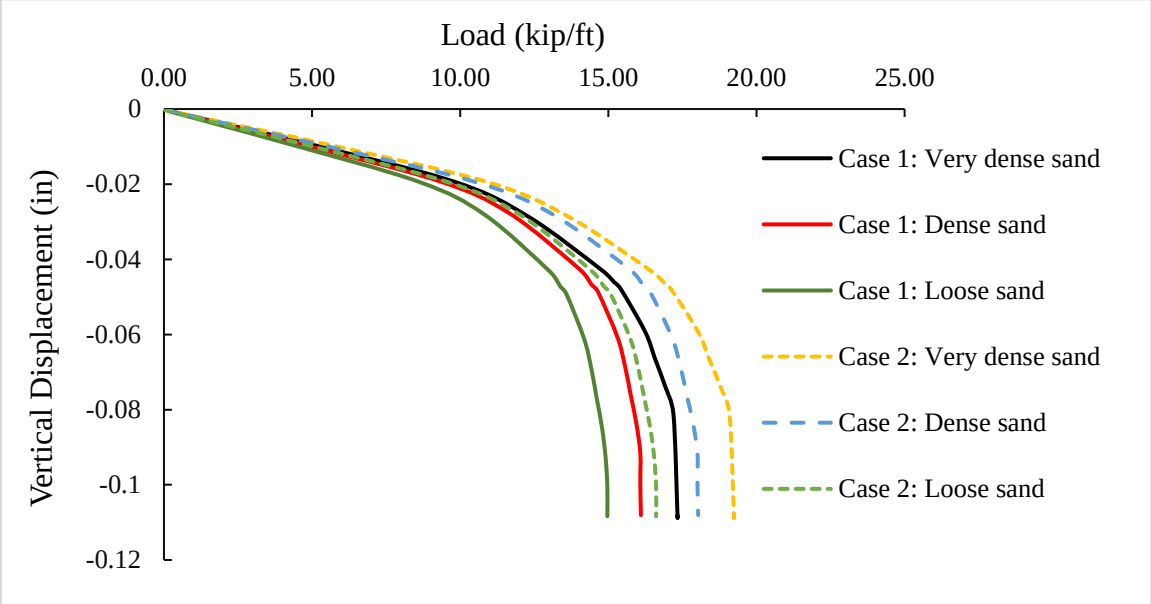

Figure 2-69. Load versus vertical displacement curve of different density sand at ratio of d/h=3; Case 1 for the free head condition and Case 2 for the fixed head condition.

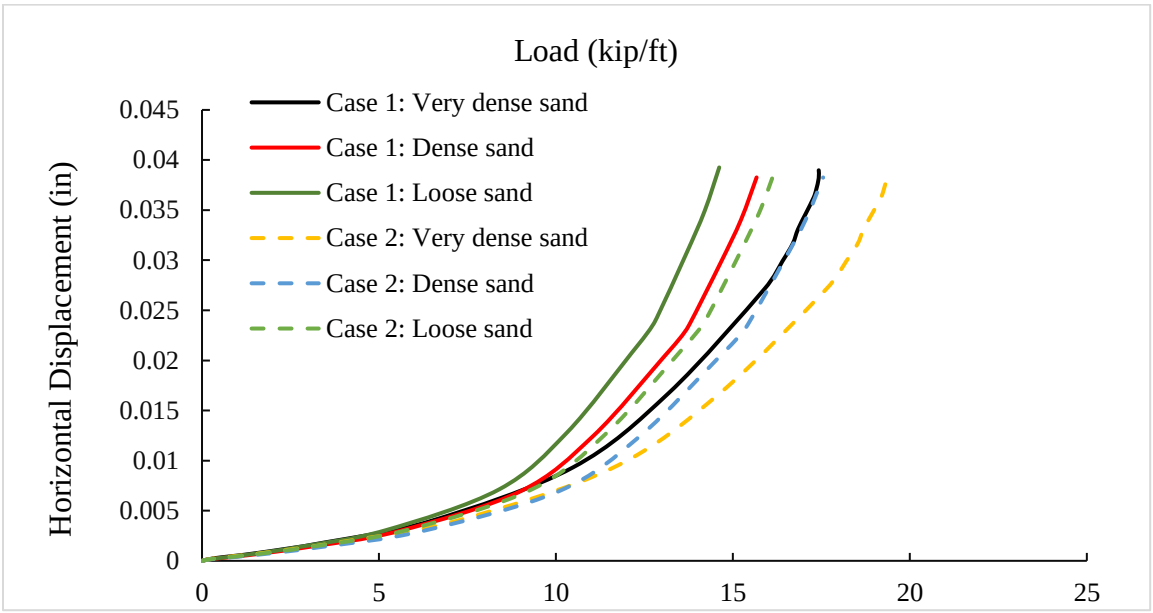

Figure 2-70. Load versus horizontal displacement curve of different density sand at ratio of d/h=3; Case 1 for the free head condition and Case 2 for the fixed head condition.

2.2.3 Effect of sand layering

2.2.3.1 Effect of penetration depth and unsupported length

We have simulated three different ratios of d/h to study the effect of the penetration depth of the pile wall on the ultimate axial capacity of the system for one layer soils. Three different (friction angle) soils are simulated in the following three cases. The retained height of soil (h), is varied at 6.56ft, 9.84ft, and 13.12 ft. Thus, three different d/h, 3, 1.67, and 1 are adopted. The soil 1 depth is 32.8ft and soil 2 depth is 6.57 ft. The soil 1 was changed from dense to loose sand in different simulations. The soil 2 was very dense sand. The material properties are also shown in Table 2-3.

In the first case, we conduct the simulation for the dense sand. Figure 2-71 shows the contours of load versus vertical displacement. Figure 2-72 plots the load versus horizontal displacement curve for the pile wall at three different ratios of d/h. Figures 33 and 34 show that the ultimate axial sheet pile wall capacity increases with an increase of the pile penetration depth. Finally, the contours of the computed plastic shear strains for a loading state are shown in Figure 2-73. The rupture surface (shear failure) is developing front interface between the pile wall and soil and to the bottom of the pile wall.

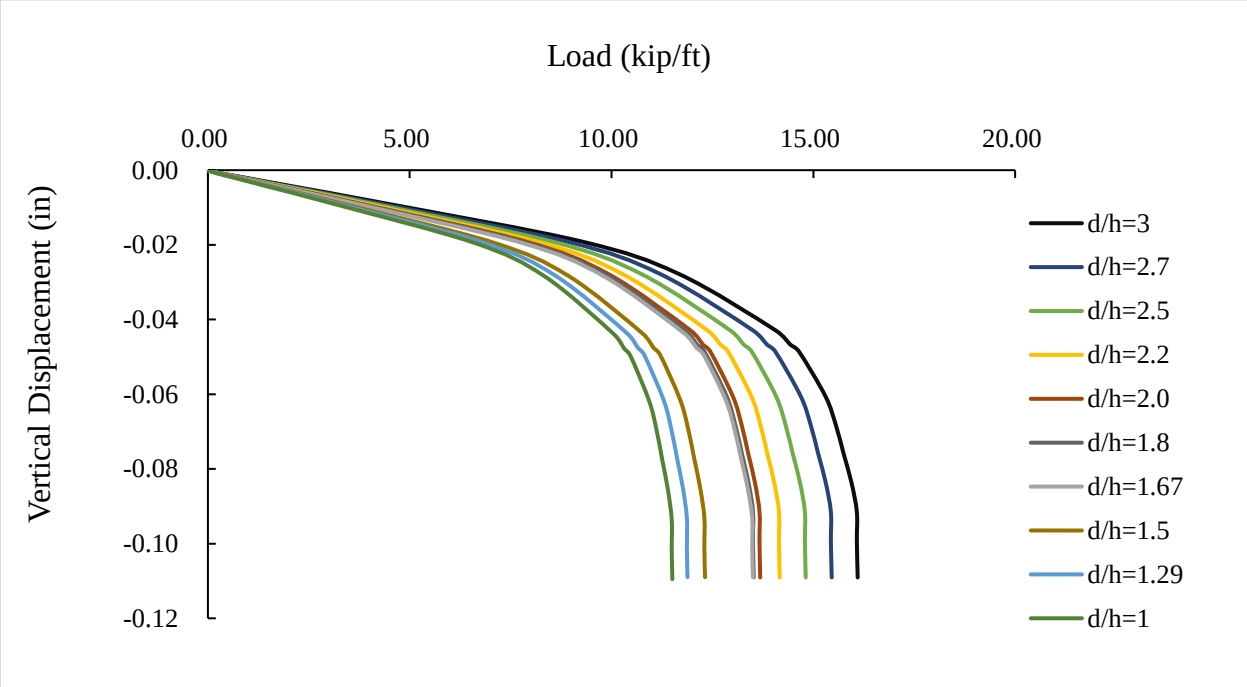

Figure 2-71. Load versus vertical displacement curve of dense sand for different ratio of d/h.

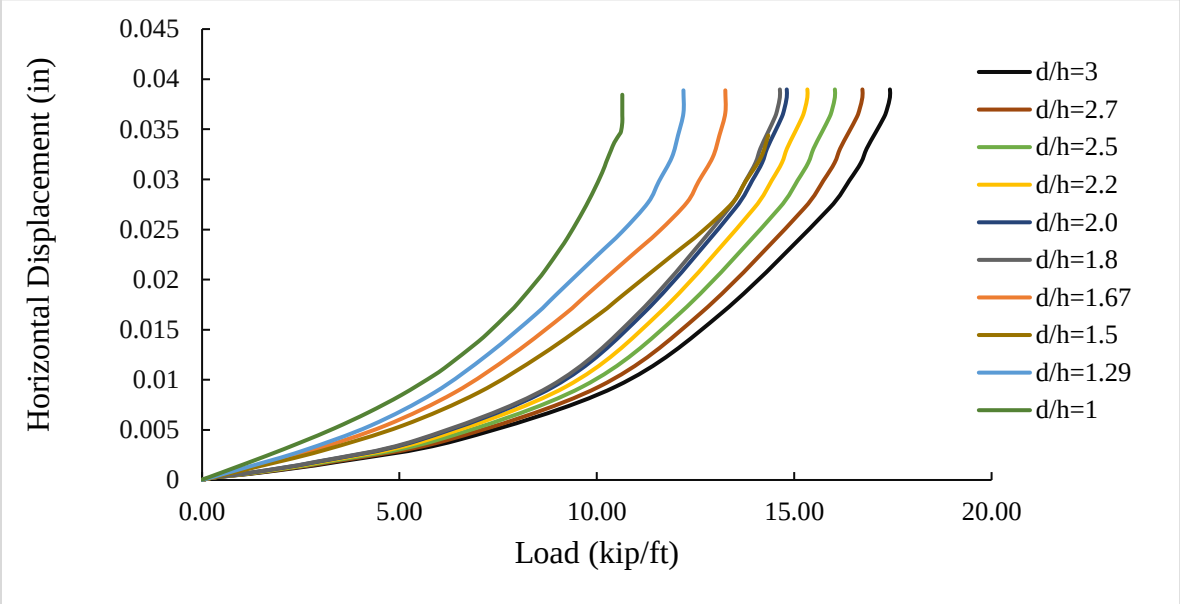

Figure 2-72 Load versus horizontal displacement curve of dense sand for different ratio of d/h.

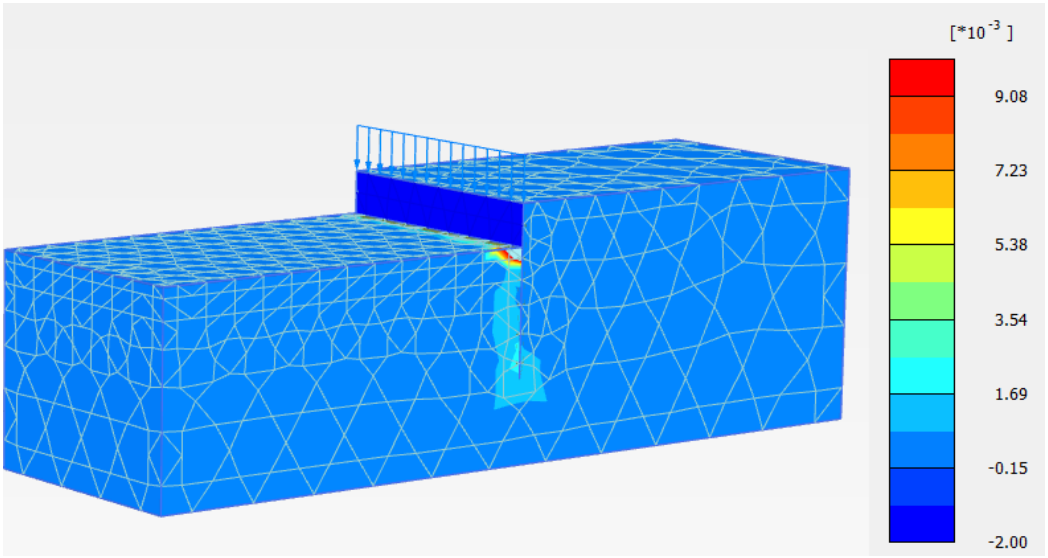

Figure 2-73. Contour of plastic shear strain of dense sand d/h = 3 at vertical displacement 0.104in.

In the second case, we conduct the simulation for the loose sand. Figure 2-74 shows the load versus vertical displacement. Figure 2-75 plots the load versus horizontal displacement curve for the pile wall at three different ratios of d/h. Figure 2-75 and Figure 2-76 show that the ultimate axial sheet pile wall capacity increases with an increase of the pile penetration depth. Finally, the contours of the computed plastic shear strains for a loading state are shown in Figure 2-76. The rupture surface (shear failure) is developing front interface between the pile wall and soil and to the bottom of the pile wall.

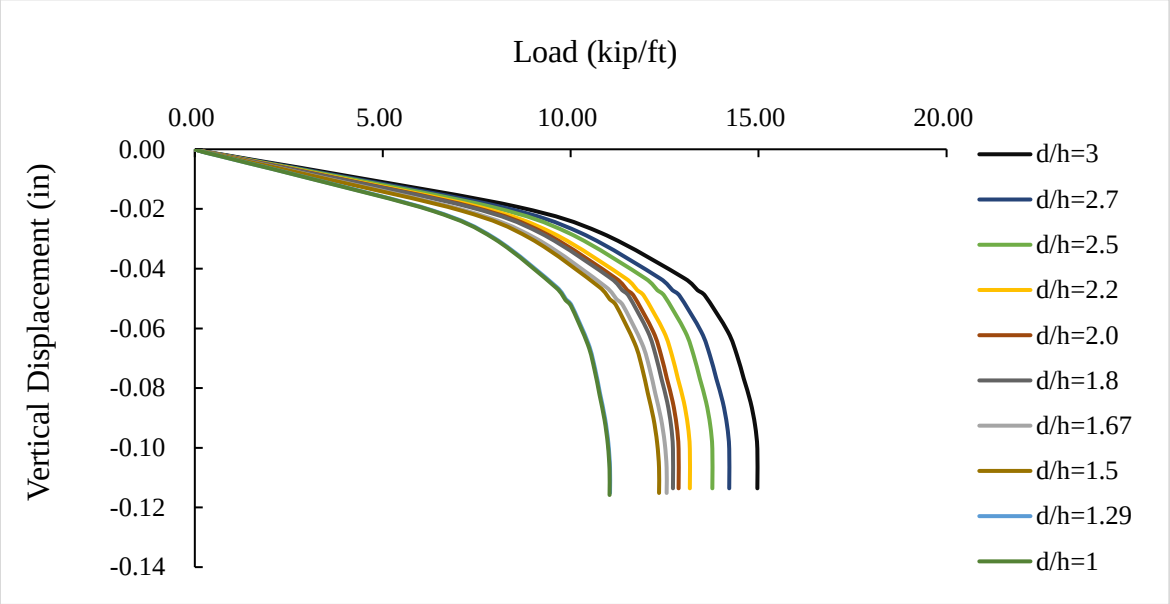

Figure 2-74. Load versus vertical displacement curve of loose sand for different ratio of d/h.

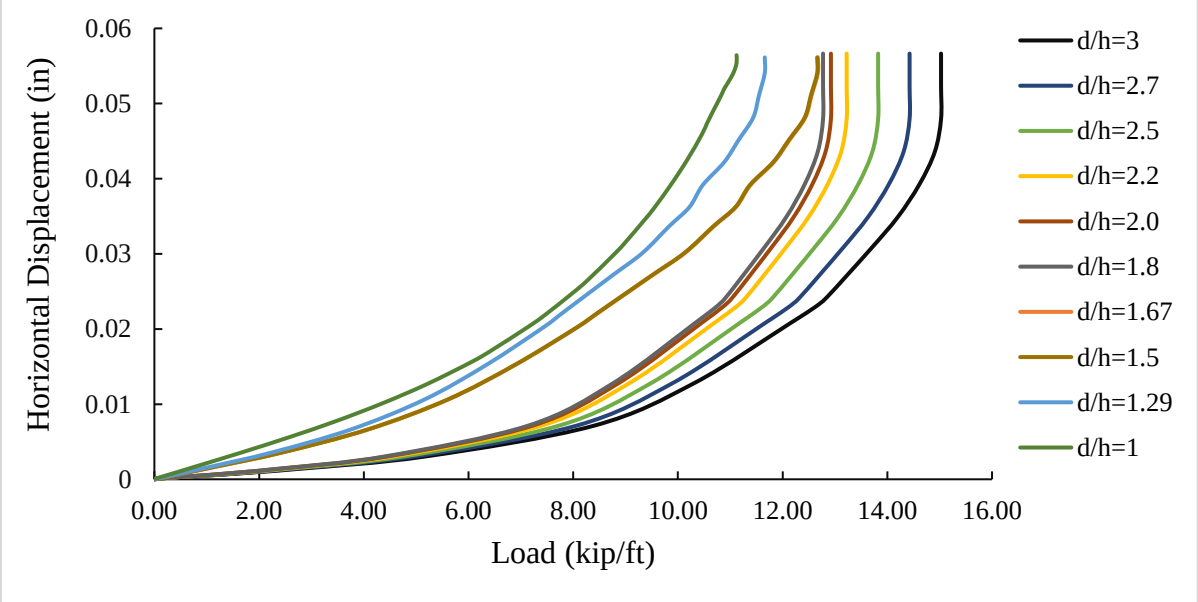

Figure 2-75. Load versus horizontal displacement curve of loose sand for different ratio of d/h.

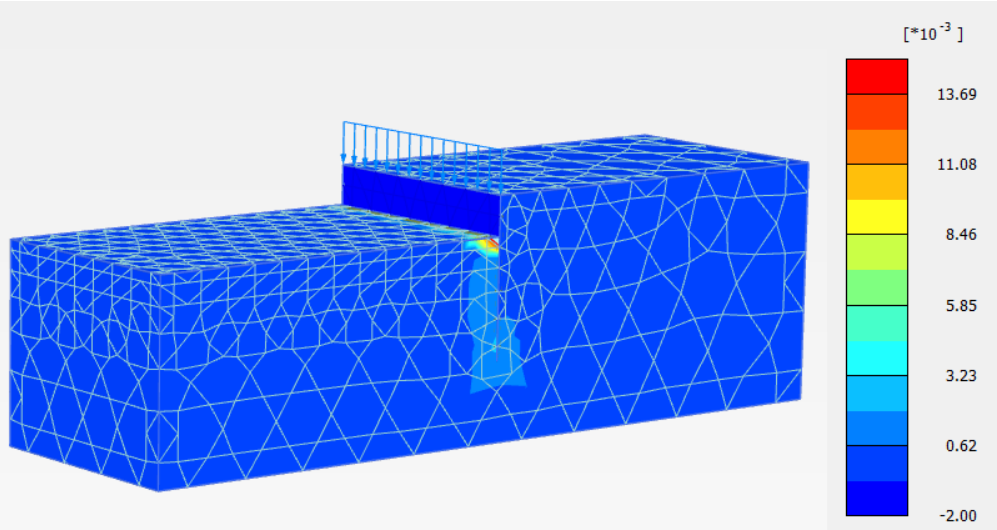

Figure 2-76. Contour of plastic shear strain of loose sand d/h = 3 at vertical displacement 0.118in.

Discussion:

In this section, the investigation mainly focused on determining the effect of the penetration depth and relative density of sand under the effect of axial loading conditions. The main conclusions that can be deduced from the numerical modeling results comparison. The numerical results obtained in the above simulations are outlined as follows:

1. The ultimate axial piled wall capacity increased with an increase in penetration depth under three different soils condition.
2. The ultimate axial piled wall capacity increased with an increasing in relative density.
3. Comparing to the simulation results in the first section of one-layer simulations, the dense sand as the second layer does not have much influence on the bearing capacity.

2.2.4 Parametric studies in layered soil (two layers)

We have simulated three different ratios of d/h to study the effect of the penetration depth of the pile wall on the ultimate axial capacity of the system for one soil layer. Three different (friction angle) soils are simulated in the following three cases. The retained height of soil (h), is varied from 6.56ft to 13.12 ft. Thus, ten different ratio of d/h are adopted. The soil 1 depth is 32.8ft and soil 2 depth is 6.57 ft. The soil 1 was changed from dense to loose sand in different simulations. The soil 2 was very dense sand. The material properties are also shown in Table 2-3.

2.2.4.1 Effect of penetration depth and unsupported length

In the first case, we did the simulation for the dense sand for layer 1. Figure 2-77 shows the plot of load versus vertical displacement. Figure 2-78 plots the load versus horizontal displacement

curve for the sheet pile wall at different ratios of d/h. Figure 2-77 and Figure 2-78 show that the ultimate axial sheet pile wall capacity increases with an increase of the pile penetration depth.

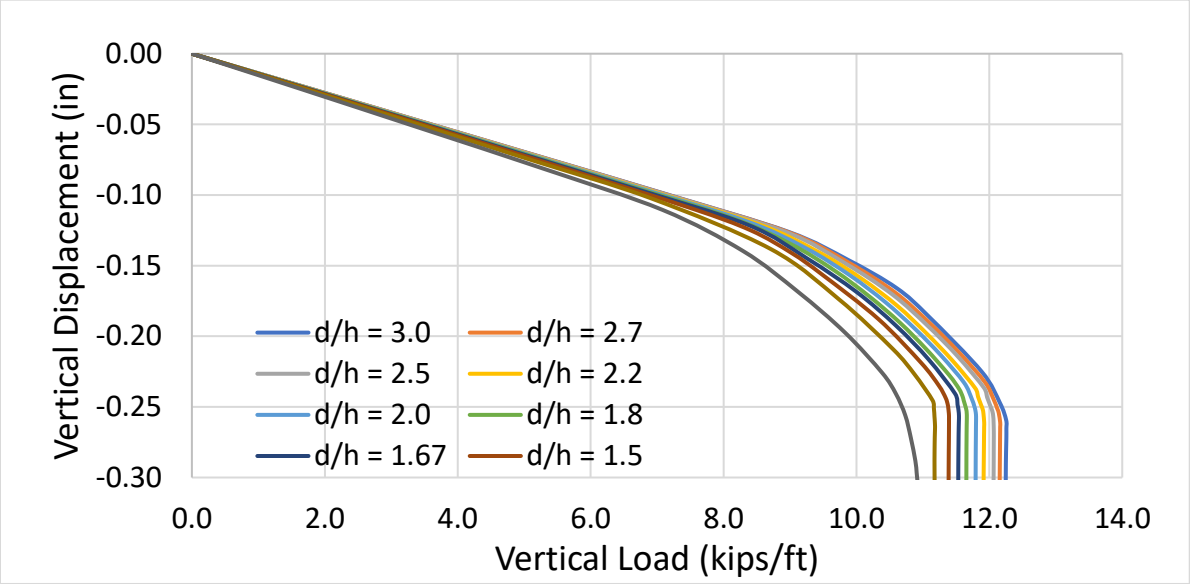

Figure 2-77. Load versus vertical displacement curve of dense sand for different ratio of d/h.

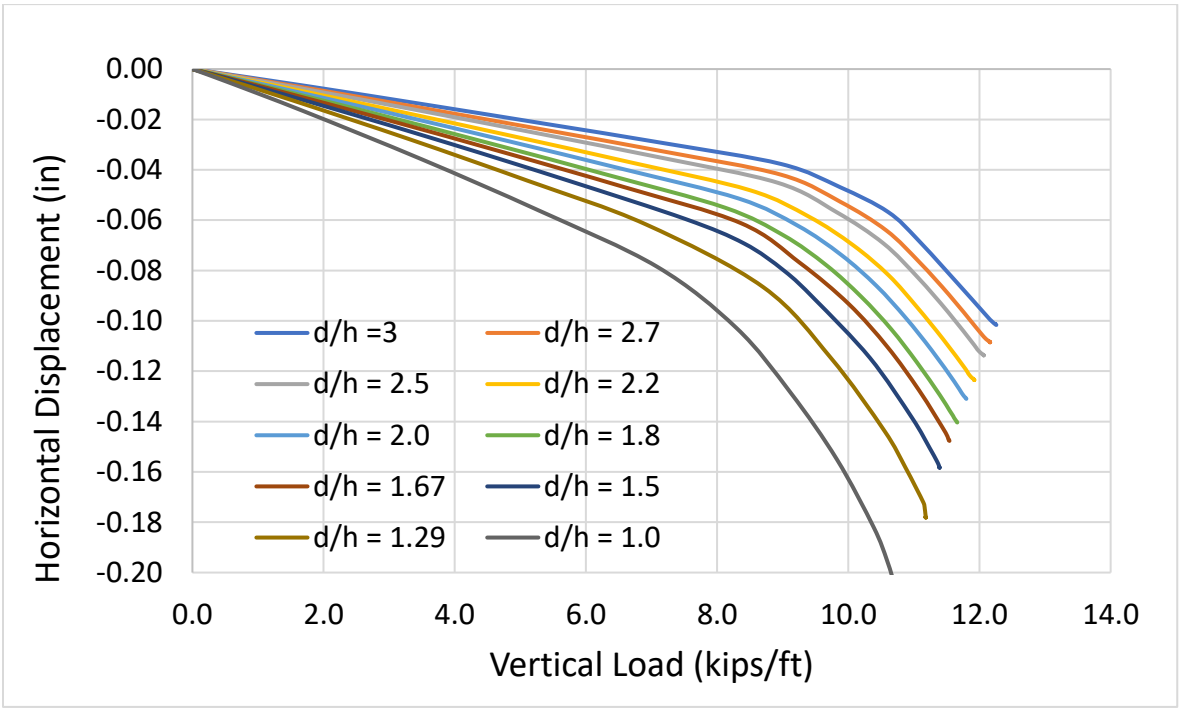

Figure 2-78 Load versus horizontal displacement curve of dense sand for different ratio of d/h.

In the second case, we did the simulation for the loose sand for layer 1. Figure 2-79 shows the load versus vertical displacement. Figure 2-80 plots the load versus horizontal displacement curve for the pile wall at three different ratios of d/h. Figure 2-79 and Figure 2-80 show that the ultimate axial sheet pile wall capacity increases with an increase in the pile penetration depth.

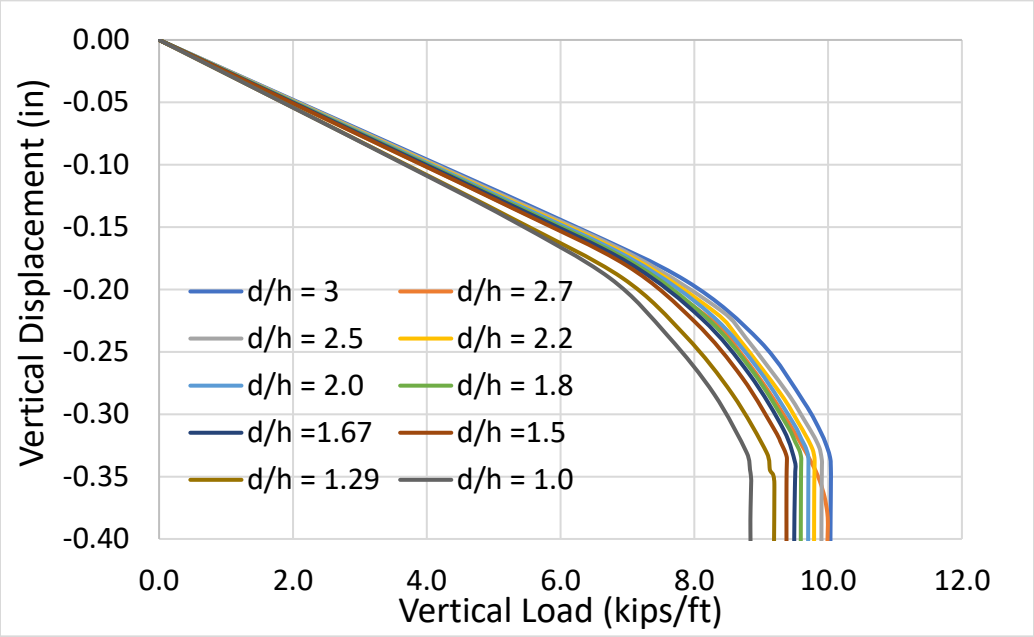

Figure 2-79. Load versus vertical displacement curve of loose sand for different ratio of d/h.

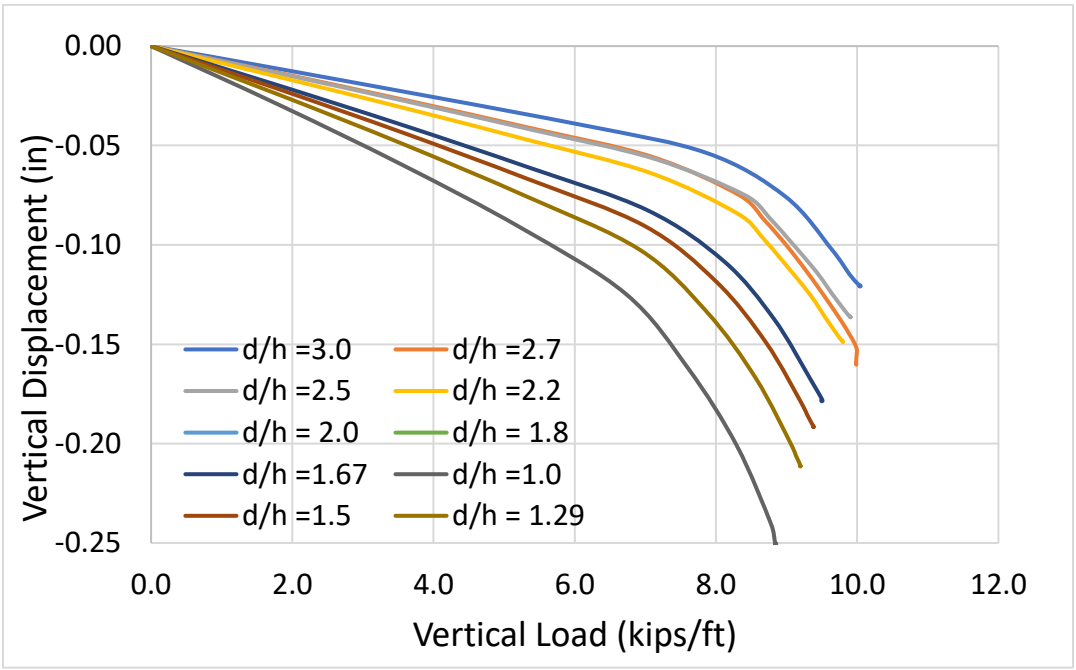

Figure 2-80. Load versus horizontal displacement curve of loose sand for different ratio of d/h.

Figure 2-81 plots the ultimate bearing capacity of the sheet pile embedded in dense and loose sand for a variety of d/h ratios. It also plots a good linear fit to these values. In Figure 2-82 - Figure 2-84, we plot the applied load against the vertical displacement of the pile in dense and loose sand top layers for d/h = 3, 1.67 and 1.0 respectively. In Figure 2-85 - Figure 2-87, we do the same for the horizontal displacement. There is clearly a marked difference in the ultimate bearing capacity of the pile in different soil layers.

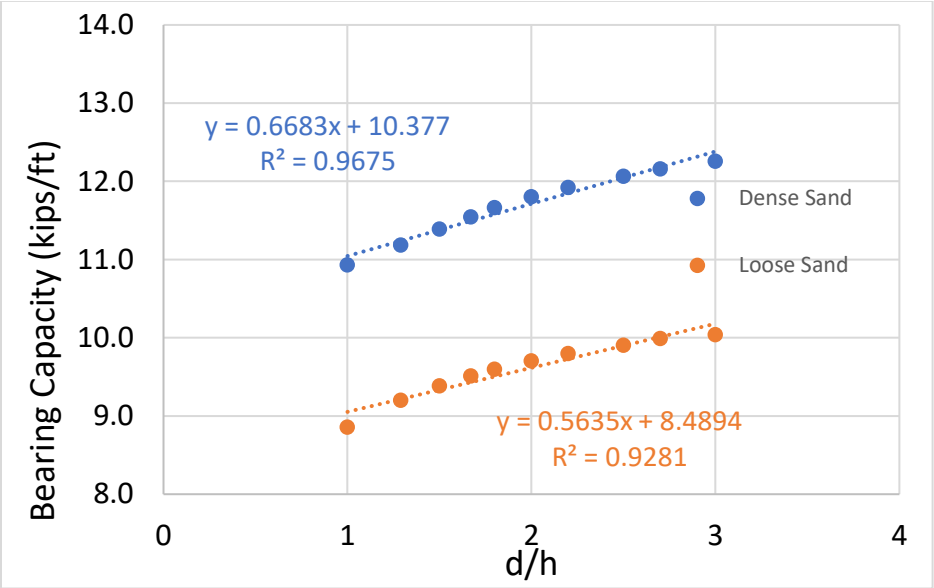

Figure 2-81 Relationship between the bearing capacity and ratio of d/h.

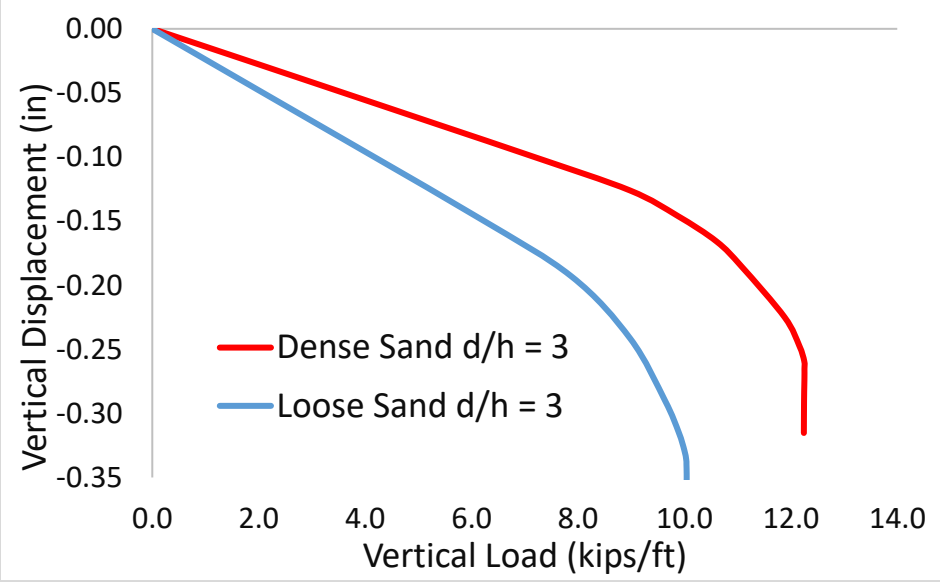

Figure 2-82 Comparison of load versus vertical displacement curve of loose sand as top layer against dense sand as the top layer for d/h =3.

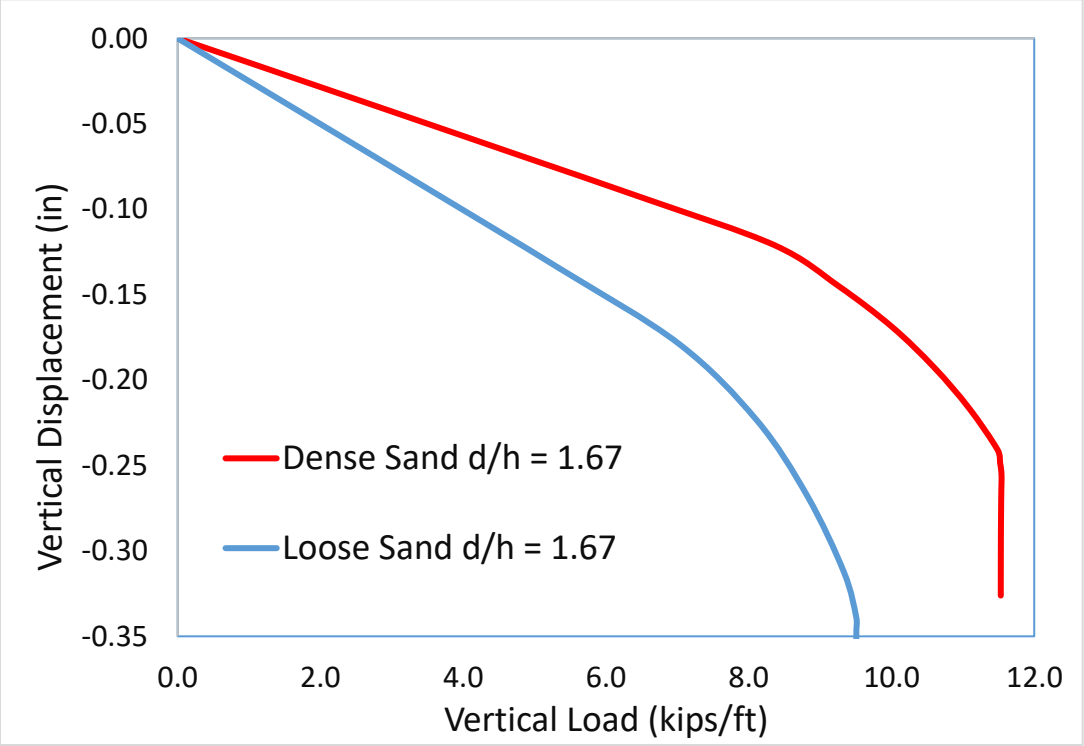

Figure 2-83 Comparison of load versus vertical displacement curve of loose sand as top layer against dense sand as the top layer for d/h =1.67.

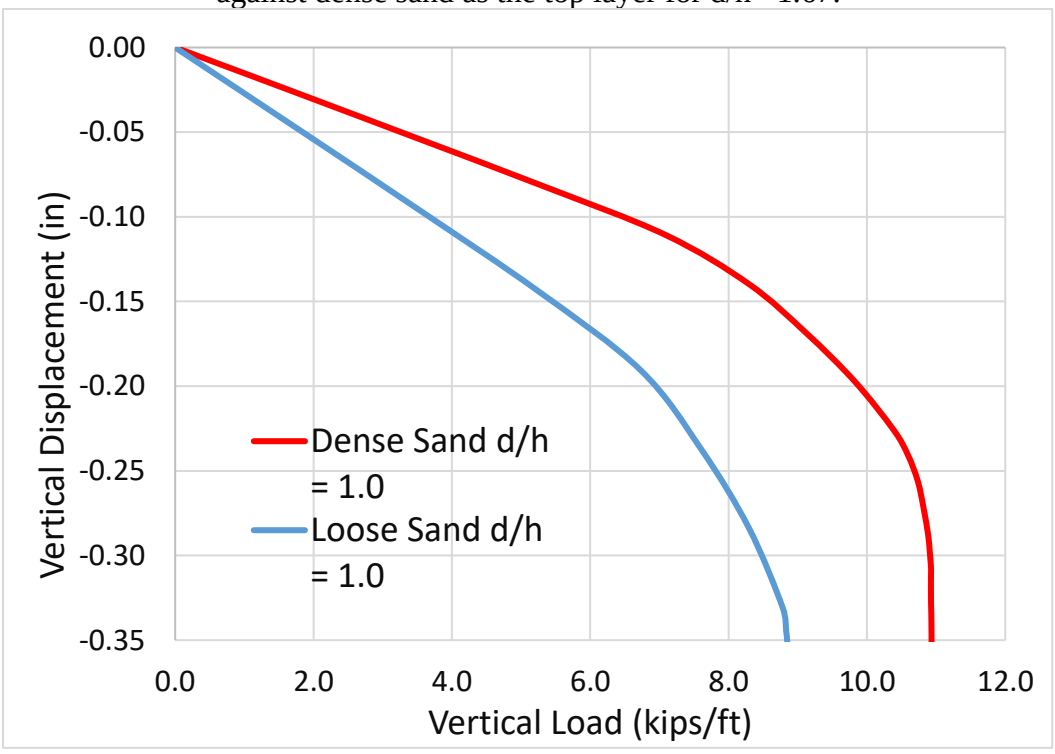

Figure 2-84 Comparison of load versus vertical displacement curve of loose sand as top layer against dense sand as the top layer for d/h =1.0.

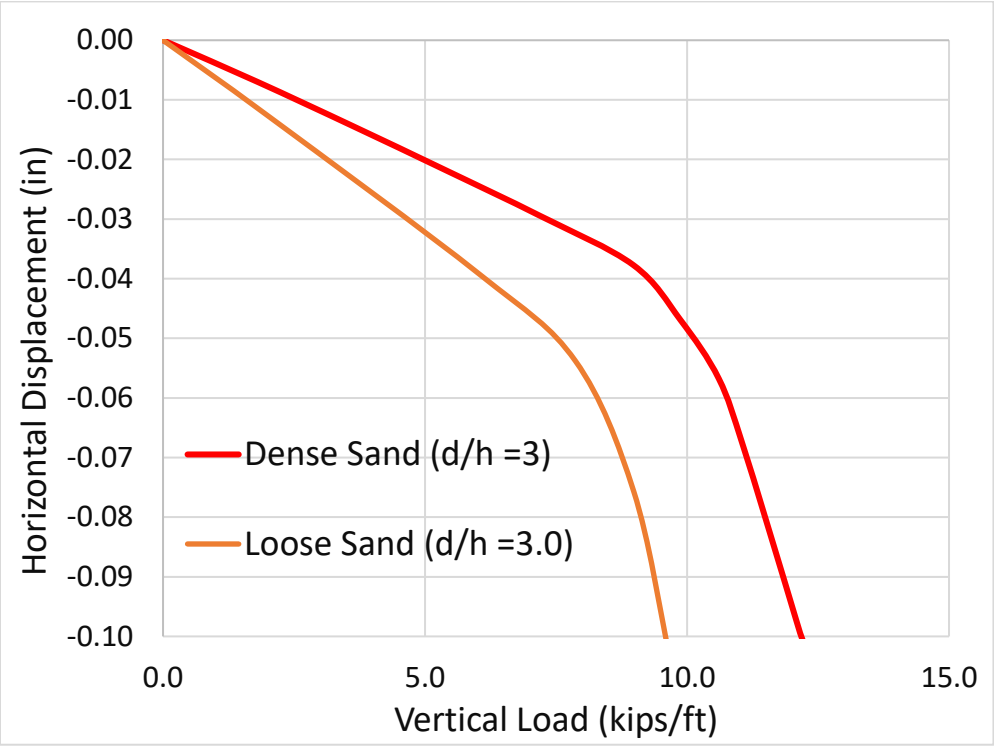

Figure 2-85 Comparison of load versus horizontal displacement curve of loose sand as top layer against dense sand as the top layer for d/h =3.0.

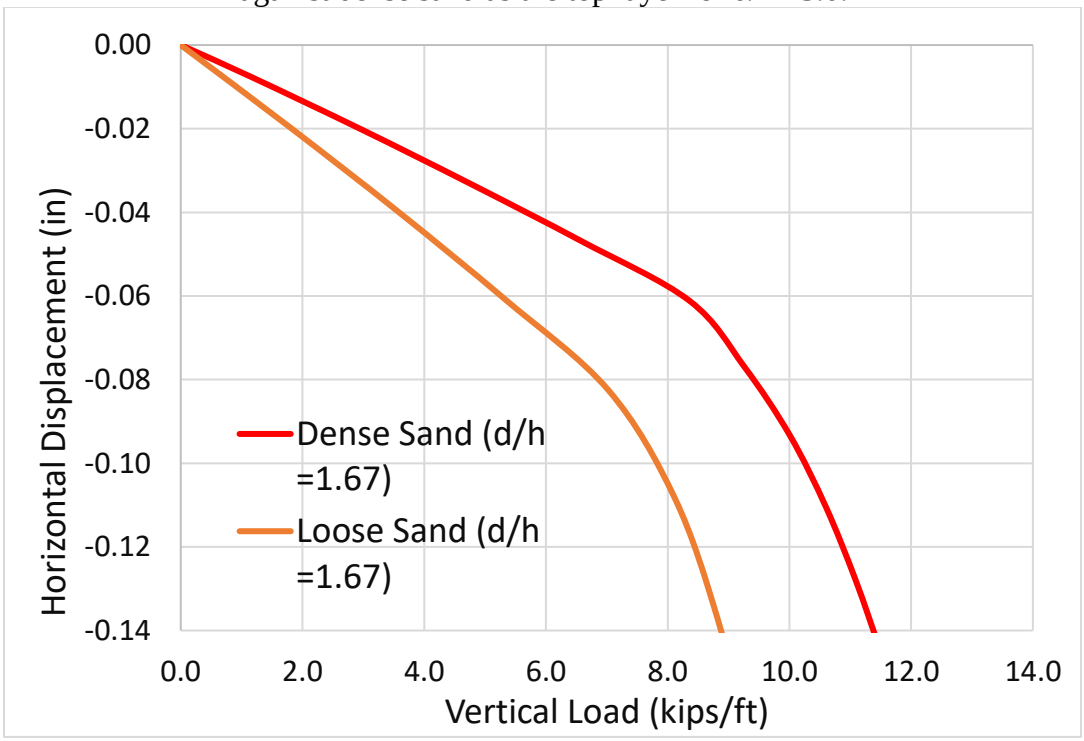

Figure 2-86 Comparison of load versus horizontal displacement curve of loose sand as top layer against dense sand as the top layer for d/h =1.67.

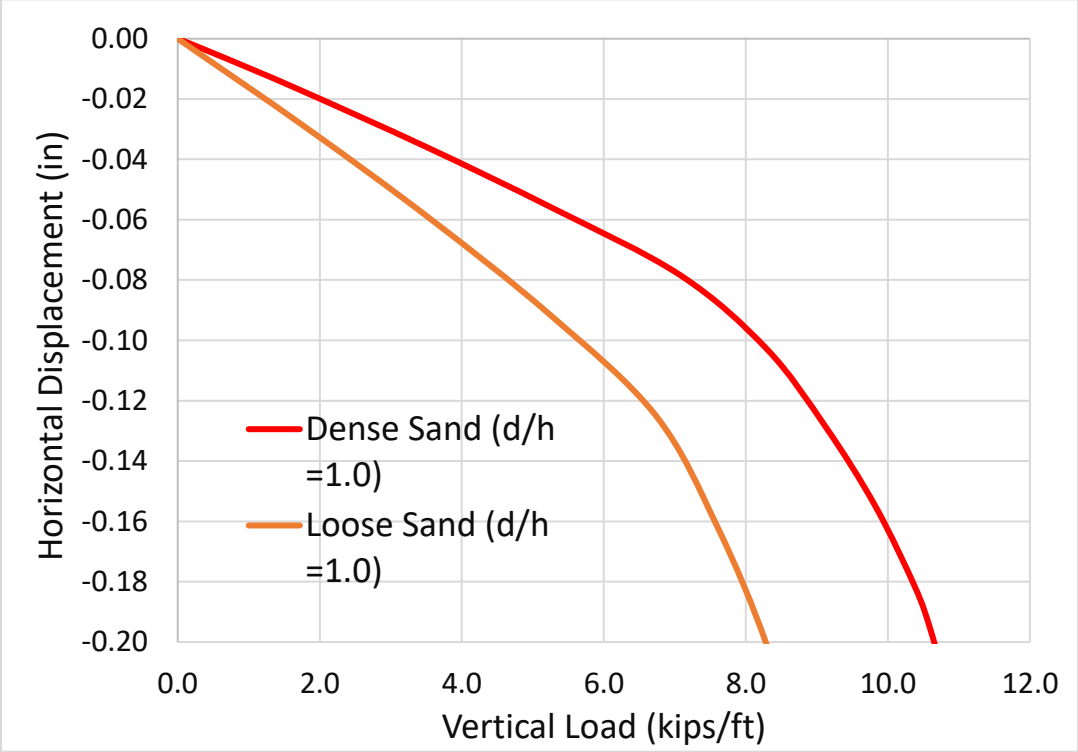

Figure 2-87 Comparison of load versus horizontal displacement curve of loose sand as top layer against dense sand as the top layer for d/h =1.0.

Discussion:

In this section, the investigation mainly focused on determining the effect of the penetration depth and relative density of sand (soil 1) under the effect of axial loading conditions for two soil layers. The main conclusions that can be deduced from the numerical modeling results are outlined as follows:

4. The ultimate axial piled wall capacity increased with an increase in penetration depth for soil 1 under same soil 2 conditions.
5. The ultimate axial piled wall capacity increased with an increasing in relative density.
6. The large difference in slope prior to achievement of maximum capacity can be explained by the differences in initial stress state caused by differences in soil density.
7. Relative density affects the allowable displacement before maximum strength is mobilized.
8. The linear fit to dense and loose sand are almost parallel to each other, implying a simple linear relationship between relative density and ultimate bearing capacity.

2.2.4.2 Effect of Sheet Pile Head Fixity

To study the influence of the sheet pile head conditions, we performed simulations with the pile head fixed in lateral directions. The topsoil (Soil 1) is assumed to be either dense sand or loose sand with the bottom soil (Soil 2) is very dense sand. We perform these tests using a ratio of d/h =3, d/h = 1.67 and finally d/h = 1. Figure 2-88 – Figure 2-90 plot the applied load against vertical

pile displacement in dense and loose top layers for three ratios of d/h = 3.0, 1.67 and 1.0 with different head conditions.

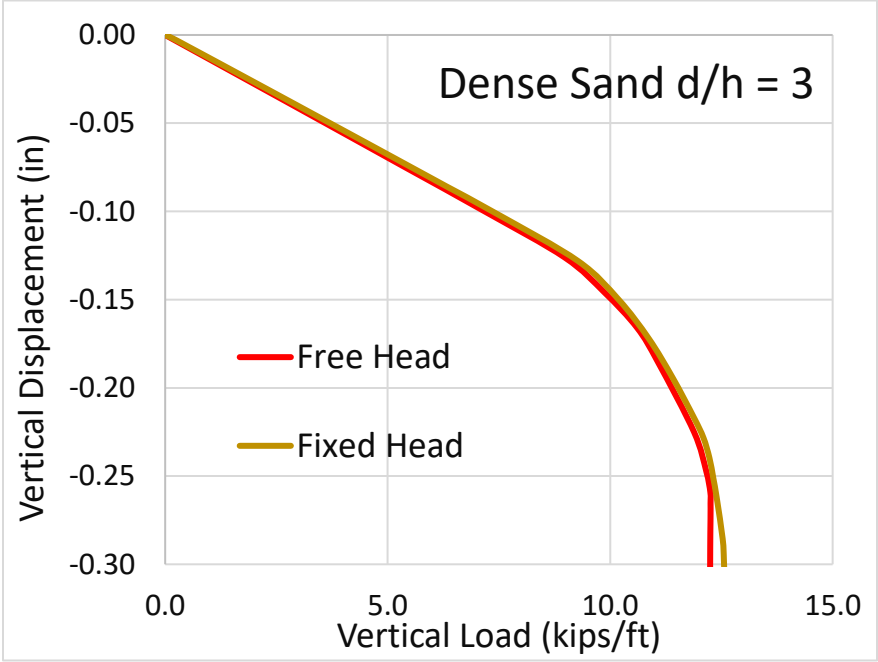

(a)

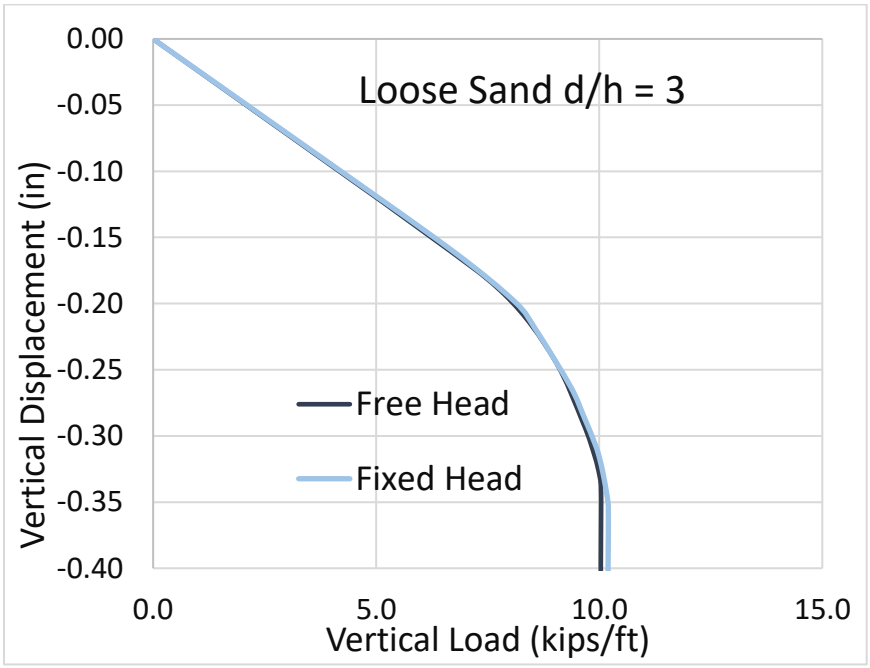

(b)

Figure 2-88 Load versus vertical displacement curve of different density sand at ratio of d/h=3 with Case 1 = free head and Case 2 = fixed head for (a) dense top soil and (b) loose top soil

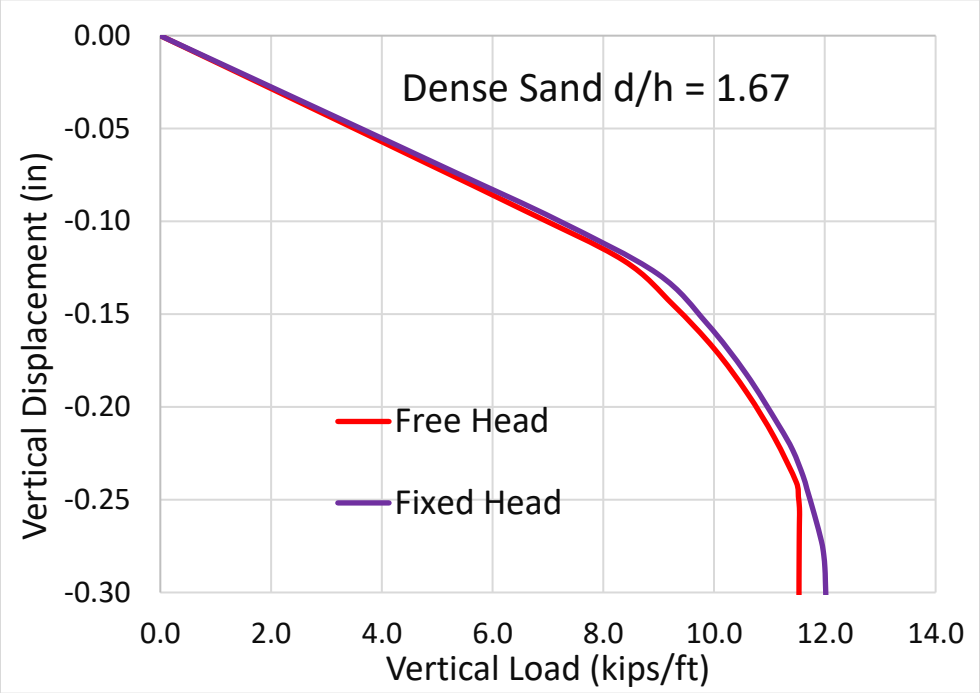

(a)

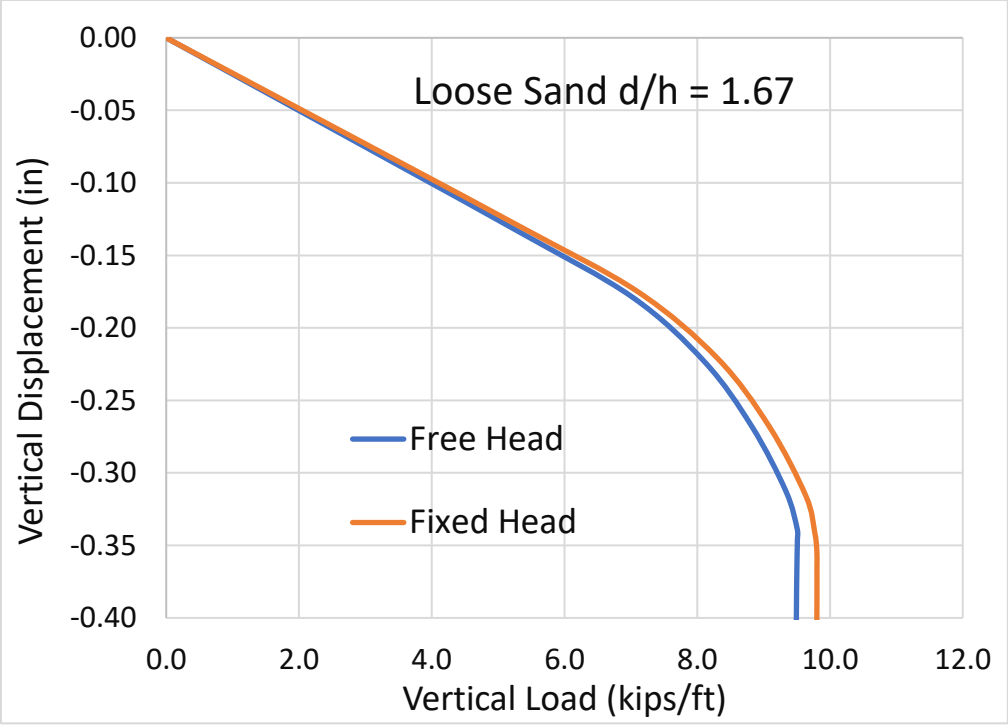

(b)

Figure 2-89 Load versus vertical displacement curve of different density sand at ratio of d/h=1.67 with free head and fixed head for (a) dense top soil and (b) loose top soil

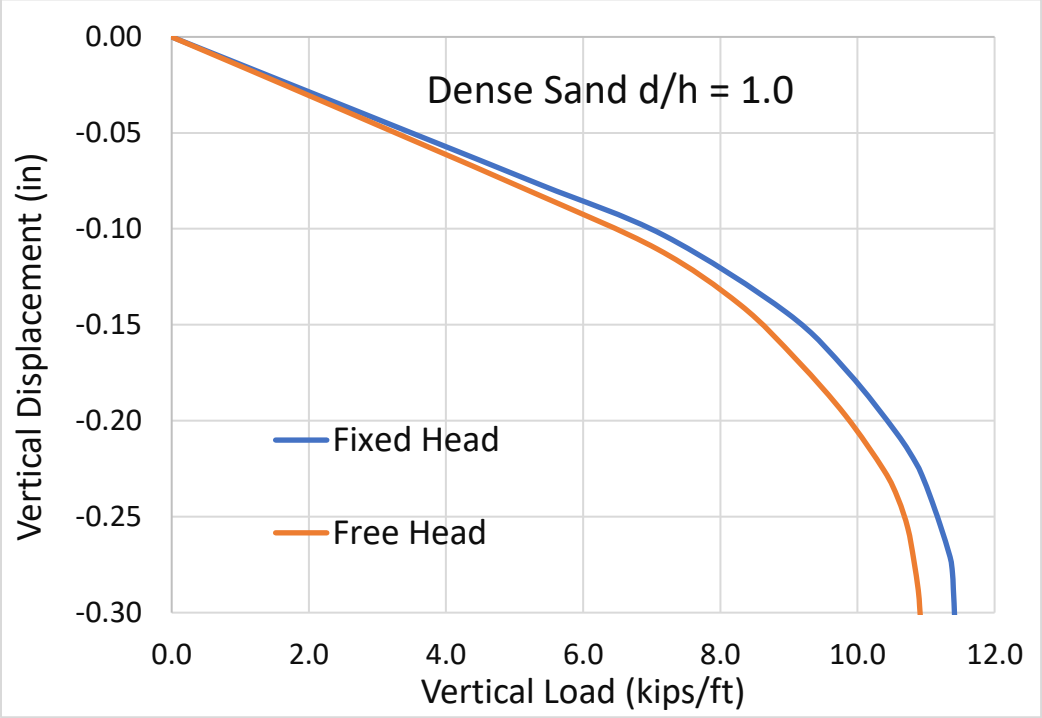

(a)

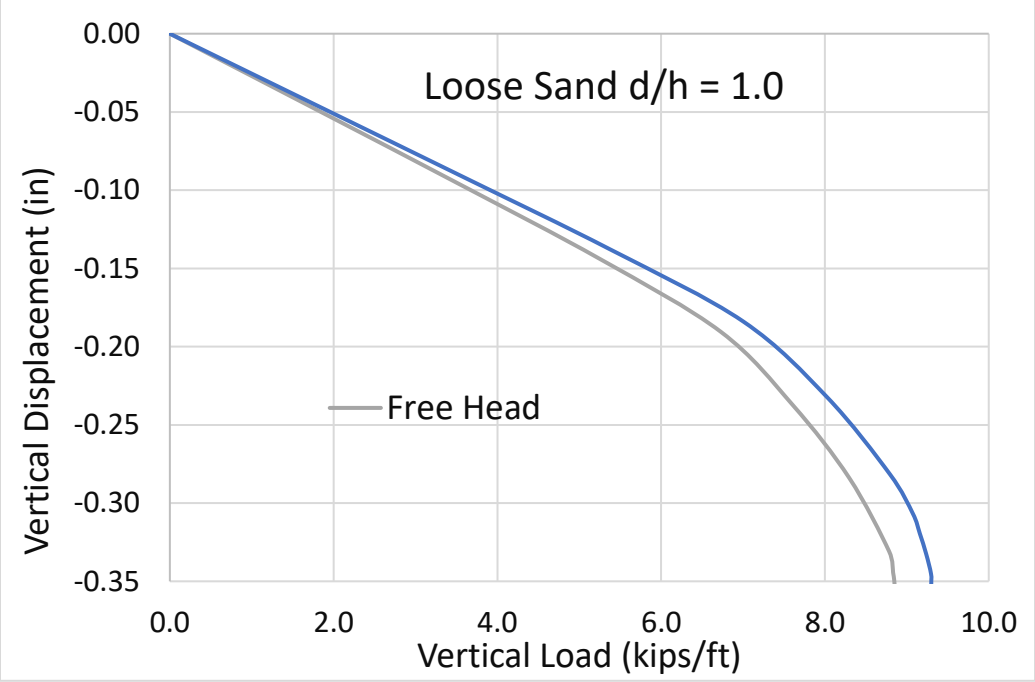

(b)

Figure 2-90 Load versus vertical displacement curve of different density sand at ratio of d/h=1.0 with Case 1 = free head and Case 2 = fixed head for (a) dense top soil and (b) loose top soil

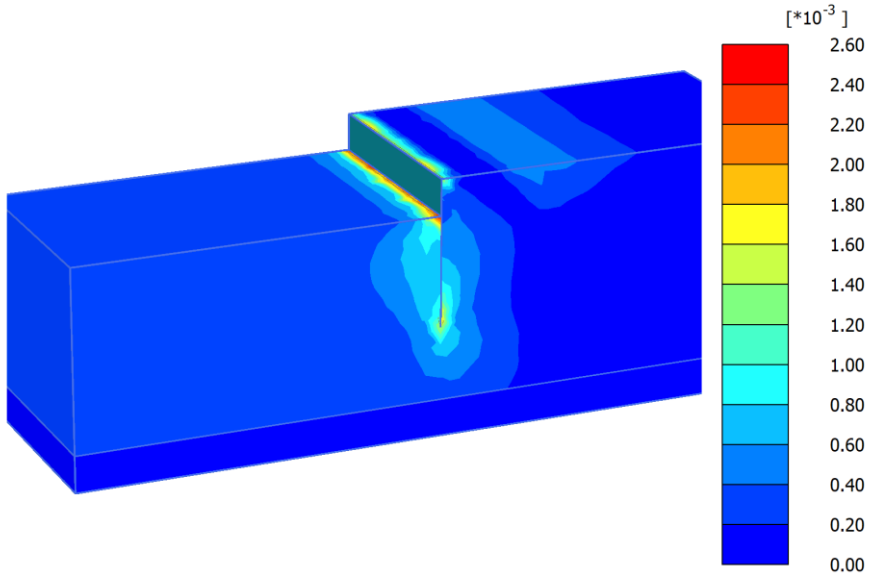

(a)

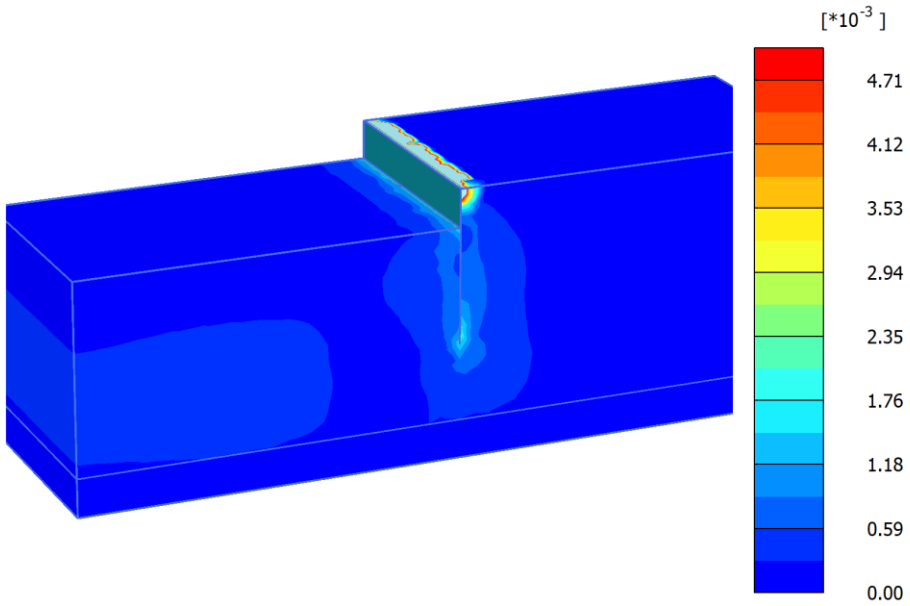

(b)

Figure 2-91 Contours of shear strains in dense sand top layer for (a) Free head condition (b) Fixed head condition for d/h = 3.0.

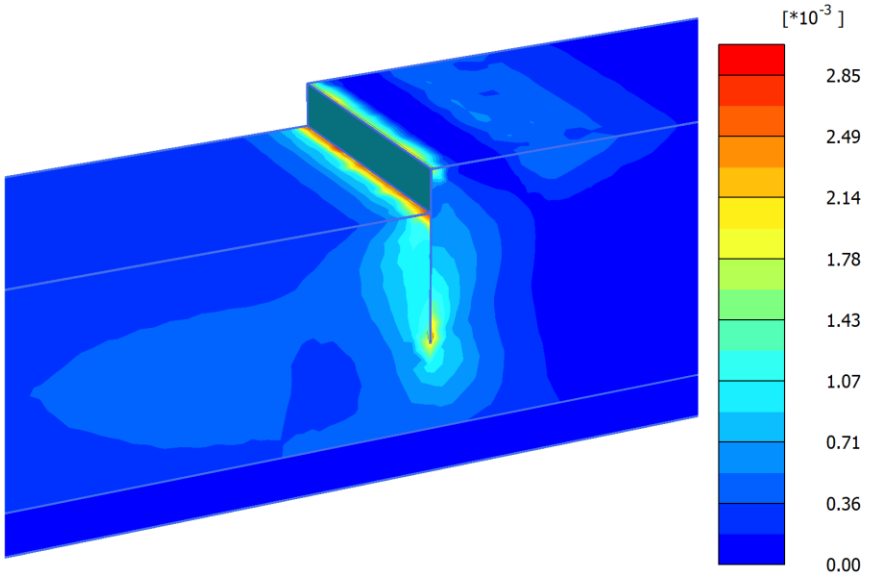

(a)

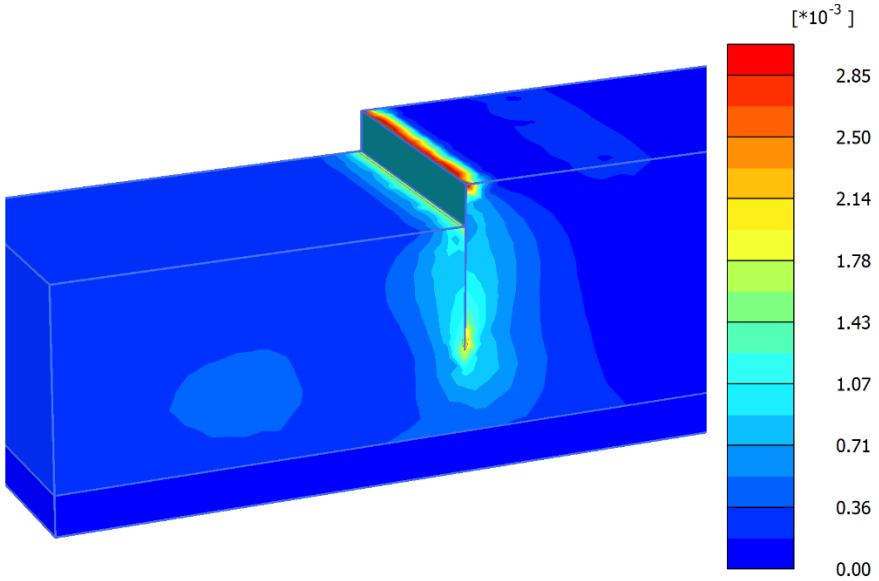

(b)

Figure 2-92 Contours of shear strains in loose sand top layer for (a) Free head condition (b) Fixed head condition for d/h = 3.0

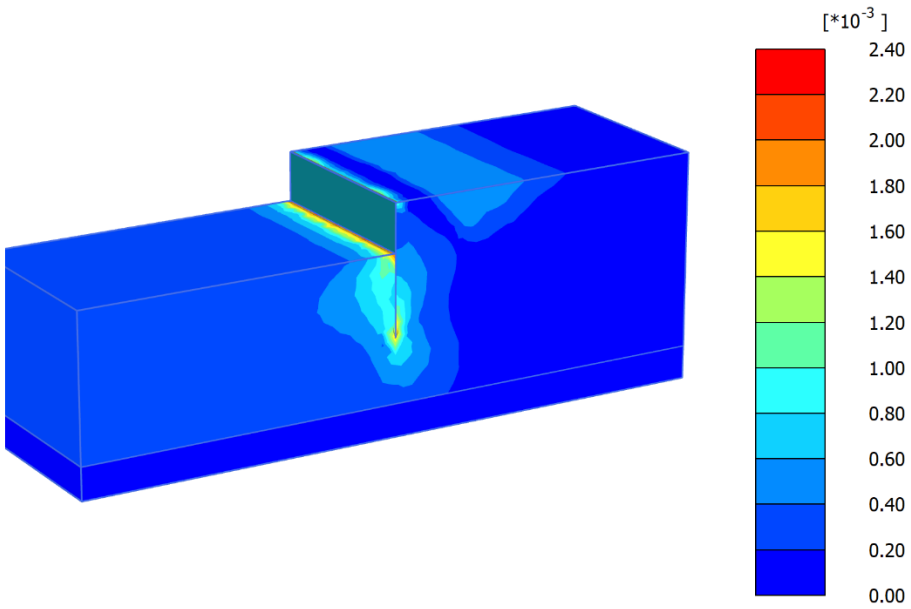

(a)

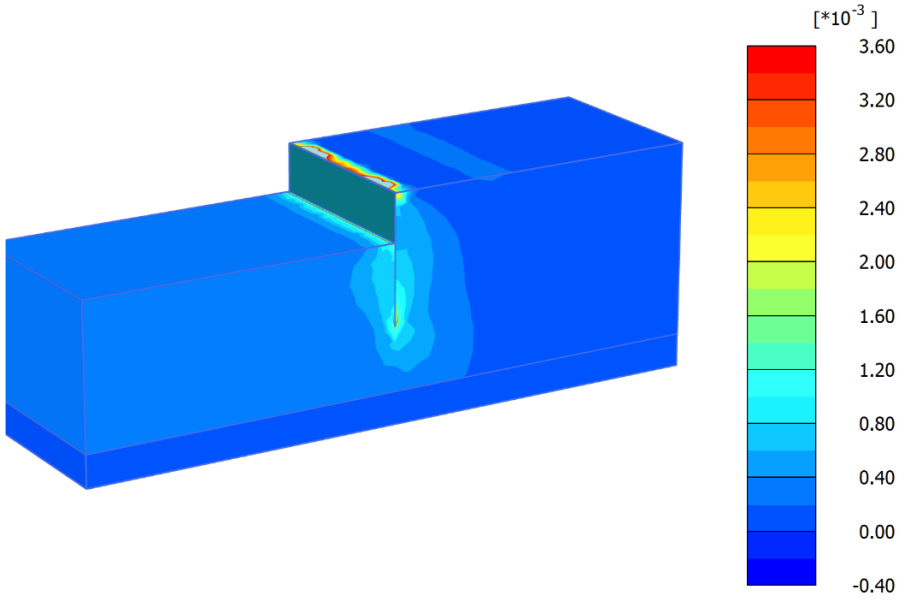

(b)

Figure 2-93 Contours of shear strains in dense sand top layer for (a) Free head condition (b) Fixed head condition for d/h = 1.67

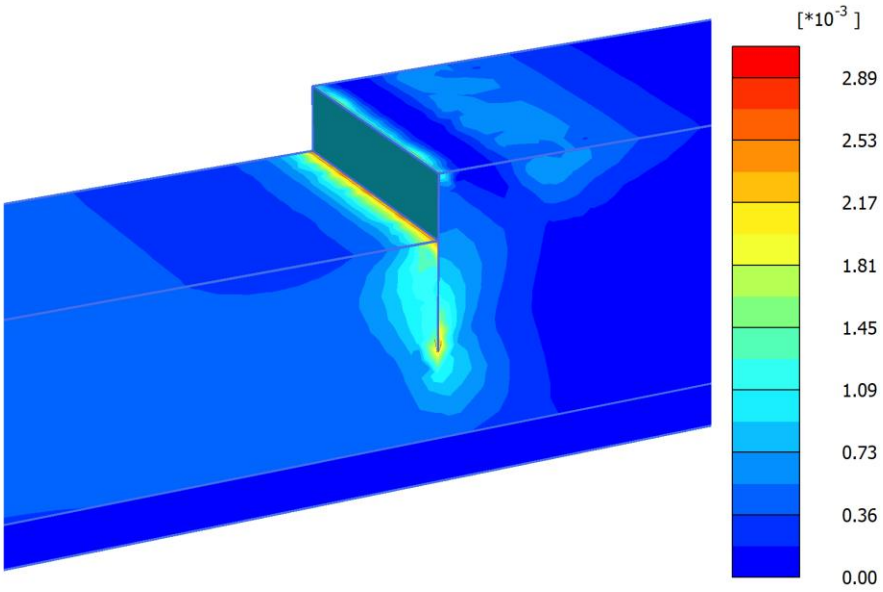

(a)

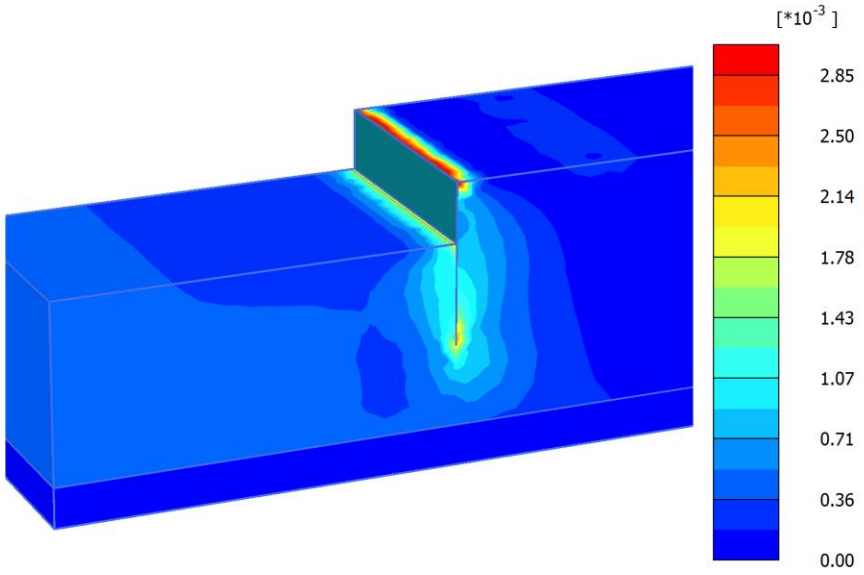

(b)

Figure 2-94 Contours of shear strains in loose sand top layer for (a) Free head condition (b) Fixed head condition for d/h = 1.67

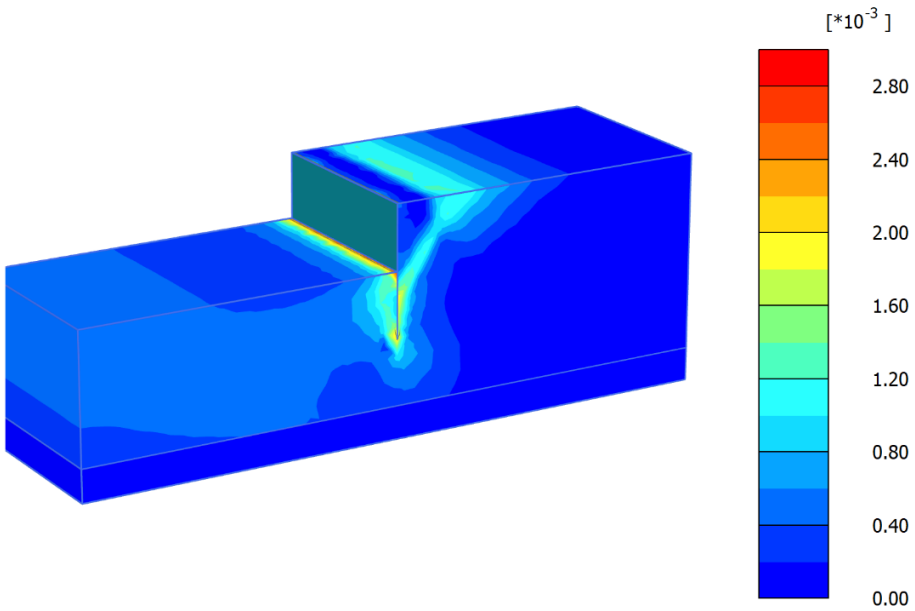

(a)

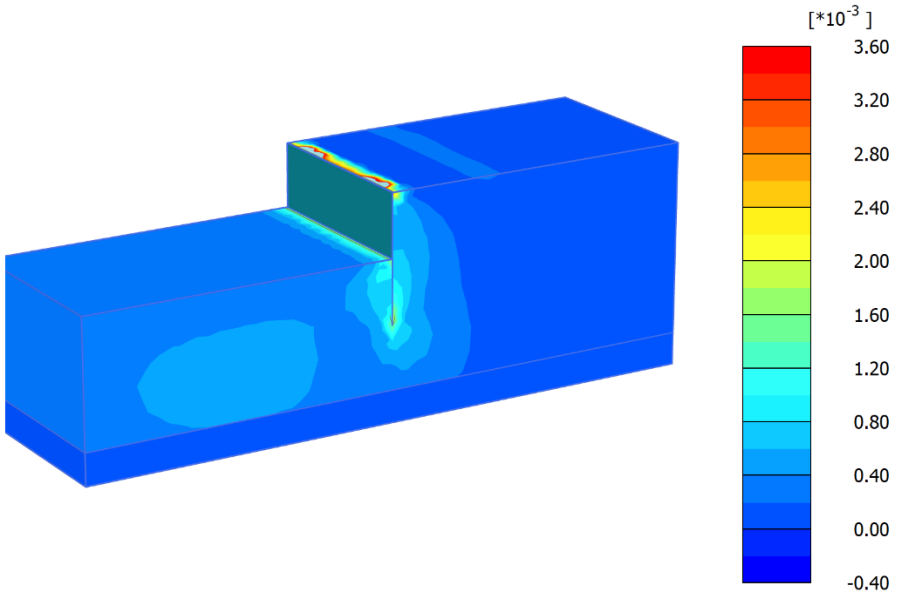

(b)

Figure 2-95 Contours of shear strains in dense sand top layer for (a) Free head condition (b) Fixed head condition for d/h = 1.0

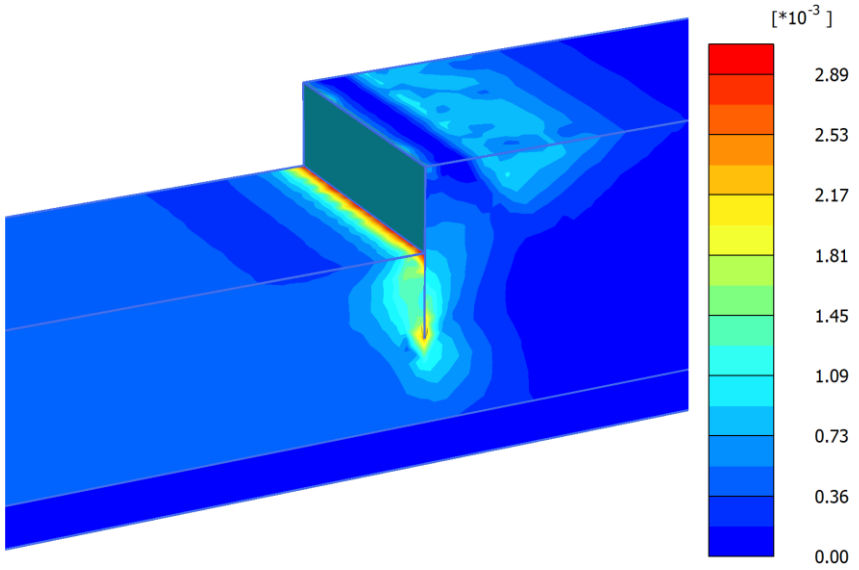

(a)

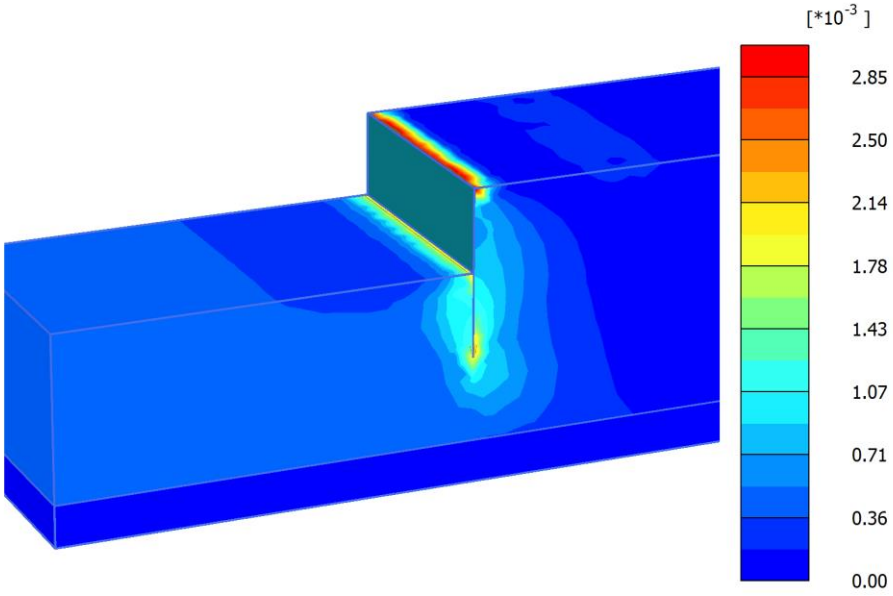

(b)

Figure 2-96 Contours of shear strains in loose sand top layer for (a) Free head condition (b) Fixed head condition for d/h = 1.0

Discussion:

From the plots of the force displacement of the pile, we can see that the fixed head condition does not show marked improvement over the free head condition for a d/h ratio = 3 irrespective of relative density of the sand. However, with smaller ratio of d/h, that is greater height of the retained soil, we see that there is marked improvement in bearing capacity for both dense and loose top layer. Figure 2-91 and Figure 2-92 plot the shear strain for (a) free and (b) fixed head in dense and loose top layer, respectively, for d/h = 3.0. Figure 2-93 and Figure 2-94 do the same for d/h = 1.67 and Figure 2-95 and Figure 2-96 do the same for d/h = 1.0. The contours of shear strain reveal that fixing the head of the pile reduces lateral deformation in the retained soil but causes intense shearing at the top of the soil-structure interface.

2.2.4.3 Effect of Surcharge Loading

Surcharge loads exert additional lateral pressures on the sheet pile wall system. Surcharge loads may result from traffic loads, equipment, construction materials, and other factors. Therefore, numerical modeling of axially loaded sheet pile walls at different surcharge intensities was conducted to investigate the effect of surcharge loads on the general behavior (e.g., axial bearing capacity, lateral movement and induced bending moment) of the sheet pile wall. The following simulations show sheet pile wall under two different surcharge loadings (design vehicular live load specified in 3.6.1.2 of ASSHTO, 2014) for three different soil conditions. The surcharge loading area is 393.7 ft^2. The soil properties are shown in Table 2-3. The ratio of d/h is 3 in each simulation.

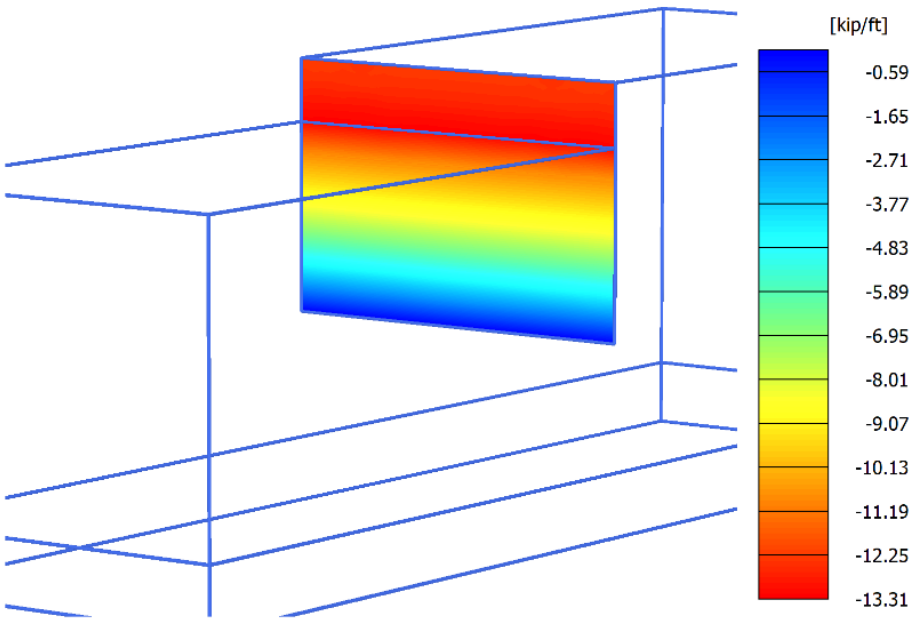

(a)

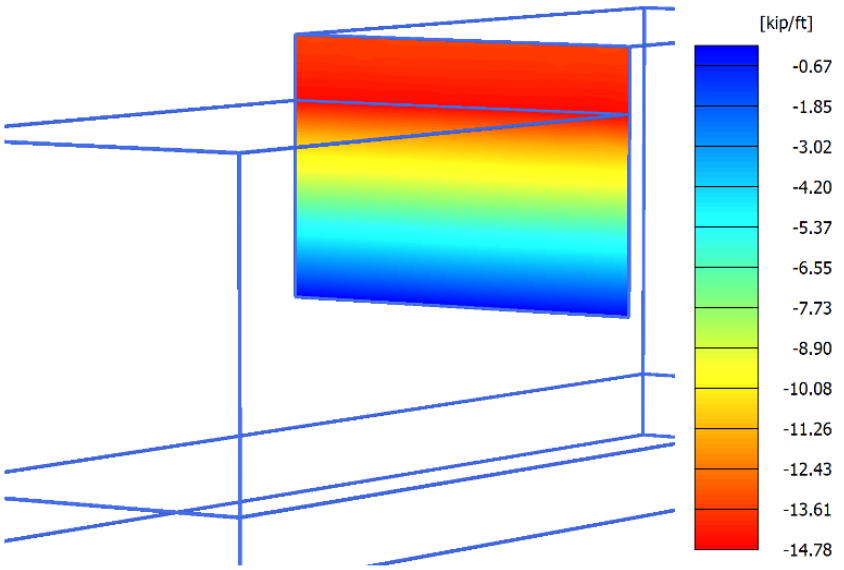

(b)

Figure 2-97 Contours of axial capacity of sheet pile wall in dense sand as top soil layer; (a) Surcharge loading 0.21 ksf; (b) Surcharge loading 0.42 ksf.

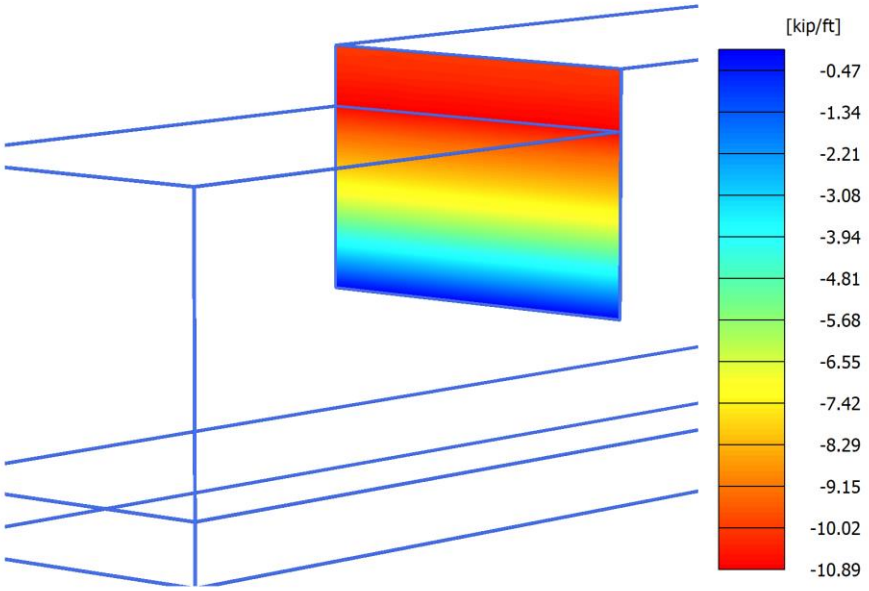

(a)

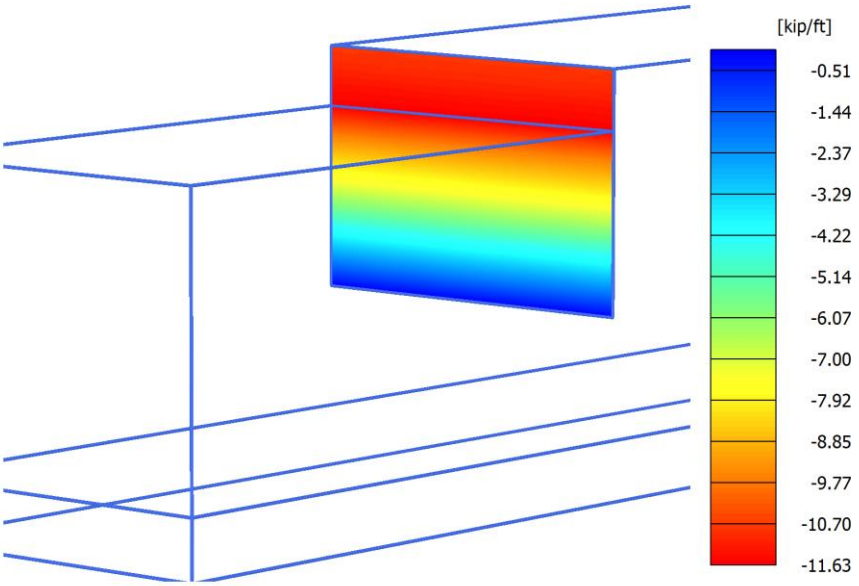

(b)

Figure 2-98 Contours of axial capacity of sheet pile wall in loose sand as top soil layer; (a) Surcharge loading 0.21 ksf; (b) Surcharge loading 0.42 ksf.

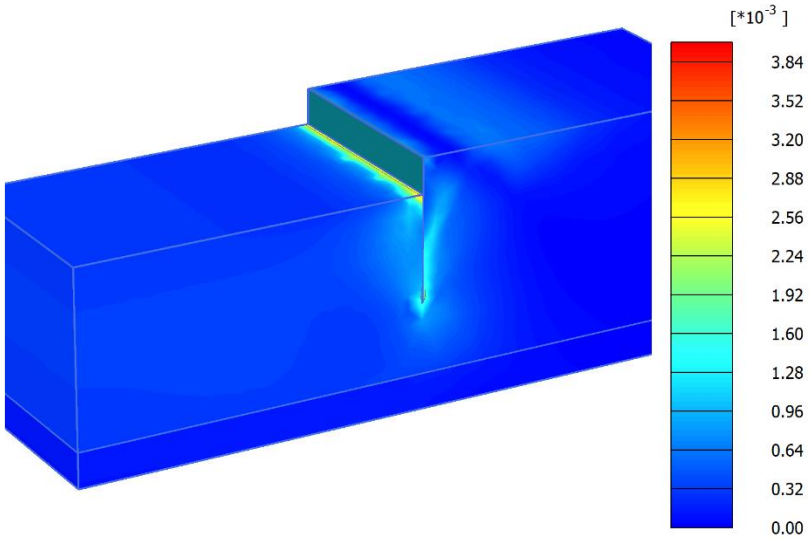

(a)

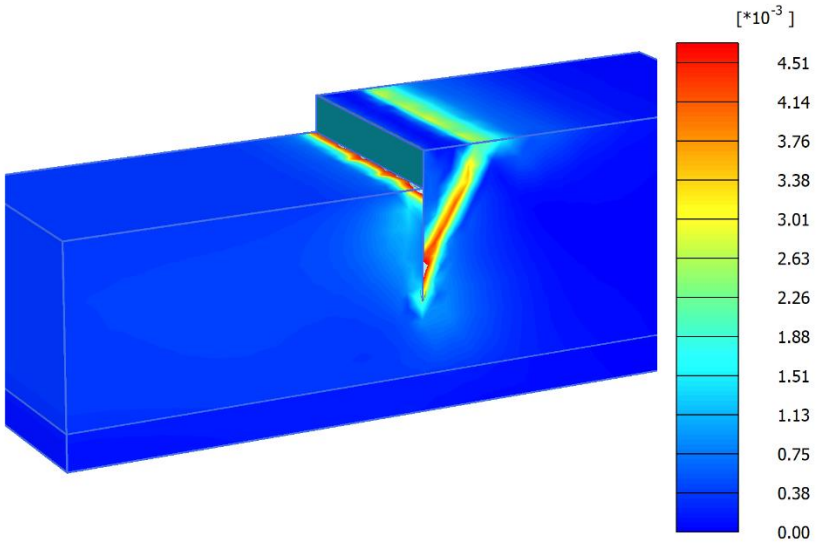

(b)

Figure 2-99 Contours of shear strain around the sheet pile wall with dense sand as top soil layer; (a) Surcharge loading $0.21\ ksf$; (b) Surcharge loading $0.42\ ksf$.

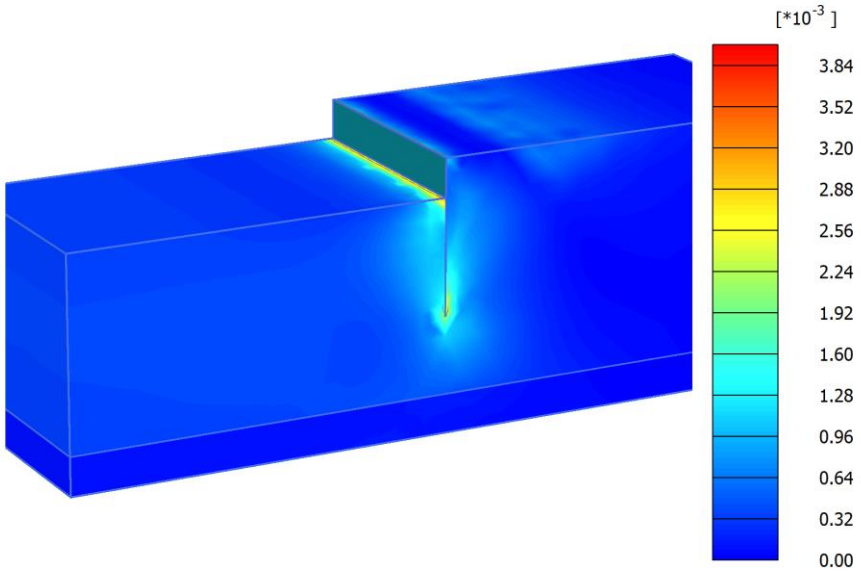

(a)

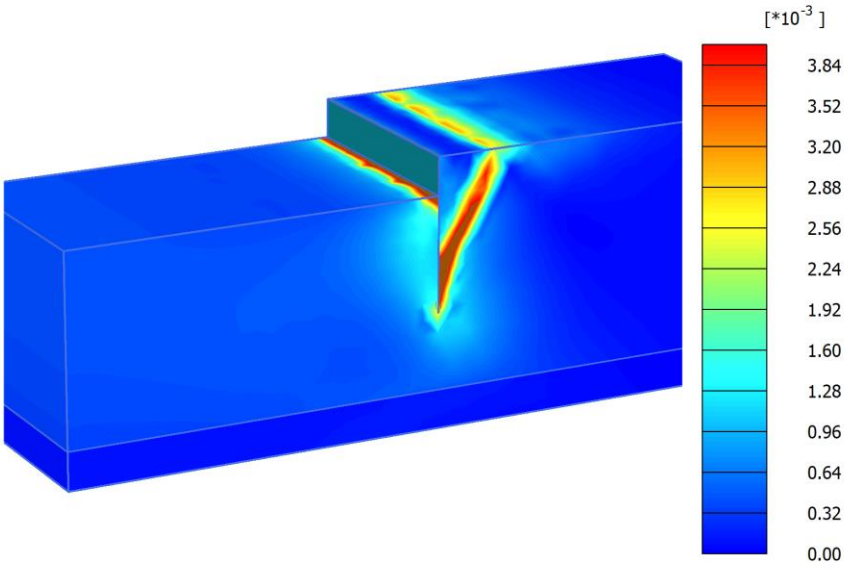

(b)

Figure 2-100 Contours of shear strain around the sheet pile wall with loose sand as top soil layer; (a) Surcharge loading $0.21\ ksf$; (b) Surcharge loading $0.42\ ksf$.

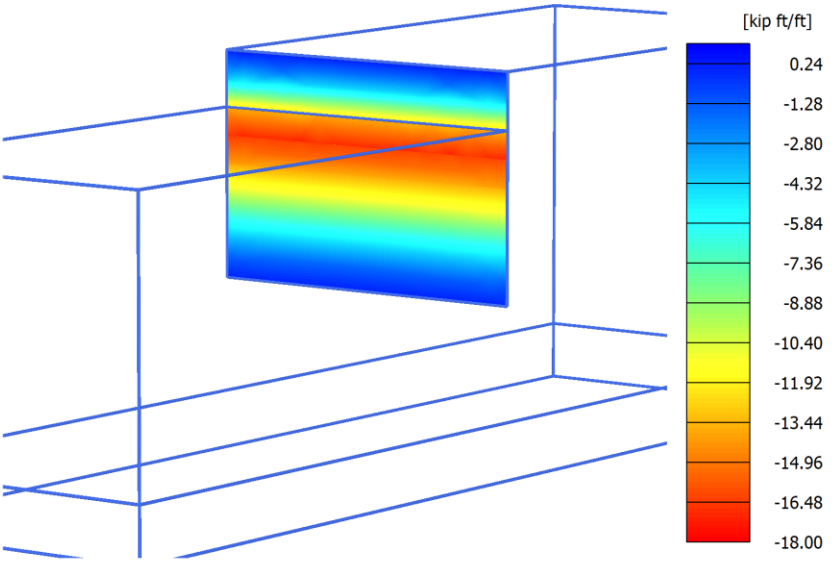

(a)

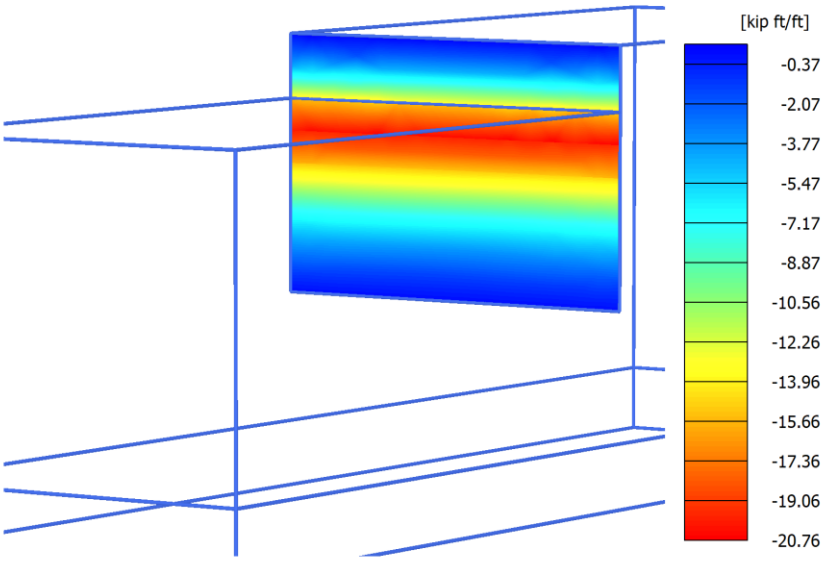

(b)

Figure 2-101 Contours of bending moments on the sheet pile wall with dense sand as top soil layer; (a) Surcharge loading $0.21\ ksf$; (b) Surcharge loading $0.42\ ksf$.

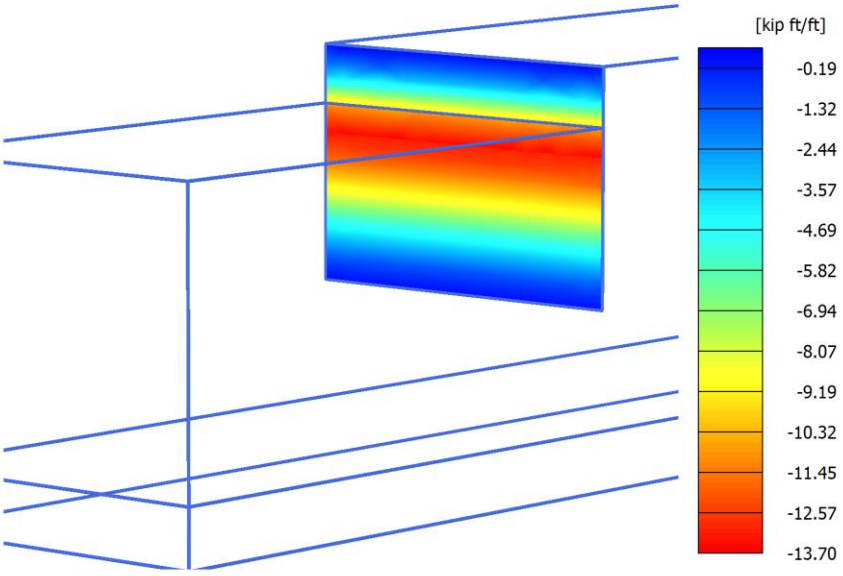

(a)

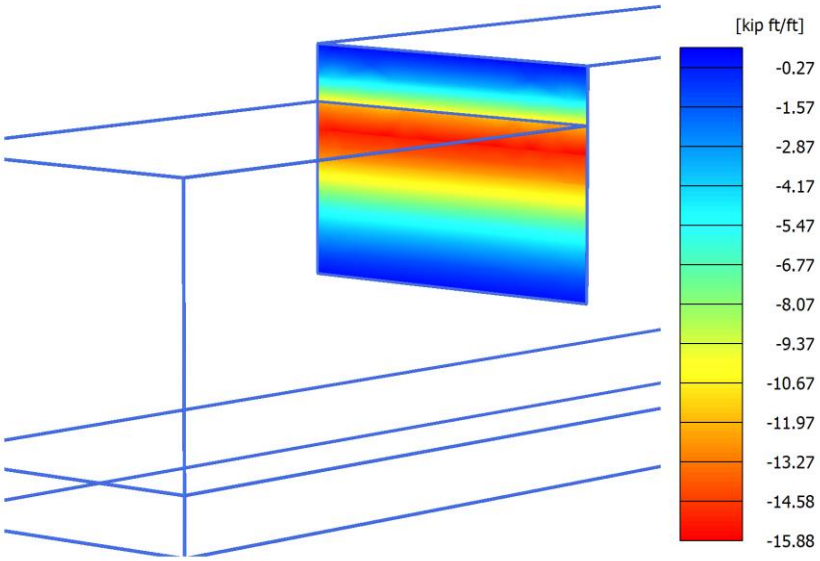

(b)

Figure 2-102 Contours of bending moments on the sheet pile wall with loose sand as top soil layer; (a) Surcharge loading $0.21\ ksf$; (b) Surcharge loading $0.42\ ksf$.

Discussion:

Figure 2-97-Figure 2-102 show, for both values of surcharge loading, the contours of axial capacity of sheet pile wall, plastic shear strain, and bending moment contour of sheet pile wall, respectively. With an increase in the surcharge load, the axial load experienced by the piles increases. Figure 2-99 and Figure 2-100 show that the surcharge of 0.42 ksf seems to trigger shear bands in the retained soil, with the dense layer experiencing greater magnitude of shear deformation. From Figure 2-101 and Figure 2-102 it is apparent that the bending moment acting on the sheet pile clearly increases with increase in the relative density of sand. The surcharge load also increases bending moments acting on the pile wall. At a surcharge intensity of $0.42\ ksf$ and d/h = 3, the maximum bending moments increased by 47% and 35% for friction angles of 32° and 27°, respectively.

Reference

Brinkgreve, R. B. J., E. Engin, W. M. Swolfs, D. Waterman, A. Chesaru, P. G. Bonnier, and V. Galavi. "Plaxis 3D 2012." *Plaxis bv* (2012).

3 CHAPTER 3: DETAILS OF PROPOSED CENTRIFUGE TESTING

3.1 Task 3a: Centrifuge modeling and procedures to conduct the centrifuge tests

Through task 3, it is planned to design and develop centrifuge load tests to investigate the problem at hand, compare centrifuge tests results with the theoretical models, and calibrate and validate the numerical models. Different geo-structural conditions will be evaluated to account for varying factors including soil layering, sheet pile wall flexural rigidity, boundary conditions of the sheet pile wall, and quasi-static loading rate. As such, the centrifuge tests are designed to help with achieving the aforementioned goals. Given in the following sections are the details of the centrifuge testing program.

3.1.1 Centrifuge test set-up

The centrifuge model tests in this study will be carried out at a centrifugal acceleration of 50 g in a rigid container. The maximum payload for the University of Florida centrifuge is 12.5 g-ton and the available basket area is approximately 0.34 m^2 (3.7 ft^2). The beam radius is 1.5 m (59 in) and the maximum centrifugal acceleration is 80 g. The rigid container to be used in our tests will have internal dimensions of (L×W×H) 558.8 mm (22 in) × 203.2 mm (8 in) × 457.2 (18 in). The rigid container will consist of three aluminum solid plates fixed to a rigid Plexiglas transparent plate. This container will have smooth walls and will make it possible to reduce the boundary effects and reasonably simulate the prototype event. By placing the sheet pile wall and instruments as far as possible from the boundaries (at the middle of the container), the boundary effects will be further minimized.

3.1.1.1 Sheet pile characteristics

Two model sheet pile walls will be machined from aluminum sheets with final prototype-scale geometry, flexural rigidity (bending stiffness), and axial stiffness values matched with those of the full-scale PZ sheet pile sections used in the geotechnical engineering industry. Using aluminum instead of steel is a typical practice in the centrifuge modeling of structural elements as it helps with increasing the thickness of the section and make it possible to machine the sections with the desirable precision using the typical computer numerical control (CNC) cutting machines (routers). The prototype-scale bending stiffness and axial stiffness of the first wall (PZS1) will be about the same as those of PZ27. The second wall (PZS2) will have bending and axial stiffness values approximately twice of those of PZS1 (and PZ27). The increase in the stiffness of PZS2 is achieved by increasing the thickness (both web and flange) from 35 mm in PZS1 to 70 mm in PZS2 and keeping all other geometrical properties (e.g. width and angles) the same. The model-scale and prototype-scale values of sheet pile sections are provided in Table 3-1. Note that the presented values in Table 3-1 are associated with the properties of the shaded areas of the sections (the pair of sheet piles) shown in Figure 3-1.

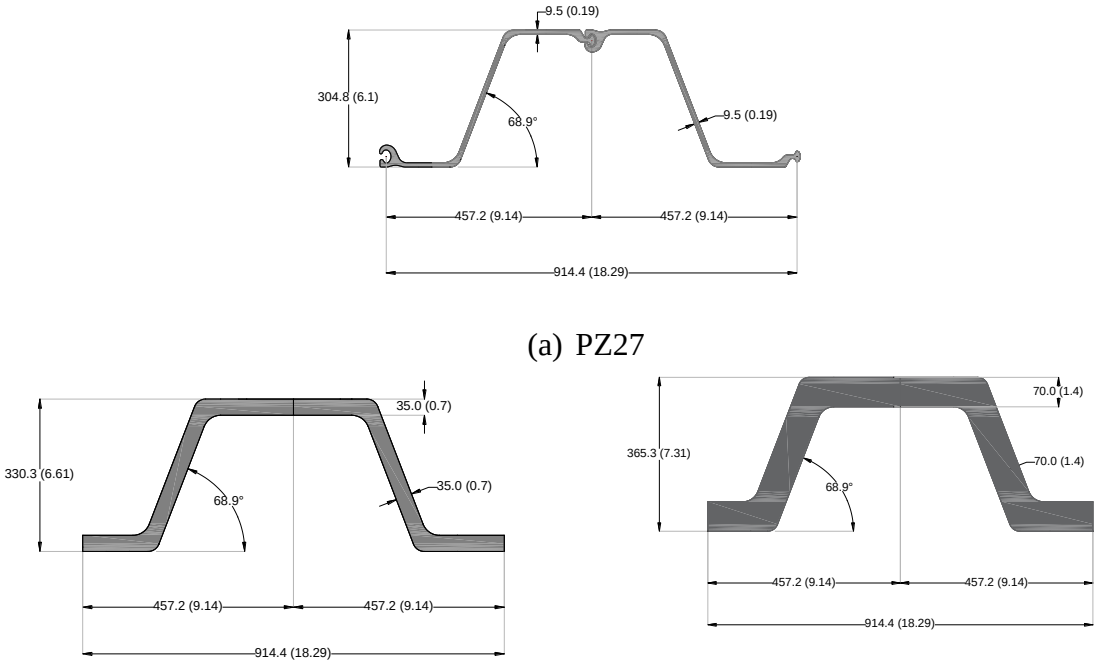

(a) PZ27

(b) PZS1

(c) PZS2

Figure 3-1. Sheet pile sections: (a) pair of PZ27 sections; (b) pair of PZS1 sections; and (c) pair of PZS2 sections; the dimensions are provided in prototype-scale (and model-scale) in millimeters.

The cantilever sheet pile wall will consist of 22 sections (11 pairs) of sheet pile elements resulting in the total prototype-scale width of 10 m. The length of the sheet pile wall will be 16.2 m (324 mm in model-scale). The prototype-scale properties of the wall are presented in Table 3-1. The PZS1 wall is shown in Figure 3-2. In this research, it is assumed that forces fully transmit in the sheet piles interlocks (i.e. welded interlocks). In placing the sheet pile walls in the centrifuge model, care will be taken to eliminate or significantly reduce boundary effects from the container walls on the sheet pile wall models. As such, the sides of the sheet pile will be greased.

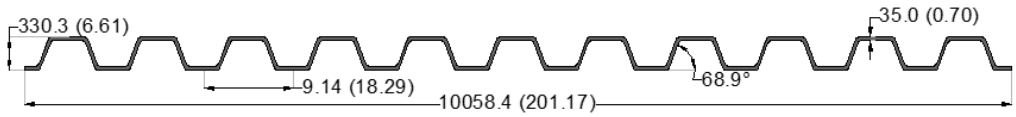

(a)

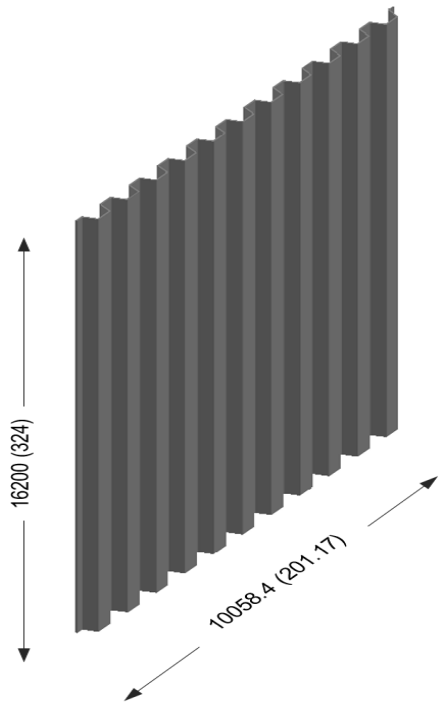

(b)

Figure 3-2. (a) Cross section; and (b) 3D view of the sheet pile wall consisted of 22 PZS1 elements; the dimensions are provided in prototype-scale (and model-scale) in millimeters.

Table 3-1. Sheet pile section dimensions and properties

	Model-scale (1 g)		Prototype-scale (50 g)		
Section	PZS1	PZS2	PZ27	PZS1	PZS2
Width (mm)	18.29	18.29	914.4	914.4	914.4
Height (mm)	6.61	7.31	304.8	330.3	365.3
Flange thickness (mm)	0.7	1.4	9.5	35	70
Web thickness (mm)	0.7	1.4	9.5	35	70
Cross Sectional Area, A (cm^2/m)	0.19	0.37	156.28	464.63	931.80

Perimeter, P (cm/m)	5.47	5.75	300.55	273.63	287.63
Moment of inertia, I (cm^4/m)	0.049	0.101	110,293.82	306,753.22	633,394.06
Material	aluminum	aluminum	steel	aluminum	aluminum
Young's modulus, E (GPa)	70	70	200	70	70
Bending stiffness, EI ($MN.m^2/m$)	3.44×10^{-5}	7.1×10^{-5}	220.59	214.73	443.38
Axial stiffness, EA (MN/m)	1.3	2.61	3,125.67	3,252.38	6,522.61

Table 3-2. Prototype-scale sheet pile wall dimensions and properties

Sheet Pile Wall	PZ27	PZS1	PZS2
Width (mm)	10058.4	10058.4	10058.4
Height (mm)	304.8	330.3	365.3
Flange thickness (mm)	9.5	35	70
Web thickness (mm)	9.5	35	70
Cross Sectional Area, A (cm^2/m)	156.28	464.63	931.80
Perimeter, P (cm/m)	300.55	273.63	287.63
Moment of inertia, I (cm^4/m)	110,293.82	306,753.22	633,394.06
Material	steel	aluminum	aluminum
Young's modulus, E (GPa)	200	70	70
Bending stiffness, EI ($MN.m^2/m$)	220.59	214.73	443.38
Axial stiffness, EA (MN/m)	3,125.67	3,252.38	6,522.61

3.1.1.2 Soil properties

In order to represent the frequently encountered geo-materials and site conditions in Florida, Florida natural sand will be used to construct normally consolidated dry sand profiles in the centrifuge tests. Based on the USCS, the mentioned soil is "SP" with coefficients of uniformity and curvature of 1.77, and 1.08, respectively. The soil gradation curve and additional soil properties are provided in Figure 3-3. Homogenous medium-dense sand profiles with relative densities of about 60% will be constructed. Two-layered soil profiles consisting of a medium-

dense sand (D_r≈60%) overlaying a dense sand layer (D_r≈90%) will be modeled as well. An air-pluviation method will be used to prepare the sand layer(s) and achieve the desired relative density and the void ratio. For this purpose, a novel pluviator designed and manufactured at the University of Florida will be used where the entire area of the centrifuge container will be covered by the pluviator; therefore, the homogeneity and uniformity of the profile will be ensured. The relative density of sand layer(s) will be controlled by maintaining a nearly constant drop height and rate. Furthermore, the profile will be constructed in layers (small lifts of about 40 mm in model-scale) and the homogeneity of each pluviated layer will be verified by weighting the soil at each layer and checking the unit weight and relative density.

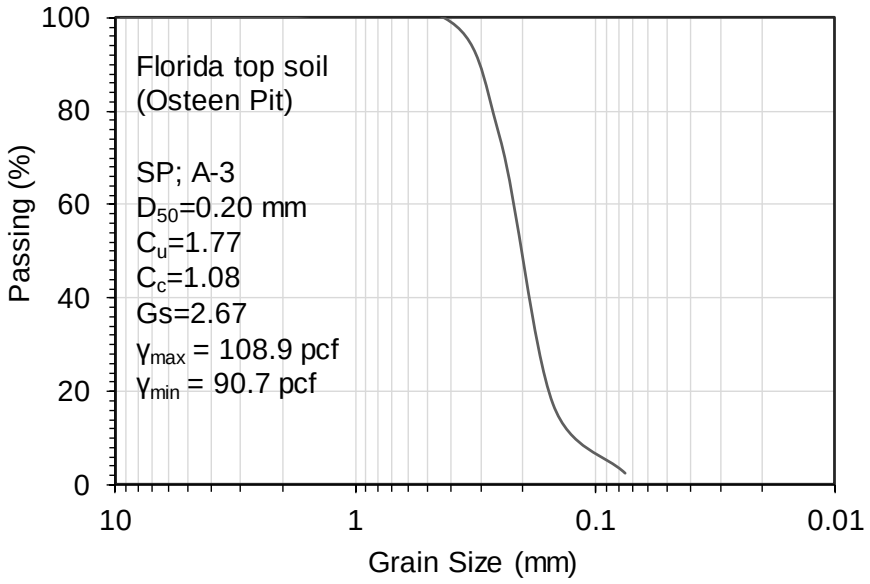

Figure 3-3. Soil gradation and properties.

3.1.1.3 Grain size effects

In modeling axially loaded deep foundations in the granular material the grain size effects should be considered. By using the Florida natural sand and the mentioned sheet pile models these criteria will be met.

3.1.1.4 Centrifuge model

To construct the soil profile in the centrifuge tests, sand will be first pluviated into the container in successive layers of about 4 cm up to the level of excavation, resulting in a total depth of 11 m (220 mm in model-scale). At this level, the cantilever sheet pile wall will be positioned using alignment racks with its toe slightly penetrating into the soil, providing support to keep the sheet pile wall in place before driving (see Figure 3-4). Sand will be then pluviated on both sides of the sheet pile wall to construct a soil profile with a total depth of 20 m (400 mm in model-scale). At the final stage, the soil in front of the sheet pile wall will be carefully excavated by a vacuum, retaining a 10.5 m (210 mm in model-scale) profile behind the wall.

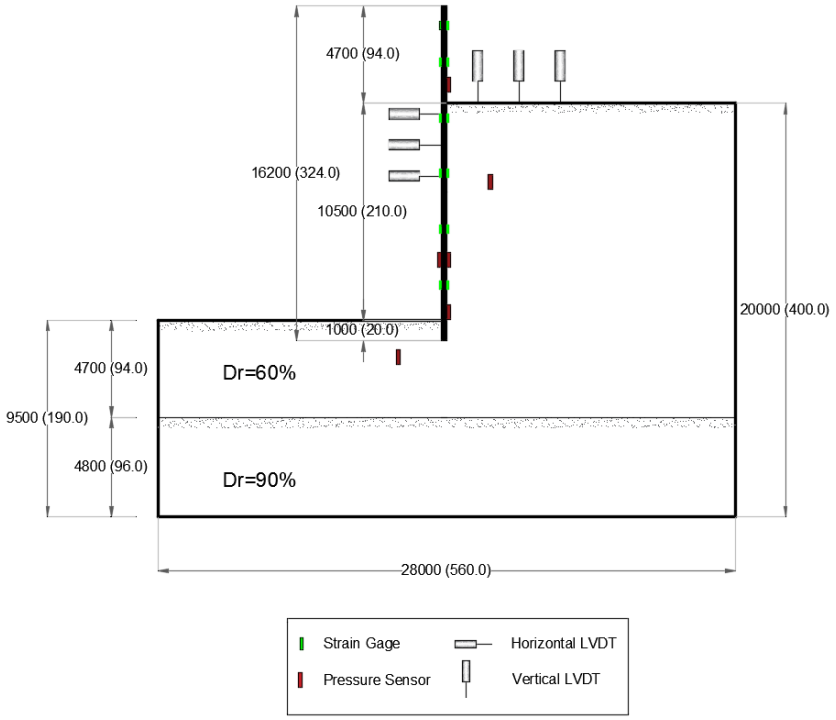

Figure 3-4. Cross section of the centrifuge model before sheet pile wall driving); the dimensions are provided in prototype-scale (and model-scale) in millimeters.

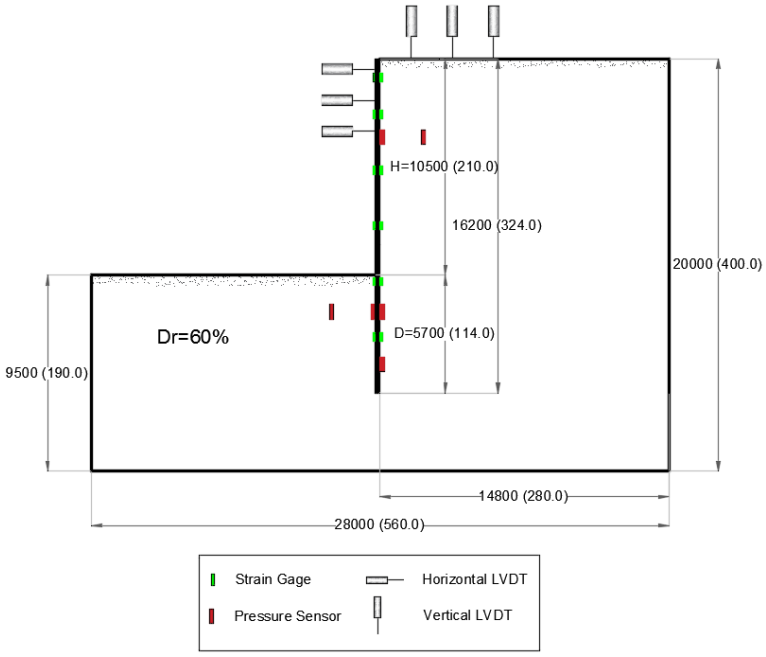

Figure 3-5. Cross section of the centrifuge model with D/H=0.54 and uniform sand (PR1); the dimensions are provided in prototype-scale (and model-scale) in millimeters.

The centrifuge model will then be carefully moved to the arm, alignment racks will be removed, and instead, the top of the wall will be supported by a helmet (cap) fixed to the actuator (refer to section 2.2.4). The schematic of this soil profile configuration (PR1) is presented in Figure 3-5. Another model configuration (PR2) with different excavation depth will be constructed using the same procedure (Figure 3-6). In PR2, the total soil profile depth, excavation depth, and penetration depth to unsupported length (free length) ratio of the wall are 20 m, 9 m, and 0.54, respectively. Further discussions in this regard are provided in section 2.2.2.

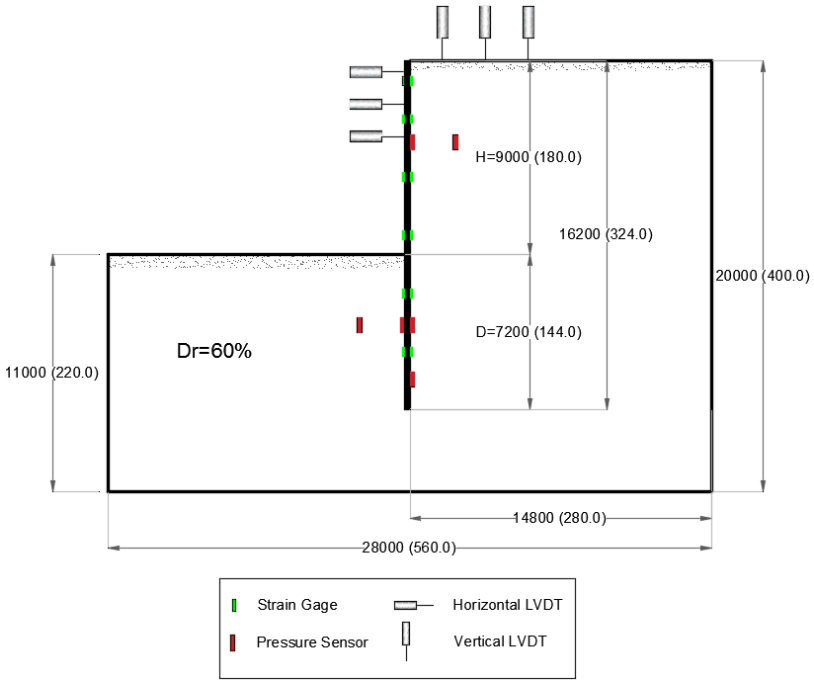

Figure 3-6. Cross section of the centrifuge model with D/H=0.8 and uniform sand (PR2); the dimensions are provided in prototype-scale (and model-scale) in millimeters.

Two additional soil profiles (PR3 and PR4) will be made where a medium-dense sand layer with a relative density of 60% will overlay on a dense sand layer with a relative density of 90%. The details of these two layered profiles are depicted in Figure 3-7 and Figure 3-8. In both of these profiles, the sheet pile wall toe will have a final penetration depth into the dense sand layer for about 1 m (20 mm in model-scale).

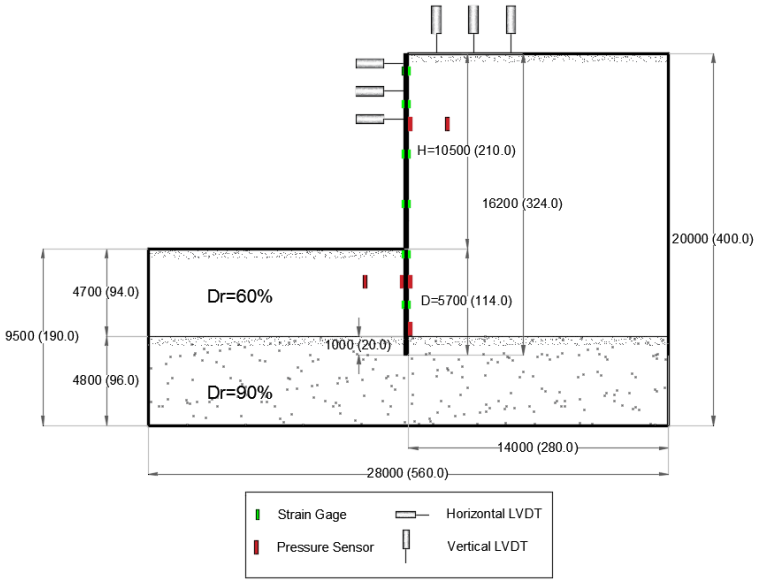

Figure 3-7. Cross section of the centrifuge model with D/H=0.54 and two-layered sand (PR3); the dimensions are provided in prototype-scale (and model-scale) in millimeters.

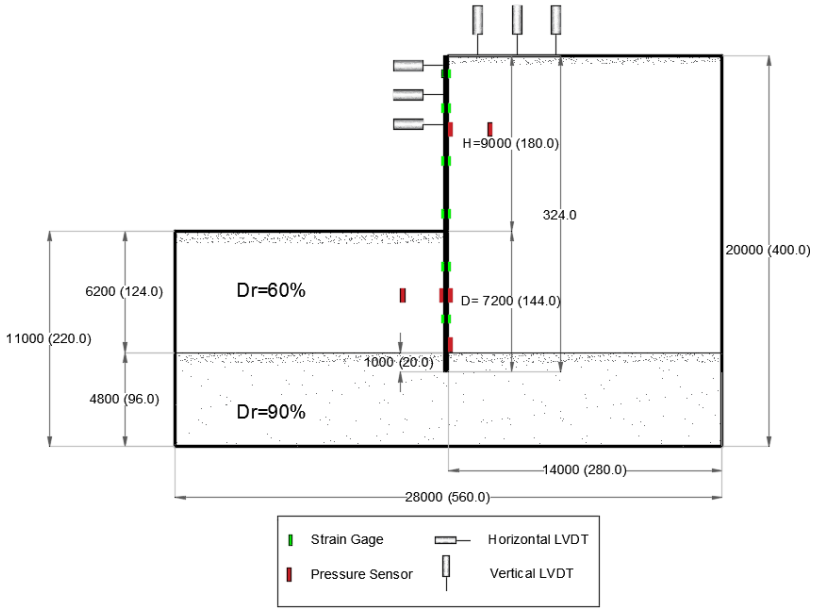

Figure 3-8. Cross section of the centrifuge model with D/H=0.8 and two-layered sand (PR4); the dimensions are provided in prototype-scale (and model-scale) in millimeters.

3.1.1.5 Instrumentation

In order to quantify the bearing capacity of sheet pile walls and evaluate both skin friction and end bearing, the SPWs will be instrumented using pairs of strain gages. This will make it possible to obtain bending moment and axial load distribution along the SPWs and quantify skin friction and

end bearing. While sheet pile walls have been used for many decades, they often provide a challenge to geotechnical engineers to predict their behavior in terms of deformations and the earth pressures sustained by them considering their flexibility. To address this problem, in addition to the strain gages, an array of horizontal Linear Displacement Transducers (LVDTs) or Linear Potentiometers (LPs) will be attached to the wall to measure its rotation and deformations during centrifuge tests. Vertical LVDTs or LPs will monitor ground surface settlement while the wall rotates around its pivot point before or during load testing. Pressure sensors will be used to monitor stresses in the soil and the wall before and during SPW driving and load testing. Preliminary numerical analyses will help with obtaining the locations of an array of strain gages and pressure sensors on the wall so that the overall behavior of the wall (e.g. bending moment, axial force, and pressure distribution on the wall) would be accurately captured. The utilized instrumentation plan is consisted with what is being used previously for instrumenting similar centrifuge models (more details can be found in section 1.4.2 of Task 1).

Prior to each centrifuge test, it is necessary to check the variation in the accuracy and linearity of each sensor. In strain gages, calibration is necessary to scale the instrument sensitivity (by adjusting gage factor or gain) in order that the registered output corresponds conveniently and accurately to some predetermined input. The pressure sensors will be calibrated prior to each test against a reference precise pressure transducer in an air-pressurized calibration chamber. The sensitivity factors of load cells and LVDTs used in this project will likely not change considering their mechanism and past experiences in using them. However, considerations will be made to make sure they remain calibrated during all tests.

3.1.1.6 Sheet pile driving and load testing

Centrifuge tests will involve driving the sheet pile walls (SPW) by pushing them in a quasi-static manner and subsequently conducting axial static and quasi-static load tests on the driven SPWs. In this project, SPW driving in sand and subsequent load testing will be performed in flight, where stresses in soil and applied forces to the sheet piles are same as those in the field. Once the SPWs are pushed in flight to the desired target depth, axial static and quasi-static load tests will be performed on the sheet piles.

In order to drive the sheet pile wall in flight and conduct the load testing, different actuating alternatives were considered and studied in detail. Pneumatic actuators were found to be inexpensive and easy to operate, however, pressure losses and compressibility of air make these actuators less efficient and less controllable for load testing of sheet piles. Utilizing a hydraulic actuator needs renovating or developing the project-specific infrastructure (e.g. an efficient hydraulic power unit, centrifuge fluid rotary union rated for simultaneous high-speeds and high-pressures, and a servo valve or proportional valve to control the actuator), which increases the costs of utilizing such an actuator. However, compared to other types of actuators, hydraulic actuators are suited to apply higher-magnitude forces. Efficiency and cost savings were two major thrusts in selecting electro-mechanical linear actuators for this project. In these actuators, an electric motor mechanically rotates a lead screw. A lead nut or ball nut capable of traveling along the lead screw can prevent or allow the actuation. The heavy-duty industrial electro-mechanical linear actuator for this project will offer both high durability and high performance. This actuator

has a stroke of 25.4 cm (10 inches) and load capacity of about 10,000 N (2,250 lbs) making it possible to be used for both driving and load testing of the SPWs. To remotely control the speed of the actuator (rate of the displacement), a solid-state relay (SSR) will be installed on the arm of the centrifuge. Depending on the model and specifications of the actuator, the required excitation voltage (12V or 24V) will be applied and an output channel on the DAQ will be used to turn the relay on and off at high speeds to modulate the voltage supplied to the actuator. This method of control is commonly called a Pulse-Width Modulation (PWM) and is same as the speed controllers for actuators used for load testing in the field. As such, the actuator will be able to apply the displacements in speed ranges as high as 4.5 mm/s and lower than 0.01 mm/s as well. The LabVIEW based user interface for controlling the centrifuge and recording data will be modified accordingly to make it possible to apply desired displacement-time histories (e.g. a sine wave) to the top of the sheet pile with preferred amplitude and frequency to drive the sheet pile, and conduct static and quasi-static load tests. The amount of the applied load and sheet pile top displacement will be recorded using a load cell and LP, respectively.

3.1.2 Centrifuge modeling scenarios

Static and quasi-static load tests will be performed on the SPW models under different scenarios simulating the variety of conditions that may frequently encounter in the field. This section explains the scenarios to be investigated by centrifuge testing.

3.1.2.1 Axial load transferring mechanisms: end bearing and skin friction

Two scenarios will be considered in investigating the axial load transferring mechanisms in sheet piles. In the first scenario, the sheet pile wall will be tested in a medium-dense sand profile with a relative density of 60% (Figures 40 and 41). It is believed that this case will represent a friction sheet pile where most of the axial load is carried through skin friction. In the second scenario, the sheet pile wall toe will be found on a dense sand layer with a relative density of 90% underlying a medium dense sand with a relative density of 60% (Figures 42 and 43). The sheet pile wall toe will be penetrated in the dense sand layer for about 1 m (20 mm in model-scale). It is believed that this case will represent an end bearing sheet pile where toe resistance plays an important role on the bearing resistance of the sheet pile. Low axial movements of the end-bearing sheet pile may result in considerable reduction in friction resistance in the upper layer.

3.1.2.2 Penetration depth and unsupported length

In order to investigate the effects of depth of penetration (D) and unsupported length (H) on the axial behavior, bearing resistance, and failure mechanism of the sheet pile walls, two different penetration depth to retained soil height ratios (D/H) of 0.54 (Figures 40 and 42) and 0.8 (Figures 41 and 43) will be considered. By changing the penetration depth, it is believed that the amount of mobilized and ultimate skin friction for the axially loaded sheet piles will be changed. The penetration depth will also determine the amount of passive resistance in front of the sheet pile under lateral earth pressure and might be capable of changing the failure mechanism. Therefore, the horizontal displacement of the sheet pile wall also depends on the penetration depth where the wall may lose its serviceability under large deformations. In cases with D/H = 0.54 the unsupported

length is increased with respect to the cases with D/H = 0.8. The influence of the unsupported length on the buckling behavior of the wall will be also investigated.

3.1.2.3 Sheet pile stiffness

The effects of bending and axial stiffness of the sheet pile elements on the bearing capacity of the axially loaded sheet piles will be studied. The prototype-scale bending stiffness and axial stiffness values of the model sheet piles will be matched with those commonly used in the field (refer to Table 4). Two sheet pile walls with PZ cross sections will be machined where the second sheet pile wall (PZS2) has higher (approximately twice) bending and axial stiffness than the first one (PZS1). Sheet pile stiffness plays an important role on its buckling especially in cases where sheet piles are driven through compressible soil layers but are terminated at depth into a relatively incompressible layer (e.g. rock or dense sand). In these cases, the maximum design load for such a sheet pile will be governed by the stresses in the sheet pile material itself, rather than the base resistance in the dense layer. The effects of stiffness change on the buckling behavior of both sheet pile sections (PZS1 and PZS2) will be investigated in all four soil profile configurations (i.e. PR1-4).

3.1.2.4 Boundary conditions

It is aimed to investigate the bearing capacity of axially loaded sheet pile walls with both fixed and free head conditions. The effects of head conditions on the deformation of the wall, lateral earth pressure on the wall, and bending moment and axial force distribution will be also investigated. In order to create fixed-head conditions, a helmet (cap) will be perfectly fitted to the top of the sheet pile wall preventing it from any rotation. In the case of free-head condition, the sheet pile will be allowed to move inside the helmet providing active earth pressure on the retained soil. In both cases, it is planned to apply a vertical load simulating the vertical loads imposed by the superstructure.

3.1.2.5 Axial load testing of sheet pile abutments

For each of the aforementioned centrifuge test scenarios described in section 2.3, separate static and quasi-static load tests will be performed. Quasi-static load tests are aimed to quantify rate effects when pushing and load testing of the sheet piles, where the results will be compared to the static load tests served as the reference case(s). To the best knowledge of the authors, axial load tests are not performed on centrifuge model sheet pile foundations so far. ASTM D1143/D1143M (2013) has explained methods for conducting static axial compressive load tests on deep foundations, which will be adopted. To do the load tests, the actuator (apparatus) will be capable of applying the desired displacement-time histories with the specified amplitude and frequency for both static and quasi-static loading. The strain gages will be used during load tests to obtain axial load distribution along the sheet pile. The main objective in performing these load tests is to investigate and confirm the capacity of sheet piles to support both vertical loads applied from the superstructure on top of it (e.g. a bridge) and lateral earth loads applied from its backfill material. By doing axial load tests on instrumented sheet pile foundations, axial load transfer curves will be obtained and relationships for load resistance versus axial deformation of the pile head for displacements ranging from zero to the ultimate limit or to an achievable maximum value will be

established. The centrifuge tests will help in coming up with a protocol for designers and practitioners to easily do the load tests on sheet piles in the field.

3.1.3 Total number of centrifuge tests

Centrifuge tests will be carried out on model cantilever sheet pile walls supporting granular fill by subjecting to varied g-levels (in steps of 10g) up to a maximum set target g-level of 50g. As stated earlier, centrifuge tests for a specified scenario will be separately conducted for static and quasi-static load testing of sheet piles. The bending moment distribution, deflections of the sheet pile wall, the settlement of the backfill, and soil stresses will be monitored during the centrifuge test. These quantities, prior to the load tests, will be served to ensure the repeatability between similar tests. The consistency of all centrifuge tests will be ensured. Four tests of select centrifuge testing scenarios including their load tests will be fully repeated to ensure about repeatability and validity of load tests as well. As it is shown in Table 3-1, a total of 36 centrifuge tests will be conducted in order to study five scenarios described in section 3.3.

Table 3-3 Summary of scenarios for centrifuge tests

	Sheet pile Embedment	Sheet pile stiffness	Sheet pile head constraints	Load testing	Total cases
Medium-dense sand	2	2	2	2	16
Two-layered Profile	2	2	2	2	16
Repeat tests					4
Sum					36

3.1.4 Element-scale laboratory tests

The stress-strain characteristics of sand will be investigated in material strength laboratory in accordance with the pertinent American Association of State Highway and Transportation Officials (AASHTO) or/and American Society for Testing and Materials (ASTM) standards. The purpose of the element-scale laboratory tests is to evaluate key shear strength parameters of the sand for use in calibration of the finite element (numerical) models and in evaluating the theoretical models to study sheet pile behavior under lateral earth pressure. State Material Office (SMO) has already performed several triaxial and direct shear tests on the sand being used in the centrifuge tests in different relative densities and normal loads. In addition to these tests, direct shear tests will be performed to study the angle of friction between the sheet pile and sand by inserting a plate

of aluminum in a shear box, with the surface of the plate flush with the plane of shearing. It is also planned to characterize soil shear strength using Isotopically Consolidate Drained Triaxial Compression tests (CIDC) on the sand samples with confining pressures and relative densities of interest.

3.2 REFERENCES

AASHTO (2014). AASHTO LRFD bridge design specifications, American Association of State Highway and Transportation Officials (AASHTO), Washington, D.C.

ASTM D1143/D1143M (2013). "Standard Test Methods for Deep Foundations Under Static Axial Compressive Load."

Azzam, W. R., and Elwakil, A. Z. (2017). "Performance of Axially Loaded-Piled Retaining Wall: Experimental and Numerical Analysis." International Journal of Geomechanics, 17(2), 04016049.

3.3 Task 3b: Centrifuge modeling and procedures to conduct the centrifuge tests

Through task 3, we will design and develop centrifuge load tests to investigate the problem at hand, compare centrifuge tests results with the theoretical models, and calibrate and validate the numerical models. Different geo-structural conditions will be evaluated to account for various factors including soil layering, sheet pile wall flexural rigidity, boundary conditions of the sheet pile wall, and quasi-static loading rates.

This current version of the report provides details and explanation on the instrumentation and the developed equipment for our centrifuge tests. The centrifuge testing plans and scenarios are explained. The centrifuge testing has been started and is continuing over the upcoming months.

3.3.1 Centrifuge test set-up

The centrifuge model tests in this study will be carried out at a centrifugal acceleration of 50 g in a rigid container. The maximum payload for the University of Florida centrifuge is 12.5 g-ton and the available basket area is approximately 3.7 ft^2. The beam radius is 59 in and the maximum centrifugal acceleration is 80 g. The rigid container to be used in our tests has internal dimensions of (L×W×H) 22 in × 8 in × 18 in. The rigid container consists of two aluminum solid plates fixed to two rigid Plexiglas transparent plates. This container has smooth walls and makes it possible to reduce the boundary effects and reasonably simulate the prototype event. By placing the sheet pile wall and instruments as far as possible from the boundaries (at the middle of the container), the boundary effects will be further minimized.

3.3.1.1 Sheet pile characteristics

Two model sheet pile walls were machined from aluminum sheets with final prototype-scale geometry, flexural rigidity (bending stiffness), and axial stiffness values matching those of full-scale PZ sheet pile sections used in the geotechnical engineering industry. It is worth mentioning that the process PZ sections are produced (e.g. hot rolling) and interlocked is different than that used for the sheet pile sections in the current centrifuge tests, resulting in likely differences in the bending behavior of the sections compared to the PZ sheet piles (bending behavior might be closer to U-shaped sheet piles). However, having similar stiffness values will help with reasonably modeling the overall bearing and failure mechanism of sheet pile walls. Compared to the other centrifuge tests (Bolton and Powrie 1987; Bolton and Powrie 1988; Madabhushi and Chandrasekaran 2005; Madabhushi and Chandrasekaran 2008; Viswanadham et al. 2009), where rigid sheet piles were used or only stiffness values of the modeled sheet piles were matched with those used in the field, in the current centrifuge tests it is tried to match the geometry (i.e. angles and width of each section) as well. Having similar geometries will help with capturing any likely soil plugging.

Using aluminum instead of steel is a typical practice in the centrifuge modeling of structural elements as it helps with increasing the thickness of the section and make it possible to machine the sections with the desirable precision using the typical computer numerical control (CNC)

cutting machines (routers). The prototype-scale bending stiffness and axial stiffness of the first wall (PZS1) was about the same as those of PZ27. The second wall (PZS2) had bending and axial stiffness values approximately twice of those of PZS1 (and PZ27). The increase in the stiffness of PZS2 is achieved by increasing the thickness (both web and flange) from 1.4 in in PZS1 to 2.8 in in PZS2 and keeping all other geometrical properties (e.g. width and angles) the same. The model-scale and prototype-scale values of sheet pile sections are provided in Table 3-1. Note that the presented values in Table 1 are associated with the properties of the shaded areas of the sections (the pair of sheet piles) shown in Figure 3-9. The cantilever sheet pile wall consisted of 22 sections (11 pairs) of sheet pile elements resulting in the total prototype-scale width of 396 in. The length of the sheet pile wall was 637.8 in. The prototype-scale properties of the wall are presented in Table 3-2. The PZS1 wall is shown in Figure 3-10. In this research, it is assumed that forces fully transmit in the sheet piles interlocks (i.e. welded interlocks) (Doubrovsky and Meshcheryakov 2015).

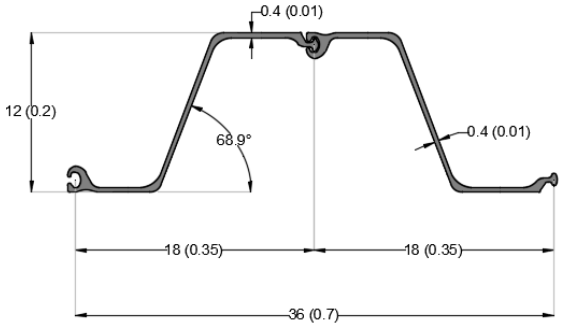

(a) PZ27

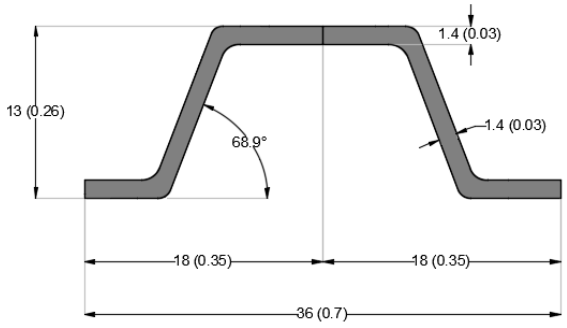

(b) PZS1

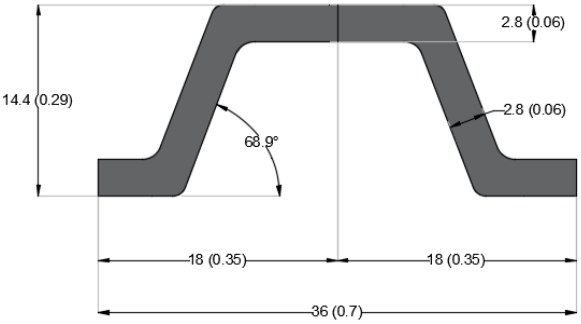

(c) PZS2

Figure 3-9. Sheet pile sections: (a) pair of PZ27 sections; (b) pair of PZS1 sections; and (c) pair of PZS2 sections; the dimensions are provided in prototype-scale (and model-scale) in inches.

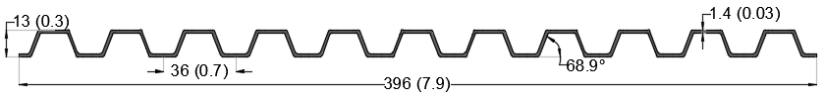

(a)

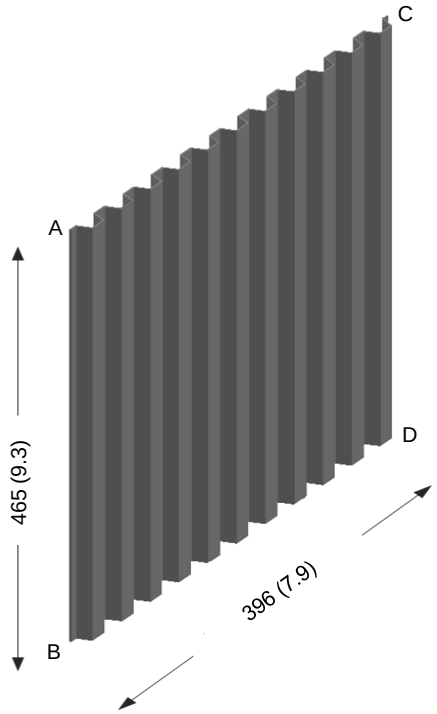

(b)

Figure 3-10. (a) Cross section; and (b) 3D view of the sheet pile wall consisted of 22 PZS1 elements; the dimensions are provided in prototype-scale (and model-scale) in inches.

Table 3-4. Sheet pile section dimensions and properties

	Model-scale (1 g)		Prototype-scale (50 g)		PZ section
Section	PZS1	PZS2	PZS1	PZS2	PZ27
Width (in)	0.7	0.7	36	36	36
Height (in)	0.26	0.29	13	14.4	12
Flange thickness (in)	0.03	0.06	1.4	2.8	0.4
Web thickness (in)	0.03	0.06	1.4	2.8	0.4
Cross Sectional Area, A (in^2/ft)	0.03	0.06	72	144.4	24.2
Perimeter, P (in/ft)	0.22	0.23	10.77	11.32	11.83

Moment of inertia, I (in^4/ft)	0.001	0.002	7,369.8	1,5217.4	2,649.8
Material	aluminum	aluminum	aluminum	aluminum	steel
Young's modulus, E (psi)	10^7	10^7	10^7	10^7	2.9×10^7
Bending stiffness, EI ($kips.in^2$/ft)	12	24.7	7.5×10^7	1.5×10^8	7.7×10^7
Axial stiffness, EA (kips/ft)	292.3	586.8	731,164	1,466,341	702,678

Table 3-5. Prototype-scale sheet pile wall dimensions and properties

Sheet Pile Wall	PZ27	PZS1	PZS2
Width (in)	396	396	396
Height (in)	12	13	14.4
Flange thickness (in)	0.4	1.4	2.8
Web thickness (in)	0.4	1.4	2.8
Cross Sectional Area, A (in^2/ft)	266.5	792.2	1,588.7
Perimeter, P (in/ft)	1301.6	1127.1	1129.9
Moment of inertia, I (in^4/ft)	3,482,438	10,347,850	20,757,205
Material	steel	aluminum	aluminum
Young's modulus, E (psi)	2.9×10^7	10^7	10^7
Bending stiffness, EI ($kips.in^2$/ft)	1.0×10^{11}	1.1×10^{11}	2.1×10^{11}
Axial stiffness, EA (kips/ft)	7,729,118	8,042,816	16,129,753

3.3.1.2 Soil properties

In order to represent the frequently encountered geo-materials and site conditions in Florida, Florida natural sand was used to construct normally consolidated dry sand profiles in the centrifuge tests. Based on the USCS, the mentioned soil was "SP" with coefficients of uniformity and curvature of 1.77, and 1.08, respectively. The AASHTO classification of the soil was A-3. The soil gradation curve and additional soil properties are provided in Figure 3-11. Homogenous medium-dense sand profiles with relative densities of about 60% were constructed. Two-layered soil profiles consisting of medium-dense sand ($D_r\approx60\%$) overlaying a dense sand layer ($D_r\approx90\%$) were modeled as well. Based on the results of direct shear tests (DST) conducted at the FDOT: State Material Office (SMO), the friction angle of this sand with a relative density of 60% was approximately 31.2°. The correlations between the peak internal friction angle (φ) with dry unit

weight (γ_d) and relative density (D_r) obtained from direct shear tests and drained triaxial compression (CIDC) tests are illustrated in Figure 3-12 and Figure 3-13, respectively.

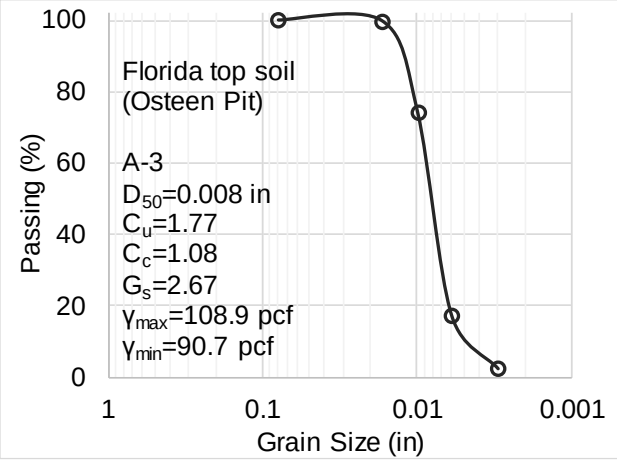

Figure 3-11. Florida sand gradation; the test was performed by SMO

Generally, the drained direct shear tests result in higher internal friction angles compared to the drained triaxial compression (CIDC) tests. However, there are some exceptions according to the literature (Lini Dev et al. 2016). For example, loose sands or find grained soils may have higher internal friction angle in triaxial compression than direct shear tests, as it is the case for the sand being used in this project. Soil density, amount of the confinement, grains shape, and ultimately, the yielding and shearing mechanism associated with each laboratory test are among the influential factors on the observed differences.

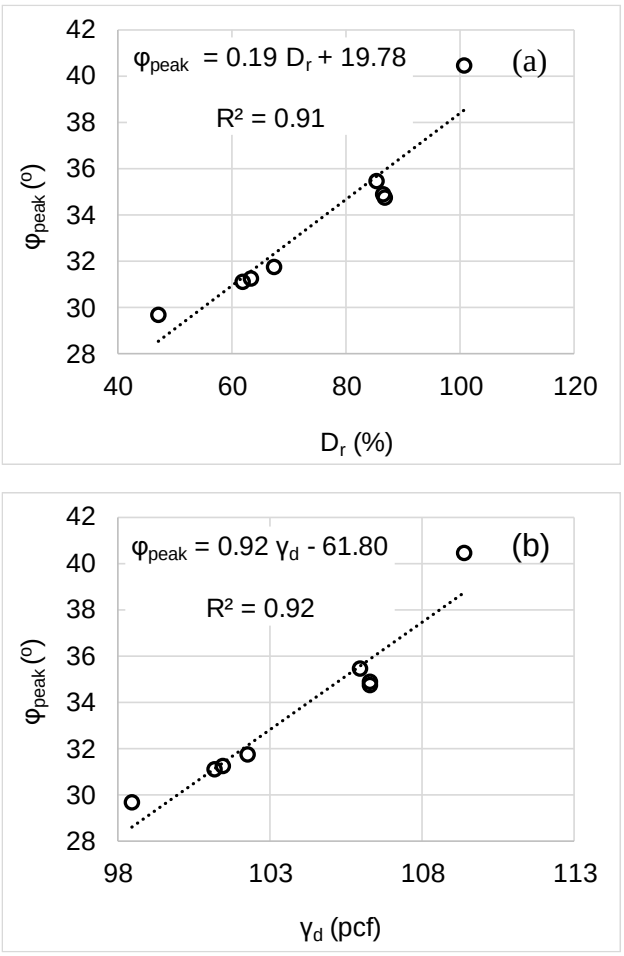

Figure 3-12. Florida sand direct shear tests results: (a) peak internal friction angle-dry unit weight correlation; and (b) peak internal friction angle-relative density correlation; the tests were performed by SMO

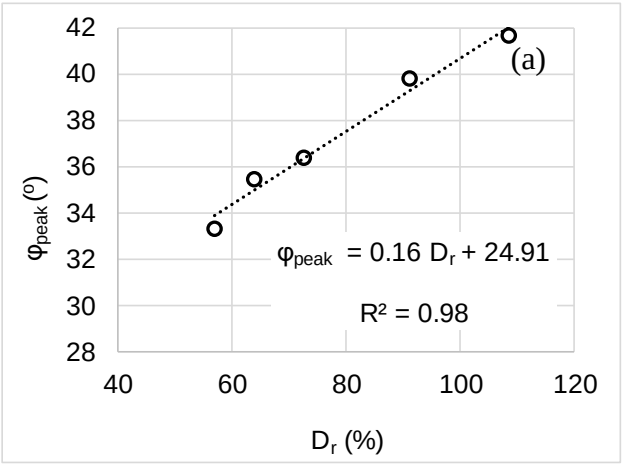

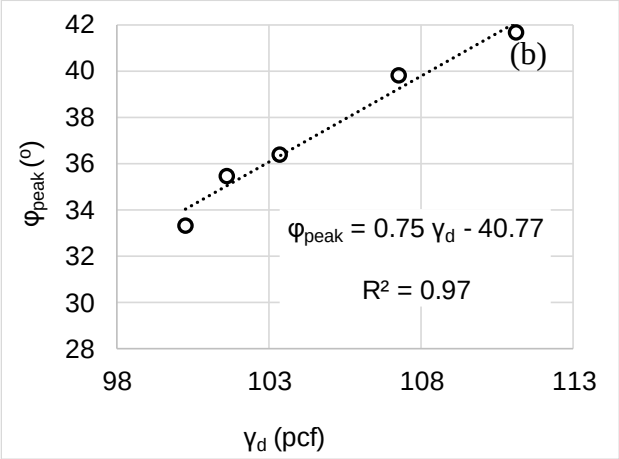

Figure 3-13. Florida sand drained triaxial compression (CIDC) tests results: (a) peak internal friction angle-dry unit weight correlation; and (b) peak internal friction angle-relative density correlation; the tests were performed by SMO

The air-pluviation method was used to prepare the sand layer(s) and achieve the desired relative density and the void ratio. For this purpose, a novel pluviator (Figure 3-14) designed and manufactured by the authors at the University of Florida was used, where the entire area of the centrifuge container was covered by the pluviator, ensuring the homogeneity and uniformity of the profile. The relative density of sand layer(s) was controlled by maintaining a constant drop height and rate. Furthermore, the profile was constructed in layers (small lifts of about 2.0 in in model-scale) and the homogeneity of each pluviated layer was verified by weighing the soil at each layer and checking the unit weight and relative density.

Figure 3-14. Pluviator used for constructing the soil profile

3.3.1.3 Grain size effects

In modeling axially loaded deep foundations in the granular material the grain size effects should be considered. McDowell and Bolton (2000) recommended the pile width to the median grain size (B/D_{50}) be greater than 20 when studying the behavior of axially loaded piles in centrifuge testing. Fuglsang and Ovesen (1987) recommended a B/D_{50} ratio greater than 30 for studying the response of a general model structure in centrifuge testing. By using the Florida natural sand and the mentioned sheet pile models these criteria are met.

3.3.1.4 Centrifuge model

The centrifuge model construction steps are shown in Figure 3-15. To construct the centrifuge model, sand was first pluviated into the container in successive layers of about 2.0 in, up to the level of excavation (dredge line), resulting in a total depth of 52.1 ft (12.5 in in model-scale). At this level, the sheet pile wall was vertically lowered on the ground surface using a level, an alignment rack at the top, and two shims at the sides. The tip of the sheet pile wall was then driven 0.8 inches into the ground surface (see Figure 3-16~~7~~). After this step, the top of the sheet pile wall was fixed using two C-clamps. Having the mentioned supports at the top and the tip of the sheet pile wall provided stability and ensured a vertical alignment before driving the sheet pile wall. To prevent any possible unwanted friction between the sheet pile wall and the container sides, the sheet pile wall was machined with a width slightly less than that of the container. The sides of the wall was then greased (A-B and C-D in Figure 2b) to reduce any possible friction between the sheet pile wall and the container and to prevent fine sand particles from falling from the retained side to the dredged side. Sand was then pluviated on both sides of the sheet pile wall to construct a soil profile with a total depth of 67.2 ft. The soil in front of the sheet pile wall was then carefully excavated by a vacuuming procedure, retaining a 15.1 ft profile behind the wall. As the final step before moving the model to the centrifuge arm, the frame holding the actuator and its helmet was placed on the container, aligning the helmet at a 0.25-inch distance above the sheet pile. On the arm, the actuator was slowly and carefully extended such that the helmet seated on the sheet pile wall and then fixed to the sheet pile wall by using the setscrews (refer to section 2.2.4). The alignment rack and C-clamps were removed before starting to spin the centrifuge.

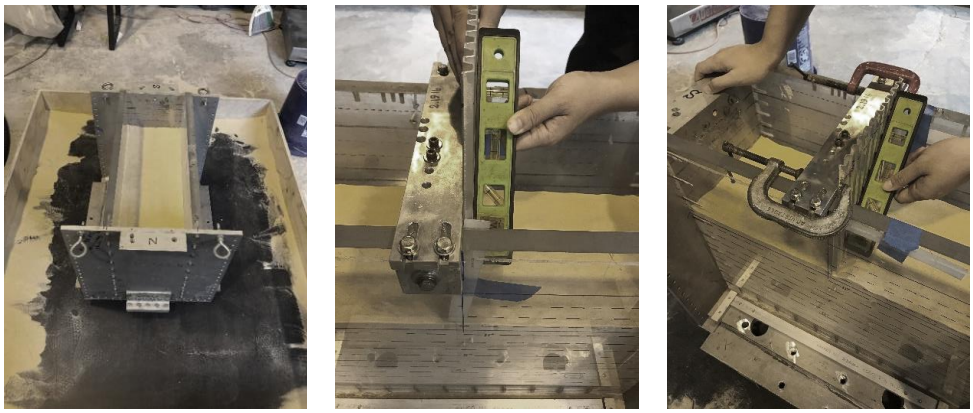

(a) (b) (c)

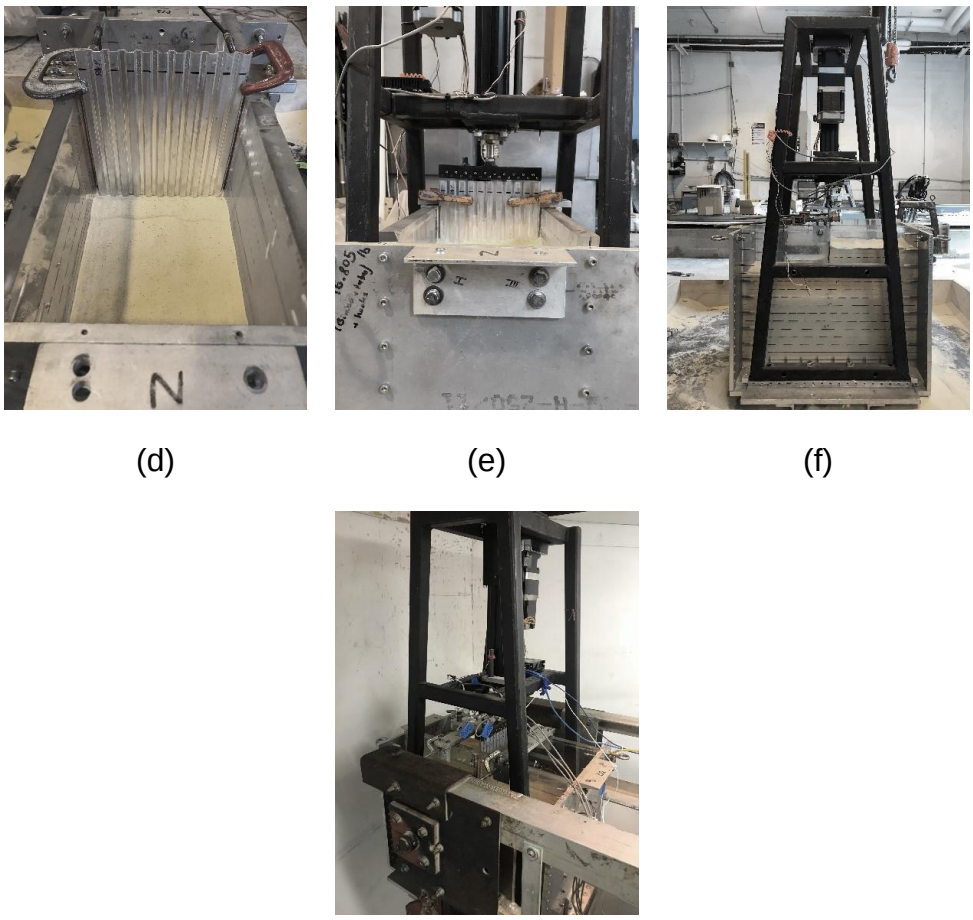

(d) (e) (f)

(g)

Figure 3-15. Centrifuge model construction steps: (a) sand is pluviated into the container up to the dredge line; (b) the sheet pile wall is lowered vertically at the center of the container using an alignment rack at the top and two shims at the sides; (c) tip of the sheet pile wall is penetrated 0.8 inches into the ground and top of it is clamped to the alignment rack, providing stability; (d) interface of the sheet pile wall-container is greased to eliminate any possible friction between the wall and container and prevent sand particles falling from the retained side to the dredged side; (e) actuator frame is attached to the container, aligning the helmet 0.25 inch above the sheet pile wall; (f) the centrifuge model is ready to be transferred to the arm; and (g) the model on the arm with sheet pile wall fixed by the helmet.

It is worth mentioning that the actual process of driving sheet pile walls in the field includes driving the sheet pile wall first and then excavating the soil to the dredge line. Alternatively, in the case of a fill, the sheet pile wall is driven first and then the retained side is filled by soil. In the current centrifuge testing project the priority is given to driving the sheet pile wall in flight such that the volume changes in sand is same as those in the prototype scale. Due to the limitations in the centrifuge modeling procedures, it was not possible to excavate or pluviate (fill) in flight; instead it was performed in 1 g prior to driving. Before load testing, the only difference on the soil stress

state between the centrifuge model and the field would be due to the relative compaction of sand above the dredge line in the centrifuge model (i.e. driving the sheet pile wall slightly copmacts the sand above the dredge line). It is believed that this compaction is not significant; however, it will be quantified during centrifuge testing.

The schematic of this soil profile configuration (PR1) is presented in Figure 3-17. Another model configuration (PR2) with different excavation depth will be constructed using the same procedure (Figure 3-18). In PR2, the total soil profile depth, excavation depth, and penetration depth to unsupported length (free length) ratio of the wall will be 67.2 ft, 56.8 ft, and 2.2, respectively. Further discussions in this regard are provided in section 2.2.2.

It is worth mentioning that the height of the sheet pile walls (H), measured from the dredge line, represent typical values used in Florida for cantilever sheet pile walls. The penetration depths (D) are calculated ensuring the walls remain stable under the applied lateral earth pressure. Having ample room (approximately 34 ft) between the tip of the sheet pile wall and the container bottom plate ensures minimizing or eliminating the boundary effects when studying the bearing capacity of the sheet piles.

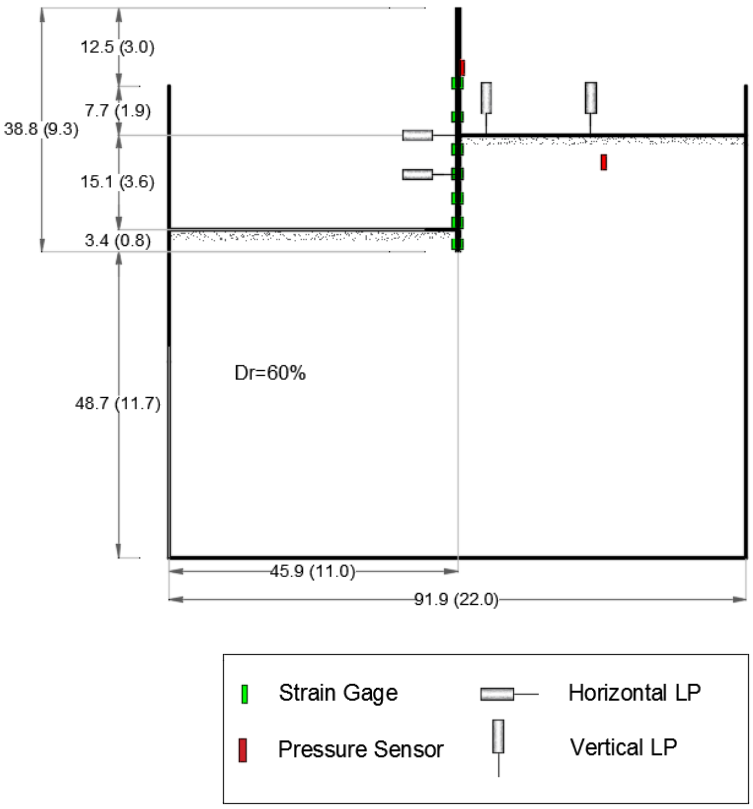

Figure 3-16. Cross section of the centrifuge model before sheet pile wall driving); the dimensions are provided in prototype-scale in feet (and in model-scale in inches).

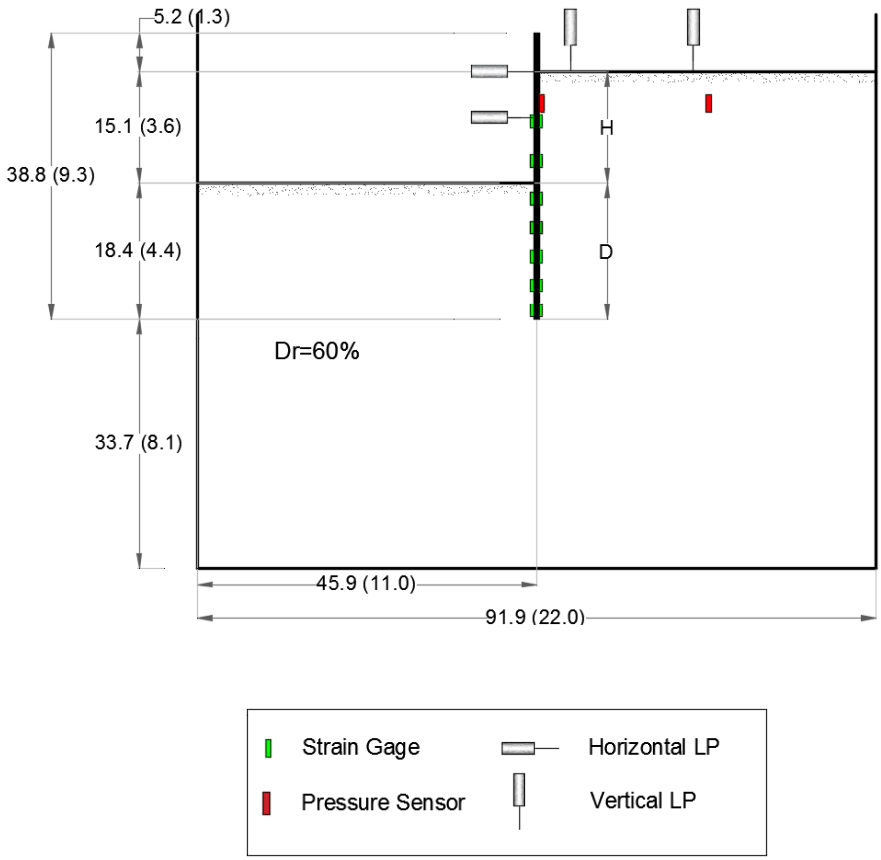

Figure 3-17. Cross section of the centrifuge model with D/H=1.2 and uniform sand (PR1); the dimensions are provided in prototype-scale in feet (and in model-scale in inches).

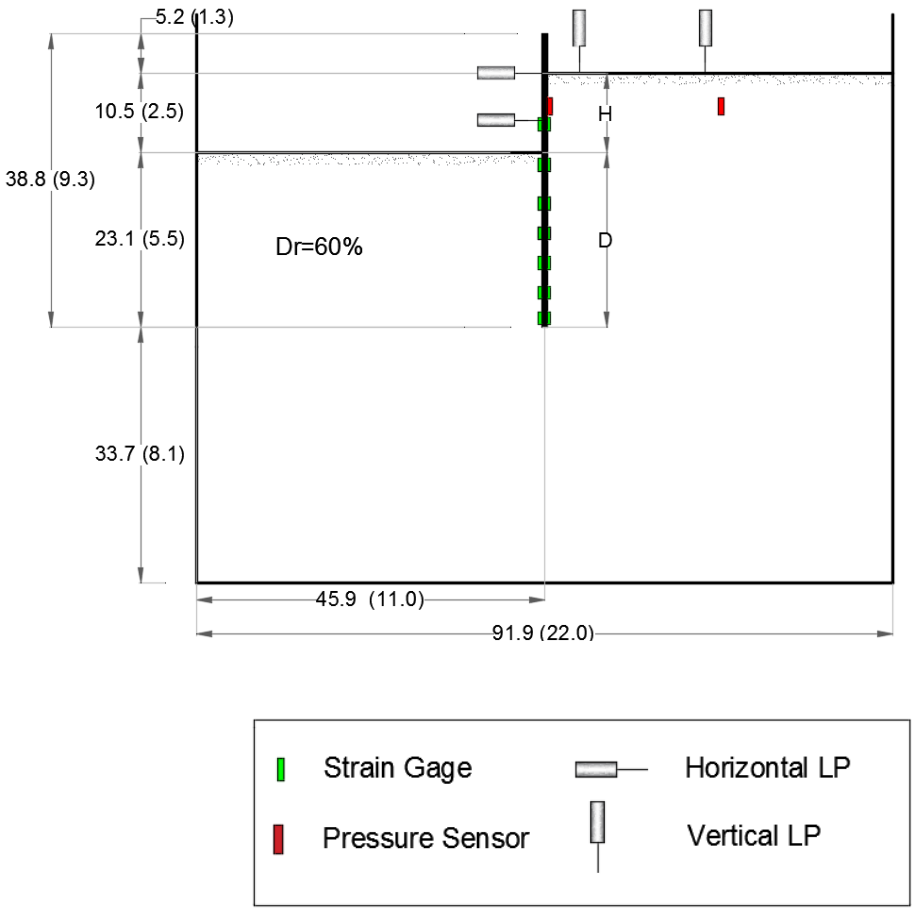

Figure 3-18. Cross section of the centrifuge model with D/H=2.2 and uniform sand (PR2); the dimensions are provided in prototype-scale in feet (and in model-scale in inches).

Two additional soil profiles (PR3 and PR4) will be made where a medium-dense sand layer with a relative density of 60% will overlay on a dense sand layer with a relative density of 90%. The details of these two layered profiles are depicted in Figure 3-19 and Figure 3-20. In both profiles, the sheet pile wall tip will have a final penetration depth into the dense sand layer for about 3.3 ft.

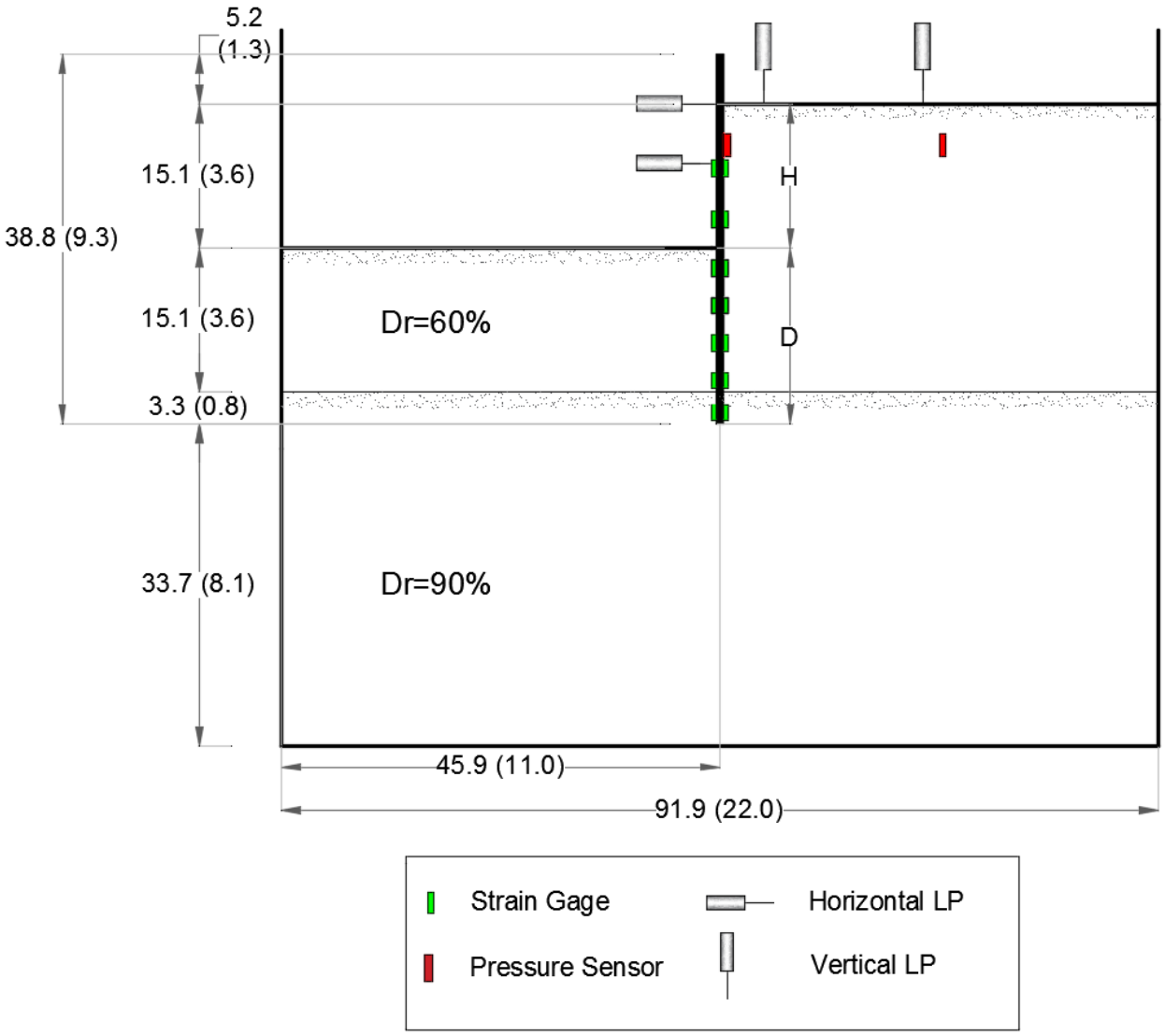

Figure 3-19. Cross section of the centrifuge model with D/H=1.2 and two-layered sand (PR3); the dimensions are provided in prototype-scale in feet (and in model-scale in inches).

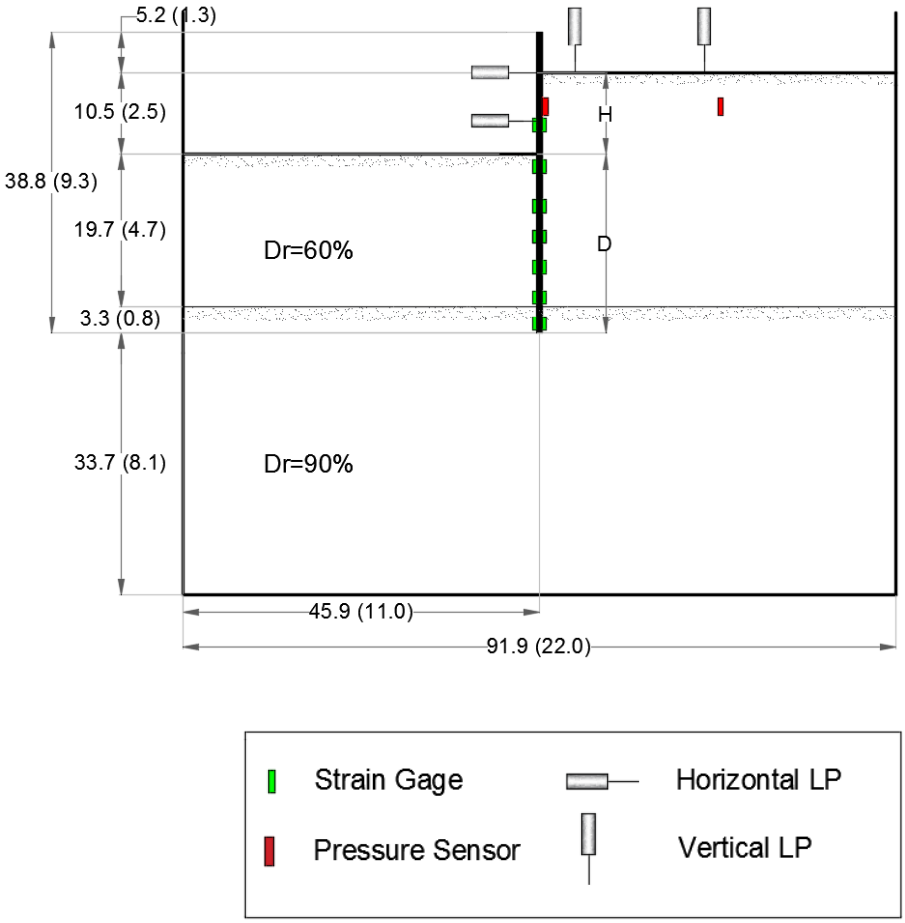

Figure 3-20. Cross section of the centrifuge model with D/H=2.2 and two-layered sand (PR4); the dimensions are provided in prototype-scale in feet (and in model-scale in inches).

3.3.2 Instrumentation

To obtain bending moment and axial load distribution, evaluate both skin friction and end bearing, and quantify the bearing capacity of sheet pile walls, the SPWs were instrumented using pairs of strain gages. In addition to the strain gages, two horizontal Linear Potentiometers (LPs) were attached to the wall to measure its rotation and deformations during centrifuge tests. Two vertical LPs monitored ground surface settlement compared to that in the free field. Pressure sensors were used to monitor stresses in the soil and the wall before and during SPW driving and load testing. Preliminary numerical analyses helped with obtaining the elevations of the strain gage pairs and pressure sensors on the wall so that the overall behavior of the wall (e.g. bending moment, axial force, and pressure distribution on the wall) would be accurately captured. Given below are more details on the selection and design of the instruments and equipment used for the current centrifuge testing.

3.3.2.1 Strain Gages

Strain Gage Selection:

Foil strain gages were used in this project (Figure 3-21). In order to optimize the strain gage performance for the specified project, obtain accurate and reliable strain measurements, ease the installation, and reduce the total costs (i.e. gage and its installation costs), the following factors should be considered when selecting a foil strain gage (Micro-Measurements 2018):

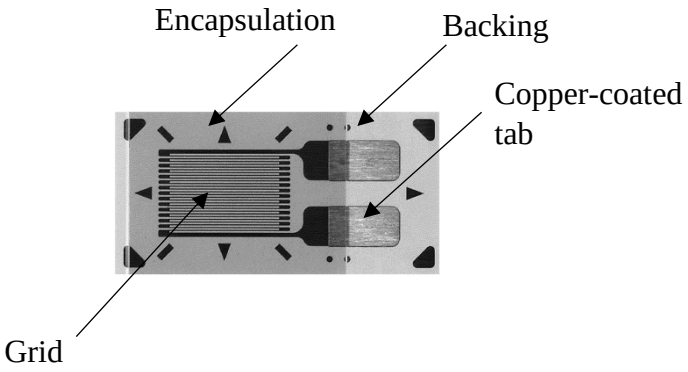

Figure 3-21. Foil strain gage used in the centrifuge tests

- ***Strain-sensitivity alloy:*** The operating characteristics of a foil strain gage is mainly determined by the strain sensitivity alloy used in the foil grid. There are several alloys that are widely used in strain gages and include constantan, annealed constantan, isoelastic, and nickel-chromium. For this project, constantan alloy, the oldest and most widely used alloy, is used. This selection is mostly due to the fact that constantan alloy provides adequately high strain sensitivity, adequate resistivity, good fatigue life and not excessive temperature coefficient of resistance. Considering the material of the test specimen, a self-temperature compensation (STC) number can be also specified to the constantan.
- ***Backing material:*** The backing material in a conventional foil strain gage provides a means for handling the foil pattern during installation, provides a readily bondable surface to adhere the gage to the specimen, and provides electrical insulation between the foil and specimen. There are several backing materials that are being used in conventional foil strain gages including polyimide and glass-fiber-reinforced epoxy-phenolic. For this project, polyimide backing material is used. It provides a tough and extremely flexible carrier and can be easily installed in flat or curved spaces with small radii. It is worth mentioning that the selection of backing material and strain sensitivity alloy are not completely independent procedures; instead, they are usually provided as a system and the designer should select a system that best fits for the specified project. As such, it appeared that CEA series by Micro-Measurements satisfy the requirements of this project. In CEA series, the constantan grid is completely encapsulated in polyimide.

- ***Grid resistance:*** The foil strain gages are available in various resistance values that might range from 30 to 5000 ohms. However, for experimental stress analysis projects, 120 ohms and 350 ohms gages are widely used and are available in the market. While 120 ohms gages may suitable for most projects, 350 ohm gages have the advantage of reducing the generated heat (by a factor of about 3) and increasing the signal to noise ratio as well. The signal to noise ratio improvement is of particular interest when working on centrifuge testing, where switches, slip rings, and other sources of random resistance changes are utilized. As such, 350 ohms strain gages are selected for this project.
- ***Gage pattern:*** The shape, number, and orientation of the grids in a multiple-grid gage dictate the sensing capability of the strain gages in different directions. Single-grid gages are ideal for the cases when the stress state at the point of measurement is known to be uniaxial and the direction of principal axes are recognized. Two-element rosette might be considered ideal for the cases when the stress state is biaxial and the direction of principal axes are known. In biaxial stress states where the direction of the principal axis are unknown, three-element rosette may be used. For the current project, uniaxial bending and axial stresses are applied to each point on the sheet pile and the direction of principal axes are known (Figure 3-22); as such, single-element grids with linear pattern (so-called UN) are selected for the strain gages.
- ***Gage size:*** A narrow grid can minimize the averaging error when a strain gage is installed in a place with a severe strain gradient perpendicular to the grid. On the other hand, wider grids can help with heat dissipation and enhance the stability of the gage. There are different size gages in the market. Gages of less than about 0.125 inches may exhibit degraded performance (i.e. maximum allowable elongation and stability). Gage lengths in the range from 0.125 in to 0.25 in are usually preferable. As such, considering the mentioned criteria and limitations and available space on the sheet pile wall, the length and width of the grid in the utilized strain gages for this project are 0.125 inches and 0.1 inches, respectively.
- ***Self-temperature compensation number:*** Some strain gages, including CEA series used for this project, come with different STC numbers to best match the thermal expansion of the structural material (specimen) they are going to adhere. As the sheet pile walls in the centrifuge testing are made of Aluminum, an STC number 13, compatible with Aluminum is used. As such, the strain gage used for this project is specified as CEA-13-125UN-350.

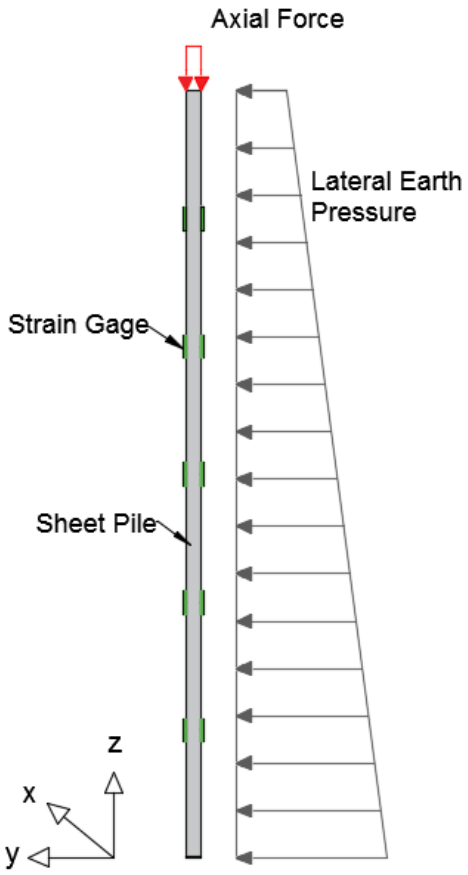

Figure 3-22. Definition of stress state relevant to the selection of grid pattern.

Strain Gage Installation:

After preparing the surface of the specimen (i.e. the sheet pile wall), the strain gages were attached to the wall by M-Bond 200 adhesive. Two leadwires were used, where they were soldered to the copper tabs of the strain gages at one end and to the terminals (positioned outside of the soil profile) in another end. Three-wire cables were then soldered to terminals in one end and attached to the NI-9236 bridge completion module in another end to form three-wire quarter-bridge circuit (see "Strain Gage Data Acquisition"). The reduced size and cross-section of leadwires compared to the three-wire cables made it possible to better secure the wires inside the soil during sheet pile wall driving and load testing. Two types of protection were used: AE-10 was first applied to both strain gage and leadwires to protect them against moisture and also adhere the leadwire to the wall. Then, application of M-Coat JA provided protection against mechanical damage.

Strain Gage Data Acquisition:

For this series of centrifuge tests, 7 pairs of strain gages were attached to the sheet pile wall. Strain gages for each pair were installed at the opposite sides (front and rear) of the wall at specific elevations. Quarter-bridge circuits were used to sense bending and axial strains, where the former was the average difference of two strain gages (at each elevation) and the latter was the average of the measured values for similar strain gages at each elevation.

As it is the case for most foil strain gages, Wheatstone bridges were used to form the sensing circuit. Wheatstone bridges are capable of detecting small resistance changes, producing a zero output voltage when strain is zero, and compensating the temperature induced resistance changes. The quarter-bridge circuits can be used in two-wire or three-wire configurations. Three-wire circuits have several benefits compared to two-wire circuits, which includes intrinsic bridge balance and automatic compensation for the effects of leadwire temperature changes on the bridge balance, and enhanced measurement sensitivity. Compared to the two-wire quarter-bridge circuit (Figure 3-23), the three-wire quarter-bridge circuit leadwire R_{L1} and strain gage R_G comprise one arm of the bridge, while the leadwire R_{L2} and resistor R_4 form the adjacent arm. As such, if the leadwires R_{L1} and R_{L2} are from the same type and length, the quarter bridge circuit will stay in balance, which might not be the case for the two-wire circuit.

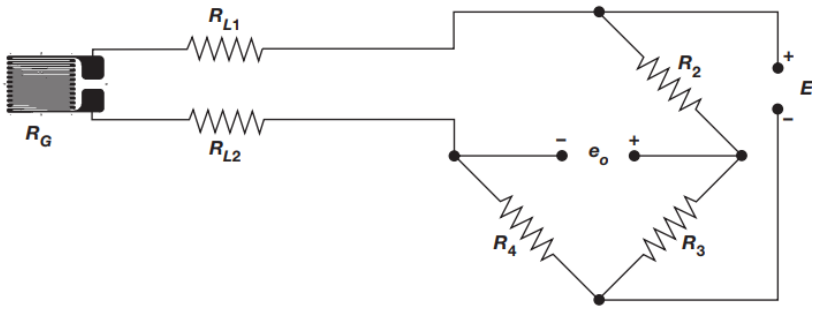

(a)

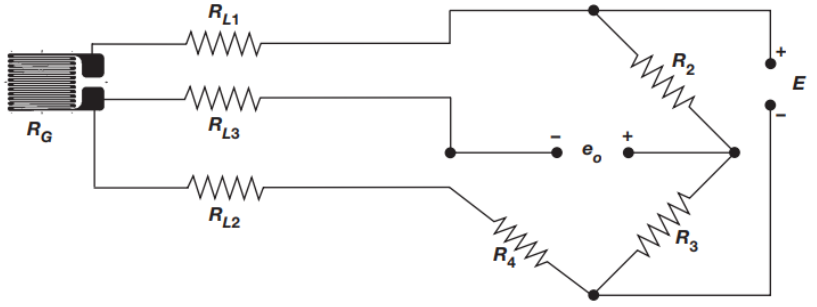

(b)

Figure 3-23. Quarter-Bridge circuits: (a) two-wire; and (b) three-wire (Micro-Measurements 2015)

3.3.2.2 Linear Potentiometers

Linear potentiometers (LPs) with 2 inch stroke were used to measure ground surface settlements and deformations of the sheet pile wall as well. These resistive sensors work as a voltage divider through a hybrid layer of plastic. LPs combine simple design with high precision (linearity of ±0.35 % for an LP with 2 inch active electrical travel) in measuring distances or positions. Shown in Figure 3-24 is a typical LP used in centrifuge tests of this project. One LP with 6 inch stroke was used as the feedback position sensor for the electric linear actuator.

Figure 3-24. Linear Potentiometer (LP) used in centrifuge tests

3.3.2.3 Pressure Sensors

Miniature pressure sensors (see Figure 3-25) with the capacity ranging from 145 psi (1 MPa) to 435 (3 MPa) were used to capture applied pressure to the soil and the wall. The pressure sensors were 0.3 inches (7.6 mm) in diameter and 0.08 inch (2 mm) in thickness, making them a reasonable candidate for the centrifuge tests.

Figure 3-25. Pressure sensor used in centrifuge tests

3.3.2.4 Electric Linear Actuator

Centrifuge tests will involve driving the sheet pile walls (SPW) by pushing them in a quasi-static manner and subsequently conducting axial static and quasi-static load tests on the driven SPWs. In this project, SPW driving in sand and subsequent load testing will be performed in flight; as such, stresses in soil and applied forces to the sheet piles will be the same as those in the field. Once the SPWs are pushed in flight to the desired target depth, axial static and quasi-static load tests will be performed on the sheet piles.

To drive the sheet pile wall in flight and conduct the load testing, different actuating alternatives were considered and studied in detail. Pneumatic actuators were found to be inexpensive and easy to operate, however, pressure losses and compressibility of air make these actuators less efficient and less controllable for load testing of sheet piles. Utilizing a hydraulic actuator needs renovating or developing the project-specific infrastructure (e.g. an efficient hydraulic power unit, centrifuge fluid rotary union rated for simultaneous high-speeds and high-pressures, and a servo valve or proportional valve to control the actuator), which increases the costs of utilizing such an actuator. However, compared to other types of actuators, hydraulic actuators are suited to apply higher-magnitude forces. Efficiency and cost savings were two major thrusts in selecting electro-mechanical (or simply electric) linear actuators for this project. Table 3-6 summarizes characteristics of pneumatic, hydraulic and electric actuators in a comparative manner.

Table 3-6. Characteristics comparison of pneumatic, hydraulic, and electric actuators, modified from Auto Motion Direct (2019)

Characteristics	**Pneumatic**	**Hydraulic**	**Electric**
Complexity	Simple	Medium	Medium/High
Peak power	Medium	Very High	High
Size	Low	Very low	Medium
Position accuracy	Good	Good	Better
Purchase cost	Low	High	High
Operating cost	Medium	High	Low
Maintenance cost	Low	High	Low
Utilities	Compressor, power, pipes	Pump, power, pipes, fluid rotary union, servo valve	Power only
Efficiency	Low	Low	High

In order to meet the technical and economical requirements of the project, it was decided to custom design the actuator. In electric actuators (Figure 3-26), an electric motor mechanically rotates a lead screw. A solid nut, ball nut, or roller nut capable of traveling along the lead screw can prevent or allow the actuation. The combination of the leadscrew, the nut, couplers, pulley, belt, and bearing was decided such that it can resist loads up to 4000 lbs. A roller nut was used as it could provide higher thrust compared to the solid nuts and ball nuts. Considering the available space in the centrifuge chamber and the overall length of the actuator, it was decided to design the leadscrew and casing such that the actuator could accommodate a 6 inch travel, making the actuator capable to be used for both driving and load testing of the SPWs.

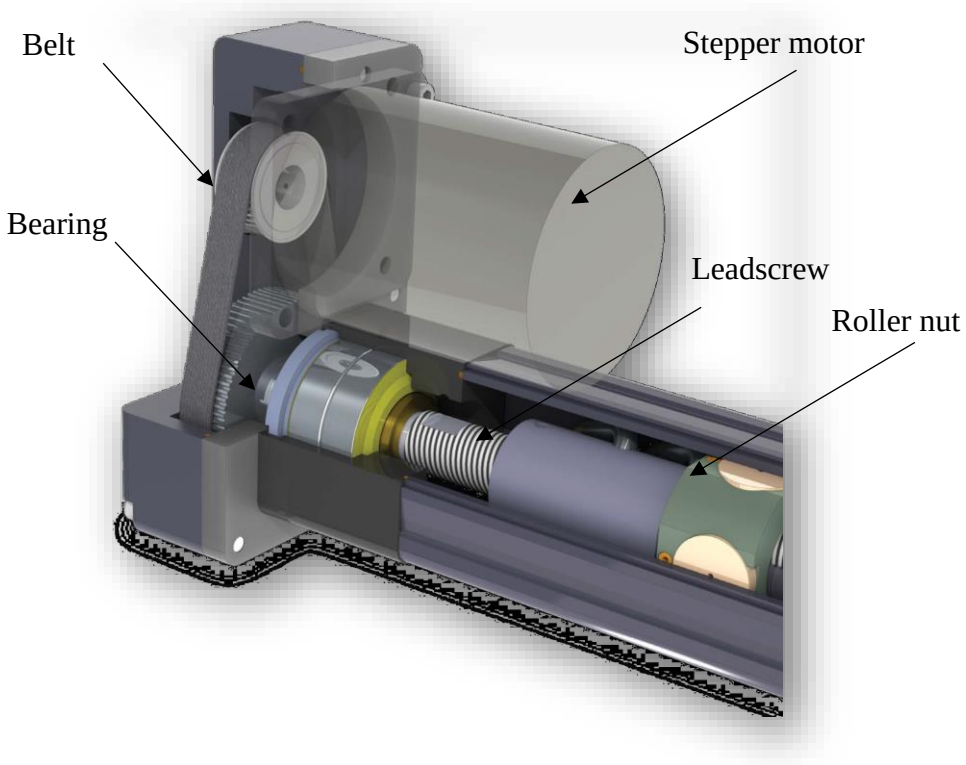

Figure 3-26. The components of the electric actuator

Stepper motors are an ideal candidate for easy and accurate positioning of electrical actuators, where their rotation angle and speed can be controlled by pulse signals. As such, a stepper motor was used to generate the required torque for the mentioned actuator utilized in the centrifuge testing. To meet the need for greater torque at low speed, a gearhead was coupled with the stepper motor. Due to their mechanical design, stepper motors can hold their position at each stop.

To remotely control the actuator (e.g. rate and amplitude of the displacement), a driver-controller was installed on the arm of the centrifuge. This driver-controller had a built-in pulse generation function that allowed the motor to be driven through a directly connected personal computer. As there is no need for an independent pulse generator, this type of driver-controller can save space and simplify wiring and might be considered as an ideal candidate for centrifuge testing. Once the excitation voltage (24V) is introduced to the driver-controller (through the personal computer), the voltage level changes repeatedly between on and off. Each on/off cycle is counted as one pulse, causing the stepper motor output shaft to turn by one step. The amount the stepper motor rotates and its speed are proportional to the number of pulse signals and speed of pulse signals sent to the driver. The control mechanism is illustrated in Figure 3-27. This actuator system made it possible to apply the displacements in speed ranges as high as 0.17 in/s and lower than 0.0004 in/s as well.

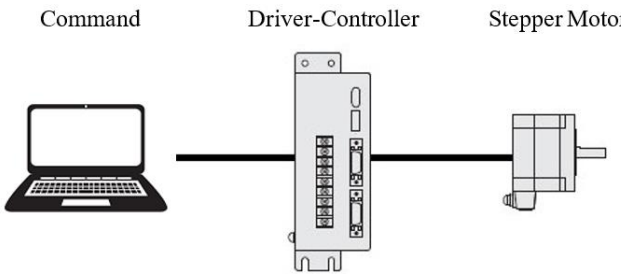

Figure 3-27. The control mechanism used for the stepper motor-actuator system

A LabVIEW based graphical user interface (GUI) for controlling the centrifuge and recording data was designed (Figure 3-28) and developed accordingly to make it possible to apply desired displacement-time histories to the top of the sheet pile with preferred amplitude and frequency to drive the sheet pile and conduct static and quasi-static load tests. The amount of the applied load and sheet pile top displacement was recorded using a load cell and a feedback position sensor (i.e. 6 inch LP), respectively. The load cell was custom design to perform in the desired loading range and fit in the actuator and helmet without using any couplers. This way, it is believed the likely load eccentricity effects are minimalized.

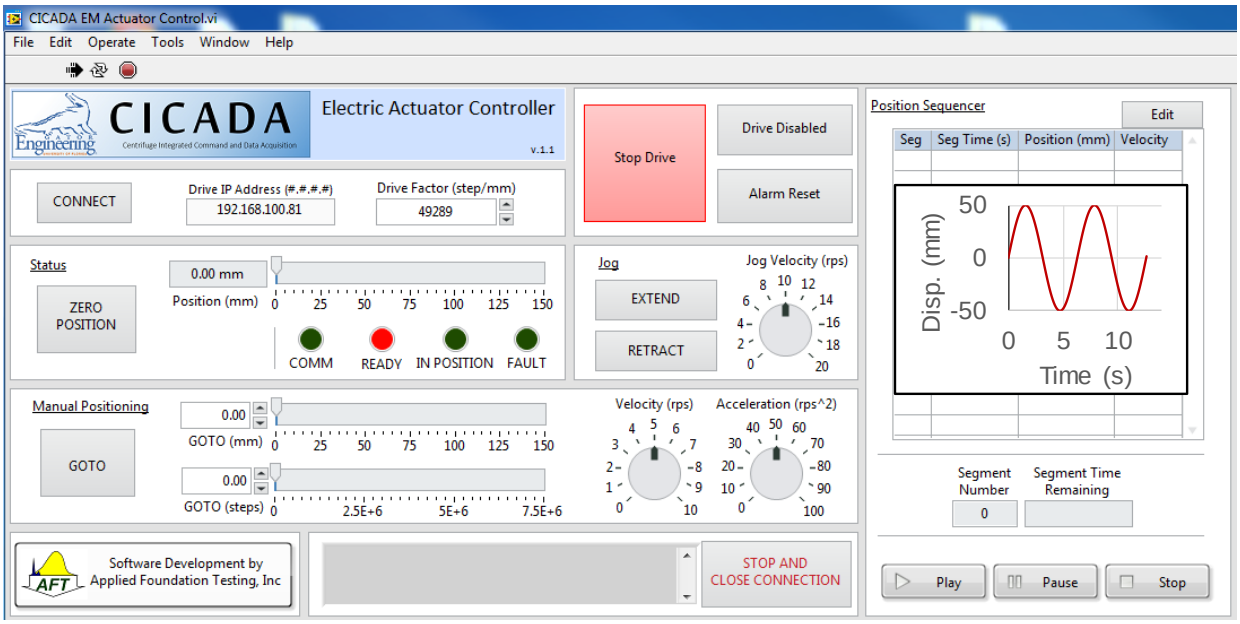

Figure 3-28. The graphical user interface (GUI) used for the stepper motor-actuator control system

Finite element analysis was conducted to design a steel frame to hold the actuator and position the sheet pile wall vertical at the middle of the container during driving and load testing. The actuator and frame were designed and fabricated in a way that the actuator was bolted through flanges to two bearing plates (welded to the frame) at top and bottom. The frame was bolted at the bottom to the container, which in turn is bolted to the rigid centrifuge swinging basket (Figure 3-29).

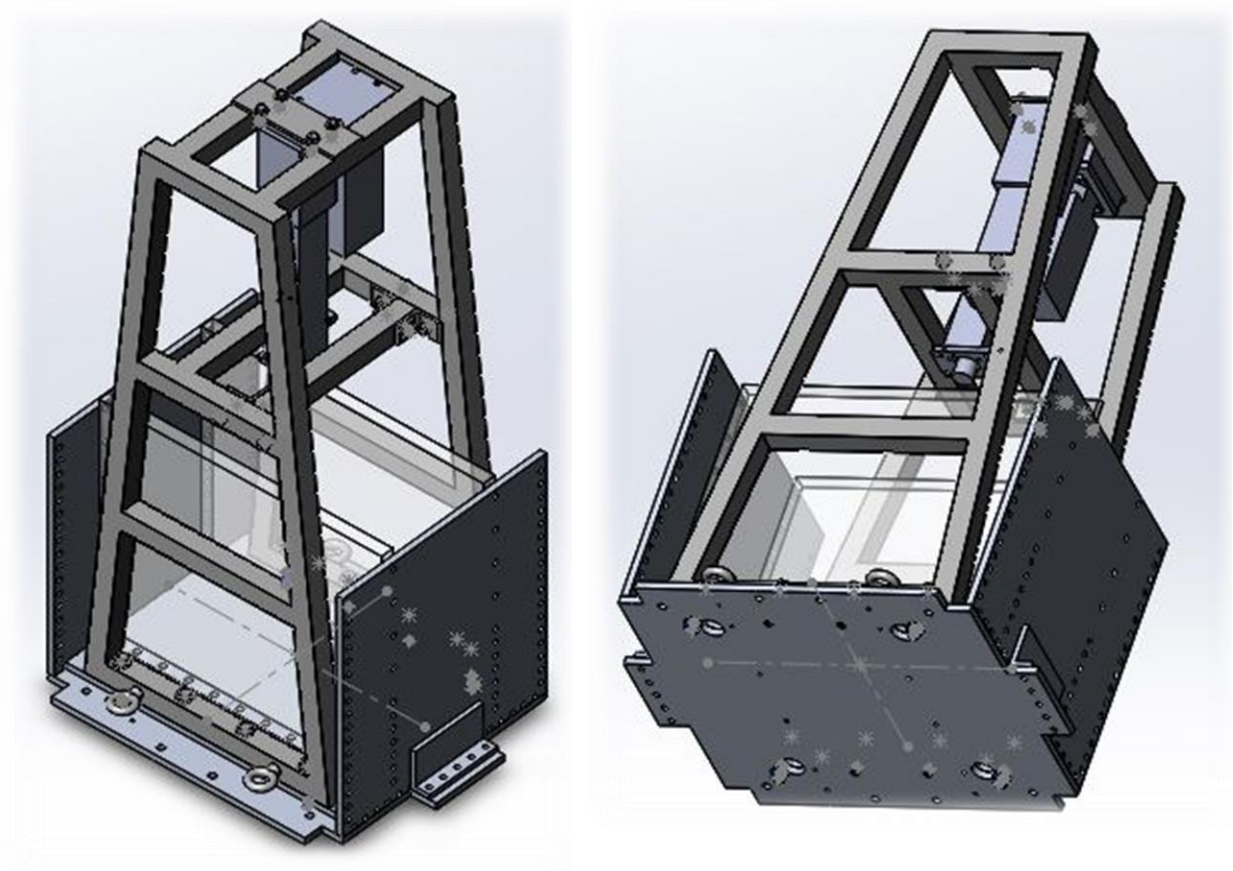

Figure 3-29. The actuator frame

Several centrifuge tests were performed to observe the overall performance of the electric actuator-frame-container in the target centrifugal acceleration level (i.e. 50g), check the mechanical design of the system under centrifugal forces, and verify the efficiency and reliability of the actuator control system. The centrifuge tests were performed at constant rates and in several different amplitudes. The displacements were recorded using a feedback LP (with 6 inch stroke) attached to the head of the actuator; as such, it monitored the position of the actuator (later the position of the top of the sheet pile wall) during the centrifuge tests. As it is depicted in Figure 3-30-Figure 3-33, there is reasonable repeatability between each test results. That is, the actuator was able to apply repeatable extensions and contractions at a constant rate and amplitude. The constant rate has been verified through depicting parallel red dashed lines for extension and parallel blue dashed lines for contraction.

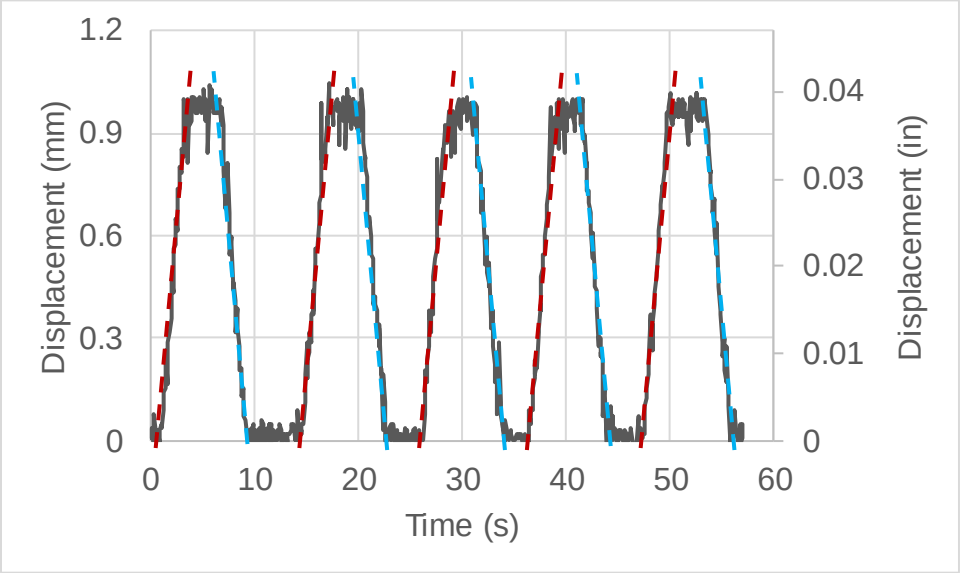

Figure 3-30. Actuator feedback during centrifuge tests performed at 50-g: results are presented in model-scale with target amplitude of 1 mm. Parallel red and blue dashed lines verify repeatability and achieved constant during extension and contraction, respectively.

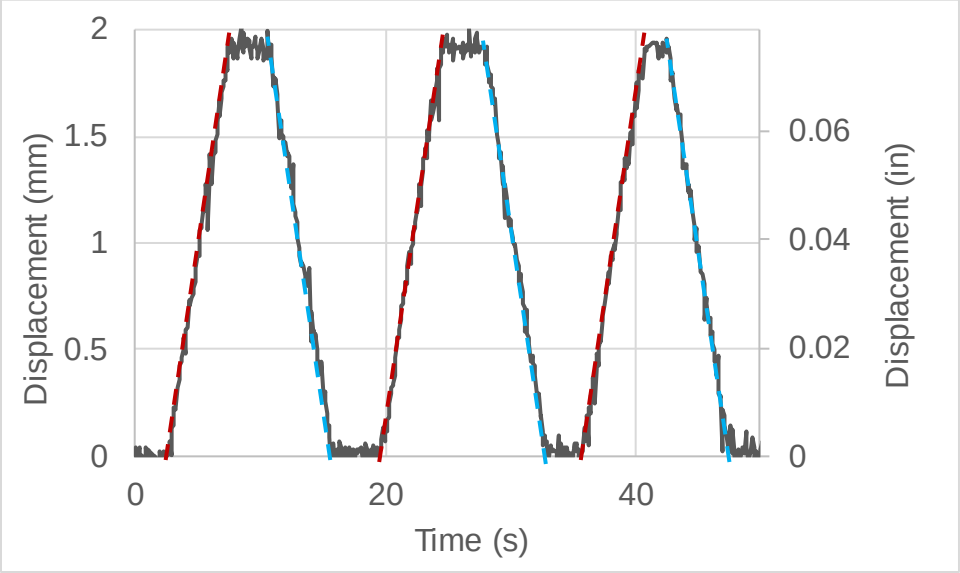

Figure 3-31. Actuator feedback during centrifuge tests performed at 50-g results are presented in model-scale with target amplitude of 1.9 mm. Parallel red and blue dashed lines verify repeatability and achieved constant during extension and contraction, respectively.

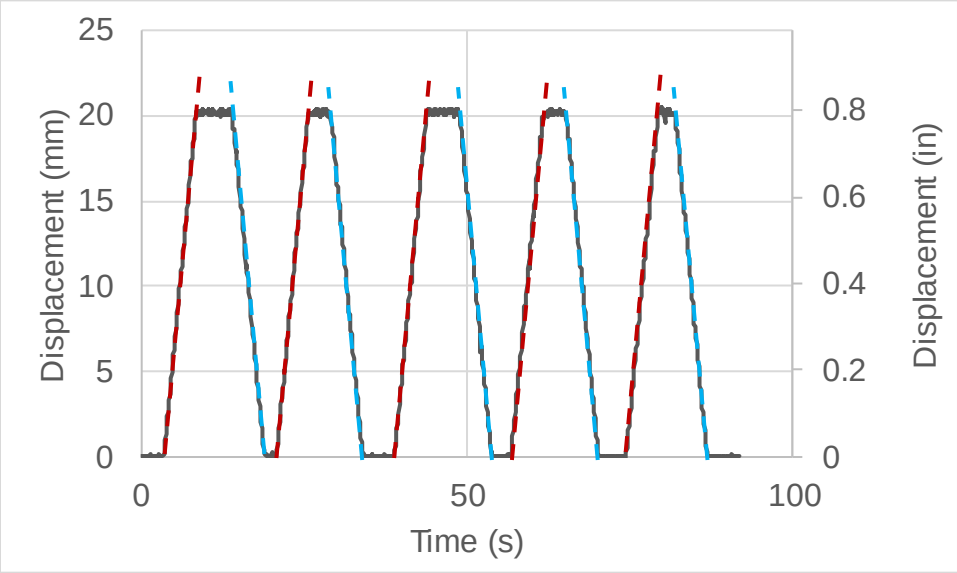

Figure 3-32. Actuator feedback during centrifuge tests performed at 50-g: results are presented in model-scale with target amplitude of 20 mm. Parallel red and blue dashed lines verify repeatability and achieved constant during extension and contraction, respectively.

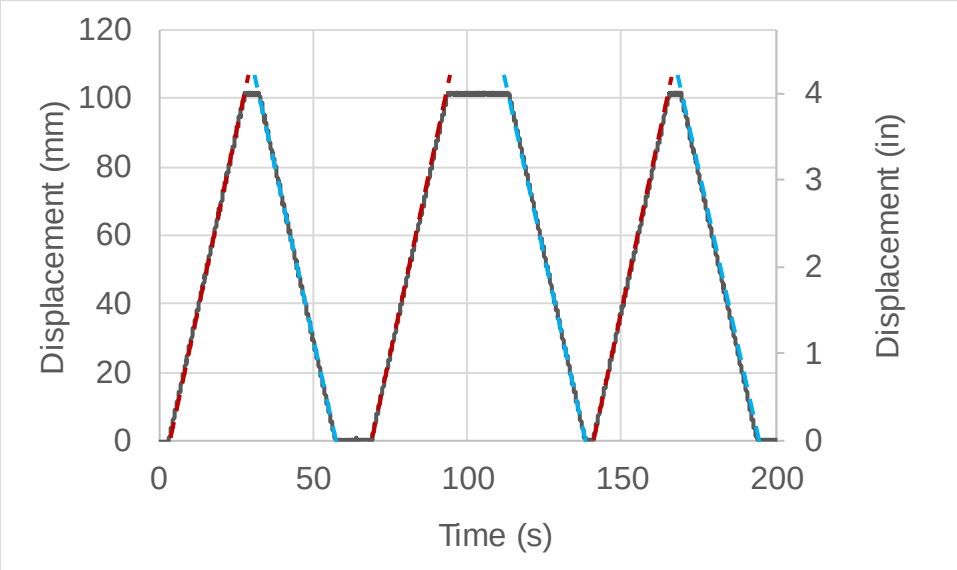

Figure 3-33. Actuator feedback during centrifuge tests performed at 50-g: results are presented in model-scale with target amplitude of 100 mm. Parallel red and blue dashed lines verify repeatability and achieved constant during extension and contraction, respectively.

3.3.2.5 Helmet

Helmets are being used in the field to drive full-scale sheet piles or piles. One important role of a helmet is connecting the hammer or pushing/driving system to the top of the pile or sheet pile. Figure 3-34 depicts a helmet used to drive a sheet pile in the field. As can be seen, the illustrated helmet seats around the sheet pile and provides a full connection to it. This concept is used for designing a small-scale helmet for centrifuge tests. The schematic sketch of the model helmet is shown in Figure 3-35. This helmet is machined from steel and is designed to be rigid. Two series of set screws in front and rear of the helmet provide full connection and a constrained boundary condition at top of the sheet pile. A photo of the helmet is presented in Figure 3-36.

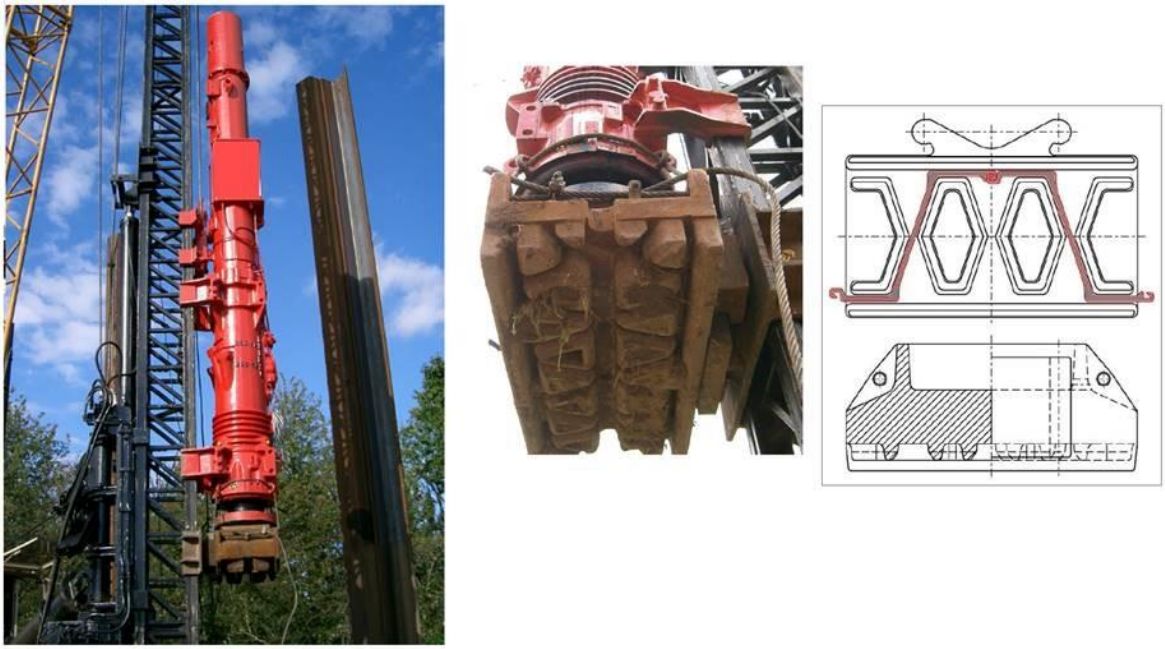

Figure 3-34. A helmet used for driving a full-scale sheet pile in the field; photo courtesy of GRL Engineers, Inc.

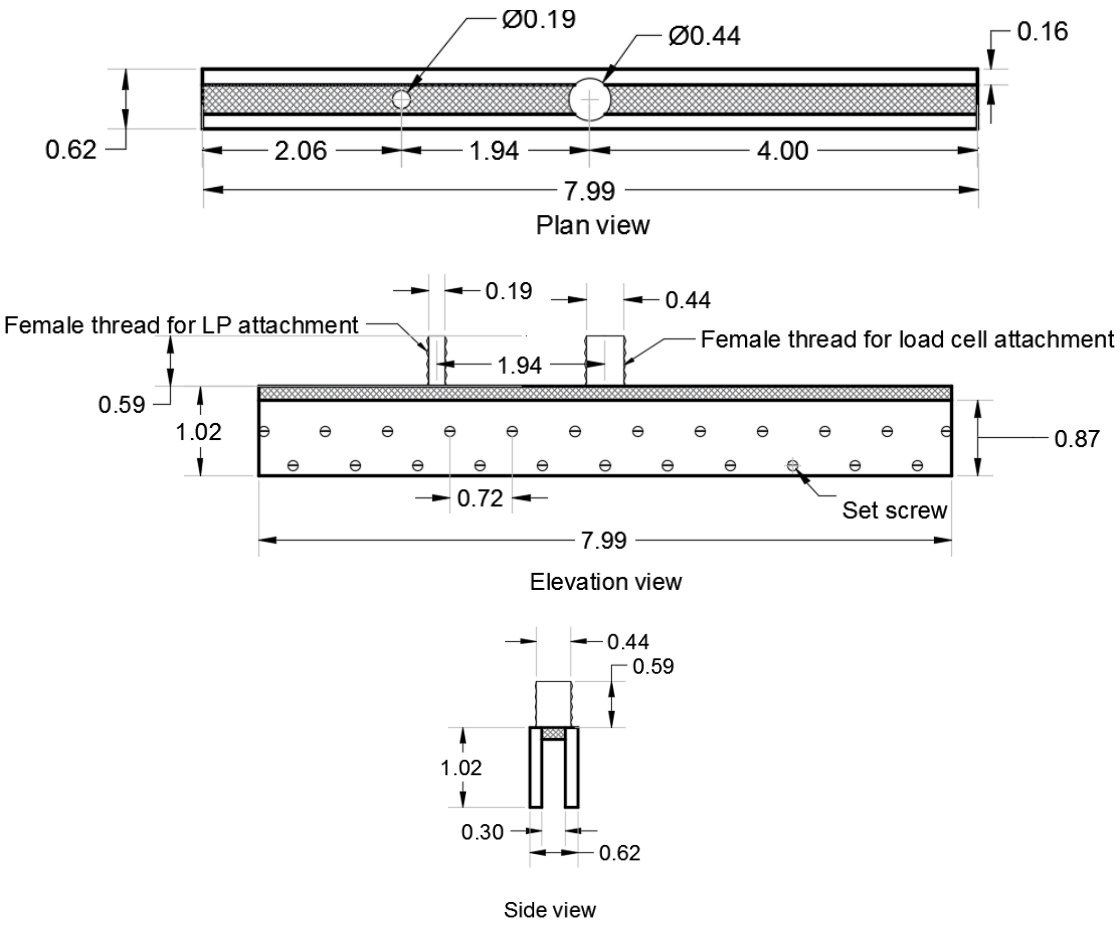

Figure 3-35. Schematic sketch of the helmet used for centrifuge tests

Figure 3-36. Helmet fixed to the model sheet pile wall

3.3.2.6 Centrifuge Tests Set-up

Shown in Figure 3-37 is the centrifuge test set-up illustrating the stepper motor, feedback LP, load cell, controller, helmet, sheet pile, container, and frame.

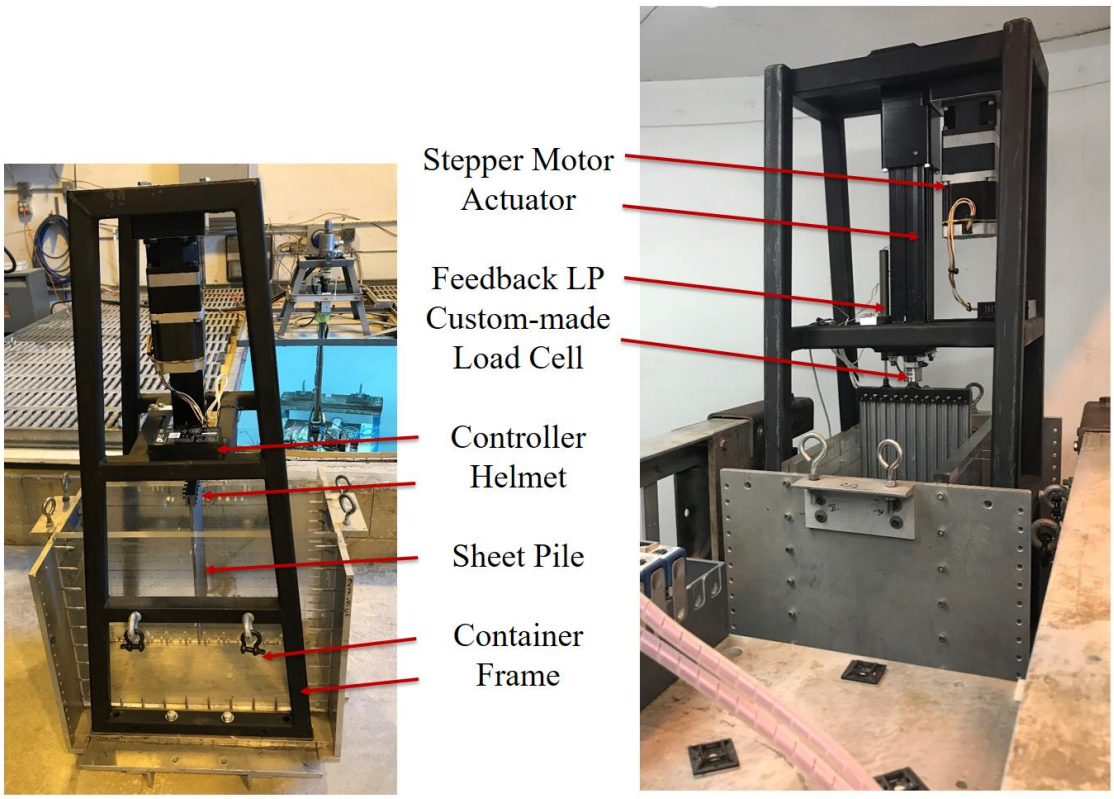

Figure 3-37. Centrifuge test set-up

3.3.3 Centrifuge modeling scenarios

Static and quasi-static load tests will be performed on the SPW models under different scenarios simulating the variety of conditions that may frequently encounter in the field. This section explains the scenarios to be investigated by centrifuge testing.

3.3.3.1 Axial load transferring mechanisms: end bearing and skin friction

Two scenarios will be considered in investigating the axial load transferring mechanisms in sheet piles. In the first scenario, the sheet pile wall will be tested in a medium-dense sand profile with a relative density of 60% (Figure 3-17 and Figure 3-18). It is believed that this case will represent a friction sheet pile where most of the axial load is carried through skin friction. In the second scenario, the sheet pile wall tip will be found on a dense sand layer with a relative density of 90% underlying a medium dense sand with a relative density of 60% (Figure 3-19 and Figure 3-20). The sheet pile wall tip will be penetrated in the dense sand layer for about 39.4 in. It is believed that this case will represent an end bearing sheet pile where tip resistance plays an important role in the bearing resistance of the sheet pile. Low axial movements of the end-bearing sheet pile may result in a considerable reduction in friction resistance in the upper layer.

3.3.3.2 Penetration depth and unsupported length

To investigate the effects of depth of penetration (D) and unsupported length (H) on the axial behavior, bearing resistance, and failure mechanism of the sheet pile walls, two different penetration depth to retained soil height ratios (D/H) of 1.2 (Figure 3-17 and Figure 3-19) and 2.2 (Figure 3-18 and Figure 3-20) will be considered. By changing the penetration depth, it is believed that the amount of mobilized and ultimate skin friction for the axially loaded sheet piles will be changed. The penetration depth will also determine the amount of passive resistance in front of the sheet pile under lateral earth pressure and might change the failure mechanism. Therefore, the horizontal displacement of the sheet pile wall also depends on the penetration depth where the wall may lose its serviceability under large deformations. In cases with D/H = 1.2 the unsupported length is increased with respect to the cases with D/H = 2.2. The influence of the unsupported length on the buckling behavior of the wall will be also investigated.

3.3.3.3 Sheet pile stiffness

The effects of bending and axial stiffness of the sheet pile elements on the bearing capacity of the axially loaded sheet piles will be studied. The prototype-scale bending stiffness and axial stiffness values of the model sheet piles will be matched with those commonly used in the field (refer to Table 2). Two sheet pile walls with PZ cross sections will be machined where the second sheet pile wall (PZS2) has higher (approximately twice) bending and axial stiffness than the first one (PZS1). Sheet pile stiffness plays an important role on its buckling especially in cases where sheet piles are driven through compressible soil layers but are terminated at depth into a relatively incompressible layer (e.g. rock or dense sand). In these cases, the maximum design load for such a sheet pile will be governed by the stresses in the sheet pile material itself, rather than the base resistance in the dense layer. The effects of stiffness change on the buckling behavior of both sheet pile sections (PZS1 and PZS2) will be investigated in all four soil profile configurations (i.e. PR1-4).

3.3.3.4 Boundary conditions

It is aimed to investigate the bearing capacity of axially loaded sheet pile walls with both fixed and free head conditions. The effects of head conditions on the deformation of the wall, lateral earth pressure on the wall, and bending moment and axial force distribution will be also investigated. To create fixed-head conditions, a helmet (cap) will be perfectly fitted to the top of the sheet pile wall preventing it from any rotation. In the case of the free-head condition, the sheet pile will be allowed to move inside the helmet providing active earth pressure on the retained soil. In both cases, it is planned to apply a vertical load simulating the vertical loads imposed by the superstructure.

3.3.3.5 Axial load testing of sheet pile abutments

For each of the centrifuge test scenarios described in section 2.3, separate static and quasi-static load tests will be performed. Quasi-static load tests are aimed to quantify rate effects when pushing and load testing of the sheet piles, where the results will be compared to the static load tests served as the reference case(s). To the best knowledge of the authors, axial load tests are not performed on centrifuge model sheet pile foundations so far. ASTM D1143/D1143M (2013) has explained methods for conducting static axial compressive load tests on deep foundations, which will be adopted. To do the load tests, the actuator (apparatus) can apply the desired displacement-time histories with the specified amplitude and frequency for both static and quasi-static loading. The strain gages will be used during load tests to obtain axial load distribution along the sheet pile. The main objective in performing these load tests is to investigate and confirm the capacity of sheet piles to support both vertical loads applied from the superstructure on top of it (e.g. a bridge) and lateral earth loads applied from its backfill material. By doing axial load tests on instrumented sheet pile foundations, axial load transfer curves will be obtained and relationships for load resistance versus axial deformation of the pile head for displacements ranging from zero to the ultimate limit or to an achievable maximum value will be established. The centrifuge tests will help in coming up with a protocol for designers and practitioners to easily do the load tests on sheet piles in the field.

3.3.4 Total number of centrifuge tests

Centrifuge tests will be carried out on model cantilever sheet pile walls supporting granular fill by subjecting to varied g-levels (in steps of 10g) up to a maximum set target g-level of 50g. As stated earlier, centrifuge tests for a specified scenario will be separately conducted for static and quasi-static load testing of sheet piles. The bending moment distribution, deflections of the sheet pile wall, the settlement of the backfill, and soil stresses will be monitored during the centrifuge test. These quantities, prior to the load tests, will be served to ensure the repeatability between similar tests. The consistency of all centrifuge tests will be ensured. Four tests of select centrifuge testing scenarios including their load tests will be fully repeated to ensure about repeatability and validity of load tests as well. As it is shown in Table 3, a total of 36 centrifuge tests will be conducted to study five scenarios described in section 3.3.

Table 3-7. Summary of scenarios for centrifuge tests

	Sheet pile Embedment	Sheet pile stiffness	Sheet pile head constraints	Load testing	Total cases
Medium-dense sand	2	2	2	2	16
Two-layered Profile	2	2	2	2	16
Repeat tests					4
Sum					36

3.3.5 Element-scale laboratory tests

The stress-strain characteristics of sand are being investigated in material strength laboratory in accordance with the pertinent American Association of State Highway and Transportation Officials (AASHTO) or/and American Society for Testing and Materials (ASTM) standards. The purpose of the element-scale laboratory tests is to evaluate key shear strength parameters of the sand for use in calibration of the finite element (numerical) models and in evaluating the theoretical models to study sheet pile behavior under lateral earth pressure. State Material Office (SMO) has already performed several Isotopically Consolidation Drained Triaxial Compression tests (CIDC) and direct shear tests (see Figures 4 and 5) on the sand being used in the centrifuge tests in different relative densities and normal loads. In addition to these tests, direct shear tests are being performed to study the angle of friction between the sheet pile and sand by inserting a plate of aluminum in a shear box (Figure 3-38), with the surface of the plate flush with the plane of shearing.

To investigate the possible variations of the angle of friction between the sand and aluminum sheet pile, and the sand and steel sheet pile (i.e. the case in the field), it is planned to perform the direct shear tests on both aluminum and steel plates. The possible changes in the interface friction angle might slightly alter the side resistance (skin friction) of the sheet pile wall. These friction angle differences (investigated through direct shear tests) will be considered in the finite element analyses and recommendations will be made considering the effects of changes in sand-interface friction angle on the bearing resistance and settlement of sheet pile walls.

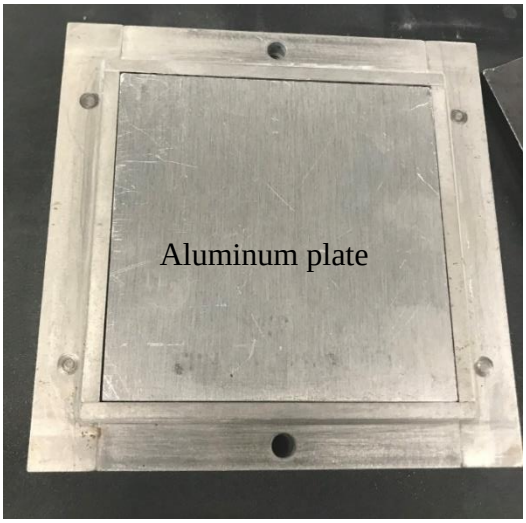

Figure 3-38. The aluminum plate used in interface shear box tests; photo courtesy of SMO

3.4 References

ASTM D1143/D1143M (2013). "Standard Test Methods for Deep Foundations under Static Axial Compressive Load."

ASTM D1143/D1143M (2013). "Standard Test Methods for Deep Foundations Under Static Axial Compressive Load." ASTM International, West Conshohocken, PA.

Auto Motion Direct (2019). <https://library.automationdirect.com>.

Bolton, M. D., and Powrie, W. (1987). "The collapse of diaphragm walls retaining clay." *Géotechnique*, 37(3), 335-353.

Bolton, M. D., and Powrie, W. (1988). "Behaviour of diaphragm walls in clay prior to collapse." *Géotechnique*, 38(2), 167-189.

Doubrovsky, M. P., and Meshcheryakov, G. N. (2015). "Physical modeling of sheet piles behavior to improve their numerical modeling and design." *Soils and Foundations*, 55(4), 691-702.

Fuglsang, L. D., and Ovesen, N. K. (1987). "The application of theory of modelling to centrifuge studies." *Centrifuge in soil mechanics*, W. J. Craig, and A. Schofield, eds., Balkema, Rotterdam, 119-138.

Lini Dev, K., Pillai, R. J., and Robinson, R. G. (2016). "Drained angle of internal friction from direct shear and triaxial compression tests." *International Journal of Geotechnical Engineering*, 10(3), 283-287.

Madabhushi, S. P. G., and Chandrasekaran, V. S. (2005). "Rotation of Cantilever Sheet Pile Walls." *Journal of Geotechnical and Geoenvironmental Engineering*, 131(2), 202-212.

Madabhushi, S. P. G., and Chandrasekaran, V. S. (2008). "Centrifuge Testing of a Sheet Pile Wall with Clay Backfill." *Indian Geotechnical Journal*, 38(1), 1-20.

McDowell, R. G., and Bolton, D. M. (2000). "Effect of particle size distribution on pile tip resistance in calcareous sand in the geotechnical centrifuge." *Granular Matter*, 2(4), 179-187.

Micro-Measurements (2015). "The Three-Wire Quarter-Bridge Circuit." Tech Tip TT-612.

Micro-Measurements (2018). "Strain Gage Selection: Criteria, Procedures, Recommendations." TechNote TN-505-6.

Viswanadham, B., Madabhushi, S. P. G., Babu, K., and Chandrasekaran, V. (2009). "Modelling the failure of a cantilever sheet pile wall." *International Journal of Geotechnical Engineering*, 3(2), 215-231.

3.5 Task 3c: Centrifuge testing observations

Through task 3c, centrifuge load tests are conducted to investigate the problem at hand and calibrate and validate the numerical models. Different geo-structural conditions were evaluated to account for various factors including soil profile layering, sheet pile wall stiffness, boundary conditions of the sheet pile wall head, and loading rate effects. This report provides the results of centrifuge tests performed on the PZS1 and PZS2 sheet pile walls with fixed (17 tests) or free (6 tests) head conditions in the PR1-PR4 profiles (Figure 3-39 and Figure 3-40). The remaining centrifuge load tests results on the sheet pile walls with free-head conditions will be included in the next report.

Details on the centrifuge models preparation, instrumentation, the centrifuge tests setup can be found in the Task 3b report.

3.5.1 Centrifuge modeling scenarios

Axial static load tests were performed on the sheet pile wall (SPW) models under different scenarios simulating a variety of conditions that may frequently encounter in the field. This section explains these investigated scenarios and discusses the findings from them. The test matrix of the centrifuge testing program is provided in Table 1.

Centrifuge tests were carried out on model cantilever sheet pile walls supporting the granular fill by subjecting to varied g-levels (in steps of 10g) up to a maximum set target g-level of 50g. The axial load and bending moment distribution and the settlement of the backfill close and far from the sheet pile wall were monitored during the centrifuge test. These quantities, prior to the load tests, were served to ensure the repeatability between similar tests. Two tests of select centrifuge testing scenarios including their load tests were fully repeated to ensure about repeatability and validity of load tests, as well.

Table 3-8. Centrifuge Testing Matrix

Test No.	Sheet Pile Wall	Head Boundary Condition	Soil Profile	CRP Rate* (in/s)
1	PZS2	Fixed	PR1	7.87×10^{-4}
2	PZS2	Fixed	PR1	7.87×10^{-4}
3	PZS2	Fixed	PR1	7.87×10^{-5}
4	PZS2	Fixed	PR3	7.87×10^{-4}
5	PZS2	Fixed	PR3	7.87×10^{-5}
6	PZS2	Fixed	PR4	7.87×10^{-5}
7	PZS2	Fixed	PR2	7.87×10^{-5}
8	PZS2	Fixed	PR2	7.87×10^{-4}
9	PZS2	Fixed	PR4	7.87×10^{-4}
10	PZS1	Fixed	PR1	7.87×10^{-5}
11	PZS1	Fixed	PR1	7.87×10^{-4}
12	PZS1	Fixed	PR3	7.87×10^{-4}
13	PZS1	Fixed	PR3	7.87×10^{-5}
14	PZS1	Fixed	PR4	7.87×10^{-5}
15	PZS1	Fixed	PR4	7.87×10^{-4}
16	PZS1	Fixed	PR2	7.87×10^{-4}
17	PZS1	Fixed	PR2	7.87×10^{-5}
18	PZS2	Free	PR1	7.87×10^{-4}
19	PZS2	Free	PR1	7.87×10^{-5}
20	PZS2	Free	PR2	7.87×10^{-5}
21	PZS2	Free	PR2	7.87×10^{-4}
22	PZS2	Free	PR3	7.87×10^{-5}

23	PZS2	Free	PR3	7.87×10^{-4}
24	PZS2	Free	PR4	7.87×10^{-4}
25	PZS2	Free	PR4	7.87×10^{-5}
26	PZS1	Free	PR3	7.87×10^{-4}
27	PZS1	Free	PR3	7.87×10^{-5}
28	PZS1	Free	PR4	7.87×10^{-5}
29	PZS1	Free	PR4	7.87×10^{-4}
30	PZS1	Free	PR1	7.87×10^{-4}
31	PZS1	Free	PR1	7.87×10^{-5}
32	PZS1	Free	PR2	7.87×10^{-4}
33	PZS1	Free	PR2	7.87×10^{-5}
34	PZS1	Free	PR1	11.81×10^{-3}
35	PZS1	Free	PR1	7.87×10^{-4}
36	PZS1	Free	PR1	7.87×10^{-5}
* Constant Rate of Penetration (CRP)				

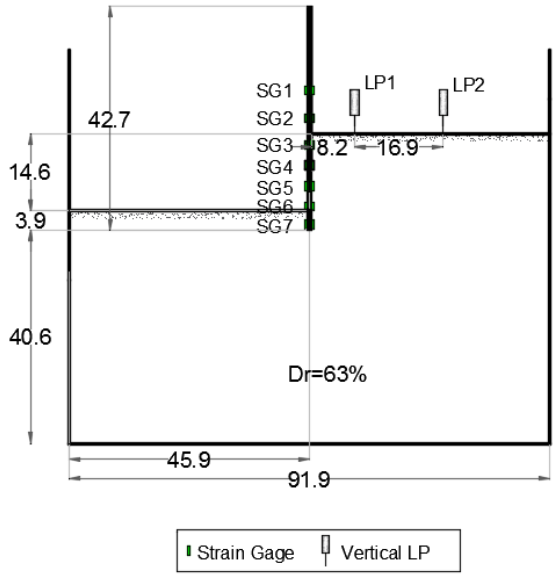

(a)

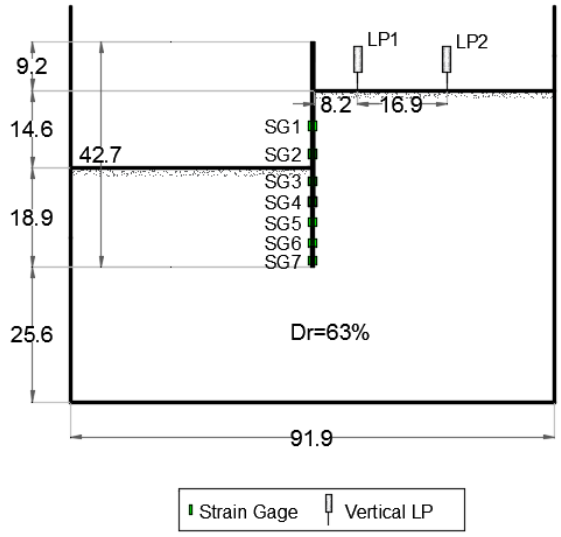

(b)

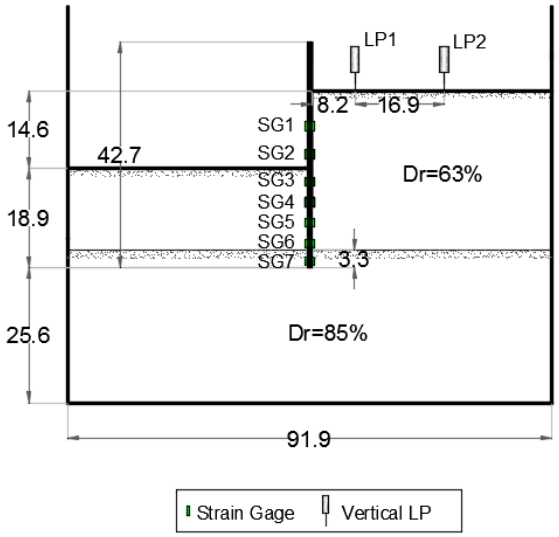

(c)

Figure 3-39. Cross-section of the centrifuge model for tests with D/H=1.3: (a) before sheet pile wall driving; (b) homogenous sand (PR1); and (c) two layers of sand (PR2). The dimensions are provided in prototype-scale in feet.

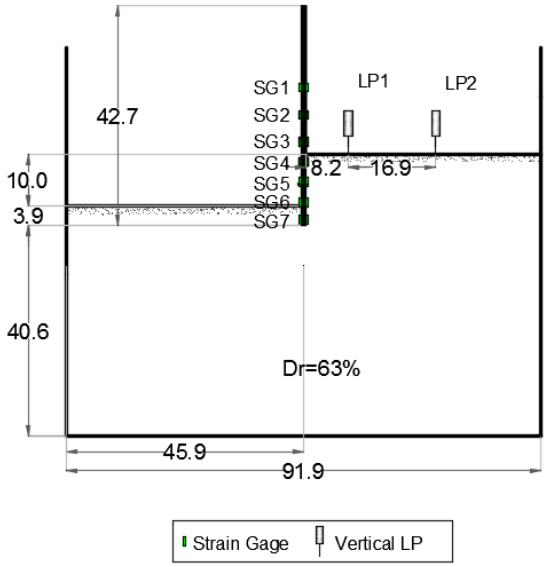

(a)

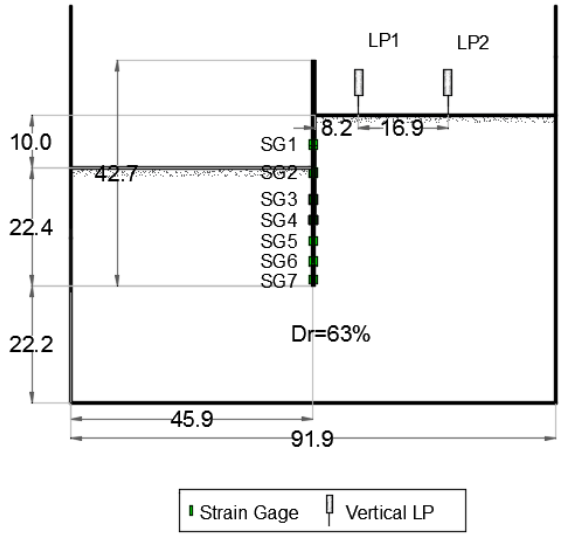

(b)

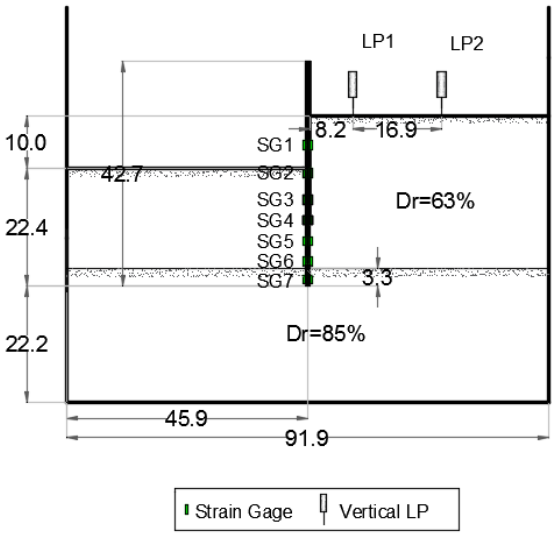

(c)

Figure 3-40. Cross-section of the centrifuge model for tests with D/H=2.24: (a) before sheet pile wall driving; (b) homogenous sand (PR3); and (c) two layers of sand (PR4). The dimensions are provided in prototype-scale in feet.

3.5.1.1 In-flight driving of sheet piles

The sheet pile walls were driven into the target depths shown in the aforementioned sand profiles (see Figure 3-39 - Figure 3-40) in flight using a combination of downward and upward axial movements. That is, after every 1.6 inches (in the model-scale) of downward movement, the sheet pile wall was moved upward for 0.4 inches. This driving pattern was continued until the sheet pile wall tip was set into its target elevation. Through this driving pattern, it was aimed to simulate the compaction and volume changes of the sand surrounding the sheet pile similar to that occurs in the field but in a simple way, in the centrifuge modeling context. Quasi-static pushing and pulling-type displacements with a speed of about 0.04 in/s (about 1 mm/s) were used. Using the precise displacement-controlled actuator and its 6 in feedback displacement transducer at the top of the sheet pile wall, it was made sure that a repeatable driving pattern and tip elevation was achieved along this series of tests. It is worth mentioning that the use of the mentioned 6 in transducer is in agreement with the requirements of ASTM D1143/D1143M (2013) for such a displacement measurement system. A photo of the centrifuge model at the end of driving (after the test) is shown in Figure 3-41.

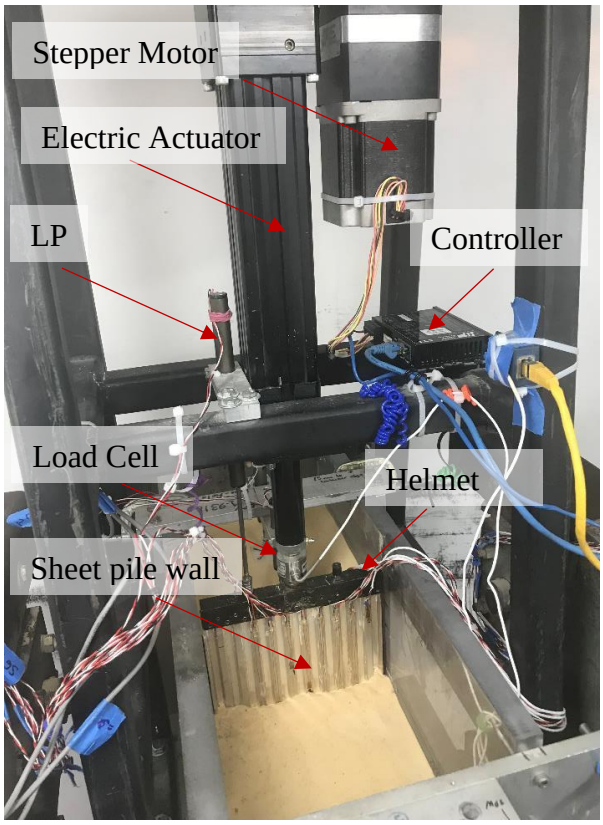

Figure 3-41. Sheet pile wall after driving (at the end of the centrifuge test)

The sheet pile wall top displacement-time history during driving and load testing in Test 11 is shown in Figure 3-42. The mentioned downward and upward movements during driving can be noticed through this figure. The upward movement during driving unloads the sheet pile wall and

as it is shown in Figure 3-43, negative (i.e. tensile) low axial loads are experienced during these moments. The sheet pile wall top displacement versus top load (measured by a load cell) during driving and load testing is depicted in Figure 3-44. The compaction of sand during the mentioned driving pattern after each downward and upward movement has been manifested in terms of an increased axial load compared to the previous stage. It is also obvious that increased confinement pressure also contributes to the increase in axial resistance when penetrating to deeper depths.

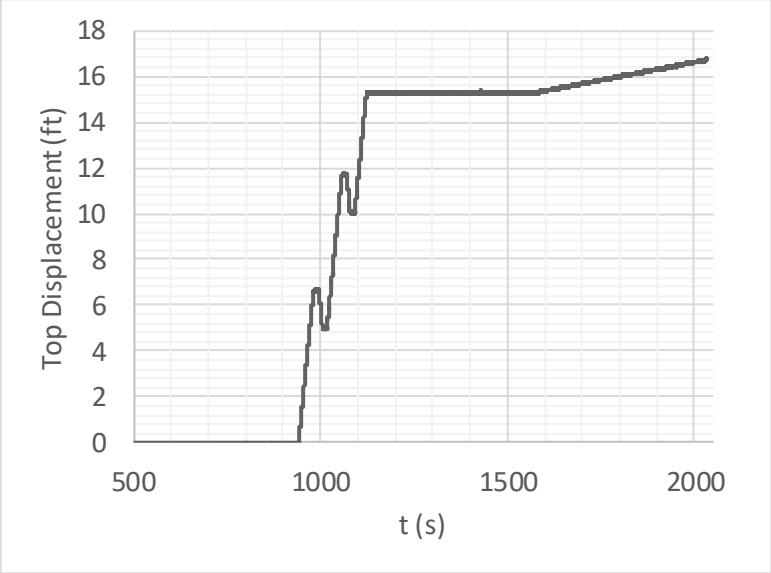

Figure 3-42. Test 11: Sheet pile wall top axial displacement-time history during driving and load testing

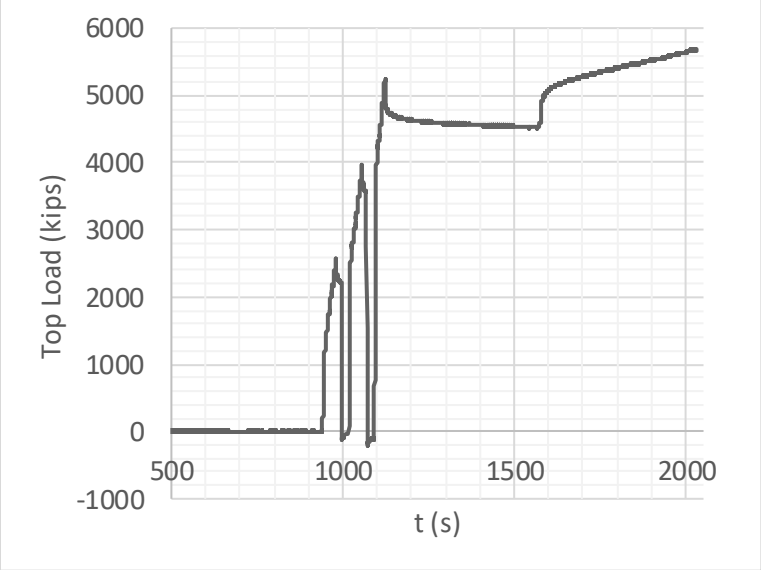

Figure 3-43. Test 11: Sheet pile wall top axial load-time history during driving and load testing

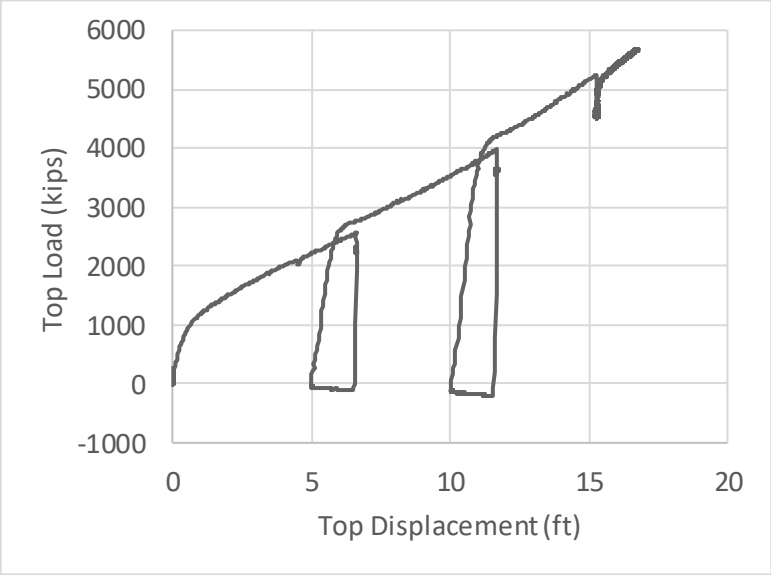

Figure 3-44. Test 11: Sheet pile wall top axial displacement versus axial load during driving and load testing

3.5.1.2 Procedure for static axial compressional load testing of cantilever sheet pile walls

ASTM D1143/D1143M (2013) has explained seven procedures (i.e. procedures A to G) for conducting static axial compressive load tests on deep foundations. The Procedure E described by ASTM D1143 designation was used for static load testing of sheet piles in this project. Procedure E describes a method for the Constant Rate of Penetration (CRP) Test. Through this procedure, the applied load varies as necessary to maintain a constant pile penetration rate of 0.03 to 0.10 in [0.75 to 2.5 mm] per minute for granular soils, or as specified by the engineer. This range of rate equals to 0.0125 to 0.0417 mm per second (4.92×10^{-4} to 1.64×10^{-3} in/s). It is worth mentioning that the British Standard (BS 8004:1986) recommends a rate of 0.025 mm/s (9.84×10^{-4} in/s) for the CRP test. As such, the load tests for this project were performed at a constant rate of 0.02 mm per second (7.87×10^{-4} in/s).

The driving factors to do the load tests using the procedure E were as follows:

- In load testing of sheet piles with fixed heads, it was observed that trying to maintain the load for about two minutes (about 100 minutes in prototype scale) by stopping the axial displacement of the sheet pile (penetration rate equal to zero) drops the applied axial load by up to about 1000 kips, which was mainly due to the relaxation of sand around the sheet pile (see Figure 3-45). Continuing to apply the axial load through applying the constant rate of penetration puts the load again at the same previous path (as shown through the red dashed line in Figure 3-45). Similar to the drilled shafts (Reese and O'Neill 1988) and H-piles (Mosher 1984) in sand, the bearing capacity (due to increase in end bearing) of the sheet piles was observed to constantly increase by the axial displacement, z. Both these

factors made using Maintained Load Testing, MLT (explained in procedure B) for performing repeatable load tests challenging. It is worth mentioning that in MLT, the individual deep foundation is axially loaded in increments of 25% to a maximum maintained load of 200% of the anticipated design load. Each load increment is maintained until the rate of axial movement does not exceed 0.01 inch (0.25 mm) per hour. After reaching the maximum load at a minimum overall test duration of 12 hour, unloading begins when the axial movement measured over a period of 1 hour does not exceed 0.01 inch. In case of failure, the failure load or the maximum possible load is maintained until the total axial movement equals 15% of the pile width or diameter.

- The CRP load testing might be considered as one of the top candidate for load testing of sheet piles considering the fact that, in both centrifuge and field load testing, the same apparatus can be used for pushing (driving) and load testing of the sheet piles (Hammers & Steel 2019; steel piling group 2019).
- The CRP testing may need less "set-up" and performing time than MLT, helping to reduce the overall costs of the load testing project.

ASTM D1143/D1143M (2013) has defined the failure load, for the purpose of terminating an axial compressive load test, "*the test load at which rapid continuing, progressive movement occurs, or at which the total axial movement exceeds 15 % of the pile diameter or width, or as specified by the engineer*." Using this definition, the axial resistances were reported at the sheet pile top total axial movement of 15 % of the average sheet pile width (D). The width of the PZS1 and PZS2 sheet piles was 13 and 14.38 inch, respectively. For comparison purposes, the width of PZS1 (i.e. the minimum value) was used as the reference for comparisons. As such, the reported resistance values relate to 15% of 13 inch or 1.95 inch of axial movement.

The axial load distribution along the sheet pile wall was obtained through the load cell (LC) located at the top of the sheet pile wall and 14 strain gages (7 pairs) along the sheet pile wall. The axial load – axial displacement response during load testing of Test 11 is presented as an example in Figure 8. T_1, T_2, T_3, T_4, T_5, T_6, and T_7 are obtained using strain gages SG1, SG2, SG3, SG4, SG5, SG6, and SG7 (see Figures 1 and 2), respectively. SG7 is located at the very bottom of the sheet pile wall and the axial load obtained by this strain gage reasonably represents the axial load carried through end bearing. Obviously, going from the sheet pile wall top to its tip, the applied axial load reduces due to the skin friction at the interface of the sheet pile wall and the sand. Evident from Figure 3-46 is the existence of significant residual stresses due to the driving of the sheet pile wall and before starting the load testing.

The increasing nature of axial load by increasing axial displacement (i.e. a strain hardening behavior) is similar to those of the axial load behavior of driven H-piles (Reese and O'Neill 1988) or drilled shafts (Reese and O'Neill 1988) in sand. The key contributors to this behavior would be sand compaction during loading and also observed soil plugging. An example photo is depicted in Figure 3-47, illustrating the observed sand plugging in centrifuge tests. It is worth mentioning that the average measured water content (due to the ambient humidity in the lab) of soil was about 0.1%.

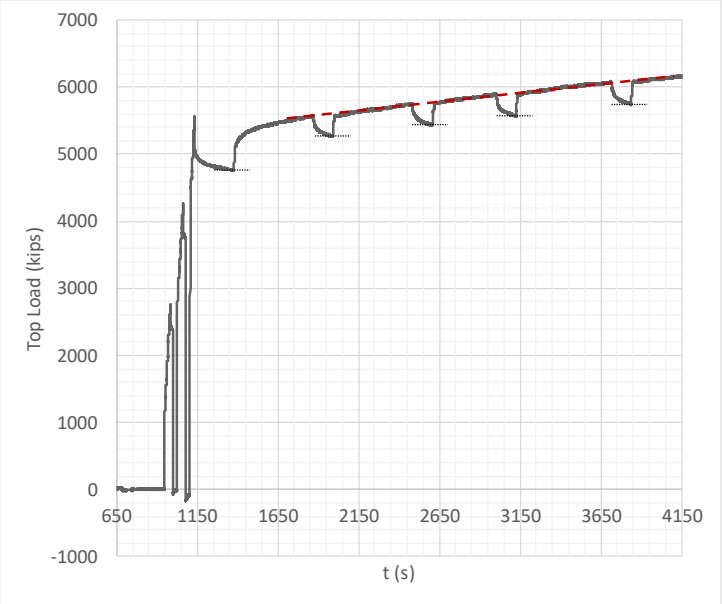

Figure 3-45. Axial compressive load tests of sheet pile walls in sand

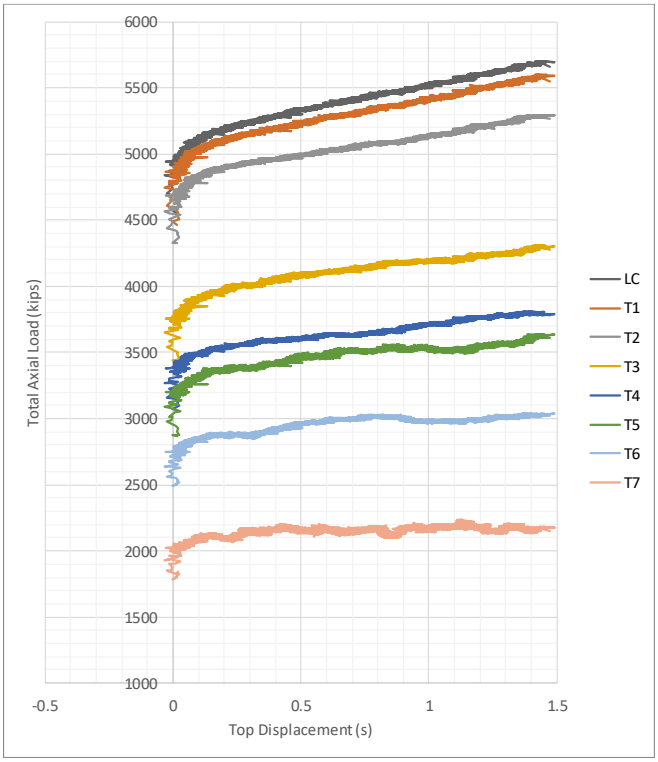

Figure 3-46. Test 11: Axial load distribution along the sheet pile wall

Figure 3-47. Soil plugging observed in centrifuge tests

3.5.1.3 Axial load transferring mechanisms: end bearing and skin friction

Two scenarios were considered in investigating the axial load transferring mechanisms in sheet piles. In the first scenario, the sheet pile wall was tested in a medium-dense sand profile with a relative density of 63%. It is believed that this case represents a friction sheet pile where most of the axial load is carried through skin friction. In the second scenario, the sheet pile wall tip was found on a dense sand layer with a relative density of 85% underlying a medium dense sand with a relative density of 63% (see Figure 3-39 - Figure 3-40). The sheet pile wall tip was penetrated in the dense sand layer for about 39.4 in. This case represented an end bearing sheet pile where the tip resistance played an important role in the bearing resistance of the sheet pile.

Shown in Figure 3-48 are the comparisons of the load tests results for the PZS1 sheet pile wall in the PR2 and PR1 profiles. As stated earlier, PR2 represents a two-layered profile (medium dense sand layer overlying a dense sand layer) and PR1 represents a homogenous medium-dense sand layer, both having D/H=1.3. The axial resistance of the sheet piles has been increased due to its penetration in the dense sand layer in the PR2 profile. Similar trends are observed when load testing at CPR=7.87×10^{-4} in/s and at a 10 times slower rate at CPR=7.87×10^{-5} in/s.

Figure 3-49 depicts the load tests results for the PZS1 sheet pile wall in the PR3 and PR4 profiles. Recall PR4 and PR3 both have D/H=2.24, with the former being a two-layered profile (medium-dense sand overlying a dense sand layer) and the latter a homogenous medium-dense sand layer. Similar to the cases with a lower D/H, the axial resistance of the sheet pile has been increased when its tip has penetrated into the dense sand layer (i.e. sheet pile in the PR4 profile). Again, similar trends are observed when load testing at CPR=7.87×10^{-4} in/s and at CPR=7.87×10^{-5} in/s. However, the gain in axial resistance in PR4 has been more than that for PR2, when comparing to the corresponding homogenous profiles. Two main factors are contributing to this observation: 1) PR4 has a higher D/H than PR2; and 2) When driving the sheet pile into D/H=2.24 profiles, it undergoes greater penetration path (or driving length) compared to the cases where the sheet pile

penetrates into the profiles with D/H=1.3. Greater driving length results in more compaction of sand around the sheet pile.

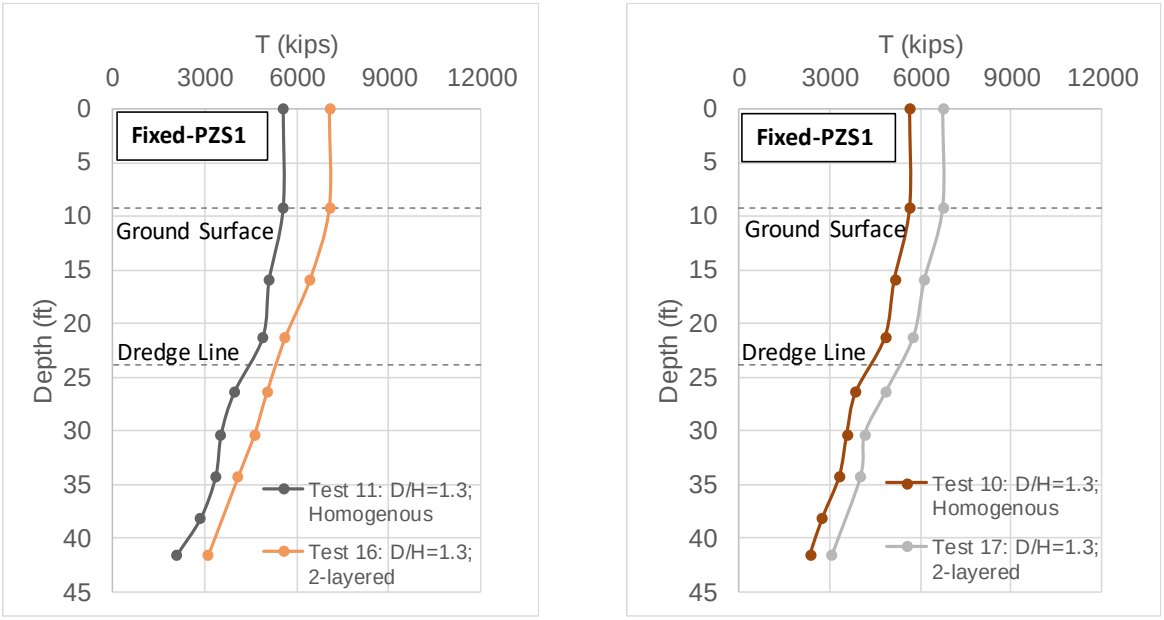

Figure 3-48. Increased axial resistance of the sheet pile wall PZS1 in the profile PR2 (tests 16 and 17) compared to that in the profile PR1 (tests 11 and 10): (a) CPR=7.87×10^{-4} in/s; and (b) CPR=7.87×10^{-5} in/s

The load testing results performed on the PZS2 sheet pile wall are presented in Figure 3-50 and Figure 3-51 for PR1-PR2 and PR3-PR4 profiles, respectively. Similar trends as those observed for PZS1 are obtained and similar discussions are applicable. Note that tests 1 and 2 are repeat tests.

Corresponding bending moment profiles are depicted in Figure 3-52 - Figure 3-55. The maximum bending moment has been obtained at 34.25 ft depth, which is generally consistent across all centrifuge load tests on sheet piles with fixed head conditions. Greater bending moments are obtained in the PR2 and PR4 (two-layered profiles) than those in PR1 and PR3 for both PZS1 and PZS2 sheet pile walls, which is mainly related to the increased axial resistance in these profiles.

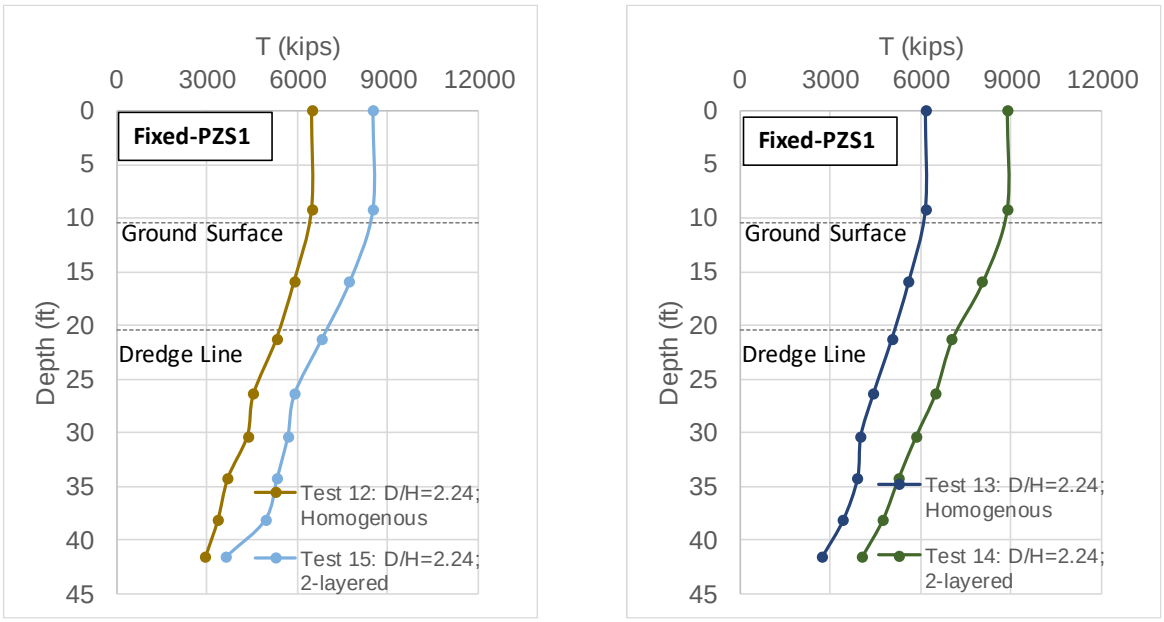

Figure 3-49. Increased axial resistance of the sheet pile wall PZS1 in the profile PR4 (tests 15 and 14) compared to that in the profile PR3 (test 12 and 13): (a) CPR=7.87×10^{-4} in/s; and (b) CPR=7.87×10^{-5} in/s

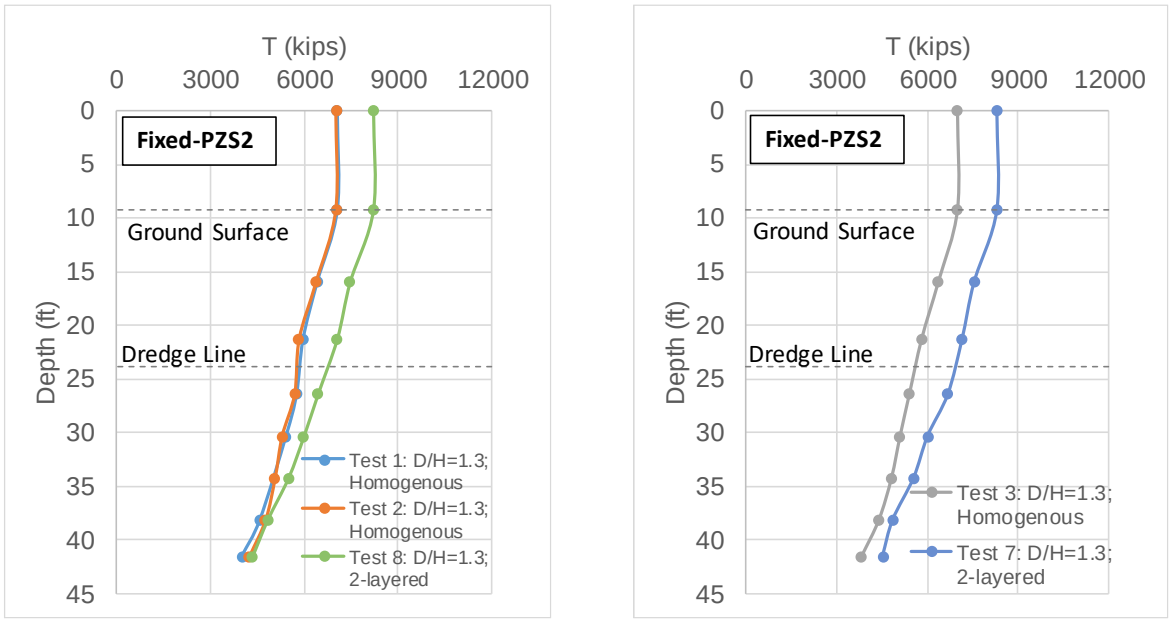

Figure 3-50. Increased axial resistance of the sheet pile wall PZS2 in the profile PR2 (tests 8 and 7) compared to that in the profile PR1 (tests 1, 2 and 3): (a) CPR=7.87×10^{-4} in/s; and (b) CPR=7.87×10^{-5} in/s. Tests 1 and 2 are repeat tests.

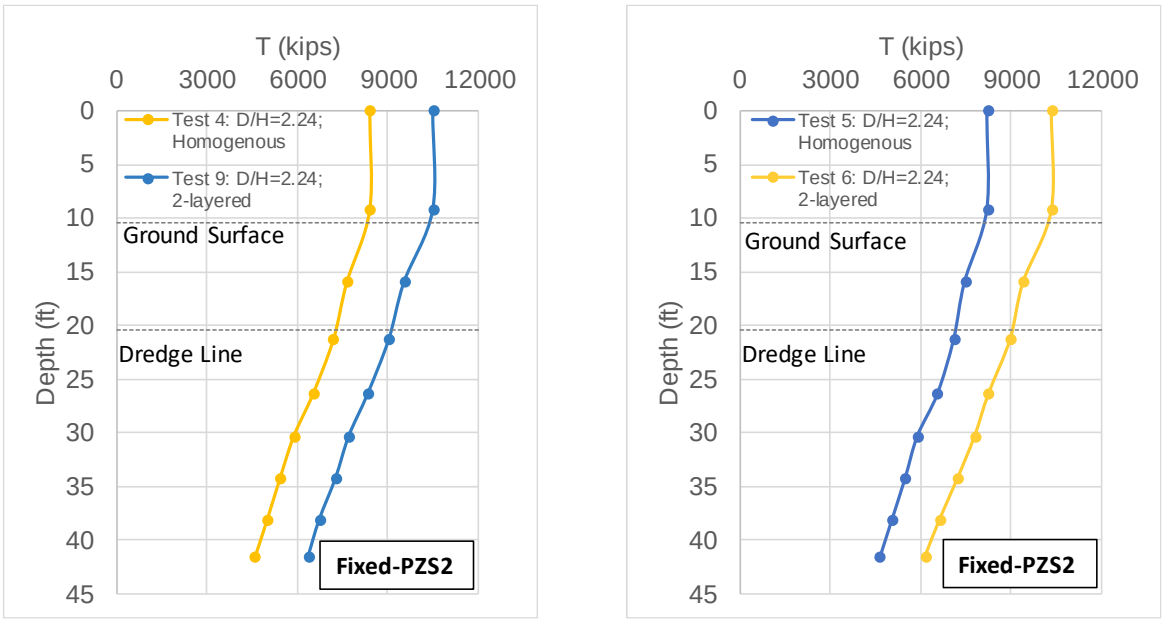

(a) (b)

Figure 3-51. Increased axial resistance of the sheet pile wall PZS2 in the profile PR4 (tests 9 and 6) compared to that in the profile PR3 (tests 4 and 5): (a) CPR=7.87×10^{-4} in/s; and (b) CPR=7.87×10^{-5} in/s

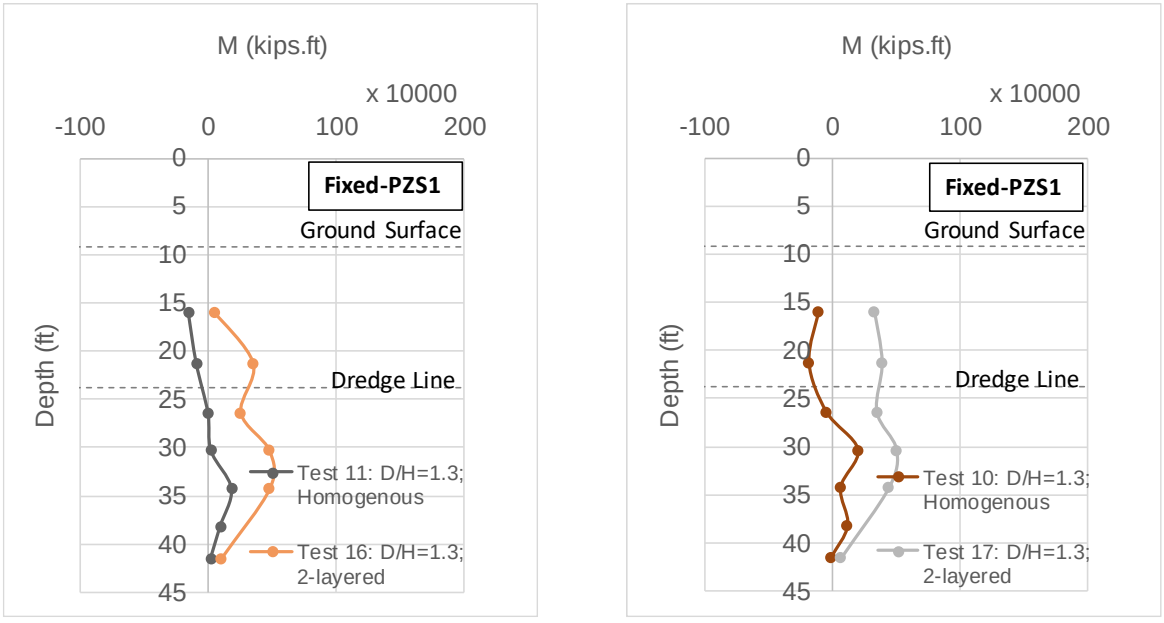

(a) (b)

Figure 3-52. Bending moment profiles of the sheet pile wall PZS1 in the profile PR2 (tests 16 and 17) compared to that in the profile PR1 (tests 11 and 10): (a) CPR=7.87×10^{-4} in/s; and (b) CPR=7.87×10^{-5} in/s

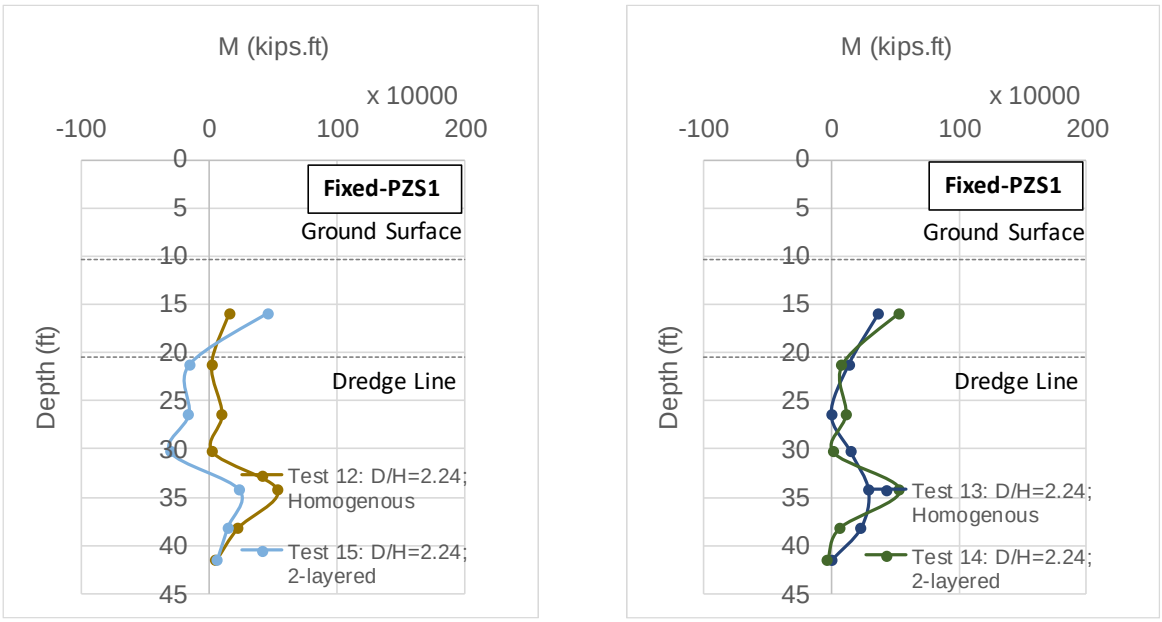

(a) (b)

Figure 3-53. Bending moment profiles of the sheet pile wall PZS1 in the profile PR4 (tests 15 and 14) compared to that in the profile PR3 (test 12 and 13): (a) CPR=7.87×10^{-4} in/s; and (b) CPR=7.87×10^{-5} in/s

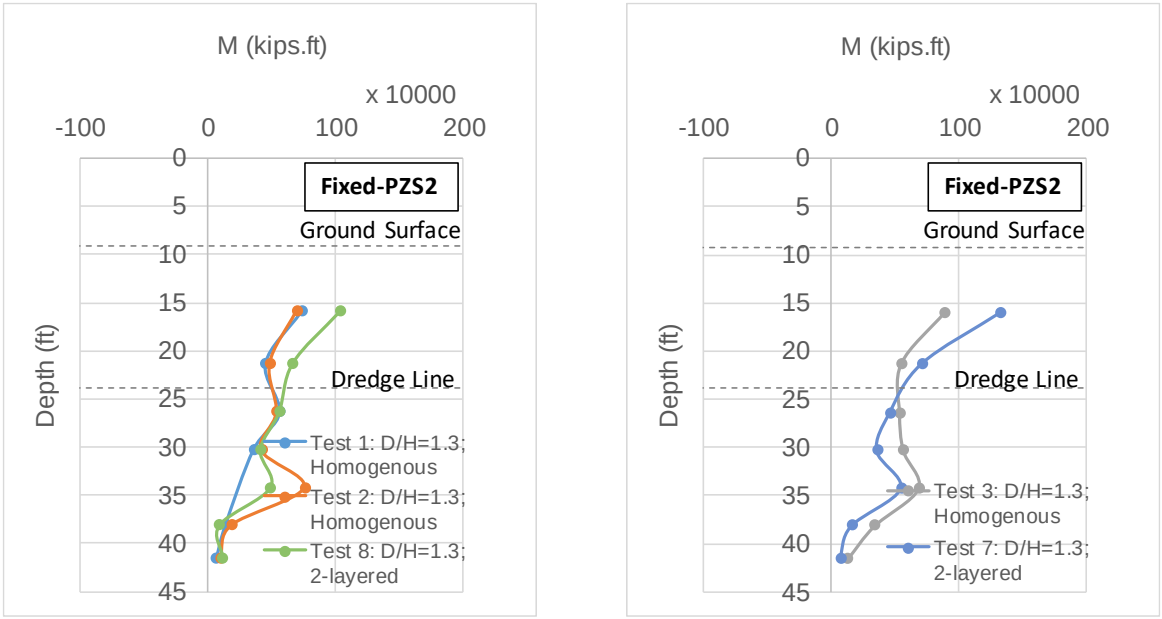

(a) (b)

Figure 3-54. Bending moment profiles of the sheet pile wall PZS2 in the profile PR2 (tests 8 and 7) compared to that in the profile PR1 (tests 1-2 and 3): (a) CPR=7.87×10^{-4} in/s; and (b) CPR=7.87×10^{-5} in/s. Tests 1 and 2 are repeat tests.

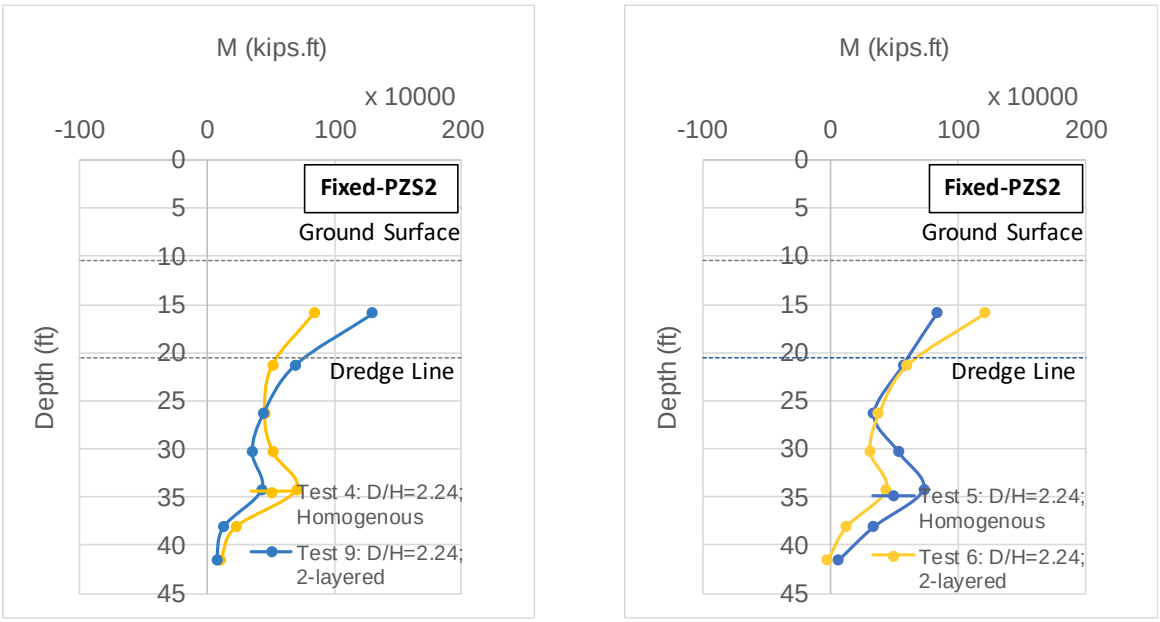

(a) (b)

Figure 3-55. Bending moment profiles of the sheet pile wall PZS2 in the profile PR4 (tests 9 and 6) compared to that in the profile PR3 (tests 4 and 5): (a) CPR=7.87×10^{-4} in/s; and (b) CPR=7.87×10^{-5} in/s

3.5.1.4 Penetration depth and unsupported length

To investigate the effects of depth of penetration (D) and unsupported length (H) on the axial behavior and bearing resistance of the sheet pile walls, two different penetration depth to retained soil height ratios (D/H) of 1.3 (Figure 3-39) and 2.24 (Figure 3-40) were considered. By changing the penetration depth, it is believed that the amount of mobilized and ultimate skin friction for the axially loaded sheet piles changes. The penetration depth also determines the amount of passive resistance in front of the sheet pile under lateral earth pressure. Therefore, the horizontal displacement of the sheet pile wall (with the free head condition) also depends on the penetration depth, where the wall may lose its serviceability under large deformations. In cases with D/H = 1.3 the unsupported length is increased with respect to the cases with D/H = 2.24.

The load test results on the PZS1 sheet pile wall in profiles PR1-PR3 (homogenous) and PR2-PR4 (two-layered) are shown in Figure 3-56 and Figure 3-57, respectively. Increasing the D/H ratio has increased the axial resistance in both homogenous and two-layered profiles. An increase in the penetration depth (D) increases skin friction; hence, the axial resistance. However, the amount of this increase in axial resistance is higher for the stratified profiles (up to 24% as can be seen in Figure 3-57) compared to those in homogenous sand profiles (about 17%, as shown in Figure 3-56). A similar trend is observed for the load tests on the PZS2 sheet pile (see Figure 3-58 - Figure 3-59) and when conducting load tests under different CPRs (i.e. 7.87×10^{-4} in/s and 7.87×10^{-5} in/s).

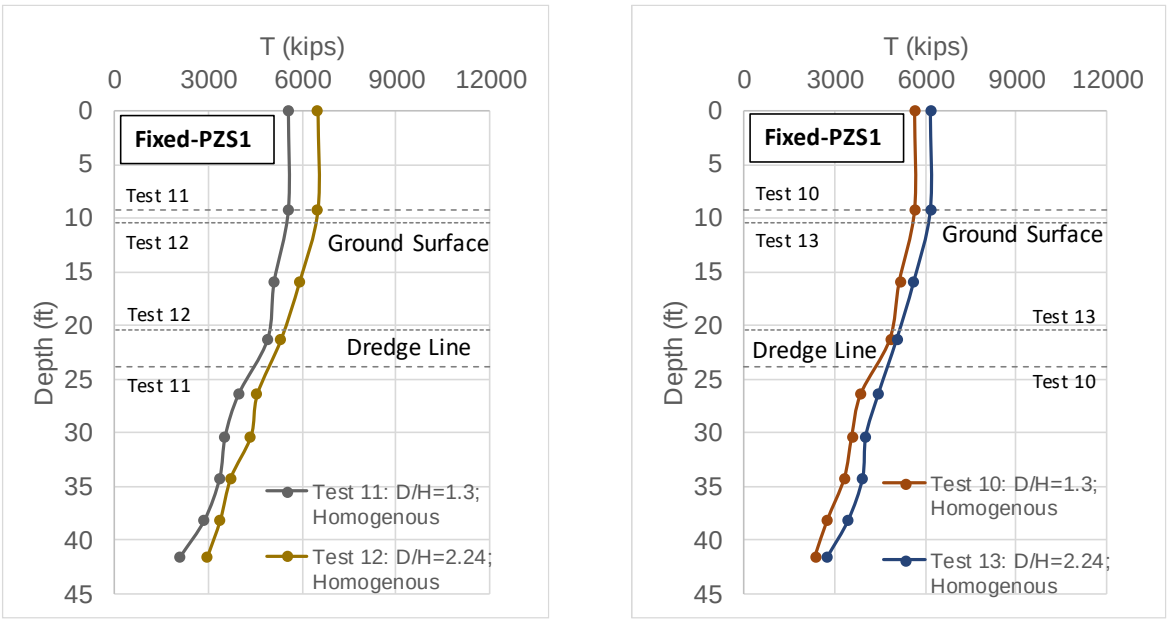

(a) (b)

Figure 3-56. Increased axial resistance of the sheet pile wall PZS1 in the profile PR3 (tests 12 and 13) compared to that in the profile PR1 (test 11 and 10): (a) CPR=7.87×10^{-4} in/s; and (b) CPR=7.87×10^{-5} in/s

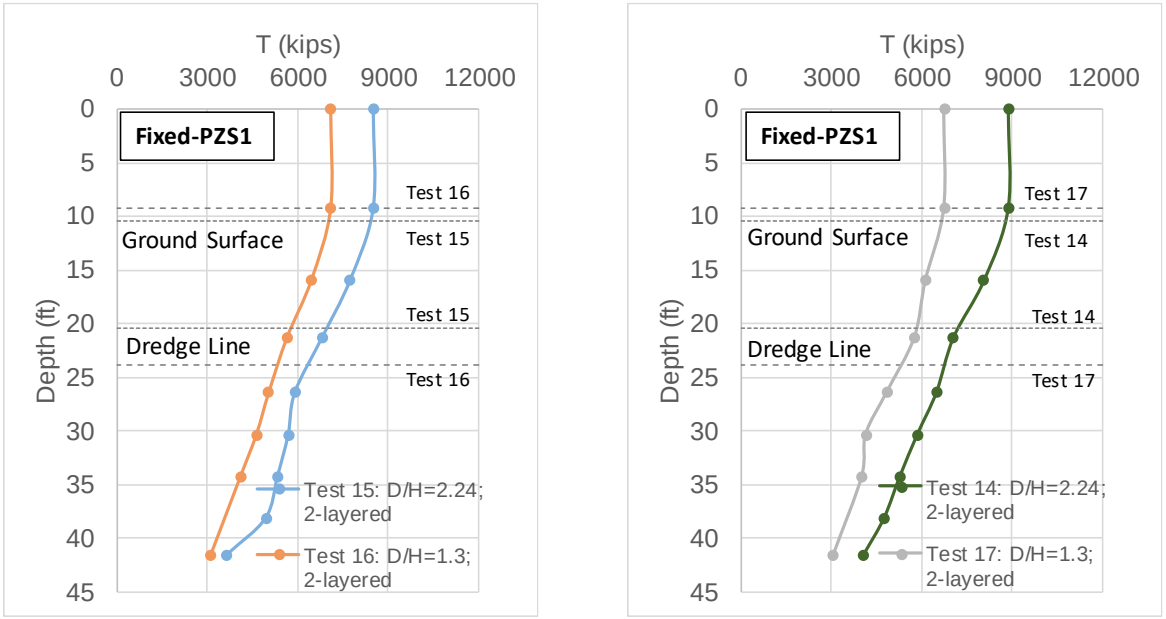

(a) (b)

Figure 3-57. Increased axial resistance of the sheet pile wall PZS1 in the profile PR4 (tests 15 and 14) compared to that in the profile PR2 (test 16 and 17): (a) CPR=7.87×10^{-4} in/s; and (b) CPR=7.87×10^{-5} in/s

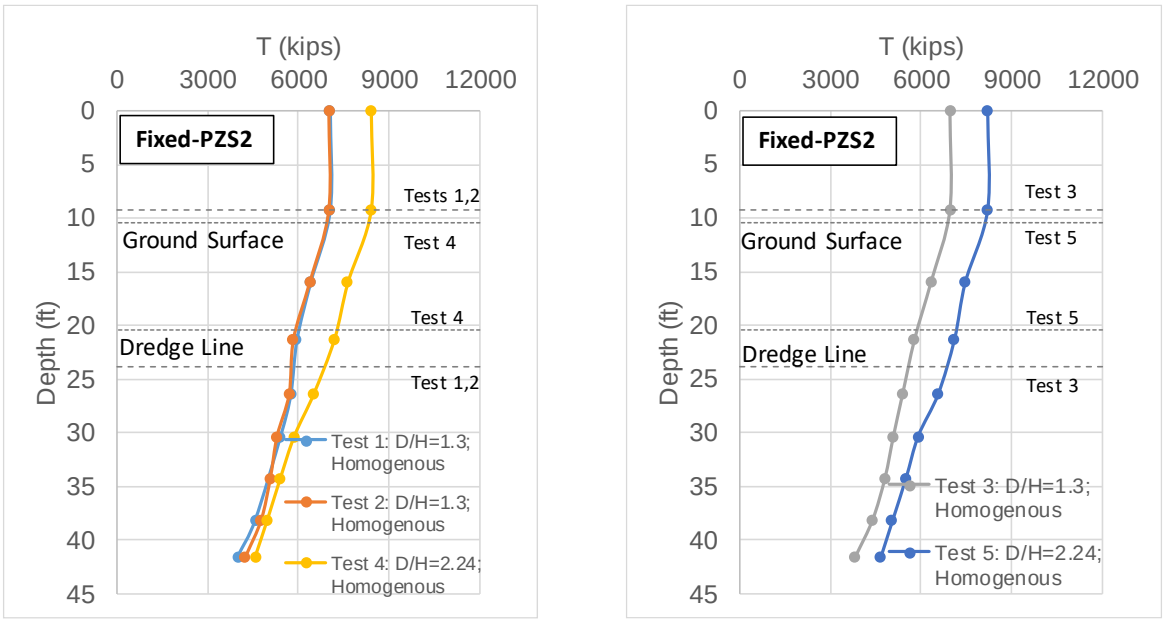

Figure 3-58. Increased axial resistance of the sheet pile wall PZS2 in the profile PR3 (tests 12 and 13) compared to that in the profile PR1 (test 11 and 10): (a) CPR=7.87×10^{-4} in/s; and (b) CPR=7.87×10^{-5} in/s

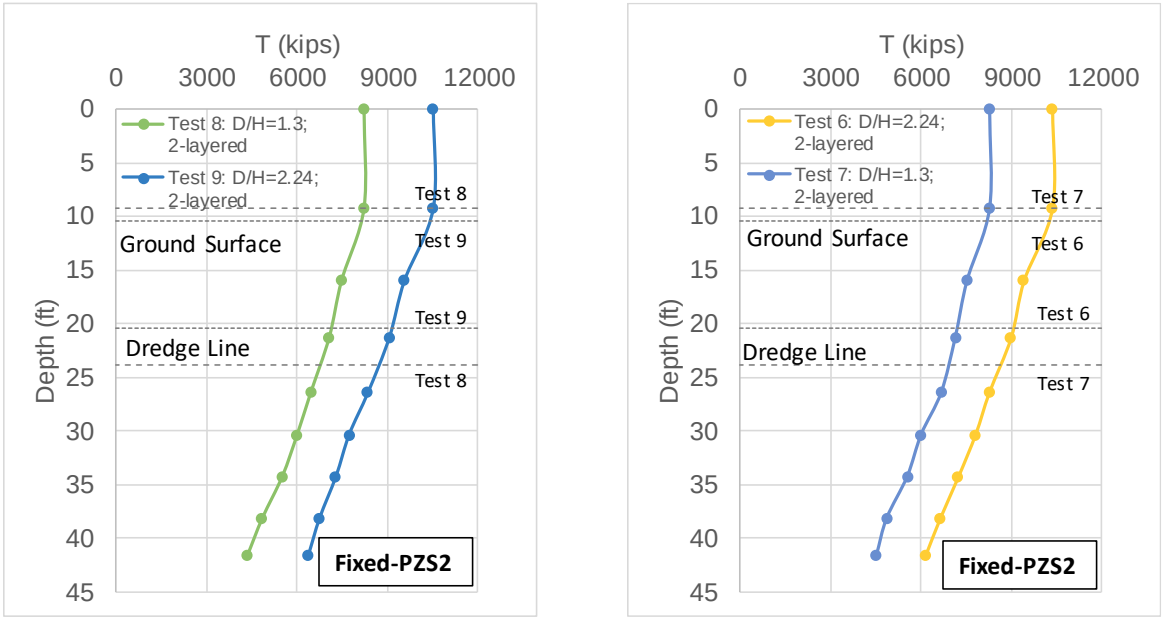

Figure 3-59. Increased axial resistance of the sheet pile wall PZS2 in the profile PR4 (tests 15 and 14) compared to that in the profile PR2 (test 16 and 17): (a) CPR=7.87×10^{-4} in/s; and (b) CPR=7.87×10^{-5} in/s

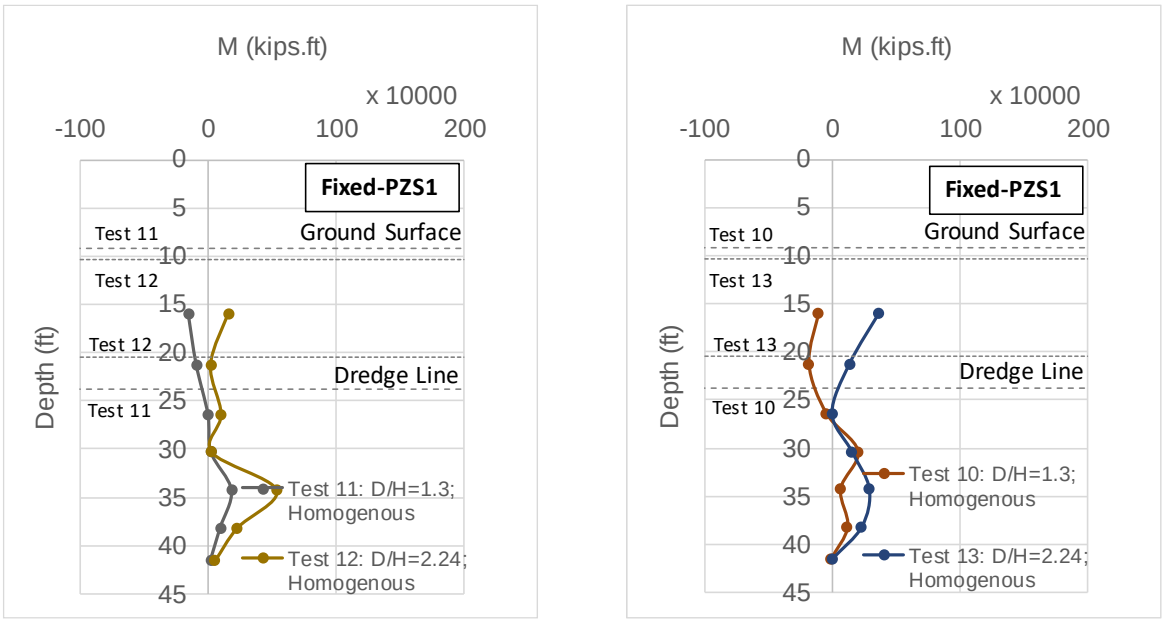

(a) (b)

Figure 3-60. Bending moment profiles of the sheet pile wall PZS1 in the profile PR3 (tests 12 and 13) compared to that in the profile PR1 (test 11 and 10): (a) CPR=7.87×10^{-4} in/s; and (b) CPR=7.87×10^{-5} in/s

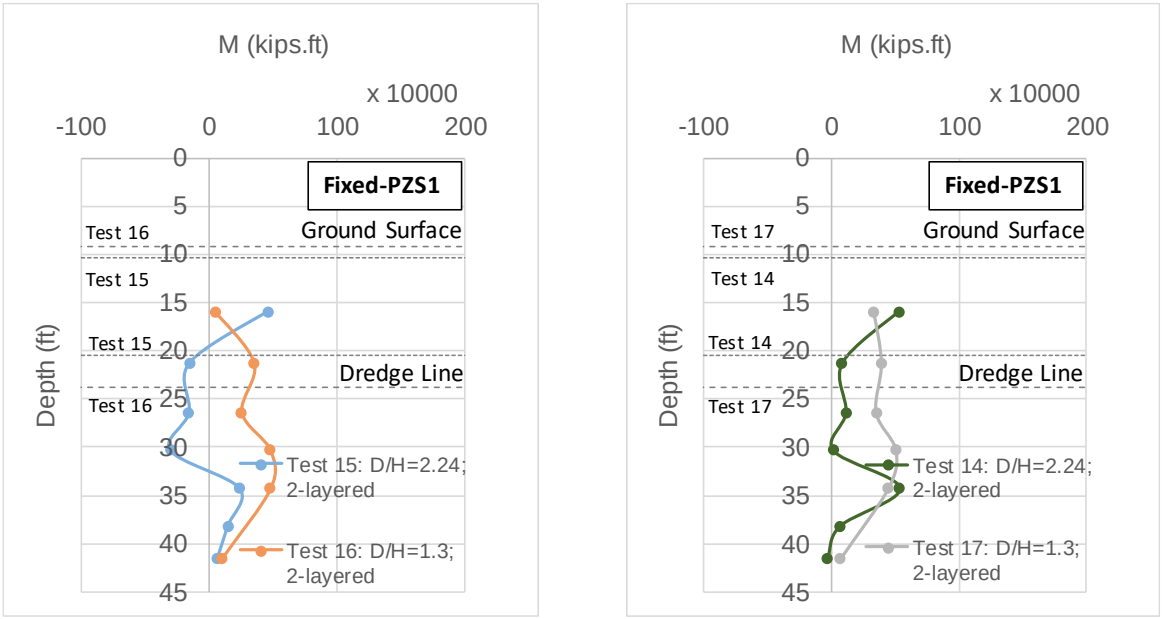

(a) (b)

Figure 3-61. Bending moment profiles of the sheet pile wall PZS1 in the profile PR4 (tests 15 and 14) compared to that in the profile PR2 (test 16 and 17): (a) CPR=7.87×10^{-4} in/s; and (b) CPR=7.87×10^{-5} in/s

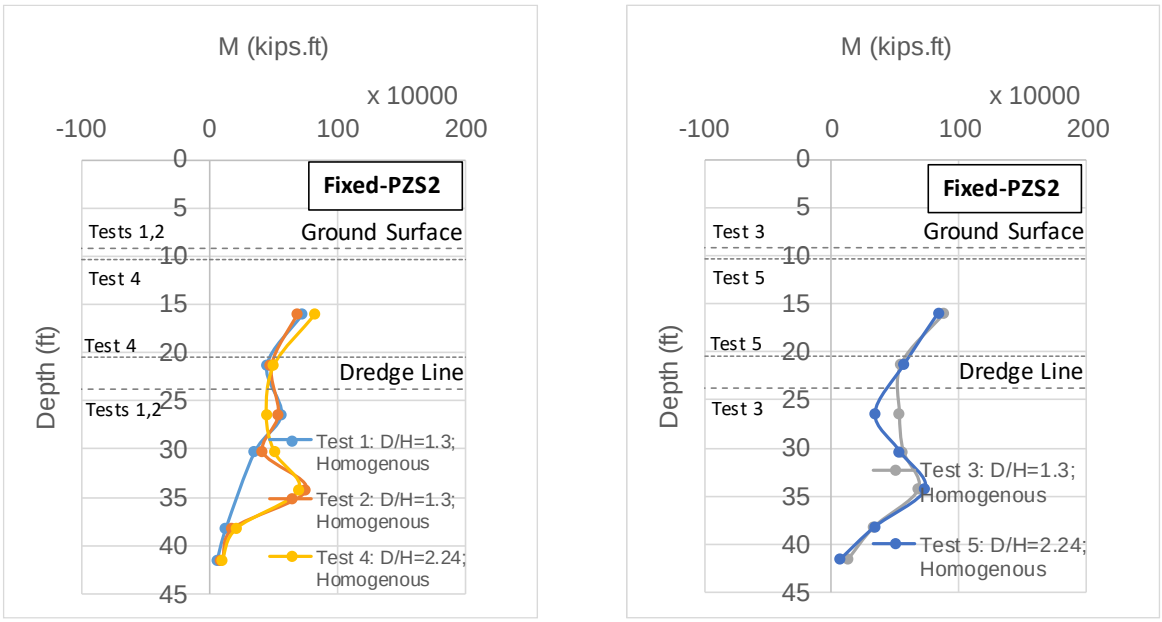

(a) (b)

Figure 3-62. Bending moment profiles of the sheet pile wall PZS2 in the profile PR3 (tests 12 and 13) compared to that in the profile PR1 (test 11 and 10): (a) CPR=7.87×10^{-4} in/s; and (b) CPR=7.87×10^{-5} in/s

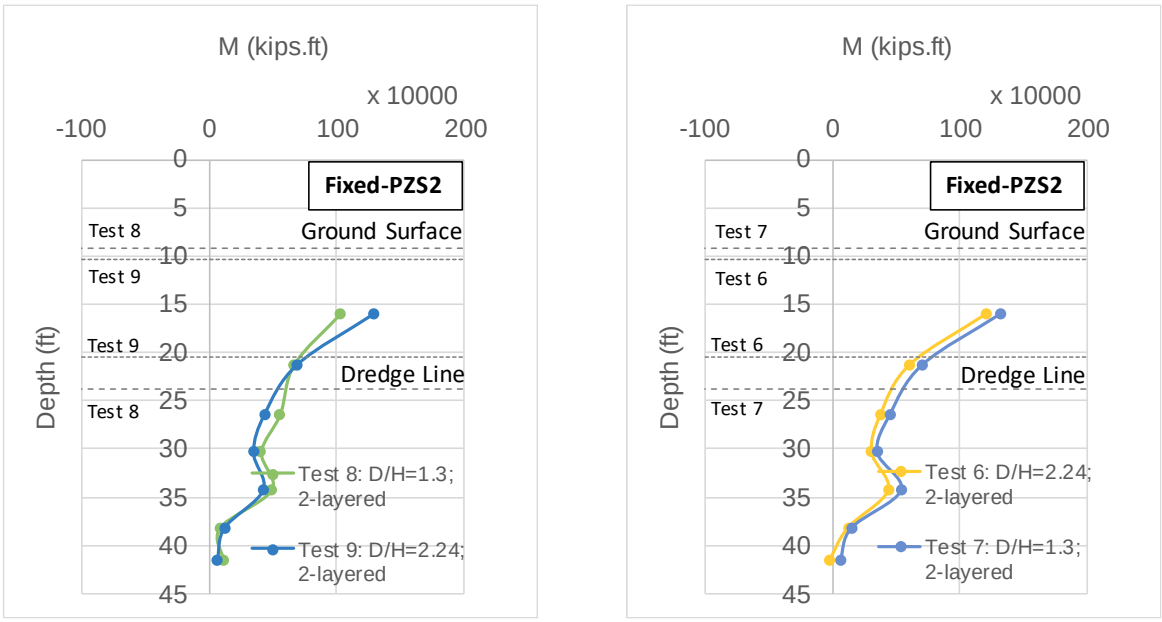

(a) (b)

Figure 3-63. Bending moment profiles of the sheet pile wall PZS2 in the profile PR4 (tests 15 and 14) compared to that in the profile PR2 (test 16 and 17): (a) CPR=7.87×10^{-4} in/s; and (b) CPR=7.87×10^{-5} in/s

Corresponding bending moment profiles are depicted in Figure 3-60 - Figure 3-63. Generally, greater maximum bending moments are obtained in the PR3 and PR4 (two-layered profiles) than those in PR1 and PR2, respectively. It is worth mentioning that tests 1 and 2 shown in Figures 20 and 24 are repeat tests and are in a reasonable agreement with each other when comparing axial load (Figure 3-58) and bending moment profiles (Figure 3-62).

3.5.1.5 Sheet pile stiffness

The effects of bending and axial stiffness of the sheet pile elements on the axial resistance of the axially loaded sheet piles were studied. The prototype-scale bending stiffness and axial stiffness values of the model sheet piles were matched with those commonly used in the field (refer to Table 2 in Tasks 3a or 3b reports). Two sheet pile walls with cross-sections similar to PZ sheet piles machined where the second sheet pile wall (PZS2) had higher (approximately twice) bending and axial stiffness than the first one (PZS1). The effects of stiffness change on the axial resistance of both sheet pile sections (PZS1 and PZS2) were investigated in all four soil profile configurations (i.e. PR1-4). Shown in Figure 3-64 - Figure 3-67 are the axial load distribution profiles for both PZS1 and PZS2 sheet piles at CPR=7.87×10^{-4} in/s and CPR=7.87×10^{-5} in/s. As it is evident, the PZS2 sheet pile has shown a greater axial resistance than the PZS1. Accordingly, the maximum bending moments tolerated by PZS2 were more than that for the PZS1 sheet pile (Figure 3-68-Figure 3-71). The main contributing factor for this observation would be the higher cross-sectional area in PZS2 compared to that in PZS1. Consequently, the soil plugging has been more in the PZS2 and has contributed more to the enhancement of the axial resistance.

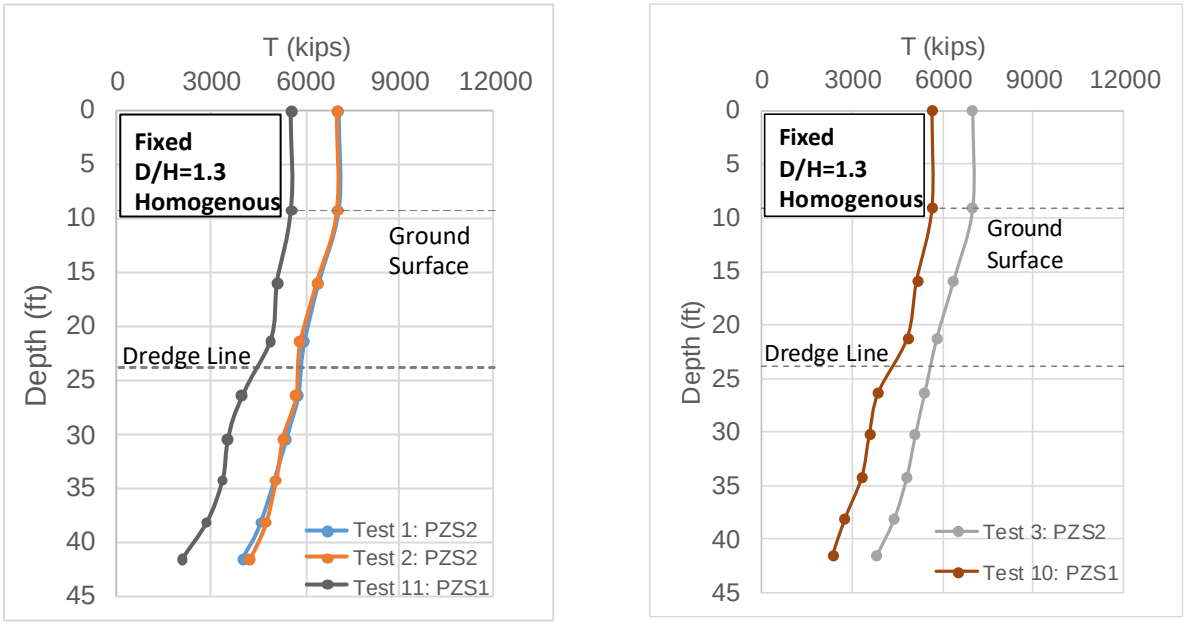

(a) (b)

Figure 3-64. Increased axial resistance of the sheet pile wall PZS2 (tests 1-2 and 3) compared to that for the sheet pile wall PZS1 (test 10 and 11) in the profile PR1: (a) CPR=7.87×10^{-4} in/s; and (b) CPR=7.87×10^{-5} in/s

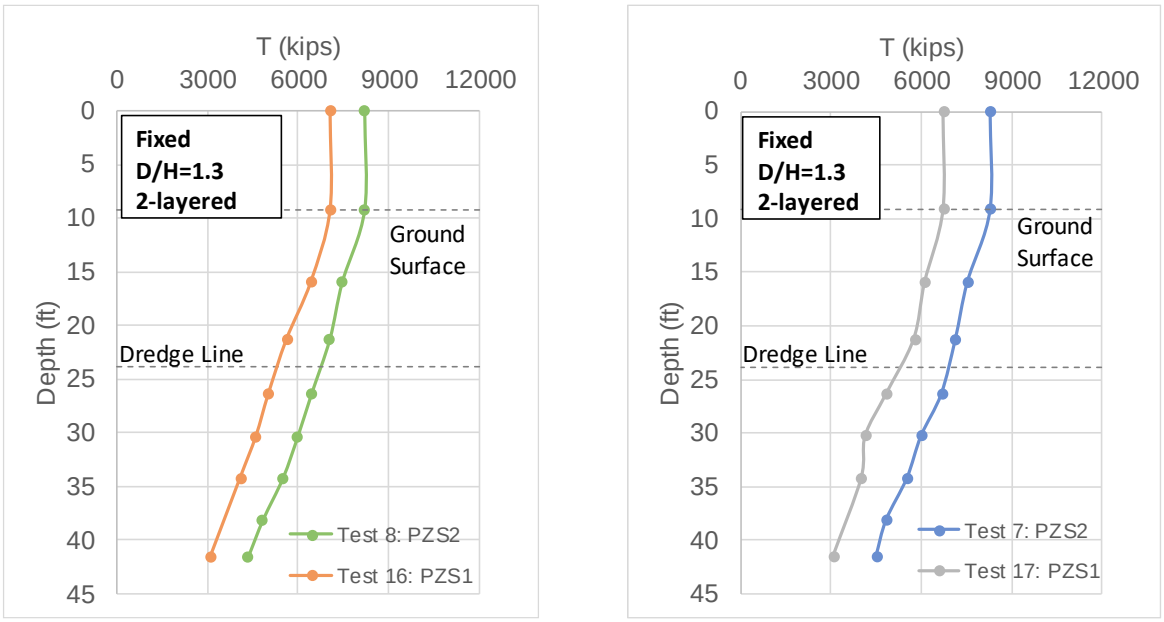

(a) (b)

Figure 3-65. Increased axial resistance of the sheet pile wall PZS2 (tests 8 and 7) compared to that for the sheet pile wall PZS1 (test 16 and 17) in the profile PR2: (a) CPR=7.87×10^{-4} in/s; and (b) CPR=7.87×10^{-5} in/s

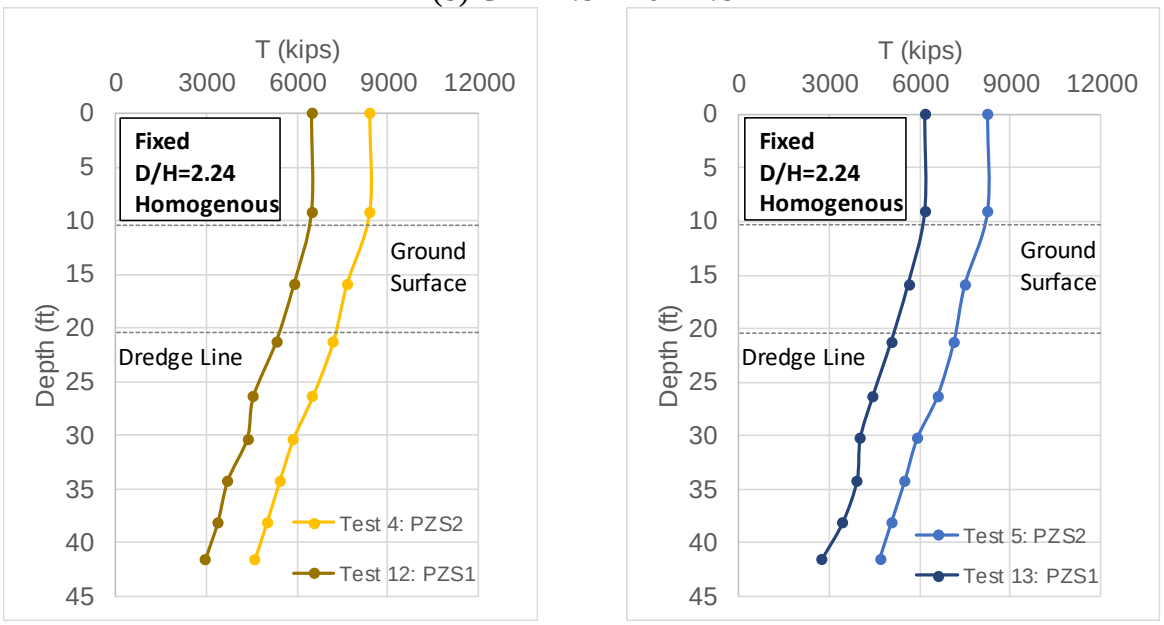

(a) (b)

Figure 3-66. Increased axial resistance of the sheet pile wall PZS2 (tests 4 and 5) compared to that for the sheet pile wall PZS1 (test 12 and 13) in the profile PR3: (a) CPR=7.87×10^{-4} in/s; and (b) CPR=7.87×10^{-5} in/s

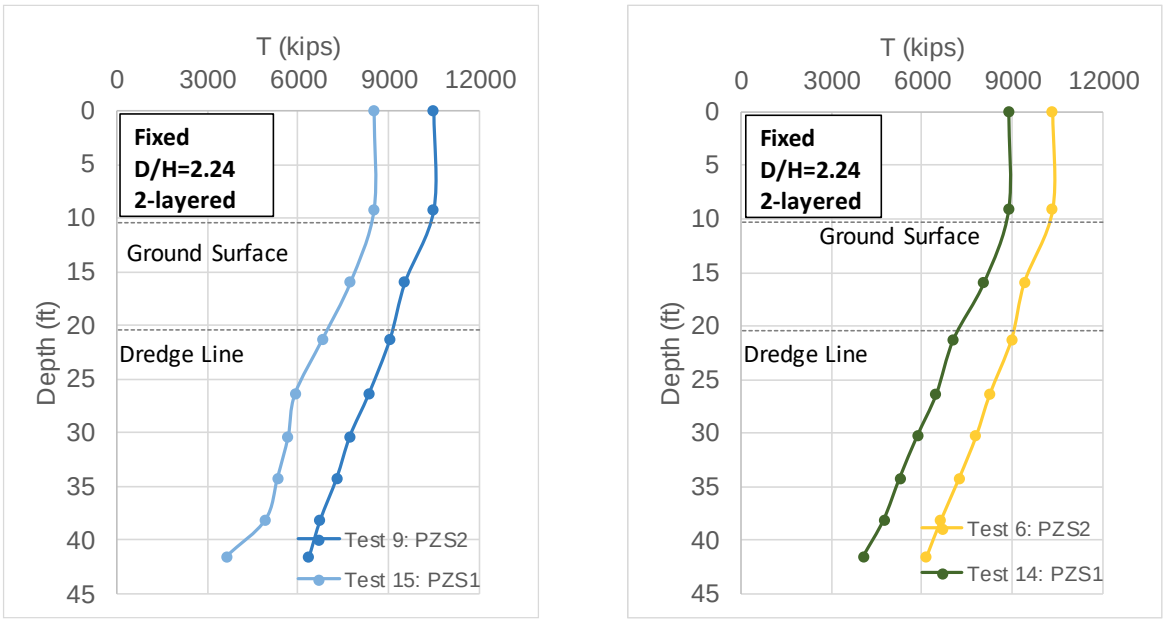

(a) (b)

Figure 3-67. Increased axial resistance of the sheet pile wall PZS2 (tests 9 and 6) compared to that for the sheet pile wall PZS1 (test 15 and 14) in the profile PR4: (a) CPR=7.87×10^{-4} in/s; and (b) CPR=7.87×10^{-5} in/s

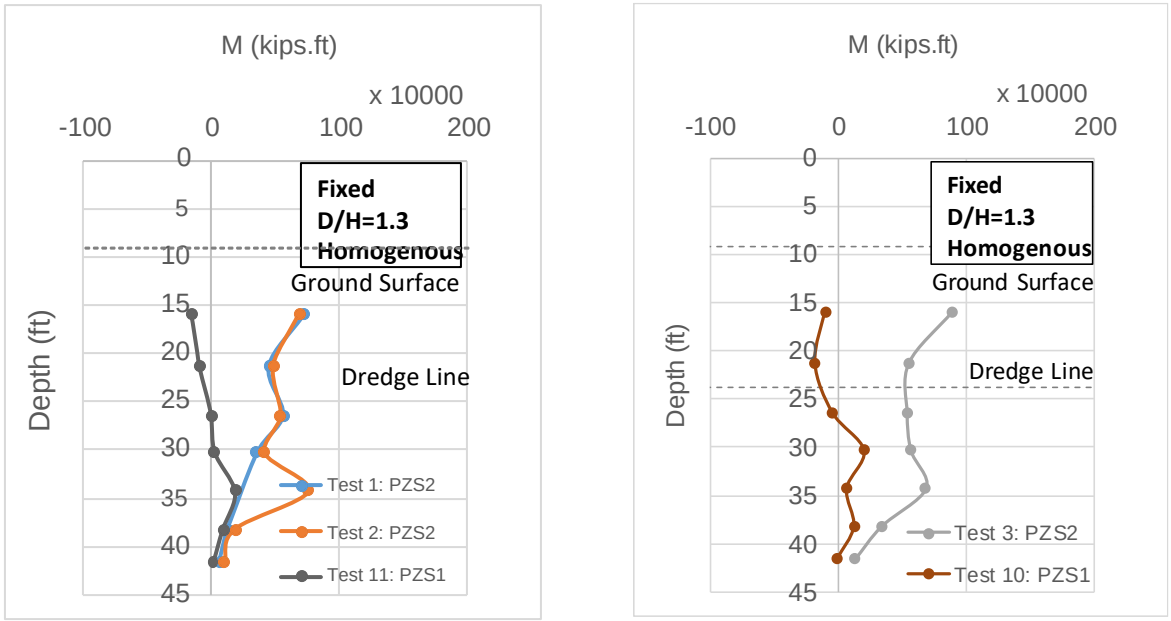

(a) (b)

Figure 3-68. Bending moment profiles of the sheet pile wall PZS2 (tests 1-2 and 3) compared to that for the sheet pile wall PZS1 (test 10 and 11) in the profile PR1: (a) CPR=7.87×10^{-4} in/s; and (b) CPR=7.87×10^{-5} in/s

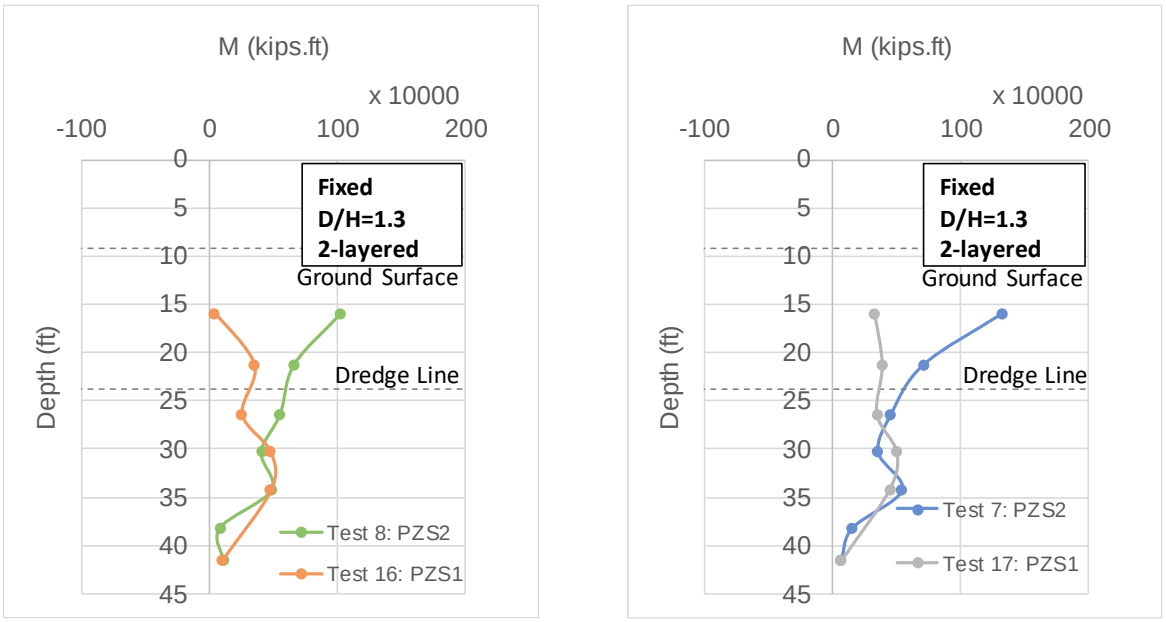

(a) (b)

Figure 3-69. Bending moment profiles of the sheet pile wall PZS2 (tests 8 and 7) compared to that for the sheet pile wall PZS1 (test 16 and 17) in the profile PR2: (a) CPR=7.87×10^{-4} in/s; and (b) CPR=7.87×10^{-5} in/s

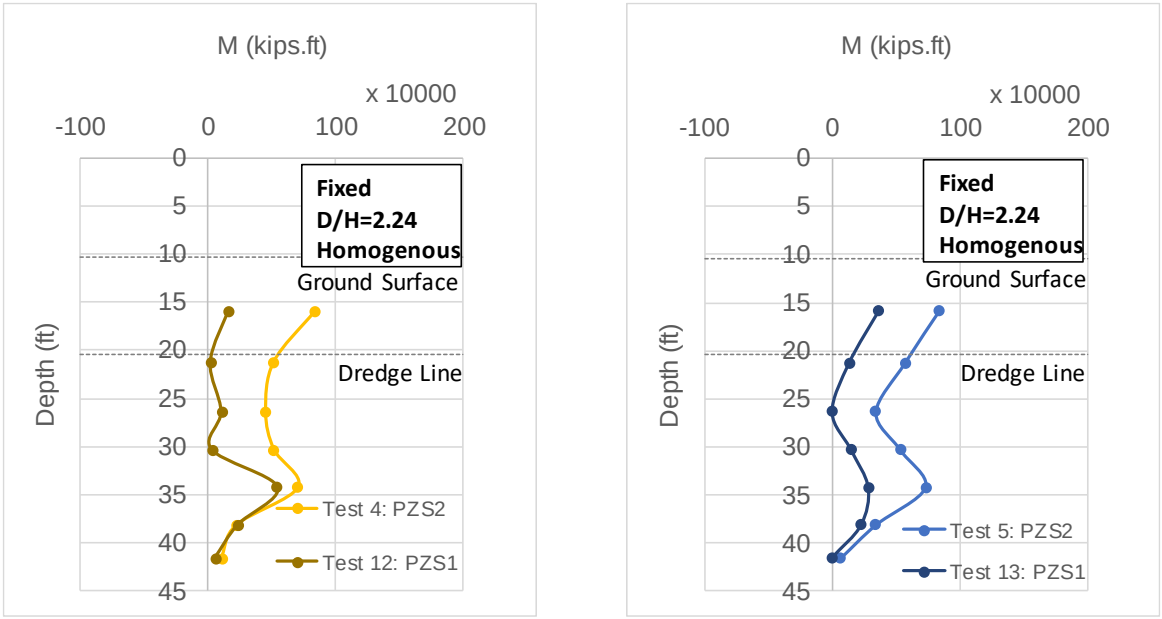

(a) (b)

Figure 3-70. Bending moment profiles of the sheet pile wall PZS2 (tests 4 and 5) compared to that for the sheet pile wall PZS1 (test 12 and 13) in the profile PR3: (a) CPR=7.87×10^{-4} in/s; and (b) CPR=7.87×10^{-5} in/s

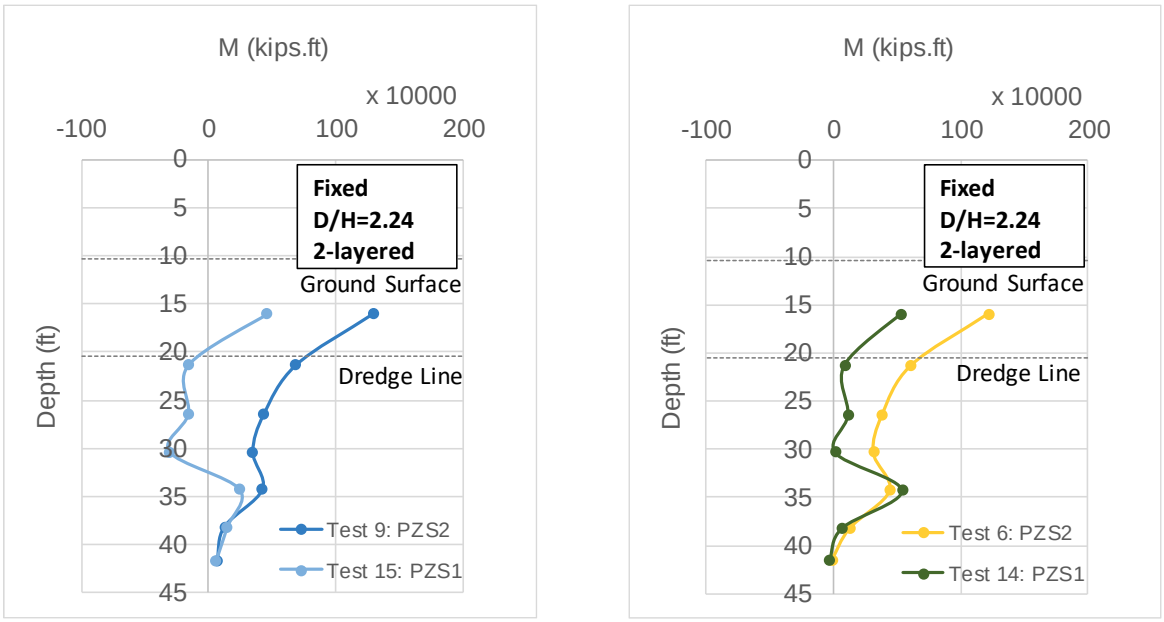

(a) (b)

Figure 3-71. Bending moment profiles of the sheet pile wall PZS2 (tests 9 and 6) compared to that for the sheet pile wall PZS1 (test 15 and 14) in the profile PR4: (a) CPR=7.87×10^{-4} in/s; and (b) CPR=7.87×10^{-5} in/s

3.5.1.6 Rate effects in load testing

To investigate the possible rate effects, another series of tests were performed at a 10 times slower rate, i.e. at CPR=7.87×10^{-5} in/s aiming to test at a closer rate to the theoretical static loading conditions and compare the results to those observed in load testing at CPR=7.87×10^{-4} in/s. Load testing at these rates was made possible due to the specific design of the mentioned electrical actuator powered by a precisely controlled stepping motor. The actuator (apparatus) could apply the desired displacement-time histories with the specified amplitude and frequency (i.e. ranging from CPR=7.87×10^{-5} to 0.197 in/s). The load test results performed on the PZS1 in profiles PR1-PR2 and PR3-PR4 are depicted in Figure 3-72 and Figure 3-73. Similar plots are presented in Figure 3-74 and Figure 3-75 for the PZS2 sheet pile wall. Changing the CPR from 7.87×10^{-4} in/s to 7.87×10^{-5} in/s has not changed the axial resistances in any of the investigated profiles. This can be contributed to the lack of any inertial and damping forces during load testing in dry sand (i.e. no excess pore water pressure generation). These findings on rate effects of CPR load testing are in agreement with those presented by Huy (2008) and observations by Hölscher et al. (2008) and Hölscher et al. (2012) in dry sand. A similar discussion is applied to the bending moment profiles presented in Figure 3-76 - Figure 3-79, where, there are no evident rate effects when comparing these profiles.

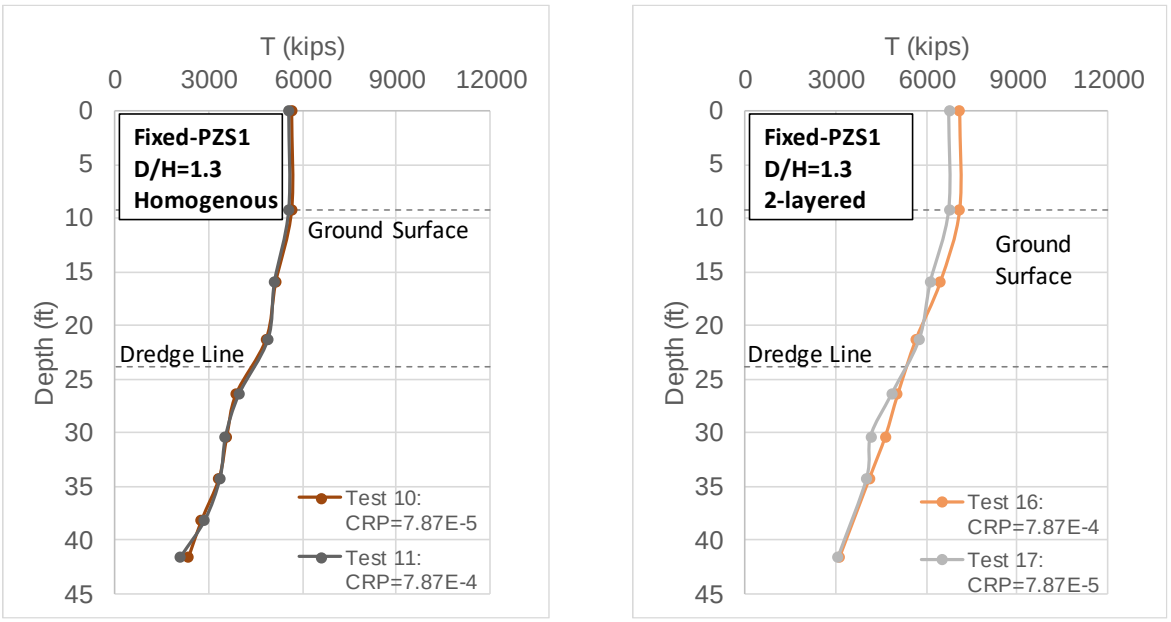

(a) (b)

Figure 3-72. Axial resistance of the sheet pile wall PZS1 in the profile (a) PR1; and (b) PR2. The tests were performed under CPR=7.87×10^{-4} in/s (tests 11 and 16) and CPR=7.87×10^{-5} in/s (tests 10 and 17)

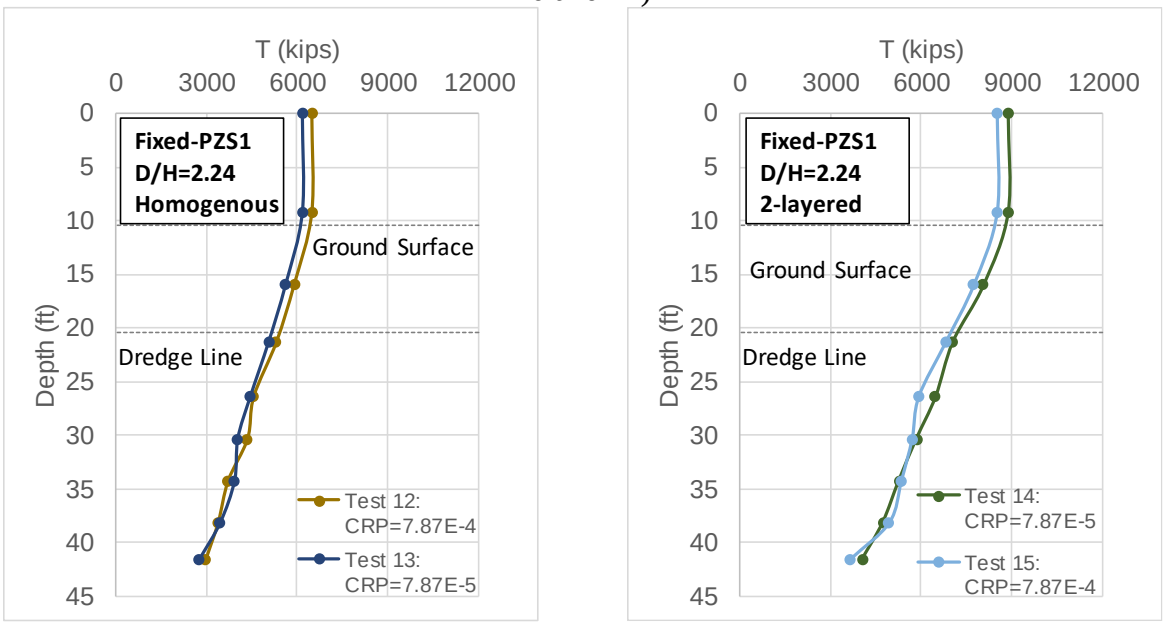

(a) (b)

Figure 3-73. Axial resistance of the sheet pile wall PZS1 in the profile (a) PR3; and (b) PR4. The tests were performed under CPR=7.87×10^{-4} in/s (tests 12 and 15) and CPR=7.87×10^{-5} in/s (tests 13 and 14)

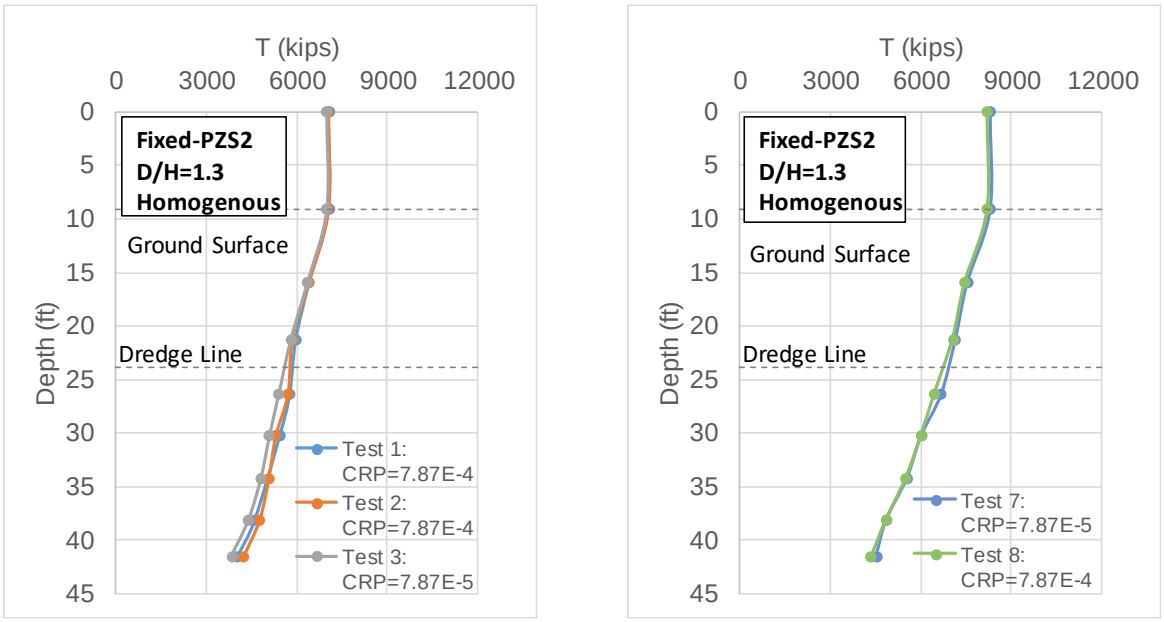

(a) (b)

Figure 3-74. Axial resistance of the sheet pile wall PZS2 in the profile (a) PR1; and (b) PR2. The tests were performed under CPR=7.87×10^{-4} in/s (tests 1-2, and 8) and CPR=7.87×10^{-5} in/s (tests 3 and 7)

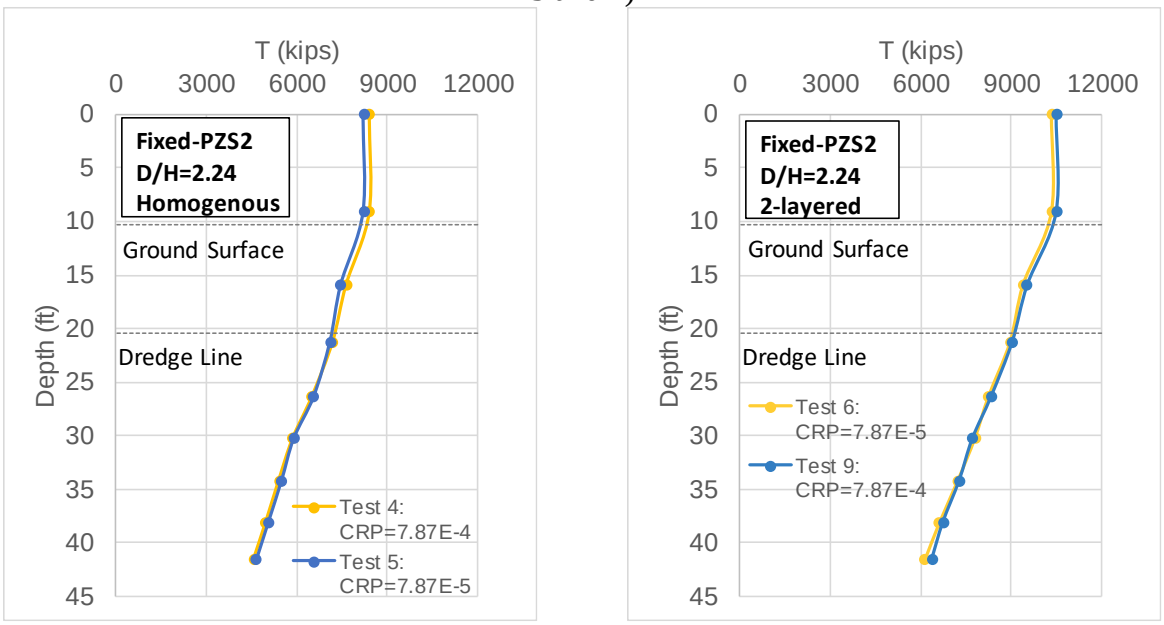

(a) (b)

Figure 3-75. Axial resistance of the sheet pile wall PZS2 in the profile (a) PR3; and (b) PR4. The tests were performed under CPR=7.87×10^{-4} in/s (tests 4 and 9) and CPR=7.87×10^{-5} in/s (tests 5 and 6)

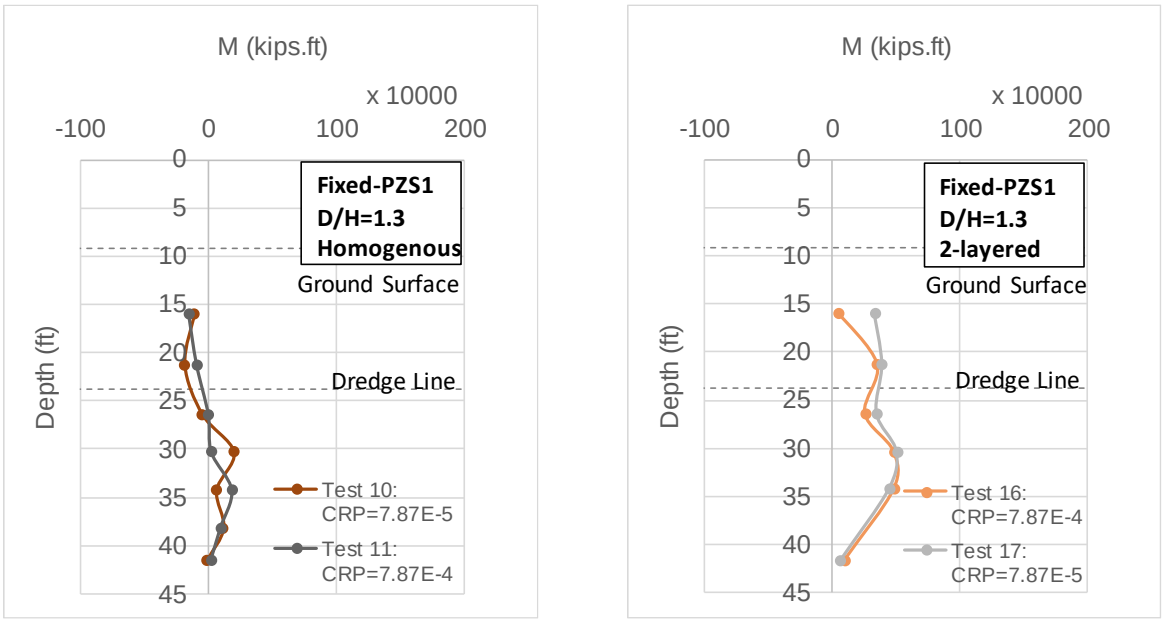

(a) (b)

Figure 3-76. Bending moment profiles of the sheet pile wall PZS1 in the profile (a) PR1; and (b) PR2. The tests were performed under CPR=7.87×10^{-4} in/s (tests 11 and 16) and CPR=7.87×10^{-5} in/s (tests 10 and 17)

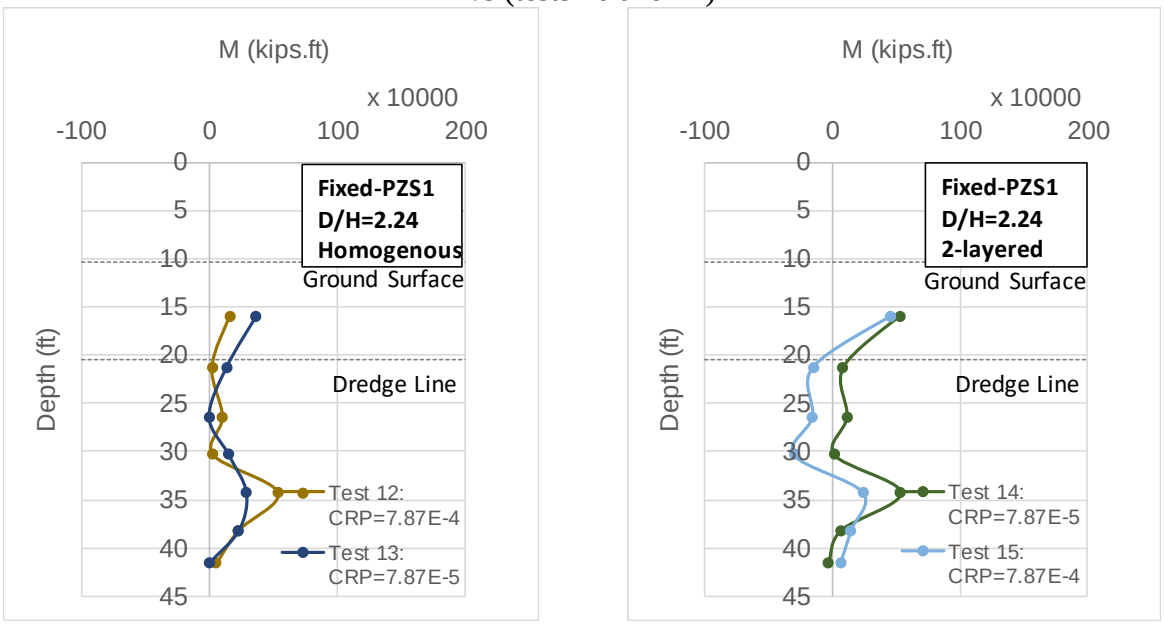

(a) (b)

Figure 3-77. Bending moment profiles of the sheet pile wall PZS1 in the profile (a) PR3; and (b) PR4. The tests were performed under CPR=7.87×10^{-4} in/s (tests 12 and 15) and CPR=7.87×10^{-5} in/s (tests 13 and 14)

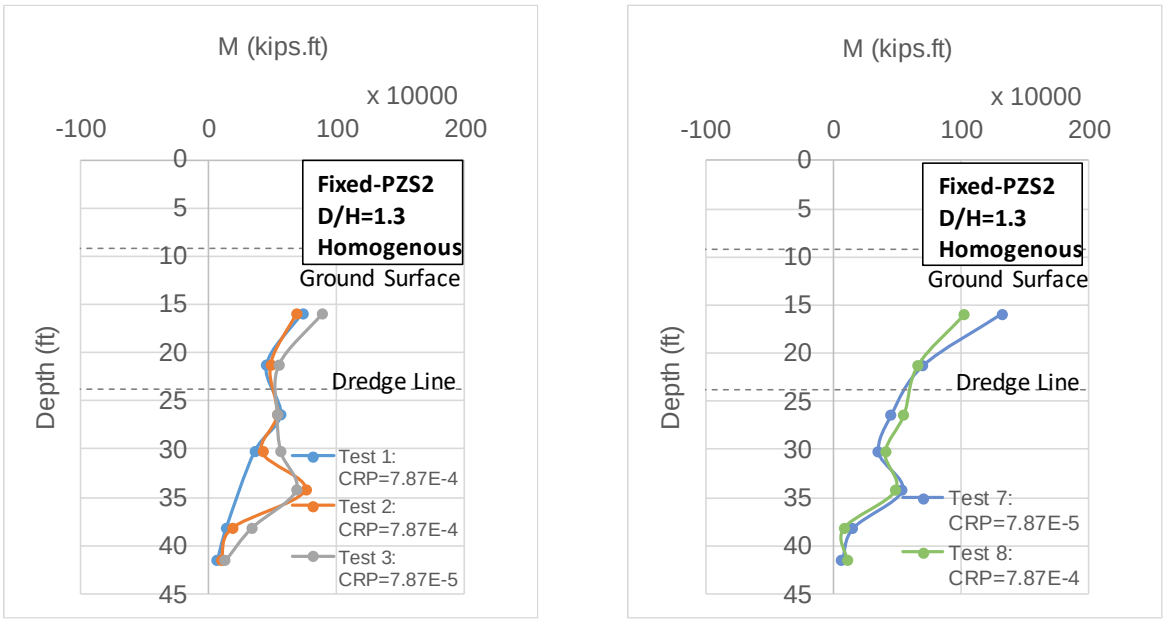

(a) (b)

Figure 3-78. Bending moment profiles of the sheet pile wall PZS2 in the profile (a) PR1; and (b) PR2. The tests were performed under CPR=7.87×10^{-4} in/s (tests 1-2 and 8) and CPR=7.87×10^{-5} in/s (tests 3 and 7)

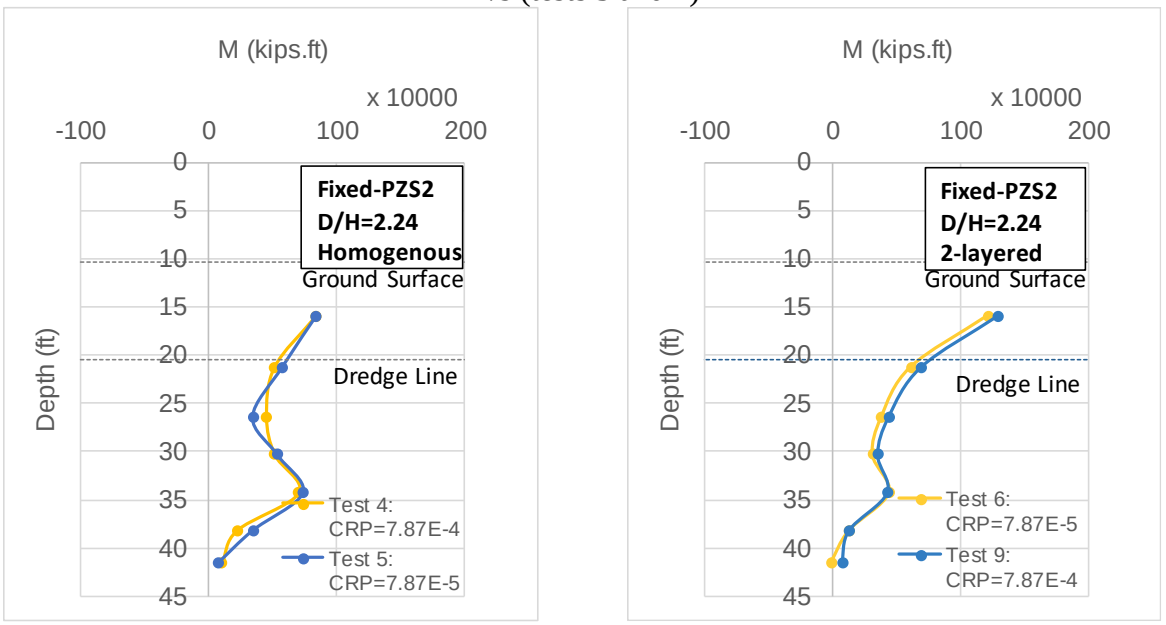

(a) (b)

Figure 3-79. Bending moment profiles of the sheet pile wall PZS2 in the profile (a) PR3; and (b) PR4. The tests were performed under CPR=7.87×10-4 in/s (tests 4 and 9) and CPR=7.87×10-5 in/s (tests 5 and 6)

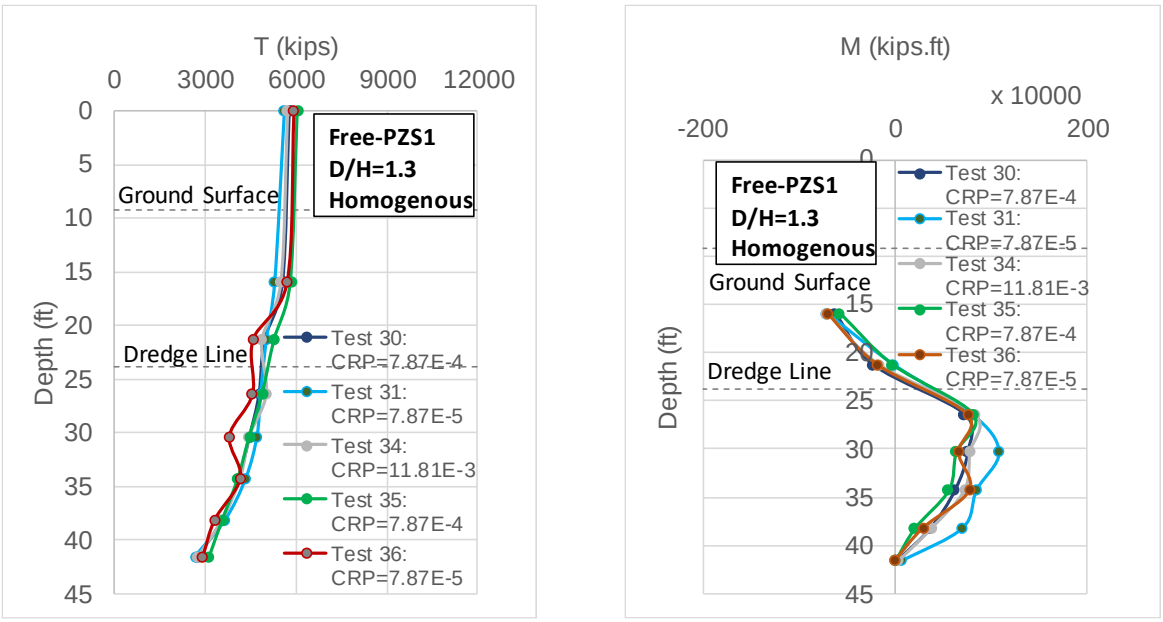

(a) (b)

Figure 3-80. (a) Axial load and (b) bending moment profiles of the sheet pile wall PZS1 in the PR1 profile. The tests were performed under CPR=7.87×10^{-5} in/s (tests 31 and 36), CPR=7.87×10^{-4} in/s (tests 30 and 35), and CPR=11.81×10^{-3} in/s (test 34).

Presented in Figure 3-80 3are axial load and bending moment profiles obtained through performing load tests on the PZS1 sheet pile wall with free-head condition. Load tests 30 and 35 and tests 31 and 36 were repeat tests performed at 7.87×10^{-4} in/s and 7.87×10^{-5} in/s, respectively. The load test No. 34 was performed at a higher rate of CPR=11.81×10^{-3} in/s. As can be seen, approximately same axial load and bending moment responses are obtained during the studied cases.

3.5.1.7 Boundary conditions

Effects of the head boundary condition (i.e. free head or fixed head) on the axial load and bending moment distribution along the sheet pile wall was investigated. To create a fixed-head condition, a helmet (cap) was perfectly fitted to the top of the sheet pile wall preventing it from any rotation at top (see the previous version of submitted report for details). In the case of the free-head condition, the sheet pile was allowed to rotate freely inside the helmet providing active earth pressure on the retained soil (see Appendix B for details). In both cases, a vertical load was applied at the sheet pile top, simulating the vertical loads imposed by the superstructure. The axial load and bending moment distribution on the PZS2 sheet pile wall obtained from free-head load tests are presented in Figure 3-81 and Figure 3-82, respectively. Similar profiles for PZS1 are shown in Figure 3-83 and Figure 3-84. While the trends in axial load distribution (for all soil profiles) are similar in fixed and free head conditions, a considerably different bending moment distribution is observed between these two scenarios.

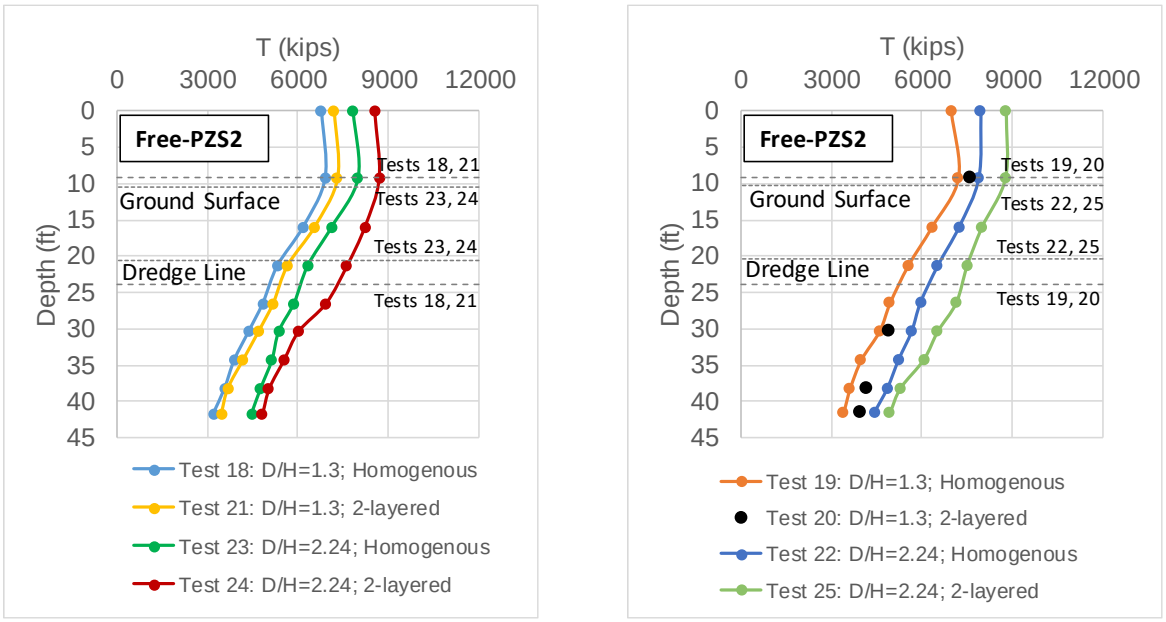

(a) (b)

Figure 3-81. Axial resistance of the sheet pile wall PZS2 in different soil profiles (a) CPR=7.87×10^{-4} in/s; and (b) CPR=7.87×10^{-5} in/s. Tests 18-19; 20-21; 22-23; and 24-25 represent the load test results in PR1; PR2; PR3; and PR4, respectively.

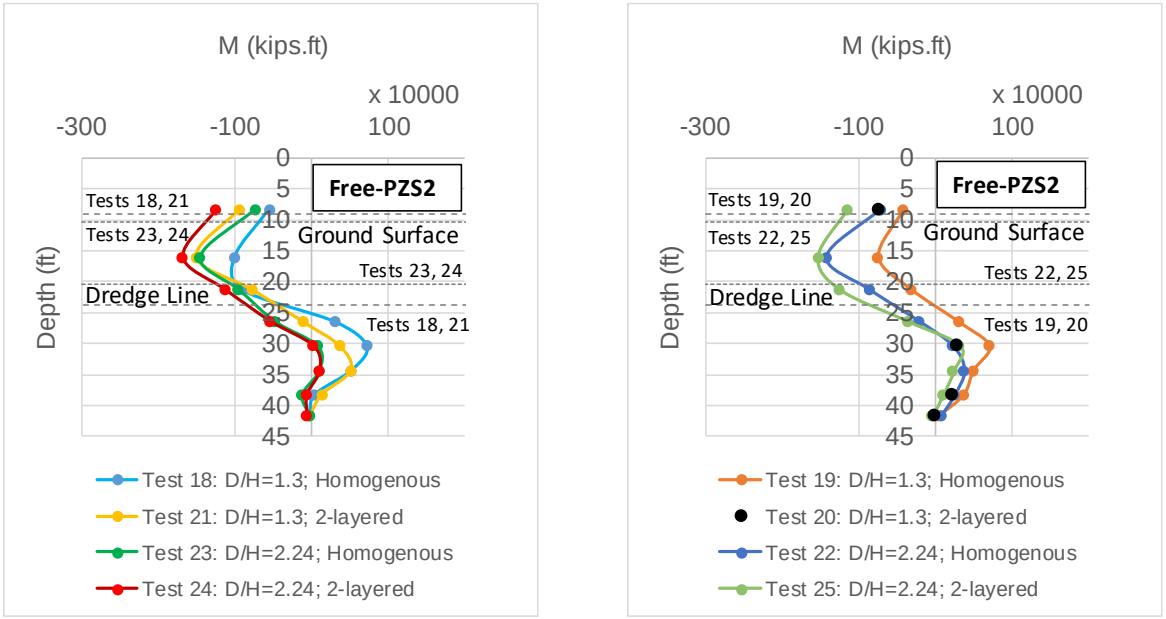

(a) (b)

Figure 3-82. Bending moment profiles of the sheet pile wall PZS2 in different soil profiles (a) CPR=7.87×10^{-4} in/s; and (b) CPR=7.87×10^{-5} in/s. Tests 18-19; 20-21; 22-23; and 24-25 represent the load test results in PR1; PR2; PR3; and PR4, respectively.

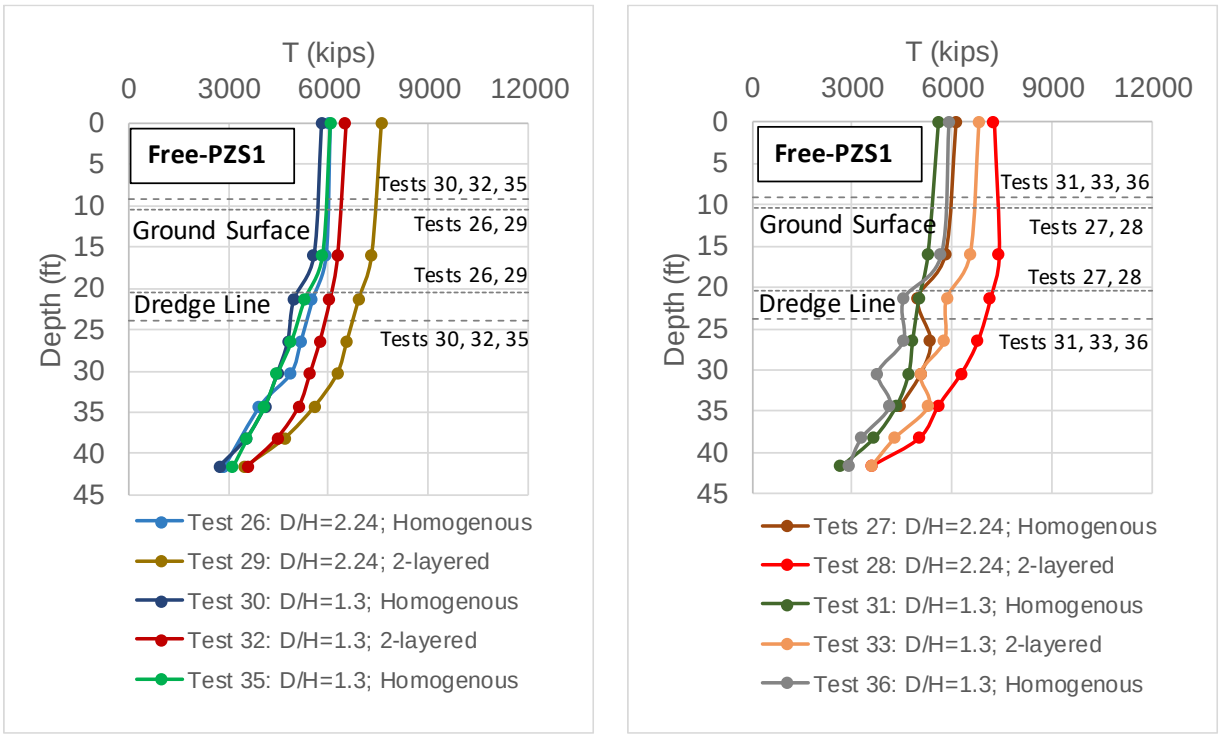

(a) (b)

Figure 3-83. Axial resistance of the sheet pile wall PZS1 in different soil profiles (a) CPR=7.87×10^{-4} in/s; and (b) CPR=7.87×10^{-5} in/s. Tests 30, 35, 31, and 36; 32-33; 26-27; and 28-29 represent the load test results in PR1; PR2; PR3; and PR4, respectively. Tests 30-35 and 31-36 are repeat tests.

As it can be seen, the bending moment values are approaching to zero at the point of load application in free-head condition tests. Having an “S” shaped bending moment profile, peak bending moments have been observed both below and above the dredge line, with maximums generally at the latter location. Considering the axial load distribution, similar to the fixed-head load tests, sheet piles in PR4 and PR1 has experienced the highest and lowest resistances. Moreover, as discussed in section 1.1.6, negligible (or no) rate effects were observed for the free-head condition tests. Due to the increased cross-sectional area, relatively higher axial resistance is obtained for PZS2.

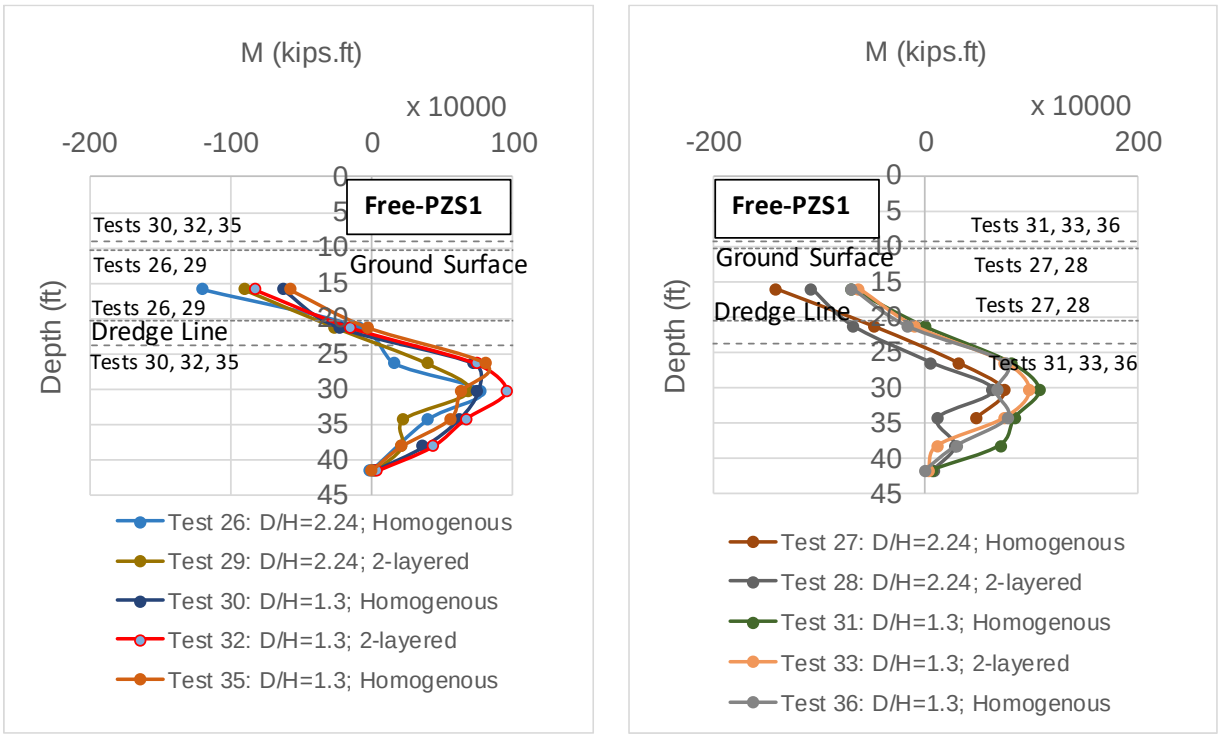

(a) (b)

Figure 3-84. Bending moment profiles of the sheet pile wall PZS1 in different soil profiles (a) CPR=7.87×10^{-4} in/s; and (b) CPR=7.87×10^{-5} in/s. Tests 30, 35, 31, and 36; 32-33; 26-27; and 28-29 represent the load test results in PR1; PR2; PR3; and PR4, respectively. Tests 30-35 and 31-36 are repeat tests.

3.5.1.1 Ground surface settlement during driving and load testing of sheet piles

The ground settlement was monitored through two LPs during (Figure 3-85) in-flight driving and load testing of sheet piles. It is believed that settlement data can be useful in construction planning in urban areas in the vicinity of the sheet piles. Settlement data were also used to cross-check the repeatability and reliability of centrifuge tests. The LP1 was installed at 8.2 ft from the sheet pile wall and the LP2 at 25.1 ft. Considering its distance from the sheet pile wall, it might be reasonable to assume the LP2 data as the ground settlement in the free-field.

As an example, the settlement data during Test 11 is presented in Figure 3-86, where the settlement in the vicinity of the sheet pile is approximately 3.2 times that in the free-field. The peak settlement values during tests 1 to 36 are presented in Figure 3-87. It can be seen that all settlement values are almost at the same magnitude in the cases of the free-field and close to the sheet pile wall.

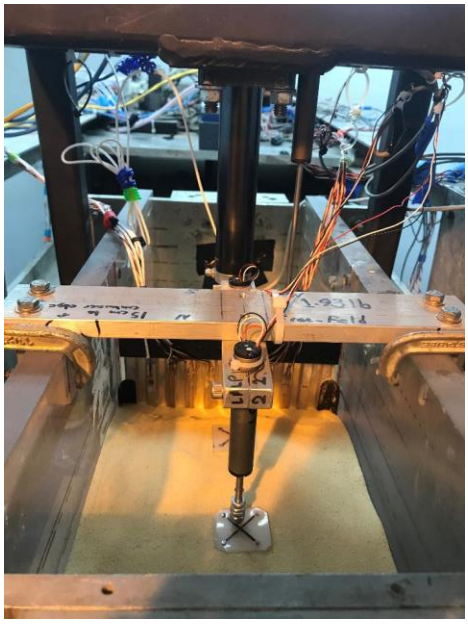

Figure 3-85. Settlement measurement by two vertical LPs

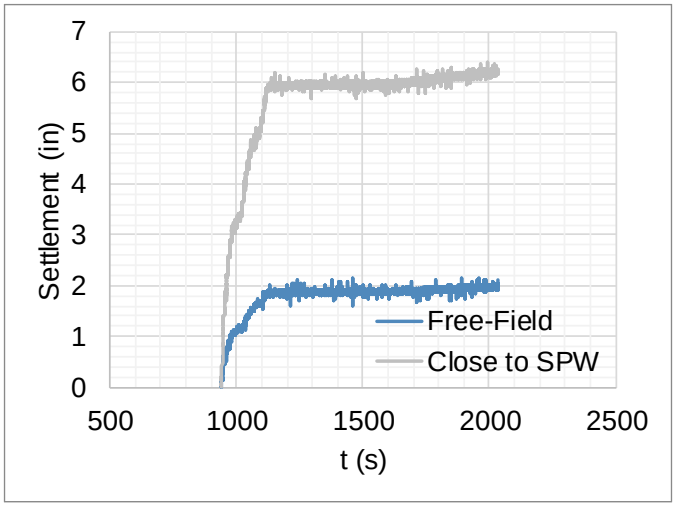

Figure 3-86. Settlement-time history during driving and load testing of the PZS1 sheet pile in PR1 during Test 11

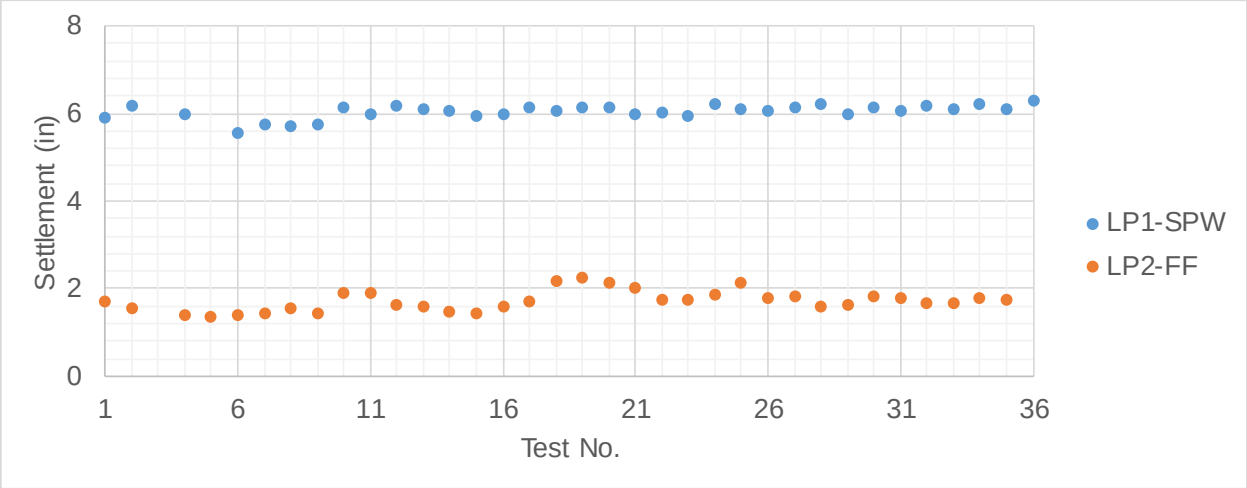

Figure 3-87. Peak ground settlement during driving and load testing of sheet piles at different presented tests

3.5.2 Conclusions and Preliminary Recommendations: centrifuge tests observations

The behavior of axially loaded sheet pile walls was investigated through centrifuge testing. As the first step, the validity and repeatability of centrifuge tests results were confirmed through performing repeat tests, comparing settlement profiles across different centrifuge tests, and comparing the axial load values obtained from the load cell and those obtained from strain gages. Static axial load tests were performed on sheet pile models in different scenarios that may frequently encounter in the field. As such, the effects of (i) existence of a dense sand layer at the sheet pile tip, (ii) sheet pile penetration depth (D) to unsupported depth (H) length ratio, (iii) sheet pile stiffness, and (iv) loading rate effects at CRP testing were studied.

Relatively high residual loads were observed during driving the sheet piles, which contributed to the overall axial capacity of the sheet piles. Soil plugging was observed during all centrifuge load tests on the studied sheet piles, which was believed to increase the axial capacity, as well. These observations are recommended to be considered when designing axially loaded sheet piles. Similar to the H-piles and drilled shafts in sand, a strain-hardening type axial load-displacement behavior was observed.

The load test results revealed that the existence of the dense sand layer at the sheet pile tip causes an increase in the axial resistance of sheet piles relative to the cases where the soil profiles were consisted of a homogenous sand layer. The amount of this increase, however, was more for the sheet piles in the profiles with a higher D/H ratio (i.e. D/H=2.24). Increasing the D/H ratio increases the skin friction; therefore, the axial resistance, in both homogenous and two-layered profiles and in either of the test series with free-head or fixed head conditions. Compared to those sheet piles in homogenous sand profiles, the amount of this increase in axial resistance was greater for the profiles with the dense sand layer at the sheet pile wall tip. Greater axial resistance was obtained in the stiffer sheet pile wall (i.e. PZS2). This was mainly attributed to the increase in the

cross-sectional area of the sheet pile wall and also an increase in the projected area, where the soil plugging occurs. It was found that generally same axial resistances were obtained when load testing of sheet piles with CPR=7.87×10^{-4} in/s and CPR=7.87×10^{-5} in/s. This was mainly due to the fact that no inertial and damping forces and excess pore water pressure were involved during load testing at these rates in dry sand. Corresponding bending moment profiles were obtained, and it was observed that the maximum in-ground bending moments generally occur at 34.25 ft depth for sheet piles with fixed head conditions. Obviously, for the fixed-head boundary condition, the maximum bending moments occur at the fixed-head (i.e. at the helmet). An increase in the axial resistance increased the maximum bending moment. In contrast, the bending moment values were approaching zero at the point of load application for the free-head condition tests. Considering an "S" shaped bending moment profile, higher magnitude bending moments were observed at both below and above the dredge line, with maximums mostly at the latter location.

3.5.3 References

ASTM D1143/D1143M (2013). "Standard Test Methods for Deep Foundations under Static Axial Compressive Load."

ASTM D1143/D1143M (2013). "Standard Test Methods for Deep Foundations Under Static Axial Compressive Load." ASTM International, West Conshohocken, PA.

Hammers & Steel (2019). "Sheet Pile Pushers." <https://www.hammersteel.com/sheet-pile-pushers.html>.

Hölscher, P., van Tol, A. F., and Huy, N. Q. (2012). "Rapid pile load tests in the geotechnical centrifuge." *Soils and Foundations*, 52(6), 1102-1117.

Hölscher, P., vanTol, A. F., and Middendorp, P. "European standard and guideline for rapid load test " *Proc., Proceedingsofthe 8th International Conference on the Application of Stress-Wave Theory to Piles*, 699–705.

Huy, N. Q. (2008). "Rapid Load Testing of Piles in Sand: Effect of Loading Rate and Excess Pore Pressure." Technical University of Delft, Delft, The Netherlands.

Mosher, R. L. (1984). "Load Transfer Criteria for Numerical Analysis of Axially Loaded Piles in Sand." U. S. Army Waterways Experiment Station, Automatic Data Processing Center, Vicksburg, Mississippi.

Reese, L. C., and O'Neill, M. W. (1988). "Drilled Shafts: Construction Procedures and Design Methods." Federal Highway Adminstration, McLean, Virginia, 564.

steel piling group (2019). "Pile Driving Installation Methods." <https://www.steelpilinggroup.org/guidance/construction/pile-driving-installation-methods/>.

Appendix A: Sheet pile – sand interface friction angle: Observations from direct shear box tests

Direct shear box tests were performed to study the sheet pile and sand interface angle of friction. This was done by inserting a plate of aluminum in a shear box (Figure A1) with its surface flush with the plane of shearing, and sand with the 67% relative density and 12 % moisture content. The provided area by the shear box was 4 in by 4 in. To investigate the possible variations of the angle of friction between the sand and aluminum sheet pile, and the sand and steel sheet pile (i.e. the case in the field), the shear box tests were performed on both aluminum and steel plates. The steel plate was made of ASTM A572 steel, Grade 50, which was the type of steel commonly being used in PZ sheet piles. The aluminum plate was made of 5052-H32 aluminum, which was the type of aluminum that was being used in the model sheet piles in the centrifuge tests.

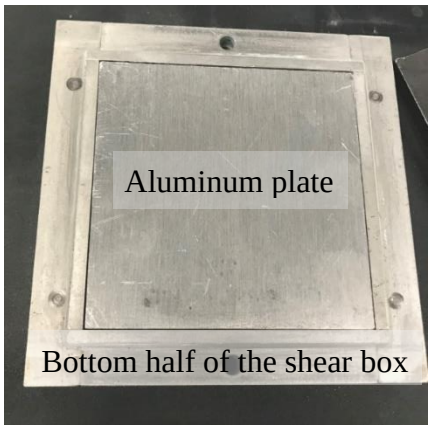

Figure A1. The aluminum plate used in interface direct shear box tests; photo courtesy of SMO

The results of the shear box tests are presented in Figure A2. These results are obtained by averaging the results of milled and un-milled plates. As can be seen, the peak interface friction angles between the sand and aluminum and steel were 26.6^{o} and 26.2^{o}, respectively. These equal to 0.81 and 0.80 of the internal friction angle of the sand at the same relative density and moisture content.

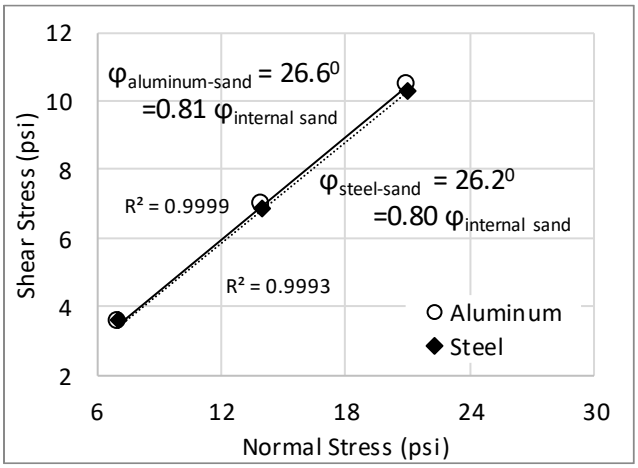

Figure A2. Sand-aluminum plate and sand-steel plate interface peak friction angles obtained through conducting direct shear box tests

Appendix B: Helmet details for free-head tests

A new helmet was designed to perform free-head load tests on sheet pile walls. The helmet had a sufficient internal width (Figure B1-a) such that the sheet pile could freely rotate inside it. To perform driving (i.e. with up and down movements, as discussed) and conduct load tests, 5 rigid rods (Figure B1-b) were passed through the helmet and the sheet pile wall and through the precisely drilled holes at the same elevations. The rods had smooth surfaces and were greased prior to each load test aiming to minimize any possible frictions and apply a distributed load along the width of the wall.

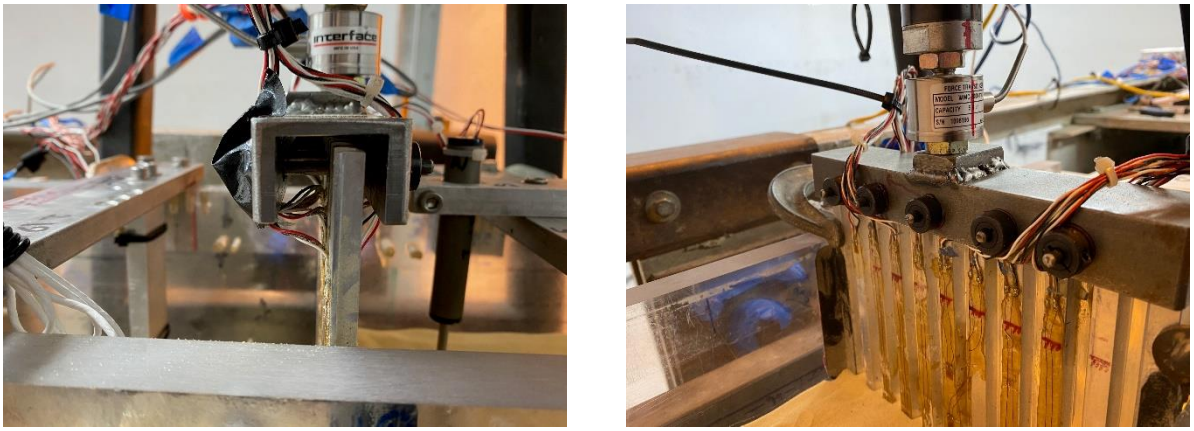

(a) (b)

Figure B1. (a) The sheet pile wall-helmet layout; and (b) the helmet and five smooth rods for performing free-head load tests

4 CHAPTER 4: NUMERICAL VALIDATION AND FIELD-TESTING PROTOCOL

4.1 Field Testing Protocol

In this section, we propose the use of the static load testing method for determining the bearing capacity of steel sheet piles. We report the choice of dimensions of sheet pile, pile installation method, static load testing procedure, and data interpretation. The results obtained from full-scale field static load tests will be compared with those from the centrifuge and numerical tests.

4.1.1 Type of steel sheet pile

In tough driving conditions, such as dense to very dense sands in our case (Dr=85%), a thicker pile should be considered. Since we expect the sheet piles to carry both axial and lateral loads as a foundation, whatever section becomes available is what will be used for driving and static load testing. Four sections are grouped to bear the loads, which gives us a width of 72 in (6ft). The length of sheet pile is determined as 25 ft based on site conditions. The maximum applied vertical load is determined based on the bearing capacity of 4 sections of sheet piles. The skin resistance and tip resistance calculated in Appendix E.

Table 1 Specifications of PZ 27 steel sheet pile

Section	**PZ 27**
Width (in)	18
Height (in)	12
Flange Thickness (in)	0.375
Web Thickness (in)	0.375
Area (in^2/ft)	7.94
Pile Weight (lbs/ft)	40.5
Wall Weight (lbs/ft^2)	27.0
Elastic Section Modulus (in^3/ft)	30.2
Plastic Section Modulus (in^3/ft)	36.49
Moment of Inertia (in^4)	184.2

4.1.2 Load application systems for static load testing

The engineer may specify a waiting period between vibro-driving of sheet pile (see Appendix c) and the static load testing. The pile load test program is designed to evaluate the actual nominal

resistance of a driven pile. Figure 1 shows the typical setup for the load applying system where the load is applied to the pile by hydraulic jack(s) acting against an anchored reaction frame.

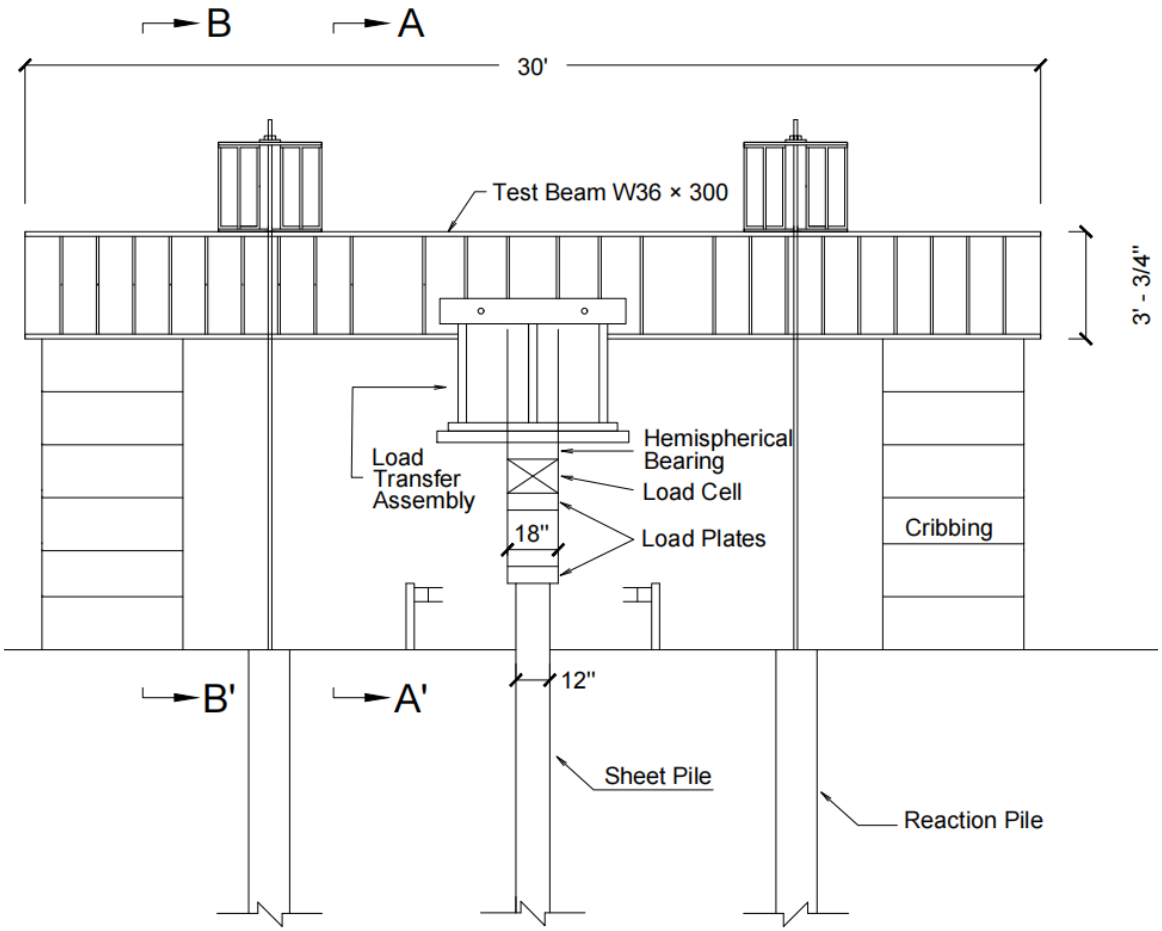

(a) Elevation

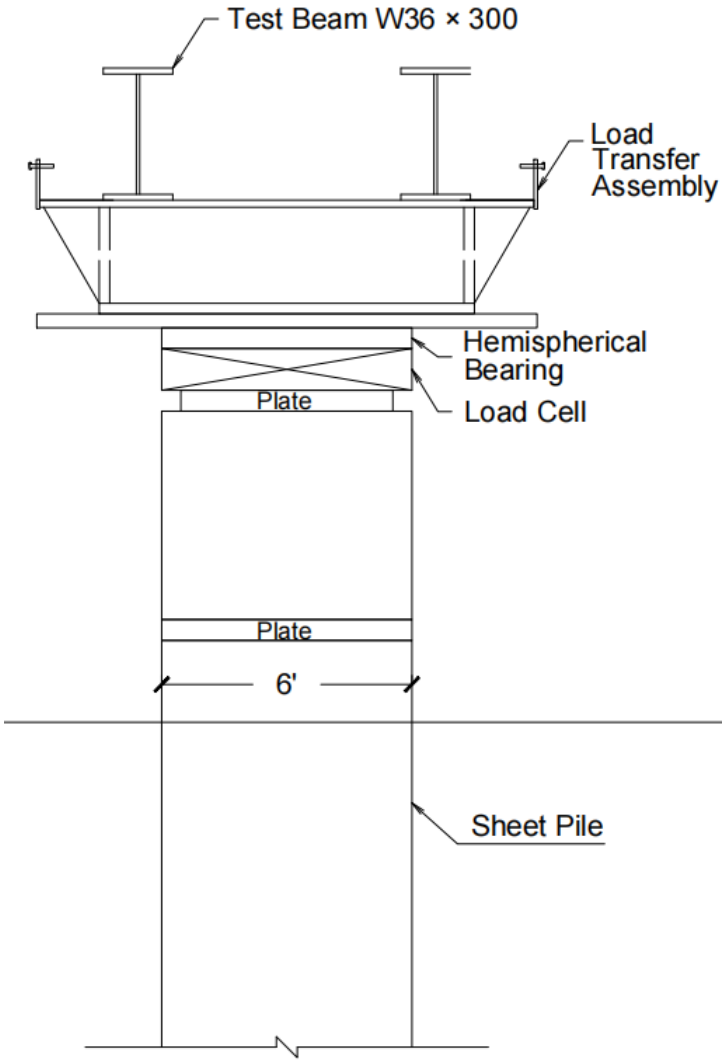
Test Beam W36 × 300
Load
Transfer
Assembly
Hemispherical
Bearing
Load Cell
Plate
Plate
6'
Sheet Pile

(b) Section A-A’

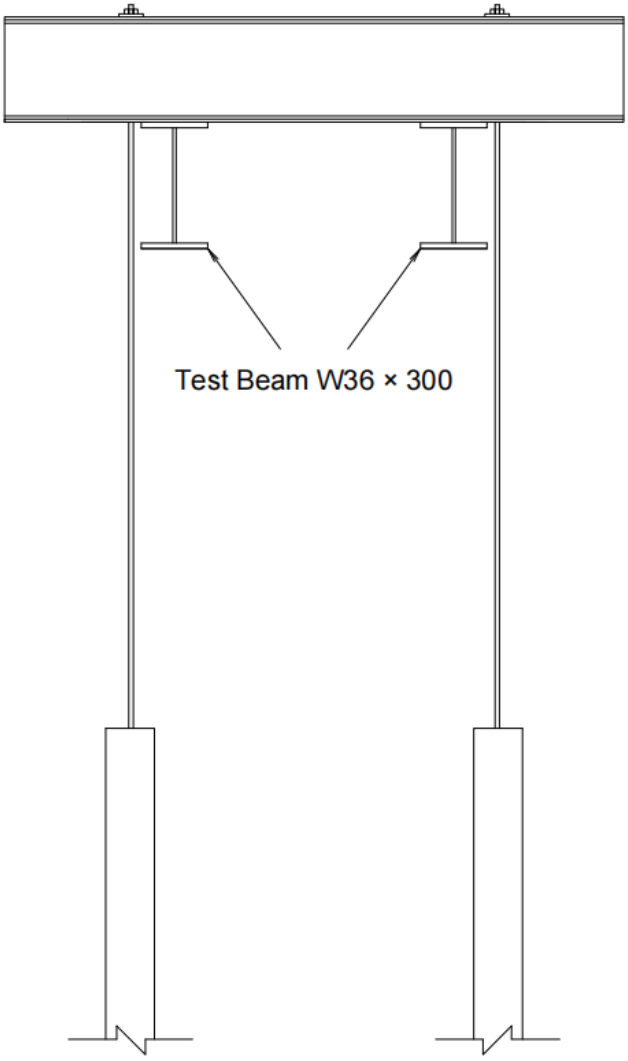

(c) Section B-B’

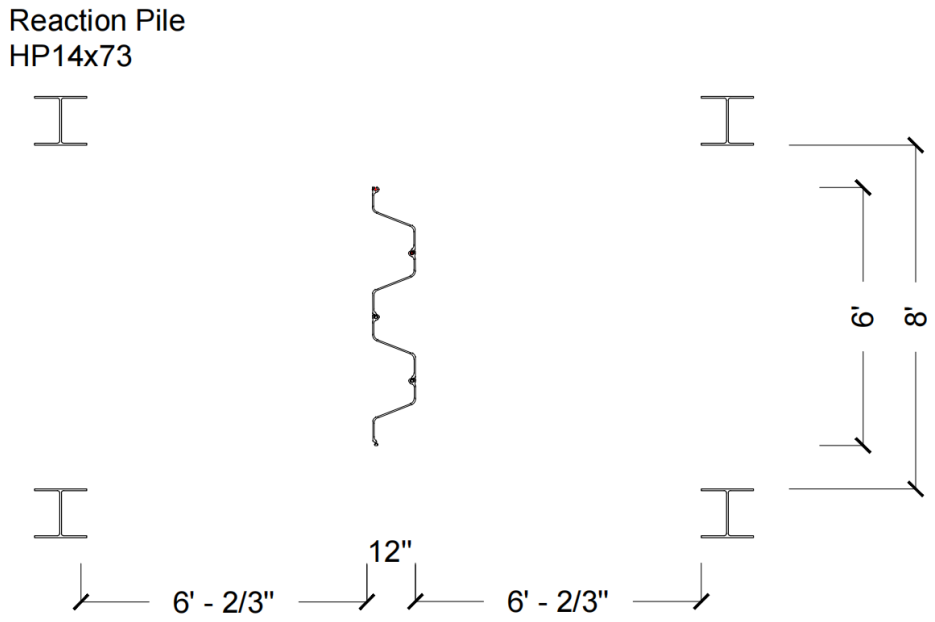

(d) Plan view

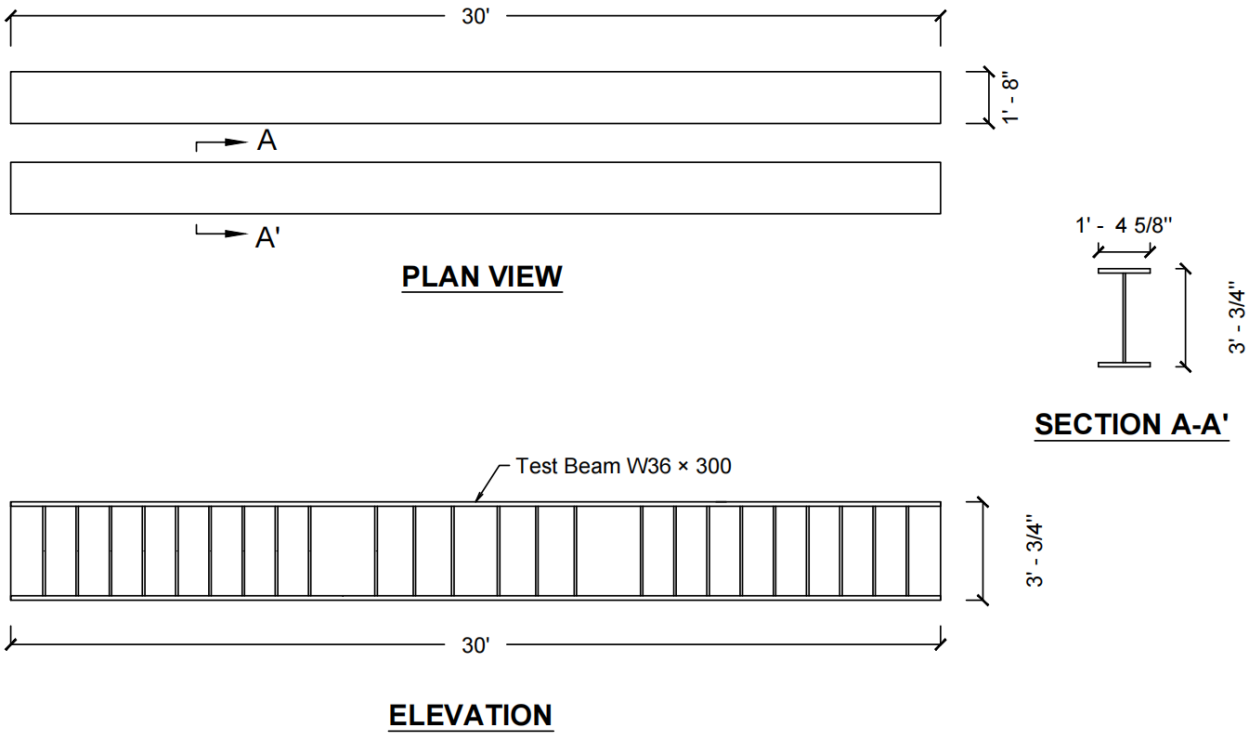

(e) Test beam

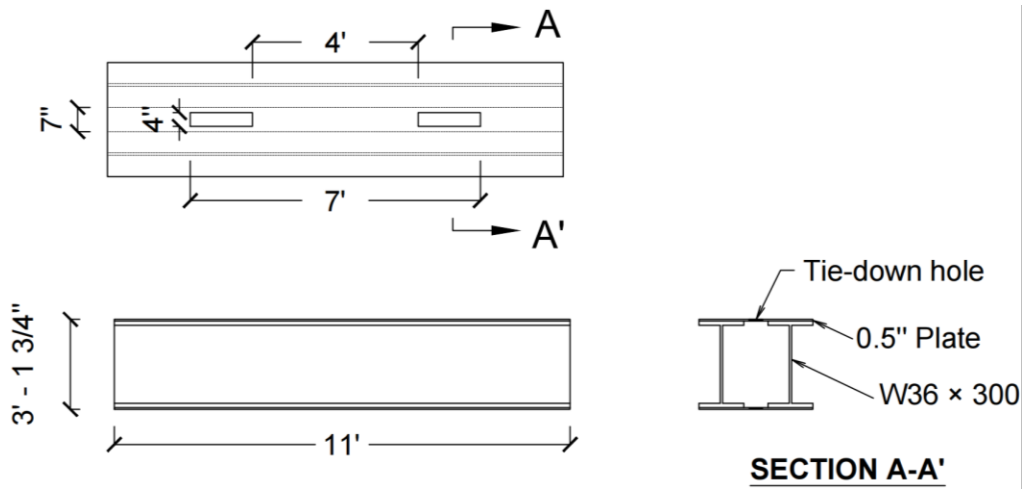

(f) Tie-down beam

Figure 4-1. Schematic of static load test setup.

4.1.3 Measuring apparatus

Provide an apparatus for measuring movement and strain of the test sheet piles that contain the following devices: wireline and scale, wooden reference beams and dial gauges, and survey level. Figure 6 show the schematic of the suggested instrumentation for measuring axial displacements of sheet pile.

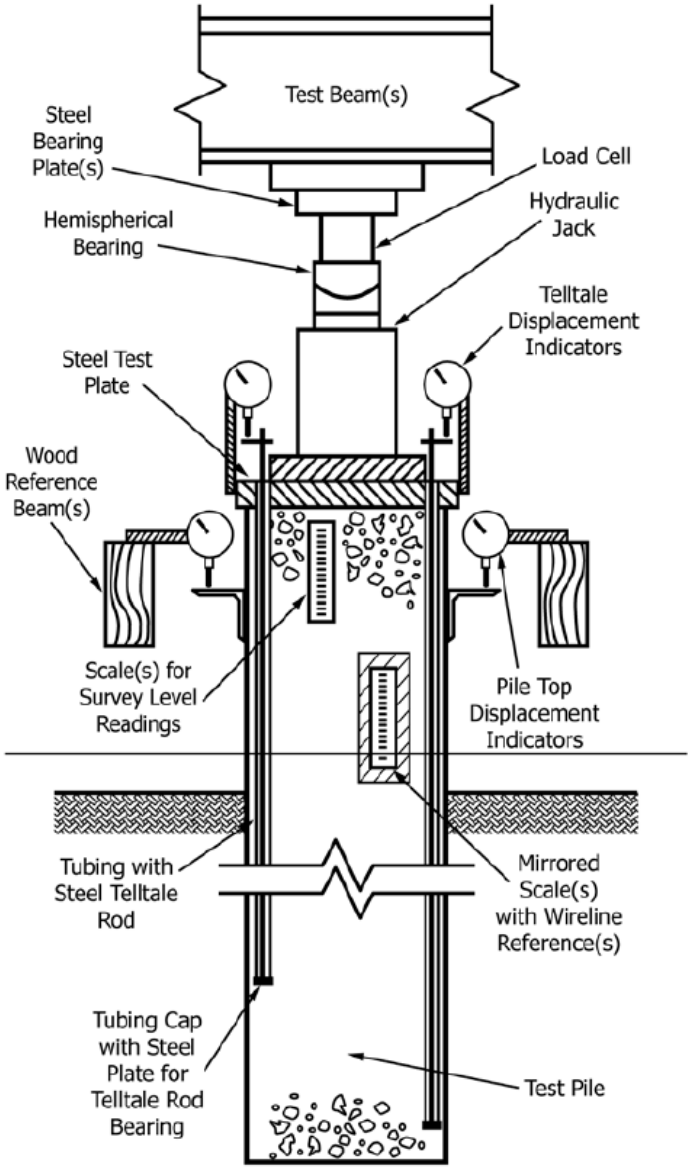

Figure 4-2. Schematic of suggested instrumentation for measuring axial displacements of sheet pile (ASTM D1143/D1143M 2020)

4.1.4 Loading procedure

The methods of testing piles are best characterized by the duration of force applied to the pile and the strain induced in the pile. Tests involving large forces maintaining a long period such as static load tests are used to assess pile load capacity. At present, the most frequently used types of static load testing are the maintained load test (MLT) and the constant rate of penetration test (CRP). MLT suits almost all subsurface conditions and pile types while CRP is limited to cohesive soils and may overestimate the ultimate capacity (Handley et al. 2006). ASTM (2020) provides an alternative loading procedure known as the modified quick test which is used in this work:

1. Place the test load in increments of 5 % of the maximum test load specified until the failure occurs.
2. Apply increments of approximately 2.5% of the maximum test load until the pile "plunges" or attains the limiting load. The Engineer may elect to stop the loading increments when the Contractor has met the failure criteria or a settlement equal to 10% of the sheet pile width is reached, whichever comes first.
3. The unloading is carried out in decrements of 10% of the maximum test load.

Table 1. Loading procedure in the modified quick test. The calculation of maximum test load is shown in Appendix E.

Cell Calibration Factors:		**0.1047**		
Max Test Load (kips) :		**45**		
Increment	**Target Load (kips)**	**Estimated Pressure (psi)**	**Hold Time (minutes)**	**Total Time (minutes)**
Initial	0	0	0	0
1	2.25	21	8	8
2	4.5	43	8	16
3	6.75	64	8	24
4	9	86	8	32
5	11.25	107	8	40
6	13.5	129	8	48
7	15.75	150	8	56
8	18	172	8	64
9	20.25	193	8	72
10	22.5	215	8	80
11	24.75	236	8	88
12	27	258	8	96
13	29.25	279	8	104
14	31.5	301	8	112
15	33.75	322	8	120
16	36	344	8	128
17	38.25	365	8	136
18	40.5	387	8	144
19	42.75	408	8	152
20	45	430	30	182

4.1.5 Failure criteria

The load test failure load is defined as the load that causes a sheet pile top deflection equal to the calculated elastic compression plus 0.15 inches plus 1/120 of the section height of sheet pile which is 12 inches for PZ-27, or 15% of the sheet pile width, whichever is greater. The criterion is applicable because the used PZ-27 sheet piles have a height of 12 inches. Consider the nominal resistance of any pile so tested as either the maximum applied load or the failure load, whichever is smaller (FDOT 2020).

4.1.6 References

AASHTO (2020). AASHTO LRFD bridge design specifications, American Association of State Highway and Transportation Officials (AASHTO), Washington, D.C.

ASTM D1143/D1143M. (2020). Standard Test Methods for Deep Foundations Under Static Axial Compressive Load. West Conshohocken, PA: ASTM International.

Baligh, F. A., & Abdelrahman, G. E. (2005). Modification of Davisson's method. In Proceedings of the International Conference on Soil Mechanics and Geotechnical Engineering (Vol. 16, No. 4, p. 2079). AA BALKEMA PUBLISHERS.

Davisson, M. 1972. High capacity piles. In Proceedings of the Soil Mechanics Lecture Series on Innovations in Foundation Construction. American Society of Civil Engineers, Illinois Section, Chicago, Ill. pp.82112.

Florida Department of Transportation (2020). Standard Specifications for Road and Bridge Construction, January 2021.

Handley, B., Ball, J., Bell, A., & Suckling, T. (2006). Federation of Piling Specialists Handbook on Pile Load Testing. FPS, Forum Court.

4.2 Validating the numerical models

In Task report 3c centrifuge load tests were conducted to investigate the problem at hand and calibrate and validate the numerical models. Different geo-structural conditions were evaluated to account for various factors including soil profile layering, sheet pile wall stiffness, boundary conditions of the sheet pile wall head, and loading rate effects. The centrifuge tests were performed on the PZS1 and PZS2 sheet pile walls with fixed (17 tests) or free (6 tests) head conditions in the PR1-PR4 profiles (Figure 0-1 and Figure 0-2).

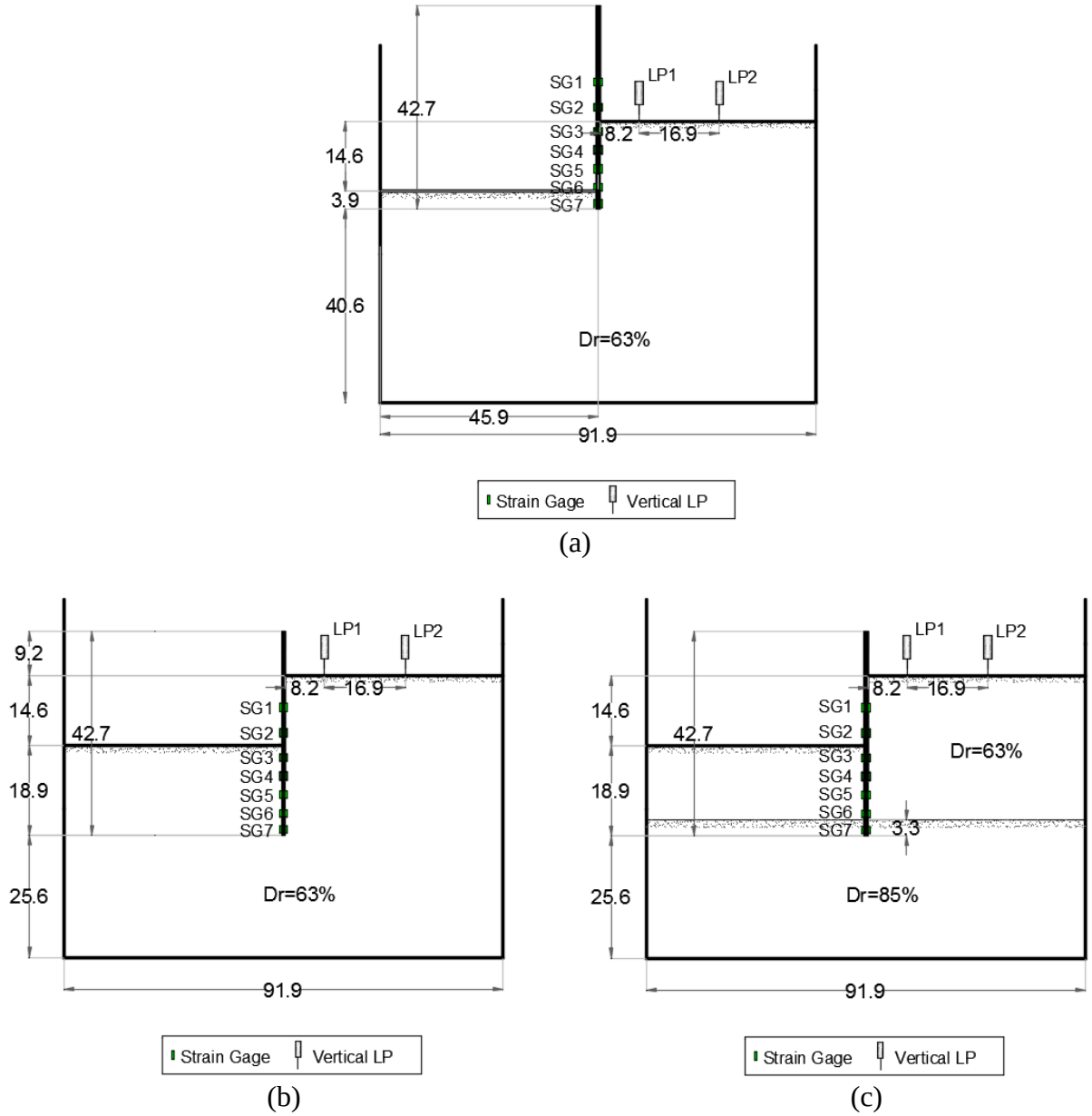

Figure 0-1. Cross-section of the centrifuge model for tests with D/H=1.3: (a) before sheet pile wall insertion; (b) homogenous sand (PR1); and (c) two layers of sand (PR2).

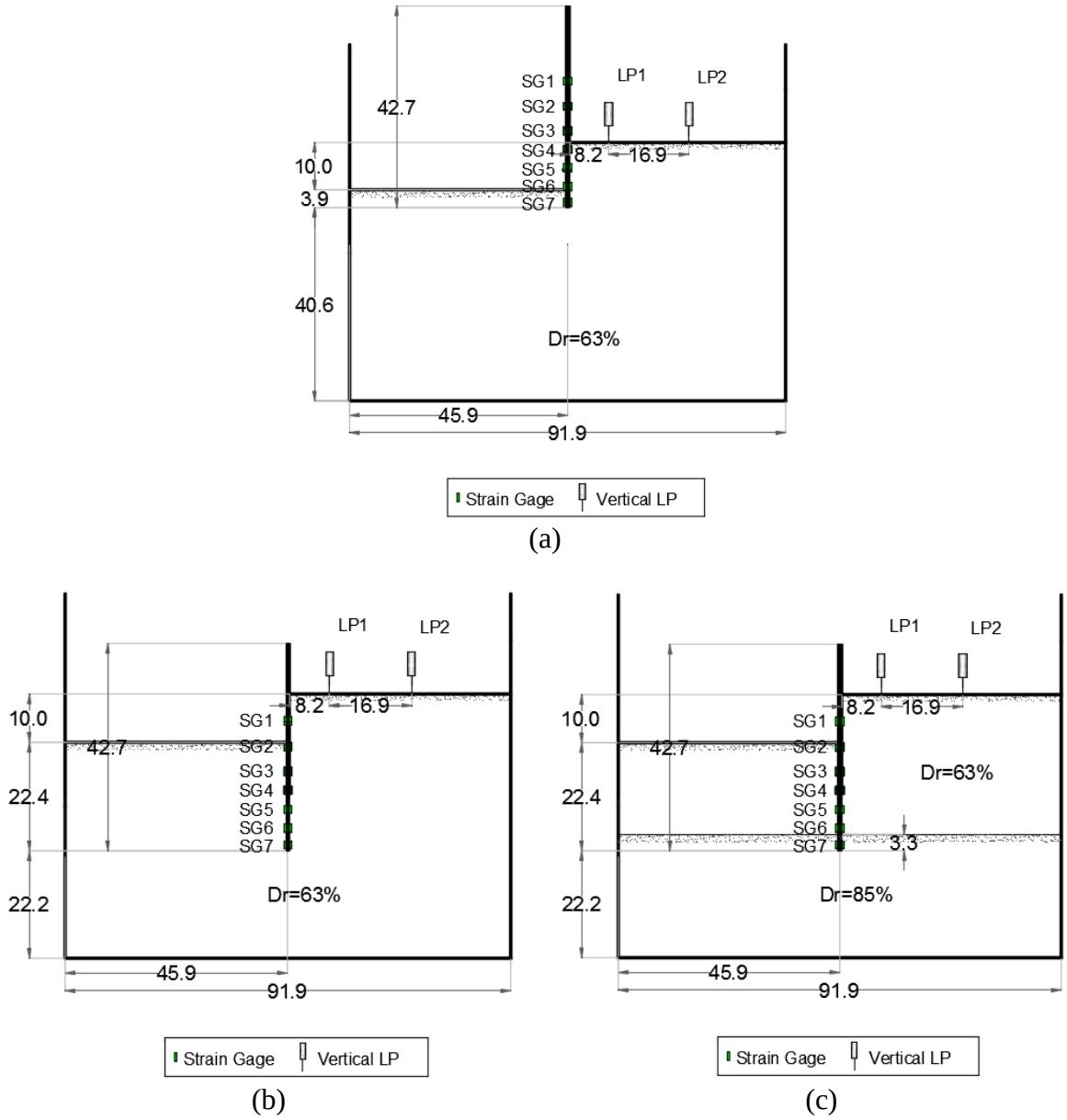

Figure 0-2. Cross-section of the centrifuge model for tests with D/H=2.24: (a) before sheet pile wall insertion; (b) homogenous sand (PR3); and (c) two layers of sand (PR4). The dimensions are provided in prototype-scale in feet.

Both sheet pile sections were tested for two different embedded pile depths in two different soil profiles, one homogeneous and the other layered. In Task Report 2, numerical simulations were performed to make predictions of the sheet pile wall capacity. Due to delays in the centrifugal tests and lab tests of the soil, SPW and their interactions certain assumptions had to be made about material properties. Therefore, load predictions from the numerical analysis could not account for the residual stresses developed, soil plugging effects or the densification of sand that occurs during the pile insertion process. Consequently, the load reported in the original numerical tests is not

indicative of the total force acting on the pile wall. To correct this, we conducted numerical simulations of the vertical bearing capacity of the sheet pile wall in identical configurations to the centrifuge tests to calibrate our numerical model. The results of the updated numerical model are then compared to the centrifuge data.

Details on the preparation of centrifuge models, instrumentation, and the centrifuge tests setup can be found in the report for Task 3b. Details on the load testing protocol, the in-flight driving of sheet piles and detailed discussion of individual tests can be found in the report for Task 3c. Axial static load tests were performed on the sheet pile wall (SPW) models under different scenarios simulating a variety of conditions that may be frequently encountered in the field. This section explains these investigated scenarios and discusses the findings from them.

Centrifuge tests were carried out on model cantilever sheet pile walls supporting the granular fill by subjecting it to varied g-levels (in steps of 10g) up to a maximum set target g-level of 50g. The axial load and bending moment distribution and the settlement of the backfill close and far from the sheet pile wall were monitored during the centrifuge test.

4.2.1 In-flight insertion of sheet piles

The sheet pile walls were inserted into the target depths shown in the sand profiles depicted in Figure 0-1 and Figure 0-2 in flight using a combination of downward and upward axial movements. Through this driving pattern, it was aimed to simulate the compaction and volume changes of the sand surrounding the sheet pile similar to that occurs in the field but in a simple way, in the centrifuge modeling context. Quasi-static pushing and pulling-type displacements with a speed of about 0.04 in/s (about 1 mm/s) were used. Using the precise displacement-controlled actuator and its 6 in feedback displacement transducer at the top of the sheet pile wall, it was made sure that a repeatable driving pattern and tip elevation was achieved along this series of tests. It is worth mentioning that the use of the mentioned 6 in transducer is in agreement with the requirements of ASTM D1143/D1143M (2013) for such a displacement measurement system.

The sheet pile wall top displacement-time history during driving and load testing from a sample test is shown in Figure 0-3(a). The mentioned downward and upward movements during driving can be noticed through this figure. The upward movement during driving unloads the sheet pile wall and as it is shown in Figure 0-3(b), negative (i.e. tensile) low axial loads are experienced during these movements. The sheet pile wall top displacement versus top load (measured by a load cell) during driving and load testing is depicted in Figure 0-4. The compaction of sand during the mentioned driving pattern after each downward and upward movement has been manifested in terms of an increased axial load compared to the previous stage. It is also obvious that increased confinement pressure also contributes to the increase in axial resistance when penetrating to deeper depths. Figure 0-5 describes the different stages of the load time history plot and identifies, by the red line, the time when a snapshot of the axial resistance through the pile is taken.

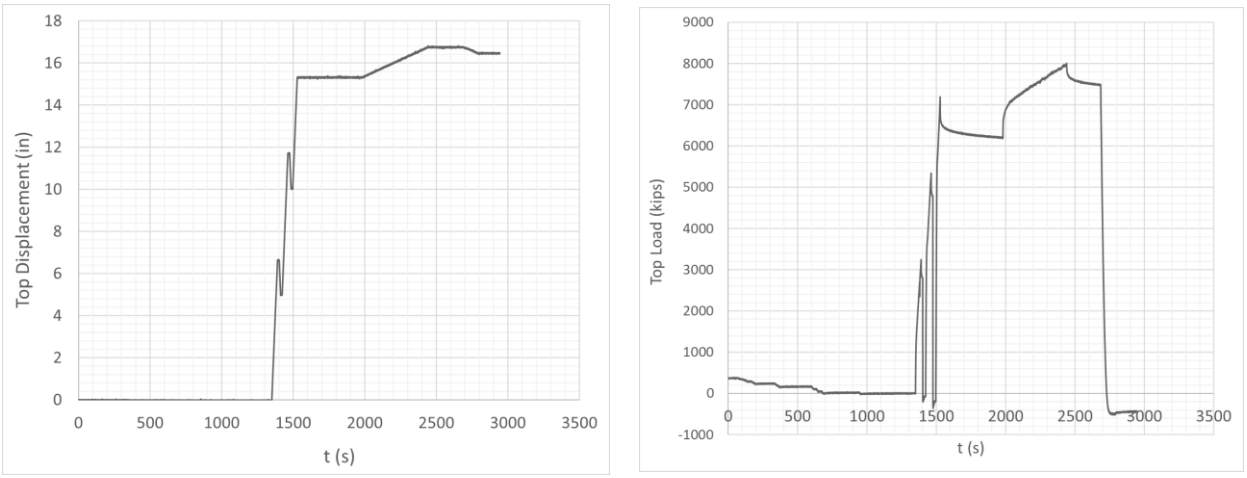

(a) (b)

Figure 0-3. (a) Sheet pile wall top axial displacement-time history during driving and load testing. (b) Sheet pile wall top axial load-time history during driving and load testing.

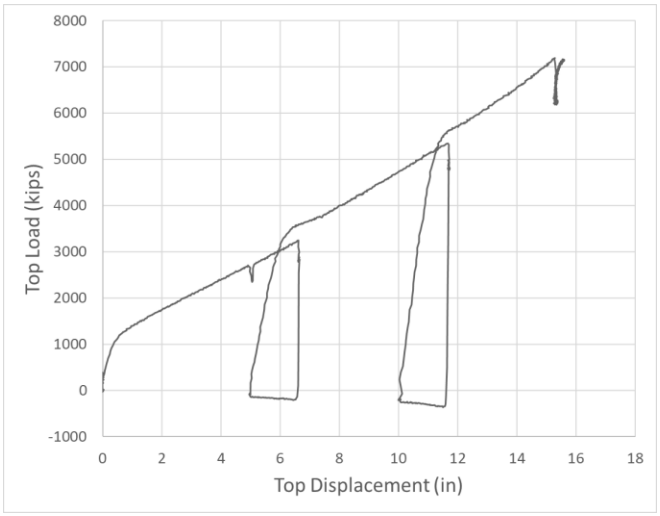

Figure 0-4 Sheet pile wall top axial displacement versus axial load during driving and load testing

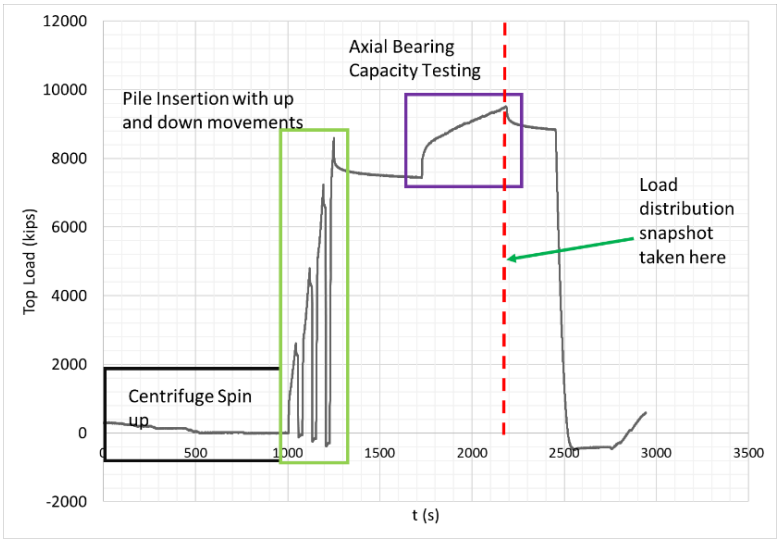

Figure 0-5 Description of the load history at the sheet pile head.

4.2.2 Procedure for static axial compressional load testing of cantilever sheet pile walls

ASTM D1143/D1143M (2013) has defined the failure load, for the purpose of terminating an axial compressive load test, "*the test load at which rapid continuing, progressive movement occurs, or at which the total axial movement exceeds 15 % of the pile diameter or width, or as specified by the engineer*." Using this definition, the nominal axial resistances were reported at the sheet pile top total axial movement of 15 % of the average sheet pile width (D). The width of the PZS1 and PZS2 sheet piles was 13 and 14.38 inch, respectively. For comparison purposes, the width of PZS1 (i.e. the minimum value) was used as the reference for comparisons. As such, the reported resistance values relate to 15% of 13 inch or 1.95 inch of axial movement. (All measurements in prototype scale.)

4.2.3 Axial load transferring mechanisms: end bearing and skin friction.

Two scenarios were considered in investigating the axial load transferring mechanisms in sheet piles. In the first scenario, the sheet pile wall was tested in a medium-dense sand profile with a relative density of 63%. It is believed that this case represents a friction sheet pile where most of the axial load is carried through skin friction. In the second scenario, the sheet pile wall tip was founded on a dense sand layer with a relative density of 85% underlying a medium dense sand with a relative density of 63% (see Figure 0-1 and Figure 0-2). The sheet pile wall tip was penetrated into the dense sand layer for about 39.4 in (1.0 m). This case represented an end bearing sheet pile where the tip resistance played an important role in the bearing resistance of the sheet pile. Both scenarios were conducted for two different sheet pile wall sections PZS1 and PZS2 with pile widths of 13 and 14.38 inch, respectively and with flange thickness of 1.4 and 2.8 inch respectively. Throughout this study, in both the numerical analysis and centrifuge tests, the sheet pile wall is 33 feet long (prototype scale) and composed of 11 pairs of wall sections. Throughout

this report, unless mentioned otherwise, all tests are conducted under a free head condition as is appropriate for cantilever sheet pile walls.

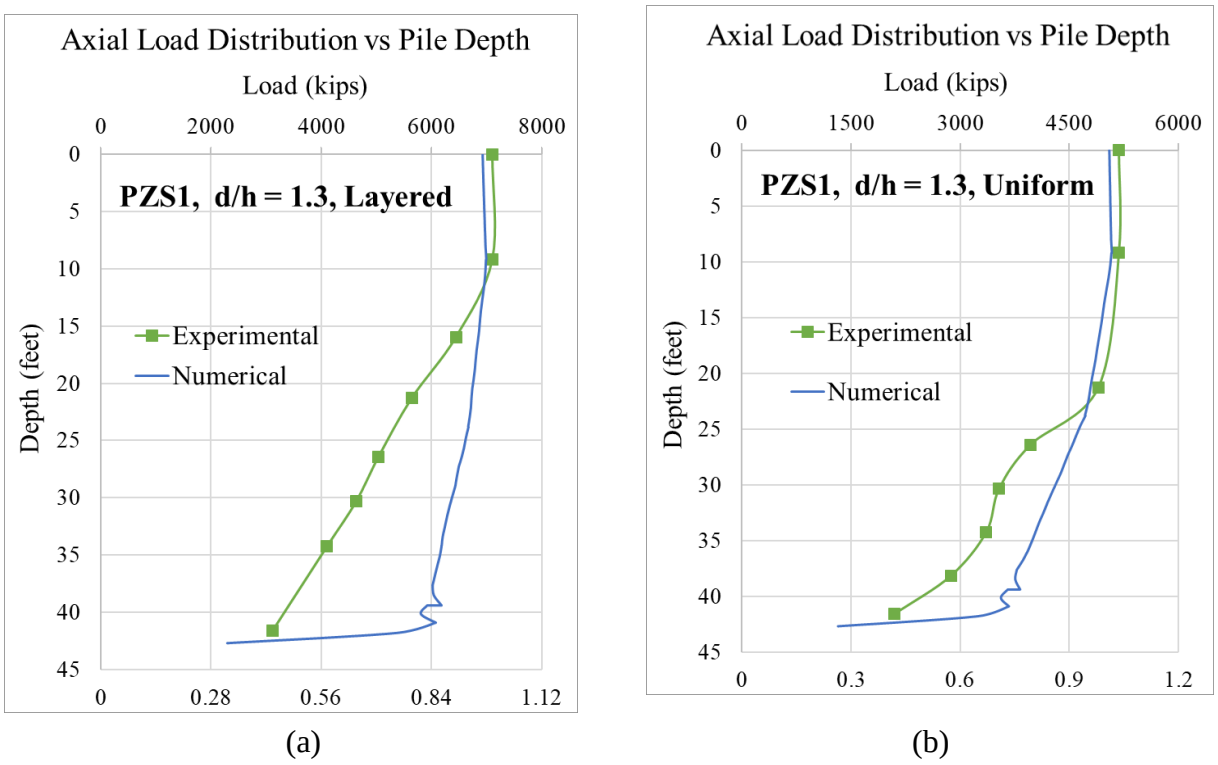

Figure 0-6. Increased axial resistance of a 33 foot long sheet pile wall (Section PZS1) in the (a) profile PR2 compared to that in the (b) profile PR1. (Note: both PR1 and PR2 have a d/h = 1.3.)

Shown in Figure 0-6 are the comparisons of total and normalized axial load distributions through the depth of the PZS1 sheet pile wall for the (a) PR2 and (b) PR1 profiles drawn at failure (defined in subsection 4.2.2). The upper horizontal axis is the absolute magnitude of the force in kips, the lower horizontal axis is the relative magnitude of the load (normalized by the maximum resistance at the pile head) and the vertical axis represents the corresponding depth along the pile wall. All figures in this section follow the same general template including those for the bending moment profiles. The experimental observations of axial resistance along the pile depth are compared to numerical predictions of the same. Unlike the ad-hoc simulations presented in Task Report 2b, here the experimentally observed resistance developed in the pile wall head at failure is used as input in the simulation. We reiterate that, the snapshot of axial load distribution or axial resistance along pile depth is taken at the red line drawn in Figure 0-5.

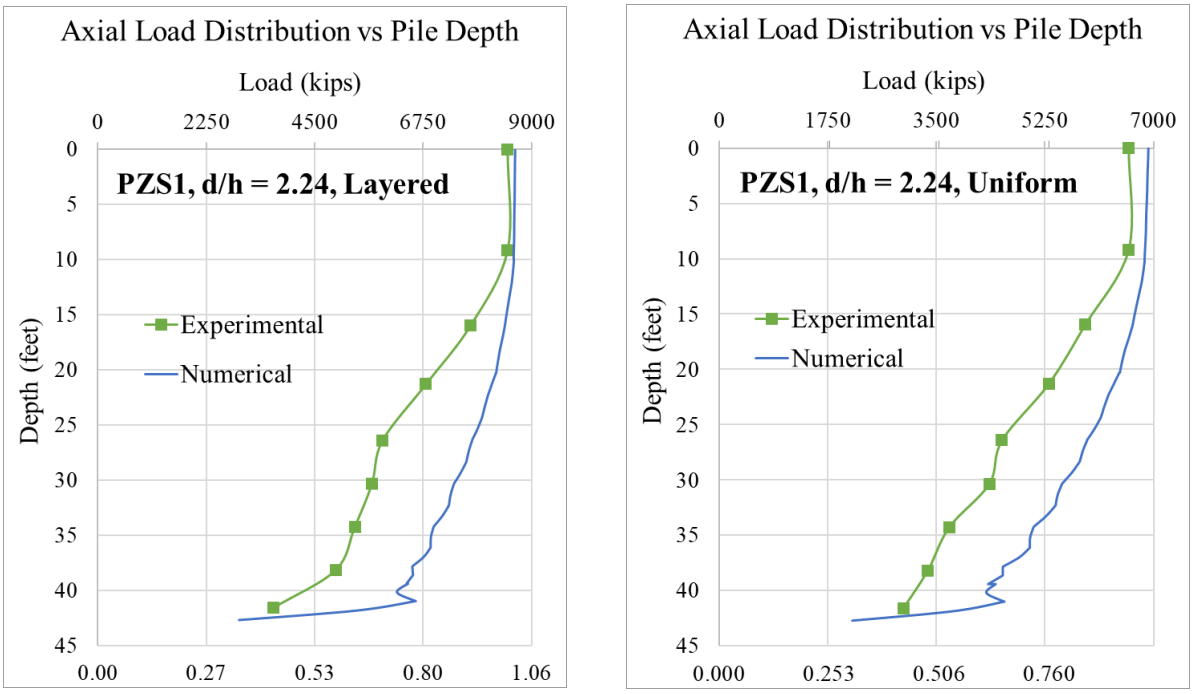

(a) (b)

Figure 0-7. Increased axial resistance of a 33 foot long sheet pile wall (Section PZS1) in the (a) profile PR4 compared to that in the (b) profile PR3. (Note: both PR3 and PR4 have a d/h = 2.24.)

As stated earlier, PR2 represents a two-layered profile (medium dense sand layer overlying a dense sand layer) and PR1 represents a homogenous medium-dense sand layer, both having embedment ratio d/h=1.3. It is evident that the bearing capacity has been increased by having the sheet pile wall tip penetrate the dense sand layer (Dr = 85%). Figure 0-7 depicts the total and normalized axial load distributions through PZS1 sheet pile wall in the (a) PR4 and (b) PR3 profiles. Recall that PR4 and PR3 both have d/h=2.24, with the former being a two-layered profile (medium-dense sand overlying a dense sand layer) and the latter a homogenous medium-dense sand layer. Similar to the cases with a lower d/h, the axial resistance of the sheet pile has been increased when its tip has penetrated into the dense sand layer (i.e. sheet pile in the PR4 profile).

While the numerical predictions of the axial resistance developed in the pile is not identical to the experimentally observed profile, the trends in the data are well matched: the numerical model is able to qualitatively predict the resistance profile developed in the sheet pile wall in both cases.

The load testing results performed on the PZS2 sheet pile wall are presented in Figure 0-8 for (a) PR2 and (b) PR1 and in Figure 0-9 for (a) PR4 (b) PR3 profiles, respectively. Larger axial resistance is observed in the centrifuge tests with the stiffer PZS2 section. As before, the centrifuge test observations are compared to results of numerical analysis but appear to be better matched for section PZS2 than for PZS1. A possible cause for this discrepancy is an improper characterization

of the soil-pile interface that does not account for the differences in soil-plugging. As discussed in the previous task report #3c, the differences between bearing capacity of section PZS1 and PZS2 might be attributable to the difference in pile width which influences the degree of soil plugging in the pile section. It is difficult to properly model soil plugging in the numerical analysis.

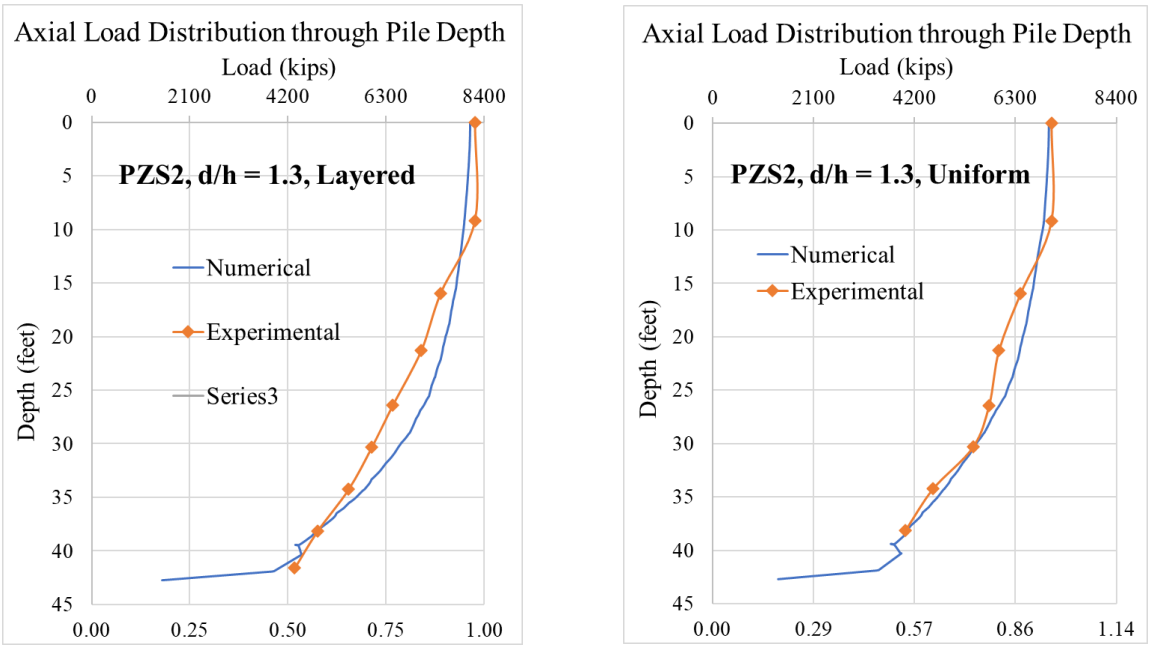

Figure 0-8. Increased axial resistance of a 33 foot long sheet pile wall (Section PZS2) in the (a) profile PR2 compared to that in the (b) profile PR1. (Note: PR2 and PR1 have a d/h = 1.3.)

Corresponding bending moment profiles are depicted in Figure 0-10 - Figure 0-13. The experimental data shows greater bending moments are developed in the PR2 and PR4 (two-layered profiles) than those in PR1 and PR3 for both PZS1 and PZS2 sheet pile walls. The numerical analysis predicts greater bending moments in the layered profiles PR2 and PR4 when using a PZS1 section (Figure 0-10 and Figure 0-11). For analyses using the PZS2 section (Figure 0-12 and Figure 0-13) the numerically predicted values of resistance show no marked difference between layered and uniform profiles. Note that in Figure 0-12 and Figure 0-13 extreme values of moment at 15-foot depth do not seem to be physically reasonable and even contradict experimental observations drawn in Figure 0-10 and Figure 0-11.

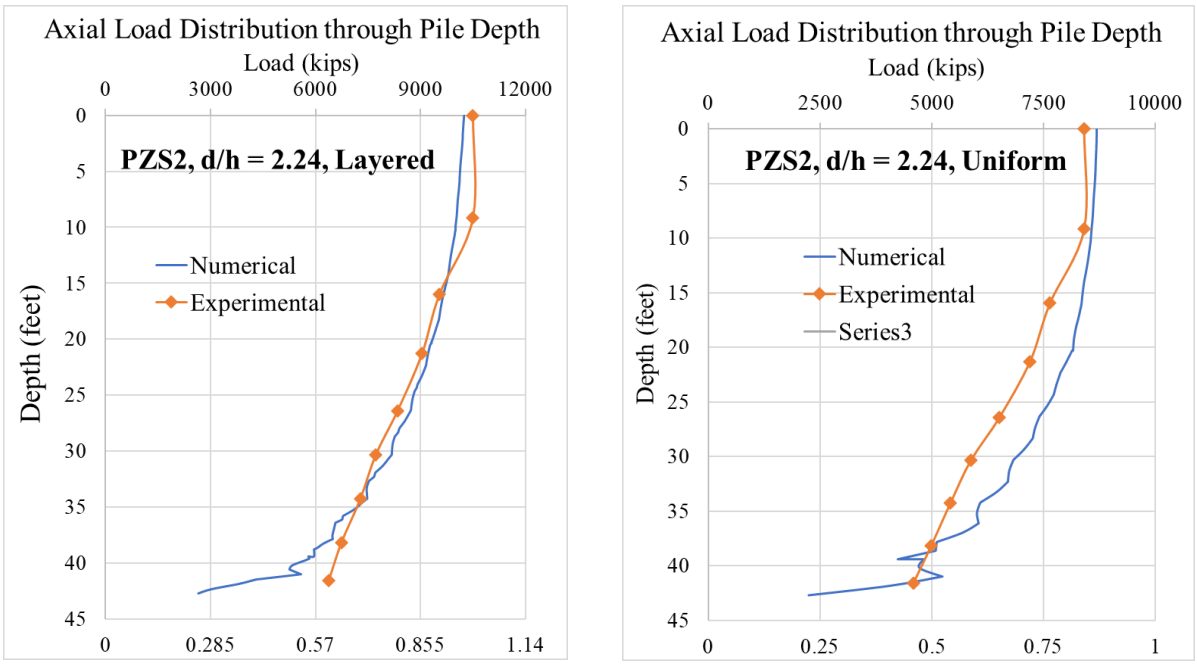

(a) (b)

Figure 0-9. Increased axial resistance of a 33 foot long sheet pile wall (Section PZS2) in the (a) profile PR4 compared to that in the (b) profile PR3. (Note: both PR3 and PR4 have a d/h = 2.24.)

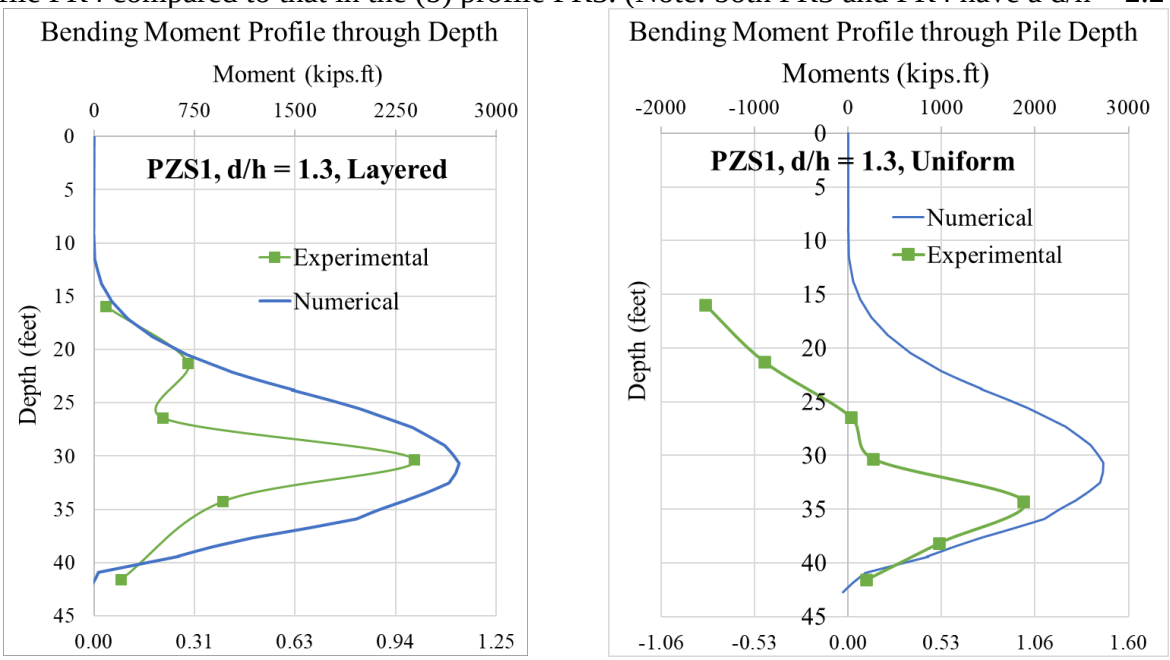

(a) (b)

Figure 0-10. Bending moment profiles in a 33 foot long sheet pile wall (Section PZS1) in (a) the profile PR2 compared to that in (b) the profile PR1. (Note: both PR1 and PR2 have a d/h = 1.3.)

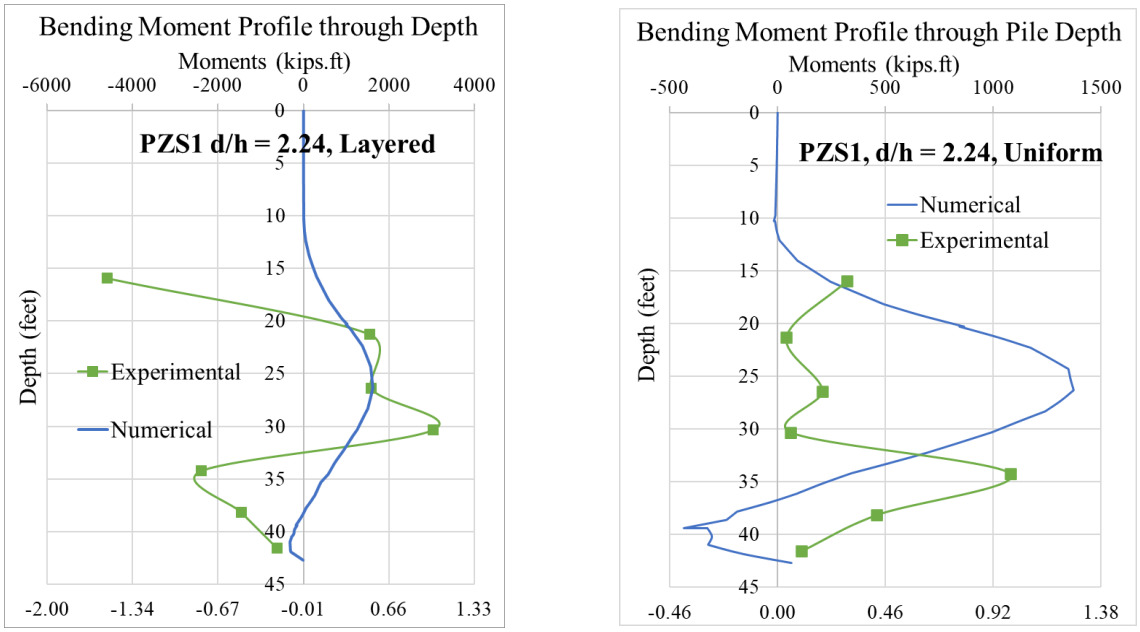

(a) (b)

Figure 0-11. Bending moment profiles in a 33 foot long sheet pile wall (Section PZS1) in (a) the profile PR4 compared to that in (b) the profile PR3. (Note: both PR3 and PR4 have a d/h = 2.24.)

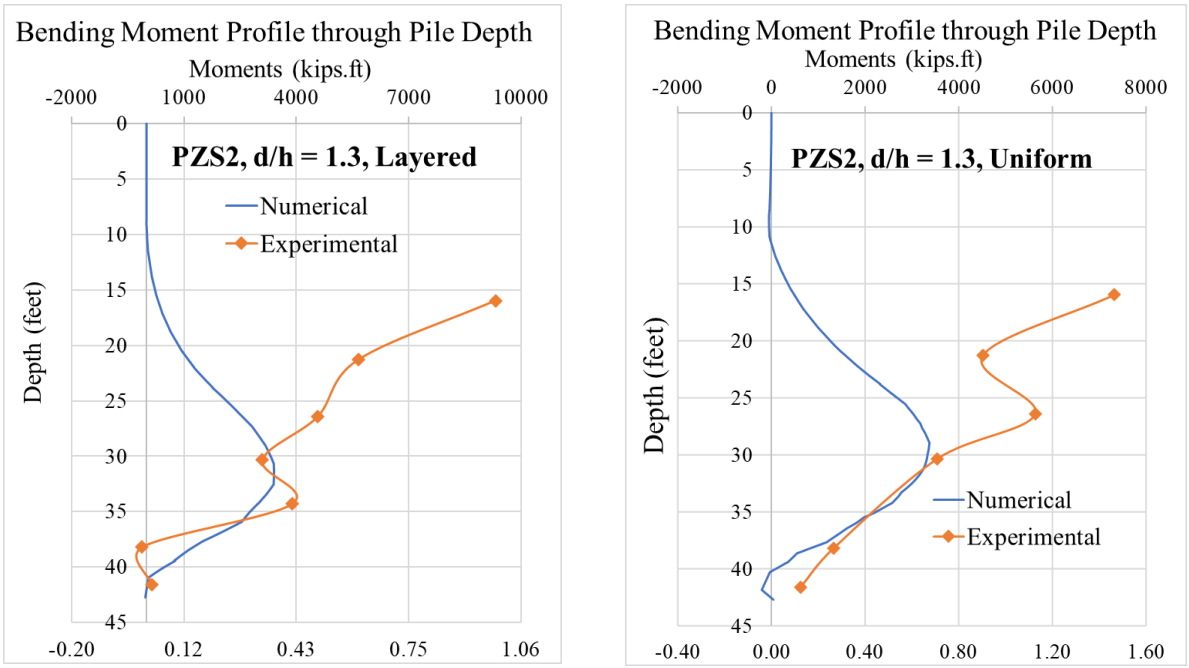

(a) (b)

Figure 0-12. Bending moment profiles of in a 33 foot long sheet pile wall (Section PZS2) in (a) the profile PR2 compared to that in (b) the profile PR1. (Note: both PR1 and PR2 have a d/h = 1.3.)

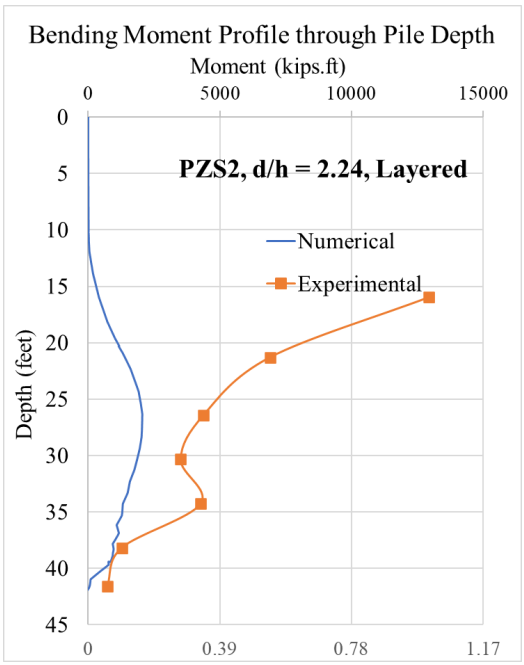

(a)

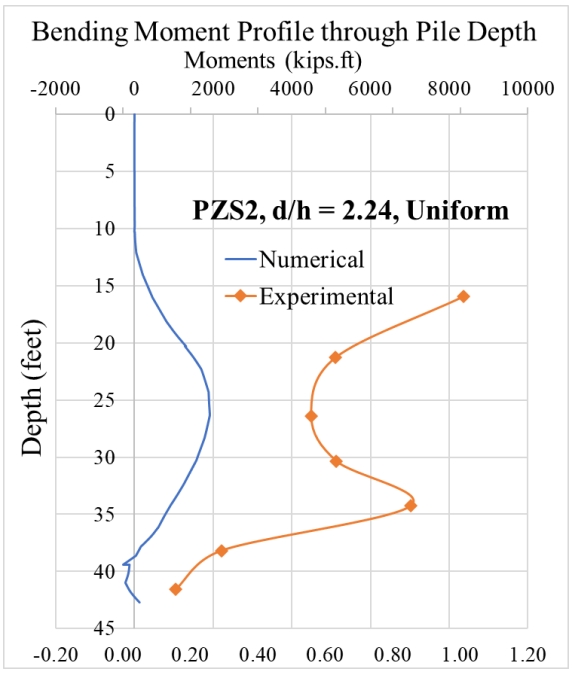

(b)

Figure 0-13. Bending moment profiles in a 33 foot long sheet pile wall(Section PZS2) in (a) the profile PR4 compared to that in (b) the profile PR3. (Note: both PR3 and PR4 have a d/h = 2.24.)

The numerical results suggest that the maximum bending moments always occur at the same location along the pile depth for a given d/h ratio, independent of the soil layering and pile stiffness. The centrifuge observations on the other hand appear inconsistent in this regard with large variations in the location of the bending moment and shape of the profile for each scenario. From static analysis of pile walls, it is known that cantilever pile walls develop a smooth bending moment profile that is zero above the dredge line and smoothly rises to a single maximum along the depth before going to zero at the tip. It is thus difficult to justify the wavy profile observed in the centrifuge tests as physically meaningful and not just instrumentation error or experimental error.

4.2.4 Penetration depth and unsupported length

To investigate the effects of depth of penetration (d) and unsupported length (h) on the axial behavior and bearing resistance of the sheet pile walls, two different penetration depth to retained soil height ratios (d/h) of 1.3 (Figure 0-1) and 2.24 (Figure 0-2) were considered. The load test results on the PZS1 sheet pile wall in profiles (a) PR3 and (b) PR1 (homogenous) and (a) PR4 and (b) PR3 (two-layered) are shown in Figure 0-14 and Figure 0-15, respectively. Increasing the d/h ratio has increased the axial resistance in both homogenous and two-layered profiles. An increase in the penetration depth (d) increases skin friction; hence, the axial resistance.

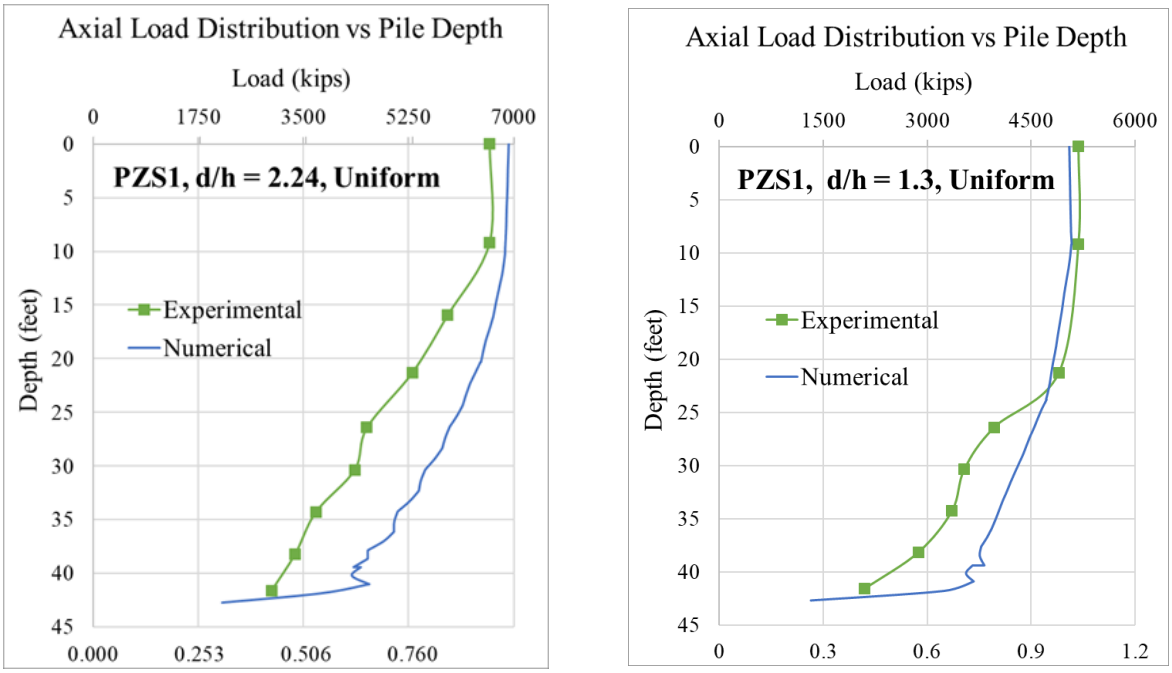

(a) (b)

Figure 0-14. Increased axial resistance in a 33 foot long sheet pile wall PZS1 in the (a) profile PR3 compared to that in the (b) profile PR1. (Note: both PR1 and PR3 are uniform soil profiles.)

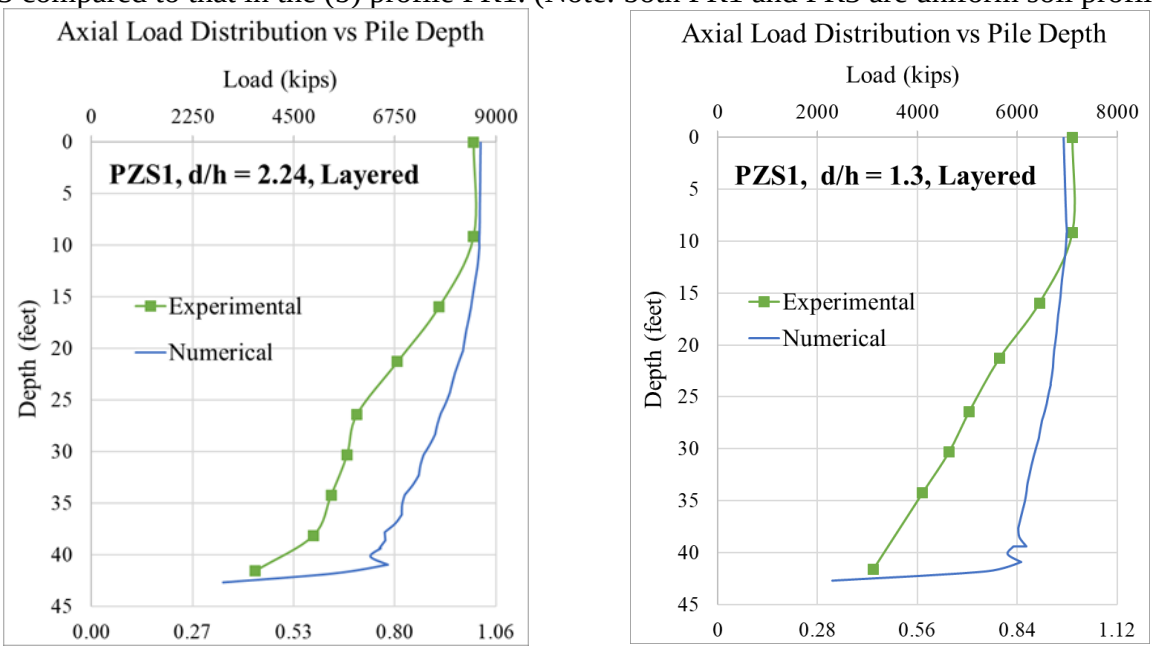

(a) (b)

Figure 0-15. Increased axial resistance in a 33 foot long sheet pile wall PZS1 in the (a) profile PR4 compared to that in the (b) profile PR2. (Note that both PR2 and PR4 are layered soil profiles.)

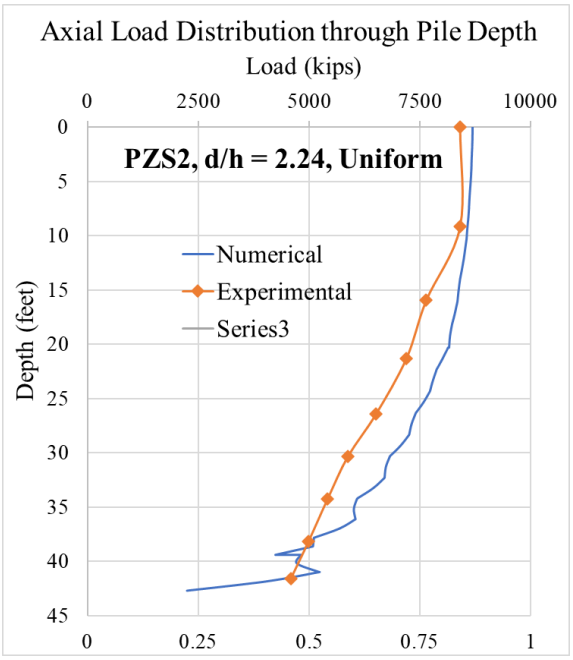

(a)

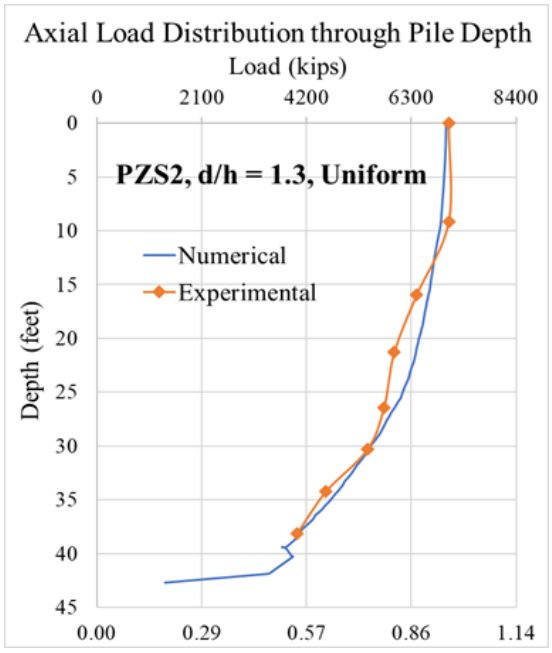

(b)

Figure 0-16. Increased axial resistance in a 33 foot long sheet pile wall PZS2 in the (a) profile PR3 compared to that in the (b) profile PR1. (Note: both PR1 and PR3 are uniform soil profiles.)

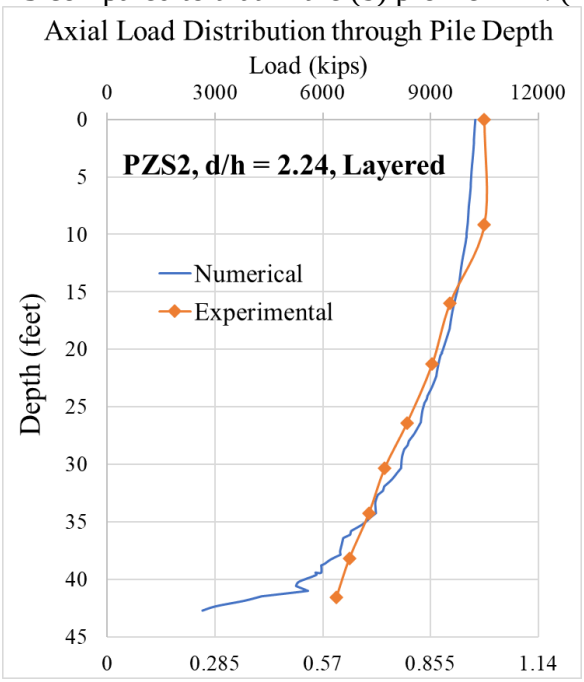

(a)

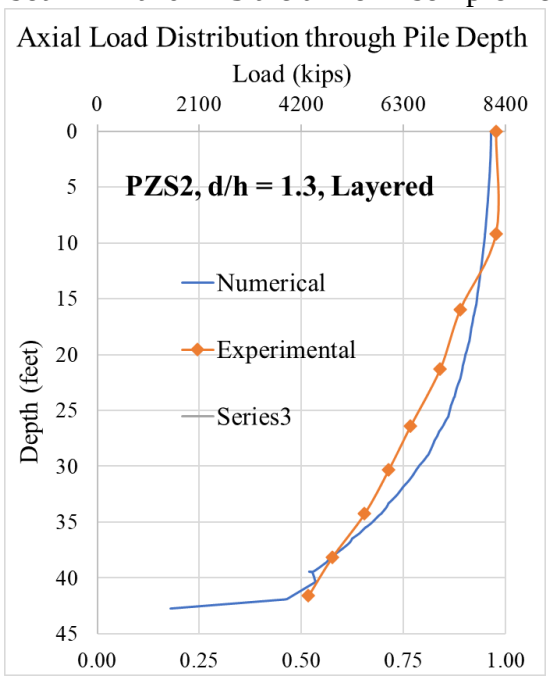

(b)

Figure 0-17. Increased axial resistance in a 33 foot long sheet pile wall PZS2 in the (a) profile PR4 compared to that in the (b) profile PR2. (Note that both PR2 and PR4 are layered soil profiles.)

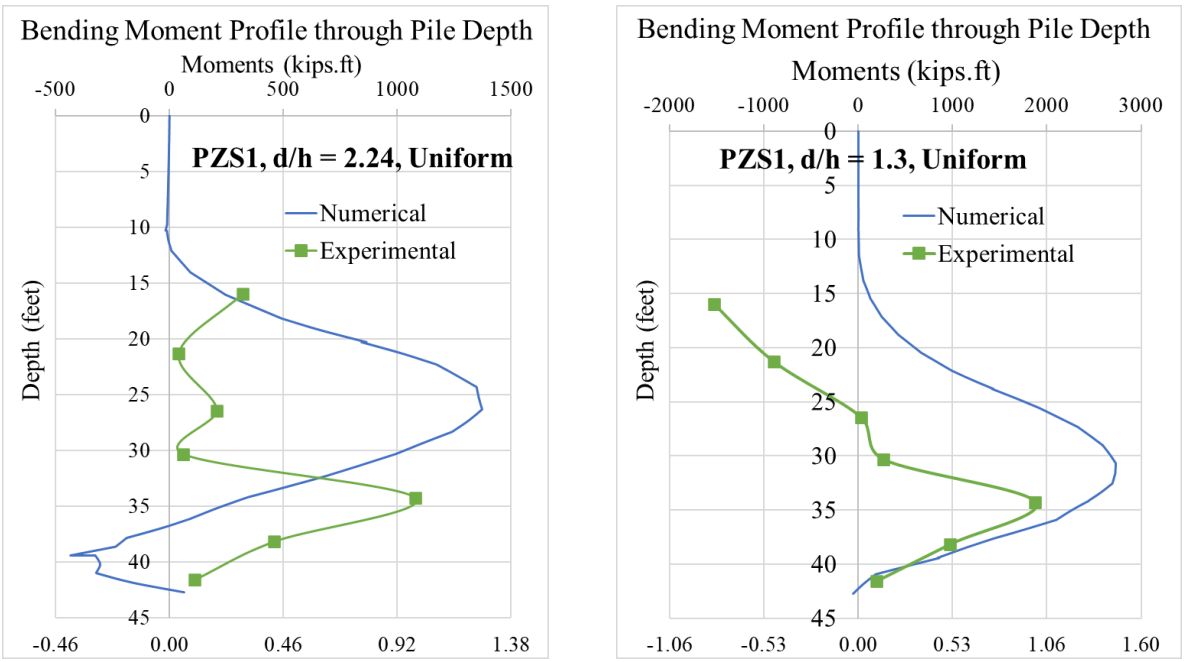

(a) (b)

Figure 0-18. Bending moment profiles in a 33 foot long sheet pile wall PZS1 in (a) the profile PR3 compared to that in (b) the profile PR1. (Note: both PR3 and PR1 are uniform soil profiles.)

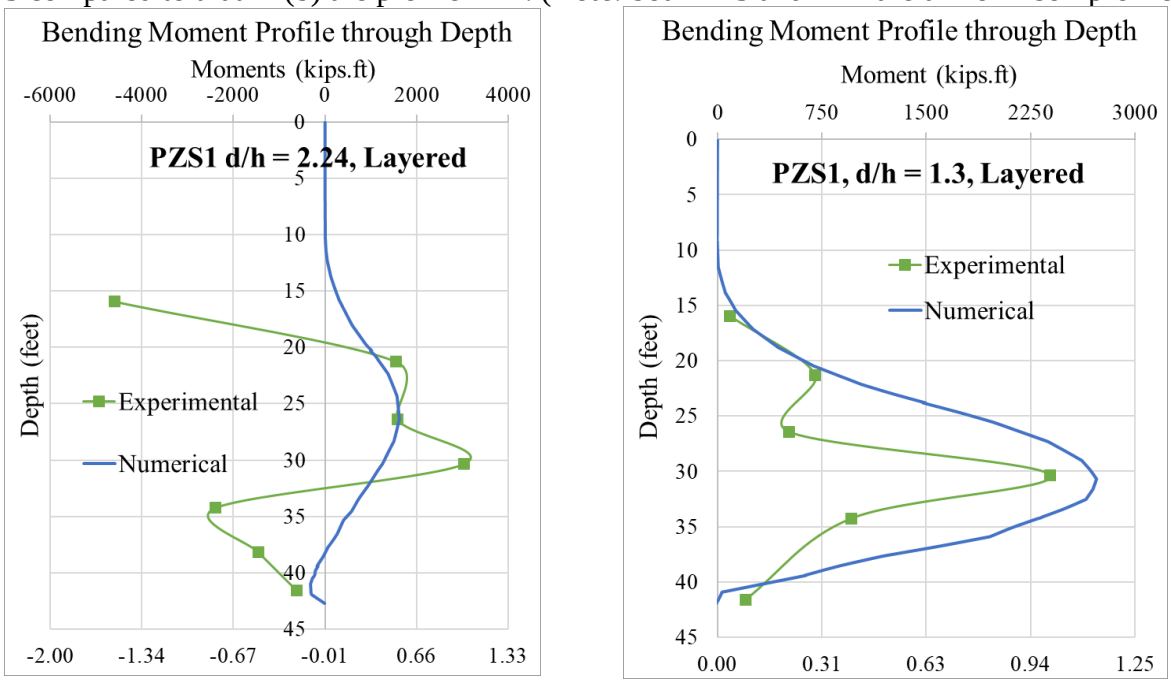

(a) (b)

Figure 0-19. Bending moment profiles in a 33 foot long sheet pile wall PZS1 in (a) the profile PR4 compared to that in (b) the profile PR2. (Note: both PR4 and PR2 are layered soil profiles.)

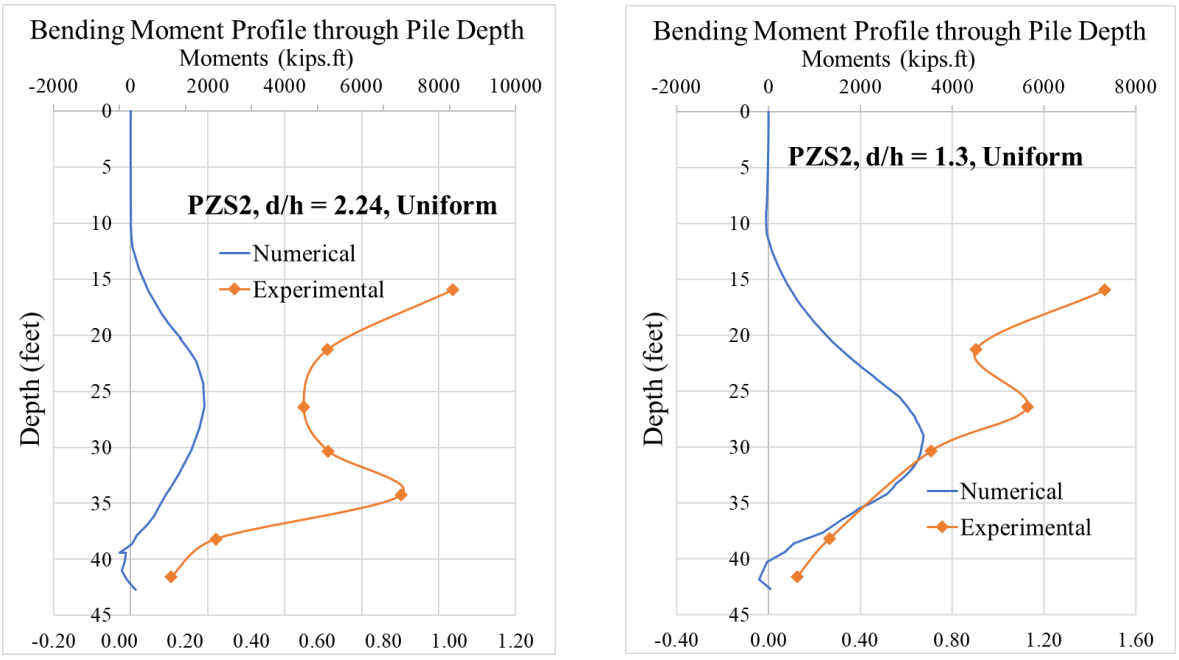

(a) (b)

Figure 0-20. Bending moment profiles in a 33 foot long sheet pile wall PZS2 in (a) the profile PR3 compared to that in (b) the profile PR1. (Note: both PR3 and PR1 are uniform soil profiles.)

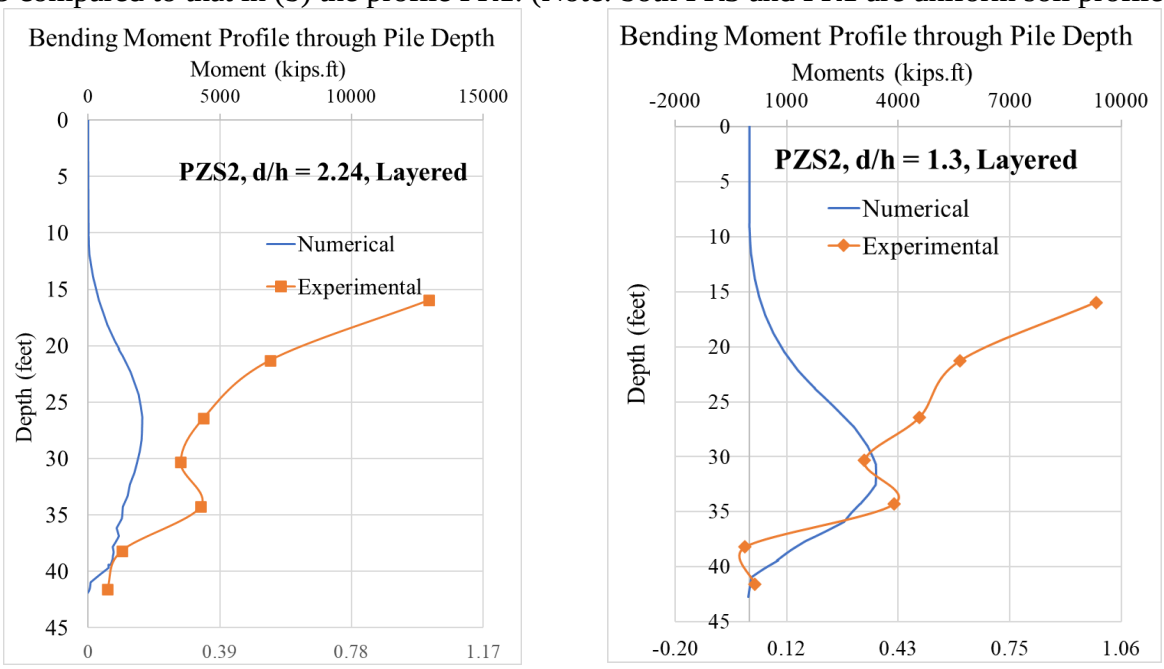

(a) (b)

Figure 0-21. Bending moment profiles in a 33 foot long sheet pile wall PZS2 in (a) the profile PR4 compared to that in (b) the profile PR2. (Note: both PR4 and PR2 are layered soil profiles.)

However, the amount of this increase in axial resistance is higher for the stratified profiles (up to 24% as can be seen in Figure 0-15) compared to those in homogenous sand profiles (about 17%, as shown in Figure 0-14). A similar trend is observed for the load tests on the PZS2 sheet pile (see Figure 0-16 and Figure 0-17).

Corresponding bending moment profiles are depicted in Figure 0-18 - Figure 0-21. For the section PZS1 pile wall (Figure 0-18 and Figure 0-19) it appears that the pile wall with d/h = 1.3 experiences greater bending moments acting on it than the corresponding pile wall with d/h = 2.24 in uniform and layered soil profiles. Moreover, for the PZS1 section pile wall the bending moments profile in centrifuge tests appear to follow the same trend as the numerical predictions. But this is not reproduced in the PZS2 section pile wall (Figure 0-20 and Figure 0-21). There appears to be an inverse correlation between axial resistance developed along the pile depth and bending moments acting on it when comparing piles with different embedment depth.

4.2.5 Sheet pile stiffness

The effects of bending and axial stiffness of the sheet pile elements on the axial resistance of the axially loaded sheet piles were studied. Two sheet pile walls with cross-sections similar to PZ sheet piles machined where the second sheet pile wall (PZS2) had higher (approximately twice) bending and axial stiffness than the first one (PZS1. Shown in Figure 0-22 - Figure 0-25 are the axial load distribution profiles for both PZS1 and PZS2 sheet piles. As it is evident, the PZS2 sheet pile develops consistently greater axial resistance than the PZS1 section pile wall. Accordingly, the experimental data reveals that the maximum bending moments experienced by PZS2 were more than that for the PZS1 sheet pile (Figure 0-26 - Figure 0-29). The numerical predictions, similarly, show a consistent trend of larger bending moments acting on the PZS2 profile when compared to the corresponding PZS1 profile. Different to the previous section, it appears that when comparing different pile walls, axial resistance and bending moments are directly correlated.

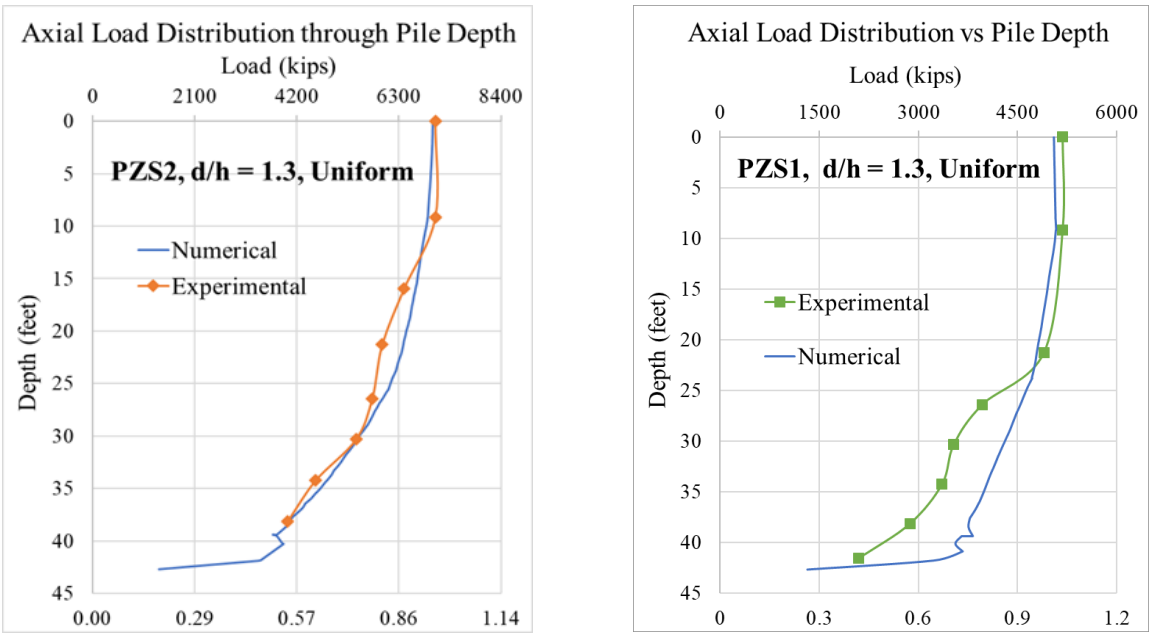

(a) (b)

Figure 0-22. Increased axial resistance in a 33 foot long sheet pile wall (a) PZS2 compared to (b) PZS1 in the profile PR1. (Note: PR1 has d/h = 1.3 and is uniform)

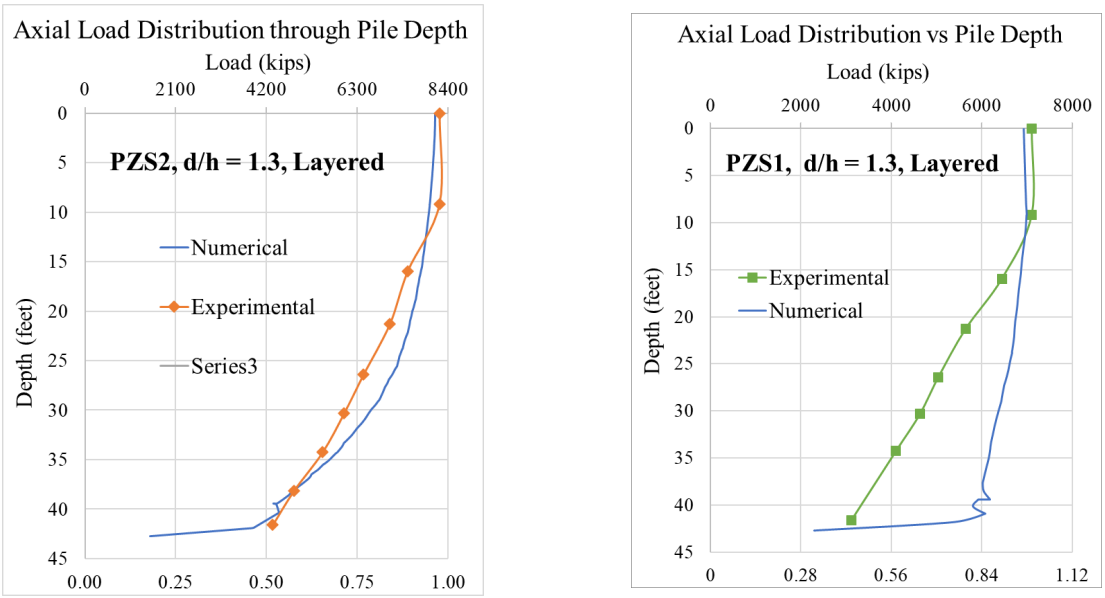

(a) (b)

Figure 0-23. Increased axial resistance in a 33 foot long sheet pile wall (a) PZS2 compared to (b) PZS1 in the profile PR2. (Note: PR2 has d/h = 1.3 and is layered)

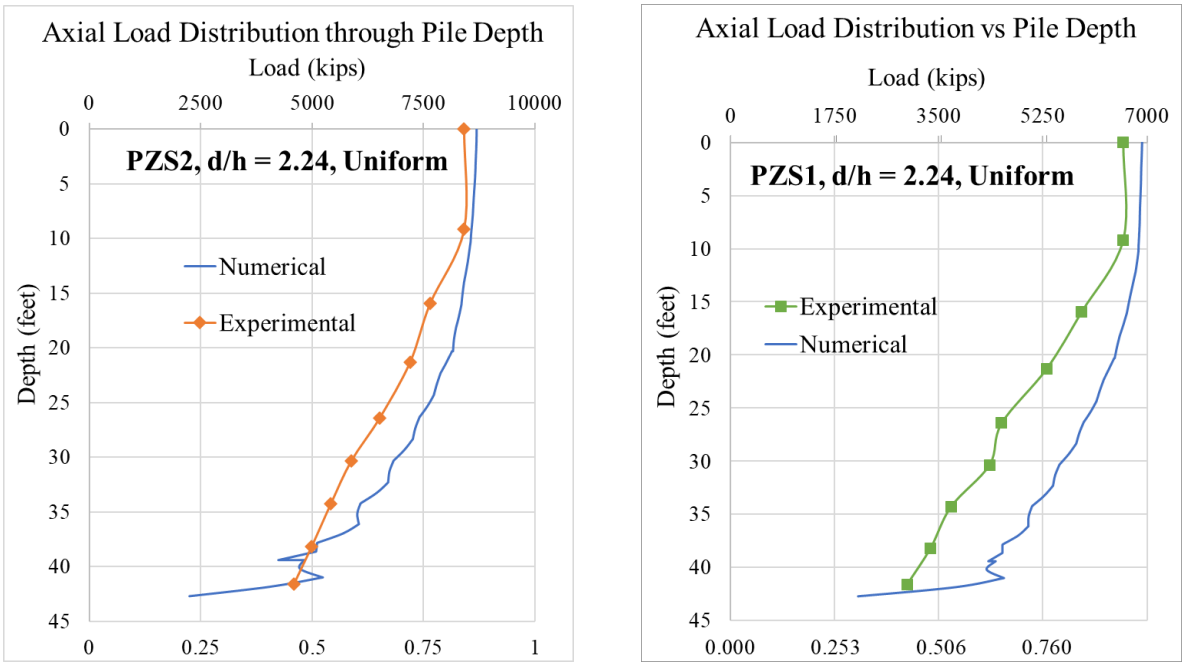

(a) (b)

Figure 0-24. Increased axial resistance in a 33 foot long sheet pile wall (a) PZS2 compared to (b) PZS1 in the profile PR3. (Note: PR3 has d/h = 2.24 and is uniform)

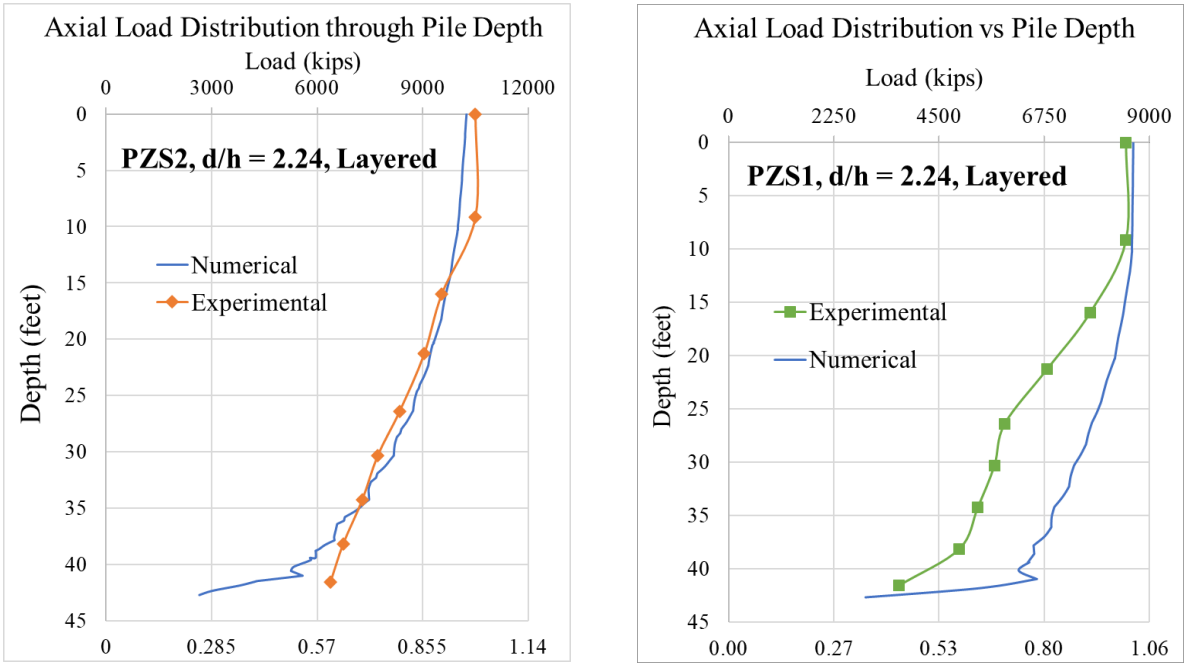

(a) (b)

Figure 0-25. Increased axial resistance in a 33 foot long sheet pile wall (a) PZS2 compared to (b) PZS1 in the profile PR4. (Note: PR4 has d/h = 2.24 and is layered.)

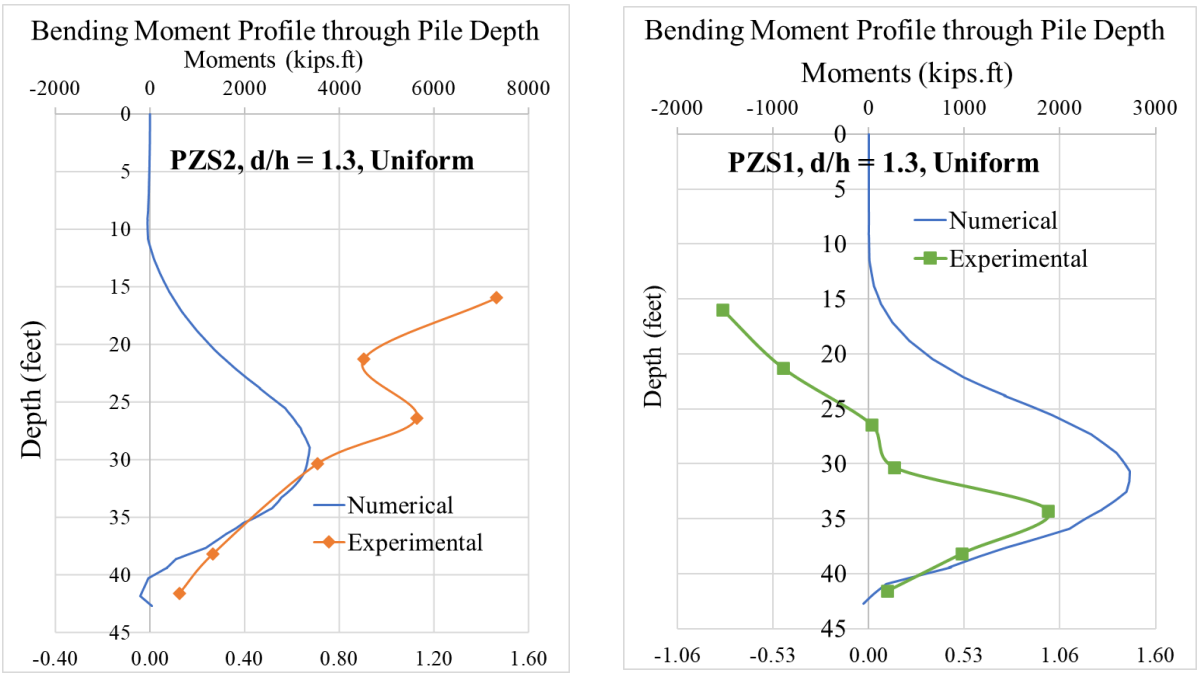

(a) (b)

Figure 0-26. Bending moment profiles in a 33 foot long sheet pile wall (a) PZS2 compared to that for the sheet pile wall (b) PZS1 in the profile PR1. (Note: PR1 has d/h = 1.3 and is uniform.)

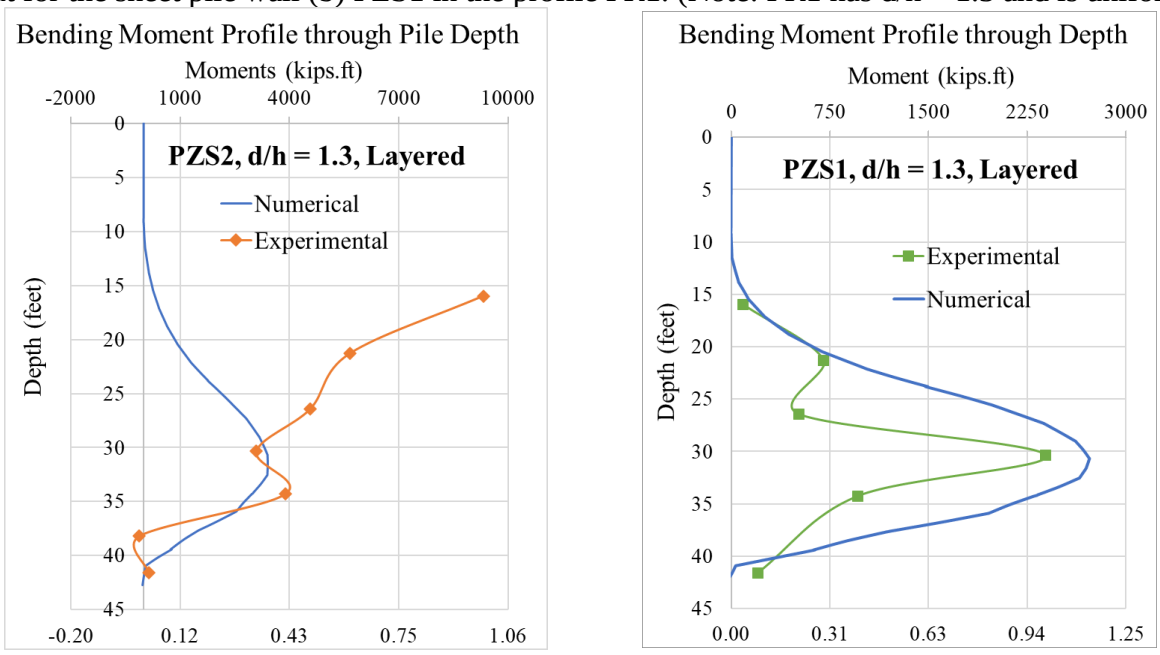

(a) (b)

Figure 0-27. Bending moment profiles in a 33 foot long sheet pile wall (a) PZS2 compared to that for the sheet pile wall (b) PZS1 in the profile PR2. (Note: PR2 has d/h = 1.3 and is layered.)

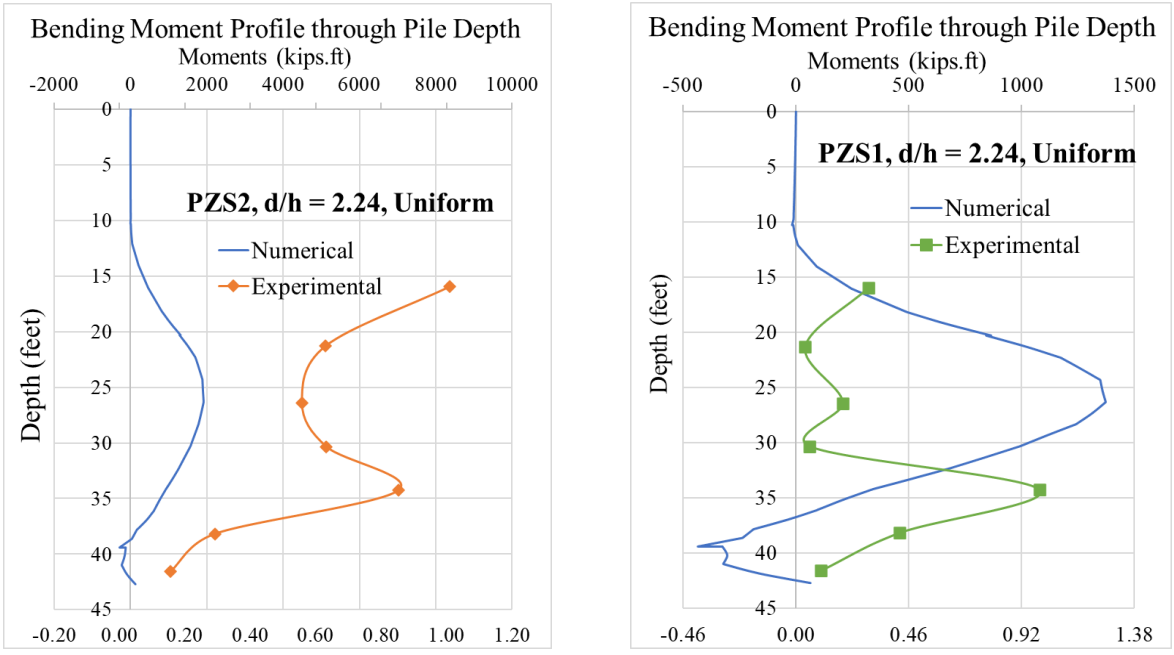

(a) (b)

Figure 0-28. Bending moment profiles in a 33 foot long sheet pile wall (a) PZS2 compared to that for the sheet pile wall (b) PZS1 in the profile PR3. (Note: PR3 has d/h = 2.24 and is uniform.)

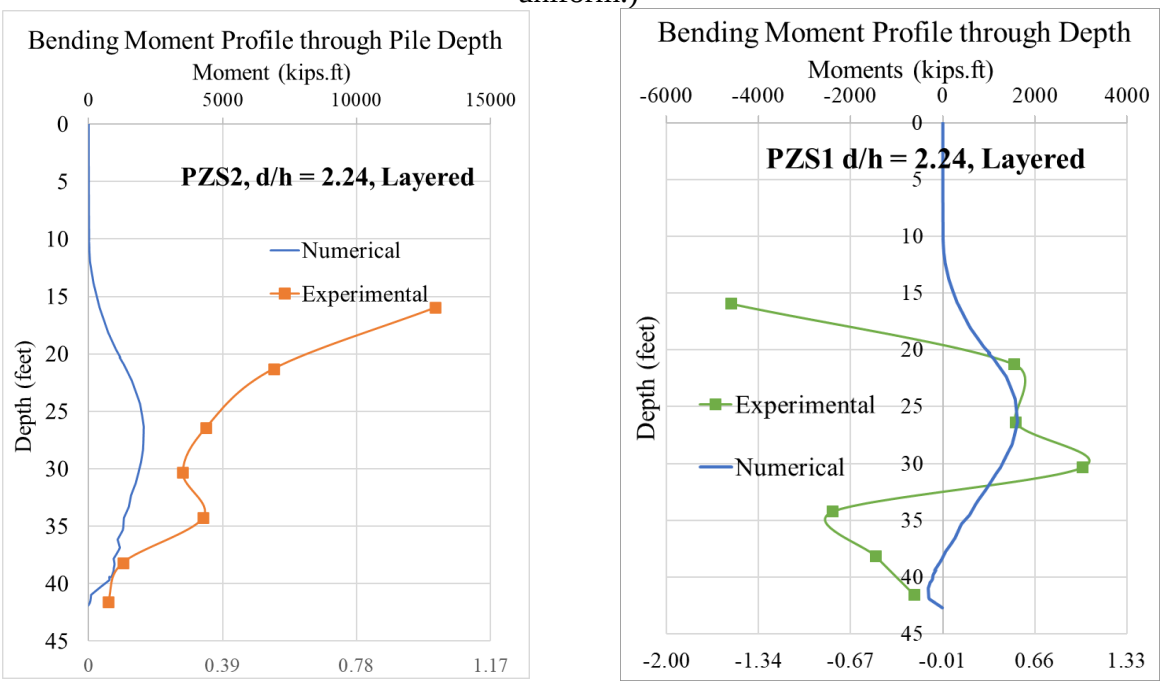

(a) (b)

Figure 0-29. Bending moment profiles in a 33 foot long sheet pile wall (a) PZS2 compared to that for the sheet pile wall (b) PZS1 in the profile PR4. (Note: PR4 has d/h = 2.24 and is layered.)

4.2.6 Sheet Pile Head Boundary Conditions

To determine the effects of the pile fixity condition centrifuge tests were carried out in the fixed and free head conditions. In the case of the free-head condition, the sheet pile could rotate freely inside the helmet providing active earth pressure on the retained soil (see Appendix B for details). In the fixed head condition, the helmet restricted the rotation of the pile wall along about the pile tip. In both cases, a vertical load was applied at the sheet pile top, simulating the vertical loads imposed by the superstructure. Axial load profiles for fixed and free head conditions were largely identical for the centrifuge tests and exactly identical in the numerical simulations and are thus not shown here. The bending moment distribution on the PZS1 sheet pile wall obtained from fixed-head load tests are presented in Figure 0-30 and Figure 0-31 for uniform and layered profiles, respectively. Similar profiles for PZS2 are shown in Figure 0-32 and Figure 0-33 for uniform and layered profiles, respectively. A considerably different bending moment distribution is observed in the fixed head condition.

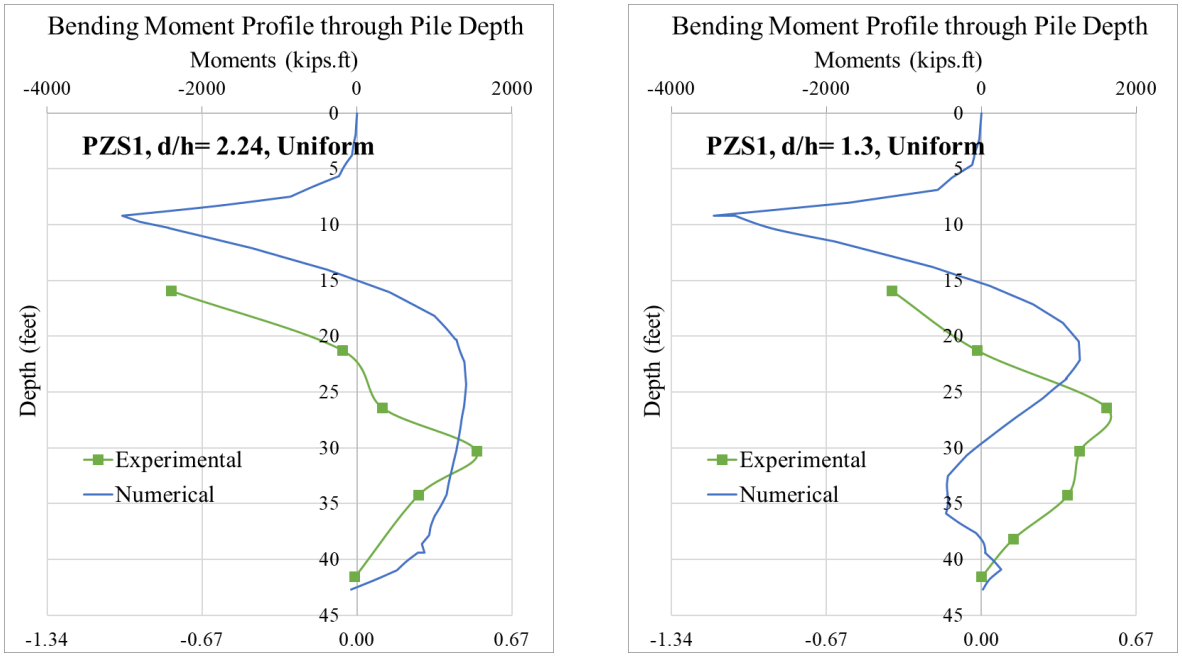

(a) (b)

Figure 0-30. Bending moment profiles in a 33 foot long sheet pile wall PZS1 in uniform soil profiles (a) PR3(d/h = 2.24) and (b) PR1 (d/h = 1.3) with a fixed head boundary condition.

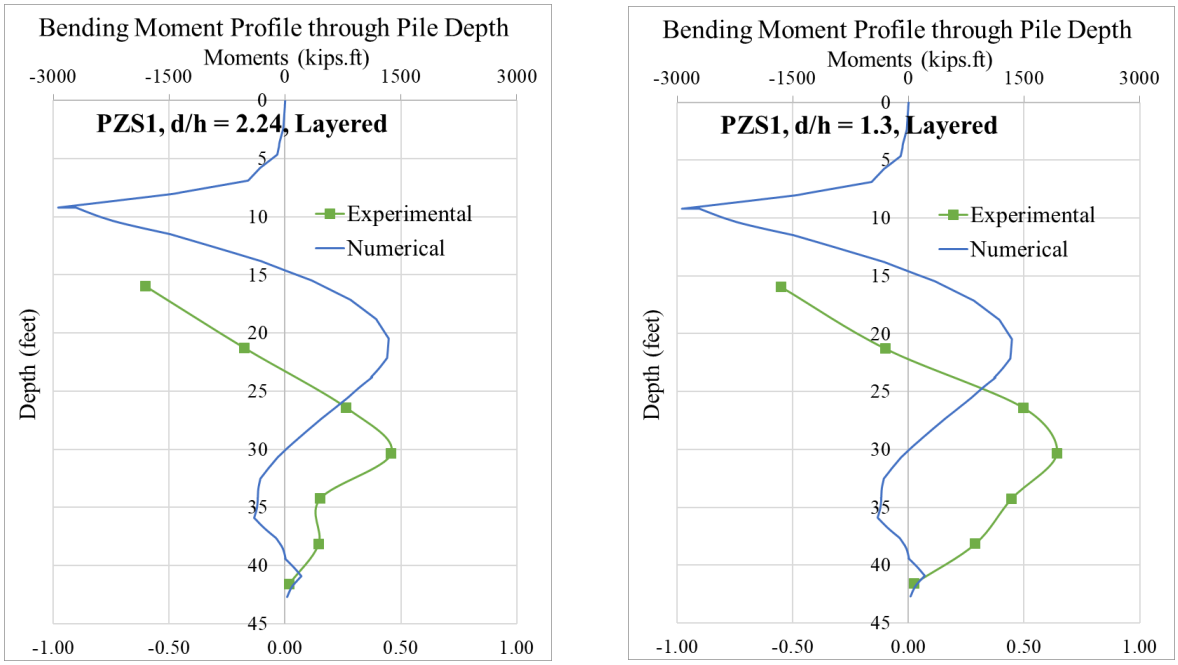

Figure 0-31. Bending moment profiles in a 33 foot long sheet pile wall PZS1 in layered soil profiles (a) PR4 (d/h = 2.24) and (b) PR2 (d/h = 1.3) with a fixed head boundary condition.

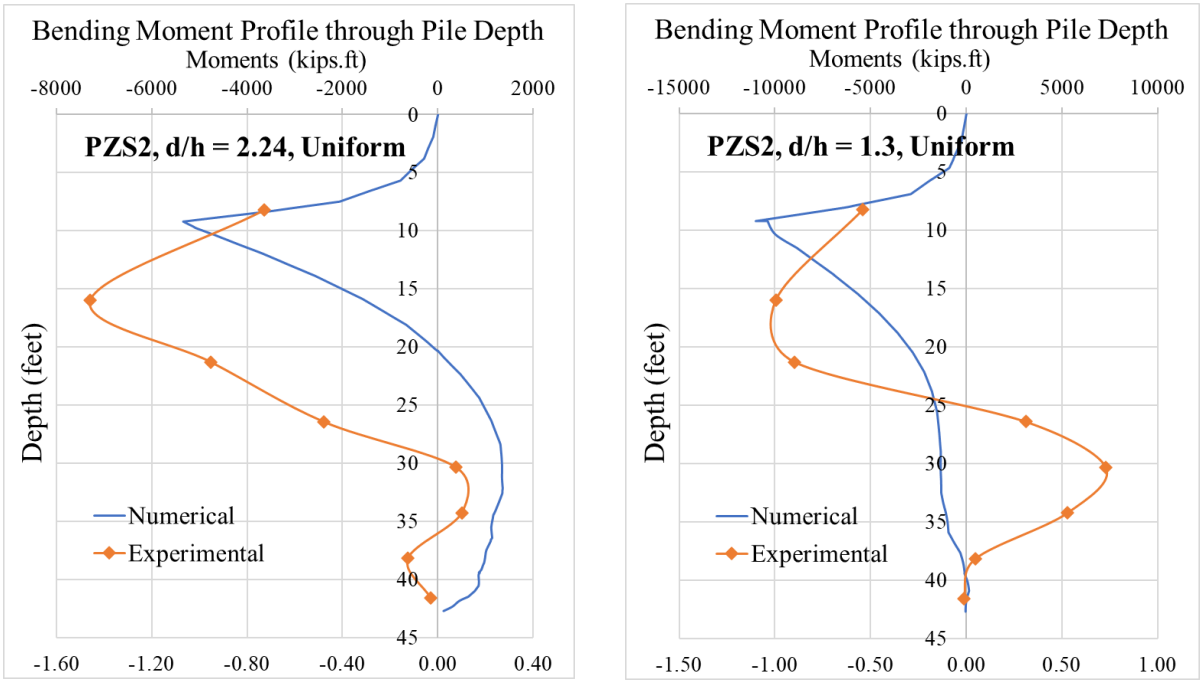

Figure 0-32. Bending moment profiles in a 33 foot long sheet pile wall PZS2 in uniform soil profiles (a) PR3 (d/h = 2.24) and (b) PR1 (d/h = 1.3) with a fixed head boundary condition.

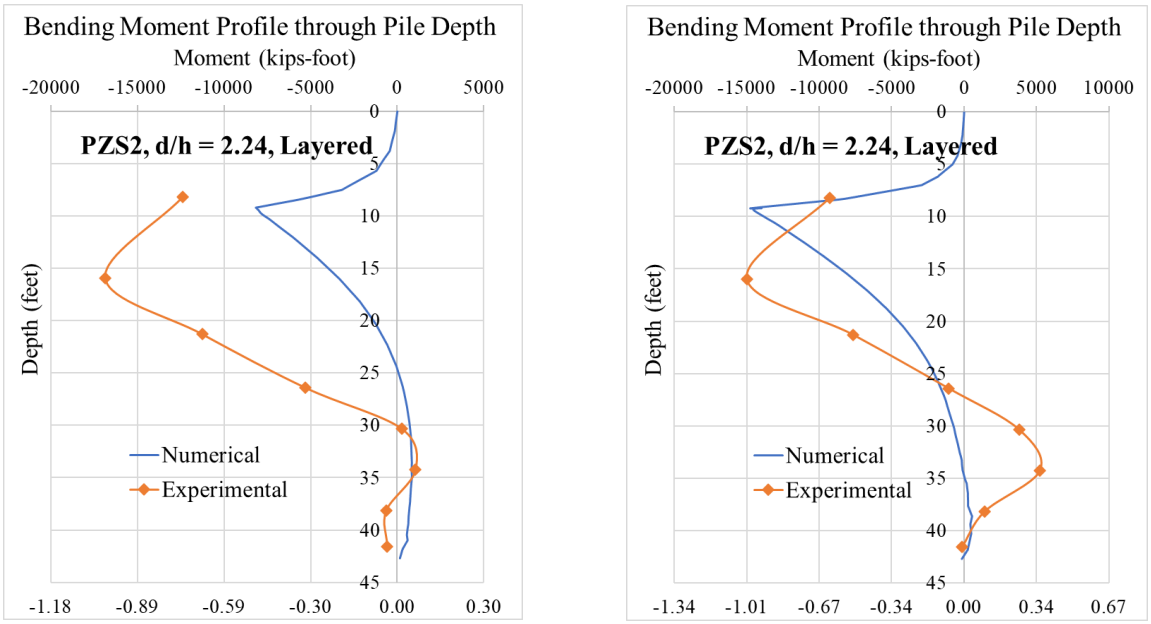

Figure 0-33. Bending moment profiles in a 33 foot long sheet pile wall PZS2 in soil profiles (a) PR4 and (b) PR2 with a fixed head boundary condition.

Having an “S” shaped bending moment profile, peak bending moments have been observed both below and above the dredge line, with maximums generally at the latter location. Contrary to the free head bending moment profiles there is better agreement in the trends of bending moment between the experimental observations and the numerical predictions for the fixed head condition. With that said, the peak negative moment develops at a location slightly above the ground level in the numerical observations whereas in the centrifuge tests they occur at the dredge line. The contradiction might be due to the way the fixed head condition was applied. In the numerical tests the pile head above the ground level was not allowed lateral motion whereas the helmet in the centrifuge tests only applied a restriction to the very top of the sheet pile wall.

4.3 Validating Load Bearing Capacity: Force displacement plots.

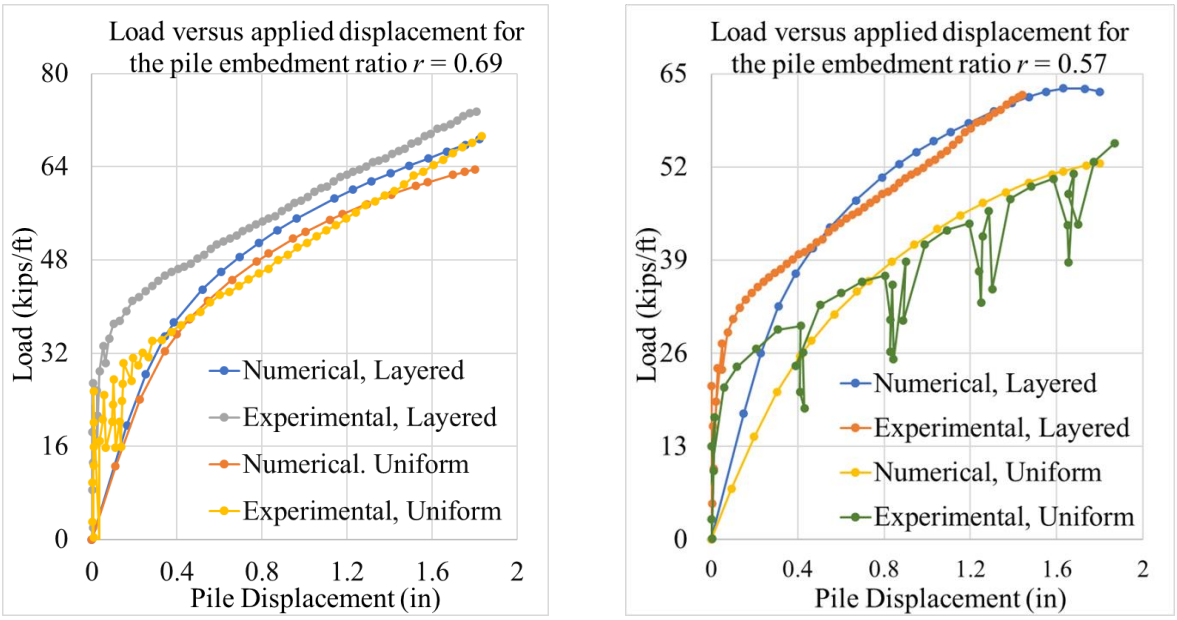

(a) (b)

Figure 0-34. Force displacement plots of the pile wall head for different soil profiles with a pile embedment ratio (a) d/h = 2.24 and (b) d/h = 1.3.

To validate the numerical model, we compare the numerical prediction of force displacement plot at the pile head to experimental observations of the same. In this case, instead of using the experimentally observed force data as a prescribed boundary condition a prescribed displacement is applied to the pile head with magnitude equal to the maximum vertical displacement provided in the centrifuge tests. Then, Figure 0-34 draws the force displacement curve of the for a pile wall in layered and uniform soil profiles for (a) d/h = 2.24 and (b) d/h = 1.3. The experimentally observed data is compared to numerical predictions of the same. It is apparent that the numerical model predicts similar failure load for a given displacement and is also capable of capturing the hardening effect of the soil under deformation. We note once again the remarkable contrast in the effects of soil layering on the bearing capacity: compare the significant gap between the failure loads in the case of (b) d/h =1.3 to the narrow one in the case of (a) d/h=2.24.

4.3.1 Design Recommendations informed by Validated Numerical Models

4.3.1.1 Relative density and bearing capacity.

Figure 2-42, Figure 2-43 and Figure 2-45 show the load versus vertical pile displacement curve for a pile embedded 3.3 ft in very dense, medium dense and loose sand profiles respectively. Ten values of embedded depth are considered for each soil profile. However, the sum of the the embedded depth (d) + retained soil height (h) is always constant. Though the total pile length is 42.7 feet (see Figure 0-1) d + h = 30 feet.

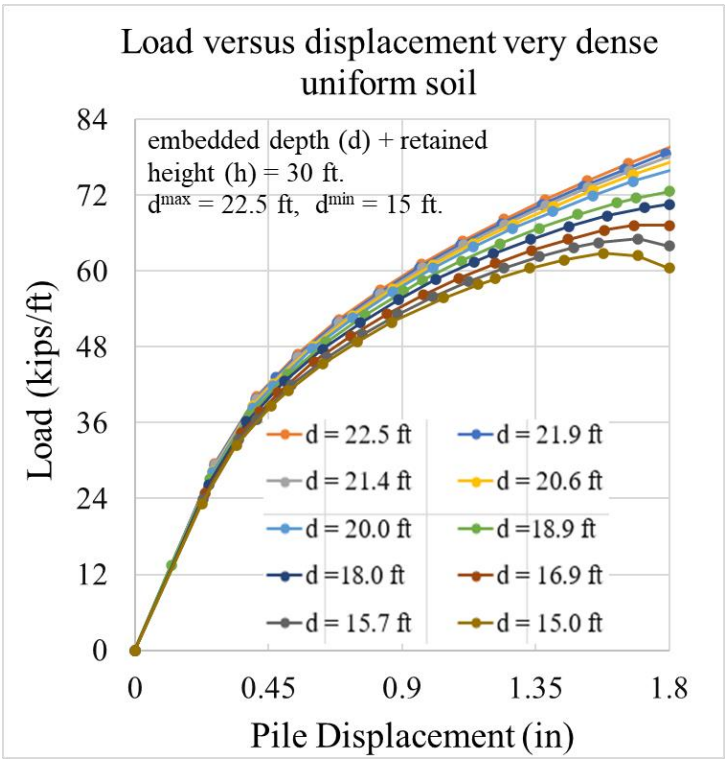

Figure 0-35. Applied load versus vertical displacement of a pile wall embedded in a very dense sand for different ratio of d/h.

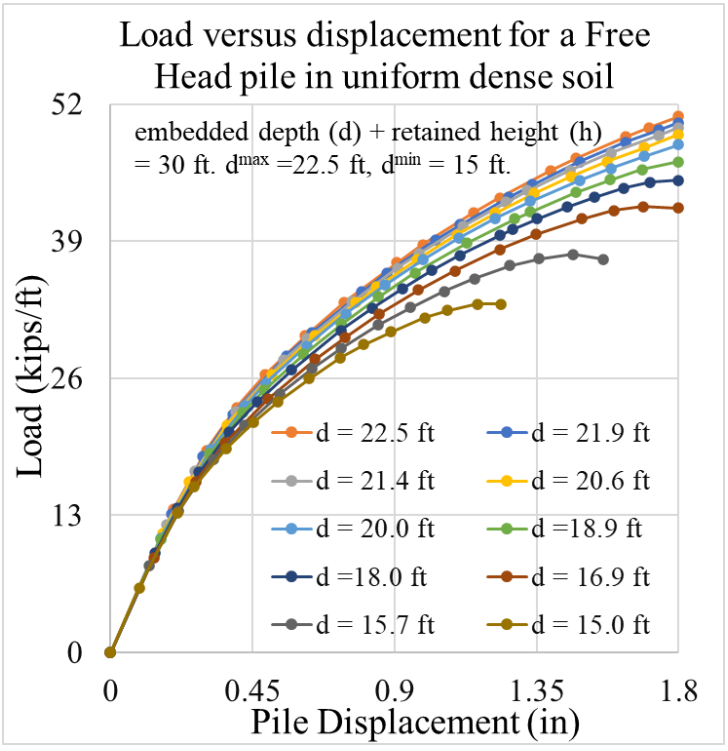

Figure 0-36. Applied load versus vertical displacement of a pile wall embedded in dense sand.

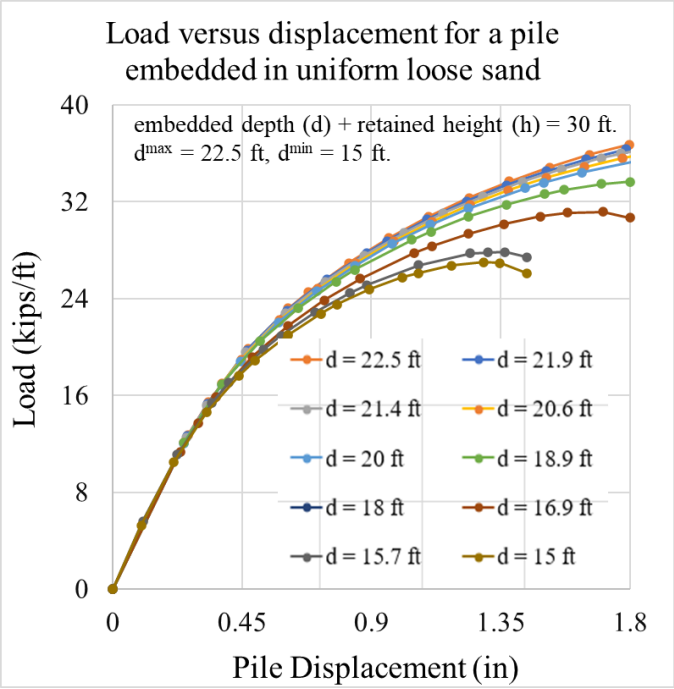

Figure 0-37. Applied load versus vertical displacement of a pile wall embedded in a loose sand for different ratio of d/h.

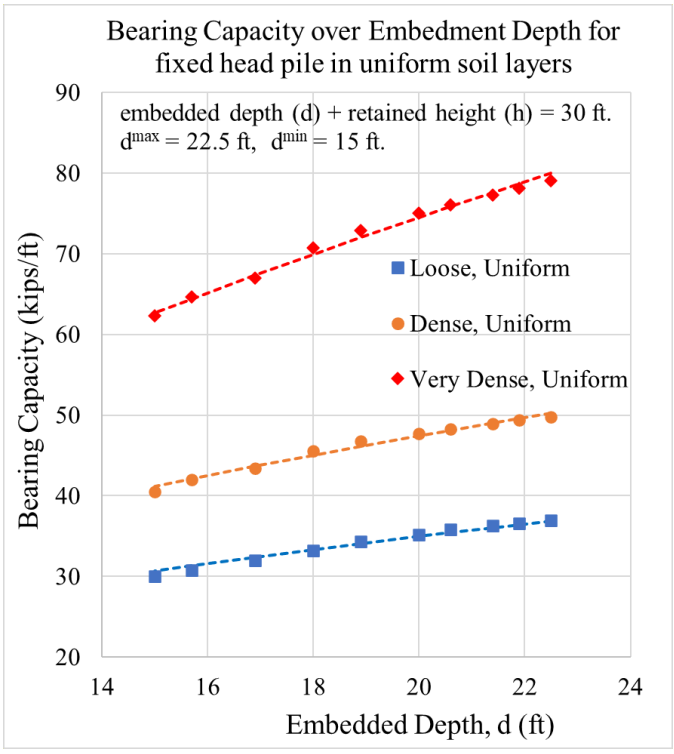

Figure 0-38 The bearing capacity of pile walls in uniform soils with different density. The dots represent data points and the dashed lines the power-law fit to the data.

The ultimate bearing capacity of sheet pile walls has a nonlinear relationship with the height of the retained soil / embedment ratio. For all three values of relative density, increasing d > 21.0 ft has very little effect on the predicted ultimate vertical bearing capacity. Based on the simulations above we can make some predictions on the relationship between the ultimate axial capacity and the embedment ratio in the soil. Figure 0-38 shows the relationship between the bearing capacity and the embedment ratio for three values of relative density. It is apparent that there is significant increase in the ultimate capacity with increasing relative density regardless of embedment depth. It is worth noting that for values smaller than d = 21.0 ft, reduction in embedment depth results in noticeable loss of bearing capacity for all three soils considered. To accurately reflect the vertical resistance of the pile the absolute value of embedment pile embedment, **d** must be used**.** On the other hand, the retained soil height **h** can reduce the bearing capacity by increasing active pressure on the pile. Therefore, we tentatively propose a three-parameter relationship between the bearing capacity Q_{ult}, soil internal friction ϕ, embedded depth and retained height **h**,

$$Q_{ult} = \left((d+h)/d\right)^{0.8421} * (tan\phi) * \mathrm{d}^{\mathrm{k}}\ kips/ft \qquad (1)$$

where, k = 1.2975 for loose sand,

k = 1.3312 for dense sand,

k = 1.444 for very dense sand.

For reference the internal friction angles are 27°, 32° and 35° for loose, dense and very dense sands respectively. The corresponding unit weights are 97.35, 101.7, and 106.2 pcf, respectively. Finally, the exponent on the ratio (0.8421) is constant for all soil properties. It is possibly a structural constant related to the material or physical properties of the sheet pile wall itself. We note that these equations are exclusive to the PZ-27 section of sheet piles and for the case of dry sand. Changing pile sections would change the surface area and the skin friction developed along the pile which would alter the bearing capacity. Similarly, the presence of water in the pores can dramatically alter the strength properties of the soil.

The relationship proposed in (1) is restricted to very specific values of the internal friction and soil unit weight. More data is needed to generate a useable relationship that is more broadly applicable. By running simulations at a constant unit weight and changing the friction angle and subsequently applying equation (1) to the data we get a broad range of values for the exponent **k** as a function of **ϕ.** Figure 0-38 plots the bearing capacity of fixed head piles in uniform, very dense sand layers for three different values of soil internal friction angle **ϕ**. Figures Figure 0-39 and Figure 0-40 do the same for dense and loose soil layers, respectively

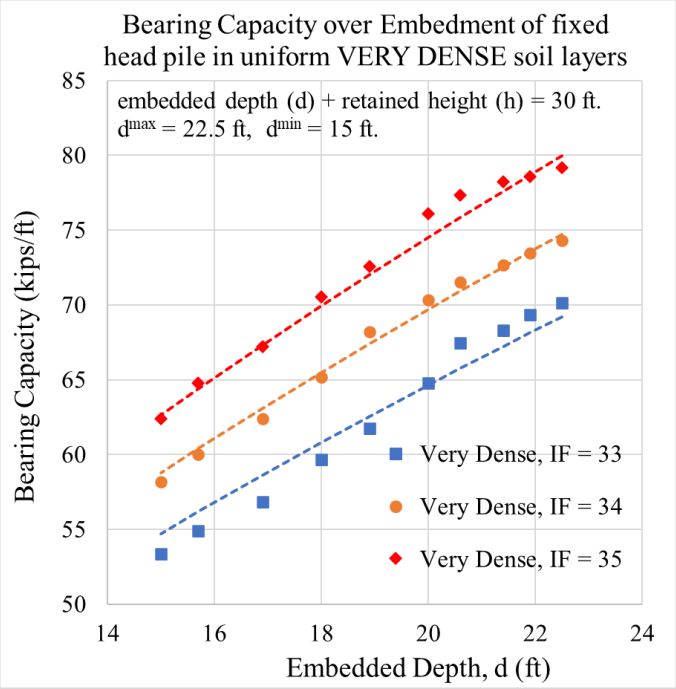

Figure 0-39 The bearing capacity of pile walls in uniform, very dense soils with different internal friction angles. The dots represent data points and the dashed lines the power-law fit to the data.

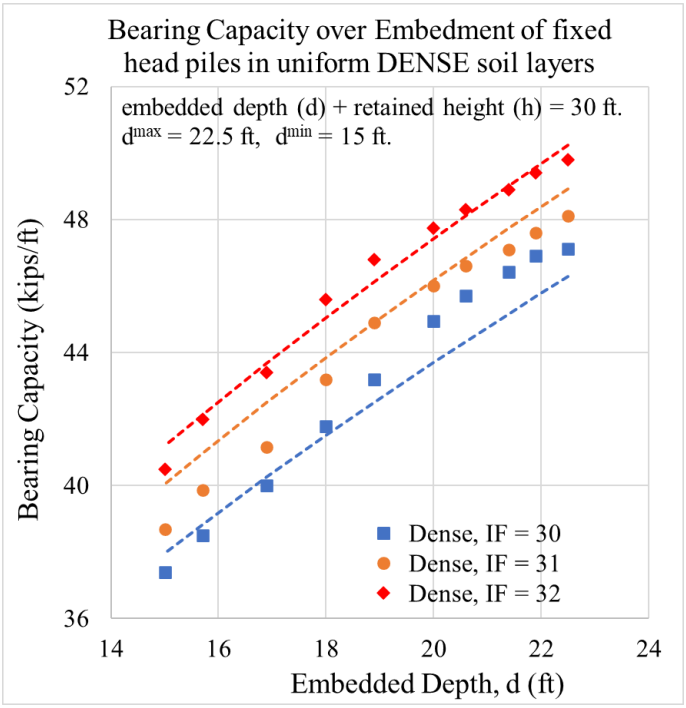

Figure 0-40 The bearing capacity of pile walls in uniform, dense soils with different internal friction angles. The dots represent data points and the dashed lines the power-law fit to the data.

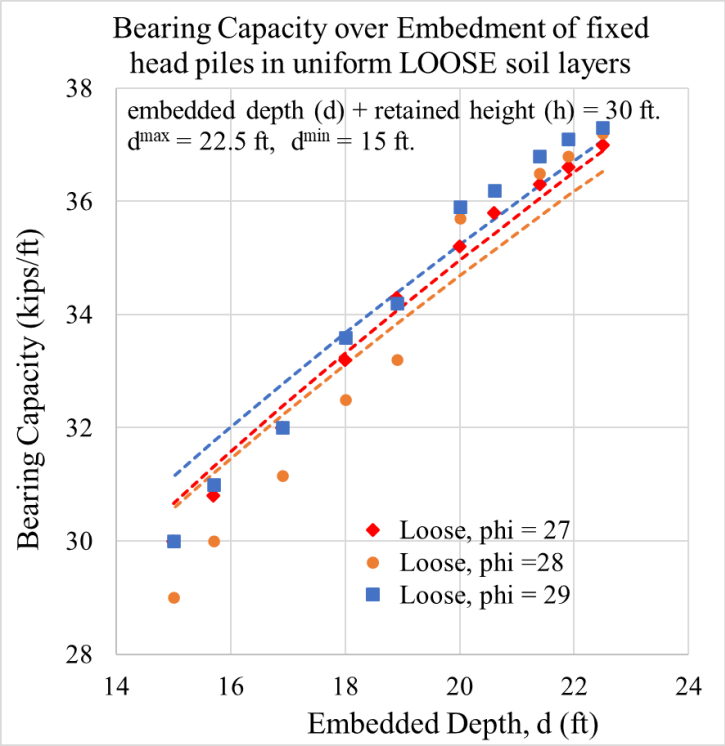

Figure 0-41 The bearing capacity of pile walls in uniform, loose soils with different internal friction angles. The dots represent data points and the dashed lines the power-law fit to the data.

Figure 0-42 plots the values of **k** derived from the simulation data. From the figure it is apparent that the **k** values occur in three different clusters with each cluster being associated with a constant unit weight for the soil. A best fit line being difficult to obtain we instead present an envelope of acceptable values using two different relationships for k:

$$\boldsymbol{k} = 0.0169\boldsymbol{\phi} + 0.8003, \tag{2}$$

$$\boldsymbol{k} = 0.025\boldsymbol{\phi} + 0.5984, \tag{3}$$

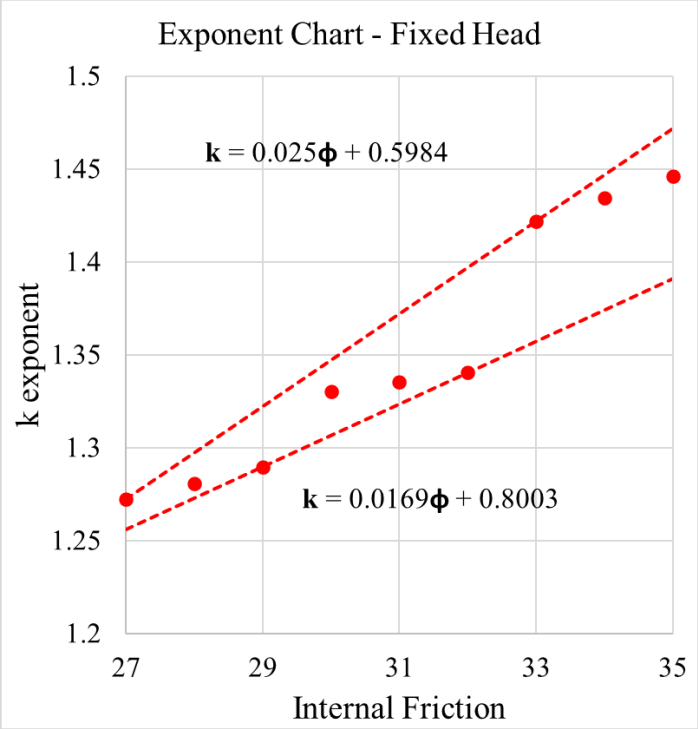

Figure 0-42 The range of values of the exponent **k** for different values of internal friction angle.

Given the wide range in the k exponent it is important to examine the performance of the proposed **k**-ϕ relationship relative to the predicted bearing capacity from the numerical simulations. We consider the specific scenario of a sheet pile wall with (d)/(d+h) = 0.66, h = 10 ft and d = 20 ft. Figure 0-43 compares the predicted bearing capacity from numerical simulations to the predictions made using equation (1) when using the different **k**-ϕ relationships.

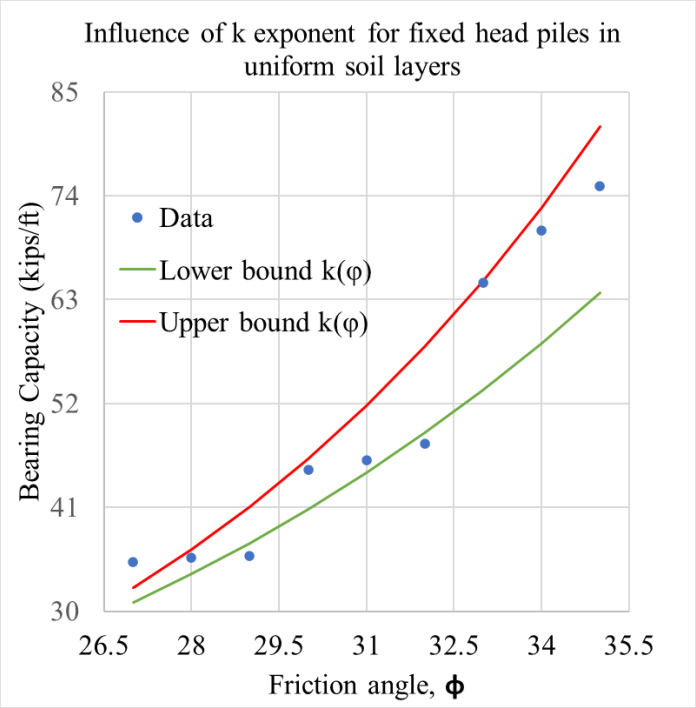

Figure 0-43 Comparison of the design equation for fixed head pile in uniform soil to the numerical data

It is apparent that using the upper bound for the k exponent in equation (1) causes it to consistently overpredict the predicted bearing capacity. But when using equation (2) in combination with the design equation (green line) we see that the predictions have a factor of safety in nearly all cases. Therefore it is our recommendation that equation (3) be neglected in favor of equation (2) to compute the **k** exponent from the soil friction angle **ϕ**.

Finally, we examine the influence of the unit weight on the proposed relationship between bearing capacity and embedment of the pile. We present the results of simulations conducted using different unit weight of soil for a constant soil internal friction angle. Three values of unit weight are considered at each internal friction angle as shown in Table 0-1. . The values in boldface are the baseline values used to develop the relationship presented in (1).

Table 0-1. Soil Unit Weights and Relative Density for simulations

Soil Classification	Internal Friction ϕ	Unit Weights (pcf)	Relative Density D_r (%)
Loose	27	94.90, **97.35**, 98.59	30, **42**, 48
Dense	32	99.83, **101.7**, 103.5	54, **63**, 72
Very Dense	35	104.4, **106.2**, 107.7	76, **85**, 92

Figure 0-44 plots the bearing capacity of pile walls embedded in loose soils with different unit weights represented by their relative density D_r. Figure 0-45 and Figure 0-46 do the same for piles embedded in dense and very dense uniform soil profiles. As expected, increasing the soil unit weight increased the ultimate bearing capacity even when the friction angle remained constant.

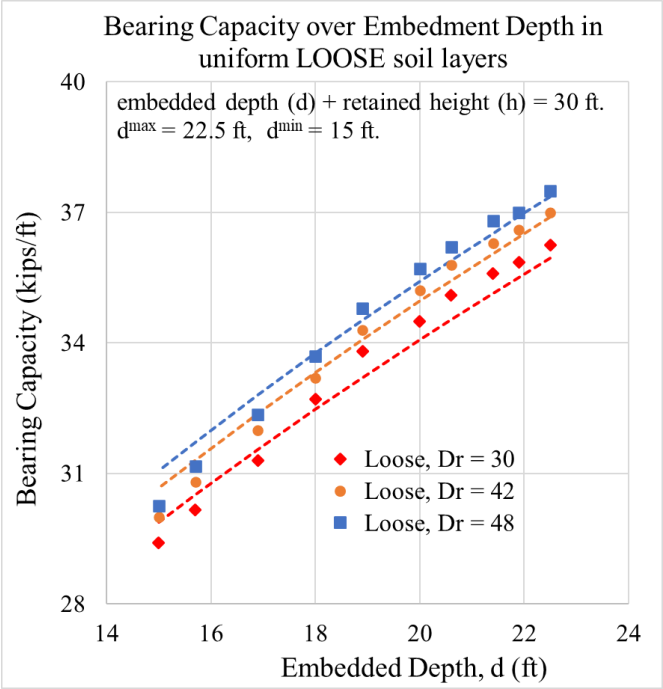

Figure 0-44 The bearing capacity of pile walls in uniform, loose soils with different unit weights. The dots represent data points and the dashed lines the power-law fit to the data.

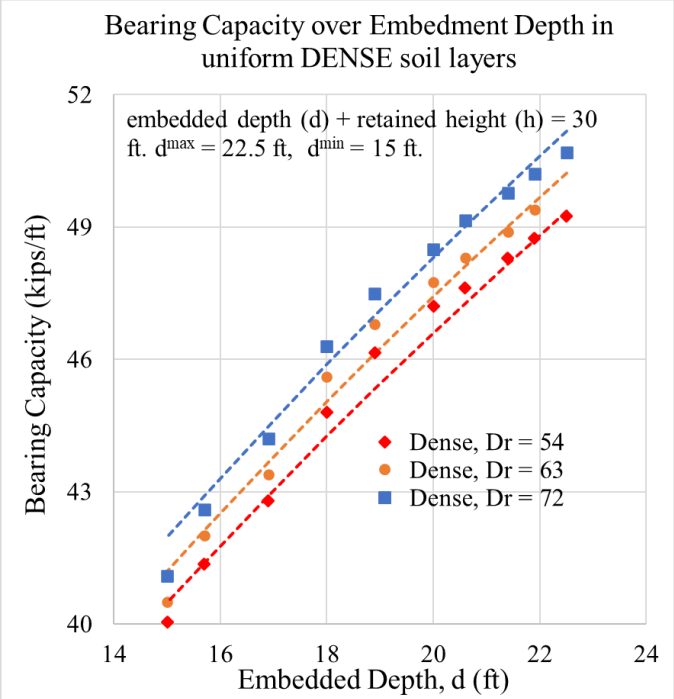

Figure 0-45 The bearing capacity of pile walls in uniform, dense soils with different unit weights. The dots represent data points and the dashed lines the power-law fit to the data.

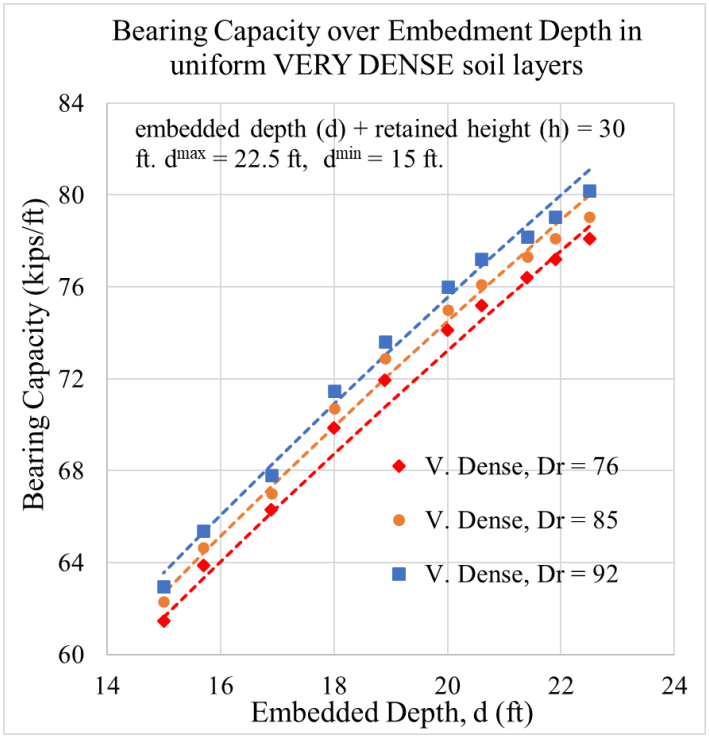

Figure 0-46 The bearing capacity of pile walls in uniform, dense soils with different unit weights. The dots represent data points and the dashed lines the power-law fit to the data.

From these results we propose the following modification to equation (1) for soil unit weights different from the ones utilized in this study,

$$Q_{ult} = \frac{\gamma'}{\gamma'_0}\left((d+h)/d\right)^{0.8421} * (tan\phi) * \mathrm{d}^{\mathrm{k}} kips/ft, \qquad (4)$$

where γ' is the design effective unit weight of the soil and γ'_0 is the baseline effective unit weight considered in this study, shown in boldface in Table 0-1. . Note that this relationship has been used to generate the power law fits shown in Figure 0-44, Figure 0-45 and Figure 0-46.

4.3.2 Effects of Soil Layering

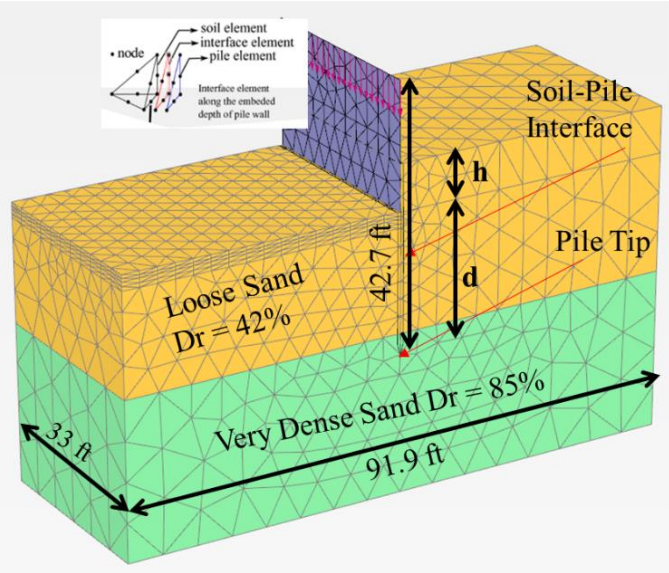

Figure 0-47 An illustration of the layered soil profile A modeled in this subsection.

In the following results, the pile tip was embedded 3.3 ft into a very dense soil layer with the pile wall being used to retain a different soil layer overlaying the very dense layer (Please see Figure 0-47 and Figure 0-48 for clarification). The top layer is soil is varied between loose and dense sand, with the bottom layer always being a very dense sand. For convenience we define, Profile A as a loose sand layer overlaying a very dense sand and Profile B as a dense sand layer overlaying a very dense sand. These scenarios are referred in this chapter as the layered profiles.

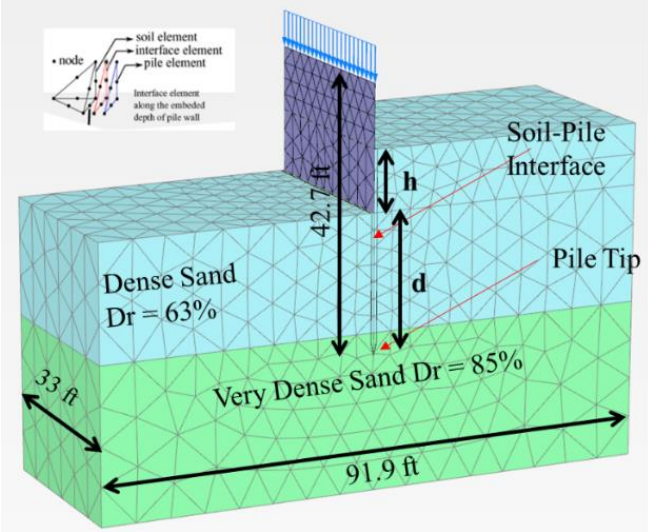

Figure 0-48 An illustration of the layered soil profile B modeled in this subsection.

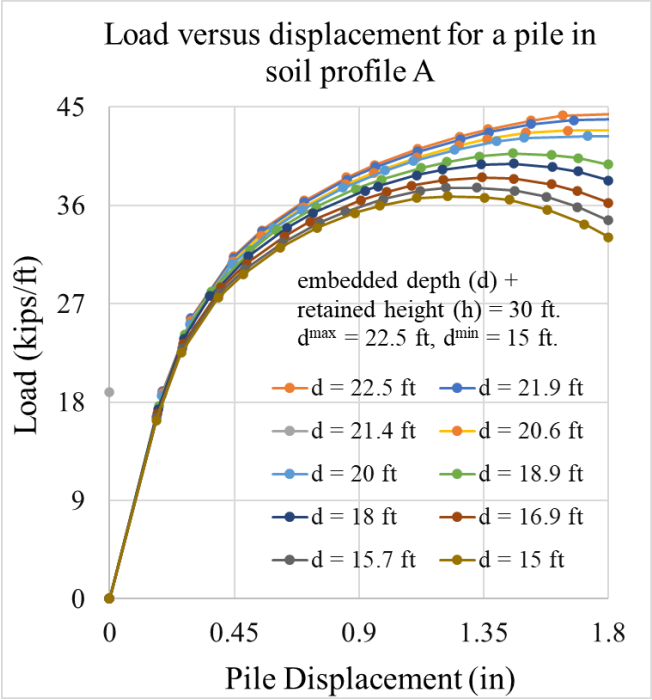

Figure 0-49 Applied load versus vertical displacement of a pile wall in soil Profile A.

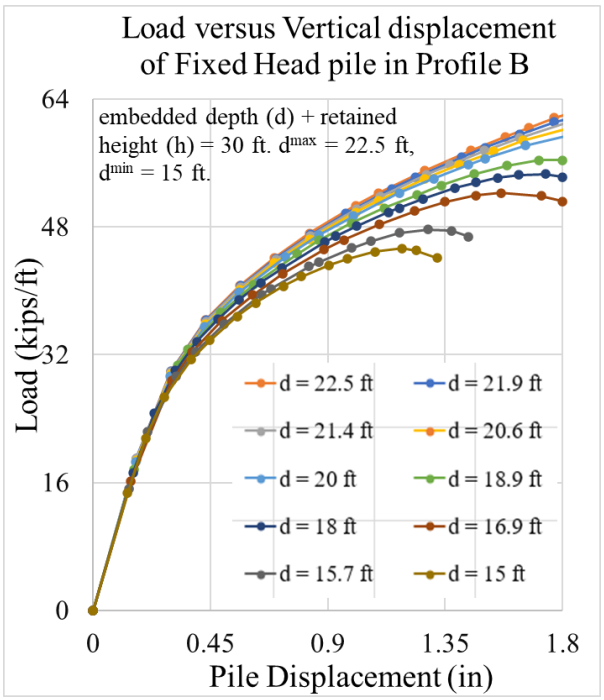

Figure 0-50 Applied load versus vertical displacement of a pile wall in soil Profile B.

The influence of soil layering is made apparent by comparing Figure 0-37 to Figure 0-49 for the loose sand top layer and Figure 0-36 to Figure 0-50 for the dense sand top layer.

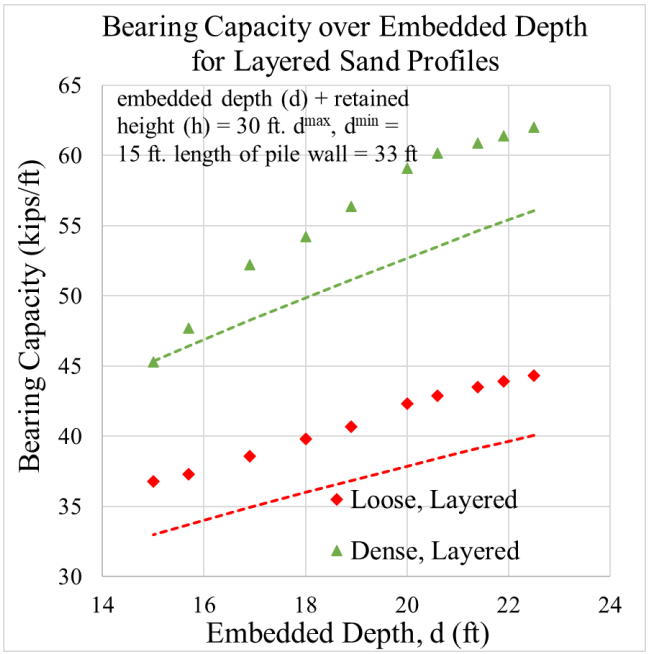

Figure 0-51 The bearing capacity of pile walls in layered soil profiles. The dots represent data points and the dashed lines the power-law fit to the data.

From Figure 0-51, we tentatively propose the following relationship for the ultimate bearing capacity of pile walls in layered sand profiles,

$$Q_{ult} = \frac{\gamma'}{\gamma'_0}\left((d+h)/d\right)^{0.8421} * (tan\phi) * d^{(k1+k2)/2}\ kips/ft\ for\ layered\ soil \quad (5)$$

where k1 and k2 are the exponents for the overlying and underlying layer of sands, respectively. We have used the equation (2), the lower bound **k-ϕ** relationship, in equation (5) to generate the fit to the data (dashed lines). It is worth noting here that the friction angle of the overlaying soil is used in the term $tan(\phi)$, which is the factor representing the skin friction. Since only 3 ft of the total 30 feet of pile is embedded in the bottom (very dense) soil layer it is assumed the resistance developed from skin friction is still the dominant component of the ultimate bearing capacity. For reference the internal friction angles are 27°, 32° and 35° for loose, dense and very dense sands respectively. In both cases, using equation (2) in equation (5) leads to significant under-prediction of the bearing capacity relative to the numerical simulation data. The design equation has a factor of safety built into it.

4.3.2.1 Head Boundary Conditions of the sheet pile

In the following results, section we discuss the influence of head boundary conditions on the predicted vertical bearing capacity of sheet pile walls.

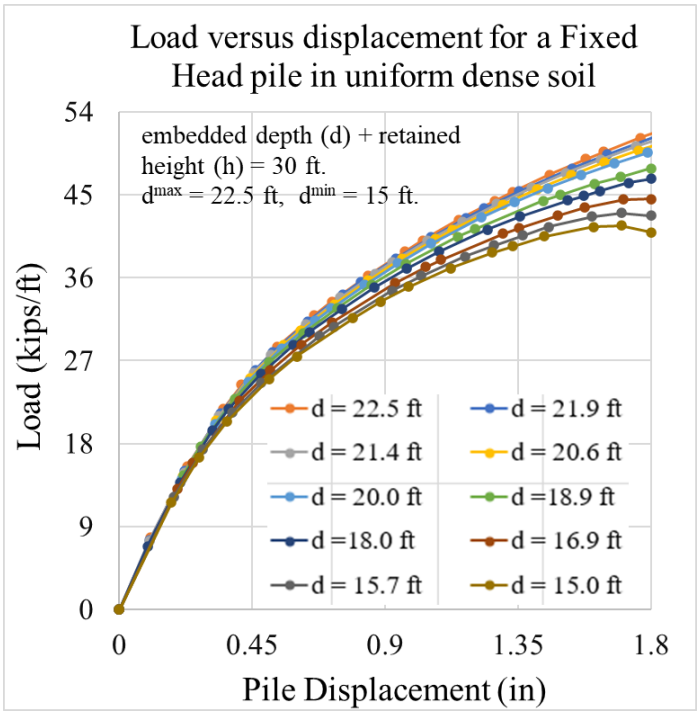

Figure 0-52 Applied load versus vertical displacement of a pile wall with a fixed head embedded in uniform dense sand profile for different values of embedded depth.

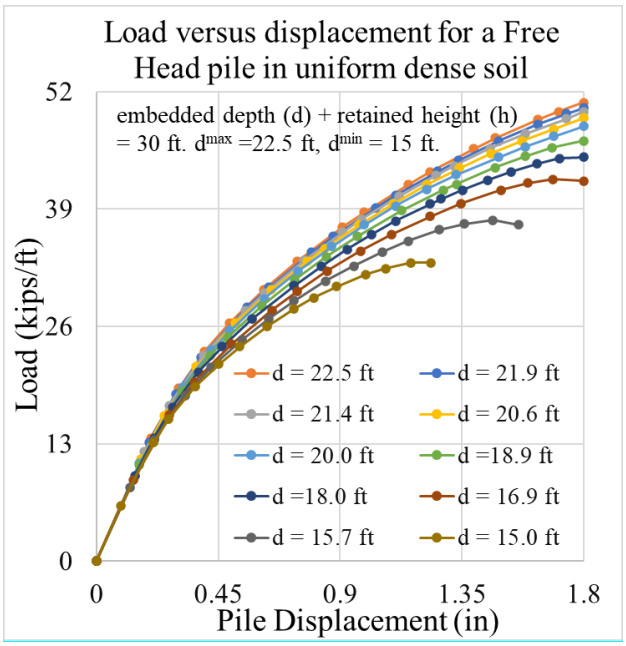

Figure 0-53 Applied load versus vertical displacement of a pile wall with a free head embedded in uniform dense sand profile for different values of embedded depth.

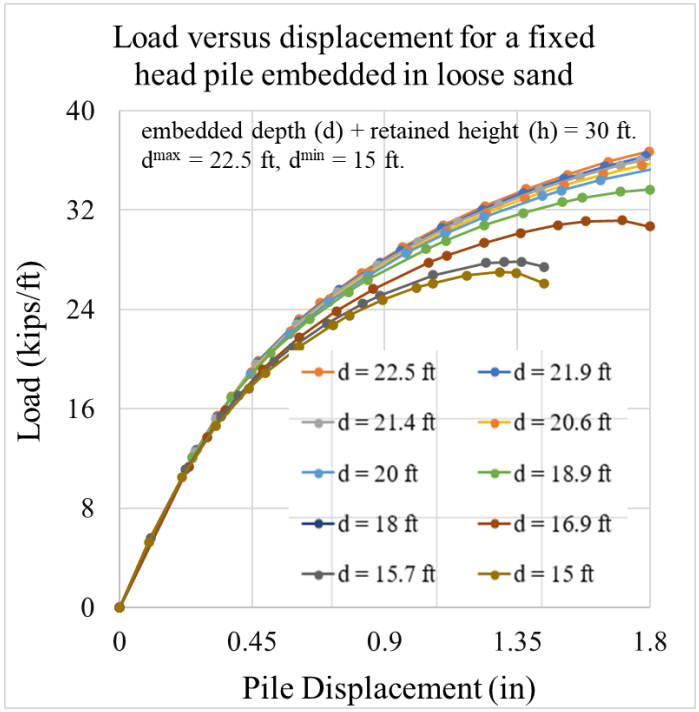

Figure 0-54 Applied load versus vertical displacement of a pile wall with a fixed head embedded in uniform loose sand profile for different values of embedded depth.

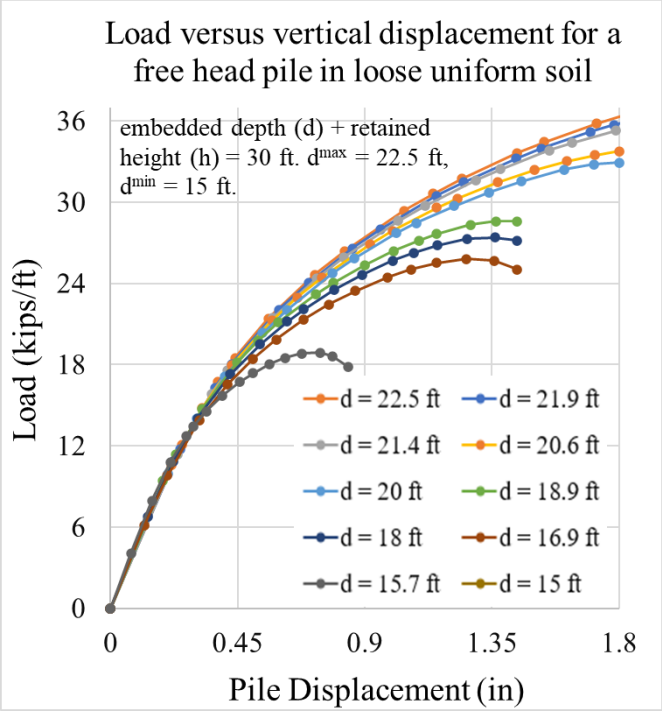

Figure 0-55 Applied load versus vertical displacement of a pile wall with a free head embedded in uniform loose sand profile for different values of embedded depth.

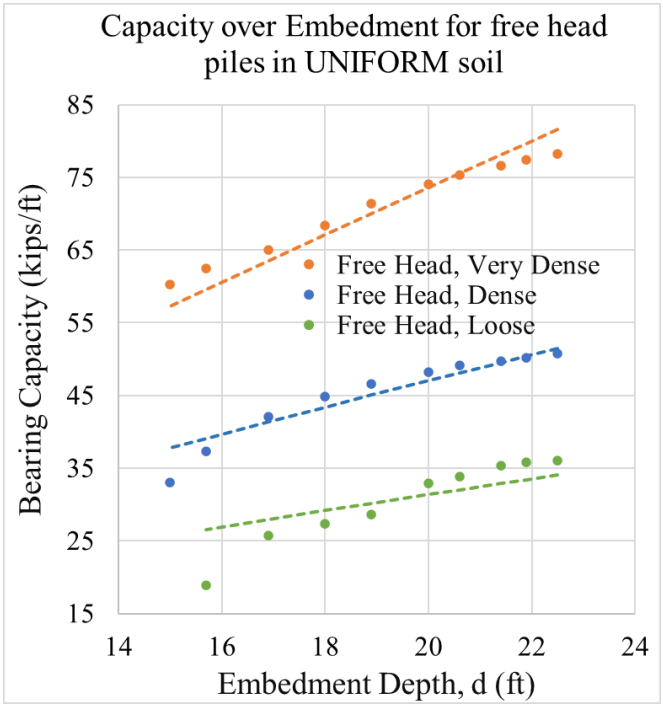

Figure 0-56 The bearing capacity of pile walls in different uniform sand profiles with different head conditions. The dots represent data points and the dashed lines the power-law fit to the data.

Figure 0-52 and Figure 0-53 plot the load applied against vertical pile displacement in dense sand profile for a fixed and free head condition, respectively. Figure 0-54 and Figure 0-55 plot the load applied against vertical pile displacement in uniform loose sand profile for a fixed and free head condition, respectively. Figure 0-56 plots the ultimate capacity against the embedment ratio for a free head pile embedded in uniform soil profiles. Comparing Figure 0-56 to Figure 0-38 it is apparent that for a pile wall embedded in dense or very dense sand, the head boundary condition only has significant effects on bearing capacity for d < 20 ft. These effects are also noticeably greater in loose sands than it is in dense sands or very dense sands. Based on the simulation data presented in Figure 0-52 - Figure 0-55, and the findings discussed in Section 2.8.1, we propose the following relationships for a free head pile in uniform soil layers,

$$Q_{ult} = \frac{\gamma'}{\gamma'_0}\left((d+h)/d\right)^{0.6} * (tan\phi) * \mathrm{d}^{\mathrm{k}}\ kips/ft, \qquad (6)$$

where, k = 1.2941 for loose sand,

k = 1.3611 for dense sand,

k = 1.473 for very dense sand.

Note the change in the exponent on the ratio $\left((d+h)/d\right)$ to 0.6 now. To reiterate, this exponent is likely a structural constant related to the pile properties. Once again we run simulations using a range of internal friction angles to gain a general range of **k** values.

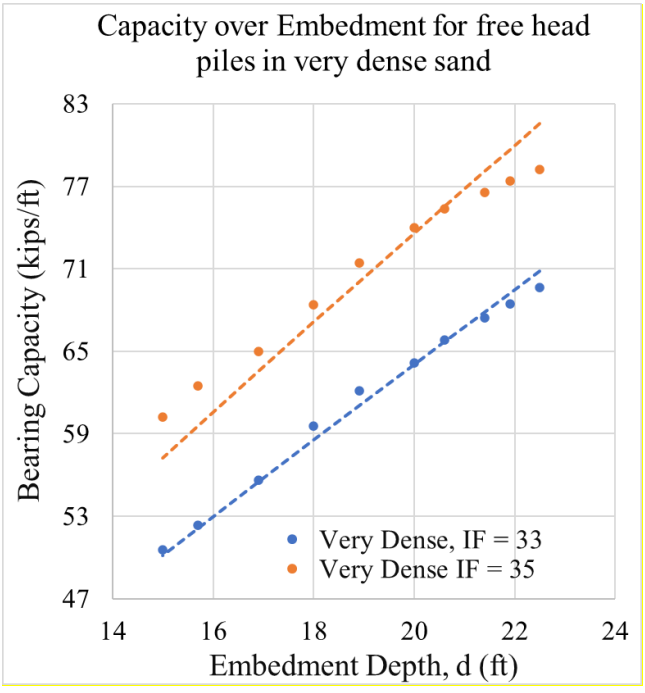

Figure 0-57 The bearing capacity of pile walls in uniform very dense sand profiles with free heads. The dots represent data points and the dashed lines the power-law fit to the data.

Figure 0-57 - Figure 0-59 compare the influence of soil friction angle on the bearing capacity of free head piles in very dense, dense and loose soil, respectively. The unit weights are constant for each type of soil. From these simulation results and the fits applied to them following equation (6), we can plot the variation of the **k** exponent with **ϕ** in the case of free head pile systems.

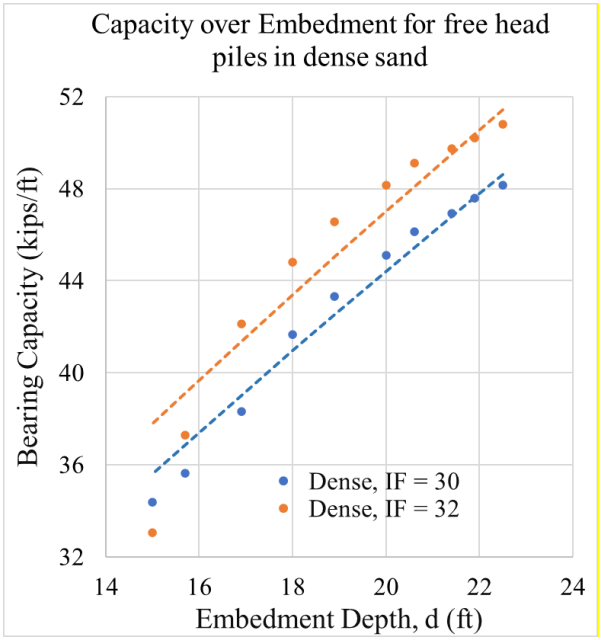

Figure 0-58 The bearing capacity of pile walls in uniform dense sand profiles with free heads. The dots represent data points and the dashed lines the power-law fit to the data.

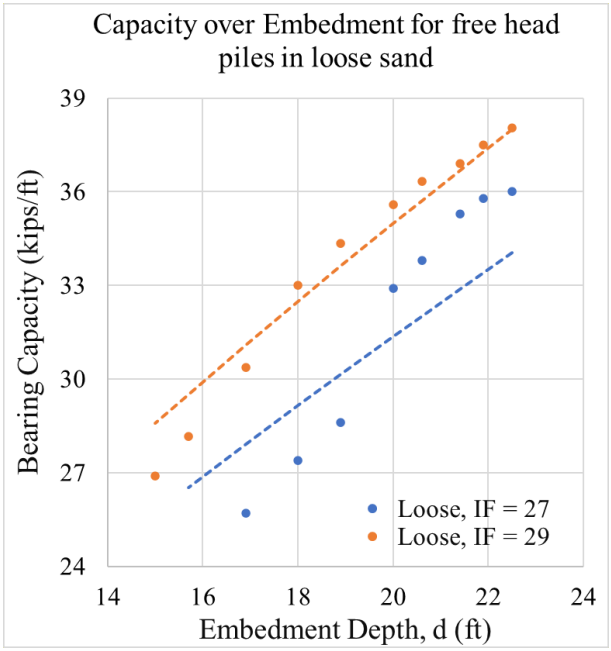

Figure 0-59 The bearing capacity of pile walls in uniform loose sand profiles with free heads. The dots represent data points and the dashed lines the power-law fit to the data.

Figure 0-60 plots the variation of the **k** exponent with the internal friction angle **ϕ** for a free head sheet pile wall in uniform soil layers.

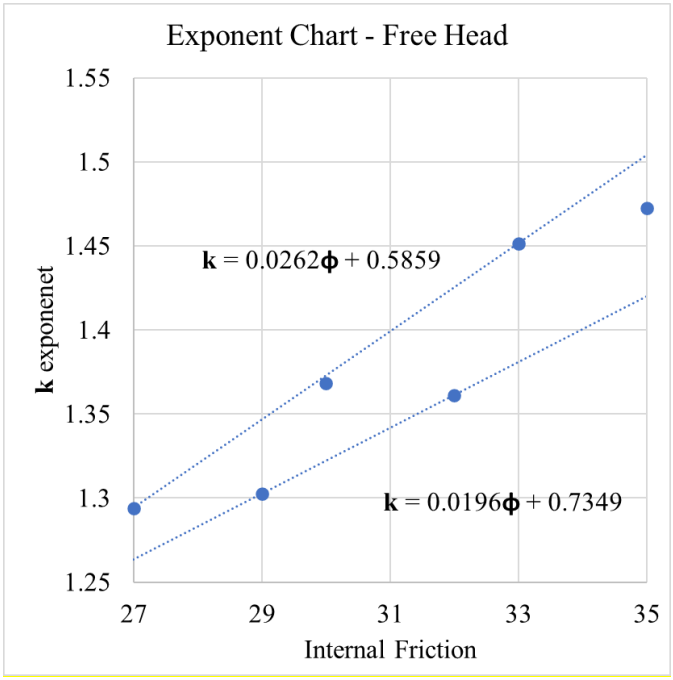

Figure 0-60 The range of values for the k exponent as a function of the soil internal friction

We present two possible relations for the **k** exponent,

$$\boldsymbol{k} = 0.0196\boldsymbol{\phi} + 0.7349, \quad (7)$$

$$\boldsymbol{k} = 0.0262\boldsymbol{\phi} + 0.5859, \quad (8)$$

Next, we examine the performance of the proposed **k- ϕ** relationships in (7) and (8) relative to the predicted bearing capacity from the numerical simulations. We consider the specific scenario of a sheet pile wall with (d)/(d+h) = 0.66, h = 10 ft and d = 20 ft. Figure 0-61 compares the predicted bearing capacity from numerical simulations (blue points) to the predictions made using the design equation (6) with the different **k- ϕ** relationships.

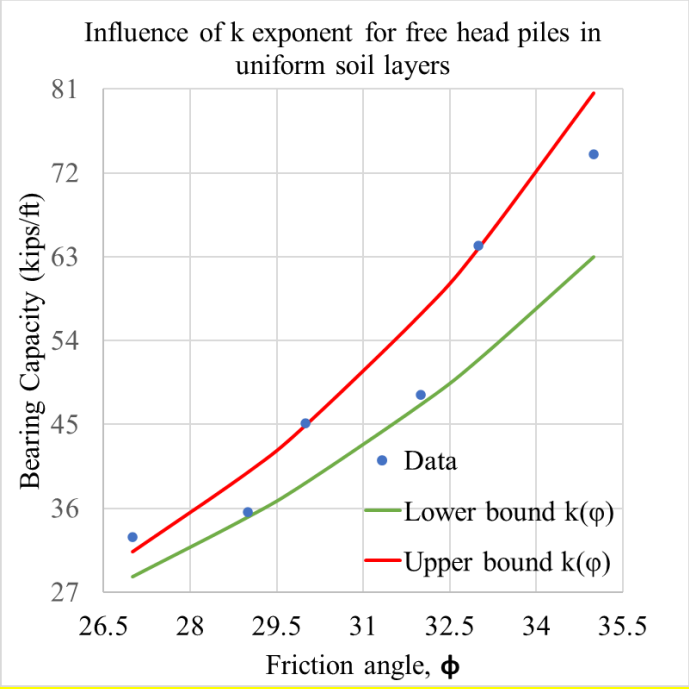

Figure 0-61 Comparison of the results from the design equation for free head pile in uniform soil to the numerical data

It is apparent that the using the lower bound **k- ϕ** relationships in (7) with the design equation in (6) yield predictions that have a natural safety factor.

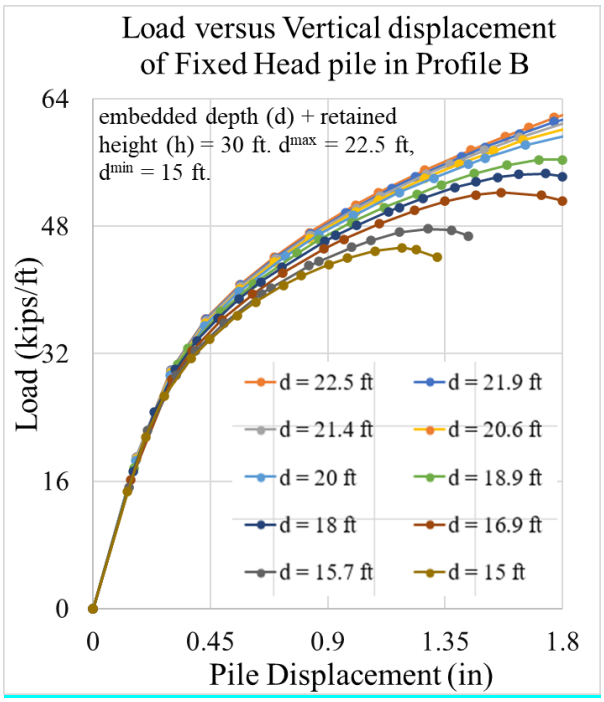

Figure 0-62 Applied load versus vertical displacement of a pile wall with a fixed head embedded in layered dense sand profile for different values of embedded depth.

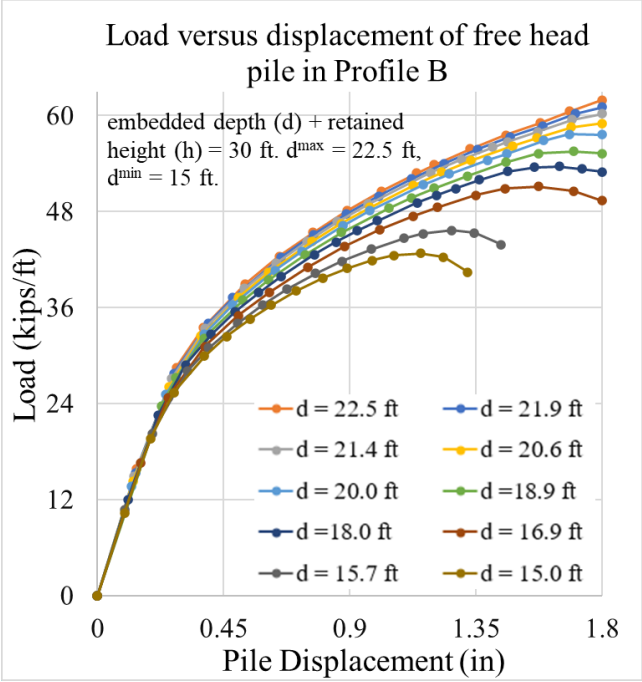

Figure 0-63 Applied load versus vertical displacement of a pile wall with a free head embedded in layered dense sand profile for different values of embedded depth.

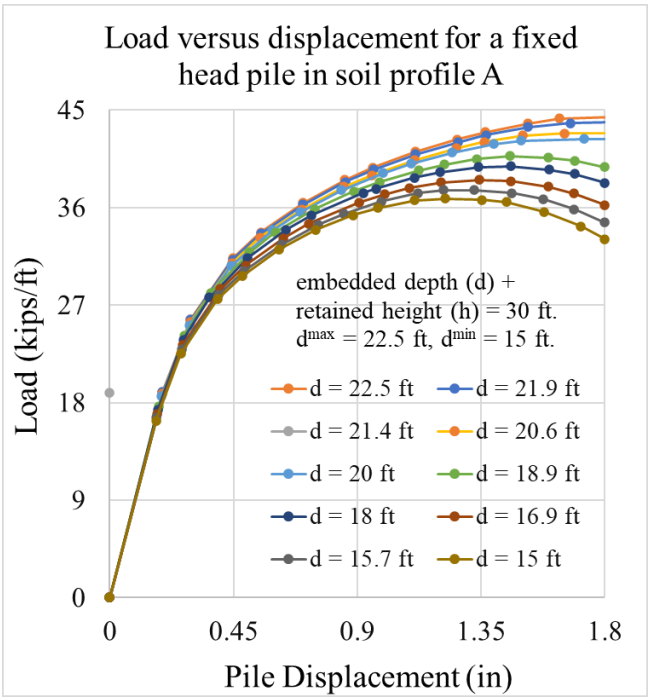

Figure 0-64 Applied load versus vertical displacement of a pile wall with a fixed head embedded in Profile A (layered loose sand) for different values of embedded depth.

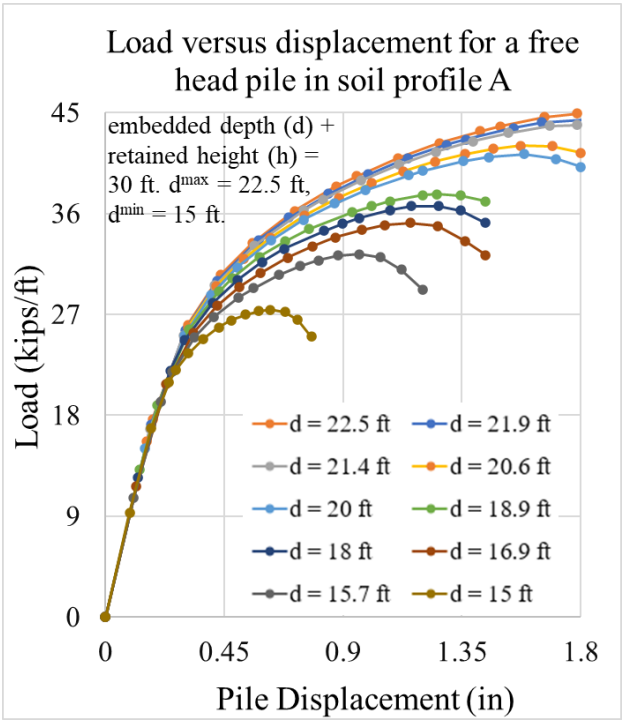

Figure 0-65 Applied load versus vertical displacement of a pile wall with a free head embedded in Profile A (layered loose sand) for different values of embedded depth.

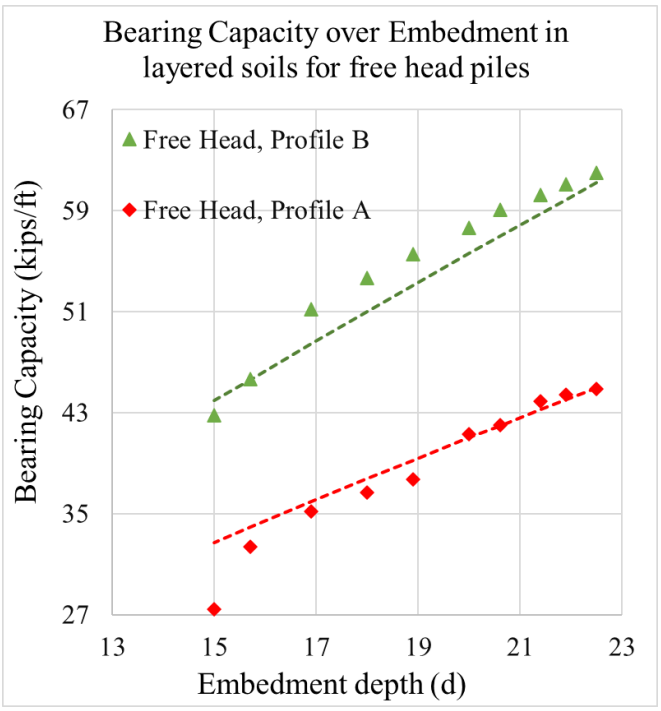

Figure 0-66 The bearing capacity of a free head pile wall in layered sand profiles.

Figure 0-66 compares the variation of bearing capacity with embedment ratio with differing head boundary conditions. Unlike the uniform soil profile, it is apparent that the head boundary condition has little influence on the bearing capacity of the pile wall in the layered soil profile, except for the smallest used values of d = 15.0 or 15.7 ft. Furthermore, greater variations are seen in the free head pile in profile A.

$$Q_{ult} = \frac{\gamma'}{\gamma'_0}\left((d+h)/d\right)^{0.6} * (tan\phi) * \mathrm{d}^{1.4171} kips/ft \text{ for Profile B and free head} \quad (9)$$

$$Q_{ult} = \frac{\gamma'}{\gamma'_0}\left((d+h)/d\right)^{0.6} * (tan\phi) * \mathrm{d}^{1.3835} kips/ft \text{ for Profile A and free head} \quad (10)$$

4.3.3 Conclusions and Recommendations: centrifuge tests observations

Numerical modeling of sheet pile walls as vertical bearing elements was validated using previously conducted centrifuge tests of sheet pile walls. Static axial load tests were performed on sheet pile models in different scenarios that may frequently encounter in the field. As such, the effects of (i) existence of a dense sand layer at the sheet pile tip, (ii) sheet pile penetration depth (d) to unsupported depth (h) length ratio, (iii) sheet pile stiffness, and (iv) pile head boundary condition. Subsequently, these experimental observations were used to inform the creation of the numerical model and validate the generated predictions: (i) by using maximum observed axial resistance as

the prescribed boundary condition for the numerical model and then (ii) by using the same prescribed displacement applied to the pile head in the centrifuge test.

Comparing plots of axial resistance along pile depth we observe that the high-density sand layer (D_r = 85%) at the sheet pile tip causes an increase in the axial resistance of sheet piles relative to the cases where the soil profiles was homogenous. The amount of this increase, however, was more for the sheet piles in the profiles with a higher d/h ratio (i.e. =2.24). When comparing the centrifuge test data of axial resistance to the numerical predictions we found that the numerical model had better fidelity in the case of the PZS2 section. It is possible this discrepancy is the result of imperfect model of soil-structure interface.

Increasing the d/h ratio increases the skin friction; therefore, the axial resistance, in both homogenous and two-layered profiles and in either of the test series with free-head or fixed head conditions. Compared to those sheet piles in homogenous sand profiles, the amount of this increase in axial resistance was greater for the profiles with the dense sand layer at the sheet pile wall tip. Greater axial resistance was obtained in the stiffer sheet pile wall (i.e. PZS2). This was mainly attributed to the increase in the cross-sectional area of the sheet pile wall and also an increase in the projected area, where the soil plugging occurs. An increase in the axial resistance did not always mean an increase in bending moments. When comparing different soil profiles axial resistance developed in the pile and bending moments acting on the pile appear to be inversely correlated. On the other hand, when comparing the effects of sheet pile stiffness, the stiffer pile develops greater axial resistance and experiences greater bending moments.

4.3.4 Example Scenario

Consider a scenario where a 15 foot column of soil, 50 feet wide needs to be retained by a sheet pile wall that also provides a vertical bearing of 2000 kips. This is equivalent to a normalized bearing capacity of $Q_{ult} = 40$ kips/ft. For simplicity assume $\frac{\gamma'}{\gamma'_0} = 1$

For a **loose soil** with internal friction angle 27° (0.506 rad) and a **fixed pile head** the minimum required depth of embedment would be:

$$k = 0.0169 * 27 + 0.8003 = 1.2566$$

$$40 = \left((d+15)/d\right)^{0.8421} * (tan\ 27) * \mathrm{d}^{1.2566}, d = 23.1\ ft$$

For a **dense sand** with friction angle 32° (0.541 rad), and a **fixed pile head** the minimum required depth of embedment would be:

$$k = 0.0169 * 32 + 0.8003 = 1.3411,$$

$$40 = \left((d+15)/d\right)^{0.8421} * (tan\ 32) * \mathrm{d}^{1.3411}, d = 14.1\ ft$$

For a **very dense sand** with friction angle 35° (0.628 rad) and a **fixed pile head** the minimum required depth of embedment would be:

$$40 = \left((d+15)/d\right)^{0.8421} * (tan\ 35) * \mathrm{d}^{1.3918}, d = 10.8\ ft$$

Consider if the l**oose soil were overlaying a very dense soil** layer (Profile B), such that the pile tip where embedded in the very dense layer. For loose soil ϕ = 28° and for very dense soil ϕ = 34°. Then the minimum required depth of embedment could be calculated as follows instead

$$k_1 = 0.0169 * 28 + 0.8003 = 1.2735$$

$$k_2 = 0.0169 * 34 + 0.8003 = 1.3749$$

$$40 = \left((d+15)/d\right)^{0.8421} * (tan\ 28) * \mathrm{d}^{(1.2735+1.3749)/2}, d = 17.7\ ft.$$

Alternatively if the **dense soil were overlaying a very dense soil** (Profile B), with ϕ = 32 and 34 respectively, then the minimum required depth would instead be,

$$40 = \left((d+15)/d\right)^{0.8421} * (tan\ 32) * \mathrm{d}^{(1.3411+1.3749)/2}, d = 13.4\ ft\ .$$

All the above scenarios assume a fixed/anchored pile head which can remarkably improve the ultimate bearing capacity of the pile wall by reducing the lateral deflection for a given axial load. For the case of cantilever sheet pile under **free head condition**, embedded in **loose, uniform sand** the required embedment would be,

$$k = 0.0196 * 27 + 0.7349 = 1.2941$$

$$40 = \left((d+h)/d\right)^{0.6} * (tan\ 27) * \mathrm{d}^{1.2941}, \quad \mathrm{d} = 25.3\ \mathrm{ft}$$

and for a pile embedded in **dense uniform sand** it would be,

$$k = 0.0196 * 32 + 0.7349 = 1.3621$$

$$40 = \left((d+h)/d\right)^{0.6} * (tan\ 32) * \mathrm{d}^{1.3621}, \quad \mathrm{d} = 15.8\ \mathrm{ft}$$

and finally for a pile embedded in very dense uniform sand it would be,

$$k = 0.0196 * 35 + 0.7349 = 1.4209$$

$$40 = \left((d+h)/d\right)^{0.6} * (tan\ 35) * \mathrm{d}^{1.4209}, \quad \mathrm{d} = 12.3\ \mathrm{ft}$$

References

Viking, K. (2002). Vibro-driveability-a field study of vibratory driven sheet piles in non-cohesive soils (Doctoral dissertation, Byggvetenskap).

McShane, G. (1991, April). Steel sheet piling used in the combined role of bearing piles and earth retaining members. In Proceedings of the 4th International Conference on Piling and Deep Foundations, Stresa, Italy (Vol. 112, p. 113).

Evans, R. R., White, D. J., & Klaiber, F. W. (2012). Modified sheet pile abutments for low-volume road bridges.

Kossakowski, P. G. (2019, April). Recent Advances in Bridge Engineering–Application of Steel Sheet Piles as Durable Structural Elements in Integral Bridges. In IOP Conference Series: Materials Science and Engineering (Vol. 507, No. 1, p. 012003). IOP Publishing.

Dunker, K. F., & Liu, D. (2007). Foundations for integral abutments. Practice Periodical on Structural Design and Construction, 12(1), 22-30.

Sylvain, M. B., Pando, M. A., Whelan, M. J., Rice, C. D., Ogunro, V. O., Park, Y., & Koch, T. Case History of a Full Scale Axial Load Test of Sheet Piles. In Geotechnical Frontiers 2017 (pp. 355-365).

North Carolina Department of Transportation. (2018). Determination of Vertical Resistance for Sheet Pile Abutments Final Report.

AMCRPS. (2019). Benefits of steel solutions in bridge design.

Evans, R. R., White, D. J., & Klaiber, F. W. (2012). Modified sheet pile abutments for low-volume road bridges.

Kossakowski, P. G. (2019, April). Recent Advances in Bridge Engineering–Application of Steel Sheet Piles as Durable Structural Elements in Integral Bridges. In IOP Conference Series: Materials Science and Engineering (Vol. 507, No. 1, p. 012003). IOP Publishing.

Dunker, K. F., & Liu, D. (2007). Foundations for integral abutments. Practice Periodical on Structural Design and Construction, 12(1), 22-30.

Sylvain, M. B., Pando, M. A., Whelan, M. J., Rice, C. D., Ogunro, V. O., Park, Y., & Koch, T. Case History of a Full-Scale Axial Load Test of Sheet Piles. In Geotechnical Frontiers 2017 (pp. 355-365).

North Carolina Department of Transportation. (2018). Determination of Vertical Resistance for Sheet Pile Abutments Final Report.

AMCRPS. (2019). Benefits of steel solutions in bridge design.

Appendix A: Helmet details for free-head tests

A new helmet was designed to perform free-head load tests on sheet pile walls. The helmet had a sufficient internal width (Figure A1-a) such that the sheet pile could freely rotate inside it. To perform driving (i.e. with up and down movements, as discussed) and conduct load tests, 5 rigid rods (Figure A1-b) were passed through the helmet and the sheet pile wall and through the precisely drilled holes at the same elevations. The rods had smooth surfaces and were greased prior to each load test aiming to minimize any possible frictions and apply a distributed load along the width of the wall.

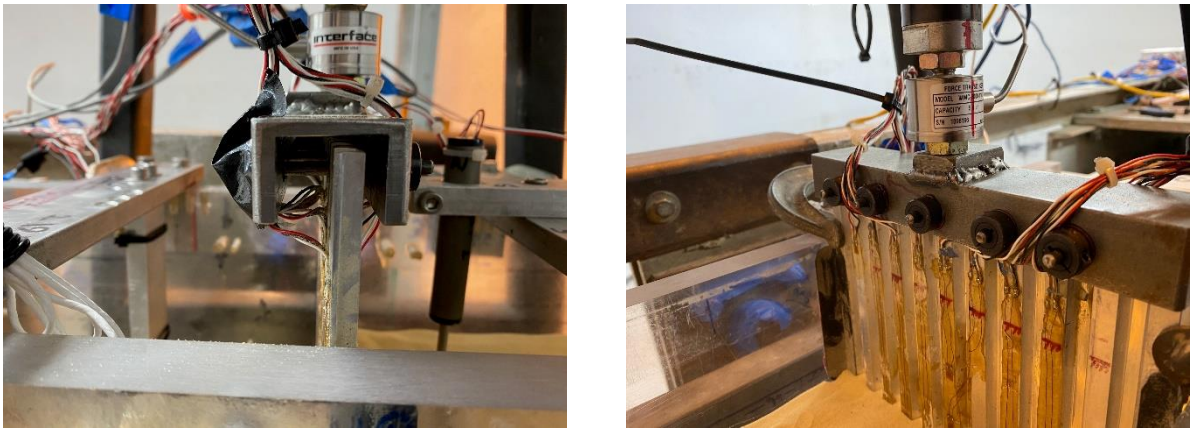

(a) (b)

Figure A1. (a) The sheet pile wall-helmet layout; and (b) the helmet and five smooth rods for performing free-head load tests

Appendix B: Installation of steel sheet pile using the vibro-driving method

The choice of a suitable driving system is of fundamental significance to successful sheet pile installation. There are three basic driving methods: impact driving, vibro-driving, and press-in piling. Though impact driving proves to be the best solution for difficult ground, it can be quite noisy and the duration of driving is usually longer than with the use of a vibratory hammer. Vibro-driving is a commonly used method due to its efficiency and good economy and has become increasingly popular since the 1970s. Vibro-driving can attain a higher production capacity while producing less damage to the sheet piles. For difficult dense grain or cohesive soils, pre-drilling and water jetting can be considered. Press-piling is not considered because this method is less economical.

We consulted some contractors, and they proposed to install sheet piles with vibratory hammer. In the proposal from Hayward Construction Group, they provide machinery to include a crane, HPSI-80 with power pack vibratory hammer. Water jetting may also be used to get to the desired depth. Figure B1 shows the excavator mounted vibratory hammer.

Figure B1. Excavator mounted vibratory hammer.

The principle of vibro-driving is reducing the resistance of the ground by vibration. Figure C2 shows principles of a vibratory hammer. The vibratory piling machine transfers vertical

vibrations to the sheet pile connected with a hydraulic clamp, which in turn transfers the vibration to the ground and forces the ground to shift. Consequently, the friction between the sheet pile and the soil is reduced, allowing the pile to be driven with less resistance. In the vibration case (gearbox), each eccentric pair turns at the same angular velocity but in opposite directions, generating a vertical vibration. The transmission of vibrations to the crane is prevented by a suppressor, a designed shock absorber. Figure B3 shows a typical telescopic leader-mounted system.

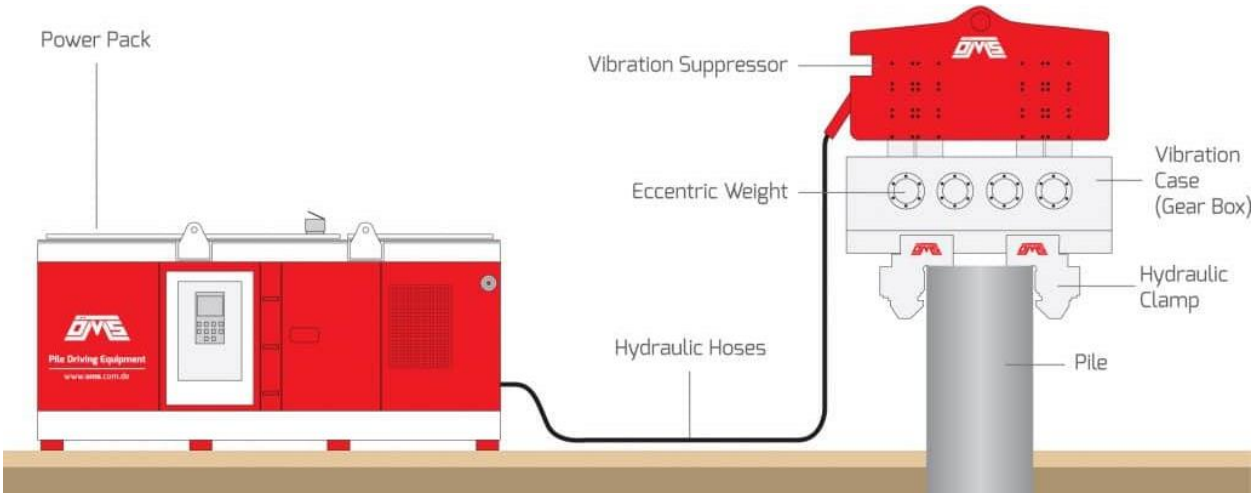

(a) Layout of a vibratory hammer.

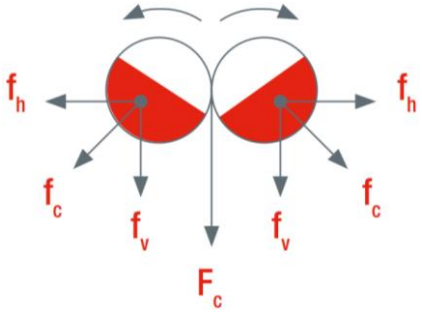

(b) Schematic of centrifugal force (f_c is the centrifugal force of each eccentric. The horizontal component f_h is offset at the same time that the vertical component f_v is added, which produces a total centrifugal force F_c).

Figure B2. Principles of a vibratory hammer (OMS Pile Driving Equipment).

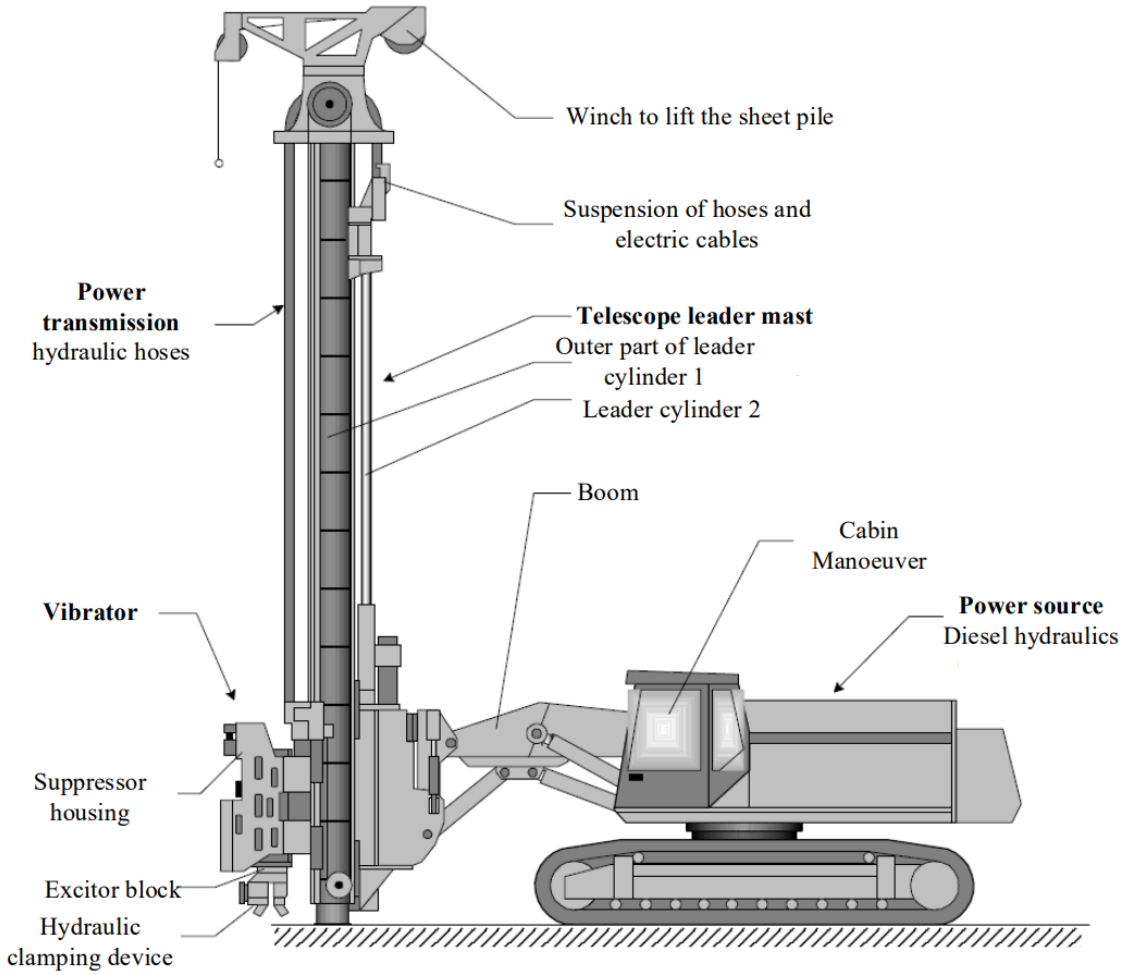

Figure B3. The main parts of telescopic leader driving system (Viking 2002)

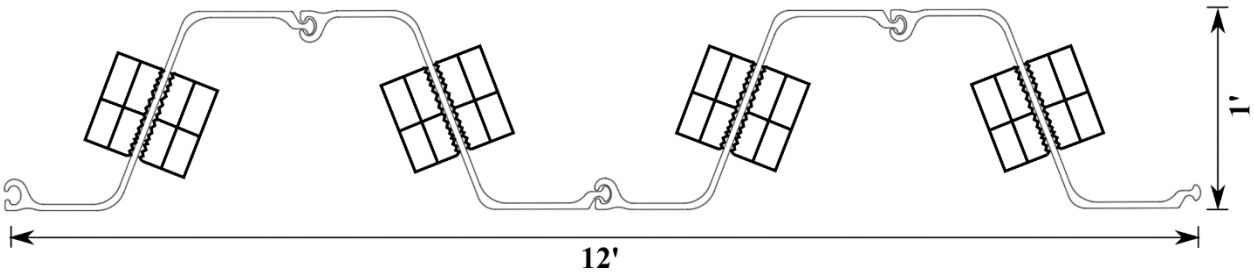

Figure B4. Schematic of arrangement of clamps.

Appendix C: Economic benefits of using steel sheet pile walls as vertical bearing elements

Traditionally, the abutment axial loads are sustained by driven piles coupled with a separate retaining structure (i.e., sheet piles) carrying lateral loads. An alternative bridge abutment design approach involving sheet piles for the double functions has been successfully used for decades (Sylvain et al., 2017). For use as the primary bearing foundation component, steel sheet piling has several potential advantages. For example, a sheet pile abutment system can retain backfill soils (i.e., lateral pressure) while simultaneously functioning as a vertical bearing element to support the bridge abutment. Thus, sheet pile bridge abutment systems require no earth embankments in front of the upper portion of the piles (McShane, 1991; Evans et al., 2012). This design has the potential to significantly reduce construction cost and time (NCDOT 2018). Alternatively, steel sheet pile bridge abutment systems can be used to circumvent unavailability or shortages of construction materials such as concrete.

The use of steel sheet piles in integral-abutment bridges significantly reduces the cost of construction and maintenance due to the eliminated number of expansion joints and bearings (Dunker et al., 2007). When used as permanent structural elements, steel sheet piles contribute to lowered project costs by eliminating the need for removal. In the tunnel project of (Kossakowski 2019), the major structural problem was solved by reducing the number of places where destructive processes could occur. Thus, they recommended the continuous integral structural elements, i.e., sheet piles, be used as combined vertical and lateral support elements.

The economy of using steel sheet pile embedded retaining wall as a bridge abutment has also been validated by field tests (Sylvain et al. 2017). The sheet pile was found to have greater axial capacity and axial stiffness as compared to the H-pile. They concluded that there is strong potential for the axial load bearing capacity of sheet piles to be considered for bridge design, and the incorporation of the axial load bearing capacity of sheet piles could provide substantial savings regarding time and money.

Short span bridges in the U.S. that are located near rivers and streams typically use sheet piles to protect the abutment against erosion and scour. In such bridges, the abutment axial load demands are usually carried by driven piles installed behind the scour protection sheet piles. An alternative bridge abutment design approach, successfully used for decades in Europe and in some projects in the U.S., involves installing sheet piles for the double function of scour protection and axial load bearing. In this manner, the maintenance cost can be greatly reduced compared to the traditional system which requires a driven pile and lateral load bearing elements.

C1 Parametric study of a sheet pile wall abutment regarding axial capacity and financial benefit

Miguel et al., (NCDOT 2018) performed a parametric study to evaluate possible technical and economic benefits of incorporating sheet pile elements as partial or total axial load bearing elements in a short span bridge. The parametric analyses are based on simplified analytical models of five bridge abutment configurations shown in Figure 0-1.

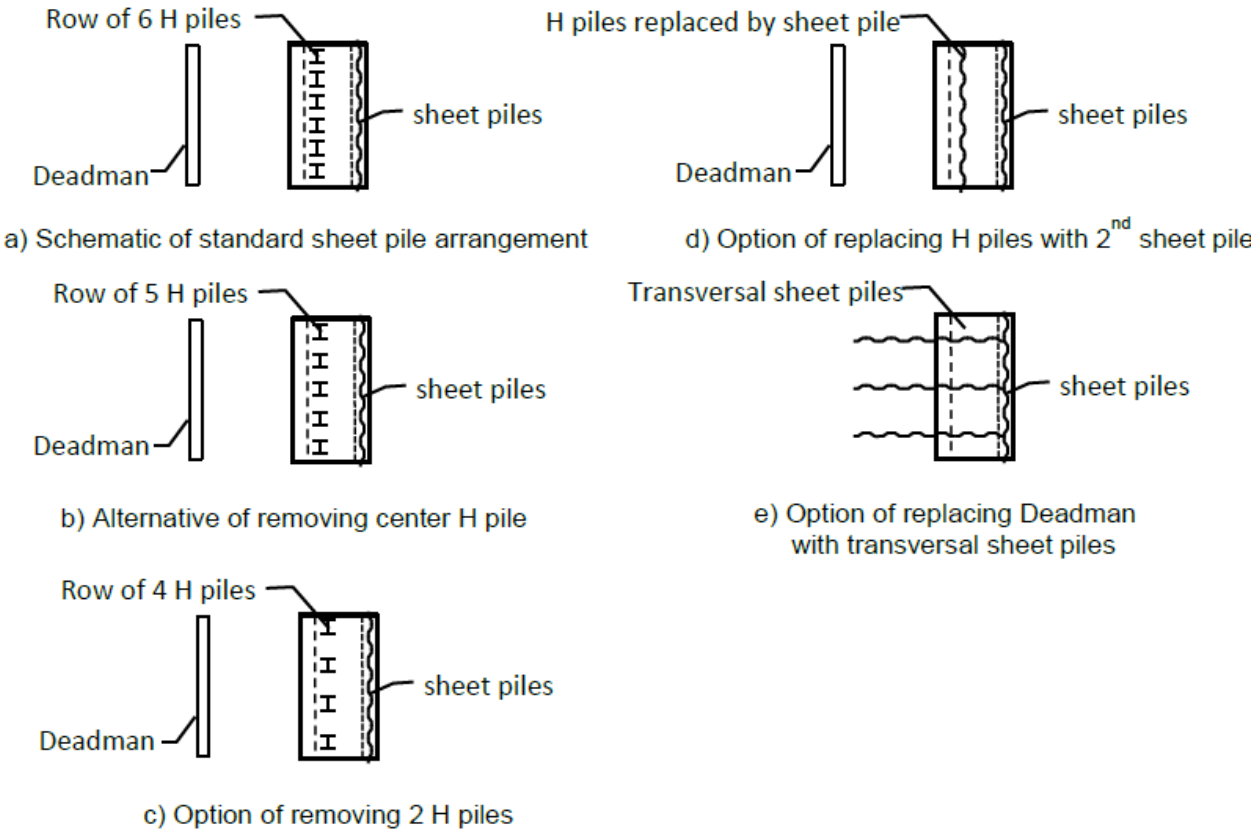

Figure C1. Different bridge abutment configurations considered in parametric study. (NCDOT 2018).

The representative bridge is shown in Figure 2. Then the investigators estimated the axial toe and skin friction capacities of the H piles and sheet piles for each abutment configuration. The total axial capacity is summarized in Table C1.

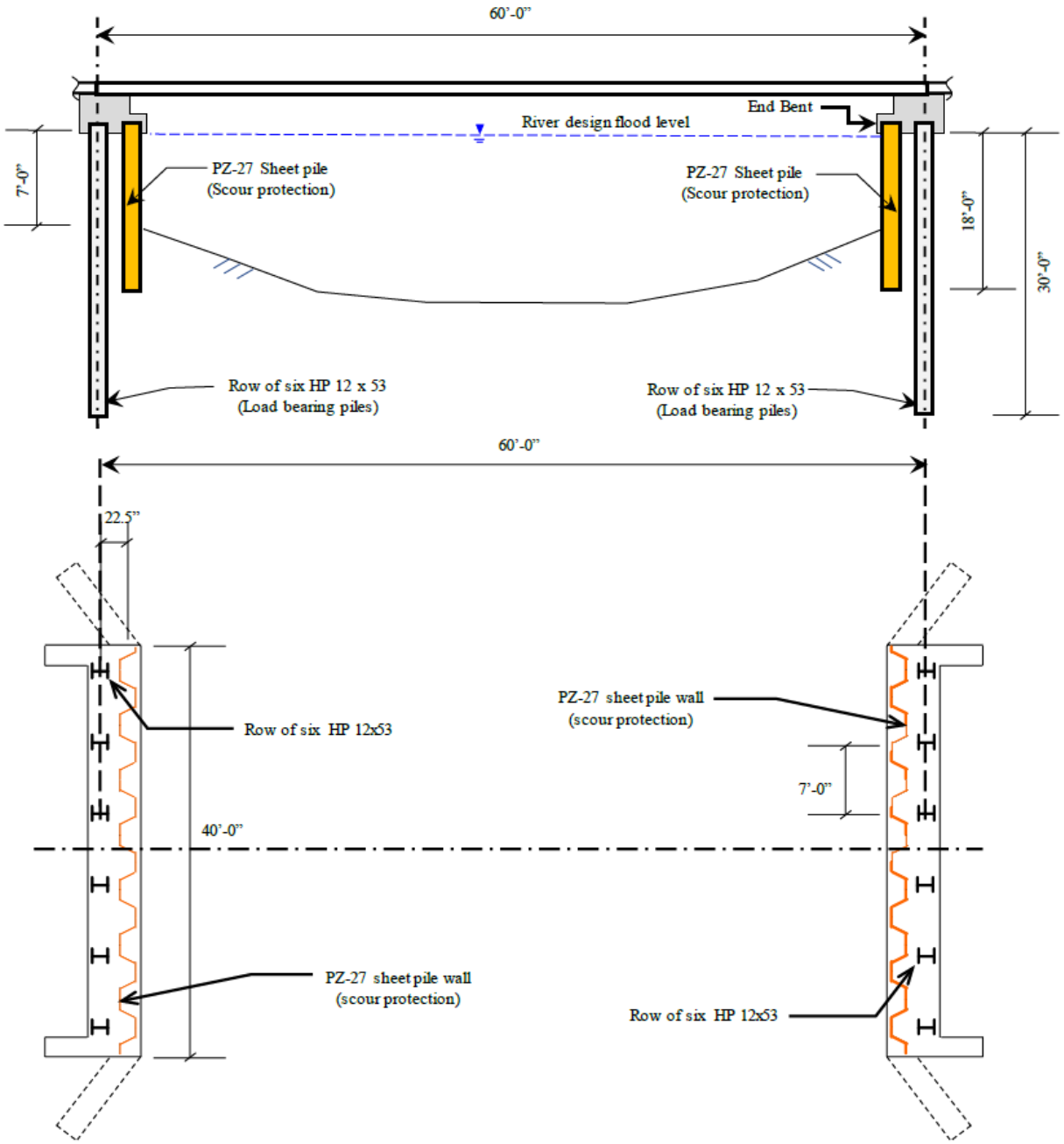

Figure C-2. Schematic of representative bridge used in parametric study.

Table C1: Summary of axial capacities and cost comparison for different abutment configurations of representative bridge.

Configuration	Description	Total axial capacity (kips)	Estimated cost of foundation elements
Baseline (Figure C0-1-a)	Six H-piles; neglecting any sheet pile contribution	426.3	$ 29,700
Baseline + sheet pile (Figure C0-1-a)	Six H-piles including contribution of PZ-27 sheet pile wall (40 ft wide, and 18 ft length)	502.0	$ 29,700
Five H-piles + sheet pile (Figure C0-1-b)	Five H-piles including contribution of PZ-27 sheet pile wall (40 ft wide, and 18 ft length)	431.0	$ 28,350
Four H-piles + extended sheet pile (Figure C0-1-c)	Four H-piles including contribution of PZ-27 sheet pile wall (40 ft wide, and 23 ft length)	436.5	$ 33,000
No H-piles + Two rows of sheet piles (Figure C0-1-d)	No H-piles + Two rows of sheet piles extended by 7 feet (L = 25 ft)	432.2	$ 60,000
Four rows of sheet piles (Figure C0-1-e)	No H-piles and four rows of sheet piles (driven to bedrock)	773.6	$ 36,000

Based on total axial capacity considerations, they found several of the proposed alternative abutment designs (Figure C-2) feasible with the elimination of one or more bearing H-piles. They performed a simplified cost comparison based on estimated cost for the HP 12 × 53 and the

PZ-27 sheet piles of $45 per linear foot and $30 per square foot, respectively. Possible cost savings when only using one contractor and hammer if only sheet piles are installed is not considered in their estimation. The axial capacities, and associated cost estimates, for the chosen geometry and simplified soil conditions, suggest that including the axial contribution of the PZ-27 sheet pile wall in the abutment design does yield technically and economically feasible alternatives.

Another case study performed by the Karlsruhe Institute of Technology assesses the associated costs and performance of a traditional concrete bridge versus a bridge whose abutments are constructed using steel sheet pile sections. This comparison is performed for a two-span superstructure with spans of 22.5 m. They concluded that choosing a bridge designed with steel sheet pile abutments and composite deck built with steel sections leads to global cost benefits such as (AMCRPS 2019):

- 7 % reduction on the construction costs.
- 3, 5 % reduction on the life cycle costs over 100 years lifetime (based on a real discount rate of 2 %);
- Up to 15 % reduction in the economic impact of the external effects during the service life of the structure.

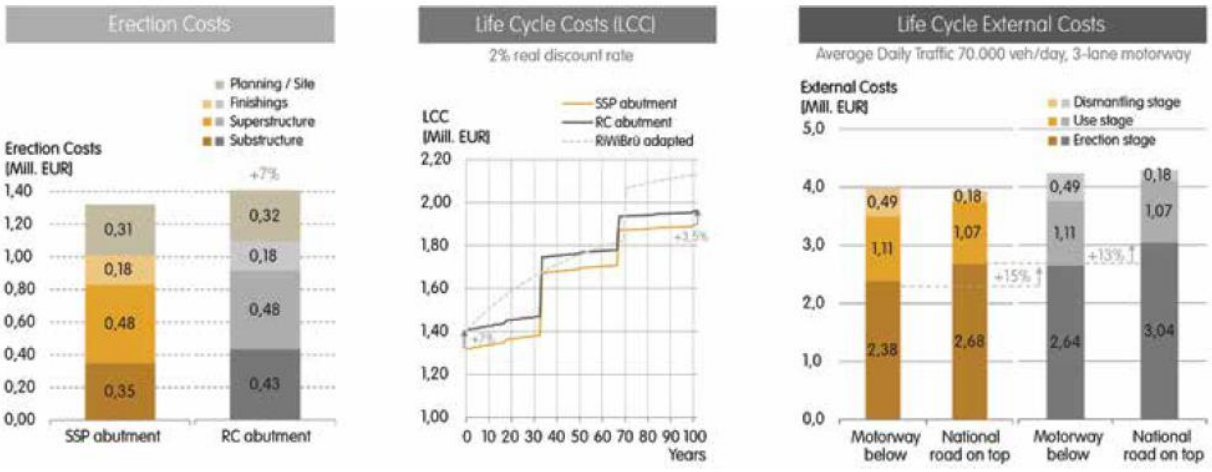

Figure C-3. Charts comparing costs of using sheet pile walls to reinforce concrete abutments

Appendix D: Predicting ultimate axial resistance of sheet piles using static load methods

Prior to static load testing, the axial load capacity of sheet piles is estimated using static methods including the SPT-based method and CPT-based method.

D.1 SPT based Brown Method

The Brown Method (Brown et al., 2001) is an empirical method that uses SPT N_{60} values for determining the pile bearing capacity. The static load tests used to develop the method incorporated a wide variety of soil types and pile types. Brown reported the average unit shaft resistance:

$$f_s = F_{vs}(A_b + B_b N_{60})$$

where

F_{vs} is factor for pile driving method (1.0 for impact or 0.68 for vibratory)

A_b and B_b are Brown's regression analysis factors based on soil type

N_{60} is SPT N-value corrected for 60% energy transfer

Table D1. Input factors for Brown's Method (FHWA GEC 012 – Volume 1).

Loading Condition	Installation Method	Soil Type	F_{vs}	A_b (ksf)	B_b (ksf/bpf)
Compression	Impact	Clay to Sand	1.0	0.555	0.040
"	"	Gravelly Sand to Boulders	1.0	0.888	0.888
"	"	Rock	1.0	2.89	2.89
Tension	Impact	Clay to Sand	1.0	0.522	0.0376
"	"	Gravelly Sand to Boulders	1.0	0.835	0.0
"	"	Rock	1.0	2.71	0.0
"	Vibratory	Clay to Sand	0.68	0.522	0.0376
"	"	Gravelly Sand to Boulders	0.68	0.835	0.0
"	"	Rock	0.68	2.71	0.0

Table D2. Calculation of skin resistance using Brown's Method.

Depth (ft)	N_{60}					**Area (ft^2)**	f_s **(ksf)**		R_s **(kips)**	
	TS1	**TS2**	**TS3**	**Min**	**Max**		**Min**	**Max**	**Min**	**Max**
0-5	5	4	8	4	13	17.92	0.46	0.69	8.19	12.32
	4	7	13							
5-10	3	8	9	3	9	17.92	0.43	0.59	7.74	10.48
	4	5	9							
	4	4	9							
	4	5	8							
10-15	4	4	5	4	9	17.92	0.46	0.59	8.19	10.48
	5	8	9							
15-20	23	9	8	8	23	17.92	0.56	0.94	10.03	16.90
		16	16							
20-22	27	15	19	15	27	7.17	0.74	1.05	5.29	7.49

**For steel sheet piling, the SCI (1998) states that the coated area of the pile shaft for friction resistance, A_s, can be conservatively taken as 80% of the surface area of the pile. Coating area (both sides) of PZ 27 sheet pile is $A_s = 4.48 \frac{ft^2}{ft}$, per section. Thus, the actual coating area is $0.8\ A_s = 3.584\ ft^2/ft$, per section.*

Thus, the range of R_s is $39.44 \sim 57.68$ kips.

The unit toe resistance is determined as follows:

$$q_p = 3.55N_{60} = 3.55(15 \sim 27) = 53.25 \sim 95.85\ ksf/ft^2.$$

For vibratory installed piles this unit toe resistance should then be multiplied by 0.56. The pile toe resistance, R_p, in kips is then calculated as follows

$$R_p = 0.56q_p\left(A_p + A_{pp}F_p\right) = 0.56q_pA_p = 4.43 \sim 7.98\ kips$$

where

$A_p = 0.1486\ ft^2$ is cross-sectional area of PZ 27 sheet pile.

A_{pp} is cross-sectional area of soil plug for open end pipe piles or H-piles at pile toe. According to the Steel Construction Institute (SCI, 1998), the development of a soil plug during driving is negligible for sheet piling. Thus, $A_{pp} = 0$.

F_p is plug mobilization factor, 0.42 for pipe piles or 0.67 for H-piles.

Thus, the range of bearing capacity of 4 PZ 27 sections is
$52.644 \sim 78.792\ kips$ $(234.17 \sim 350.48\ kN)$

$$R_r = \phi_{stat}(R_s + R_p) = 4 * 0.3 * (R_s + R_p)$$

where $\phi_{stat} = 0.3$ for SPT method.

Table D3. Resistance Factors for Driven Piles (AASHTO Table 10.5.5.2.3-1).

Condition/Resistance Determination Method		Resistance Factor
Nominal Bearing Resistance of Single Pile—Static Analysis Methods, φ_{stat}	Side Resistance and End Bearing: Clay and Mixed Soils	
	α-method (Tomlinson, 1987; Skempton, 1951)	0.35
	β-method (Esrig & Kirby, 1979; Skempton, 1951)	0.25
	λ-method (Vijayvergiya & Focht, 1972; Skempton, 1951)	0.40
	Side Resistance and End Bearing: Sand	
	Nordlund/Thurman Method (Hannigan et al., 2005)	0.45
	SPT-method (Meyerhof)	0.30
	CPT-method (Schmertmann)	
	End bearing in rock (Canadian Geotech. Society, 1985)	0.50 0.45

D.2 CPT based Method

The CPT-based Laboratoire Central des Ponts et Chaussees (LCPC) method was developed by Bustamante and Gianeselli (1982) to predict the pile bearing capacity. A series of 197 full-scale static load tests were carried out on various soil and pile types. The LCPC method utilizes primarily q_c values to develop both shaft and toe resistance. The unit skin friction q_s is calculated by dividing the cone resistance by a coefficient which is a function of pile type and installation method:

$$q_s = \frac{q_c}{\alpha}$$

Table D4. Values of coefficients α for calculating the skin friction (reproduced from Bustamante & Gianeselli, 1982).

Nature of soil	q_c $(10^5 Pa)$	Coefficient α				Maximum value of q_s $(10^5$ Pa)					
		Category									
		I		II		I		II		III	
		I A	I B	II A	II B	I A	I B	II A	II B	III A	III B
Soft clay and mud	<10	30	30	30	30	0.15	0.15	0.15	0.15	0.35	-
Moderately compact clay	10 to 50	40	80	40	80	0.35	0.35	0.35	0.35	0.8	≥1.2
Silt and loose sand	≤50	60	150	60	120	0.35	0.35	0.35	0.35	0.8	-
Compact to stiff clay and compact silt	>50	60	120	60	120	0.35	0.35	0.35	0.35	0.8	≥2.0
Soft chalk	≤50	100	120	100	120	0.35	0.35	0.35	0.35	0.8	-
Moderately compact sand and gravel	50 to 120	100	200	100	200	0.35	0.35	0.35	0.35	0.8	≥2.0
Weathered to fragmented chalk	>50	60	80	60	80	1.2	0.8	1.2	1.2	1.5	≥2.0
Compact to very compact sand and gravel	>120	150	300	150	200	1.2	0.8	1.2	1.2	1.5	≥2.0

Table D5. Calculation of skin resistance using LCPC method.

Depth (ft)	**Area (ft^2)**	q_c **(ksf)**	q_c/p_a	α	$q_s = q_c/\alpha$	q_s/p_a	**Max.** q_s/p_a	**Corrected** q_s	R_s **(kips)**
0-2.5	8.96	25	12.0	80	0.31	0.15	0.35	0.31	2.80
2.5-6	12.54	53	25.4	120	0.44	0.21	0.35	0.44	5.54
6-10	14.34	47	22.5	120	0.39	0.19	0.35	0.39	5.61
10-12.5	8.96	47	22.5	120	0.39	0.19	0.35	0.39	3.51
12.5-22	34.05	141	67.5	200	0.71	0.34	0.8	0.71	24.00
								Total	**41.47**

*$p_a = 10^5\ Pa = 2.08854\ ksf$ *is the reference pressure. Type IIB: Driven metal piles is employed in our case.*

$$R_s = 41.47\ kips$$

The tip resistance is calculated as:

$$R_p = q_{ca} k_c A_{cross}$$

where

q_{ca} is the equivalent cone resistance. Here we assume it is equal to q_c at the level of the pile point, i.e.,$q_c = q_{ca} = 141\ ksf = 67.5 \times 10^5\ Pa$.

k_c is penetrometer bearing capacity. Driven metal piles belong to Group II. Thus, $k_c = 0.5$.

$A_p = 0.1486\ ft^2$ is cross-sectional area of PZ 27 sheet pile.

$$R_p = q_c k_c A_{cross} = 10.4763\ kips$$

Table D6. Values of bearing capacity factors k_c for the calculation of the limit point resistance (Bustamante & Gianeselli, 1982).

Nature of soil	q_c $(10^5 Pa)$	**Factor** k_c	
		Group I	**Group II**
Soft clay and mud	<10	0.4	0.5
Moderately compact clay	10 to 50	0.35	0.45
Silt and loose sand	≤50	0.4	0.5

Compact to stiff clay and compact silt	>50	0.45	0.55
Soft chalk	≤50	0.2	0.3
Moderately compact sand and gravel	50 to 120	0.4	0.5
Weathered to fragmented chalk	>50	0.2	0.4
Compact to very compact sand and gravel	>120	0.3	0.4

** Our case corresponds to moderately compact sand and gravel, and driven metal piles involved in Group II.*

Total bearing resistance of 4 PZ 27 sections:

$$R_r = \phi_{stat}(R_s + R_p) = 4 * 0.45 * (41.47 + 10.4763) kips = 93.5\ kips = 415.91\ kN$$

Table D7. Resistance Factors for Driven Piles (AASHTO Table 10.5.5.2.3-1).

Condition/Resistance Determination Method		Resistance Factor
Nominal Bearing Resistance of Single Pile—Static Analysis Methods, φ_{stat}	Side Resistance and End Bearing: Clay and Mixed Soils	
	α-method (Tomlinson, 1987; Skempton, 1951)	0.35
	β-method (Esrig & Kirby, 1979; Skempton, 1951)	0.25
	λ-method (Vijayvergiya & Focht, 1972; Skempton, 1951)	0.40
	Side Resistance and End Bearing: Sand	
	Nordlund/Thurman Method (Hannigan et al., 2005)	0.45
	SPT-method (Meyerhof)	0.30
	CPT-method (Schmertmann)	0.50
	End bearing in rock (Canadian Geotech. Society, 1985)	0.45

**No resistance factor for LCPC method is specified. We use 0.5 following CPT-method (Schmertmann).*

D.3 Prediction from numerical simulation of the test pile

Four sections are grouped to bear the loads, which gives us a pile wall of width of 72 in (6ft). The length of sheet pile is determined as 25 ft based on site conditions. The pile is embedded 22 ft into the soil. The soil properties are reproduced from Mcvay et al. (2014).

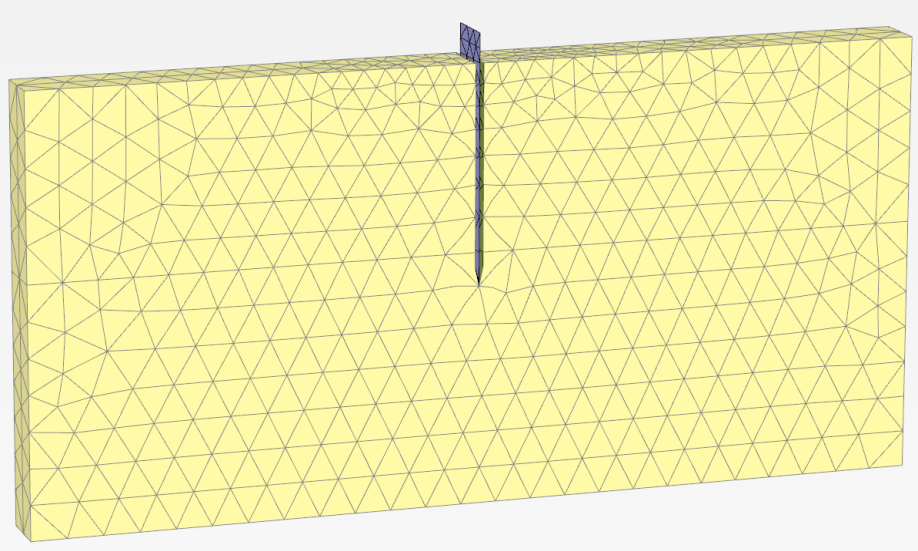

Figure D-1 The problem geometry

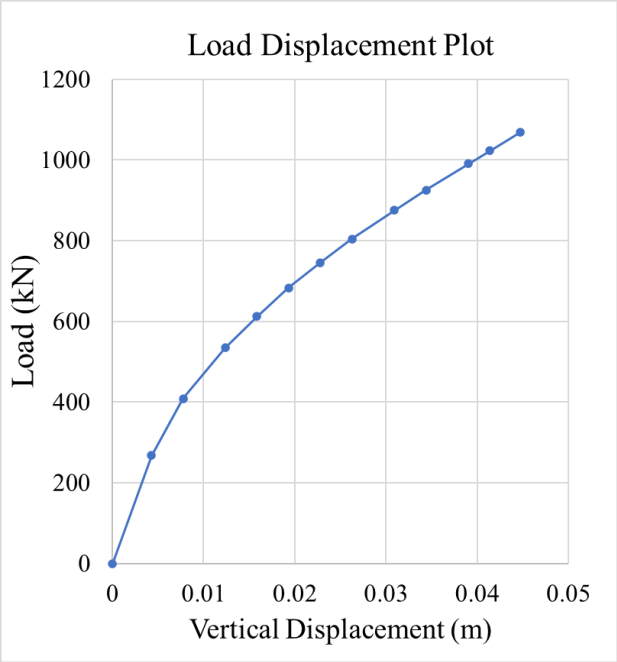

Figure D-2 The load displacement curve for sheet pile.

Figure D-2 plots the applied load over vertical displacement of the pile wall. ASTM D1143/D1143M (2013) has defined the failure load, for the purpose of terminating an axial compressive load test, "*the test load at which rapid continuing, progressive movement occurs, or at which the total axial movement exceeds 15 % of the pile diameter or width, or as specified by the engineer*." Using this definition, the axial resistances were reported at the sheet pile top total

axial movement of 15 % of the average sheet pile width (D) which is 13 in. In other words, the bearing capacity of the sheet pile is the load which causes a settlement of 0.046 m in the pile. **From the figure it is apparent that the predicted bearing capacity of the pile wall is 1070 kN.**

D.4 Prediction from the proposed design equations

The soil boring profiles from Figure D-3 indicate N60 values ranging from 3 to 9 (very loose to loose sand) for the upper 18ft. Between 18ft and 22ft the N values are between 16 and 23 (medium dense sand). Using Boring TS-1, the following average N60 may be estimated for the sand between 2.5ft and 22 ft below ground.

From 2.5 and 18ft: N60 avg =4

From 18 and 22ft: N60 avg =16

Weighted average N60= (4x15.5' +16x4')/19.5'=6.5 blows/ft, (loose sand)

$\phi = 30^0$ may be assumed.

Assume $\gamma' = 105$ pcf. For loose sand $\gamma_0 = 97.35$ pcf $\quad \frac{\gamma'}{\gamma_0} = \frac{105}{97.35} \quad = 1.08$

For ϕ=30^0, k= 0.0169 * 30 + 0.8003 = 1.3073

From the power-law fits derived for **loose uniform sands**, the predicted bearing capacity is determined using the following relationship,

$$Q_{ult} = 1.08 * \left((22+0)/22\right)^{0.8421} * (tan\ 30) * 22^{1.3073} = 35.47\ kips/ft$$

where ϕ is the friction angle. Therefore,

$Q_{ult} = 6ft * (35.47) = \mathbf{212.82\ kips}$ OR $\boldsymbol{Q_{ult} = 947\ kN}$

Alternatively, the layered equation can be applied to determine the bearing capacity of the sheet pile wall. First the exponents can be computed as follows

$\phi_1 = 30,\ k_1 = 1.3073, \quad \phi_2 = 33,\ k_2 = 0.0169 * 33 + 0.8003 = 1.358$where we have assumed that the medium dense sand has friction angle 33°. Then the predicted bearing capacity determined using the following relationship,

$$Q_{ult} = 1.08 * \left((22+0)/22\right)^{0.8421} * (tan\ 30) * 22^{1.3073 + 1.358/2} = 38.357\ kips/ft$$

$$Q_{ult} = 6ft * 38.357 = \mathbf{230.14\ kips} \text{ OR } \boldsymbol{Q_{ult} = 1023.7\ kN}$$

D.5 Soil properties (FDOT BDK75-977-41 Field Testing of Jet-Grouted Piles and Drilled Shafts)

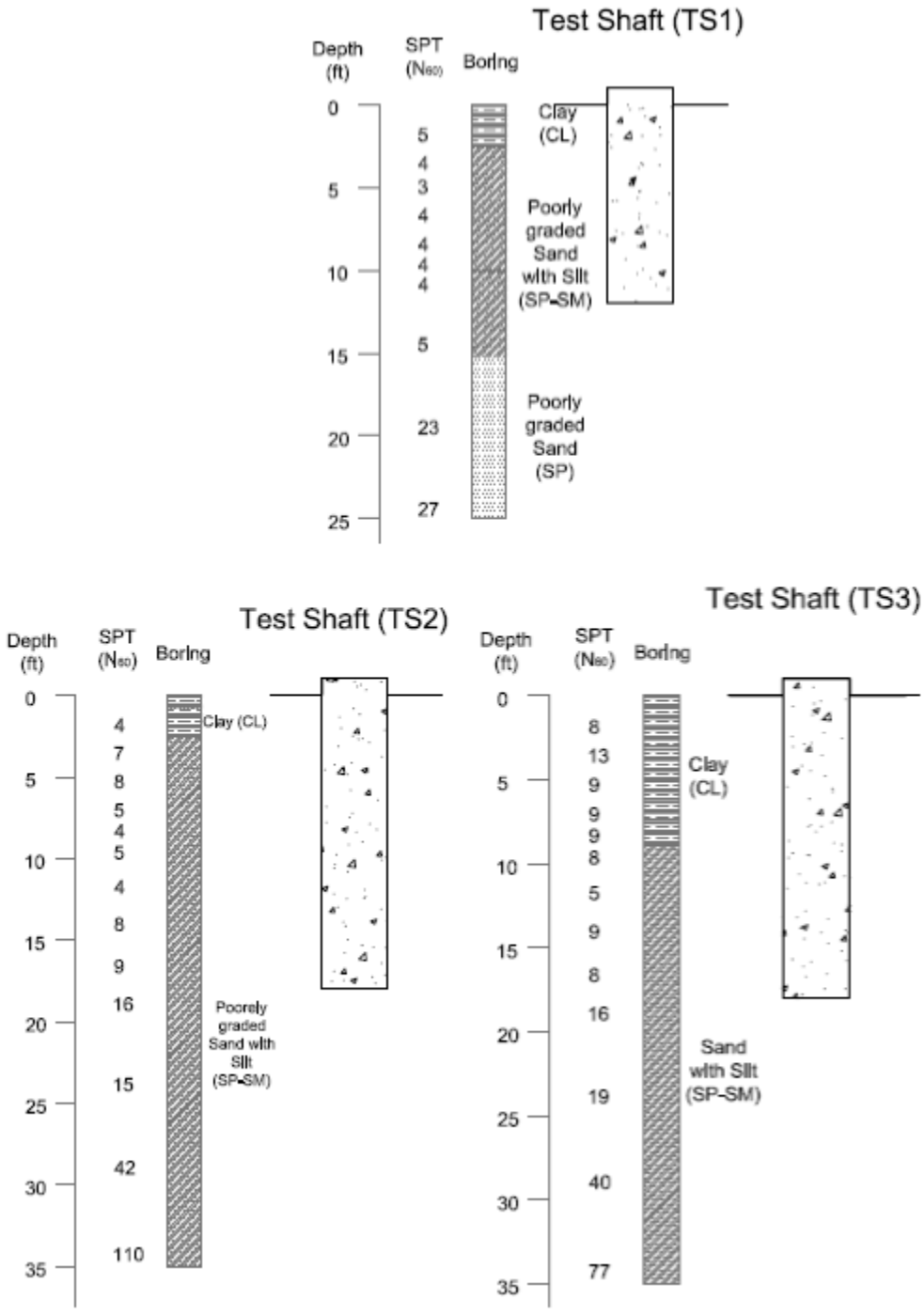

Figure D-3 Soil classification (USC) and N_{60} at the location test drilled shafts (McVay et al., 2014).

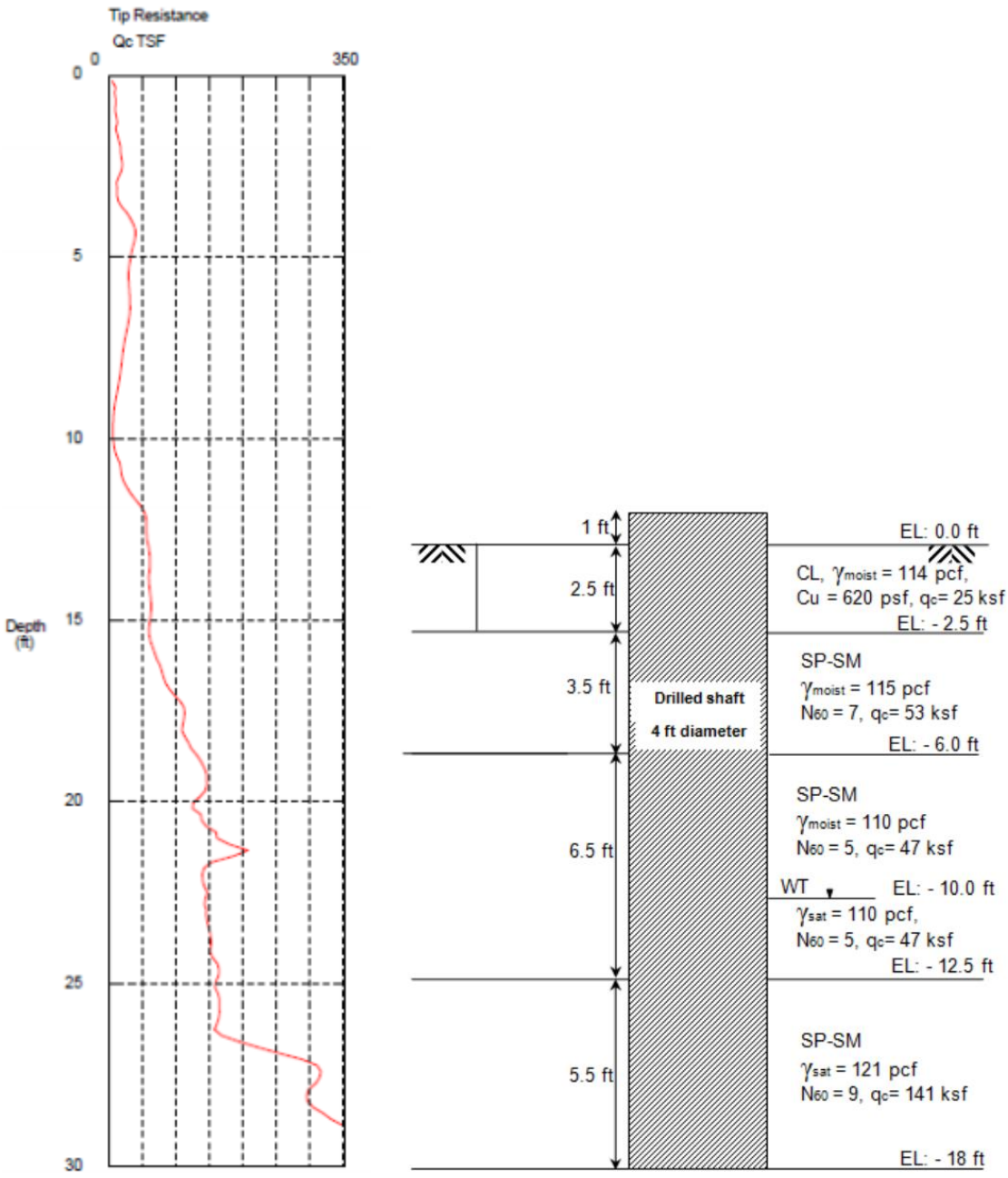

Figure D-4 CPT boring data near test pile TS2 (McVay et al., 2014).